ASTM INTERNATIONAL
Selected Technical Papers

Advances in Electrochemical Techniques for Corrosion Monitoring and Laboratory Corrosion Measurements

STP 1609

Editors:
Sankara Papavinasam | Raul B. Rebak
Lietai Yang | Neal S. Berke

SELECTED TECHNICAL PAPERS
STP1609

Editors: Sankara Papavinasam, Raul B. Rebak, Lietai Yang, and Neal S. Berke

Advances in Electrochemical Techniques for Corrosion Monitoring and Laboratory Corrosion Measurements

ASTM STOCK #STP1609
DOI: 10.1520/STP1609-EB

ASTM International, 100 Barr Harbor Drive, PO Box C700, West Conshohocken, PA 19428-2959
Printed in the U.S.A.

Library of Congress Cataloging-in-Publication Data

Names: Papavinasam, Sankara, 1962- editor. | Rebak, Raul B. (Raul Basilio), 1956- editor. | Yang, Lietai, 1958- editor. | Berke, Neal Steven, 1952- editor. | ASTM Committee G-1 on Corrosion of Metals, sponsoring body.

Title: Advances in electrochemical techniques for corrosion monitoring and laboratory corrosion measurements / edited by Sankara Papavinasam, Raul B. Rebak, Lietai Yang, Neal S. Berke.

Description: West Conshohocken, PA : ASTM International, [2019] | Series: ASTM stock #STP1609 | Includes bibliographical references.

Identifiers: LCCN 2018040917 (print) | LCCN 2018045260 (ebook) | ISBN 9780803176645 (ebook) | ISBN 9780803176638 (pbk.)

Subjects: LCSH: Corrosion and anti-corrosives--Measurement--Congresses. | Nondestructive testing--Congresses. | Electrochemical analysis--Congresses.

Classification: LCC TA462 (ebook) | LCC TA462 .A2377 2019 (print) | DDC 620.1/12230287--dc23

LC record available at https://lccn.loc.gov/2018040917

ISBN: 978-0-8031-7663-8

Peer Review Policy

Each paper published in this volume was evaluated by two peer reviewers and at least one editor. The authors addressed all of the reviewers' comments to the satisfaction of both the technical editor(s) and the ASTM International Committee on Publications.

The quality of the papers in this publication reflects not only the obvious efforts of the authors and the technical editor(s), but also the work of the peer reviewers. In keeping with long-standing publication practices, ASTM International maintains the anonymity of the peer reviewers. The ASTM International Committee on Publications acknowledges with appreciation their dedication and contribution of time and effort on behalf of ASTM International.

Citation of Papers

When citing papers from this publication, the appropriate citation includes the paper authors, "paper title," STP title, STP number, book editor(s), ASTM International, West Conshohocken, PA, year, page range, paper doi. A citation is provided on page one of each paper.

Printed in Atlanta, GA
March, 2019

Memorial

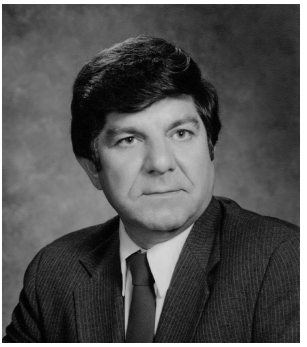

This book of selected technical papers is dedicated to the memory of our great friend, colleague, leader, and mentor, Dr. Robert (Bob) Baboian. His leadership and support of electrochemical methods in corrosion testing will long be remembered.

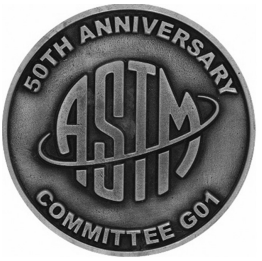

Front and back photos of the memento that Bob distributed at ASTM Committee G01's 50th Anniversary, November 2014.

Foreword

THIS COMPILATION OF Selected Technical Papers, STP1609, *Advances in Electrochemical Techniques for Corrosion Monitoring and Laboratory Corrosion Measurements*, contains peer-reviewed papers that were presented at a symposium held November 13–14, 2017, in Atlanta, Georgia, USA. The symposium was sponsored by ASTM International Committee G01 on Corrosion of Metals and Subcommittee G01.11 on Electrochemical Measurements in Corrosion Testing.

Symposium Chairs and STP Editors:

Sankara Papavinasam
CorrMagnet Consulting Inc.
Ottawa, Ontario, Canada

Raul B. Rebak
GE Global Research
Schenectady, NY, USA

Lietai Yang
Corr Instruments, LLC
Elk Grove, CA, USA

Neal S. Berke
Tourney Consulting Group, Ltd.
Kalamazoo, MI, USA

Contents

Overview

The global cost of corrosion is estimated at US $2.5 trillion, equivalent to approximately 3.4 % of global Gross Domestic Product (GDP). Studies have indicated that an appropriate application of current knowledge on corrosion control can reduce one third of the cost. ASTM Committee G01 on Corrosion of Metals plays an important role in developing knowledge on corrosion control.

ASTM Committee G01 on Corrosion of Metals was formed in 1964 to promote knowledge, stimulate research, collect engineering data, and develop standard test methods, practices, guides, classifications, specifications, and terminology relating to corrosion and methods for corrosion-protection of metals.

Most corrosion takes place by electrochemical mechanisms. Therefore, electrochemical techniques and tests play pivotal roles in understanding corrosion and in developing appropriate strategies to control corrosion. ASTM Subcommittee G01.11 on Electrochemical Measurements in Corrosion Testing was established in 1965 to address three issues that had been inhibiting the development of electrochemical tests:

- A lack of reproducibility of electrochemical tests and the lack of understanding of the variations in results,
- The absence of standardized procedures for carrying out the tests, and
- The use of several conventions to present electrochemical data that made interpreting the test results difficult.

To address these issues, G01.11 has been organizing symposia on the developments on electrochemical measurements and monitoring, publishing Selected Technical Papers (STPs), and developing standards on promising techniques. At present G01.11 has 19 standards under its jurisdiction and has published over 6 STPs.

The three most recently published STPs by ASTM G01.11 are:

- STP1506, *Advances in Electrochemical Techniques for Corrosion Monitoring and Measurement*, Ed. S. Papavinasam, N. S. Berke, and S. Brossia (2009)
- STP1277, *Electrochemical Noise Measurement for Corrosion Applications*, Ed. J. R. Kearns, J. R. Scully, P. R. Roberge, D. L. Reichert, and J. L. Dawson (1996)
- STP1188, *Electrochemical Impedance: Analysis and Interpretation*, Ed. J. R. Scully, D. C. Silverman, and M. W. Kendig (1993)

To further knowledge, ASTM G01.11 organized a two-day symposium in Atlanta, Georgia, USA, on November 13–14, 2017. The objectives of the symposia were to:

- Pay tribute to one of the eminent scientists, adherent users and promotor of electrochemical techniques, good friend to many, and enthusiastic mentor of young professionals, Dr. Robert Baboian;
- Provide a forum for discussing the recent advances in electrochemical techniques to monitor corrosion in the field and measure corrosion in the laboratory;
- Identify opportunities to develop new standards on specific techniques and methodologies;
- Promote use of electrochemical techniques in field application; and
- Publish an STP.

At the symposium, 30 presentations were made by experts from Argentina, China, Canada, India, Italy, and the USA. Twenty peer-reviewed papers from the symposium are collected in this STP. The papers are arranged in six sections:

- Dr. Robert Baboian Memorial Lecture
- Plenary Sessions
- Application of Electrochemical Techniques in the Field
- Advancement in Electrochemical Techniques in Measuring Corrosion in the Laboratory
- Investigation of Material and Electrolyte Properties Using Electrochemical Techniques
- Integration of Electrochemical Techniques with Other Techniques and Tools

It is hoped that the papers in this STP will provide the state-of-the-art electrochemical techniques for measuring and monitoring corrosion, both in the laboratory and in the field; increase the use of standards on electrochemical techniques in academic institutes in educating next-generation professionals; and lead to the development of new ASTM standards.

Symposium Chairs and STP Editors:

Sankara Papavinasam
CorrMagnet Consulting Inc.
Ottawa, Ontario, Canada

Raul B. Rebak
GE Global Research
Schenectady, NY, USA

Lietai Yang
Corr Instruments, LLC
Elk Grove, CA, USA

Neal S. Berke
Tourney Consulting Group, Ltd.
Kalamazoo, MI, USA

STP 1609, 2019 / available online at www.astm.org / doi: 10.1520/STP160920170202

Harvey P. Hack[1]

Development and Use of ASTM Standard G5

Citation

Hack, H. P., "Development and Use of ASTM Standard G5," *Advances in Electrochemical Techniques for Corrosion Monitoring and Laboratory Corrosion Measurements*, *ASTM STP1609*, S. Papavinasam, R. B. Rebak, L. Yang, and N. S. Berke, Eds., ASTM International, West Conshohocken, PA, 2019, pp. 1–10, http://dx.doi.org/10.1520/STP160920170202[2]

ABSTRACT

The author first discusses the life of Dr. Robert Baboian, a leader within the corrosion and electrochemical field; a contributor to ASTM G5, *Standard Reference Test Method for Making Potentiodynamic Anodic Polarization Measurements*; a leader within ASTM International, NACE International (formerly the National Association of Corrosion Engineers), the International Organization for Standards, and the Electrochemical Society; a world-renowned corrosion researcher and promoter; the recipient of many awards in his field; and a good friend to many in the corrosion field throughout the world. The author then discusses the importance and history of the development of ASTM G5, a seminal work of ASTM Committee G01 on Corrosion of Metals. Finally, the apparatus, test procedure, and acceptance criteria for this standard are summarized.

Keywords

corrosion, electrochemistry, polarization, Baboian

Robert Baboian

Robert Baboian (**Fig. 1**) was born on November 17, 1934, in Watertown, MA. He graduated from Watertown High School in 1952 and then served in the U.S. Army,

Manuscript received October 16, 2017; accepted for publication February 2, 2018.

[1]Northrop Grumman Corporation, 895 Oceanic Dr., Annapolis, MD 21409, USA http://orcid.org/0000 0001 9887 2285

[2]ASTM Symposium on *Advances in Electrochemical Techniques for Corrosion Monitoring and Laboratory Corrosion Measurements* on November 13 14, 2017 in Atlanta, GA, USA.

FIG. 1 Robert Baboian, 1934–2015.

stationed in Germany from 1953 to 1955. He received a B.S. in chemistry from Suffolk University in 1959 and a Ph.D. in physical chemistry from Rensselaer Polytechnic Institute in 1964 on electrochemistry of titanium, zirconium, and hafnium in molten salts. He then did postdoctoral research as a Ford Foundation Fellow at the University of Toronto from 1964 to 1966 where he developed a high temperature solution calorimeter for molten salts and liquid metals. He was married to Roberta J. (Sanderson) Baboian, whom he met during the summer of 1958 and married on June 20, 1959.

Bob was employed at Texas Instruments (TI) in Attleboro, MA, for 30 years prior to his retirement in 1996. His initial work at TI led to fused salt processes for the electrodeposition of titanium, removal of plastics from metals, recovery of scrap metals, and production of gall resistant coatings. After establishing the Corrosion Laboratory in 1968, he initiated work on design and evaluation of corrosion resistant materials and devices for corrosion control. He developed fundamental principles for galvanic corrosion, established electrochemical techniques for investigation of corrosion reactions and developed devices for corrosion control, and established test methods and design criteria for clad metal systems.

He gained international recognition for this work and assisted in establishing a major business opportunity at TI based on corrosion resistant materials and devi ces. He pioneered the use of electrochemical techniques for galvanic corrosion. His use of polarization, zero resistance ammeter, and potential techniques in the study of galvanic effects has been published widely. At the time of his retirement, Bob was a principal fellow of the company, the highest honor that the company gives for technological achievement. During his career, he became an internation ally recognized expert in the field of corrosion, lecturing throughout the world on galvanic corrosion; he received 15 U.S. patents, edited 13 books, and authored more than 180 technical articles. He was listed in *Who's Who in the East* and in *American Men and Women of Science*.

Bob provided key contributions in the application of a wide range of clad met als for corrosion control. These include stainless steel clad aluminum for trim and bumpers, clad transition materials for joining dissimilar metals, clad materials for batteries, steel clad copper concentric neutral wire, copper clad stainless steel cable shielding, various clad metals for heat exchangers, a wide range of clad coinage materials, and platinum clad niobium for anodes. Platinum clad niobium strip and wire has gained worldwide use for cathodic protection anodes. This is due to the key contributions Bob made in testing and design of these clad materials for this application. His publications on mechanisms of degradation and platinum con sumption rates have been widely cited and are responsible for the introduction and wide use of these anodes for cathodic protection in North America. He made major contributions to the development of clad metals for U.S. coinage, developing the environmental tests for coinage materials used by the U.S. Mint and performing these tests in the development of new clad coinage materials for the U.S. penny and dollar coins.

Bob was deeply involved in technical volunteer organizations, including ASTM International, NACE International (formerly the National Association of Corrosion Engineers), the American Chemical Society, SAE International, ASM International, the International Organization for Standards (ISO), the Electrochemical Society, and the Sea Horse Institute. He served on the board of directors of ASTM Interna tional for three years, was treasurer, and was chairman of the board in 1987. He was the chairman of Committee G01 on Corrosion of Metals for four years, and he was the chairman of the Committee G01 Awards Committee, the Sam Tour Award Committee, and the Francis L. LaQue Memorial Award Committee. He also served as chairman of ASTM Committee G01.95, the United States Technical Advisory Group to ISO Technical Committee 156 on Corrosion of Metals, and provided sig nificant leadership to that activity during the critical formation period. He chaired several symposia for ASTM and edited several special technical publications (STPs), including the Silver Anniversary Symposium for ASTM Committee G01, which resulted in the publication, *Corrosion Testing and Evaluation: Silver Anniversary Volume*, ASTM STP1000 [1]. He organized and edited both the first and second editions of ASTM Manual 20, *Corrosion Tests and Standards: Application and*

Interpretation [2]. He received many awards from ASTM, including the Committee G01 Certificate of Appreciation, the ASTM Award of Merit, and the Francis L. LaQue Memorial Award.

Bob earned the Vittorio de Nora Award for contributions to the field of electro chemical engineering and technology from the Electrochemical Society. He also served on the executive committee and the board of directors of NACE Internation al. He served on the NACE Committee on Preservation of Historic Artifacts and the publications committee. He also served on seven specific technology groups and five technical exchange groups. He received numerous awards for technology and his service from NACE and other organizations, including the NACE Frank New man Speller Award for excellence in corrosion engineering and the T. J. Hull Award for excellence in publications. He was a fellow of ASTM, NACE, and SAE, and a NACE Certified Corrosion Specialist. He was an adjunct professor at the University of Rhode Island and a lecturer at Johns Hopkins University and the University of Virginia. He was a National Park Service volunteer and served as a corrosion consultant on the restoration of the Statue of Liberty during the 1980s. Bob was a coeditor of the NACE book *The Statue of Liberty Restoration* [3] and a frequent speaker on the subject. He was elected to chair the Gordon Research Conference on Corrosion, a very prestigious position in the scientific community. Bob organized and led many symposia for NACE, and he was tireless in promoting the dissemina tion of knowledge about corrosion testing and prevention. He was particularly interested in electrochemical techniques, and this interest resulted in two major symposia and compilations of papers on this subject. Moreover, his interests extended broadly to almost every aspect of corrosion technology, and this was reflected in his editing of the second and third editions of the *NACE Corrosion Engineer's Reference Book* [4]. At the time of his death, he was working on revising the NACE corrosion course book, *Basic Corrosion* [5]. However, his greatest contri butions probably were his leadership, enthusiasm, and encouragement for many of us to join with him in friendship and in the ongoing battle to fight the ravages of corrosion damage. Bob's leadership extended beyond technical meetings to after hours events; he was a frequent organizer of groups for meals and entertainment. His friends were legion, as are the memories of amusing and happy events with Bob leading the charge.

Bob died at home on November 3, 2015. He lived his life through his children, grandchildren, and great grandchildren. He was an avid fisherman, having fished throughout the United States but mainly on Cape Cod, MA, Marco Island, FL, and Slacks Pond in Greenville, RI. He is survived by a son, Robert C. (and his wife Rachel), and two daughters, Laura Thibodeau (and her fiancé Frank Gillespie) and Rosann Maneca (and her husband Tony Maneca). He was predeceased by daughter Susan (Baboian) Frost and a sister, Mary (Baboian) Balyosian. He also leaves six grandchildren (Jamie Nezat, Nicholas Baboian, Thomas Thibodeau, and Justin, Andrew, and Ava Maneca), two great grandchildren (Olivia Nezat and Cora Baboian), and three brothers (Jacob, Charles, and Richard).

History of ASTM G5, *Standard Reference Test Method for Making Potentiodynamic Anodic Polarization Measurements*

When ASTM Committee G01 on Corrosion of Metals was first established in 1964, the first standard that they wrote was ASTM G1, *Standard Practice for Preparing, Cleaning, and Evaluating Corrosion Test Specimens* [6], a logical beginning for the fledgling committee. Their second standard, ASTM G2, *Standard Test Method for Corrosion Testing of Products of Zirconium, Hafnium, and Their Alloys in Water at 680°F (360°C) or in Steam at 750°F (400°C)* [7], was rushed through at the behest of the nuclear industry. Because electrochemical corrosion testing was becoming popular at that time, Committee G01 then wrote ASTM G3, *Standard Practice for Conventions Applicable to Electrochemical Measurements in Corrosion Testing* [8]. This was followed by ASTM G4, *Standard Guide for Conducting Corrosion Tests in Field Applications* [9].

At the time, many corrosion experimenters were new to the field of electro chemical corrosion testing, and they were getting inconsistent results. Sometimes these results were due to improper selection or operation of equipment; sometimes they were due to improper control of solution chemistry; and sometimes they were due to improper setup or gas leakage in the test glassware. This would generate anomalous results, particularly in deaerated tests of stainless steel alloys. In addition, crevice effects were generating test anomalies. At about that time, Princeton Applied Research (PAR, now EG&G/Princeton Applied Research), a potentiostat manufactur er, developed a specimen mounting technique using a conical shaped polytetra fluoroethylene (Teflon®) gasket that would minimize the probability of initiation of crevice corrosion at the specimen mounting and electrical connection point.

Committee G01 took it upon itself to help researchers figure out if they had all aspects of their test set up correctly by writing ASTM G5, *Standard Reference Test Method for Making Potentiostatic and Potentiodynamic Anodic Polarization Meas urements* [10]. This standard used the new PAR gasket mounting system to avoid crevice effects and picked a test system that was particularly sensitive to solution chemistry. In addition, they chose a deaerated environment and picked a stainless steel alloy that was particularly sensitive to exposure to oxygen. The system chosen was anodic polarization of Type 430 stainless steel in 30°C deaerated 1N sulfuric acid scanned at a ramped potential scan rate of 0.6 V/h (or 50 mV every 5 min in steps). Since this test is also very sensitive to metal chemistry, a supply of reference material was obtained to ensure that anyone performing this test would be using material from the same heat and lot. When all testing parameters were properly controlled, this system would generate an anodic polarization curve with two pas sive areas, the location and magnitude of which could be used to determine if ade quate deaeration was achieved. This curve was also sensitive to potential scan rate and had narrow enough peaks to be used to check reference electrode potentials as well. ASTM G5 also describes the details of the potentiostat, glassware, counter

electrodes, reference electrodes, salt bridge, specimen cleaning, and pre exposure conditions.

It turned out that this choice of materials and test system was so sensitive to proper setup that if the experimenter could adequately reproduce the curves in the standard, then it was ensured that they could do almost any other type of electro chemical test that they wanted, being confident in their potentiostat, reference elec trode, glassware setup, deaeration setup, and experimental technique. Production of ASTM G5 was so important to Committee G01 that the work of developing it was placed well ahead of work that most new committees perform that of standardiza tion of terminology. Therefore, it was not until much later that Committee G01 got around to writing their corrosion terminology standard, ASTM G15, *Standard Ter minology Relating to Corrosion and Corrosion Testing* (withdrawn 2010) [11].

Over the years, ASTM G5 has changed. Initially, the experimenter could scan the set potential either manually in 50 mV steps or by using an automated poten tial ramp. However, in recent years, computerized potentiostats have become ubiquitous and make the more accurate ramp technique easier to use than poten tial stepping. So, the step procedure was deemphasized in the standard. Statistical probability bands were placed around the standard curves. Descriptions were added to explain what deviations from the standard reference plots could mean, particularly if the observed deviations were due to instrumental or oxygen effects. Other glassware besides that from PAR was allowed, as were a variety of deaera tion gasses.

In the early 1990s, the supply of standard reference material, originally obtained in 1987, ran out and a new supply was obtained in 1992. It was soon deter mined through round robin testing that testing the new material gave a different set of curves from the original material. Over the next few years, there was contro versy regarding what would cause this effect, but it was eventually resolved that whatever the cause a new set of reference curves would need to be generated, along with the associated statistics. After many delays, this was accomplished, and the present ASTM G5 contains reference curves for both sets of reference alloys.

The last change in ASTM G5 occurred fairly recently. When determining whether this standard has been passed by a given laboratory, some issues arose con cerning evaluation of results. With curve bands being the only data given, and since test data must fall within these bands in order to have an acceptable test, there were labs having tests rejected because one point fell outside of the band, even when this was one point out of thousands. Recently, a table has been added to ASTM G5 with a list of four potentials and the range of permitted currents at those potentials. This concentrates the acceptance criteria on those areas of the curves that are the most critical in terms of determining if lab technique is adequate, while reducing the number of data points that must fall within a specified range to a manageable num ber. New precision and bias information has also been incorporated.

ASTM G5 has been so popular that certification agencies have used it to certify corrosion testing laboratories. This has given the standard an economic importance

not realized when it was first written. It is the mainstay for corrosion electrochemists to this day. The scan rate of 0.6 mV/h, originally chosen somewhat randomly just for this test, has become almost a standard for potentiodynamic testing of many other corrosion systems.

Apparatus for ASTM G5

The original apparatus for ASTM G5, an electrochemical cell from PAR, is still shown in the standard (**Fig. 2**), although other apparatuses are permitted. Other manufacturers now make suitable apparatuses for performing this test. The test cell uses a Luggin probe salt bridge arrangement, thus ensuring that the laboratory doing the testing can use this type of equipment correctly.

Detailed requirements for the potentiostat are stated, including the preset potential accuracy, the potential range, the current output range, the input impedance and accuracy of the electrometer, and the accuracy of the current measurement circuitry. A wiring diagram is also included to ensure that the experimenter connects the potentiostat to the test cell correctly.

The original PAR electrode holder using a conical polytetrafluoroethylene washer to seal against the specimen end is still shown in the standard (**Fig. 3**). The specimen

FIG. 2 Apparatus, ASTM G5.

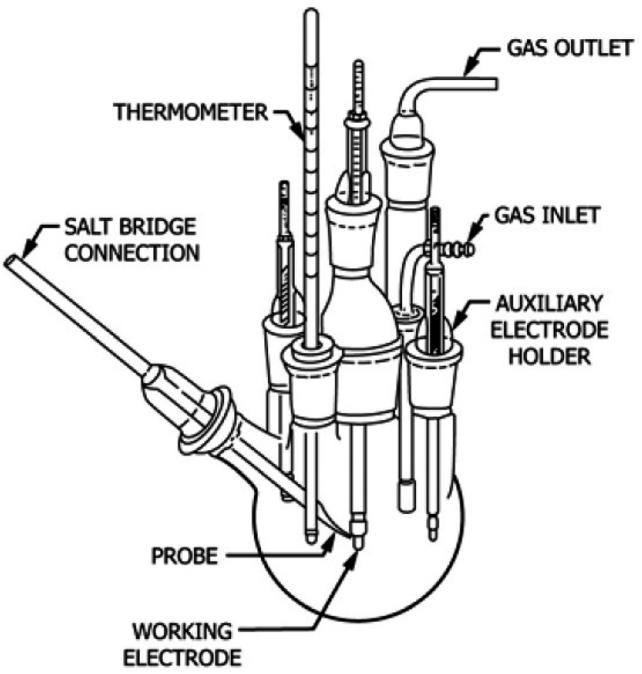

FIG. 3 Specimen mounting, ASTM G5.

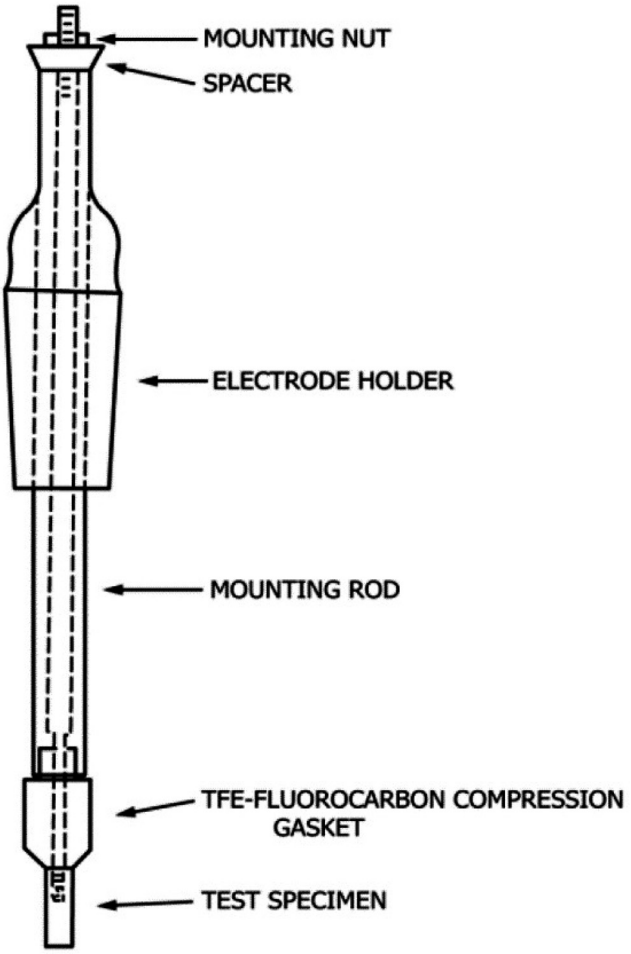

is a cylinder 9.5 mm in diameter and 12.7 mm long with a threaded hole in one end into which a mounting rod is screwed. The specimen itself is made from AISI Type 430 stainless steel (UNS S43000) that has been mill annealed and air cooled.

Two platinum rods or platinum sheets are specified for the auxiliary electrodes, with instructions given on how to increase the effective surface area by platinizing. Graphite is also permitted for these electrodes. The reference electrode type specified is a saturated calomel electrode, although some experimenters use other types of reference electrodes such as silver/silver chloride and correct the measured potentials for the difference using information such as that contained in ASTM G3.

TABLE 1 Compliance limits from ASTM G5.

Potential, Volts (versus SCE)	Min	Max
0.450	5.16	13.86
0.100	2.61	15.60
0.000	25.75	13.48
+0.400	0.883	1.669

ASTM G5 Test Procedure

The detailed procedure in ASTM G5 requires preparing a 1.0 N solution of sulfuric acid using reagent grade acid and distilled water. Test temperature is 30 ± 1°C. Suggested deaeration gasses and bubbling rates are presented. The standard also details the method for surface preparation, including wet sanding and degreasing, and tightening mounting in the electrode holder.

Once immersed, the open circuit potential of the specimen is recorded for 55 min, after which the potential is scanned from the corrosion potential through +1.60 V versus saturated calomel electrode at a sweep rate of 0.6 V/h. The method of plotting the data is also given.

ASTM G5 Acceptance Criteria

Although full reference curves, including scatter bands, are given for this test, compliance limits are only needed for the four potentials given in the standard (Table 1).

All test measurements must fall within these current limits (in uA/cm^2 at the given potentials) for the test results to be in compliance with ASTM G5.

The last part of the standard consists of two nonmandatory appendices. The first of these is designed to help experimenters whose test data are not in compliance. It shows an example curve for a test where crevice corrosion effects are in evidence. If test results deviate from the reference plots in this manner, then the experimenter can assume that they mounted the specimen incorrectly. An example curve is also given showing deviations from the reference plots due to instrumental effects, allowing the experimenter to determine that their electronic equipment must be checked. The last curve shows the effect of inadequate solution deaeration. If the test data resemble this curve, then air leaks and the quality and flow rate of the deaeration gas should be checked.

The last appendix is a set of recommended data fields for those wishing to computerize the data from the test.

Conclusions

ASTM G5 is one of the oldest standards from ASTM Committee G01 on Corrosion of Metals. It has been continuously updated to remain current and has gained wide

acceptance among electrochemists as a method for ensuring that electrochemical equipment and procedures are correct. It has been used as a compliance check for certifying laboratories performing electrochemical measurements. As such, it is one of the most important corrosion tests produced by ASTM International.

ACKNOWLEDGMENTS

The author wishes to acknowledge the contributions of Sheldon Dean in gathering information on the life of Robert Baboian, but more importantly, he wishes to acknowledge the contributions of Dr. Baboian, who contributed greatly to the devel opment and updating of ASTM G5 and to many other ASTM corrosion standards. Besides being a leader within the corrosion and electrochemical field; a leader within ASTM International, NACE International, the International Organization for Stand ards, and the Electrochemical Society; a world renowned corrosion researcher and promoter; and the recipient of many awards in his field, he was also a good friend to many in the corrosion field throughout the world. He will be missed.

References

[1] Baboian, R. and Dean, S. W., Eds., *Corrosion Testing and Evaluation: Silver Anniversary Volume, ASTM STP1000*, ASTM International, West Conshohocken, PA, 1990, http://dx.doi.org/10.1520/STP1000-EB

[2] Baboian, R., Ed., *Corrosion Tests and Standards: Application and Interpretation*, ASTM MNL20, ASTM International, West Conshohocken, PA, 2005, http://dx.doi.org/10.1520/MNL20-2ND-EB

[3] Baboian, R., Ed., *The Statue of Liberty Restoration*, NACE, Houston, TX, 1990.

[4] Baboian, R., Ed., *NACE Corrosion Engineer's Reference Book*, NACE, Houston, TX, 2016.

[5] *NACE Basic Corrosion Course*, NACE, Houston, TX, 1982.

[6] ASTM G1-02 (2017)e1, *Standard Practice for Preparing, Cleaning, and Evaluating Corrosion Test Specimens*, ASTM International, West Conshohocken PA, 2017, www.astm.org

[7] ASTM G2/G2M-06 (2011)e1, *Standard Test Method for Corrosion Testing of Products of Zirconium, Hafnium, and Their Alloys in Water at 680°F (360°C) or in Steam at 750°F (400°C)*, ASTM International, West Conshohocken, PA, 2011, www.astm.org

[8] ASTM G3-14, *Standard Practice for Conventions Applicable to Electrochemical Measurements in Corrosion Testing*, ASTM International, West Conshohocken PA, 2014, www.astm.org

[9] ASTM G4-01 (2014), *Standard Guide for Conducting Corrosion Tests in Field Applications*, ASTM International, West Conshohocken PA, 2014, www.astm.org

[10] ASTM G5-14e1, *Standard Reference Test Method for Making Potentiodynamic Anodic Polarization Measurements*, ASTM International, West Conshohocken PA, 2014, www.astm.org

[11] ASTM G15-08, *Standard Terminology Relating to Corrosion and Corrosion Testing* (withdrawn 2010), ASTM International, West Conshohocken, PA, 2008, www.astm.org

STP 1609, 2019 / available online at www.astm.org / doi: 10.1520/STP160920170195

Sheldon W. Dean, Jr.[1]

Recent Developments in Standards for Electrochemical Corrosion Testing

Citation

Dean, Jr., S. W., "Recent Developments in Standards for Electrochemical Corrosion Testing," *Advances in Electrochemical Techniques for Corrosion Monitoring and Laboratory Corrosion Measurements*, *ASTM STP1609*, S. Papavinasam, R. B. Rebak, L. Yang, and N. S. Berke, Eds., ASTM International, West Conshohocken, PA, 2019, pp. 11–31, http://dx.doi.org/10.1520/STP160920170195[2]

ABSTRACT

Electrochemical methods are now widely used in corrosion testing and evaluation. About one-third of all research articles recently published on corrosion science and technology have some electrochemical components in the studies reported. New methods continue to be developed and standardized. The purpose of this paper is to highlight the newer standards and discuss changes made to existing standards developed by ASTM Subcommittee G01.11 on Electrochemical Methods. Among the newer methods discussed are ASTM G192, *Standard Test Method for Determining the Crevice Repassivation Potential of Corrosion-Resistant Alloys Using a Potentiodynamic-Galvanostatic-Potentiostatic Technique*, and ASTM G217, *Standard Guide for Corrosion Monitoring in Laboratories and Plants with Coupled Multielectrode Array Sensor Method*. Older standards that have been updated are also discussed, including ASTM G5, *Standard Reference Method for Making Potentiodynamic Anodic Polarization Measurements*, and ASTM G69, *Standard Test Method for Measurement of Corrosion Potentials of Aluminum Alloys*. Some outstanding issues with existing standards and suggestions for new standards are provided in the discussion.

Manuscript received October 11, 2017; accepted for publication January 25, 2018.

[1]Dean Corrosion Technology, Inc., 306 Marshall Lndg., Glen Mills, PA 19346, USA http://orcid.org/0000 0003 0611 7384

[2]ASTM Symposium on *Advances in Electrochemical Techniques for Corrosion Monitoring and Laboratory Corrosion Measurements* on November 13 14, 2017 in Atlanta, GA, USA.

Keywords
repassivation potential, anodic polarization, corrosion potential, electrode potential, coupled multielectrode array sensor, corrosion monitoring, nonuniform corrosion, repeatability, reproducibility, protection potential

Introduction

In 1964, the Board of Directors of ASTM International created Committee G01 to develop standards for the growing field of corrosion technology [1]. Previously, the "A" committees had subcommittees that handled corrosion testing standards related to the ferrous metals, and Committee B 3 handled nonferrous alloy corro sion standards. These groups were incorporated into the new Committee G01 [2].

Electrochemical corrosion standards were assigned to Subcommittee G01.11, and this subcommittee has been a significant contributor to the overall efforts of Committee G01 since its creation. A previous paper summarized ten of the twenty one standards currently assigned to Subcommittee G01.11 as a keynote lecture dur ing the 2007 symposium entitled "Advances in Electrochemical Techniques for Corrosion Monitoring and Measurement" [2].

The purpose of this paper is to review some of the standards developed after the 2007 symposium and to discuss some of the changes that have been made to the standards covered in the earlier paper. However, ASTM G215, *Standard Guide for Electrode Potential Measurement*, is not included in this paper because it is cov ered in a separate paper [3].

This review discusses the theories that form the basis of the new standards together with an explanation of the procedures that are to be used in carrying out the methods. In the discussion that follows, the accuracy and reliability of some of the methods will be covered. Thereafter, some suggestions for improving these standards and developing new standards will be presented.

Table 1 shows a listing of all of the standards Subcommittee G01.11 has devel oped. The type of standard is also shown and whether the document applies to cor rosion monitoring.

Test methods produce a result usually in the form of a quantity or decision, such as whether the product is acceptable or not. Reference test methods are used to pro vide results that can be compared to accepted values so that the investigator can be confident that the procedure used produces results that agree with other laboratories. The results of these methods are now also being used by certification organizations to certify that a laboratory is competent to carry out the procedure.

A standard practice is a set of instructions to carry out a procedure that does not produce a result but represents a consensus as to the correct way to carry out the procedure. In some cases, several different procedures are covered if they are all useful in certain circumstances.

A standard guide covers a general area to provide information that may be use ful for carrying out a procedure but without a mandatory component.

TABLE 1 ASTM standards assigned to ASTM Subcommittee G01.11 as of 2017.

No.	ASTM Designation	Type	Subject	T	M
1	G3	SP	Convention		
2	G5	RTM	Polarization Scan	X	
3	G59	RTM	Polarization Resistance	X	X
4	G61	RTM	Cyclic Polarization	X	
5	G69	TM	Al Corrosion Potential	X	
6	G71	G	Galvanic Corrosion	X	X
7	G82	G	Galvanic Series	X	
8	G96	G	Polarization and Electric Resistance		X
9	G100	TM	Cyclic Galvanostat Polarization Al	X	
10	G102	G	Calculation Procedures		
11	G106	SP	Electrochem. Impedance	X	
12	G108	TM	EPR	X	
13	G142	SP	H Uptake and Permeation	X	
14	G150	TM	Critical Pitting Temperature	X	
15	G189	G	Corrosion under Insulation	X	
16	G192	TM	Crevice Repassivation Potential	X	
17	G199	G	Electrochem. Noise	X	X
18	G215	G	Electrode Potential	X	X
19	G217	G	CMAS		X

Note: T document used for testing; M document used for monitoring; RTM reference test method; TM test method; SP standard practice; G guide; Al aluminum; EPR electrochemical reactivation; H hydrogen; CMAS coupled multielectrode array sensor.

ASTM G5, *Standard Reference Method for Making Potentiodynamic Anodic Polarization Measurements*

The ASTM G5 standard [4] was one of the first standards developed by Committee G01. It was developed as a reference test method because investigators were beginning to use potentiostatic and potentiodynamic scans in corrosion testing, and they needed a technique to demonstrate that they were able to carry out the procedure and obtain results that were reproducible and in agreement with the results that other investigators obtained. The original procedure used a stepwise potentiostatic procedure employing 50 mV steps every 5 min from the corrosion potential to 1.600 V versus a saturated calomel electrode (SCE). When potentiostats became available with automatic scanning ability, the method was revised to use this capability thereby reducing the need for continuous operator attention during the scan.

The ASTM G5 standard was very successful because a large number of investigators were attempting to use potentiodynamic scans as part of their work. The standard not only provided an envelope of acceptable performance, it also showed

how problems with the method affected the results. However, the results created an issue as to how to develop a quantitative evaluation of precision for the method. The original potentiostatic approach had more than 420 potentials where a current measurement was made. The potentiodynamic system converted the stepwise scan to a continuous scan, so there were no longer discrete points for evaluation. The use of an envelope to contain the range of acceptable behavior was a practical approach for most investigators, but it raised questions as to how evaluate minor points where a scan might diverge from the envelope. This issue became critical when organizations that were engaged in certifying the performance of laboratories began to use the ASTM G5 standard in their evaluation.

As a result, a statistical evaluation was carried out using a computer to deter mine the standard deviation for many current density points along the scan. The results of these calculations are plotted in **Fig. 1** showing the ± 3 reproducibility standard deviation ranges from the logarithmic average. This plot shows some wig gles in the envelope that were not present in the original envelope curves. The issue of how to judge the acceptability of a laboratory's performance remained. To resolve this issue, it was decided to determine the standard deviation of the loga rithm of the current densities at four critical points in the scan. The points were

FIG. 1 Standard potentiodynamic polarization envelope at ± 3 standard deviations based on logarithms of the data points and showing the reproducibility ranges at the five selected potentials, from ASTM G5 14 [4].

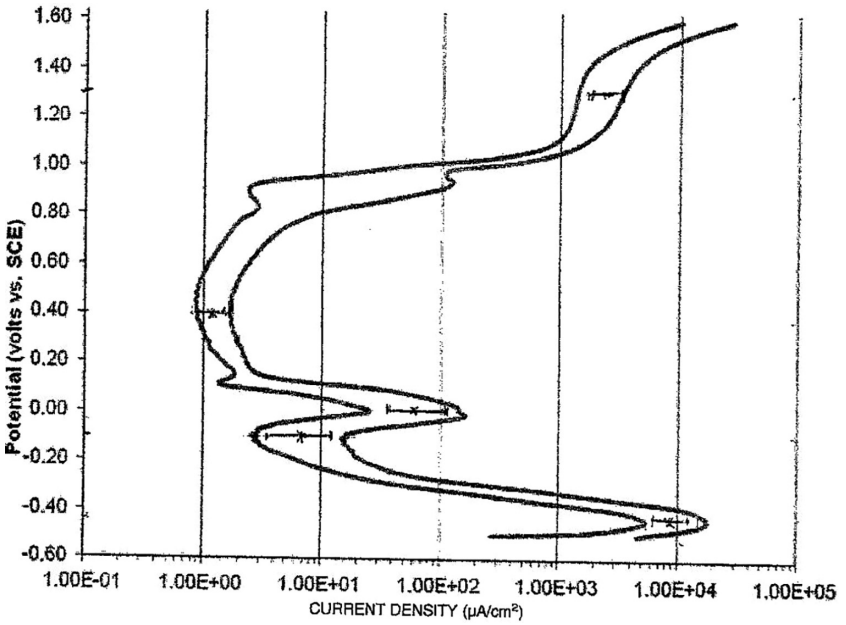

chosen where the slope of the curve was close to vertical so minor errors in the elec trode potential measurements would have little influence on the resulting current density. The four points were:

- The primary passivation potential: −0.450V versus SCE
- The first passivation potential minimum: −0.100 V versus SCE
- The secondary passivation potential: 0.000 V versus SC.
- The secondary passivation minimum: 0.400 V versus SCE

The compliance limits were determined at these four potentials as the average of the logarithms of the current densities with a range of ± 3 standard deviations.

In addition, the precision statistics were calculated using the same four points but with an additional point at 1.300 V versus SCE as the transpassive limit. Fig. 1 also shows the reproducibility limits. The reproducibility is based on 2.8 times the reproducibility standard deviation at the five potentials chosen.

The decision to use three standard deviations for the compliance limits was a compromise based on the concept that the probability of rejecting an acceptable result should be less than 0.01. In fact, having four points to make that judgment reduces the probability further, but because of the likelihood that a common factor could affect all four points in the same direction, it is not possible to determine a probability with certainty.

ASTM G69, *Standard Reference Method for Making Potentiodynamic Anodic Polarization Measurements*

This test method uses corrosion potential as an indicator of the solid solution content of certain alloying elements in aluminum alloys. Copper and zinc, in par ticular, affect the corrosion potentials of aluminum alloys when they are in solid solution in the alloy. However, if they precipitate to form intermetallic com pounds, their effect on the corrosion potential diminishes [5]. The ASTM G69 method takes advantage of this behavior to reveal the solid solution content of these elements [6]. The test method is a rapid and inexpensive way to verify whether certain high strength aluminum alloys, in particular the 2XXX and 7XXX alloys, have been properly heat treated.

The method employs a 1.0 M sodium chloride (NaCl) solution containing 3 g/L of hydrogen peroxide. The specimen is immersed in this solution for either 30 min or 60 min, and the corrosion potential is measured during the final 10 min using an SCE reference electrode.

Although the method was developed more than 50 years ago, the precision was not formally determined at that time. Later, an issue was raised about the effect of the surface preparation of the specimens. The original method used a No. 00 steel wool mechanical abrasion to prepare the surface. However, later work showed that particles of the steel wool were incorporated into the aluminum alloy surface during

this treatment. Several other preparation treatments were suggested as alternatives, so an interlaboratory program was initiated to determine how the surface preparation affected the results.

The following treatments were evaluated:

- No. 00 steel wool abrasion
- No. 320 silicon carbide abrasive cloth abrasion
- No. 320 aluminum oxide abrasive cloth abrasion
- 1 min immersion in 93°C solution containing 5 mL/L of 48 % hydrofluoric acid and 50 mL/L of reagent grade nitric acid
- 1 min immersion in 10 % sodium hydroxide (NaOH) solution at 71°C
- 30 sec immersion in 12 N hydrochloric acid (HCl) at room temperature (22°C)
- 1 min immersion in 5 N HCl at room temperature (22°C)
- 5 min immersion in 1 N sulfuric acid (H_2SO_4) at 60°C

Unfortunately, the results of this program were not evaluated at the conclusion of the study. This analysis was completed recently, and the precision statement was added to the method.

The interlaboratory test results showed that the chemical treatment steps were equivalent to the mechanical treatments in terms of the potentials and the standard deviations, except for the AA5052 H32 (UNS A95052) specimens [7]. This alloy showed repeatability and reproducibility standard deviations about 20 % higher than the other alloys when the chemical treatments were used. The reason for this effect was not determined.

ASTM G148, *Standard Practice for Evaluation of Hydrogen Uptake, Permeation, and Transport in Metals by an Electrochemical Technique*

This standard practice was developed as an electrochemical technique to quantitatively measure the uptake, permeation, and transport of hydrogen in metals [8]. This technique had been developed by Devanathan and Stachurski and published in 1962 [9]. The technique has been used by several investigators since then, so there was a desire to have a standardized approach for carrying out the measurements and evaluating the results.

The approach used in this practice is to employ a thin membrane of the alloy in question and electrodeposit hydrogen on one surface of the membrane. Hydrogen that is transported through the membrane is oxidized electrochemically as it exits the membrane. Because both the electrodeposition and oxidation are electrochemical reactions, their rates can be expressed as electrical currents. The transient behavior can be used to determine the diffusivity and retention of hydrogen in the metal.

Microstructural features such as grain boundaries, stacking faults, inclusions, and precipitates can affect the transport and retention of hydrogen in metals.

This technique can be used to determine the extent to which these features affect the hydrogen transport kinetics. This can be a significant finding when evaluating hydrogen embrittlement, blister formation, and other hydrogen related issues.

A typical apparatus is shown in Fig. 2. Although this type of apparatus has gen erally been constructed for operation at ambient pressure and ambient temperature, modifications could be made to allow for operation at elevated temperature or pres sure, or both. The test apparatus consists of a galvanostatic cell to deposit hydrogen on one side of the membrane and a potentiostatic cell to carry out the oxidation on the opposite side.

Typical results for a test are shown in Fig. 3. This figure shows the normalized transient current flowing to oxidize the hydrogen on the exit side of the cell as a function of exposure time plotted on a logarithmic scale. The plot of the expected behavior based on Fick's law calculations for lattice diffusion is also shown in this figure. The experimental results are shown for membranes of the same alloy with

FIG. 2 Hydrogen permeation cell with double junction reference electrodes used for electrochemical charging, from ASTM G148 97 [8].

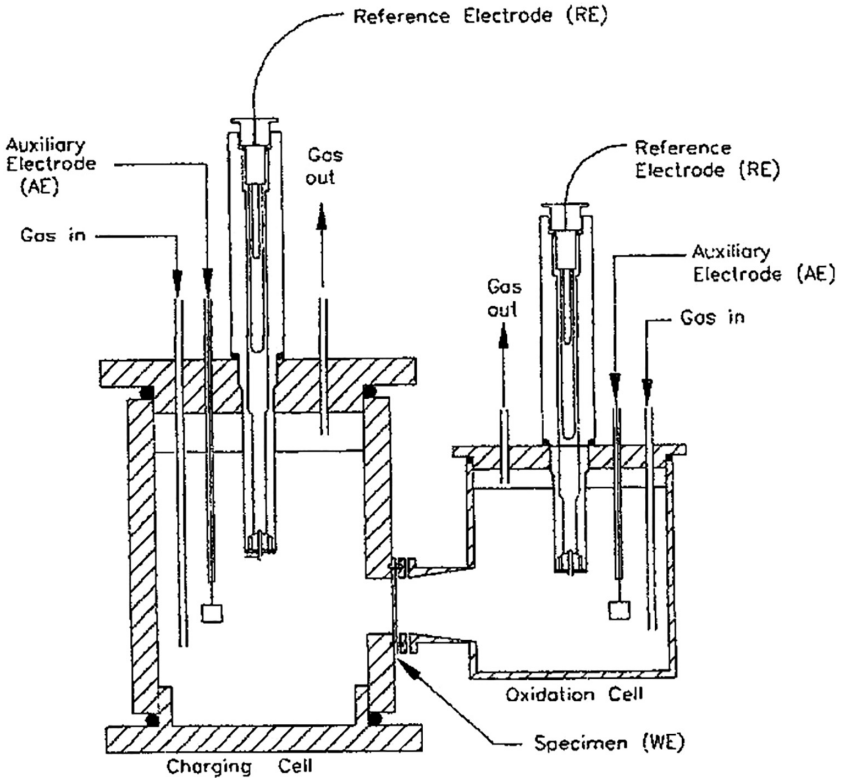

FIG. 3 Permeation transients for BS 970 410S21 stainless steel in acidified NaCl at 77°C, from ASTM G148 97 [8].

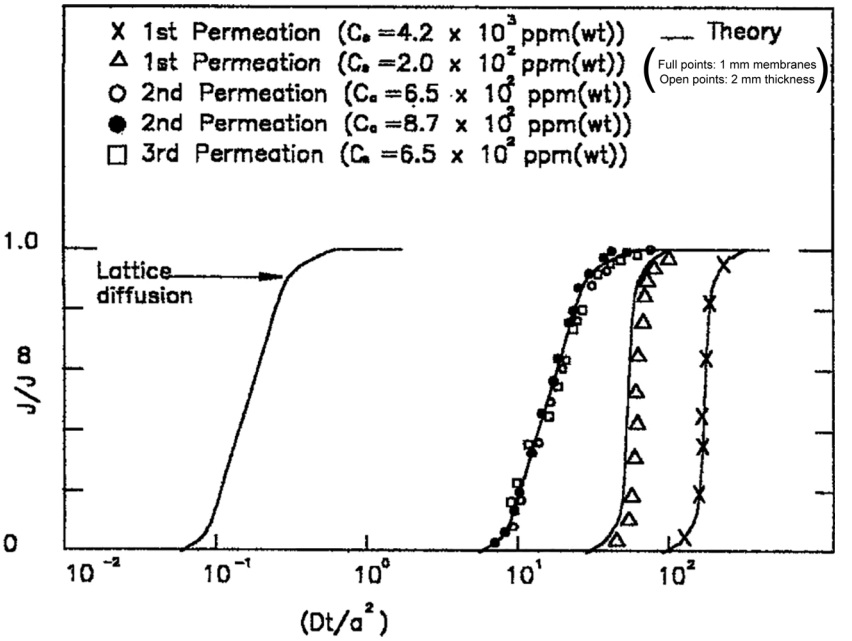

1 mm and 2 mm thicknesses and three sequential runs. The membranes were allowed to have the hydrogen diffuse out of the membrane between runs. The delayed exit and steep rise of the rate of permeation indicate the presence of traps in the metal that retain the hydrogen in the matrix rather than allowing it to freely diffuse. Revers ible traps release the hydrogen between runs, but irreversible traps retain it.

More recent studies have been directed at finding the effect of tensile stress on the trapping phenomenon [10]. This work showed that elastic strain increased the permeation rate slightly, but plastic strain increased it greatly during the time when the deformation was occurring.

This technique uses electrochemical measurements to detect the hydrogen flux. This phenomenon is not necessarily related to corrosion issues, but hydrogen entry and permeation often occur during corrosion, so the information obtained from this type of procedure is certainly of interest in many situations.

ASTM G189, *Standard Guide for Laboratory Simulation of Corrosion under Insulation*

Corrosion under thermal insulation is an important failure mechanism that has occurred in chemical manufacturing facilities and similar facilities, such as

power plants. In these cases, the rate of attack is often greater than what would be expected based on static immersion testing. Although the reasons for this acceleration have not been clearly determined, the problem has been widely observed. In order to study the mechanism of corrosion and to establish whether protective measures will be effective, the ASTM G189 standard guide was developed [11].

In this case, the corrosion rate of the metal is determined by either mass loss or a potentiodynamic scan to obtain a polarization resistance value, or both. The test specimens are produced by cutting 0.187 in. (4.75 mm) wide rings from a 2 in. pipe (Fig. 4). These rings are electrically isolated from each other by nonconductive gaskets. In this design, a total of six specimen rings are used with seven isolating spacers. A heater is used to maintain the heat transfer fluid within the pipe at the proper temperature level. A reservoir and a micrometering pump (0.5 to 5 ml/min) are also required to supply the test solution to the assembly at the desired rate. Fig. 5 shows the assembly.

The test is carried out after assembling the apparatus and checking it to be sure it is leak tight. The heater is turned on to bring the unit up to temperature.

FIG. 4 Ring specimens and nonconductive spacer, from ASTM G189 07 [11].

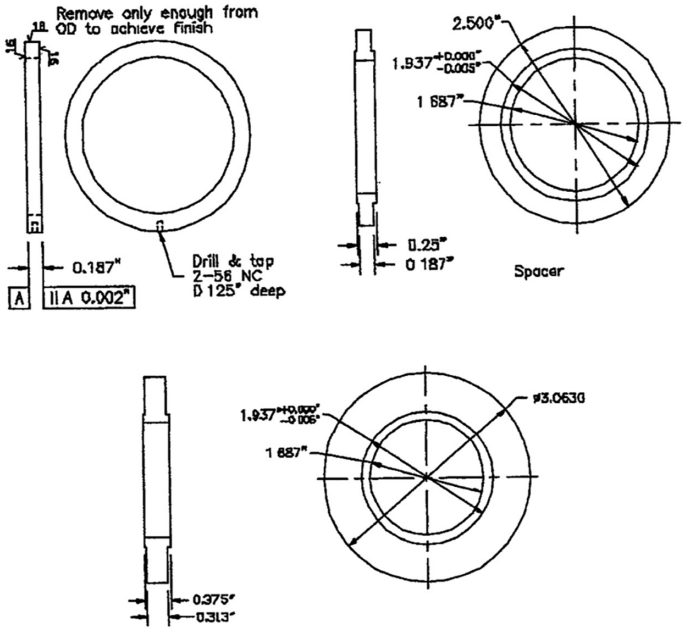

Top Left—Configuration of the ring specimen.
Top Right—Nonconductive spacer.
Bottom—Nonconductive large spacer (dam) located between the two sides of the CUI-Cell.

FIG. 5 Schematic diagram of CUI apparatus, from ASTM G189 07 [11].

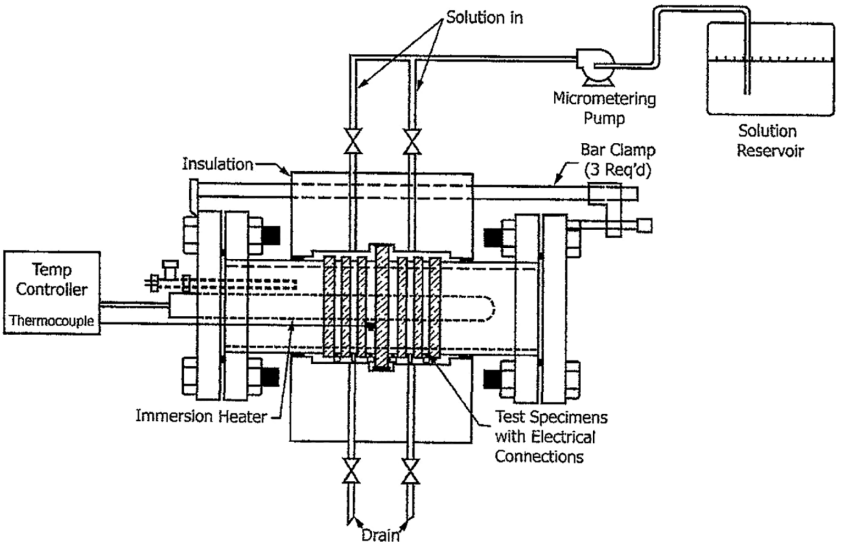

The operating temperature is specified by the organization sponsoring the test. A solution is prepared to be placed into the reservoir before the test is run. The recommended solution is prepared from purified water with 100 ppm NaCl and the pH adjusted to 6.0 with a 1 M sulfuric acid (H_2SO_4) solution. The test solution is pumped into the annulus between the insulation and the specimens at a rate sufficient to keep the annulus filled with solution. The bottom drain valve should be opened enough to allow several drops per minute of solution to exit the appa ratus. The test is typically carried out for 72 or 96 h, but longer durations can be used if desired.

In cases where mass loss measurements are desired, the specimen rings are cleaned to remove corrosion products and weighed to obtain a mass loss. When polarization resistance measurements are used, the potentiodynamic scan technique described in ASTM G59, *Standard Test Method for Conducting Potentiodynamic Polarization Resistance Measurements*, is recommended [12]. Measurements should be made every 30 min during the initial 4 h and during the drying interval if a wet dry cycle is used. In cases where more accurate corrosion rates are desired, the Tafel slopes of the polarization curves can also be obtained by scanning over a larger potential range, such as ± 200 mV from the corrosion potential. ASTM G102, *Standard Practice for Calculation of Corrosion Rates and Related Information from Electrochemical Measurements*, has procedures for estimating Tafel slopes if an approximate rate is adequate [13]. However, mass loss measurements may be a better choice when greater accuracy is required.

ASTM G192, *Standard Test Method for Determining the Crevice Repassivation Potential of Corrosion-Resistant Alloys Using a Potentiodynamic-Galvanostatic-Potentiostatic Technique*

Crevice corrosion is a long standing concern in the use of corrosion resistant alloys in difficult environments such as seawater. Conventional stainless steels such as Types 304 and 316 (UNS S30400 and S31600) are particularly susceptible to this form of attack. A variety of other alloys have been developed that have better resistance to this type of attack, but it has been particularly difficult to find a suitable procedure for ranking the resistance of these alloys. Approaches based on the composition have been used, but a quantitative method based on performance has been desired. ASTM G61, *Standard Test Method for Conducting Cyclic Potentiodynamic Polarization Measurements for Localized Corrosion Susceptibility of Iron , Nickel , or Cobalt Based Alloys* [14], was developed for this purpose, but it does not provide a definitive end point for evaluating alloys.

ASTM G192 [15] was developed to determine the repassivation potential of alloys such as stainless steels. This parameter was observed to be a key indicator of the resistance of the alloys to crevice corrosion. The concept is that the passive film breaks down in crevices because of the development of acidity in crevices. This mechanism is driven by the electrode potential of the alloy, with the system becoming more aggressive as the potential increases. Once crevice corrosion begins, the acidity stabilizes, and the corrosion continues. If the potential decreases thereafter, the corrosion will not cease until a critical potential is reached. This potential has been termed the "repassivation potential." A similar value can be obtained with the ASTM G61 method, although in this case it is designated as the "protection potential." The ASTM G192 procedure has a reproducibility standard deviation of 10.6 mV, while the ASTM G61 procedure showed a reproducibility standard deviation of about 23 mV.

This method was developed by Tsujikawa and Hisamatsu [16,17], and although it is more time consuming than the ASTM G61 method, its greater precision has made it a desirable choice for evaluating the crevice corrosion resistance of alloys in difficult environments.

The concept used in this method is to place a specimen with a standard multiple crevice former device in the test environment. **Fig. 6** shows a typical prismatic specimen. The multiple crevice washer system described in ASTM G78, *Standard Guide for Crevice Corrosion Testing of Iron Base and Nickel Base Stainless Alloys in Seawater and Other Chloride Containing Aqueous Environments*, may be used [18]. The recommended solution is a 1 M NaCl solution at 90°C purged with 99.99 % nitrogen gas. The specimen is equilibrated for 1 h and then a potentiodynamic scan is initiated at a rate of +0.167 mV/s from a potential 100 mV below its corrosion

FIG. 6 Prismatic test electrode for crevice corrosion test, from ASTM G192 08 [15].

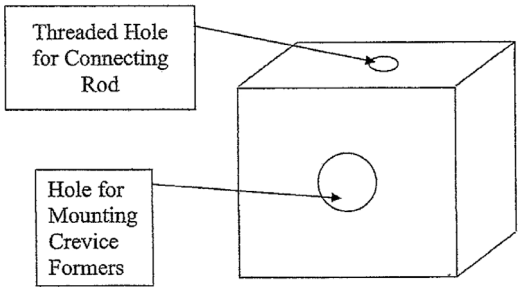

potential. The scan is terminated when the current density reaches 2 μA/cm^2. At that point, the current is held constant for 2 h to allow the crevice corrosion to become established. Then, the potential is decreased by 10 mV and held for 2 h. If the current increases during this period, the potential is decreased another 10 mV and held for another 2 h. This procedure is continued until the current density does not increase during the 2 h hold period. The potential at this point is the crevice repassivation potential for the specimen. **Fig. 7** shows a typical potential and current plot versus exposure time for this method. Note that the specimen used in this example has an area of 3 cm^2.

ASTM G199, *Standard Guide for Electrochemical Noise Measurement*

Many investigators have noticed when carrying out electrochemical measurements that spontaneous fluctuations occur, even when no observable changes have occurred. These fluctuations have been attributed to a variety of sources, including initiation and propagation of localized corrosion processes, gas bubble formation and release, and breakdown of passivity [19]. These fluctuations have been designated as electro chemical noise and their monitoring has been proposed as a technique for monitor ing both general corrosion and localized corrosion processes, especially pitting.

The ASTM G199 standard guide [20] covers three approaches for monitoring electrochemical noise. Method A is based on the use of a zero resistance ammeter (ZRA) and uses two identical electrodes connected to the terminals of this instru ment. A third electrode is used as a reference electrode to monitor the electrode potential of the test electrodes. This reference electrode can be either an electrode identical to the other two or a standard reference electrode. However, a standard ref erence electrode such as the SCE is a better choice in many cases because it tends to be stable and noise free. **Fig. 8** shows a schematic diagram of the setup used in this case. The current flowing between the two test electrodes is measured and recorded as a function of exposure time, along with the electrode potential of the couple.

FIG. 7 Example of the current and electrode potential versus exposure time plot, from ASTM 192 08 [15].

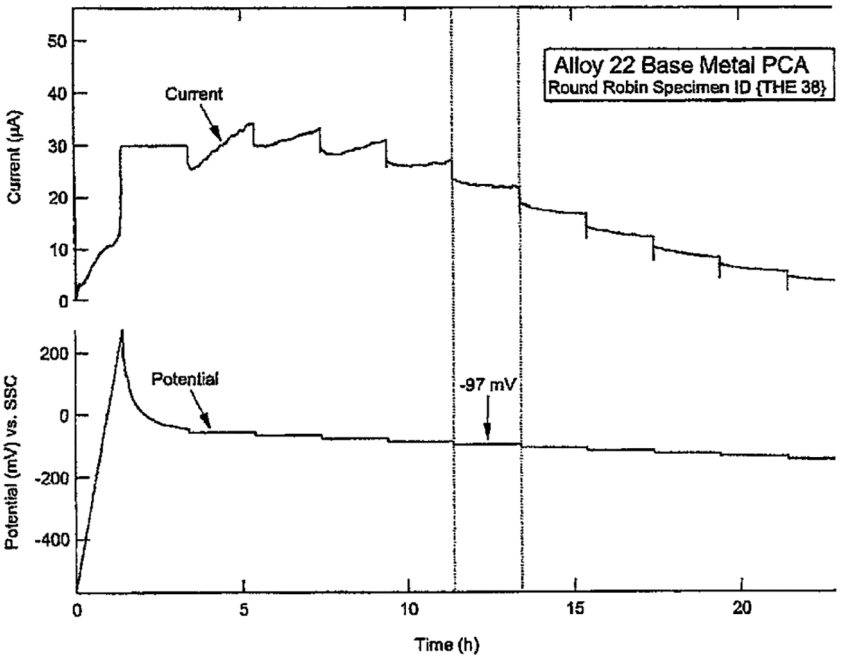

FIG. 8 ZRA based electrochemical noise setup, from ASTM G199 09 [20].

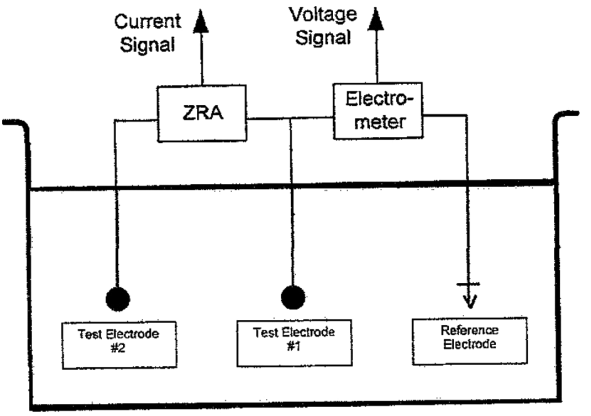

Method B uses a potentiostat to maintain the specimen electrode at a constant electrode potential while measuring and recording the current required to achieve this potential as a function of the exposure time. The reference electrode used

to control the electrode potential may be either a standard reference electrode or an electrode identical to the test electrode. The auxiliary electrode may be either a third identical electrode or a nonconsumable platinum electrode. This electrode is used to supply the current needed to maintain the specimen at a constant potential. The current fluctuations are usually converted to current density values by dividing by the exposed specimen area, and they are used in the subsequent calculations.

Method C uses a galvanostat to maintain a constant current flow between two specimen electrodes while a third electrode is used to monitor the electrode potential of the specimen electrodes. This approach is useful in cases where it is desired to observe the noise generated by electrochemical activity, such as cathodic protection, or other activities where the surface in question may be polarized. As in the other methods, the reference electrode may be either a standard reference elec trode or an electrode identical to the test electrode. The fluctuations of electrode potential during the exposure provide the data used for the analysis of the noise.

The results of these types of studies can be used to estimate the general corro sion rate of the metals tested by obtaining standard deviations of the potential spikes and current spikes during the exposure. The ratio of potential standard devi ation to current density standard deviation is termed the "electrochemical noise resistance," R_n. It is thought to be equivalent to the polarization resistance, R_p, and can be used to calculate the corrosion rate by means of the Stern Geary relationship [13]. This calculation requires information on the Tafel slopes of the anodic and cathodic reaction kinetics in cases where these reactions are limited by the charge transfer processes.

Pitting information has also been derived from electrochemical noise measure ments. The values of the pitting factor, pitting index, and pitting indicator are described in ASTM G199. Several other types of localized corrosion information have been derived from electrochemical noise measurements, although they have not been researched as extensively.

ASTM G217, *Standard Guide for Corrosion Monitoring in Laboratories and Plants with Coupled Multielectrode Array Sensor Method*

In many situations, the corrosion of metals shows substantial variation over the exposed area. This nonuniform corrosion can occur for a variety of reasons, includ ing the formation of deposits on the metal surface. When this occurs, traditional monitoring techniques such as polarization resistance and electrical resistance monitoring as described in ASTM G96, *Standard Guide for Online Monitoring of Corrosion in Plant Equipment* (*Electrical and Electrochemical Methods*) [21], may not adequately reveal the rate of penetration that is occurring. The multielectrode electrode array technique described in ASTM G217 provides an electrochemical technique that can reveal such nonuniform corrosion [22].

The coupled multielectrode array sensor (CMAS) consists of a large number of electrodes mounted together but insulated from each other so that the net electrical current flowing through each electrode can be monitored. Typically, between 8 and 25 electrodes are used in each sensor, but larger numbers could be used if desired. In cases where uniform corrosion is occurring, there will be no current flowing between the electrodes, but if nonuniform corrosion is occurring, some electrodes will have a net cathodic current while others will have a net anodic current. These currents must balance out so that no current leaves or enters the coupled array. However, it is possible to measure the currents flowing from and to each electrode by means of a zero voltage ammeter (ZVA).

The ZVA is a device that measures the current by means of a shunt resistor that produces less than 1 mV potential drop across the shunt. A ZRA may also be used, but the ZVA concept is simpler and better suited for cases where many electrodes are being measured. In either case, a multichannel recorder is required to monitor the current flowing from each electrode.

The anodic current can be converted to a corrosion rate by means of Faraday's law [13]. However, it must be noted that the currents measured in this apparatus are not the actual total corrosion currents; they are only the nonuniform corrosion currents.

Fig. 9 shows a schematic diagram of the CMAS system. The electrodes are usually wires that are precoated with an insulating material before being embedded in an epoxy or similar polymeric material. The surface of the sensor is polished so that the ends of the wires are exposed to the test environment thereby becoming the electrode surfaces. The other ends of the wires are connected to the multichannel voltmeter or similar multiplexing device. Each electrode is then connected to a

FIG. 9 Wiring diagram for CMAS probes to multichannel ZVA formed with (a) multiple ZRAs and (b) multiple shunt resistors, from ASTM G217 16 [22].

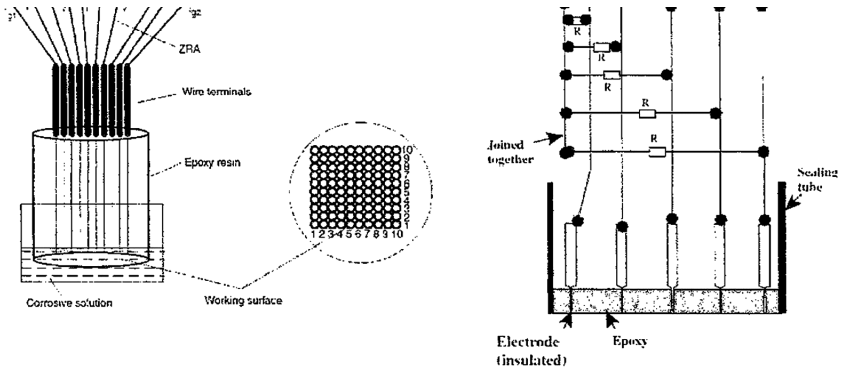

shunt resistor, which is connected to a common terminal, so that the potential drop across each shunt can be monitored.

The CMAS technique can be used to monitor inhibited systems where deposits can form. It may also be used to monitor cathodic protection systems. In this case, it is necessary to connect the common terminal of the sensor to the protected metal and to place the probe close to the protected metal. In cases where the protection system is operating properly, the current flowing will be the same for all of the electrodes.

As a practical matter, the variation in current flows among the electrodes may vary by a factor of five or more. The variation in actual corrosion rates is generally smaller, but values up to a factor of two have been reported.

Discussion

REVISIONS TO EXISTING STANDARDS

In reviewing the standards that Subcommittee G01.11 has developed during the past decade, it is clear that the subcommittee has been active in a number of different areas. The changes made to ASTM G5 and ASTM G69 represent a growing recognition that standards provide not only a set of steps for carrying out a test procedure but also a reference point for evaluating the performance of an operator and the organization that supports the operator. The addition of compliance limits for ASTM G5 is an example of how this concept can be executed. In this case, the decision to have four reference points on the polarization scan was significant. The selection of these points was an important feature of the approach. Choosing regions of the scan where the current density was insensitive to electrode potential was a valuable approach for minimizing the effect of minor reference electrode variations.

The decision to use three standard deviations to calculate the compliance limits was an interesting departure from the generally accepted approach for ASTM precision determinations where 2.8 times the standard deviation is the recommended procedure. It could be argued that this approach represents a willingness to accept minor errors in the procedure if they do not affect the result significantly. The original argument for the decision was to reduce the probability of rejecting an acceptable result to a level of 0.01. However, in this case, because four points are used the actual probability is most likely less.

The other decision made in this case was to use the logarithm of the current density rather than the actual value in calculating averages and standard deviations. This decision makes the acceptable range on a logarithmic plot appear centered around the average values rather than offset toward the high end limit. The implication in this case is that the percentage error is the same for values greater than the average as well as those less than the average.

In the case of ASTM G69, the initial motivation for the interlaboratory test program was to determine if the various alternative pretreatment steps were equivalent. The study showed that there was no difference in results for all of the pretreatments

except in the case of the 5052 H32 specimens. In the case of this alloy, all of the chemical pretreatments showed significantly greater repeatability and reproducibili ty standard deviations than the mechanical pretreatments. Unfortunately, the rea son for this effect was not discovered. However, the results demonstrated that the presence of steel wool fragments in the mechanically prepared surfaces did not affect the results in any significant way. The level of precision for this method was also remarkable. The repeatability standard deviation of 3.0 mV and reproducibility standard deviation of 7.0 mV indicates that the commercially obtained SCE (calo mel) electrodes are very reliable for this type of testing.

RECENT STANDARDS

In the past decade, six new standards have been developed by Subcommittee G01.11. These standards include four guides and two test methods. Three of these documents cover approaches for corrosion monitoring. Guides are most often used in cases where the environment is not specified and where the technique may be applied in a variety of circumstances. As a result, it is usually not possible to specify all of the procedural steps that would be necessary for a standard practice. Guides usually provide important information on how to obtain useful results and avoid errors. They are used for monitoring situations where the desired result is not nec essarily a decision point but rather an indication that further investigation is proba bly in order.

Test methods are used to provide a result. Test methods must have a precision statement that shows the range of acceptable results if the method is carried out according to the procedure. Repeatability statistics are intended to provide an approach for judging whether an operator is performing the method properly. Reproducibility statistics are intended to provide information for judging a labora tory system, including the operator, equipment, and data management system as it applies to the test method. When test methods are used to make decisions on the suitability of materials or other items for the intended service, it is vital to have limits of acceptability for the results.

The two test methods developed in the past decade, ASTM G150, *Standard Test Method for Electrochemical Critical Pitting Temperature Testing of Stainless Steels and Related Alloys* [23], and ASTM G192 are both for the purpose of deter mining the relative performance of corrosion resistant alloys for pitting and crevice corrosion resistance in difficult environments. These methods were developed to provide an electrochemical approach for evaluating these alloys with the purpose of replacing older methods. The ASTM G150 test method was intended to use a 700 mV electrode potential versus SCE as the driving force to cause pitting of these alloys to determine the critical pitting temperature. Previously, ASTM G48, *Standard Test Methods for Pitting and Crevice Corrosion Resistance of Stainless Steels and Related Alloys by Use of Ferric Chloride Solution*, Method C, for nickel based alloys, and Method E, for stainless steels, used a ferric chloride solution to determine the critical pitting temperature [24].

ASTM G192 was developed to provide a method with better reproducibility than ASTM G61 for determining crevice corrosion resistance. ASTM G61 was intended to provide an estimate of the protection potential for crevice corrosion, but the ASTM G192 method determined the repassivation potential. Both of these potentials are reasonable measures of the crevice corrosion resistance, but the repassivation potential appears to be a better defined value and therefore should be better at discriminating among alloys with similar performances.

AREAS FOR FUTURE WORK

In reviewing the work of the G01.11 Subcommittee against the list of eight forms of corrosion that Fontana and Greene enumerated [25], one area that seems to be missing is dealloying. Although this form of corrosion does not occur with many of the corrosion resistant alloys in use today, it is still an issue with some copper and nickel based alloys. Copper alloys with good resistance to this form of corrosion are available, but unfortunately they are not used in many applications where corrosion failures occur. A reliable test method might encourage engineers responsible for specifying materials for applications where this form of corrosion can occur to require their choices to pass the test.

Although ASTM G61 was developed in 1986 and reapproved in 2014, it is deficient because it does not have a report section, and there is no method for calculating a protection potential from the data obtained. Report sections are essential in test methods because they provide the minimum requirements for a laboratory supplying a report to a client on the results obtained.

The term "repassivation potential" is used in ASTM G192 as a measure of an alloy's resistance to crevice corrosion. However, this term is not defined in this standard, nor is it defined in ASTM NACE/ASTM G193, *Standard Terminology and Acronyms Related to Corrosion* [26]. It would be helpful to have a definition of this term clarifying how it is related to protection potentials measured in ASTM G61 and ASTM G100, *Standard Test Method for Conducting Cyclic Galvanostaircase Polarization* [27]. ASTM Committee J01 should be encouraged to handle this task.

There are now several standards that have been developed for similar purposes. For example, the ASTM G96 standard covers corrosion monitoring for general corrosion using the polarization resistance method. ASTM G59, ASTM G106, and ASTM G199 can also be used for determining polarization resistance. It could be very useful to have a standard that explained the advantages and disadvantages for each of these approaches to assist investigators who are entering the field in selecting the method that meets their needs. This concept might also be helpful for investigators dealing with pitting or crevice corrosion and for those who would like to use electrochemical techniques for obtaining the information they need related to these problems.

Finally, there have been some concerns that have developed when comparing the results of electrochemical measurements with other techniques such as mass

loss or thickness loss measurements. It would be desirable to have some studies carried out to compare these approaches and determine if there are any biases in these techniques. For example, a review paper by Frankel [28] showed corrosion rates for carbon steel measured by polarization resistance and other electrochemical techniques in sulfuric acid solutions that were significantly lower than those obtained by mass loss measurements. It would be helpful if the reasons for this lack of agreement were determined.

Conclusions

1. ASTM Subcommittee G01.11 has provided six new electrochemical standards related to corrosion testing and monitoring during the last decade. These standards have been important contributions to the field for many industries.
2. New standards have been developed for evaluating pitting and crevice corrosion. These documents provide greater precision than previous methods.
3. Corrosion monitoring continues to be an important application where electrochemical measurements are necessary and valuable.
4. Improvements in electrochemical techniques continue to be an important direction for future work. Precision studies using interlaboratory test programs are important in establishing reliable methods with clearly defined limits. The use of reference test methods for determining whether a laboratory can meet standardized compliance requirements is a new development.
5. ASTM G61 should be revised to include a technique for determining the protection potential of the alloy and also to include a report section.
6. New standards that provide guidelines for selecting methods for monitoring and testing would be helpful for investigators entering the field.
7. Studies that compare the various methods for determining corrosion rates and related parameters could be very useful in determining if there are any biases in these methods.

References

[1] ASTM International, "Foreword," *Corrosion Testing and Evaluation, Silver Anniversary Volume, ASTM STP1000*, R. Baboian and S. W. Dean, Eds., ASTM International, West Conshohocken, PA, 1990, http://dx.doi.org/10.1520/STP1000-EB

[2] Dean, S. W., "Development of Electrochemical Standards for Corrosion Testing," *J. ASTM Intl.,* Vol. 4, No. 9, http://dx.doi.org/10.1520/JAI101198

[3] ASTM G215-17, *Standard Guide for Electrode Potential Measurement*, ASTM International, West Conshohocken, PA, 2017, www.astm.org

[4] ASTM G5-14e1, *Standard Reference Test Method for Making Potentiodynamic Anodic Polarization Measurements*, ASTM International, West Conshohocken, PA, 2014, www.astm.org

[5] Brown, R. H., Fink, W. L., and Hunter, M. S., "Measurement of Irreversible Potentials as a Metallurgical Research Tool," *T. Am. I. Min. Met. Eng.,* Vol. 143, 1941, pp. 115–123.

[6] ASTM G69-12, *Standard Test Method for Measurement of Corrosion Potentials of Aluminum Alloys*, ASTM International, West Conshohocken, PA, 2012, www.astm.org

[7] ASTM Research Report RR G01-1024, "Interlaboratory Study to Establish Precision Statement for ASTM G69, *Standard Test Method for Measurement of Corrosion Potentials of Aluminum Alloys*, ASTM International, West Conshohocken, PA, 2012.

[8] ASTM G148-97, *Standard Practice for Evaluation of Hydrogen Uptake, Permeation, and Transport in Metals by an Electrochemical Technique*, ASTM International, West Conshohocken, PA, 2018, www.astm.org

[9] Devanathan, M. A. V. and Stachurski, Z., "The Adsorption and Diffusion of Electrolytic Hydrogen in Palladium," *P. Roy. Soc. Lond. A Mat.,* Vol. 270, No. 1340, 1962, pp. 90–102.

[10] Zheng, C. and Wang, C., "Effect of Stress on Hydrogen Permeation for X70 Carbon Steel in Seawater," *Mater. Performance,* Vol. 56, No. 8, 2017, pp. 54–58.

[11] ASTM G189-07, *Standard Guide for Laboratory Simulation of Corrosion under Insulation*, ASTM International, West Conshohocken, PA, 2013, www.astm.org

[12] ASTM G59-97, *Standard Test Method for Conducting Potentiodynamic Polarization Resistance Measurements*, ASTM International, West Conshohocken, PA, 2014, www.astm.org

[13] ASTM G102-89, *Standard Practice for Calculation of Corrosion Rates and Related Information from Electrochemical Measurements*, ASTM International, West Conshohocken, PA, 2015, www.astm.org

[14] ASTM G61-86, *Standard Test Method for Conducting Cyclic Potentiodynamic Polarization Measurements for Localized Corrosion Susceptibility of Iron-, Nickel-, or Cobalt-Based Alloys*, ASTM International, West Conshohocken, PA, 2018, www.astm.org

[15] ASTM G192-94, *Standard Test Method for Determining the Crevice Repassivation Potential of Corrosion-Resistant Alloys Using a Potentiodynamic-Galvanostatic-Potentiostatic Technique*, ASTM International, West Conshohocken, PA, 2014, www.astm.org

[16] Tsujikawa, S. and Hisamatsu, Y., "On the Repassivation Potential for Crevice Corrosion," *Corros. Eng.,* Vol. 29, No. 1, 1980, pp. 37–40.

[17] Akashi, M., Nakayama, G., and Fukuda, T., "Initiation Criteria for Crevice Corrosion of Titanium Alloys Used for HLW Disposal Overpack," Paper 98158, *Proceedings of Corrosion/98*, San Diego, CA, March 22–27, 1998, NACE International, Houston, TX.

[18] ASTM G78-15, *Standard Guide for Crevice Corrosion Testing of Iron-Base and Nickel-Base Stainless Alloys in Seawater and Other Chloride-Containing Aqueous Environments*, ASTM International, West Conshohocken, PA, 2015, www.astm.org

[19] Kearns, J., Scully, J. R., Roberge, P. R., Reichert, D. L., and Dawson, J. L., *Electrochemical Noise Measurement for Corrosion Applications, ASTM STP1277*, ASTM International, West Conshohocken, PA, 1996, http://dx.doi.org/10.1520/STP1277-EB

[20] ASTM G199-09, *Standard Guide for Electrochemical Noise Measurement*, ASTM International, West Conshohocken, PA, 2014, www.astm.org

[21] ASTM G96-90, *Standard Guide for Online Monitoring of Corrosion in Plant Equipment (Electrical and Electrochemical Methods)*, ASTM International, West Conshohocken, PA, 2018, www.astm.org

[22] ASTM G217-16, *Standard Guide for Corrosion Monitoring in Laboratories and Plants with Coupled Multielectrode Array Sensor Method*, ASTM International, West Conshohocken, PA, 2016, www.astm.org

[23] ASTM G150-13, *Standard Test Method for Electrochemical Critical Pitting Temperature Testing of Stainless Steels and Related Alloys*, ASTM International, West Conshohocken, PA, 2018, www.astm.org

[24] ASTM G48-11, *Standard Test Methods for Pitting and Crevice Corrosion Resistance of Stainless Steels and Related Alloys by Use of Ferric Chloride Solution*, ASTM International, West Conshohocken, PA, 2015, www.astm.org

[25] Fontana, M. G. and Greene, N. D., "Introduction," *Corrosion Engineering,* McGraw Hill, New York, 1984, p. 2.

[26] ASTM NACE/ASTM G193-12d, *Standard Terminology and Acronyms Relating to Corrosion*, ASTM International, West Conshohocken, PA, 2012.
[27] ASTM G100-89, *Standard Test Method for Conducting Cyclic Galvanostaircase Polarization*, ASTM International, West Conshohocken, PA, 2015, www.astm.org
[28] Frankel, G. S., "Electrochemical Techniques in Corrosion: Status, Limitations, and Needs," *J. ASTM Int.*, Vol. 5, No. 2, 2008, http://dx.doi.org/10.1520/JAI101241

STP 1609, 2019 / available online at www.astm.org / doi: 10.1520/STP160920170247

Carol F. Glover,[1] Michael J. Hutchinson,[1] Veronica N. Rafla,[1]
Leslie G. Bland,[1] and John R. Scully[1]

Progress in Development of Electrochemical Methods in Corrosion Science and Engineering

Citation

Glover, C. F., Hutchinson, M. J., Rafla, V. N., Bland, L. G., and Scully, J. R., "Progress in Development of Electrochemical Methods in Corrosion Science and Engineering," *Advances in Electrochemical Techniques for Corrosion Monitoring and Laboratory Corrosion Measurements*, *ASTM STP1609*, S. Papavinasam, R. B. Rebak, L. Yang, and N. S. Berke, Eds., ASTM International, West Conshohocken, PA, 2019, pp. 32–58, http://dx.doi.org/10.1520/STP160920170247[2]

ABSTRACT

The role and impact of four electrochemical techniques in the study of various corrosion applications are discussed; these are scanning vibrating electrode technique, coupled multielectrode array technique, scanning electrochemical microscope, and atomic emission spectroelectrochemistry. A common theme is an ability to monitor corrosion phenomena in situ on a local electrochemical scale with high resolution of electrochemical and, in some cases, chemical reaction rates. In all cases, the techniques presented here are discussed in the context of specific corrosion problems carried out in full immersion conditions. Examples taken from the current literature, and new data, are presented to demonstrate the use and advantages of these techniques, or a combination of these techniques, as powerful tools for industrially important applications.

Manuscript received December 11, 2017; accepted for publication February 9, 2018.
[1]University of Virginia, Center for Electrochemical Science and Engineering, Dept. of Materials Science and Engineering, 395 McCormick Ave., Charlottesville, VA 22904, USA C. F. G. http://orcid.org/0000 0002 9220 622X, M. J. H. http://orcid.org/0000 0001 7057 4825, V. N. R. http://orcid.org/0000 0002 9315 9437, L. G. B. http://orcid.org/0000 0002 8764 4962, J. R. S. http://orcid.org/0000 0001 5353 766X
[2]ASTM Symposium on *Advances in Electrochemical Techniques for Corrosion Monitoring and Laboratory Corrosion Measurements* on November 13 14, 2017 in Atlanta, GA, USA.

This includes assessment of the galvanic interactions and throwing power of metal-rich primer coatings for active corrosion protection, corrosion/corrosion resistance mechanisms of new metal alloys, the effect of pretreatments on coating integrity, current distributions within a crevice, and pitting corrosion.

Keywords
SVET, multielectrode arrays, SECM, AESEC, corrosion

Introduction

The current article describes four in situ experimental techniques that are key players in the study of corrosion, all of which afford insights that are not possible with conventional electrochemical methods. The roles of the scanning vibrating electrode technique (SVET), coupled multielectrode arrays (CMEAs), the scanning electrochemical microscope (SECM), and atomic emission spectroelectrochemistry (AESEC) are discussed in terms of their unique capabilities and their limitations. With the exception of the AESEC method, where the main advantage is resolution of chemical species in electrochemistry, the techniques presented here are particularly advantageous for the study of localized corrosion, providing spatial resolution of local corrosion events as a function of time. This article aims to provide a comparison through which it is demonstrated that certain techniques can be utilized to mitigate the limitations of others through complementary experiments; a summary of this can be found in **Table 1**.

SVET

INTRODUCTION TO SVET

SVET is a well established tool for assessing localized corrosion phenomena in situ for specimens corroding in full immersion conditions [1 14]. Specifically, SVET measures the potential drop generated by ionic currents in solution emanating from a corrosion cell reflecting the size, shape, and spatial distribution of anodic (positive) current and cathodic (negative) currents. The electrochemical potential of a vibrating platinum (Pt) microelectrode (ME) is measured between two points in the electrolyte at a fixed height and perpendicular to the sample surface. Corrosion activity may be estimated quantitatively without any electrical or mechanical perturbation of the corroding surface. As the sample is nondestructively tested, in that it is not damaged or altered in any way, repeat scanning of the same corroding surface builds up a time resolved series of data, illustrating the progression of electrochemical processes. The movement and development of corrosion features over the surface can be monitored and used to measure propagation rate kinetics, for example, by tracking the progression of local anodic maxima. Through numerical integration, the component of normal current density (j_z) data from individual

TABLE 1 Advantages and limitations of the SVET, CMEA, SECM, and AESEC techniques.

Technique	Advantages	Limitations
SVET	• Measurements made in situ • Spatially resolved local electrochemical activity • Semiquantitative current density measurements as a function of time • Nonperturbing • Height scanning possible	• Interactions occurring between anodes and cathodes where spacing is less than tip height are not detectable • Measurements not concurrent • Full immersion conditions only • Planar samples only
CMEA	• Measurements made in situ • Spatially resolved electrochemical measurements made concurrently and instantaneously • Full immersion or thin film conditions • Nonperturbing • Nonplanar samples and complex geometries possible	• Spatial resolution limited to the size of the matrix • Test specimens difficult to produce (but can be used multiple times)
SECM	• Measurements made in situ • Spatially resolved local electrochemical and chemical activity • Measuring current as a function of the reactions occurring both at the electrode tip and at the substrate of the test specimen • Height scanning possible	• Measurements not concurrent
AESEC	• In situ monitoring of chemical and electrochemical dissolution products of a freely corroding surface	• No spatially resolved dissolution • Flow cell required

surface plots can be converted into time dependent net anodic (J_{at}) and cathodic (J_{ac}) current density values [15]. Compiling all J_{at} values from an experiment and plotting against immersion time enables an estimate of the corrosion rate in the case of separate anodes and cathodes. This can be converted into mass loss, for example, either metal dissolution (taken from J_{at} values) or H_2 evolution (taken from J_{ac} values). The SVET has some limitations, and it is typical for complementary measurements to be made in order to verify quantitative data, such as gravimetric or volumetric measurements. The technique can only provide an estimate of current density data as each scan can take several minutes depending on the size of the exposed area to be mapped. The very nature of the scanning probe means that data for the whole surface are not recorded instantaneously; however, an alternative method that surpasses this limitation is the coupled multielectrode arrays technique (discussed in the next section). A further limitation of the SVET is low detection efficiency in cases where the spacing between anodes and cathodes is so small that the current flux lines pass below the plane of scan of the

vibrating probe [7]. However, for localized corrosion with large spaced anodes and cathodes, SVET detection efficiency is high.

A wealth of literature exists documenting the utilization of SVET to investigate corrosion problems, including the study of corrosion of bare metals and their alloys to elucidate fundamental corrosion mechanisms [8,13,16 19], the study of galvanic activity [2,6,20] at cut edges [21 24] and weld joints [4,25 27], the influence of inhibitors [5,7,18,28 30], modified surfaces [31], pitting corrosion [1,7,9,15,32,33], scribed coatings [29,34,35], and the study of metal rich coatings [36,37]. An example of the latter will be given in greater detail in the following section.

SVET THEORY OF OPERATION

An SVET probe consists of a Pt micro disc electrode typically ranging from 5 to 125 μm in diameter that is scanned at a fixed height across the surface of a sample in an electrolyte under full immersion conditions. The probe is vibrated at constant frequency and peak to peak amplitude (A_{pp}) and measures a peak to peak SVET voltage signal (V_{pp}). Calibration is necessary to convert to normal current density (j_z) by applying Ohm's Law, where A_{pp} and V_{pp} are related by Eq 1:

$$V_{pp} = j_z(A_{pp}/\kappa) \tag{1}$$

where κ is the solution conductivity. It is possible to measure A_{pp} using a strobe light; however, this method is difficult and provides poor accuracy. An alternative method can be applied whereby a quantity $G = \kappa/A_{pp}$ may be obtained by a "point source" method [38]; V_{pp} measurements are made where an external galvanostatic current is set up in the solution of interest and an even current distribution over the surface of a hemisphere is assumed and the maximum obtained at the center (**Fig. 1**). The area that encompasses the emanating current is mapped with the SVET probe at a fixed probe height, z. Applied current density is calculated by dividing applied current, $i_{applied}$, by the surface area of a hemisphere ($2\pi z^2$); G is obtained by taking the gradient when plotting maximum V_{pp} versus $i_{applied}/(2\pi z^2)$ for a range of $i_{applied}$; G is then applied to Eq 1 to obtain j_z [38].

EXAMPLE OF CORROSION STUDY USING SVET: THE GALVANIC THROWING POWER OF A MAGNESIUM-RICH PRIMER ON PRETREATED AA2024-T351 IN FULL IMMERSION

Metal rich primer coatings can offer sacrificial protection when applied to an electrochemically more noble substrate [39 43]. The galvanic protection potential of such a system is dictated by mixed potential theory and can be mediated by electrical and ionic resistances between the metal rich coating (anode) and the substrate (cathode) that will limit protection. Such resistances can derive from the barrier properties of a pretreatment at the coating/substrate interface. Traditional corrosion experiments, such as electrochemical impedance spectroscopy and open circuit potential measurements can provide information in terms of overall barrier properties and the global potential of the coating systems, respectively. In the current

FIG. 1 Schematic diagrams of a point current source method where the Pt tip is scanned over an electrode embedded in epoxy, cutting through the lines of flux of an emanating current, and it is assumed that, in the plane of scan, current emanating from the point source is distributed evenly over the surface of a hemisphere.

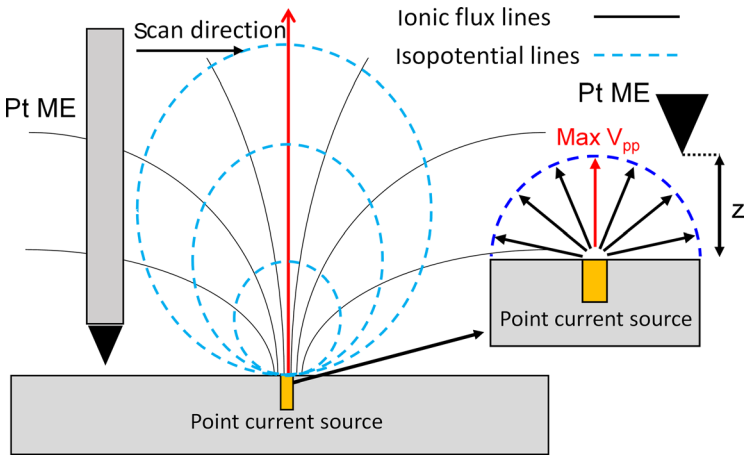

example, SVET is utilized to probe the distance over which an Mg rich primer coating can afford protection to an AA2024 aluminum (Al) alloy substrate with a nonfilm forming pretreatment at a large defect [44]. This is known as the "galvanic throwing power."

Experimental Procedure

The experimental area of interest was an AA2024 T351 Al alloy specimen with a nonfilm forming pretreatment overcoated with an Mg rich epoxy primer of area 3 mm by 10 mm. On the same surface, a large defect of area 11 mm by 10 mm was created to expose the bare substrate. The specimen was immersed in 2 M aqueous sodium chloride solution ($NaCl_{(aq)}$) with the area of interest facing upward. The SVET probe was scanned over the surface at hourly intervals over a period of 24 h, producing current distribution maps like the one given in Fig. 2b. Representative current density profiles across the coating/defect interface (as shown in Fig. 2a) were taken at selected time intervals. Total anodic and total cathodic current density values were measured in five sections of equal size moving progressively away from the coating (shown in Fig. 3a).

SVET Example: Results and Discussion

Fig. 2a shows the current density profiles given at 4 h, 14 h, and 24 h across the coating/defect interface. Pitting corrosion can be observed in the defect region denoted by the local anodic maxima; this is also shown in the current density map

FIG. 2 Results from an SVET study where current density values were mapped over the interface between an Mg rich primer coating and a bare Al alloy AA2024 surface defect when fully immersed in 2 M $NaCl_{(aq)}$ where: (a) shows representative current density profiles across the interface at 4 h, 14 h, and 24 h; (b) shows an example of an SVET derived current density distribution map 14 h; and (c) shows an optical image of the specimen surface after 24 h of immersion time.

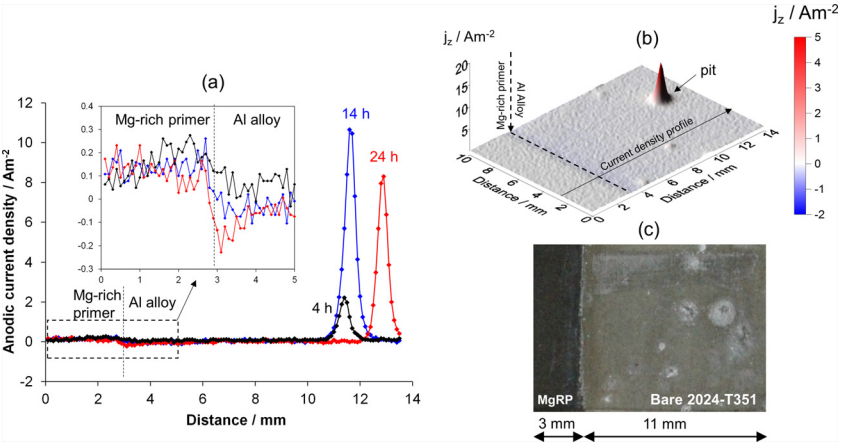

FIG. 3 (a) Schematic diagram showing the five regions of the defect area on the bare Al alloy AA2024 surface where total net anodic and total net cathodic current density values were detected as a function of time. Plots are shown of (b) the total net anodic and (c) the total net cathodic current density values measured in the five specified regions of the defect area, respectively.

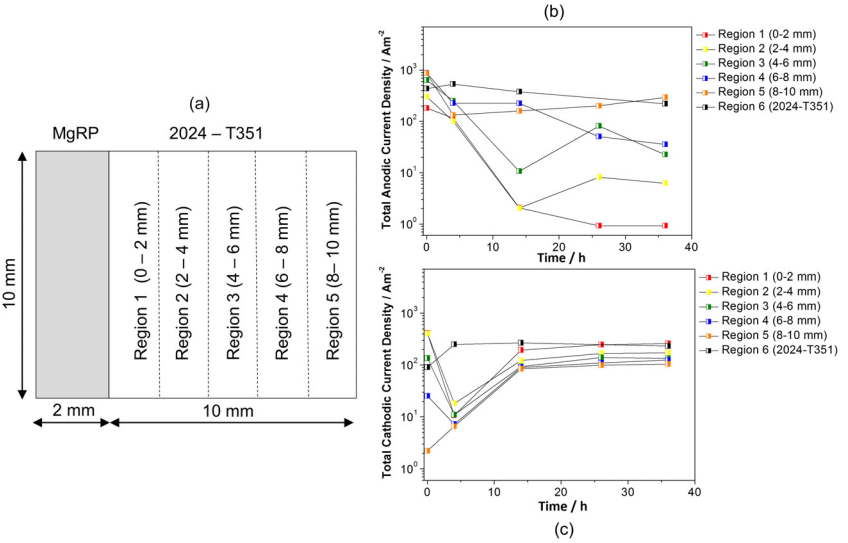

given in Fig. 2b and visually in the photographic image in Fig. 2c. The profiles demonstrate that no pitting occurs within 7 mm of the Mg rich primer coating. Furthermore, it can be observed that the coating and substrate are galvanically coupled where the coating is anodic to the substrate. The current density baseline is shown more clearly in the inset of Fig. 2a. Fig. 3b shows that, after 14 h, total anodic current density increases with increasing distance from the coating/defect interface while the opposite is true for the total cathodic current density (Fig. 3c). The SVET is used here to demonstrate that the coating and substrate are galvanically coupled, but this effect is limited to 7 mm rather than the entire exposed substrate in the defect region.

CMEAs

INTRODUCTION

The key advantage of the CMEA technique is that multiple electrochemical measurements are taken concurrently and instantaneously, enabling the measurement of real time local corrosion processes that take place on an electrode surface [45,46]. Sharing the same principle as SVET, close packed CMEAs (which will be the main focus of this section) enable temporal and spatial measurement of electrochemical processes, providing information about net local anodes and cathodes. However, rather than utilizing a scanning probe, CMEAs are an assortment of electrically isolated, separately addressable electrodes, coupled through zero resistance ammeters. This forms a galvanically coupled electrode surface designed to closely simulate a planar electrode surface, allowing localized current to be mapped on the scale of the electrode sizes and monitored over time in full, alternate, and thin electrolytes.[3]

CMEAs can be designed to satisfy specific corrosion problems to replicate common real life configurations in terms of material, geometry, physical arrangement, and environment, including thin film and full immersion conditions as well as crevices and recesses. Several examples are available in the literature [42,45,47,48]. CMEAs can be built with either nominally identical electrodes to simulate large planar electrodes or a combination of different electrode materials, to simulate complex alloys with nonuniform composition and structure. Budiansky et al. demonstrated that far spaced configurations, in contrast to close packed, can be optimized for high throughput experiments capable of elucidating the statistical distributions of flaws under different variables and their effect on corrosion processes [45]. CMEAs have also been used to investigate the spreading of intergranular corrosion by cooperative interactions where CMEAs were constructed from sensitized 304 stainless steel to understand the origins of persistent interactions in localized corrosion sites [48]. It was interesting to note that while intergranular

[3]Perfectly uniform corrosion will indicate zero electrochemical current on each electrode during open circuit potential testing.

corrosion was limited to isolated electrodes, chemical and electric fields coupled across electrodes. King, Lee, and Scully utilized CMEAs to study the effect of immersion conditions on the "galvanic throwing power" of a magnesium rich primer system for AA2024 T351 substrates [42]. First, they were able to demonstrate that, for continuous, thin electrolyte layers, throwing power extended across an entire 6 mm array. Second, for tortuous electrolyte geometries (resulting from drying or isolated droplet formation due to low initial salt deposition density), throwing power is limited by the reduction in length of ionically conductive pathways [42]. Moreover, galvanic interaction just before drying increases significantly at the galvanic interface, which was highly concentrated in Cl^-. Budiansky et al. built an artificial crevice made from a 316 stainless steel CMEA and monitored the current through each individual electrode within the crevice. They were able to demonstrate for the first time that, in conditions where the potential inside and outside are equal, and pitting corrosion resistance is modest, corrosion initiates on the outside in a region adjacent to the crevice mouth and subsequently progresses inside [45]. Another finding was that, in the case of a reduction in cathode area, the crevice anodes reorganized to a few surviving anodic sites deep within a crevice. In the current article, an example study is presented that combines some of the configurations described here. The galvanic corrosion of AA7050 T7451 and 316 stainless steel in both a general planar electrode geometry configuration and a fastener geometry configuration is outlined in the next section.

EXAMPLE OF CORROSION STUDY USING CMEAS

Investigation of Galvanic Corrosion of AA7050-T7451 and 316 Stainless Steel in a General Planar Electrode Geometry and a Fastener Geometry

High strength aluminum alloys and stainless steel are widely used in the aerospace industry in fastener applications [42,45,47–50]. While a vast amount of work has been performed regarding the localized corrosion of high strength aluminum alloys, there is a lack of literature on the unique factors and environments present in a rivet hole combined with a galvanic couple [51–55]. Furthermore, there are unanswered questions regarding how these factors and environments affect the current distribution inside and outside a fastener hole. One method to examine hidden corrosion is X ray tomography [49,56–60]; however, there was no instantaneous electrochemical information. The work presented here utilizes CMEAs in a fastener like geometry to understand the effect of various environmental and physical factors on the electrochemical current distribution in a typical Al SS galvanic couple fastener.

CMEA Example: Experimental Procedure

Fig. 4 shows schematic representations of CMEA geometrical configurations where (a) shows a flat galvanic geometric array where six AA7050 electrodes and six SS 316 electrodes were embedded in an AA7050 T7451 plate, and (b) shows a simulated fastener arrangement representing a cross section at a fastener plate assembly where

FIG. 4 CMEA schematic of the (a) flat galvanic geometric array where six AA7050 electrodes and six SS 316 electrodes were embedded in an AA7050 T7451 panel in a flat arrangement; (b) galvanic fastener geometric array where 22 AA7050 electrodes were embedded in an AA7050 panel and 20 SS 316 electrodes were embedded in an SS 316 panel and arranged in a geometry representing a fastener with an adjustable gap between a 316 SS rivet and 7050 T741 plate where the separately addressable electrodes in each panel are facing. (Note: The electrodes in the schematic have been deliberately turned outward so that each electrode can be seen.)

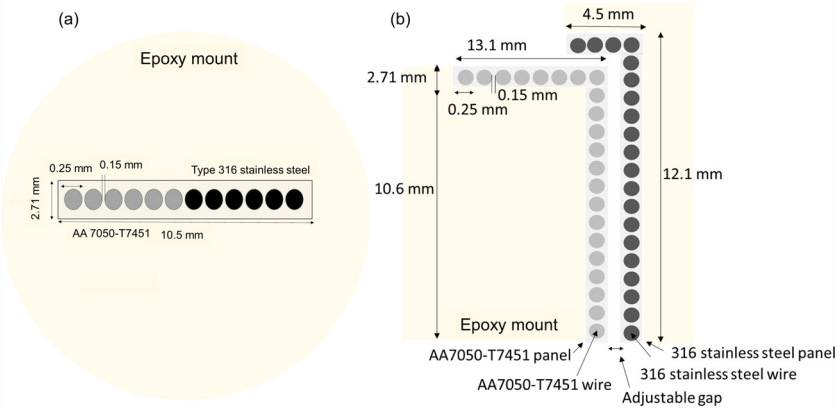

22 AA7050 electrodes were embedded in an AA7050 panel and 20 SS 316 electrodes were embedded in an SS 316 panel (the ends of each wire, i.e., the individual flush mounted microdisc electrodes, are shown here facing outward to illustrate the place ment of microdisc electrodes). In all cases, electrodes were separately addressable and constructed from electrically isolated wires 250 μm in diameter with a spacing of approximately 150 μm. CMEAs were tested in a controlled relative humidity (RH) chamber set to 98 % RH. The CMEA resin epoxy was masked using polyamide elec trochemical tape to control the thickness of a thin water layer to approximately 70 μm. The electrolyte used in this study was 0.6 M NaCl pH 5.5. The individual wires used to build an CMEA need to be electrically isolated using an insulating var nish, and the exposed ends that form the electrodes can be flush mounted into epoxy resin or embedded in a panel of the material of interest. The latter was used in this study due to the higher wettability of Al and its oxides; this was particularly impor tant for the fastener geometry, which required the electrolyte solution to wick inside and completely fill the crevice.

A Scribner Associates, Inc. Model MMA910B (Southern Pines, NC) was employed and is capable of providing a graphical interface to display the array and data acquisition of each ME current. The instrument is capable of galvanically coupling and measuring up to 100 working electrode current channels and contains

an individual zero resistance ammeter dedicated to each current channel with a measureable current range of 3.3 nA to 100 uA per channel. Furthermore, the applied potentiostatic or potentiodynamic potential can be controlled in ten groups of ten electrodes such that specific groups of electrodes can be controlled at a desired potential. Current distribution maps are produced where red denotes anodic current and blue denotes cathodic current. Charge conservation for ME array experiments can be validated in accordance with mixed potential theory, where the sum of anodic current is equal to the sum of cathodic current (Eq 2):

$$\sum i_{anodic} = \sum i_{cathodic} \tag{2}$$

CMEA Example: Results and Discussion

Current measurements over a 24 h period for the flat galvanic geometric CMEA are shown in Fig. 5, where the solid and dotted lines represent the 7050 T7451 Al alloy flush mounted electrodes and the 316 stainless steel flush mounted electrodes, respectively. Al flush mounted electrodes A4 and A5 had high positive anodic current and electrode S6 of 316 stainless steel had the most negative cathodic current. Fig. 5 shows that, initially, all Al electrodes were anodic and SS electrodes were cathodic. After 3 h at 98 % RH, Al electrodes A1, A2, and A3 switched polarity to become cathodic. Al wire A4 became a strong anode and Al electrode A5 became a weak anode. This observed change in polarity may be attributed to S phase aluminum copper magnesium (Al_2Cu_2Mg) intermetallic particles (IMPs) dealloying leaving behind a copper (Cu) rich remnant that becomes mechanically detached and

FIG. 5 Net CMEA current recorded over 24 h for the flat galvanic geometric array, where solid lines represent the current for AA7050 electrodes and dotted lines are those for SS 316 electrodes. The key at the bottom of the image shows the position of each wire in the array.

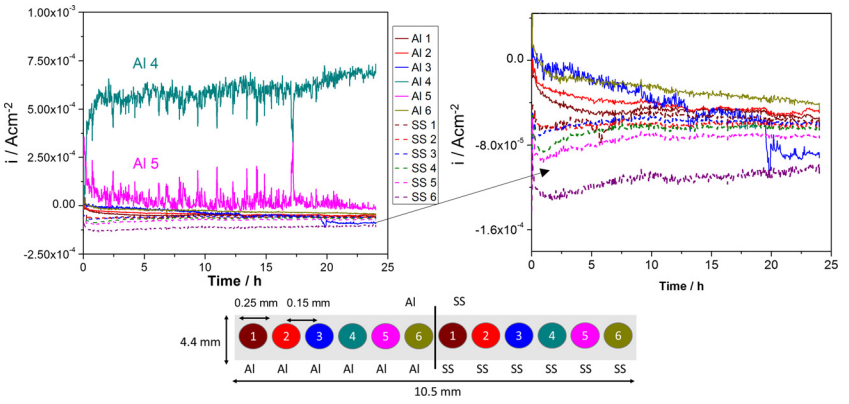

electrochemically replated on the 7050 T7451 Al alloy surface. Such sites can become strong sites for oxygen reduction. Thus, selected 7050 T7451 electrodes became cath odes, a fact that has been suggested in previous publications but never proven [50,59 64]. All SS wires remained cathodic throughout the 24 h exposure.

Regarding the fastener, the galvanic fastener geometric array enabled the cur rent distribution to be determined inside an artificial crevice. The location of each of the electrodes is given in **Fig. 6a**, and the wires of interest are highlighted (S9, S14, S17, A4, A7, A9, A10, and A11). **Fig. 6b** gives the current measurements for a 3 h period. It can be observed that three SS electrodes (S9, S14, and S17), which were located deep within the fastener crevice, were dominant cathodes throughout. The current measured in electrodes A9 and A11 is shown to reach the highest max imum anodic values of 1.5 to 2.0 $\times$ 10^{-3} Acm^{-2}, albeit intermittently.

SECM

INTRODUCTION

SECM enables time resolved mapping on the micrometer length scale of heteroge neous reactions on the surface of a corroding specimen. In this technique, the SECM ME "sensing" tip is an electrochemical mapping sensor that exploits the reaction rate of a mediator, added to the test solution, as a method to indirectly sense the local reactivity of the test substrate. The principle of SECM is similar to that of a typical three electrode electrochemical cell; however, in this case, two

FIG. 6 (a) CMEA results (for a fastener arrangement with adjustable gap) give the location of each wire in the array and the wires of interest (S9, S14, S17, A4, A7, A9, A10, and A11) are highlighted. (b) Plots of the measured current over 3 h for the fastener galvanic geometric array, where solid lines are AA7050 electrodes and dotted lines are SS 316 electrodes.

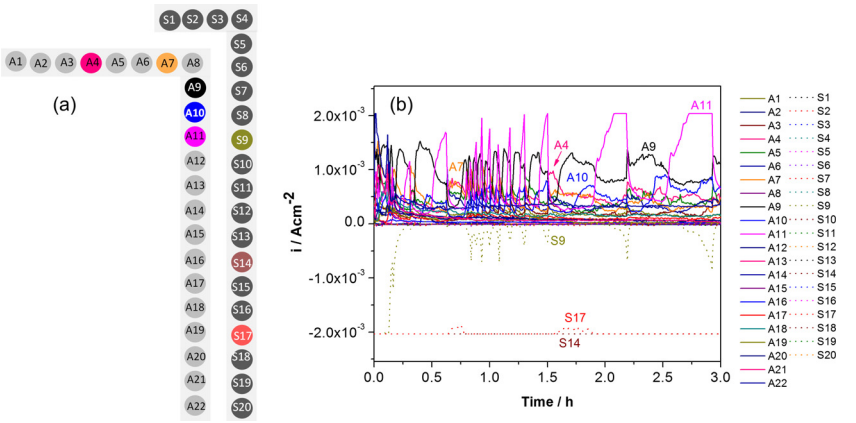

cells, controlled by a bi potentiostat, are utilized, where the ME or the specimen surface (or both) act as the working electrodes sharing a counter and reference electrode [65].

The ME is immersed in electrolytic solution and positioned above the specimen surface at a set distance. As the tip scans across the surface of the specimen, an SECM current reading is taken directly at the ME tip as a function of the reactions occurring both at the tip and at the substrate. There are several variations of SECM mode of operation that can be selected, which are dictated by the specimen surface properties, experimental environment, and tip geometry. The feedback mode and sample generation/tip collection mode will be discussed in greater detail here as they are the most relevant for corrosion monitoring.

A body of publications exists describing the use of SECM for characterizing heterogonous corrosion rates for specific applications such as pitting [66 68] and metastable pitting [69 73], galvanic corrosion of dissimilar metals or metal alloys [2,74,75], and the breakdown of protective coating systems [36,37,76]. In a previous study, Simõet al. employed SECM to study coupled iron zinc (Fe Zn) cells [2], demonstrating the ability to map the heterogeneous galvanic corrosion reaction rate at an interface to study the interaction between the two metals [2]. Another well established application of SECM is to map the localized breakdown and reac tions occurring on protective coatings [77 79]. Gonzalez Garcia et al. demonstrated the self healing capabilities of an inhibitor pigment added to shape memory polyurethane [79]. Other studies have assessed the galvanic interactions between metal rich primers and a substrate of interest [36,37,80,81]. A unique capability of SECM is that measurements can be carried out in the presence of nonaqueous electrolytes, such as ethylene glycol [82] or methanol [83], to suppress fast substrate reaction rates, which produce gases that may disrupt sensing strategies. This ensures that all important corrosion activity is captured. This is particularly advan tageous for studying the corrosion of magnesium and its alloys where corrosion progresses at a very fast rate. In the current article, an example is presented where SECM is used in feedback mode to study localized dissolution at IMPs on a com mercially important Mg alloy AZ31B wrought bass plate in an NaCl/methanol mix solution.

SECM THEORY OF OPERATION

Tip Geometry and Reactions

SECM enables the mapping of electrochemically active microstructural features on the specimen surface with micrometer length scale resolution. This is dependent on the size and shape of the ME tip, which typically is 10 μm to 25 μm in diameter. A redox mediator is added to the test electrolyte. Tip geometry and height effects the diffusion characteristics at both tip and substrate and can be described as: (a) planar, (b) spherical, (c) disk, or (d) conical [84]. The tip currents obtained from each geometry varies, and a relevant diffusion equation must be applied. For the example described here, the planar geometry and an infinite flat planar

surface is assumed. For this, the steady state current at the tip (when positioned away from the substrate) can be demonstrated by the plane/thin layer expression:

$$j = 4nFADC^*/d \tag{3}$$

where d is the spacing between substrate and tip, C^* is the bulk concentration of the given mediator species, D is the mediator species diffusion coefficient, and F is Faraday's constant.

The Use of Mediators

A redox mediator typically is used as a supportive reactant in the electrolyte solu tion and, if selected carefully, can be used to control which particular reactions are probed during an experiment [2,75,83,85]. A full description of mediator selection can be found elsewhere; however, a brief example is Ferrocene methanol (FcMeOH) where the oxidation of $\mathrm{FCMeOH} \rightarrow \mathrm{FCMeOH}^+ + \mathrm{e}$ occurs at the tip and FcMeOH^+ diffuses to the surface where it reduces back to FcMeOH [82].

Mode of Operation

The *feedback* mode and *tip generation/substrate collection* (TG/SC) mode have been extensively used for corrosion monitoring [36,37,80,81]. In feedback mode, the ME tip is used as both the source and the current detector [86,87], and a redox media tor, in its reduced form, is added to the electrolyte solution. The SECM measures the current at the ME tip while simultaneously applying a positive potential (to the ME tip) to oxidize the mediator species in the bulk. The rate of this oxidation reac tion is governed by the diffusion of the reduced species from the bulk solution to the ME tip according to Eq 3. The selection of an appropriate mediator is dictated by the properties of the specimen material such that the oxidized species produced at the tip will be reduced back to its original form at the specimen surface. When the vertical position of the tip is changed from "far away" from the specimen into close proximity (i.e., less than 100 μm) to the specimen, the current response mea sured at the ME tip will affect whether the SECM is operating in positive or nega tive feedback mode. When the substrate is a conductor (i.e., a bare metal surface), the amount of available reduced species will increase; this is because those mediator species oxidized by the ME tip will be reduced at the substrate. In the presence of a conducting substrate, the SECM will operate in *positive feedback* mode. When the substrate is an insulator (a polymer coating, for example), the SECM will operate in *negative feedback* mode as there will be no replenishment of the reduced species at the surface. Furthermore, the diffusion of the reduced species from the bulk to the tip will be greatly hindered by the presence of the insulating specimen surface [88]. In such cases, the measured current decreases due to the depleted mediator species at the surface of the substrate.

In *tip generation/substrate collection* (TG/SC), both the ME tip and the speci men surface can be used as working electrodes and current detectors. In the same way as in feedback mode, the tip is held at a potential to drive an electrochemical

oxidation reaction. However, in this case, the substrate is concurrently held at a potential such that the oxidation products of the ME tip reaction are reduced [86,89]. Therefore, oxidized species produced at the ME tip diffuse across the gap and are collected at the substrate. In the opposing direction, the reduced species generated at the substrate diffuse to the ME tip for collection. Concurrent measurement of the current at the tip (i_{tip}) and the substrate ($i_{substrate}$) can be used to obtain a value for collection efficiency ($i_{substrate}/i_{tip}$). This value can provide information regarding the kinetics of reactions, particularly where certain species undergo conversion to electrochemically inactive species in irreversible reactions.

EXAMPLE OF CORROSION STUDY USING SECM: CHARACTERIZATION OF Mg-Alloy AZ31B in Chloride Conditions

The extremely negative electrochemical potential of Mg renders Mg alloys highly susceptible to microgalvanic corrosion from various IMPs, or secondary phases within the alloy [68]; reaction rates are high and difficult to capture with conventional corrosion testing techniques. The current study utilizes SECM, performed in sample feedback mode, to probe sites' fast hydrogen evolution in order to assess localized dissolution at IMPs on a commercially important Mg alloy AZ31B wrought base plate. A hexaammineruthenium(III)chloride ($Ru(NH_3)_6Cl_3$) mediator was employed where the reduction of $Ru(NH_3)_6^{3+}$ occurs at actively corroding sites following the half cell reaction $Ru(NH_3)_6^{3+} + e \rightarrow Ru(NH_3)_6^{2+}$ along with the subsequent oxidation of $Ru(NH_3)_6^{2+}$ at the tip. A solution of aqueous NaCl mixed with methanol is used to reduce reaction rates but preserves the same mechanism as in a fully aqueous environment. The findings are compared to scanning electron microscope (SEM) imaging.

SECM Example: Experimental Procedure

SECM mapping was carried out at hourly intervals up to 3 h on an AZ31B (Mg Zn Al) wrought base plate. The specimen was fully immersed in 0.1 M NaCl(aq) consisting of 50 wt.% water + 50 wt.% methanol and 1 mM $Ru(NH_3)Cl_6$ mediator. A scan rate of 100 μm/s was used with a step size of 10 μm. The tip was positioned 30 μm away from the specimen surface and polarized at −100 mV versus saturated calomel electrode (SCE) where Ru(II) is oxidized to Ru(III). The specimen was imaged using SEM after removal from the experimental solution.

SECM Example: Results and Discussion

Fig. 7a shows an SECM map of the surface as imaged by the ME after approximately 1 h of immersion in the experimental electrolyte. Small spots of intense current (approximately 1,000 pA) relative to the background (approximately 500 pA) can be observed. Approximately 3 h after immersion, a separate set of intense current spots are visible, and the original areas are now seen to be similar to the background (Fig. 7b). These results indicate that corrosion sites change with time, and initially corrosion is dictated by IMPs that form local galvanic cells. The SEM micrograph

FIG. 7 (a) Scanning electrochemical microscope (SEM) scan of current on an AZ31B specimen taken immediately after immersion. (b) SEM image of an AZ31B specimen taken after 3 h of immersion. Scan was taken in 0.1 M NaCl with $[Ru(NH_3)_6]Cl_3$ as the mediator in 50 wt.% methanol + 50 wt.% H_2O. Scan was run at 100 μm/s with a step size of 10 μm. The tip was positioned 30 μm away from the specimen surface and polarized to 100 mV. (c) SEM secondary electron micrograph of AZ31B as received surface showing various IMPs.

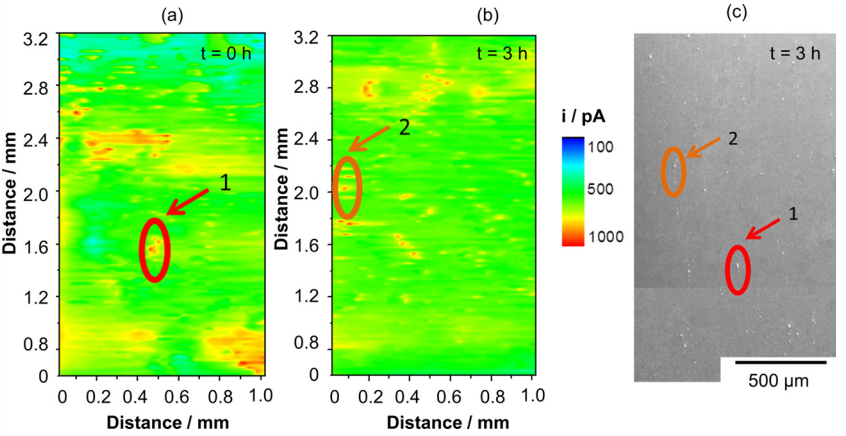

given in Fig. 7c can be used to correlate the regions of high current suggesting that active microgalvanic cells exist at sites where heterogeneously spaced IMP clusters are located. These sites were previously shown to be Al Mn particles [90].

Atomic Emission Spectroelectrochemistry (AESEC)

INTRODUCTION TO AESEC

One drawback in direct current and alternating electrochemistry is that measuring electron flow proportional to various half cell reactions does not indicate chemical specificity. AESEC is an approach that monitors chemical and electrochemical dis solution of a freely corroding surface in situ. An inductively coupled plasma atomic emission spectrometer connected downstream from an electrochemical flow cell screens the spent effluent stream to provide data about the dissolved ele ments present in the solution as a function of time. With the use of a polychroma tor, multiple elements may be assessed simultaneously, revealing element specific information such as selective dissolution and dealloying [91 95], cathodic dissolu tion [93,95,96], structure dependent dissolution behavior [97,98], alloy influences on dissolution and multielement alloy behavior [99 101], oxide and coating disso lution [94,101,102], and fundamental dissolution mechanisms [94,99,103]. Precise

chemical control of the solution environment at the electrode surface enables studies to be conducted that are analogous to real life situations. Furthermore, the technique can facilitate multistage experiments such as rapid changes in pH, complexing environments, and aeration conditions.

Studies reported in the available literature demonstrate the advantages of the AESEC method over conventional corrosion testing methods. Ogle et al. [93] reported the use of AESEC for assessing the stability of a phosphate conversion coating on galvanized steel when subjected to the highly alkaline conditions observed at the substrate/coating interface during the cathodic disbondment process. While cathodic disbondment is an electrochemical process, the physical destruction of a conversion coating at the interface is purely chemical, and conventional electrochemical testing methods, which rely on current or potential measurements, are not suitable for this type of phenomenon. As such, the authors utilized the AESEC method to measure the time dependent dissolution of all the individual metallic components of the phosphate layer in a high pH solution and were subsequently able to correlate exactly how the different element additions present in the phosphating bath influenced the corrosion protection [93].

In another study, AESEC was utilized to study structural dependencies on dealloying, offering an explanation for the mechanisms of dissolution for amorphous and crystalline alloys, which have been previously shown to be dissimilar [98]. Duarte et al. [97] used the AESEC method to study the dissolution of an amorphous stainless steel (Fe 15Cr 14Mo 15C 6B) compared to an annealed (800°C) nanocrystalline specimen of the same composition when exposed to sulfuric acid (H_2SO_4). Using a multi element inductively coupled plasma mass spectroscopy, it was shown that soluble molybdenum was released preferentially and that this was exacerbated with an increased degree of crystallinity [97]. Chromium enrichment was demonstrated on the amorphous specimen in contrast to stoichiometric dissolution observed on the annealed specimens [97].

AESEC may also be used to study soluble valence by measuring the total dissolution mass balanced with the applied charge. Zhou et al. [94] and Hutchison et al. [99] studied the dissolution of Cu in this way for exposure to various media. They demonstrated that Cu dissolves in the cupric (Cu^{2+}) state for simulated tap waters and sulfuric acid, but it dissolves in the cuprous state (Cu^{+}) for HCl and an artificial perspiration solution [94,99]. Oxide enrichment of alloying elements, inferred from a lack of measured soluble release, can be characterized using ex situ techniques, such as X ray photoelectron spectroscopy and transmission electron microscopy energy dispersive spectroscopy, enabling a complete description of a corroded system and elucidating the role of alloying on passivation phenomena [104]. In the current article, an example is presented where the effects of alloying additions on the soluble and insoluble release of elements from copper tin (Cu Sn) alloys is evaluated in a two stage process. The former are analyzed following specimen exposure to artificial perspiration solution (pH 6.5), and the latter are analyzed following exposure to a deaerated citrate buffer solution (CBS, pH 5.0) to chemically dissolve

and allow quantification of corrosion product films. The experimental procedure, results, and discussion are given as follows.

THEORY OF OPERATION

The procedural setup and flow cell geometry of a typical AESEC experiment are shown in the schematic given in Fig. 8. An electrochemical flow cell pumps electrolyte from the reservoir through a tube in which the working area of the specimen of interest is embedded. Typical flow rates are in the order of 2 mL/min to 3 mL/min with flow cell volumes and working electrode areas on the order of 0.25 mL and 0.5 cm^2 to 1 cm^2, respectively [105]. A bypass valve enables the user to conveniently select whether the electrolyte solution bypasses the flow cell, for calibration of standards and background intensity, or passes through the flow cell for an AESEC measurement (Fig. 8a). Photons ($h\nu$) emitted from the ionized atoms in the plasma are collected using both monochromatic and polychromatic spectrophotometers (Fig. 8b). Electronics allow real time monitoring of the emission intensity of up to 30 elements simultaneously from the polychromator plus one additional element from the monochromator. Furthermore, multiple input signals from the potentiostat/galvanostatic electrochemical measurements, for example, current

FIG. 8 Schematic diagram of an AESEC experiment. (a) Electrochemical flow cell with electrolyte reservoir and peristaltic pump. The valve is used to switch between a bypass (for background intensities) and an AESEC measurement. (b) Inductively coupled plasma atomic emission spectrometer. Photons ($h\nu$) emitted from the ionized atoms in the plasma are collected using both monochromatic and polychromatic spectrophotometers. (c) Electronics allow real time monitoring of the emission intensity of up to 30 elements from the polychromator plus one from the monochromator as well. In addition, multiple input signals from the potentiostat/galvanostatic electrochemical measurements (e.g., current density j) and potentials (E) can be correlated to the emission intensity in real (albeit delayed) time. The emission intensity is used to calculate the flow rate of specific elements, v_i.

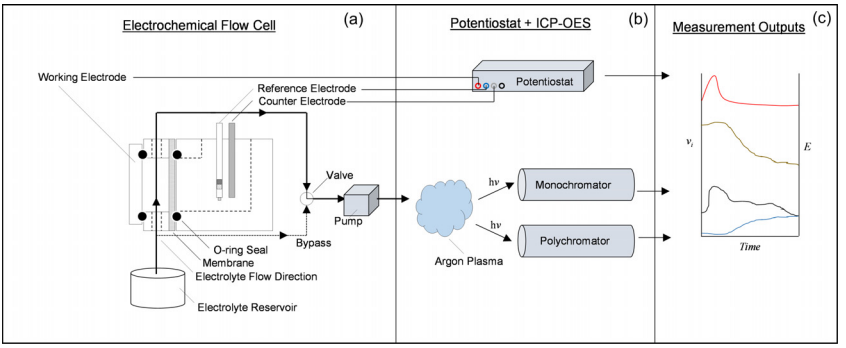

density (j), and potentials (E) can be correlated directly to the emission intensity in real time, albeit slightly delayed due to flow (Fig. 8b). The emission intensity is used to calculate the concentrations of specific elements. It follows that the instantaneous dissolution rate from the corroding system in the flow cell can be directly obtained from the monitored element concentration obtained from the spectrometer as described by Eq 4:

$$v_i = C_i f / A \tag{4}$$

where:

v_i = instantaneous downstream flow concentration of species i (nmol s^{-1} cm^{-2}),
C_i = measured concentration of element i (nmol cm^{-3}),
f = flow rate (cm^2 s^{-1}), and
A = working electrode area (cm^{-2}).

For direct comparison, the applied current can be converted to an "effective" electron flow density (Eq 5):

$$v_e = j_e / nF \tag{5}$$

where:

v_e = effective electron transfer rate,
j_e = applied current density,
n = valence, and
F = Faraday's constant.

In the absence of insoluble corrosion product formation, the applied current compared with the measured downstream flux of chemical species concentrations provides a direct evaluation of both Faradaic and non Faradaic species reaction rates.

EXAMPLE OF CORROSION PHENOMENA STUDIED USING AESEC: THE ANODIC DISSOLUTION OF COPPER TIN ALLOYS AND THE FATE OF ALLOYING ELEMENTS IN ARTIFICIAL PERSPIRATION SOLUTION

The release of soluble Cu from Cu alloys facilitates an antimicrobial surface effective against even antibiotic resistant bacteria strains such as methicillin resistant staphylo coccus aureus [106]. The influence of alloying elements on soluble Cu release and tarnishing (oxide formation) from Cu alloys is of interest in this antimicrobial application. A two stage AESEC investigation is an ideal method to study both the directly soluble release and the oxides formed related to alloying contents.

Experimental Procedure

The experimental setup for the current example is given in Fig. 9a, where a two phase procedure was carried out. In the first stage, commercially pure Cu (UNS C11000), commercial alloys of Cu 4.5Sn 0.1Zn (UNS C51000), and Cu 9.7Sn 0.1Zn (UNS C52480) specimens were subjected to 10 min of open circuit immersion in synthetic perspiration solution, followed by a 20 min anodic pulse of 0, 5, 20, or 80 μA/cm^2, during which Cu ion release was recorded. In the second stage, specimens were allowed to stabilize for 10 min before switching the influent electrolyte to deaerated

FIG. 9 (a) Schematic diagram of in situ AESEC. Galvanostatic pulse conducting in artificial perspiration solution. The citrate dissolution stage was conducted in a deaerated CBS (pH 5.0). The gray shaded integrated areas under curves represent moles. (b) The dashed blue line indicates applied current [e] and the solid black lines indicate AESEC measured species release [Me^{x+}] expressed as nmol/s.

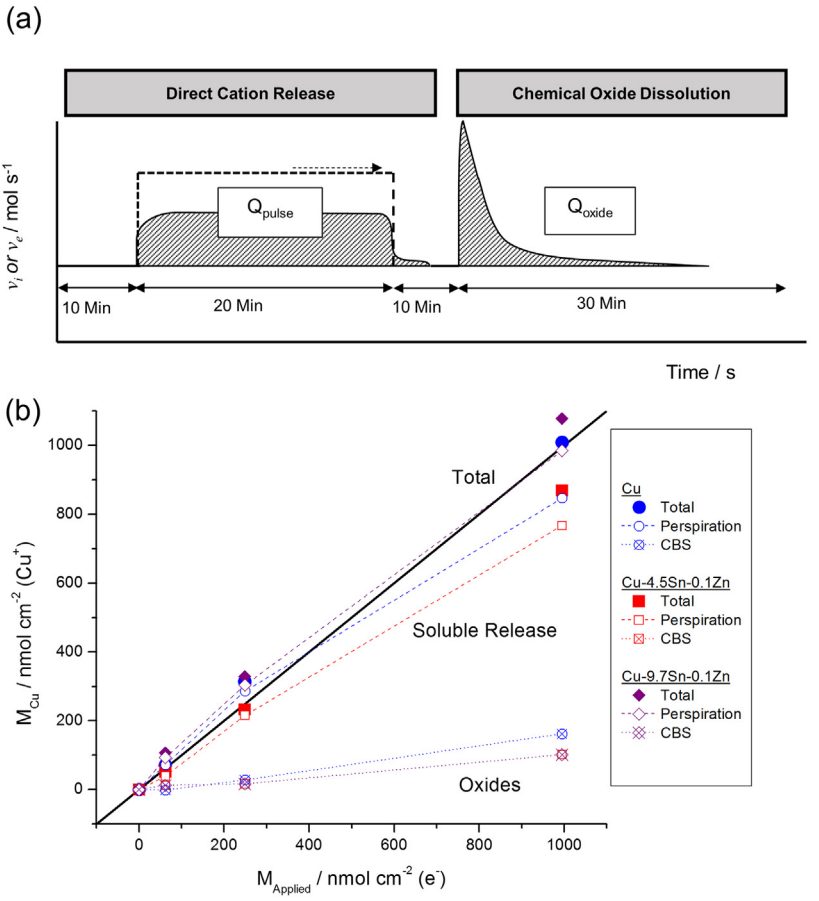

CBS [94,99], a chelating chemical that is known to dissolve Cu oxides [94]. Cu ion release was recorded for a further 30 min to capture all ions from the dissolved oxide layer. Deaeration of CBS ensured no further corrosion took place in this stage.

Results and Discussion

AESEC analysis was utilized to elucidate the fate of Cu, whether in oxides or in so lution, and to deduce the dominant valence states of soluble Cu, that is, either cu pric (Cu^{2+}) or cuprous (Cu^+) in the case of corrosion of pure Cu, Cu 4.5Sn 0.1Zn, and Cu 9.7Sn 0.1Zn after exposure to artificial perspiration. **Fig. 9a** [99] shows the

total amount of soluble Cu ions released in the first experimental phase and insoluble Cu ions released through dissolution in CBS in the second phase. As the mass measured agreed directly (1:1) with the charge applied, cuprous valence state was confirmed for both soluble release and oxide. Sn oxides were not quantifiable as they are insoluble in artificial perspiration and CBS; however, a quantitative measure of total Cu corrosion products was made possible by integrating the chemical dissolution of Cu oxides preformed in the first stage using flowing deaerated CBS. The majority of the applied current went into the direct formation of soluble Cu cations (Fig. 9b). Only 5 % to 10 % of the applied current went into insoluble product formation (Fig. 9b). This demonstrates that alloying with Sn led to an increase in the ratio of soluble Cu release despite the same applied current and lower Cu content of the alloy. In summary, the AESEC approach, in combination with other straightforward diagnostics, assesses the fate of the elements during corrosion processes that could give rise to chemical or electrochemical effects.

Summary

Recent developments in corrosion testing techniques were presented with the unique capabilities of four important methods that enable in situ spatial and local measurement of corrosion phenomena described in detail, which are summarized here and in Table 1.

- SVET enables the measurement of local current density distributions on corroding surfaces, in full immersion conditions, where anodic and cathodic activity is spatially resolved as a function of time. The integration of anodic and cathodic current density data with respect to area enables corrosion rates to be determined and converted to metal mass loss and cathodic reaction rates, respectively. It is demonstrated that SVET can be used to observe pitting corrosion and determine the galvanic throwing power of a metal rich primer coating where the baseline anodic and cathodic current densities of coating and substrate are measured.
- The CMEA technique is a powerful tool for the study of localized corrosion behavior and can be conducted in conjunction with various galvanic geometries and in thin or wet/dry electrolytes. The ability to interrogate each electrode at open circuit potential enables investigations into the current distribution within irregular geometries, providing local information that is impossible to obtain with conventional, global corrosion monitoring techniques.
- SECM enables the spatial resolution of a specified electrochemical reaction occurring on a corroding surface in full immersion conditions through fixing the tip at a potential of interest to sample a redox mediator, which signals substrate reactivity. Nonaqueous solutions can be incorporated to slow down reaction rates and avoid copious gas evolution.
- The AESEC technique enables monitoring of chemical and electrochemical dissolution of a freely corroding or polarized surface as a function of time. The technique enables precisely controlled environments to replicate in service conditions. The fate of the elements in a corroding system can account for

those released electrochemically and chemically. Diagnostics using an alternative solution can ensure that all corrosion product is accounted for.

ACKNOWLEDGMENTS

We acknowledge support from Office of Naval Research (ONR) Multidisciplinary University Research Initiatives (MURI) "Understanding Atomic Scale Structure in Four Dimensions to Design and Control Corrosion Resistant Alloys" on Grant Number N00014 16 1 2280; National Science Foundation, Division of Materials Research on Grant Number 1309999; Center of Performance and Design of Nuclear Waste Forms and Containers, an Energy Frontier Research Center funded by the U.S. Department of Energy, Office of Science, Basic Energy Sciences under Award number DE SC0016584; and U.S. Department of Defense, Office of the Undersecretary of Defense Corrosion University Pilot Program under the direction of Daniel Dunmire.

References

[1] Isaacs, H. S., "The Localized Breakdown and Repair of Passive Surfaces during Pitting," *Corros. Sci.,* Vol. 29, Nos. 2–3, 1989, pp. 313–323.

[2] Simões, A. M., Bastos, A. C., Ferreira, M. G., Gonzáz-Garcia, Y., González, S., Souto, R. M., "Use of SVET and SECM to Study the Galvanic Corrosion of an Iron–Zinc Cell," *Corros. Sci.,* Vol. 49, No. 2, 2007, pp. 726–739.

[3] Williams, G., Birbilis, N., and McMurray, H. N., "Controlling Factors in Localized Corrosion Morphologies Observed for Magnesium Immersed in Chloride Containing Electrolyte," *Faraday Discuss.,* Vol. 180, 2015, pp. 313–330.

[4] Atz Dick, P., Knornschild, G. H., and Dick, L. F. P., "Anodising and Corrosion Resistance of AA 7050 Friction Stir Welds," *Corros. Sci.,* Vol. 114, 2017, pp. 28–36.

[5] Lin, J., Battocchi, D., and Bierwagen, G. P., "Inhibitors for Prolonging Corrosion Protection of Mg-Rich Primer on Al Alloy 2024-T3," *J. Coat. Technol. Res.,* Vol. 14, No. 3, 2017, pp. 497–504.

[6] Souto, R. M., Gonzáz-Garcia, Y., Bastos, A. C., and Simões, A. M., "Investigating Corrosion Processes in the Micrometric Range: A SVET Study of the Galvanic Corrosion of Zinc Coupled with Iron," *Corros. Sci.,* Vol. 49, No. 12, 2007, pp. 4568–4580.

[7] Williams, G., Coleman, A. J., and McMurray, H. N., "Inhibition of Aluminium Alloy AA2024-T3 Pitting Corrosion by Copper Complexing Compounds," *Electrochim. Acta,* Vol. 55, No. 20, 2010, pp. 5947–5958.

[8] Williams, G., Gusieva, K., and Birbilis, N., "Localized Corrosion of Binary Mg-Nd Alloys in Chloride-Containing Electrolyte Using a Scanning Vibrating Electrode Technique," *Corrosion,* Vol. 68, No. 6, 2012, pp. 489–498.

[9] Zlatev, R., Valdez, B., Stoytcheva, M., Ramos, R., and Kiyota, S., "Solution Conductivity Influence on Pitting Corrosion Studies by SVET," *Int. J. Electrochem. Sci.,* Vol. 6, 2011, pp. 2746–2757.

[10] Isaacs, H. S. and Ishikawa, Y., "Applications of the Vibration Probe to Localized Current Measurements," presented at *CORROSION 1985*, Boston, MA, March 25, 1985.

[11] Isaacs, H. S., "The Measurement of the Galvanic Corrosion of Soldered Copper Using the Scanning Vibrating Electrode Technique," *Corros. Sci.,* Vol. 28, No. 6, 1988, pp. 547–588.

[12] Ishikawa, Y. and Isaacs, H. S., "Electrochemical Behaviour of Pits Developed on Aluminium in a Dilute Chloride Solution," *Corros. Eng.,* Vol. 33, No. 3, 1984, pp. 147–152.
[13] Fajardo, S., Glover, C. F., Williams, G., and Frankel, G. S., "The Source of Anodic Hydrogen Evolution on Ultra High Purity Magnesium," *Electrochim. Acta,* Vol. 212, 2016, pp. 510–521.
[14] Glover, C. F. and Williams, G., "Inhibition of Localized Corrosion of Hot Dip Galvanized Steel by Phenylphosphonic Acid," *J. Electrochem. Soc.,* Vol. 164, No. 7, 2017, pp. C407–C417.
[15] Williams, G. and McMurray, H. N., "Pitting Corrosion of Steam Turbine Blading Steels: The Influence of Chromium Content, Temperature, and Chloride Ion Concentration," *Corrosion,* Vol. 62, No. 3, 2006, pp. 231–242.
[16] Cano, Z. P., Kish, J. R., and McDermid, J. R., "On the Evolution of Cathodic Activity during Corrosion of Magnesium Alloy AZ31B in a Dilute NaCl Solution," *J. Electrochem. Soc.,* Vol. 163, No. 3, 2016, pp. C62–C68.
[17] Fajardo, S., Glover, C. F., Williams, G., and Frankel, G. S., "The Evolution of Anodic Hydrogen on High Purity Magnesium in Acidic Buffer Solution," *Corrosion,* Vol. 73, No. 5, 2017, pp. 482–493.
[18] Williams, G., Grace, R., and Woods, R. M., "Inhibition of the Localized Corrosion of Mg Alloy AZ31 in Chloride Containing Electrolyte," *Corrosion,* Vol. 71, No. 2, 2015, pp. 184–198.
[19] Williams, G. and McMurray, H. N., "Localized Corrosion of Magnesium in Chloride-Containing Electrolyte Studied by a Scanning Vibrating Electrode Technique," *J. Electrochem. Soc.,* Vol. 155, No. 7, 2008, pp. C340–C349.
[20] Deshpande, K. B., "Effect of Aluminium Spacer on Galvanic Corrosion between Magnesium and Mild Steel Using Numerical Model and SVET Experiments," *Corros. Sci.,* Vol. 62, 2012, pp. 184–191.
[21] Ogle, K., Morel, S., and Jacquet, D., "Observation of Self-Healing Functions on the Cut Edge of Galvanized Steel Using SVET and pH Microscopy," *J. Electrochem. Soc.,* Vol. 153, No. 1, 2006, pp. B1–B5.
[22] Simões, A. M. and Fernandes, J. C. S., "Studying Phosphate Corrosion Inhibition at the Cut Edge of Coil Coated Galvanized Steel Using the SVET and EIS," *Prog. Org. Coat.,* Vol. 69, No. 2, 2010, pp. 219–224.
[23] Thébault, F., Vuillemin, B., Oltra, R., Ogle, K., and Allely, C., "Investigation of Self-Healing Mechanism on Galvanized Steels Cut Edges by Coupling SVET and Numerical Modeling," *Electrochim. Acta,* Vol. 53, No. 16, 2008, pp. 5226–5234.
[24] Worsley, D. A., Williams, D., and Ling, J. S. G., "Mechanistic Changes in Cut-Edge Corrosion Induced by Variation of Organic Coating Porosity," *Corros. Sci.,* Vol. 43, No. 12, 2001, pp. 2335–2348.
[25] Bertoncello, J. C. B., Manhabosco, S. M., and Dick, L. F. P., "Corrosion Study of the Friction Stir Lap Joint of AA7050-T76511 on AA2024-T3 Using the Scanning Vibrating Electrode Technique," *Corros. Sci.,* Vol. 94, 2015, pp. 359–367.
[26] Kish, J. R., Birbilis, N., McNally, E. M., Glover, G. F., Zhang, X., McDermid, J. R., and Williams, G., "Corrosion Performance of Friction Stir Linear Lap Welded AM60B Joints," *JOM,* Vol. 69, No. 11, 2017, pp. 2335–2344.
[27] Kish, J. R., Williams, G., McDermid, J. R., Thuss, J. M., and Glover, C. F., "Effect of Grain Size on the Corrosion Resistance of Friction Stir Welded Mg Alloy AZ31B Joints," *J. Electrochem. Soc.,* Vol. 161, No. 9, 2014, pp. C405–C411.
[28] Pirhady Tavandashti, N., Ghorbani, M., Shojaei, A., Mol, J. M. C., Terryn, H., Baert, K., and Gonzáz-Garcia, Y., "Inhibitor-Loaded Conducting Polymer Capsules for Active Corrosion Protection of Coating Defects," *Corros. Sci.,* Vol. 112, 2016, pp. 138–149.
[29] Gnedenkov, A. S., Sinebryukhov, S. L., Mashtalyar, D. V., and Gnedenkov, S. V., "Localized Corrosion of the Mg Alloys with Inhibitor-Containing Coatings: SVET and SIET Studies," *Corros. Sci.,* Vol. 102, 2016, pp. 269–278.

[30] Sullivan, J., Cooze, N., Gallagher, C., Lewis, T., Prosek, T., and Thierry, D., "In Situ Monitoring of Corrosion Mechanisms and Phosphate Inhibitor Surface Deposition during Corrosion of Zinc–Magnesium–Aluminium (ZMA) Alloys Using Novel Time-Lapse Microscopy," *Faraday Discuss.,* Vol. 180, 2015, pp. 361–379.

[31] Pieretti, E. F., Manhabosco, S. M., Dick, L. F. P., Hinder, S., and Costa, I., "Localized Corrosion Evaluation of the ASTM F139 Stainless Steel Marked by Laser Using Scanning Vibrating Electrode Technique, X-Ray Photoelectron Spectroscopy and Mott-Schottky Techniques," *Electrochim. Acta,* Vol. 124, 2014, pp. 150–155.

[32] Franklin, M. J., White, D. C., and Isaacs, H. S., "Pitting Corrosion by Bacteria on Carbon Steel, Determined by the Scanning Vibrating Electrode Technique," *Corros. Sci.,* Vol. 32, No. 9, 1991, pp. 945–952.

[33] Krawiec, H., Vignal, V., and Oltra, R., "Use of the Electrochemical Microcell Technique and the SVET for Monitoring Pitting Corrosion at MnS Inclusions," *Electrochem. Commun.,* Vol. 6, No. 7, 2004, pp. 655–660.

[34] Raps, D., Hack, T., Wehr, J., Zheludkevich, M. L., Bastos, A. C., Ferreira, M. G. S., and Nuyken, O., "Electrochemical Study of Inhibitor-Containing Organic-Inorganic Hybrid Coatings on AA2024," *Corros. Sci.,* Vol. 51, No. 5, 2009, pp. 1012–1021.

[35] Yasakau, K. A., Zheludkevich, M. L., Karavai, O. V., and Ferreira, M. G. S., "Influence of Inhibitor Addition on the Corrosion Protection Performance of Sol–Gel Coatings on AA2024," *Prog. Org. Coat.,* Vol. 63, No. 3, 2008, pp. 352–361.

[36] Simões, A., Battocchi, D., Tallman, D., and Bierwagen, G., "Assessment of the Corrosion Protection of Aluminium Substrates by a Mg-Rich Primer: EIS, SVET and SECM Study," *Prog. Org. Coat.,* Vol. 63, No. 3, 2008, pp. 260–266.

[37] Simões, A., Battocchi, D., Tallman, D., and Bierwagen, G., "SVET and SECM Imaging of Cathodic Protection of Aluminium by a Mg-Rich Coating," *Corros. Sci.,* Vol. 49, No. 10, 2007, pp. 3838–3849.

[38] McMurray, H. N., Williams, D., and Worsley, D. A., "Artifacts Induced by Large-Amplitude Probe Vibrations in Localized Corrosion Measured by SVET," *J. Electrochem. Soc.,* Vol. 150, No. 12, 2003, pp. B567–B573.

[39] Nanna, M. E. and Bierwagen, G. P., "Mg-Rich Coatings: A New Paradigm for Cr-Free Corrosion Protection of Al Aerospace Alloys," *J. Coat. Technol. Res.,* Vol. 1, No. 2, 2004, pp. 69–81.

[40] Kannan, B., King, A. D., and Scully, J. R., "Effect of Pretreatments on Alloy 2024-T351 Corrosion Protection by Magnesium-Rich, Nonchromium Primer (MgRP): Laboratory Characterization in Full Immersion," *Corrosion,* Vol. 71, No. 9, 2015, pp. 1093–1109.

[41] Kannan, B. and Scully, J. R., "Performance of a Magnesium-Rich Primer on Pretreated AA2024-T351 in Selected Laboratory and Field Environments: Conversion Coating Pretreatments," *Corrosion,* Vol. 72, No. 11, 2016, pp. 1363–1384.

[42] King, A., Lee, J. S., and Scully, J. R., "Galvanic Couple Current and Potential Distribution between a Mg Electrode and 2024-T351 under Droplets Analyzed by Microelectrode Arrays," *J. Electrochem. Soc.,* Vol. 162, No. 1, 2015, pp. C12–C23.

[43] King, A. D., Kannan, B., and Scully, J. R., "Environmental Degradation of a Mg-Rich Primer in Selected Field and Laboratory Environments: Part 2—Primer and Topcoat," *Corrosion,* Vol. 70, No. 5, 2014, pp. 536–557.

[44] Kannan, B., Glover, C. F., McMurray, H. N., Williams, G., and Scully, J. R., "Performance of a Magnesium-Rich Primer on Pretreated AA2024-T351 in Full Immersion: a Galvanic Throwing Power Investigation Using a Scanning Vibrating Electrode Technique," *J. Electrochem. Soc.,* Vol. 165, No. 2, 2018, pp. C27–C41.

[45] Budiansky, N. D., Bocher, F., Cong, H., Hurley, M. F., and Scully, J. R., "Use of Coupled Multi-Electrode Arrays to Advance the Understanding of Selected Corrosion Phenomena," *Corrosion,* Vol. 63, No. 6, 2007, pp. 537–554.

[46] Yang, L., Sridhar, N., Pensado, O., and Dunn, D. S., "An In-Situ Galvanically Coupled Multielectrode Array Sensor for Localized Corrosion," *Corrosion,* Vol. 58, No. 12, 2002, pp. 1004–1014.

[47] Cong, H. and Scully, J. R., "Use of Coupled Multielectrode Arrays to Elucidate the pH Dependence of Copper Pitting in Potable Water," *J. Electrochem. Soc.,* Vol. 157, No. 1, 2010, pp. C36–C46.

[48] Budiansky, N., Hudson, J. L., and Scully, J. R., "Origins of persistent Interaction among Localized Corrosion Sites on Stainless Steel," *J. Electrochem. Soc.,* Vol. 151, No. 4, 2004, pp. B233–B243.

[49] Rafla, V. N., King, A. D., Glanvill, S., Davenport, A., and Scully, J. R., "Operando Assessment of Galvanic Corrosion between Al-Zn-Mg-Cu Alloy and a Stainless Steel Fastener using X-Ray Tomography," *Corrosion,* Vol. 74, No. 1, 2018, pp. 5–23.

[50] Young, P. S. and Payer, J. H., "Stages of Damage Evolution for Al 2024-T3 around Fasteners in Marine Atmosphere," *Corrosion,* Vol. 71, No. 10, 2015, pp. 1278–1293.

[51] Burns, J. T., Kim, S., and Gnagloff, R. P., "Effect of Corrosion Severity on Fatigue Evolution in Al–Zn–Mg–Cu," *Corros. Sci.,* Vol. 52, No. 2, 2010, pp. 498–508.

[52] Holroyd, N., "Environment-Induced Cracking of High-Strength Aluminum Alloys," *Environment-Induced Cracking of Metals*, H. S. Isaacs, Ed., NACE International, Houston, TX, 1990, p. 311–346.

[53] Little, D. A., Connolly, B. J., and Scully, J. R., "An Electrochemical Framework to Explain the Intergranular Stress Corrosion Behavior in Two Al–Cu–Mg–Ag Alloys as a Function of Aging," *Corros. Sci.,* Vol. 49, No. 2, 2007, pp. 347–372.

[54] Turnbull, A., "The Environmentally Small/Short Crack Growth Effect: Current Understanding," *Corros. Rev.,* Vol. 30, Nos. 1–2, 2012, pp. 1–17.

[55] Wang, S.-S., Frankel, G. S., Jiang, J.-T., Chen, J.-F., Dai, S.-L., and Zhen, L., "Mechanism of Localized Breakdown of 7000 Series Aluminum Alloys," *J. Electrochem. Soc.,* Vol. 160, No. 10, 2013, pp. C493–C502.

[56] Connolly, B. J., Horner, D. A., Fox, S. J., Davenport, A. J., Padovani, C., Zhou, S., Turnbull, A., et al., "X-Ray Microtomography Studies of Localized Corrosion and Transitions to Stress Corrosion Cracking," *Materials Sci. Tech.,* Vol. 22, No. 9, 2006, pp. 1076–1085.

[57] Knight, S. P., Salagaras, M., and Trueman, A. R., "The Study of Intergranular Corrosion in Aircraft Aluminium Alloys Using X-Ray Tomography," *Corros. Sci.,* Vol. 53, No. 2, 2011, pp. 727–734.

[58] Knight, S. P., Salagaras, M., Wythe, A. M., De Carlo, F., Davenport, A. J., and Trueman, A. R., "In Situ X-Ray Tomography of Intergranular Corrosion of 2024 and 7050 Aluminium Alloys," *Corros. Sci.,* Vol. 52, No. 12, 2010, pp. 3855–3860.

[59] Rafla, V., Davenport, A., and Scully, J. R., "Determination of Cathodic and Anodic Charge from Operando X-Ray Tomography Observation of Galvanic Corrosion of Aluminum Alloy 7050-T7451 and 304 Stainless Steel in a Simulated Fastener," *Corrosion,* Vol. 71, No. 11, 2015, pp. 1300–1303.

[60] Rafla, V., King, A. D., Glanvill, S., Parsons, A., Davenport, A., and Scully, J. R., "Operando Observation of Galvanic Corrosion Between Aluminum Alloy 7050-T7451 and 304 Stainless Steel in a Simulated Fastener Arrangement Using X-Ray Tomography," *Corrosion,* Vol. 71, No. 10, 2015, pp. 1171–1176.

[61] Birbilis, N. and Buchheit, R. G., "Investigation and Discussion of Characteristics for Intermetallic Phases Common to Aluminum Alloys as a Function of Solution pH," *J. Electrochem. Soc.,* Vol. 155, No. 3, 2008, pp. C117–C126.

[62] Buchheit, R., Martinez, M. A., and Montes, L. P., "Evidence for Cu Ion Formation by Dissolution and Dealloying the Al2CuMg Intermetallic Compound in Rotating Ring-Disk Collection Experiments," *J. Electrochem. Soc.,* Vol. 147, No. 1, 2000, pp. 119–124.

[63] Vukmirovic, M. B., Dimitrov, N., and Sieradzki, K., "Dealloying and Corrosion of Al Alloy 2024 T 3," *J. Electrochem. Soc.,* Vol. 149, No. 9, 2002, pp. B428–B439.

[64] Xu, D. K., Birbilis, N., and Rometsch, P. A., "Effect of S-Phase Dissolution on the Corrosion and Stress Corrosion Cracking of an As-Rolled Al–Zn–Mg–Cu Alloy," *Corrosion,* Vol. 68, No. 3, 2012, http://dx.doi.org/10.5006/1.3688501

[65] Kwak J. and Bard, A. J., "Scanning Electrochemical Microscopy. Theory of the Feedback Mode," *Anal. Chem.,* Vol. 61, No. 11, 1989, pp. 1221–1227.

[66] Luo, H., Li, X. G., Dong, C. F., and Xiao, K., "Effect of Solution Treatment on Pitting Behavior of 2205 Duplex Stainless Steel," *Arab. J. Chem.,* Vol. 10, Suppl. 1, 2017, pp. S90–S94.

[67] González-Garcia, Y., Burstein, G. T., González, S., and Souto, R. M., "Imaging Metastable Pits on Austenitic Stainless Steel In Situ at the Open-Circuit Corrosion Potential," *Electrochem. Commun.,* Vol. 6, No. 7, 2004, pp. 637–642.

[68] Izquierdo, J., Nagy, L., Bitter, I., Souto, R. M., and Nagy, G., "Potentiometric Scanning Electrochemical Microscopy for the Local Characterization of the Electrochemical Behaviour of Magnesium-Based Materials," *Electrochim. Acta,* Vol. 87, 2013, pp. 283–293.

[69] Davoodi, A., Pan, J., Leygraf, C., and Norgren, S., "Integrated AFM and SECM for In Situ Studies of Localized Corrosion of Al Alloys," *Electrochim. Acta,* Vol. 52, 2007, pp. 7697–7705.

[70] Yuan, Y., Li, L., Wang, C., and Zhu, Y., "Study of the Effects of Hydrogen on the Pitting Processes of X70 Carbon Steel with SECM," *Electrochem. Commun.,* Vol. 12, No. 12, 2010, pp. 1804–1807.

[71] Gabrielli, C., Joiret, S., Keddam, M., Perrot, H., Portail, N., Rousseau, P., and Vivier, V., "Development of a Coupled SECM-EQCM Technique for the Study of Pitting Corrosion on Iron," *J. Electrochem. Soc.,* Vol. 153, No. 3, 2006, pp. B68–B74.

[72] Still, J. W. and Wipf, D. O., "Breakdown of the Iron Passive Layer by Use of the Scanning Electrochemical Microscope," *J. Electrochem. Soc.,* Vol. 144, No. 8, 1997, pp. 2657–2665.

[73] Casillas, N., Charlebois, S. J., Smyrl, W. H., and White, H. S., "Scanning Electrochemical Microscopy of Precursor Sites for Pitting Corrosion on Titanium," *J. Electrochem. Soc.,* Vol. 140, No. 9, 1993, pp. L142–L145.

[74] Andreatta, F., Terryn, H., and de Wit, J. H. W., "Effect of Solution Heat Treatment on Galvanic Coupling between Intermetallics and Matrix in AA7075-T6," *Corros. Sci.,* Vol. 45, No. 8, 2003, pp. 1733–1746.

[75] Souto, R. M., González-Garcia, Y., Battistel, D., and Daniele, S., "On the Use of Mercury-Coated Tips in Scanning Electrochemical Microscopy to Investigate Galvanic Corrosion Processes Involving Zinc and Iron," *Corros. Sci.,* Vol. 55, 2012, pp. 401–406.

[76] Tefashe, U. M., Dauphin-Ducharme, P., Danaie, M., Cano, Z. P., Kish, J. R., Botton, G. A., and Mauzeroll, J., "Localized Corrosion Behavior of AZ31B Magnesium Alloy with an Electrodeposited Poly (3, 4-Ethylenedioxythiophene) Coating," *J. Electrochem. Soc.,* Vol. 162, No. 10, 2015, pp. C536–C544.

[77] Souto, R., González-Garcia, Y., González, S., and Burstein, G. T., "Imaging the Origins of Coating Degradation and Blistering Caused by Electrolyte Immersion Assisted by SECM," *Electroanal.,* Vol. 21, No. 23, 2009, pp. 2569–2574.

[78] Souto, R. M., González-García, Y., Izquierdo, J., and González, S., "Examination of Organic Coatings on Metallic Substrates by Scanning Electrochemical Microscopy in Feedback Mode: Revealing the Early Stages of Coating Breakdown in Corrosive Environments," *Corros. Sci.,* Vol. 52, No. 3, 2010, pp. 748–753.

[79] González-García, Y., Mol, J. M. C., Muselle, T., De Graeve, I., Van Assche, G., Scheltzens, G., Van Mele, B., and Terryn, H., "SECM Study of Defect Repair in Self-Healing Polymer Coatings on Metals," *Electrochem. Commun.,* Vol. 13, No. 2, 2011, pp. 169–173.

[80] Lu, X., Zuo, Y., Zhao, X., and Tang, Y., "The Improved Performance of a Mg-Rich Epoxy Coating on AZ91D Magnesium Alloy by Silane Pretreatment," *Corros. Sci.,* Vol. 60, 2012, pp. 165–172.

[81] Bierwagen, G., Brown, R., Battocchi, D., and Hayes, S., "Active Metal-Based Corrosion Protective Coating Systems for Aircraft Requiring No-Chromate Pretreatment," *Prog. Org. Coat.,* Vol. 67, No. 2, 2010, pp. 195–208.

[82] Asmussen, R. M., Binns, W. J., Jakupi, P., Dauphin-Ducharme, P., Tefashe, U. M., Mauzeroll, J., and Shoesmith, D., "Reducing the Corrosion Rate of Magnesium Alloys Using Ethylene Glycol for Advanced Electrochemical Imaging," *Corros. Sci.,* Vol. 93, 2015, pp. 70–79.

[83] Bland, L. G., Schaller, R. F., and Scully, J. R., "Utilization of a Partially Non-Aqueous Electrolyte for the Spatial Mapping of Mg Corrosion Using a Model Mg–Al Electrode," *Magnesium Technology 2017*, K. N. Solanki, D. Orlov, A. Singh, and N. R. Neelameggham, Eds., Springer, Cham, Switzerland, 2017, pp. 421–428.

[84] Mirkin, M. V., Fan, F.-R. F., and Bard, A. J., "Scanning Electrochemical Microscopy Part 13. Evaluation of the Tip Shapes of Nanometer Size Microelectrodes," *J. Electroanal. Chem.,* Vol. 328, Nos. 1–2, 1992, pp. 47–62.

[85] Dauphin-Ducharme, P., Asmussen, R. M., Tefashe, U. M., Danaie, M., Binns, W. J., Jakupi, P., Botton, G. A.,Shoesmith, D. W., and Mauzeroll, J., "Local Hydrogen Fluxes Correlated to Microstructural Features of a Corroding Sand Cast AM50 Magnesium Alloy," *J. Electrochem. Soc.,* Vol. 161, No. 12, 2014, pp. C557–C564.

[86] Bard, A. J., Fan, F.-R. F., Kwak, J., and Lev, O., "Scanning Electrochemical Microscopy. Introduction and Principles," *Anal. Chem.,* Vol. 61, No. 2, 1989, pp. 132–138.

[87] Zhou, J., Zu, Y., and Bard, A. J., "Scanning Electrochemical Microscopy: Part 39. The Proton/Hydrogen Mediator System and Its Application to the Study of the Electrocatalysis of Hydrogen Oxidation," *Electroanal. Chem.,* Vol. 491, Nos. 1–2, 2000, pp. 22–29, https://dx.doi.org/10.1016/S0022-0728(00)00100-5

[88] Kwak, J. and Bard, A. J., "Scanning Electrochemical Microscopy," *Anal. Chem.,* Vol. 61, No. 17, 1989, pp. 1794–1799.

[89] Bertoncello, P., "Advances on Scanning Electrochemical Microscopy (SECM) for Energy," *Energ. Environ. Sci.,* Vol. 3, No. 11, 2010, pp. 1620–1633.

[90] Bland, L. G., Rincon Troconis, B. C., Santucci, R. J., Jr., Fitz-Gerald, J. M., and Scully, J. R., "Metallurgical and Electrochemical Characterization of the Corrosion of AZ31B-H24 Tungsten Inert Gas Weld: Isolated Weld Zones," *Corrosion,* Vol. 72, No. 10, 2016, pp. 1116–1132.

[91] Gharbi, O., Birbilis, N., and Ogle, K., "In-Situ Monitoring of Alloy Dissolution and Residual Film Formation during the Pretreatment of Al-Alloy AA2024-T3," *J. Electrochem. Soc.,* Vol. 163, No. 5, 2016, pp. C240–C251.

[92] Ogle, K., Mokaddem, M., and Volovitch, P., "Atomic Emission Spectroelectrochemistry Applied to Dealloying Phenomena II. Selective Dissolution of Iron and Chromium during Active–Passive Cycles of an Austenitic Stainless Steel," *Electrochim. Acta,* Vol. 55, No. 3, 2010, pp. 913–921.

[93] Ogle, K., Tomandl, A., Meddahi, N., and Wolpers, M., "The Alkaline Stability of Phosphate Coatings I: ICP Atomic Emission Spectroelectrochemistry," *Corros. Sci.,* Vol. 46, No. 4, 2004, pp. 979–995.

[94] Zhou, P., Hutchison, M. J., Scully, J. R., and Ogle, K., "The Anodic Dissolution of Copper Alloys: Pure Copper in Synthetic Tap Water," *Electrochim. Acta,* Vol. 191, 2016, pp. 548–557.

[95] Shkirskiy, V., Maltseva, A., Ogle, K., and Volovitch, P., "Environmental Effects on Selective Dissolution from ZnAlMg Alloy under Low Frequency Alternating Current Perturbations," *Electrochim. Acta,* Vol. 238, 2017, pp. 397–409.

[96] Mokaddem, M., Volovitch, P., Rechou, F., Oltra, R., and Ogle, K., "The Anodic and Cathodic Dissolution of Al and Al-Cu-Mg Alloy," *Electrochim. Acta,* Vol. 55, No. 11, 2010, pp. 3779–3786.

[97] Duarte, M. J., Klemm, J., Klemm, S. O., Mayrhofer, K. J. J., Stratmann, M., Borodin, S., Romero, A. H., et al. "Element-Resolved Corrosion Analysis of Stainless-Type Glass-Forming Steels," *Science,* Vol. 341, No. 6144, 2013, pp. 372–376.

[98] Horton, D. J. and Scully, J. R., "The Effect of the Amorphous and Crystalline States on Preferential Corrosion of Hf from a Cu75Hf20Dy05 Alloy," *Metall. Mater. Trans. A,* Vol. 43, No. 8, 2012, pp. 2706–2720.

[99] Hutchison, M. J., Zhou, P., Ogle, K., and Scully, J. R., "Enhanced Electrochemical Cu Release from Commercial Cu-Sn Alloys: Fate of the Alloying Elements in Artificial Perspiration," *Electrochim. Acta,* Vol. 241, 2017, pp. 73–88.

[100] Volovitch, P., Serdechnova, M., and Ogle, K., "Aqueous Corrosion of Mg-Al Binary Alloys: Roles of Al and Mg," *Corrosion,* Vol. 68, No. 6, 2012, pp. 557–570.

[101] Vu, T. N., Mokaddem, P., Volovitch, P., and Ogle, K., "The Anodic Dissolution of Zinc and Zinc Alloys in Alkaline Solution. II. Al and Zn Partial Dissolution from 5% Al-Zn Coatings," *Electrochim. Acta,* Vol. 74, 2012, pp. 130–138.

[102] Jiang, L., Volovitch, P., Sundermeier, U., Wolpers, M., and Ogle, K., "Dissolution and Passive Film Formation of Sn and Sn Coated Steel Using Atomic Emission Spectroelectrochemistry," *Electrochim. Acta,* Vol. 58, 2011, pp. 322–329.

[103] Shkirskiy, V., King, A. D., Gharbi, O., Volovitch, P., Scully, J. R., Ogle, K., and Birbilis, N., "Revisiting the Electrochemical Impedance Spectroscopy of Magnesium with Online Inductively Coupled Plasma Atomic Emission Spectroscopy," *ChemPhysChem,* Vol. 16, No. 3, 2014, pp. 536–539.

[104] Laurent, B., Gruet, N., Gwinner, B., Miserque, F., Rousseau, K., and Ogle, K., "Dissolution and Passivation of a Silicon-Rich Austenitic Stainless Steel during Active-Passive Cycles in Sulfuric and Nitric Acid," *J. Electrochem. Soc.,* Vol. 164, No. 13, 2017, pp. C892–C900.

[105] Shkirskiy, V., Maciel, P., Deconinck, J., and Ogle, K., "On the Time Resolution of the Atomic Emission Spectroelectrochemistry Method," *J. Electrochem. Soc.,* Vol. 163, No. 3, 2016, pp. C37–C44.

[106] Michels, H., Moran, W., and Michel, J., "Antimicrobial Properties of Copper Alloy Surfaces, with a Focus on Hospital-Acquired Infections," *Int. J. Metalcast.,* Vol. 2, No. 3, 2008, pp. 47–56.

STP 1609, 2019 / available online at www.astm.org / doi: 10.1520/STP160920170227

Andrew Fahim,[1] Pouria Ghods,[2] Rouhollah Alizadeh,[2]
Mustafa Salehi,[2] and Sarah Decarufel[2]

CEPRA: A New Test Method for Rebar Corrosion Rate Measurement

Citation

Fahim, A., Ghods, P., Alizadeh, R., Salehi, M., and Decarufel, S., "CEPRA: A New Test Method for Rebar Corrosion Rate Measurement," *Advances in Electrochemical Techniques for Corrosion Monitoring and Laboratory Corrosion Measurements*, *ASTM STP1609*, S. Papavinasam, R. B. Rebak, L. Yang, and N. S. Berke, Eds., ASTM International, West Conshohocken, PA, 2019, pp. 59–80, http://dx.doi.org/10.1520/STP160920170227[3]

ABSTRACT

The corrosion rate of rebar in concrete traditionally has been determined using polarization methods such as the potentiodynamic technique, galvanostatic pulse technique, potentiostatic pulse technique, and, in some cases, the electrochemical impedance spectroscopy technique in laboratory applications. These techniques are very slow, and all require having an electrical connection to the rebar, which makes them impractical in the field. In this paper, the recently developed technique of Connectionless Electrical Pulse Response Analysis (CEPRA) will be introduced. The CEPRA method, which eliminates the need to have a rebar connection, is based on the concept that the voltage response of the corroding rebar is different from that of the noncorroding rebar once subjected to variable frequencies of an AC current applied on the concrete surface using the four-probe Wenner array configuration. However, direct measurement of the low-frequency impedance of rebar in concrete is very time-consuming and vulnerable to noise interruption; hence, in the CEPRA method, a narrow current pulse is applied for a short period of time (for a couple of seconds). Using the recorded voltage and the applied current, the low-frequency

Manuscript received November 10, 2017; accepted for publication May 15, 2018.
[1]Dept. of Civil Engineering, University of New Brunswick, 17 Dineen Dr. #B 19, Fredericton, NB, E3B 5A3, Canada http://orcid.org/0000 0002 6210 2390
[2]Giatec Scientific Inc., 245 Menten Place, Suite 300, Nepean, ON, K2H 9E8, Canada
[3]ASTM Symposium on *Advances in Electrochemical Techniques for Corrosion Monitoring and Laboratory Corrosion Measurements* on November 13 14, 2017 in Atlanta, GA, USA.

impedance response of rebar in concrete can be extracted, which can be used to determine the state of corrosion in reinforced concrete structures. The details of the CEPRA technique and equivalent electrical circuit models will be discussed in this paper. Laboratory and finite element modeling results will be presented to compare the traditional corrosion rate measurement techniques with the CEPRA method.

Keywords
corrosion monitoring, rebar corrosion, concrete durability, nondestructive testing, connectionless corrosion monitoring, CEPRA

Introduction

In recent decades, several nondestructive electrochemical techniques were developed to monitor the corrosion rate of steel embedded in concrete. Such techniques rely on the method of determining the polarization resistance of metallic electrodes subjected to an electrochemical potential excitation. The polarization resistance theory was coined by Stern and Geary [1] and has been widely used to monitor instantaneous corrosion rates. These techniques are based on the assumption that there is a linear relationship between a small polarization around the electrode's open circuit potential (ΔE less than 20 mV) and the current required to induce this potential shift (ΔI). In such cases, the polarization resistance (R_p) is calculated as the ratio of the shift in potential (from open circuit potential) to the polarizing current used to induce this potential shift. By determining R_p, the corrosion rate (i_{corr}), in $\mu A/cm^2$, can be calculated using the Stern and Geary equation shown in Eq 1 [1]:

$$i_{corr} = \frac{\beta}{AR_p} \tag{1}$$

where:
β = Tafel constant (in mV),
A = area polarized by the applied current (in cm^2), and
R_p = ratio of the change in voltage to the change in current, (in ohms).

The typical method of determining the polarization resistance includes connecting a device that uses one of the potential perturbing methods (e.g., the potentiostatic technique) to the rebar network. This is done through inducing damage to the concrete cover in order to establish such a connection. The aforementioned device then measures the electrode's open circuit potential and applies a certain prespecified amount of current, or a potential shift, to polarize the reinforcement network. Subsequently, the potential response following the application of this polarizing current is monitored and fitted to the theoretical response of circuits representing the reinforced concrete system (typically, the Randles circuit) in order to determine the polarization resistance. This method has been frequently applied in laboratory studies and research applications [2–5]. However, it has not been widely used for field applications in the civil engineering community due to the following

reasons: (1) The concrete cover has to be damaged in order to establish a connection to the rebar network; (2) the polarized area has been a large source of uncertainty, even with the use of the so called guard ring electrodes, especially in cases of macrocell corrosion and passive reinforcements [6 9]; (3) a number of these techniques, such as electrochemical impedance spectroscopy (EIS), are very time consuming; and (4) existing techniques that do not require a long measurement time (e.g., certain commercial devices implementing the galvanostatic pulse technique with a measurement time of 10 s) do not provide reliable results for the passive cases due to the large amount of time required for passive electrodes to reach quasi steady state conditions [10].

In recent years, a number of studies have observed that the reinforcement network can be polarized through the application of an external polarization such as that typical of the case of using a Wenner array probe in the vicinity of a reinforcement [11 14]. The earliest work on this method was reported by Monteiro, Morrison, and Frangos [11], in which the authors demonstrated that when an experimental setup similar to that of a Wenner probe is used in the reinforcement vicinity, and the applied current from the two outer probes is swept from very high to very low frequencies, the frequency dependent characteristics of the interface are reflected in the complex ratio of potential difference between the inner electrodes to the applied current. This concept was further developed in [12,15,16], and by using this connectionless method, results were obtained that were qualitatively similar to those of classical EIS measurements. However, these studies also showed that the results obtained through such a method do not directly reflect the actual impedance of the system. The obtained results were found to be directly affected by the relative direction between the Wenner array and the reinforcing bar, the probes' spacing, the concrete cover depth, and the concrete resistivity [12,15,16]. This is because a portion of the current, applied by the outer probes of the Wenner array, flows explicitly through the electrolyte/concrete and another portion polarizes the reinforcement. The current polarizing the reinforcement depends on the aforementioned factors and cannot be directly determined. Furthermore, the obtained potential difference between the two inner probes in such a setup is not directly the potential shift exhibited by the working electrode. Several studies [13,14,17] have shown that the polarization resistance can be obtained through such a method if the concrete resistivity is known. This is because a knowledge of the concrete resistivity provides a measure of the amount of current flowing explicitly in the electrolyte/concrete as opposed to that polarizing the electrode.

The Connectionless Electrical Pulse Response Analysis (CEPRA) Technique

Although the aforementioned studies clearly indicate the applicability of this method, the experimental and analytical procedures used in the CEPRA technique are rather different. In typical DC measurements of the polarization resistance, the

steel concrete system is represented, simplistically, as a Randles circuit. If an AC current, at a wide range of frequencies, is applied to this circuit (similar to typical EIS measurements) and the potential response is monitored, then the circuit components can be analyzed by observing the changes in real impedance, imaginary impedance, and phase shifts [6]. In the case of the Randles circuit, in the very high frequency range, the impedance caused by the double layer capacitance tends to reach negligible values, and this double layer acts as a short circuiting element, leading to most of the current flowing through the electrolyte/concrete resistance and the short circuit caused by the double layer capacitance. Therefore, at the very high frequency ranges, the electrolyte/concrete resistance can be measured directly as the impedance modulus. At the very low frequency ranges, the impedance caused by the double layer capacitance tends to reach very high values, leading to most of the current flowing through the electrolyte/concrete resistance and the polarization resistance. Therefore, at the low frequency range, their summation can be found directly as the impedance modulus.

In the connectionless technique, there is a higher system complexity. If a current pulse or a step voltage is applied from the two outer probes of a Wenner probe, this current has two primary flow paths. One path is normal to the metallic electrode, which causes the charging of the double layer capacitance or the polarization of the electrode (depending on the frequency of the applied current); another path is parallel to the metallic electrode, in which the current applied by one of the probes is consumed by the other. The portion of current flowing in each of these paths is dependent on the applied current's frequency, the concrete cover characteristics (cover depth and resistivity), the polarization resistance value, the rebar diameter, and the double layer capacitance. These are all interrelated factors that affect the current flow path and the obtained results. This system can be represented schematically using the circuit model shown in Fig. 1.

FIG. 1 Circuit model used to represent the CEPRA technique.

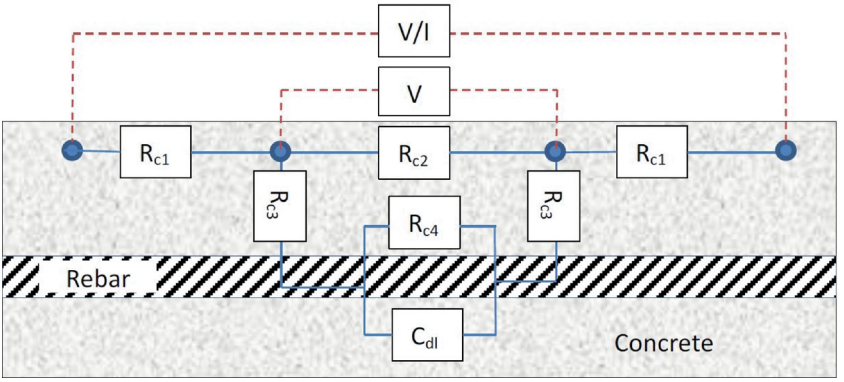

In this case, R_{c1} represents the probes' contact resistance, and all of the current is faced by this resistance. This approach clearly identifies the two major current flow paths in the concrete medium through R_{c2} and R_{c3}, where R_{c2} represents the current flow path between the two probes (the path not polarizing the rebar) and R_{c3} repre sents the current flow path that polarizes the rebar or charges the double layer capac itance. The magnitude of current passing by each of these resistors is dependent on (1) the magnitude of their resistance, (2) the impedance caused by the capacitance or the extent of charging of this capacitance, (3) the magnitude of the polarization resis tance, (4) the concrete cover depth and reinforcement diameter, and (5) the frequen cy of the applied current. This circuit can be solved in order to determine the polarization resistance (R_{c4} in Fig. 1) if the current applied from the two outer probes is swept from very high to very low frequencies. However, this is a very time consuming measurement that may take several minutes to a few hours depending on the circuit's time constant. Alternatively, the components of this system can be retrieved if the response (i.e., voltage difference between the two inner probes) to a narrow DC/AC current or voltage pulse applied from the outer probes for a short period of time is fitted to the theoretical transient obtained from this circuit. In these cases, the measured voltage response as a factor of time is similar to that of a charging RC circuit, as shown in Eq 2, assuming that the electrolyte/concrete capacitance is negligible (same assumption as that in all of the other monitoring techniques)

$$V_{in}(t) = V_{ex}\left(A - Be^{-Dt}\right) \tag{2}$$

where:

V_{ex} = constant voltage applied through the external electrodes and

V_{in} = potential difference measured between the two inner electrodes.

The model shown in Fig. 1 was solved in order to determine the variables A, B, and D. It was found that these variables follow functions shown in Eqs 3–5. By mea suring the voltage response over time, A, B, and D can be calculated by fitting Eq 2 to the measured data. These factors can then be used to calculate the circuit compo nents shown in Fig. 1. This solution approach is rather complicated compared to the Randles circuit used by all of the other techniques or that used in Andrade and Martínez [13]. However, such a circuit can be solved using more complicated solu tion procedures if the cover depth is known. This is because the cover depth pro vides an indirect measure of the ratio of current flowing through R_{c2} to that flowing through R_{c3}.

$$A = f(R_{c1}, R_{c2}, R_{c3}, R_{c4}) \tag{3}$$

$$B = g(R_{c1}, R_{c2}, R_{c3}, R_{c4}) \tag{4}$$

$$D = h(R_{c1}, R_{c2}, R_{c3}, R_{c4}, C_{dl}) \tag{5}$$

The commercial device used to implement this technique uses a four probe Wenner array with an electrode spacing of 50 mm. The outer probes are used to apply a narrow DC/AC step voltage for a short period of time (6 s in this study), and the

potential difference between the two inner probes is simultaneously monitored with a relatively high sampling rate. The current applied in this setup is typically in the range of 0.5 to 2 mA, depending on concrete resistivity and cover depth. (Note that this is not the polarizing current because a large portion of this applied current flows explicitly inside the concrete between the two outer probes, as will be demon strated later.) The obtained transient is then fitted to Eq 2 to yield the constants *A*, *B*, and *D*, which are used to calculate the system components shown in **Fig. 1**.

Experimental Methods

A total of 16 reinforced concrete blocks were cast for this portion of the study. The blocks, presented in **Fig. 2**, were each 300 mm (L) by 300 mm (W) by 100 mm (H) and were reinforced with two black steel reinforcements at the same cover depth. The concrete mix design used is shown in **Table 1**. This mixture was selected to obtain relatively high corrosion activity on the reinforcements in a short time due to the higher permeability and lower resistivity of this concrete. Four dosages of admixed chlorides were used in this test to provide a wide range of corrosion activity and concrete resistivity. The admixed chloride dosages were 0 %, 1.5 %, 3 %, and 6 % by weight of cement. For each of the admixed chloride percentages, four blocks were cast with the mix design shown in **Table 1**. Three of these blocks had rebar at different cover depths (each block had two reinforcements at either 20, 40, or 70 mm cover

FIG. 2 Schematic representation of the test blocks.

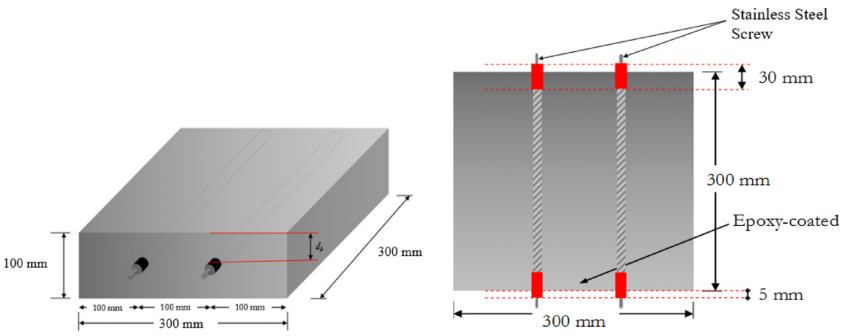

TABLE 1 Mix design used for the laboratory test blocks.

Constituent	Amount (kg/m^3)
GU cement	265
Coarse aggregate (<19 mm)	1,055
Fine aggregate	940
Water	165

Note: GU = general use.

depth) in which 10M rebar was used (nominal diameter = 11.3 mm). For the fourth block, 20M rebar (nominal diameter = 19.5 mm) was used with 40 mm of cover depth to study the effect of reinforcement area on the results.

Thirty two reinforcements were prepared for this study for the 16 blocks outlined. The end 3 cm of the reinforcements was epoxy coated to prevent atmospheric corro sion and contamination from the exposure to the atmosphere at the part of the rein forcement protruding from the concrete. The reinforcements were then thoroughly sandblasted to remove any prior corrosion by products or mill scale. Finally, all of the reinforcements were weighed and the weight was recorded to the nearest 0.01 g.

Four molds were prepared allowing for the three blocks with different cover depths and the block with 20M reinforcement to be cast at once with the same concrete mix ture. Four concrete mixtures, shown in Table 1, were conducted, with each mix incorpo rating a different percentage of admixed chlorides (0 %, 1.5 %, 3 %, and 6 % by weight of cement). The concrete was cast in accordance with ASTM C192, *Standard Practice for Making and Curing Concrete Test Specimens in the Laboratory* [18]. Casting was done in two layers, with each layer tamped 30 times. The surface was finished using a steel trowel, and specimens were covered with wet burlap and wrapped in plastic for 24 h. Specimens were then removed from the formwork after 1 day and placed into a sealed container with an approximately 3 cm deep layer of water to ensure the avail ability of the required moisture for corrosion propagation.

Weekly corrosion rate measurements were taken on all of the slabs using the CEPRA technique. After 7 months, the specimens were removed from the contain ers and left to dry for a month during which time measurements were taken weekly to analyze the effect of the increased resistivity on the results. At the end of the expo sure period (a total of 8 months), reinforcements were extruded by inducing a longitu dinal crack along the reinforcement using a jackhammer. The mass loss of the reinforcements was found according to Procedure C.3.5 of ASTM G1, *Standard Practice for Preparing, Cleaning, and Evaluating Corrosion Test Specimens* [19].

Finite Element Modeling

In order to study the current propagation behavior and the time dependent poten tial response during the application of the CEPRA technique, a finite element model was developed. This section deals with the model formulation, constitutive relation ships, input parameters, and parameters studied.

CONSTITUTIVE RELATIONSHIPS

In order to model the polarization behavior of the reinforcement, Faradaic and capacitive processes were assumed to apply at the steel surface. The electrochemical Faradaic kinetics governing the polarization behavior occurring at the reinforce ment surface can be modeled with the use of the Butler Volmer equation shown in Eq 6 [20]:

$$j = j_o\left(10^{\frac{\eta}{b_a}} - 10^{\frac{-\eta}{b_c}}\right) \tag{6}$$

where:
j = net current density,
j_o = exchange current density,
η = change in potential (Φ) from the equilibrium potential (Φ_{eq}) of the electrode (Φ Φ_{eq}),
b_a = anodic Tafel coefficient, and
b_c = cathodic Tafel coefficient.

The effects of the charge storage process (caused by the double layer capaci tance) can be incorporated into the model assuming that the electrode surface behaves as a perfect capacitor during the charge storage or release process. The cor responding current charge/discharge at any time for such a capacitor can be repre sented as shown in Eq 7 [21]:

$$j_{cap} = C_{dl}\frac{\partial E}{\partial t} \tag{7}$$

where:
C_{dl} = electrode's double layer capacitance and
$\partial E/\partial t$ = change in potential with respect to time.

Using this approach, the current at the steel concrete interface after the appli cation of a polarizing current is the sum of the Faradaic process (Butler Volmer kinetics) and the capacitive currents. The total time dependent current can then be expressed as shown in Eq 8 [21]:

$$j = j_o\left(10^{\frac{\eta}{b_a}} - 10^{\frac{\eta}{b_c}}\right) + C_{dl}\frac{\partial E}{\partial t} \tag{8}$$

In order to solve for the potential and current density distribution at the surface of the reinforcement, assuming electrical charge conservation and isotropic con ductivity, Ohm's law, shown in Eq 9, and charge conservation law, shown in Eq 10, are used for the concrete domain, assuming that concrete is a homogeneous medium with a uniform electrical resistivity [22]:

$$j = \frac{-1}{\rho}\nabla E \tag{9}$$

$$\nabla j = 0 \tag{10}$$

where:
j = current density (A/m^2),
∇E = potential gradient, and
ρ = resistivity of the concrete medium (Ohm.m).

FINITE ELEMENT MODELING PROCEDURE

Three dimensional simulations were performed using a COMSOL® 5.2 software package (COMSOL Group, Stockholm, Sweden). The domain of the problem, shown in **Fig. 3**, was chosen to represent a reinforced concrete member 1 m in length, 0.3 m in width, and 0.2 m in height, with a rebar embedded at a certain

FIG. 3 Domain of the finite element model: (a) reinforcement surface, (b) concrete domain, (c) external boundaries, and (d) Wenner probe.

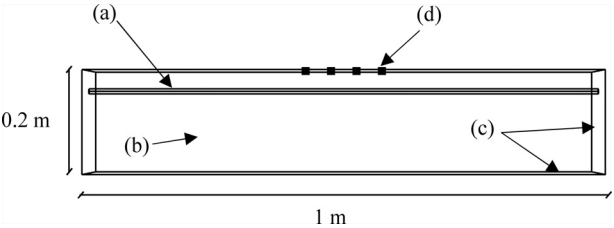

cover depth (variable parameter). At the steel concrete interface (boundary *a*), Eq 8 was used as a Dirichlet type boundary condition to find the time dependent polarization behavior of the electrode. In the concrete domain (domain *b*), Eq 9 and Eq 10 were used to solve for the potential and current density distributions. External boundaries (boundary *c*) were modeled as electrically insulated boundaries (Neumann boundary conditions with a specified normal current of zero). The CEPRA technique was modeled as a Wenner array, with four probes having a probe spacing of 50 mm in which the two outer probes were used to apply a current of 0.5 and −0.5 mA. The potential difference between the two inner probes was recorded using the CEPRA technique. The four probes were modeled as perfect point objects.

Solutions were performed using a MUMPS solver (MUltifrontal Massively Parallel Sparse direct Solver) inputted in the software (COMSOL Group, Stockholm, Sweden). This solver makes use of the multifrontal method Gaussian elimination and is based on the lower upper decomposition matrix solving procedure. It should be noted, however, that other solvers available in the software were tried and their solutions were identical for the problem under consideration. However, the primary difference was the convergence time. The relative tolerance used was 0.001.

In such a system, the summation of the current at the reinforcement surface and at the two current applying electrodes is expected to be zero. This was used in order to discretize the mesh and minimize errors due to the mesh elements' size and approximations [23]. This was conducted by trying several different mesh combinations for the concrete domain and the three different boundaries shown in Fig. 3 until the summation of current was negligible (less than 0.1 % of the applied current). It was found that the optimum mesh configuration varies greatly depending on the cover depth (due to the distance between the reinforcement surface boundary and external boundary) and concrete resistivity (due to potential gradients being different in high resistivity systems compared to low resistivity systems), among other factors.

MODEL INPUTS AND INVESTIGATED PARAMETERS

The model was solved for cases representing passive reinforcements and cases representing actively corroding reinforcements. This was done by changing the input

parameters in the Butler Volmer equation according to Table 2. The anodic and cathodic beta coefficients for the active case were chosen to yield a beta coefficient of 26 mV, which is the value typically used for corrosion in reinforcing steel studies [24]. The exchange current density for the active case was adapted from that used by Marchand et al. [25] for the same purpose of this study. However, the effect of this parameter was studied separately. The exchange current density for the passive cases was adapted from the model outlined by Pour Ghaz, Isgor, and Ghods [22]. The beta coefficients for the passive case were chosen to yield a beta coefficient close to 52 mV, which is the value typically used for corrosion of reinforcing steel studies [24]. The anodic beta coefficient for the passive case also reflects passivation control and the ineffectiveness of anodic potential polarizations in increasing the anodic current for the passive case. This number is based on the mean value obtained in experimental work done by the authors, which will be presented in a subsequent paper. The equilibrium potentials were obtained from Pour Ghaz, Isgor, and Ghods [22]. For each of the passive and active cases, the parameters were studied as shown in Table 3.

Experimental Results

Fig. 4 presents the corrosion rate measurements collected by this method throughout the exposure period. The presented results are averages of two replicate reinforcements embedded in the same concrete specimen. It is evident that the method was able to capture the effect of admixed chloride contents on the measured corrosion rates. The rebar specimens embedded in chloride free concrete showed the

TABLE 2 Model inputs for active and passive cases.

Input	Passive Case Parameters	Active Case Parameters
j_o	10^{-5} A/m^2	0.1 A/m^2
b_a	5 V	0.12 V
b_c	0.12 V	0.12 V
Φ_{eq}	0.16 V	0.78 V
C_{dl}	Variable	Variable

TABLE 3 Parameters investigated.

Independent Variable	Cases
Cover depth	20, 40, 70, and 100 mm
Resistivity	20, 50, 100, 200, 500, and 1,000 ohm.cm
Reinforcement diameter	10, 20, and 30 mm
i_o (for the active case)	0.01, 0.05, 0.1, and 0.5 A/m^2

FIG. 4 Corrosion rate measurements obtained throughout the exposure period for rebar with a: (a) 20 mm cover, (b) 40 mm cover, (c) 70 mm cover, and (d) 20M diameter.

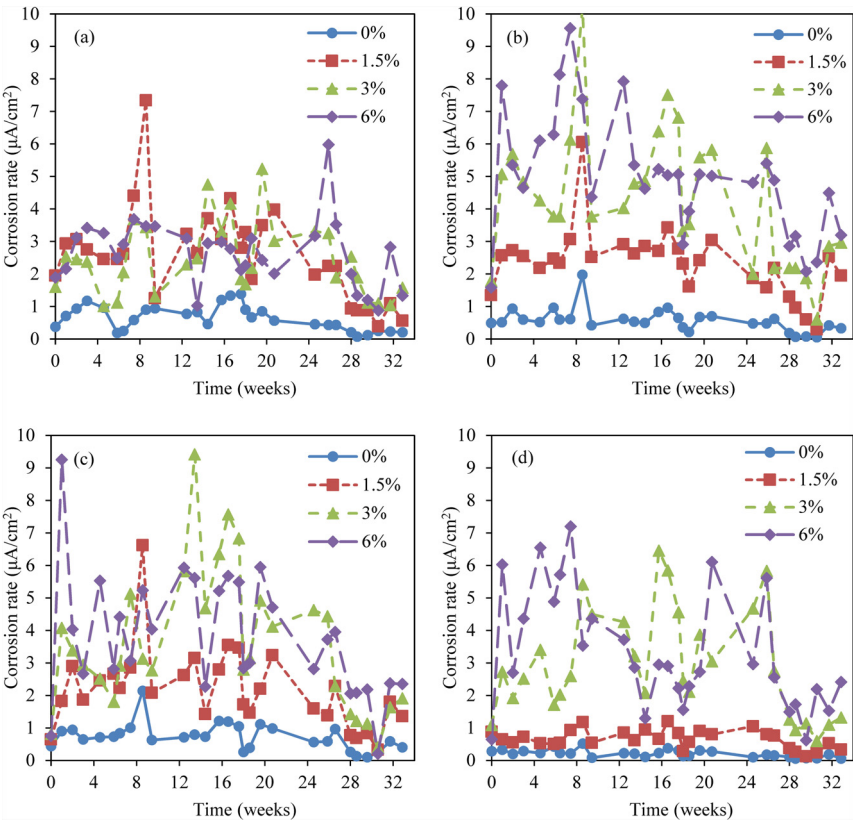

lowest corrosion rates, and the corrosion rate generally was found to increase with increasing admixed chloride contents up to 3 % after which no significant increase in corrosion activity is found. Fig. 5 presents the weighted average corrosion rate determined by the CEPRA technique plotted versus the actual corrosion rate obtained by determining the mass loss. The actual corrosion rate was obtained us ing the ASTM G1 procedure. The average electrochemically predicted corrosion rate was obtained by integrating the corrosion rates obtained by the technique throughout the monitoring period (shown in Fig. 4) divided by the total period of exposure. Note that the measurements labeled dry are the average of measurements conducted during the drying month mentioned earlier on specimens with no admixed chlorides. The dashed lines show the range of correlations accepted in the literature [2].

FIG. 5 Results obtained from the CEPRA technique compared to the actual corrosion rate (a) as a factor of admixed chloride percentage and (b) as a factor of cover depth and reinforcement diameter.

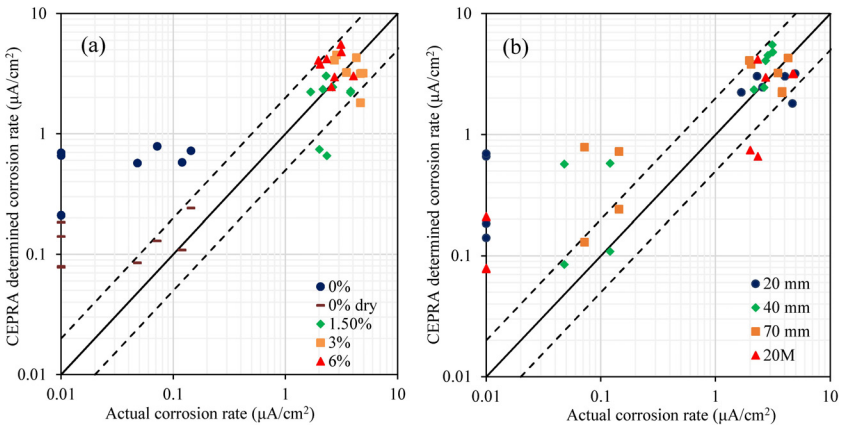

The results clearly indicate the applicability of using the technique to measure corrosion rates. For the actively corroding specimens (specimens with admixed chlorides), the predicted corrosion rates generally agreed well with the actual corro sion rates. Results for 21 out of 24 specimens fell in the range of results typically accepted in the literature, which is one half to two times the actual corrosion rates [2]. The three specimens that did not fall in the typically accepted range still showed corrosion rates that were 0.35 to 0.45 times the actual corrosion rate, which is close to the lower accepted range. This correlation is similar to, if not better than, those typically reported for well established corrosion monitoring techniques applied for steel in concrete [26 30], especially for cases of low resistivity [28]. The success of the outlined method did not appear to be affected by the reinforced concrete system characteristics in this case. This correlation was obtained similarly for a wide range of resistivities (obtained using different admixed chloride percentages), cover depths, or reinforcement diameters.

For the passive specimens (specimens without admixed chlorides) in the dry condition, the results showed corrosion rates in the range of 0.2 μA/cm^2 or less, which is in the range that is typically accepted in the literature for passive reinforce ments [10,26,29]. The same reliability in determining passive corrosion rates was obtained for the case of saturated concrete with 20M reinforcements. It has to be noted that this success in determining corrosion rates for passive reinforcements was obtained with a measurement time of only 6 s, which is much lower than the typical time required for other techniques for passive conditions [10]. This is due to the effect of this technique in shortening the time to steady state conditions, as

demonstrated further through modeling results, and due to the exponential curve fitting procedure used.

An overestimation of passive corrosion rates was found for the case of saturated specimens with 10M reinforcements, where the results fall in the range of 0.6 to 0.8 $\mu A/cm^2$. This is relatively higher than the range of corrosion rates expected for specimens without admixed chlorides (an order of magnitude of difference between actual and estimated corrosion rates) but is similar to results obtained for galvano static devices using short measurement times and nonmodulated confinement [10,29], and it still allows differentiating of passive and active reinforcements. It should be noted that the specimens showing 0.6 to 0.8 $\mu A/cm^2$ in saturated condi tions started to show results lower than 0.4 $\mu A/cm^2$ after 1 day of drying, which represents cases of semisaturated concrete that better resemble field cases. (Note that in the saturated condition, these specimens were not allowed to dry since casting.) The substantial difference between the results obtained in the dry and saturated con ditions is expected and will be discussed further through modeling results. It will be demonstrated, through modeling, that this overestimation of corrosion rates only occurs for cases of saturated, low resistivity concrete with small diameter reinforce ments (which represents the limitation of this method), and it will be shown that the case used in this study (concrete with a water cementitious material ratio of 0.6 in saturated conditions reinforced with 10M rebar) served as a worst case scenario com pared to cases available in the field. This is evidenced by the good estimation of pas sive corrosion rates for dry, or semisaturated, concrete and for reinforcements with larger diameters in saturated concrete, which better represent field conditions.

Finite Element Modeling Results

Fig. 6 shows modeling results on the effect of concrete resistivity, cover depth, rein forcement diameter, and exchange current density on the current distribution on the rebar surface for the case of actively corroding reinforcements. The base case was for a cover depth of 40 mm, a resistivity of 40 ohm.m, a reinforcement diameter of 10 mm, and an exchange current density of 0.1 A/m^2. Each of the parameters was swept from the base case as shown. The presented results are all obtained at steady state (at a time long enough that the double layer capacitance is charged). The negative sign indicates anodic polarization, while the positive sign indicates cathodic polarization.

The resistivity was found to influence the amount of current reaching the rein forcement in the range of low resistivities (20 200 ohm.m), where more current polarizes the reinforcement area as resistivity increases. However, in the range of higher resistivities (higher than 200 ohm.m), there was little to no influence of resis tivity on the current reaching the reinforcement. The effect of resistivity on the polar izing current is simply due to the availability of two current consumption boundaries in this technique, as opposed to one in typical three electrode linear polarization resistance techniques. In typical techniques, any current that is applied by the counter

FIG. 6 Effect of (a) resistivity (in ohm.m), (b) cover depth (in m), (c) rebar diameter (in m), and (d) exchange current density (in A/m^2) on the distribution of polarizing current for a uniformly corroding rebar.

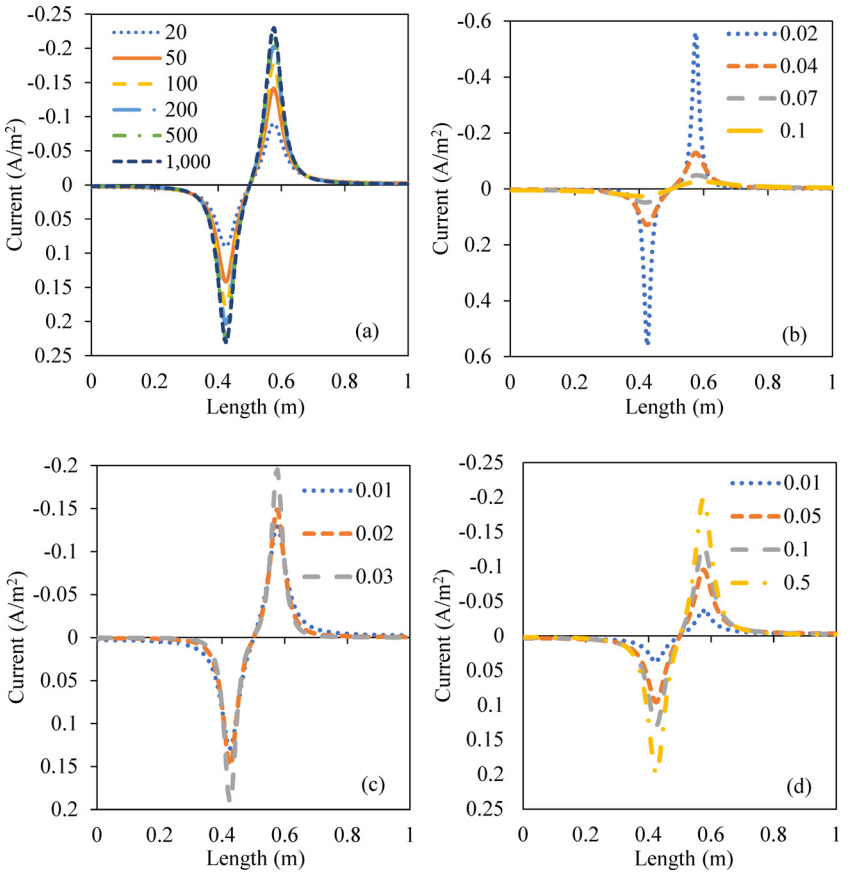

electrode is consumed by the reinforcement if current leakage/storage is considered negligible at steady state. In the CEPRA technique, if a certain amount of current is applied from the positive (anodic) probe, it can be consumed by either the negative (cathodic) probe or in polarizing the reinforcement. As the resistivity between the two current applying/receiving probes increases, more current preferentially polarizes the reinforcement instead of flowing between the two probes. Therefore, the current reaching the reinforcement increases as the resistivity increases. However, the polarized area shown by the technique is not strongly dependent on resistivity, and confinement happens for all of the resistivities, which is very different from typical galvanostatic techniques in which confinement was found to be highly dependent on resistivity [7,31,32].

The effect of the cover depth showed that the current reaching the reinforcement decreases as the cover depth increases. This is because larger (higher) concrete covers allow for a larger area for the polarizing current to flow between the two current applying probes instead of polarizing the reinforcement. For lower covers, the current preferentially polarizes the reinforcement instead of flow in the electrolyte/concrete. The effect of the cover depth on the polarized area shows that lower covers lead to lower polarized areas and more localized polarization under the probe, while higher covers lead to more dispersion of the applied current in the concrete cover, which is in agreement with the effect observed for other corrosion monitoring techniques [6,7]. This may explain the reason for the underestimation of the corrosion rate for one of the 20 mm cover depth reinforcements when assuming that the full reinforcement is polarized. The same trend is observed for the effect of the reinforcement diameter. As the reinforcement diameter increases, more current can reach the reinforcement due to a higher electrode area available to consume this current. It seems that the area polarized by the technique tends to slightly decrease as the reinforcement diameter increases due to the higher current consumption area available, which decreases the ability of the lateral propagation of the polarizing current. This may explain the underestimation of corrosion rate found for two of the 20M reinforcement specimens.

The influence of exchange current density, or equivalently the polarization resistance, on the area polarized by the technique is very similar to that observed for resistivity. This is because the portion of current flowing in the path polarizing the reinforcement, as opposed to that parallel to the reinforcement, is determined by the relative values of concrete resistivity and polarization resistance. Lower polarization resistances encourage more current to reach the reinforcement instead of flowing explicitly in the concrete. Nevertheless, the polarized area shown by the technique is not strongly dependent on polarization resistance (in the range of active corrosion rates), and confinement happens regardless of the polarization resistance value, which is very different from typical galvanostatic techniques in which confinement was found to be highly dependent on polarization resistance [7,31].

Although the current reaching the reinforcement is variable, it is well estimated through the model outlined in this paper as evidenced by the accuracy of the technique for actively corroding reinforcements. Furthermore, these results clearly indicate that the dependency of confinement success on factors such as concrete resistivity, cover depth, reinforcement diameter, and exchange current density are very marginal, and the polarized area changes with very low magnitudes. The polarized length for this technique varied, for the cases shown and for other cases not presented in this paper, for a wide range of concrete resistivities, cover depths, reinforcement diameters, and exchange current densities, from 50 cm (in cases of very large cover depths and small reinforcement diameters) to 30 cm (in cases of very small cover depth and large reinforcement diameters). This variance in polarized area is much lower than that typically found for other techniques [7,9,32]. If, for instance, the polarized area is assumed to be 40 cm for all of these cases, the error

due to this assumption will not exceed 25 %. This ability to confine the polarized current, without the use of confinement techniques, stems from the current regulating nature of this technique, where the current reaching the reinforcement is variable and depends on characteristics of the steel concrete system. This is very different from the currently used techniques where confinement is essential. For instance, it has been shown that achieving confinement using the guard ring tech nique is very challenging in very low resistivity systems due to the higher tendency of the polarizing current to disperse laterally [7,28]. This effect does not occur in the CEPRA technique because the current reaching the reinforcement decreases as resistivity decreases, leading to a lower effect of resistivity on confinement success.

Fig. 7 shows the effect of concrete resistivity on current distribution for the case of a passive reinforcement. These results were obtained for a cover depth of 40 mm and a diameter of 10 mm. As demonstrated previously, higher resistivities generally lead to higher amounts of current reaching the reinforcement. For low resistivities (Fig. 7b), it was found that confinement occurs only in the branch of the reinforce ment near the cathodic probe while the full reinforcement area near the anodic probe is polarized up to 0.5 m in this case. This is simply due to the challenge of polarizing a passive electrode anodically. This is due to the electrode's very low exchange current density and the very high anodic Tafel slope (due to passivation control) leading to the reinforcement having a very limited ability to consume the anodic polarizing current. On the other hand, for cathodic polarizations, passive reinforcements tend to become better current consumers because the cathodic Tafel slope is much lower than the anodic one (if no diffusion limitation exists). This leads to a limitation of the CEPRA model due to the lack of symmetry between the two sides of the reinforcements, which means that R_{c3} (shown earlier) will not be

FIG. 7 Effect of resistivity (in ohm.m) on current distribution for the case of a passive rebar.

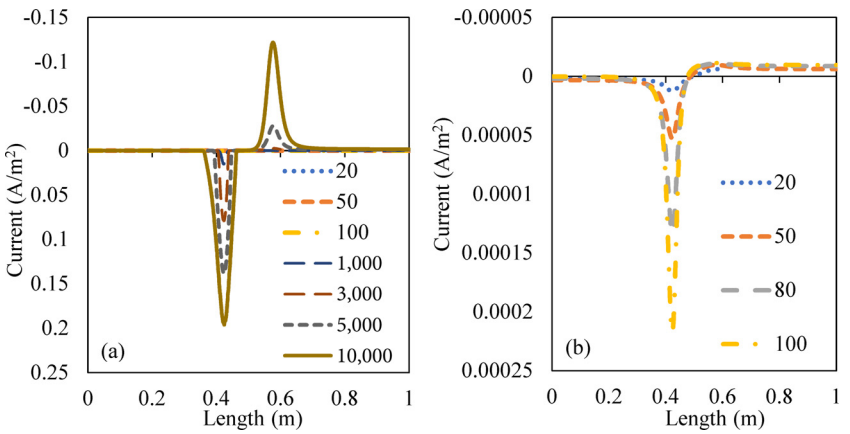

the same under the two probes (R_{c3} will be identical for both sides only if the anodic and cathodic beta coefficients are equal). In the case of high resistivity systems, the symmetry is restored and confinement occurs, which leads to a better estimate of passive corrosion rates. This can partially explain the better estimate of passive cor rosion rates in cases of semisaturated or dry concrete. This limitation of confining anodic polarizations for passive electrodes is similar for all the techniques using an odic polarizations [8,31,32].

It should be also noted that the CEPRA model assumes that high and low frequency current propagation behaviors follow the same path. This is essential in applying the model successfully. Fig. 8 shows the typical current propagation path for the case of a passive reinforcement at the high frequency range (1 μs after cur rent application). This is the same path as that for high and low frequency responses for active reinforcements. These paths are identical to Fig. 8 and are, therefore, not presented herein. Fig. 9 shows the typical current propagation path for the case of a passive reinforcement, with low resistivity concrete (40 ohm.m), at the low frequency range (500 s after current application). As mentioned previously, the high and low frequency paths are rather similar in cases of actively corroding electrodes (both similar to Fig. 8), which explains the validity of the model and the accuracy obtained through it. However, this is not the case for the passive reinforce ment in low resistivity concrete because in the high frequency portion, the rein forcement's double layer acts as a relatively good current consumer (causing a short circuit effect), while at the low frequency region, this reinforcement acts as

FIG. 8 High frequency current path (evaluated 1 μs after current application) for a case representing passive reinforcements. (Note that this is identical to the current path for high and low frequency responses for active reinforcements.)

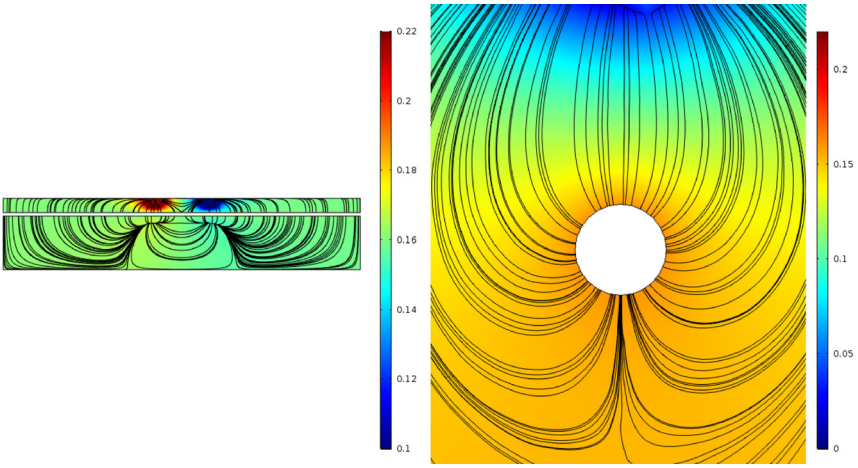

FIG. 9 Low frequency current path (evaluated at steady state) for a case representing passive reinforcements in low resistivity concrete.

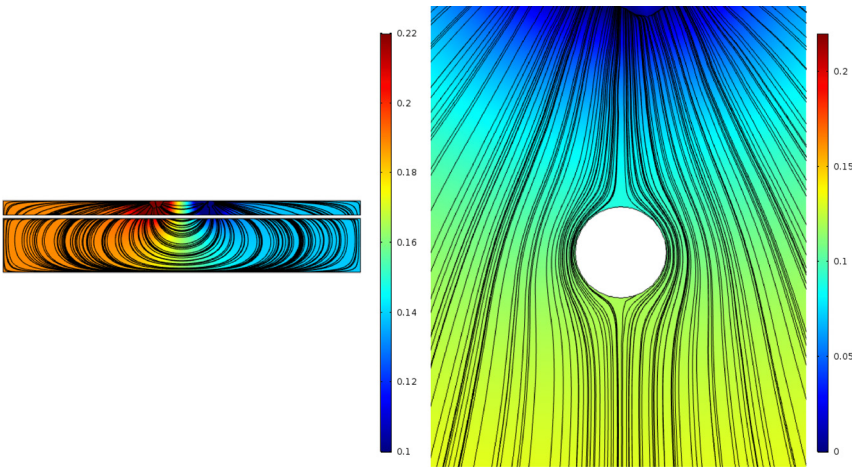

a current insulator (due to the high R_p) and hardly any current polarizes the rein forcement. It is clear that in the low frequency ranges for the passive reinforce ments, the electrode tends to encourage current flow in a different path than that for the high frequency response (around and beneath the reinforcement). The low and high frequency current paths will tend to become more similar, and subse quently provide better results, when the current polarizing the reinforcement in the low frequency range increases. This polarizing current increases as the electrode's area available for current consumption increases or as the system resistivity increases, which explains the good results obtained for the dry or semisaturated (high resistivity) cases, as well as cases with large reinforcement diameters (these cases better simulate field conditions). This may indicate that the overestimation found in the case of saturated, low resistivity concrete with small diameter passive rebar is not characteristic of the technique and only occurs in such scenarios.

Fig. 10 and Fig. 11 illustrate the potential difference between the two inner probes as a factor of time for a case of resistivity of 40 ohm.m, a cover depth of 40 mm, and a reinforcement diameter of 10 mm for a passive and active rebar, respectively. It is clear that the technique substantially reduces the time to reaching quasi steady state conditions compared to other techniques [10,26,29]. A measurement time of 10 s was found to provide adequate information about the polarization be havior of the reinforcement up to capacitance values in the range of 1 F/m^2 for the passive case (88 % of the steady state polarization was achieved in 10 s) and 5 F/m^2 in the active case (91 % of the steady state polarization was achieved in 10 s). This has been a major challenge for determining the passive reinforcements corrosion

FIG. 10 Effect of the double layer capacitance (in F/m^2) on the obtained time transient for the case of a passive rebar up to (a) 100 s and (b) 10 s.

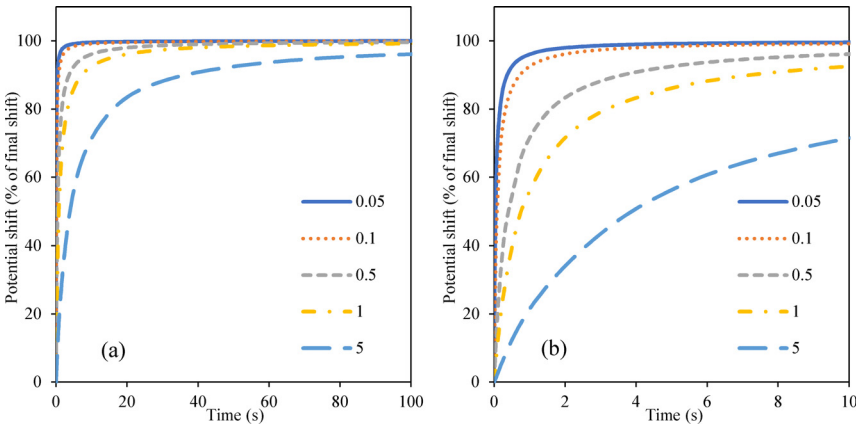

FIG. 11 Effect of the double layer capacitance (in F/m^2) on the obtained time transient for the case of an active rebar up to (a) 100 s and (b) 10 s.

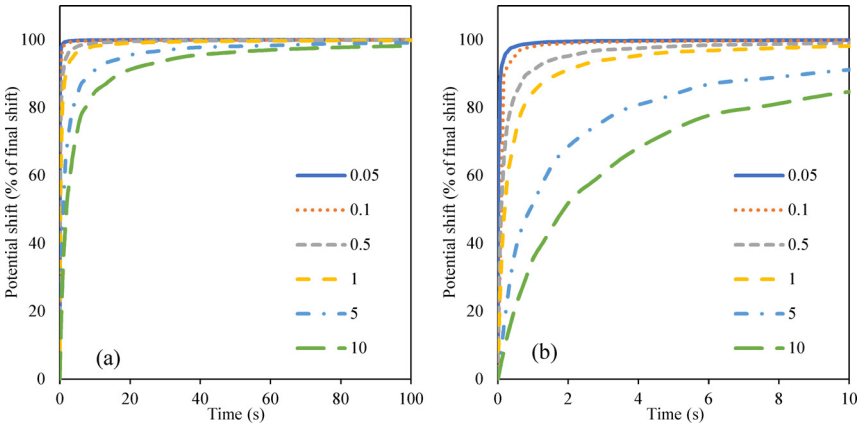

rates [10], especially with the very low exchange current density assumed in this model (10^{-5} A/m^2). The shortening of the measurement time associated with this technique has been previously proven experimentally [12,33], theoretically [33], and numerically by the current study. The primary reason for this is that the polarizing current is very low in the area found in the middle of the reinforcement. Another reason is the lower electrode area contributing to the polarization. However, this changes if the resistivity reaches very high values due to the higher current

received by the reinforcement, where higher resistivities lead to higher times to quasi steady state conditions. This shortening of the time to steady state conditions leads to the technique's ability to determine corrosion rates in the passive cases in very few seconds, as evidenced by the experimental results. Such a feature is not applicable for techniques with constant applied currents.

Conclusions

This paper outlined the theory behind the CEPRA technique and introduced its use. From experimental and numerical work investigating the mode of application and reliability of the technique, the following conclusions can be drawn:

- The technique showed an accuracy in estimating the corrosion rates for actively corroding reinforcements that was similar to other well established techniques that require a reinforcement connection and a longer measure ment time.
- The technique showed success in determining passive corrosion rates in the case of dry or semisaturated, high resistivity concrete and in the case of large reinforcement diameters. However, the technique overestimated the corrosion rates for passive cases when testing saturated concrete with small reinforce ment diameters.
- The CEPRA technique was found to decrease the time to steady state condi tions for passive reinforcements considerably.
- The polarized area for the CEPRA technique has shown to vary in lower mag nitudes compared to other techniques, without the use of confinement techni ques, due to the self regulating current for this technique.

ACKNOWLEDGMENTS

The authors would like to acknowledge Dr. Michael Thomas, from the University of New Brunswick, for his contribution to the experimental study, and Dr. O. Burkan Isgor, from Oregon State University, for his help throughout the model development process. This research project was funded partially by the National Science and Engi neering Research Council of Canada and by Giatec Scientific Inc., who provided the device used to perform the corrosion rate measurements.

References

[1] Stern, M. and Geary, A. L., "A Theoretical Analysis of the Shape of Polarization Curves," *J. Electrochem. Soc.,* Vol. 104, No. 1, 1957, pp. 56–63.

[2] Alonso, C., Andrade, C., and Gonzalez, J. A., "Relation between Concrete Resistivity and Corrosion Rate of the Reinforcements in Carbonated Mortar Made with Several Cement Types," *Cement Concrete Res.,* Vol. 18, No. 5, 1988, pp. 687–698.

[3] Glass, G. K., Page, C. L., Short, N. R., and Zhang, J. Z., "The Analysis of Potentiostatic Transients Applied to the Corrosion of Steel in Concrete," *Corros. Sci.*, Vol. 39, No. 9, 1997, pp. 1657–1663.

[4] Pech-Canul, M. A. and Castro, P., "Corrosion Measurements of Steel Reinforcement in Concrete Exposed to a Tropical Marine Atmosphere," *Cement Concrete Res.*, Vol. 32, No. 3, 2002, p. 491.

[5] Andrade, C., Alonso, C., and Sarria, J., "Corrosion Rate Evolution in Concrete Structures Exposed to the Atmosphere," *Cem. Concr. Compos.,* Vol. 24, No. 1, 2002, pp. 55–64.

[6] Kranc, S. C. and Sagués, A. A., "Polarization Current Distribution and Electrochemical Impedance Response of Reinforced Concrete When Using Guard Ring Electrodes," *Electrochim. Acta,* Vol. 38, No. 14, 1993, pp. 2055–2061.

[7] Wojtas, H., "Determination of Corrosion Rate of Reinforcement with a Modulated Guard Ring Electrode; Analysis of Errors Due to Lateral Current Distribution," *Corros. Sci.*, Vol. 46, No. 7, 2004, pp. 1621–1632.

[8] Poursaee, A. and Hansson, C. M., "Galvanostatic Pulse Technique with the Current Confinement Guard Ring: The Laboratory and Finite Element Analysis," *Corros. Sci.*, Vol. 50, No. 10, 2008, pp. 2739–2746.

[9] Nygaard, P. V., Geiker, M. R., and Elsener, B., "Corrosion Rate of Steel in Concrete: Evaluation of Confinement Techniques for On-Site Corrosion Rate Measurements," *Mater. Struct.*, Vol. 42, No. 8, 2009, pp. 1059–1076.

[10] Martinez, I., Andrade, C., Rebolledo, N., Luo, L., and De Schutter, G., "Corrosion-Inhibitor Efficiency Control: Comparison by Means of Different Portable Corrosion Rate Meters," *Corrosion*, Vol. 66, No. 2, 2010, https://dx.doi.org/10.5006/1.3319663

[11] Monteiro, P. J. M., Morrison, H. F., and Frangos, W., "Nondestructive Measurement of Corrosion State of Reinforcing Steel in Concrete." *ACI Mater. J.*, Vol. 95, No. 6, 1998, pp. 704–709.

[12] Zhang, J., Monteiro, P. J. M., and Morrison, H. F., "Noninvasive Surface Measurement of Corrosion Impedance of Reinforcing Bar in Concrete—Part 1: Experimental Results," *ACI Mater. J.*, Vol. 98, No. 2, 2001, pp. 116–125.

[13] Andrade, C. and Martínez, I., "Metal Corrosion Rate Determination of Different Solutions and Reinforced Concrete Specimens by Means of a Noncontacting Corrosion Method," *Corrosion*, Vol. 66, No. 5, 2004, https://dx.doi.org/10.5006/1.3430465

[14] Keddam, M., Nóvoa, X. R., and Vivier, V., "The Concept of Floating Electrode for Contact-Less Electrochemical Measurements: Application to Reinforcing Steel-Bar Corrosion in Concrete," *Corros. Sci.*, Vol. 51, No. 8, 2009, pp. 1795–1801.

[15] Zhang, J., Monteiro, P. J. M., and Morrison, H. F., "Noninvasive Surface Measurement of Corrosion Impedance of Reinforcing Bar in Concrete—Part 2: Forward Modeling," *ACI Mater. J.*, Vol. 99, No. 3, 2002, pp. 242–249.

[16] Zhang, J., Monteiro, P. J. M., Morrison, H. F., and Mancio, M., "Noninvasive Surface Measurement of Corrosion Impedance of Reinforcing Bar in Concrete—Part 3: Effect of Geometry and Material Properties," *ACI Mater. J.*, Vol. 101, No. 4, 2004, pp. 273–280.

[17] Keddam, M., Nóvoa, X. R., Puga, B., and Vivier, V., "Impedance Based Method for Non-Contact Determination of the Corrosion Rate in Buried Metallic Structures," *Eur. J. Environ. Civ. En.*, Vol. 15, No. 7, 2011, pp. 1097–1103.

[18] ASTM C192, *Standard Practice for Making and Curing Concrete Test Specimens in the Laboratory*, ASTM International, West Conshohocken, PA, 2016, www.astm.org

[19] ASTM G1-03 (2017)e1, *Standard Practice for Preparing, Cleaning, and Evaluating Corrosion Test Specimens*, ASTM International, West Conshohocken, PA, 2017, www.astm.org

[20] Frankel, G. S., "Fundamentals of Corrosion Kinetics," *Active Protective Coatings*, A. E. Hughes, J. M. C. Mol, M. L. Zheludkevich, and R. G. Buchheit, Eds., Springer, Dordrecht, The Netherlands, 2012, pp. 17–32.

[21] Kranc, S. and Sagues, A. A., "Modeling the Time-Dependent Response to External Polarization of a Corrosion Macrocell on Steel in Concrete," *J. Electrochem. Soc.*, Vol. 144, No. 8, 1997, pp. 2643–2652.

[22] Pour-Ghaz, M., Isgor, O. B., and Ghods, P., "The Effect of Temperature on the Corrosion of Steel in Concrete. Part 1: Simulated Polarization Resistance Tests and Model Development," *Corros. Sci.*, Vol. 51, No. 2, 2009, pp. 415–425.

[23] Clement, A., Laurens, S., Arliguie, G., and Deby, F., "Numerical Study of the Linear Polarization Resistance Technique Applied to Reinforced Concrete for Corrosion Assessment," *Eur. J. Environ. Civ. En.*, Vol. 16, Nos. 3–4, 2012, pp. 491–504.

[24] Andrade, C. and González, J. A., "Quantitative Measurements of Corrosion Rate of Reinforcing Steels Embedded in Concrete Using Polarization Resistance Measurements," *Mater. Corros.*, Vol. 29, No. 8, 1978, pp. 515–519.

[25] Marchand, J., Laurens, S., Protière, Y., and Samson, E., "A Numerical Study of Polarization Tests Applied to Corrosion in Reinforced Concrete," *ACI Special Publication,* Vol. 312, 2017, pp. 1–12.

[26] Luping, T., "Calibration of the Electrochemical Methods for the Corrosion Rate Measurement of Steel in Concrete," NORDTEST Project No. 1531–01, SP Swedish National Testing and Research Institute, Borås, Sweden, 2005.

[27] Law, D. W., Cairns, J., Millard, S. G., and Bungey, J. H., "Measurement of Loss of Steel from Reinforcing Bars in Concrete Using Linear Polarisation Resistance Measurements," *NDT & E Int.*, Vol. 37, No. 5, 2004, pp. 381–388.

[28] Andrade, C. and Martińez, I., "Calibration by Gravimetric Losses of Electrochemical Corrosion Rate Measurement Using Modulated Confinement of the Current," *Mater. Struct.*, Vol. 38, No. 9, 2004, pp. 833–841.

[29] Poursaee, A., "An Analysis of the Factors Influencing Electrochemical Measurements of the Condition of Reinforcing Steel in Concrete Structures," Ph.D. thesis, University of Waterloo, Waterloo, Ontario, Canada, 2007.

[30] Pradhan, B. and Bhattacharjee, B., "Performance Evaluation of Rebar in Chloride Contaminated Concrete by Corrosion Rate," *Constr. Build. Mater.*, Vol. 23, No. 6, 2009, pp. 2346–2356.

[31] Flis, J., Sehgal, A., Li, D., Kho, Y., Sabotl, S., Pickering, H., Osseo-Asare, K., and Cady, P. D., "Condition Evaluation of Concrete Bridges Relative to Reinforcement Corrosion Volume 2: Method for Measuring the Corrosion Rate of Reinforcing Steel," Strategic Highway Research Program, Washington, DC, 1993.

[32] Mitzithra, M. E., "Detection of Corrosion of Reinforced Concrete on Cooling Towers of Energy Production Sites," Ph.D. thesis, Universite De Toulose, Toulose, France, 2013.

[33] Lim, Y. C., Noguchi, T., and Shin, S. W., "Formulation of a Nondestructive Technique for Evaluating Steel Corrosion in Concrete Structures," *ISIJ Int.*, Vol. 49, No. 2, 2009, pp. 275–283.

STP 1609, 2019 / available online at www.astm.org / doi: 10.1520/STP160920170228

Madeline Lee[1] and Ryan Tinnea[1]

Use of Alternating Current Impedance Spectra as a Supplemental Verification of Rebar Passivation in Two Marine Viaducts

Citation

Lee, M. and Tinnea, R., "Use of Alternating Current Impedance Spectra as a Supplemental Verification of Rebar Passivation in Two Marine Viaducts," *Advances in Electrochemical Techniques for Corrosion Monitoring and Laboratory Corrosion Measurements*, *ASTM STP1609*, S. Papavinasam, R. B. Rebak, L. Yang, and N. S. Berke, Eds., ASTM International, West Conshohocken, PA, 2019, pp. 81–90, http://dx.doi.org/10.1520/STP160920170228[2]

ABSTRACT

Cathodic protection (CP) systems were installed on a viaduct in Ketchikan, Alaska, in 2001. Three CP styles were implemented to meet the changing protection needs in several marine environments over varying elevations. The systems installed included galvanic thermal spray zinc metallizing installed on cast-in-place pile caps and precast deck panels in the upper splash and atmospheric zones; fiberglass-reinforced plastic jackets with embedded galvanic zinc mesh anodes installed on the pile caps and piling in the tidal and lower splash zones; and submerged aluminum anodes protecting the piling in the submerged zone. A 2017 inspection found that the systems were still providing protection to most of the cathodically protected areas. In contrast, areas not originally protected with CP showed severe cracking and delamination exacerbated by corrosion of the reinforcing steel. Depolarization testing of CP systems in concrete is often a lengthy process that can take weeks to months to fully achieve. The extreme tidal changes in Ketchikan provided further challenges

Manuscript received November 15, 2017; accepted for publication March 13, 2018.

[1]Tinnea & Associates, LLC, 2018 E. Union St., Seattle, WA 98122, USA

[2]ASTM Symposium on *Advances in Electrochemical Techniques for Corrosion Monitoring and Laboratory Corrosion Measurements* on November 13 14, 2017 in Atlanta, GA, USA.

as measured corrosion potentials in many areas were influenced by tide level. As a result, passivation verification technique (PVT) testing was utilized to provide additional support to the depolarization data. PVT is an alternating current technique that provides a qualitative analysis of the condition of the reinforcing steel by measuring changes in phase angle over a partial spectrum—100, 10, 1, 0.1, and 0.01 Hz. These PVT and depolarization measurements are used to determine if the reinforcing steel is exhibiting passive or active behavior and whether the reinforcement is corroding or protected.

Keywords
cathodic protection, passivation verification, GECOR, rebar, thermal spray zinc, adhesion testing, depolarization

Introduction

Ketchikan, Alaska, is a popular cruise destination located in a temperate rain forest. With an average yearly rainfall of 153 in, it is one of the rainiest cities in the United States [1]. There are two main roads in town, Tongass Avenue and Water Street. Portions of both are constructed on viaducts, with residential properties and busi nesses often on the seaward side and, like the viaducts, supported by piles. The Tongass Avenue Viaduct was constructed in 1956 and is 18 m wide and 526 m long. The viaduct is composed of prestressed piles and beams with cast in place pile caps, deck, and slab spans. Tides in Ketchikan are extreme, and the sea eleva tion can change by more than 7.5 m in a given day [2]. For this reason, installing and inspecting cathodic protection (CP) systems can be a challenge. In marine envi ronments, the rate of corrosion of steel in concrete can be influenced by elevation, water temperature, wave action, and amount of exposure [3]. As a result, CP sys tems on the viaducts are split into three zones to adequately protect marine piling: the submerged (buried) zone, the tidal zone, and the upper splash and atmospheric zone. The lower portion of the piling is in either the submerged zone or is below grade. It is always fully submerged or buried and hence is protected using sub merged indium activated aluminum anodes. The tidal zone may be underwater depending on the tides, and it is mainly comprised of the upper parts of the piling and the lower portions of the pile caps. They are protected with fiberglass reinforced jackets and galvanic zinc mesh in the pile caps. The decking and the remainder of the pile caps are located in the splash zone, and they are typically out of the water except during extreme storms hitting at or near high tide. This area is protected by thermal spray zinc metallizing. **Fig. 1a** and **b** shows how the bulk alumi num anodes will protect both unjacketed pilings and areas of jacketed pilings, depending on the tide level.

This CP system configuration was only installed on about three quarters of each of the viaducts. The other quarter did not receive any protection because, at the time, they were slated for demolition and backfilling. Before that work was initi ated, changes in coastal management requirements precluded filling, so those

FIG. 1 (a) Piling during low tide and (b) piling during high tide.

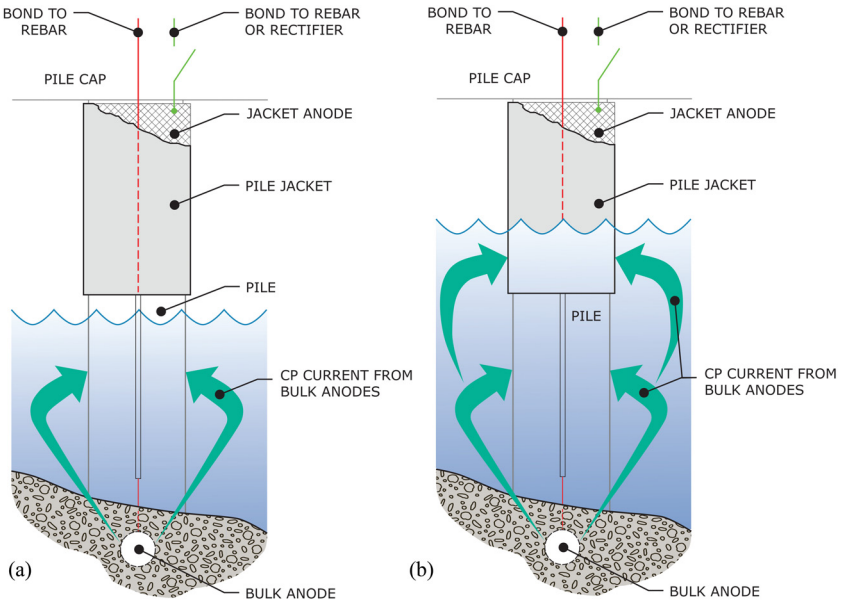

sections have continued in use. This situation allows for a comparison to be drawn between the two areas and shows how well the CP system protected the structures compared to the unprotected structures that were constructed at the same time and that have served in an identical environment.

Experimental

A variety of testing methods was used to analyze each part of the CP system. An ini tial visual inspection was conducted that identified cracking and spalling of the con crete and any damage to the CP systems. Acoustic sounding per ASTM D4580 03, *Standard Practice for Measuring Delaminations in Concrete Bridge Decks by Sounding*, was also used to identify areas of delamination in nonjacketed areas [4]. The current output of each element of the CP system was measured at the rectifier. The main tests used to assess the function of the CP system were depolarization and passivation verification technique (PVT) testing.

DEPOLARIZATION

Portable data loggers were placed in test stations to record the depolarization of the elements of the two viaducts with respect to time by disconnecting cur rent at the junction boxes (Fig. 2). Compared to CP systems installed in soil or water, CP systems in moist concrete typically require long depolarization times

FIG. 2 Junction box where current is interrupted for depolarization testing.

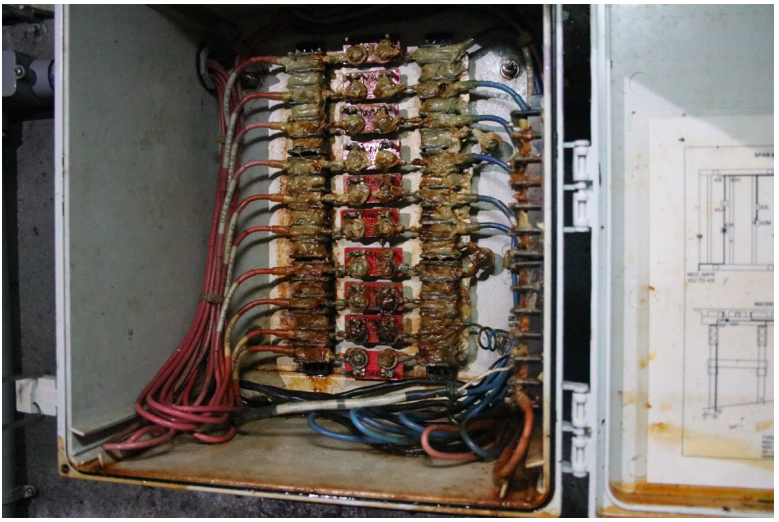

due to the high resistivity of the electrolyte and concrete and the slow diffusion rate of oxygen. Given the weather in Ketchikan and the presence of fiberglass reinforced plastic jackets, full depolarization of the systems would not occur unless disconnected for weeks or months [5]. To calculate those final depolarized potentials without this extended wait time, the potentials were logged once per minute as they depolarized for 1 to 2 days. Those potentials were plotted to establish a trend. The data were extrapolated along a natural log curve to determine and estimate the fully depolarized potential. The final depolarized potential can be compared to the instant off potential to determine the effectiveness of the CP system.

According to NACE SP0290, *Impressed Current Cathodic Protection of Reinforcing Steel in Atmospherically Exposed Concrete Structures*, a minimum depolarization of 100 mV, shown as the difference between the final depolarized potential and the instant off potential, indicates full protection of the reinforcing steel. If the depolarized potential is more electropositive than −200 mV to a copper copper sulfate (−85 mV_{SSC}), then the steel is considered passivated regardless of the magnitude of depolarization [6].

PVT TESTING

PVT is an alternating current technique used to analyze the effectiveness of a CP system without the need to interrupt current flow from the system [7–9]. In other tests such as linear polarization resistance testing, the direct current from the CP system interferes with readings because the equipment is unable to differentiate

current from the macro cell formed by the CP system and that of localized corro sion in rebar [3]. PVT utilizes electrochemical impedance spectroscopy (EIS) to provide a qualitative evaluation of the state of the rebar under the tested area. Five different current frequencies are applied to the structure at 0.01, 0.1, 1, 10, and 100 Hz at an amplitude of ±100 mV. Only five frequencies were measured instead of a larger range, such as in normal EIS testing, to decrease the length of time for each test. The change in phase angle from the generated frequencies is analyzed, and the results are reported as "not protected," "moderately protected," or "well protected." The test also records the potential versus the copper copper sulfate reference electrode [3,7 9].

These tests were completed using a GECOR 9™ portable corrosion testing device shown in **Fig. 3a**. The device consists of a 7 cm diameter counter electrode (CE) surrounded by an 18 cm diameter guard electrode (GE) and measures poten tials against a copper/copper sulfate reference electrode located in the center of the CE. The CE applies an electrical current to the rebar being tested, or working elec trode, at the varying frequencies listed previously. The GE works to polarize the rebar immediately adjacent to the rebar being tested, and this ring is controlled using the two reference electrodes located between the CE and the GE, which reduces current attenuation from the CE and allows for a more accurate estimation of the surface area of rebar analyzed (**Fig. 3b**).

To perform PVT testing, the reinforcement in the concrete is first located using a portable rebar locator. Then, the thermal spray zinc over the top of the rebar is removed with a pneumatic needle gun. It was determined that needle gun scalers are best for removing thermal spray zinc, as grinders only smeared the metalizing [5]. A moist sponge is placed between the PVT meter's sensor and concrete to ensure electrical contact. Each test takes approximately 15 min, so it is useful to hold the sensor in place with a strap or other apparatus rather than in hand, which can lead to the apparatus slipping and requiring the test to be redone.

FIG. 3 (a) GECOR 9 sensor and (b) schematic of GECOR 9 applying current to rebar.

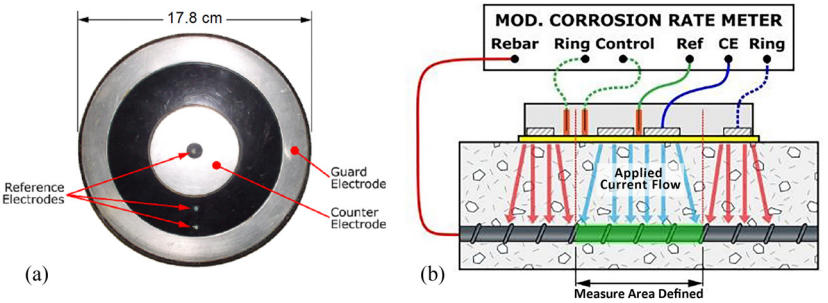

Results

An initial visual inspection indicated the existing CP system is effective and has successfully protected the piles. It is not unusual for some minor cracking or spalling to occur after a CP system is installed. During construction, some areas may appear sound, but previous rebar corrosion has generated stresses very near the point that will crack the concrete. Even absent further corrosion after the CP system is installed, thermal cycles or additional passing of large trucks or buses can cause that "almost spall" or crack to fail. On a few bents, some cracking was found, but the location, shape, and orientation of the cracks suggests the damage was caused by mechanical loads and not by corrosion of the reinforcement.

On the bents not cathodically protected, extensive corrosion related damage can be found on the piling and pile caps. Many spalls, cracks, and delaminations due to rebar corrosion were observed. Additionally, at locations where cracking was likely initially caused by flexing of the concrete, chloride ingress at those cracks caused significant corrosion of the underlying rebar and led to severe damage. These areas exemplify the significant difference between CP protected areas and nonprotected areas (**Fig. 4a,b**).

DEPOLARIZATION

The decay in potential was recorded at eight bent locations. In five of the tests, the final depolarized potential was found to be greater than −85 mV versus an embedded silver silver chloride (SSC) reference electrode, indicating passive behavior. Two locations had potentials close enough to the −85 mV_{SSC} standard (within 10 mV) to be considered passive given the testing was performed during the very wet winter months. These conditions restrict oxygen availability at the rebar, and oxygen is necessary for depolarization to occur. The other location, Bent 26, had a projected total depolarization difference of 406 mV, which exceeds the NACE standard 100 mV requirement and shows the CP system is protecting that area.

FIG. 4 (a) Cracking on bent without CP and (b) cracking on Bent 19 with CP.

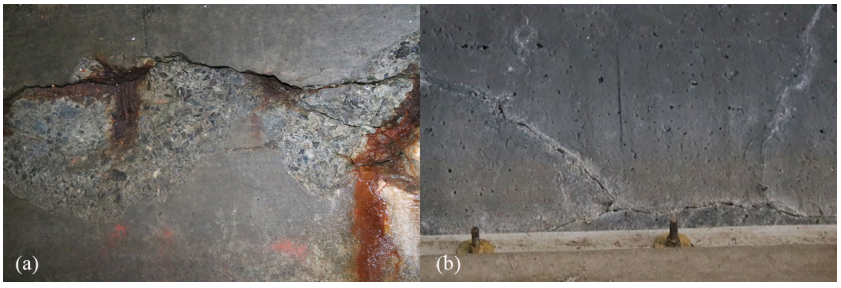

FIG. 5 Depolarization trends for Tongass Avenue.

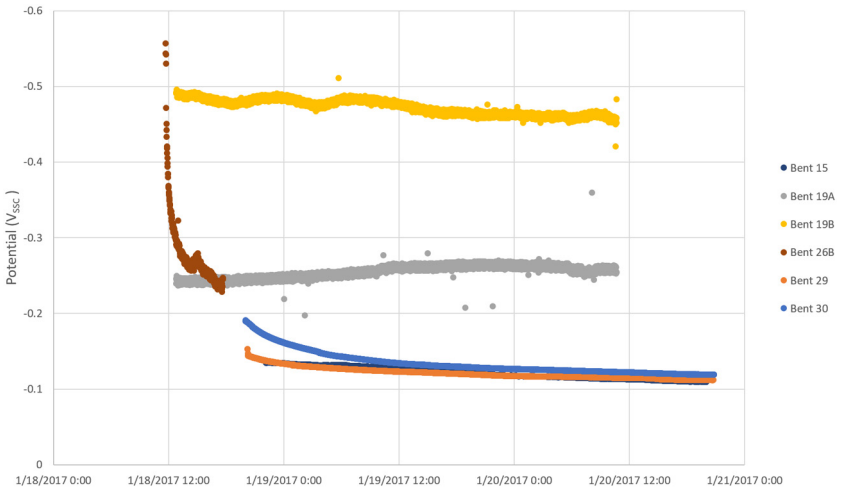

Fig. 5 documents the depolarization trends and Table 1 shows the initial and final depolarization values.

PVT TESTING

PVT testing was performed on areas with and without CP. Tests on areas with CP showed full protection, or passivation, of the reinforcing steel, indicating that the CP system was providing protection to these areas. On the unprotected locations outside of the bents included in the Tongass Avenue CP system, the PVT found the rebar to be actively corroding, which yielded a "not protected" result from the PVT meter (Table 2).

TABLE 1 Depolarization results for Tongass Avenue.

Location	Instant-Off Potential	Final Depol Potential	Difference	Projected Final Potential	Difference	Meets Requirements?
Bent 13	89 mV	132 mV	43 mV	65 mV	24 mV	Yes
Bent 15	135 mV	109 mV	26 mV	80 mV	55 mV	Yes
Bent 19A	25 mV	25 mV	0 mV	25 mV	0 mV	Yes
Bent 19B	49 mV	45 mV	4 mV	35 mV	14 mV	Yes
Bent 26	556 mV	235 mV	321 mV	150 mV	406 mV	Yes
Bent 29	153 mV	111 mV	42 mV	100 mV	53 mV	Yes
Bent 30	191 mV	112 mV	79 mV	95 mV	96 mV	Yes
Bent 34	152 mV	97 mV	55 mV	90 mV	62 mV	Yes

TABLE 2 PVT results taken versus a copper copper sulfate electrode.

Tongass Passivation Verification Results

Location	In CP System	Potential	Level of Protection
Bent 26	Yes	112 mV	Well protected
Bent 35	Yes	174 mV	Well protected
Bent 35	Yes	203 mV	Well protected
Bent 40	No	438 mV	Not protected
Bent 40	No	331 mV	Not protected
Bent 40	No	221 mV	Not protected

Discussion

The results of the PVT testing and the depolarization indicate that the structure with CP is protected. When the testing was performed on areas without CP, the results showed that the structure was not protected. The areas protected showed minor cracking but were in generally good condition and will be operational for years into the future. The areas outside the CP system showed spalling and delami nations in the concrete that may be indicative of structural issues. Fig. 6a shows cracking in the protected region of the viaduct versus cracking and exposed rebar in the unprotected area in Fig. 6b. The CP system prolonged the life of the viaduct for years and prevented the need for repairs.

PVT, unlike general EIS testing, uses five specific testing frequencies instead of a wide range of frequencies. In EIS testing, alternating current voltage is applied to the system at a wide range of frequencies. A Randles circuit models the system, and each part of the circuit has a different response to varying frequencies. Using a wide range of frequencies allows for the EIS data to be deconvoluted so that different components of the Randles circuit can be analyzed. EIS has a range of issues that

FIG. 6 (a) Cracking in areas within the CP system compared to (b) areas outside of the CP system.

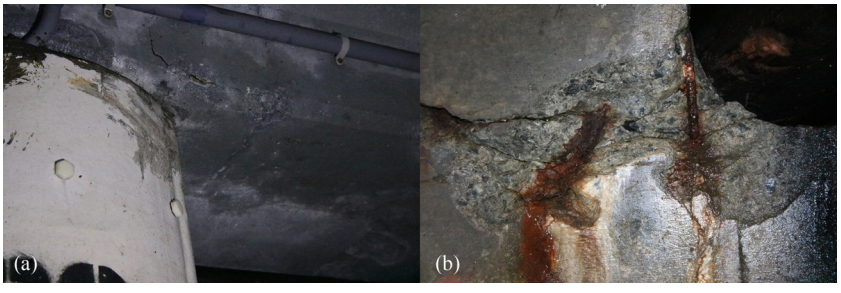

make it difficult to use in the field. The system must be stable to obtain valid EIS measurements.

The PVT method employs only five different frequencies. This dramatically reduces test time. In field conditions, it is often difficult to control things like tem perature, so the rebar electrochemical environment will change with time. Unlike EIS testing that could take hours, PVT testing takes only around 15 min, which well addresses stability concerns. A trade off with using only five frequencies is that each element of the theoretical Randles circuit cannot be analyzed in detail. Instead, only a general level of protection is provided by the test. However, most bridge owners only need to know if the CP system is working or not and do not need to know the instantaneous corrosion rate.

Conclusions

1. PVT can be used to accurately verify the level of protection in an operating CP system.
2. The PVT meter has some limitations:
   a. The meter can only determine if the reinforcing steel is passive or not pas sive and cannot provide any quantitative data as to the CP system's function.
   b. The meter still has engineering obstacles to overcome and is not ruggedized for harsh field conditions.
3. The installation of a CP system in these marine viaducts extended the life of the structures and reduced the cost of lifetime repairs.

References

[1] Western Regional Climate Center, "Ketchikan, Alaska—Climate Summary," WRCC, 2005, http://web.archive.org/save/https://wrcc.dri.edu/cgi-bin/cliMAIN.pl?akketc (accessed Oct. 10, 2017).

[2] National Oceanic and Atmospheric Administration, "Datums for 9450460, Ketchikan AK," NOAA, 2011, http://web.archive.org/web/20171108204412/https://tidesandcurrents.noaa.gov/datums.html?id 9450460 (accessed Oct. 10, 2017).

[3] Tinnea, J. S. and Tinnea, R. J., "Cathodic Protection Evaluation Final Report ODOT Contract PSK28885," Oregon Department of Transportation, Salem, OR, 2014, pp. 1–81.

[4] ASTM D4580-03, *Standard Practice for Measuring Delaminations in Concrete Bridge Decks by Sounding*, ASTM International, West Conshohocken, PA, 2003, www.astm.org

[5] Broomfield, J. P. and Tinnea, J. S., *Cathodic Protection of Reinforced Concrete Bridge Components Contract C-102B*, National Academy of Sciences, Washington, DC, 1992, 79 p.

[6] NACE SP0290-2007, *Impressed Current Cathodic Protection of Reinforcing Steel in Atmospherically Exposed Concrete Structures*, NACE International, Houston, TX, 2007, https://web.archive.org/web/20181017185630/https://nace.org/home.aspx (accessed Oct. 17, 2017).

[7] Martinez, I., Andrade, C., Vennesland, O., Evensen, U., Polder, R. B., and Leggedor, J., "Efficiency Control of Cathodic Protection Measured Using Passivation Verification Technique in Different Concrete Structures," *Corrosion*, Vol. 63, No. 9, 2007, pp. 880–892.

[8] Andrade, C., Lasa, I., Martinez, I., Novoa, X. R., Rincon, O., and Martinez, M., "Cathodic Protection Efficiency Measurements Made on Concrete Bridges Using a New Technique Called Passivity Verification Technique (PVT) without Disconnecting the Protective Current," *NACE International*, 2004, pp. 1–11.

[9] Martinez, I. and Andrade, C., "Application of EIS to Cathodically Protected Steel: Tests in Sodium Chloride Solution and in Chloride Contaminated Concrete," *Corros. Sci.*, Vol. 50, No. 10, 2008, pp. 2948–2958.

STP 1609, 2019 / available online at www.astm.org / doi: 10.1520/STP160920170222

Fritz J. Friedersdorf,[1] Jeff C. Demo,[1] Nathan K. Brown,[1] and Patrick C. Kramer[1]

Electrochemical Sensors for Continuous Measurement of Corrosion and Coating System Performance in Outdoor and Accelerated Atmospheric Tests

Citation

Friedersdorf, F. J., Demo, J. C., Brown, N. K., and Kramer, P. C., "Electrochemical Sensors for Continuous Measurement of Corrosion and Coating System Performance in Outdoor and Accelerated Atmospheric Tests," *Advances in Electrochemical Techniques for Corrosion Monitoring and Laboratory Corrosion Measurements*, *ASTM STP1609*, S. Papavinasam, R. B. Rebak, L. Yang, and N. S. Berke, Eds., ASTM International, West Conshohocken, PA, 2019, pp. 91–113, http://dx.doi.org/10.1520/STP160920170222[2]

ABSTRACT

Organic coatings are the primary means of protecting structures from atmospheric corrosion in harsh environments. Environmental compliance and a desire for increased performance continue to drive the development of new coatings; however, this process may take many years. Corrosion tests for coatings development, qualification, and selection often provide poor correlation to service performance. Conventional tests and characterization procedures may not assess the most relevant degradation mechanisms of loss of barrier properties, localized corrosion, and galvanic attack. Furthermore, these tests do not yield information on interactions between specific environmental parameters and material degradation or the kinetics of failure. To improve coating evaluations, electrochemical sensors and data acquisition systems have been

Manuscript received November 7, 2017; accepted for publication March 15, 2018.

[1]Luna Innovations Inc., 706 Forest St., Suite A, Charlottesville, VA 22936, USA F. J. F. http://orcid.org/0000 0002 5148 5488, J. C. D. http://orcid.org/0000 0003 1733 4755, N. K. B. http://orcid.org/0000 0002 4599 7575, P. C. K. http://orcid.org/0000 0002 8686 8091

[2]ASTM Symposium on *Advances in Electrochemical Techniques for Corrosion Monitoring and Laboratory Corrosion Measurements* on November 13 14, 2017 in Atlanta, GA, USA.

developed to measure coating performance and corrosion continuously during atmospheric tests. The sensing elements are incorporated in multisensor test panels that can be cleaned, coated, and scribed like conventional coating test panels. The multisensor panels support measurement of coating barrier properties, free corrosion, and galvanic corrosion. The barrier properties and free corrosion are measured using impedance-based methods, and galvanic corrosion is quantified using a zero resistance ammeter. Local measurements of panel surface temperature, air temperature, and relative humidity are used to correlate degradation rates and barrier properties to environmental conditions. The simultaneous environmental measurements also provide records that can be used to ensure the validity of performance comparisons between separate tests and within a single test. A description of the sensors, electrochemical measurements, and methods for coating testing are reported.

Keywords

atmospheric corrosion, coating degradation, electrochemical impedance spectroscopy, zero resistance ammeter, accelerated testing

Introduction

Corrosion increases maintenance costs and reduces the availability of commercial and military aircraft and ultimately can reduce aircraft service life and degrade structural integrity. Studies by the U.S. Department of Defense conclude that 25 % of maintenance costs are associated with corrosion, while for newer fleets of aircraft used by commercial aviation, corrosion may account for 10 % of total maintenance costs [1,2].

Organic coating systems are the primary means of corrosion protection for air craft. A coating system may consist of cleaning processes, pretreatment, primer, and topcoat. Traditionally, these protective coatings have been solvent borne sys tems containing hexavalent chromium compounds to inhibit corrosion. The desire to achieve improved corrosion performance and reduce the use of volatile organic solvents and hexavalent chromium have been driving the development and qualifi cation of new coating systems. The introduction of new coatings can take years, and poor performance can result in costly removal and replacement. Besides aes thetics, the capacity of protective coating systems to prevent localized corrosion and damage that might transition into cracks is important to maintaining aircraft struc tural integrity.

Historically, corrosion testing for coatings development, qualification, and selection has been done using accelerated corrosion test chambers, outdoor expo sure tests, and demonstration trials. Concern about the correlation of accelerated tests with service performance has resulted in numerous efforts to develop more representative testing [3 5]. These efforts have resulted in a number of cyclic corro sion tests, and wet and dry cycling are widely recognized as being important in determining the aggressiveness of an atmospheric exposure test [6 8]. Corrosion

test cycles typically are described by environmental factors such as time, tempera ture, and humidity; test solution chemistry and flow rates (collection volumes); and mass loss requirements using standard alloy coupons [9]. The environmental fac tors, solution chemistry, collection volumes, and mass loss conditions are all easily measured parameters, but the significance and level of control required during tran sitions from wet to dry states or vice versa to achieve consistent results are not well known. Although cycling is recognized as important to achieving the desired level of aggressiveness and morphology of corrosion attack, it is difficult to quantify the amount of corrosion that occurs during these transitions.

Atmospheric corrosion testing of coatings has relied heavily on test panels that can be conveniently processed and prepared in large quantities. The coated panels are often scribed to produce controlled damage to the coating prior to exposure. These panels typically are rated after set times to obtain comparative results for materials tested simultaneously, from previous tests, other laboratories, or relative to defined performance requirements. A number of criteria may be used for rating coating and corrosion performance after a given test time such as blistering and creep back from a scribe [10]. These evaluation criteria are cumulative measure ments and provide very little information on the kinetics of the degradation pro cess. Furthermore, the simple panel design and ratings methods are primarily cosmetic assessments for the capacity of a coating to reduce alloy free corrosion at a coating defect. The evolution of the coating condition, reaction to a set of specific environmental conditions, and other corrosion mechanisms are not assessed using scribed panels and post test analysis.

More complex sample designs have been developed to obtain measurements that assess coating performance and corrosion mechanisms that are more relevant to structural integrity [11 13]. In some instances, these more complex sample designs have been instrumented to obtain measurements of corrosion rate during testing, and recently, electrochemical sensor techniques have been standardized for continuous measurement of coating condition during testing [11,14,15]. Elec trochemical sensors for measuring time of wetness, atmospheric corrosion, and coating performance have been utilized by a number of researchers [16 19]. There is a recognized, but as yet unmet, need to improve the correlation between outdoor and accelerated tests, increase the reliability of atmospheric corrosion tests, and obtain a more complete understanding and quantification of coating performance and corrosion to support the development, qualification, and selec tion of coatings.

The present study is focused on integrating standardized environmental and electrochemical sensors into a test system that can be used by the coatings commu nity to monitor exposure conditions and continuously track coating performance. It is expected that these sensors and measurement systems will enable (1) improved understanding of atmospheric corrosion and coating performance; (2) develop ment, standardization, and control of accelerated tests; and (3) more reliable and application relevant coatings testing.

Experimental Methods

A coating and corrosion evaluation system is described that is used to measure environmental parameters, alloy free corrosion (i_c), galvanic corrosion (i_g), and coating barrier properties. These electrochemical sensors were developed to meet test method American National Standards Institute/NACE International (ANSI/NACE) TM0416 2016 [14]. Multiple test systems have been used to characterize corrosion test chamber conditions and perform accelerated tests and outdoor exposure evaluations of aerospace coatings systems. The focus of this work has been the measurement system development, although some coating and corrosion test data are reported.

MEASUREMENT SYSTEM

The corrosion and coating evaluation system includes three major components: the multisensor panel (MSP), docking platform, and base station laptop (Fig. 1). Each MSP includes a free corrosion sensor, galvanic corrosion sensor, and coating barrier property sensor. The docking platform is a multichannel data acquisition device that supports three MSPs, a temperature sensing panel and relative humidity (RH) and air temperature measurements. The complete assembly of docking platform with MSPs and temperature sensor panel are designed for operation in accelerated corrosion test chambers and outdoor exposure sites. The docking platform performs continuous data acquisition, processing, and storage throughout an exposure test. The base station is used to enter test specific data, visualize the data during the test, and retrieve the data from the docking platform.

Corrosion and Coating Measurement Techniques

Electrochemical measurement methods and instrumentation are used to determine the corrosion rate and perform coating property measurements. The free corrosion

FIG. 1 (a) Coating evaluation system with (b) docking platform for data collection from multisensor panels.

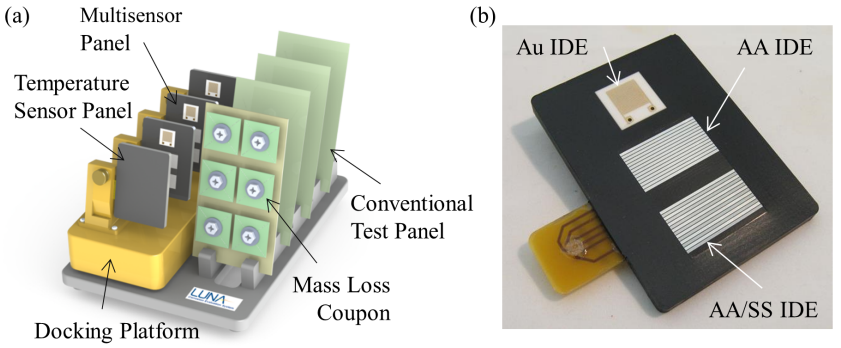

rate is measured using a laminated interdigitated electrode (IDE) that is fabricated from a 0.813 mm UNS [20] A97075 (AA7075 T6) sheet with the rolling direction oriented normal to the exposure test surface. The two electrode sensor has 14 digits, with an area of approximately 144 mm^2 for one electrode of the IDE. The dielectric material separating the laminated IDE is an epoxy fiberglass prepreg sheet that results in an electrode separation distance of approximately 0.1 mm. The aluminum free corrosion sensor is excited using a 10 mV peak to peak 0.5 Hz AC signal. The free corrosion measurement is the root mean square current response to the excitation voltage reported in units of microamperes. Cumulative free corrosion is the integral of the free corrosion rate reported in microcoulombs. Given that the corrosion mechanism for AA7075 T6 is pitting, the measurements of free corrosion cannot be used directly to estimate mass loss or thickness loss without additional empirical correlations between the sensor output and actual corrosion damage measurements, such as mass loss measurements [14].

Galvanic corrosion is measured using an IDE, with similar dimensions as the free corrosion sensor except one electrode is fabricated from a 0.032 in. (0.813 mm) UNS S31600 (SS316) sheet. Galvanic corrosion rate is measured using a zero resistance ammeter.

Coating barrier properties are quantified using a gold IDE that is a thick film printed electrode on a 0.6 mm thick alumina substrate. The coating impedance magnitude is measured using a 10 mV peak to peak AC excitation signal at a high frequency of 25 kHz and a low frequency of 10 Hz. The frequency range was selected based on the instrumentation limits and to achieve measurements that are sensitive to surface and bulk properties of the coated sensor [19].

Environmental Parameters

Each docking platform records air temperature (T_a), RH, and panel surface temperature (T_s) (Table 1). Knowing the air temperature, RH, and panel surface temperature, an effective RH can be calculated for the panel surface according to Eq 1, where variables a and b are 17.625 and 243.04°C, respectively [21].

$$RH_{eff} = RH \times \exp\left[\frac{aT_a}{b + T_a}\right] \times \exp\left[\frac{-aT_s}{b + T_s}\right] \quad (1)$$

TABLE 1 Environmental sensors used in docking platform.

Sensor	Parameter	Span	Accuracy	Repeatability
Sensirion SHT75[a]	RH	0 to 100 % RH	± 1.8 % RH	± 0.1 % RH
	Air Temp.	40 to 123°C	± 0.3°C	± 0.1°C
U.S. Sensor PPG102A1[b]	Surface Temp.	50 to 500°C	± 0.5°C	± 0.1°C

[a]Sensirion, Staefa ZH, Switzerland.
[b]U.S. Sensor, Orange, CA.

TEST MATERIALS

The MSP is designed to be cleaned, pretreated, coated, and scribed like a conven tional corrosion test panel. The MSPs and conventional 4 by 6 in. (10 by 15 cm) AA7075 T6 corrosion test panels were pretreated using a chromate conversion coating (MIL DTL 5541 Type I Class 1A). A variety of primers have been tested, including a chromate containing solvent borne primer (Cr SB, MIL PRF 23377J, Type 1 Class C2), a nonchromate solvent borne primer (NC SB, MIL PRF 23377J, Type I Class N), and a nonchromate waterborne primer (NC WB, MIL PRF 85582 Type II Class N). A single topcoat was used with all the aforementioned primers (MIL PRF 85285 Type 1 F7925 Gloss White). All the coatings were spray applied to the MSPs and conventional test panels.

ACCELERATED AND OUTDOOR TESTING

Both cyclic accelerated corrosion tests and outdoor exposures have been performed using the coating evaluation system. Four separate laboratories tested docking plat forms according to ASTM G85 11, *Standard Practice for Modified Salt Spray* (*Fog*) *Testing*, Annex 5 [22]. A single test cycle is a 1 h salt fog at room temperature fol lowed by 1 h dry off at 35°C. The salt solution contains 0.05 % sodium chloride and 0.35 % ammonium sulfate. The ASTM G85 A5 method was chosen as a rela tively simple test cycle that all four of the participating laboratories were capable of performing.

Outdoor testing was done at the Battelle (Columbus, OH) exposure site near Daytona Beach, FL; the Boeing (Chicago, IL) exposure site on Whidbey Island, WA; and Wright Paterson Air Force Base, Dayton, OH. The docking platforms were placed unsheltered on exposure racks at all test sites and within simulated air craft structures (SASs) at Whidbey Island and Daytona Beach. The SAS boxes were fabricated from aluminum sheet stock and comprised of bottom, top, and side panels to achieve an overall size of 23.5 by 20 by 8.835 in. (60 by 51 by 22 cm). The SAS boxes had bolted joints to form a nonhermetically sealed enclosure.

Initial testing was performed to evaluate the system response to environmen tal conditions within a single accelerated corrosion chamber. Testing was per formed using four docking platforms to obtain an estimate of measurement system variability with regard to environmental measurements. Subsequent tests utilized a single coating system (NC SB) evaluated at four laboratories using three docking platforms each and three MSPs per docking platform. Outdoor exposures also used three docking platforms for each of the sheltered and unsheltered test conditions.

Results

Test results are given for the environmental testing at a single laboratory, single coating system evaluation at multiple laboratories; some preliminary testing with multiple coatings in accelerated tests and outdoor exposures is also given.

ENVIRONMENTAL

Initial environmental testing was done using four docking platforms located in four separate quadrants of a corrosion test chamber. A typical cycle of ASTM G85 A5 as measured by a docking platform is given in **Fig. 2**. The ASTM G85 A5 test cycle was run for 330 h and then the docking platforms were moved to new positions within the chamber for completion of the approximately 1,300 h of testing. The average RH and temperature were calculated for each docking platform before and after being moved at 330 h. Pairing the before and after data by chamber quadrant posi tion yields a strong correlation between docking platform surface temperature and RH (**Fig. 3**). The standard deviation of the average surface temperature within the chamber is 0.79°C and the average RH standard deviation is 1.8 %. Based on corre lation of the docking platforms for each quadrant before and after 330 h, the aver age surface temperature and RH standard deviations are 0.16°C and 0.32 %, respectively. The correlation based on chamber position indicates that the measure ment system variability is better than the within chamber average temperature and RH position variability.

Four laboratories performed ASTM G85 A5 cyclic accelerated corrosion tests using three docking platforms each. Besides within chamber position dependency, significant differences in the chamber test cycles were observed among the laborato ries (**Fig. 4**). One laboratory repeated the 1,125 h ASTM G85 A5 test three times and within laboratory variability was apparent, but it was not as extreme as the between laboratory differences.

FIG. 2 Docking platform measurement of panel temperature and RH for one cycle of the ASTM G85 A5 corrosion test.

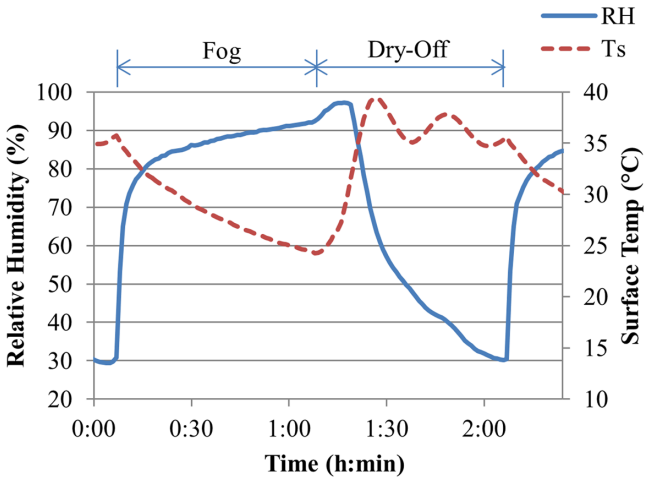

FIG. 3 Docking platform average panel (a) surface temperature and (b) RH for four docking platforms placed in different chamber positions before and after 330 h of testing. Each quadrant position in the chamber was measured by two different docking platforms.

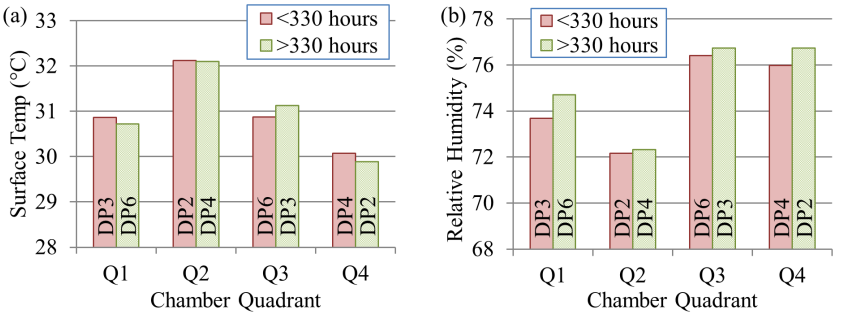

FIG. 4 Plots of effective RH versus surface temperature for two cycles of the accelerated corrosion test. The test was done at four laboratories (L1 L4), and three docking platforms were tested at each laboratory.

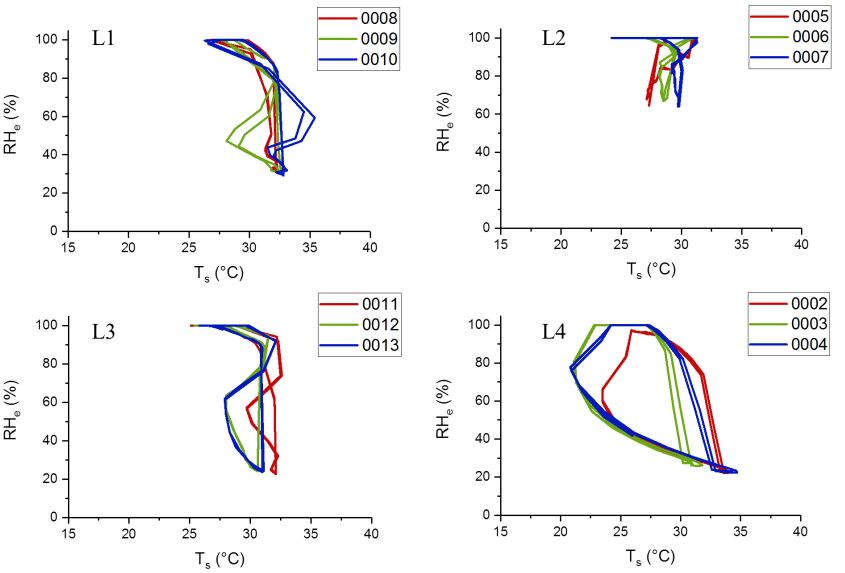

In outdoor environments, RH and temperature tend to have inverse approxi mately linear dependence, where RH is low when air temperature is high during the day and RH is high at night when the temperature is low (Fig. 5). Sheltered and

FIG. 5 Outdoor environmental data for unsheltered docking platforms at the (a) Whidbey Island and (b) Daytona Beach exposure sites.

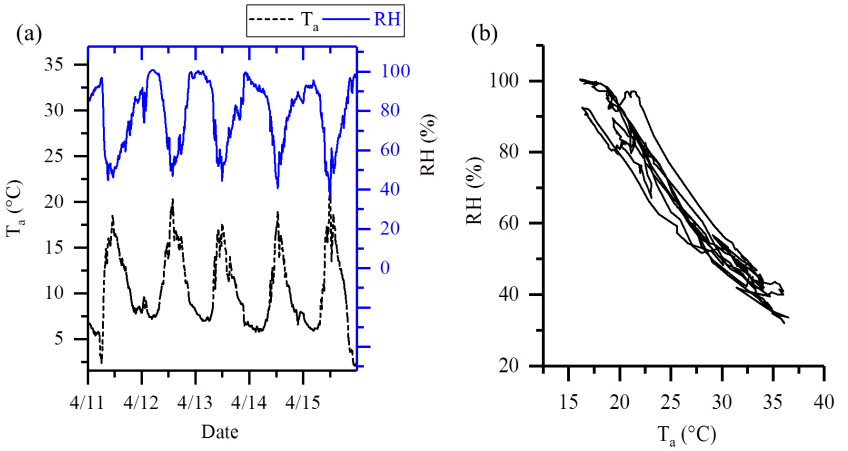

unsheltered environmental conditions were similar, with air temperature in the SAS box being equal to or slightly higher than the unsheltered docking platform. The slightly elevated temperature had the expected effect of reducing the RH in the SAS box. Also, the unsheltered temperature and RH have more high frequency var iation with time, which is superimposed on the larger diurnal cycling, as compared to the sheltered system within the SAS box (Fig. 6). There is a high degree of

FIG. 6 Air temperature and RH for sheltered and unsheltered docking platforms exposed at the Daytona Beach exposure site.

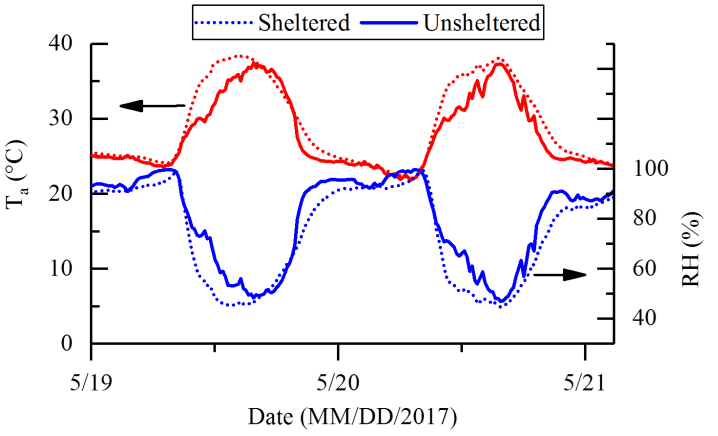

correlation, coefficient of determination (R^2) of 0.99, between the air temperature and surface temperature measurements for a given docking platform sheltered in an SAS box at Daytona Beach. For the same location, the correlation was less ($R^2 = 0.92$) between the air temperature and surface temperature for an unsheltered docking platform. Similar correlations exist for RH and effective RH given that Eq 1 uses RH and air and surface temperature to calculate effective RH. Since there is a high degree of correlation between these parameters, air temperature and RH are used in the following results and analysis. The influence of differences between air and surface temperature are of interest but beyond the scope of this investigation.

CORROSION

Both accelerated and outdoor corrosion testing were performed using the coating evaluation system with conventional scribed panels tested in parallel. Environmental, corrosion, and barrier property data were recorded at 5 and 15 min intervals for accelerated and outdoor tests, respectively.

Accelerated Cyclic Corrosion Testing

The corrosion rate was measured continuously during the cyclic accelerated corrosion tests, and cumulative corrosion was quantified by integrating the measurement with respect to time. The cyclic corrosion tests were run for approximately 1,125 h, with conventional coated test panels pulled in triplicate at 350, 625, and 1,125 h. The corrosion rate varied with environmental conditions where higher humidity produced higher corrosion (**Fig. 7**). Cyclic corrosion testing produced reasonably repeatable observations of high corrosion rate during wetting and drying transitions with low corrosion rates at the high and low RH extremes (**Fig. 8**).

FIG. 7 (a) Free corrosion (i_c) and (b) galvanic corrosion (i_g) rate for NC SB coated MSPs as a function of RH and temperature for the cyclic accelerated corrosion test (L2).

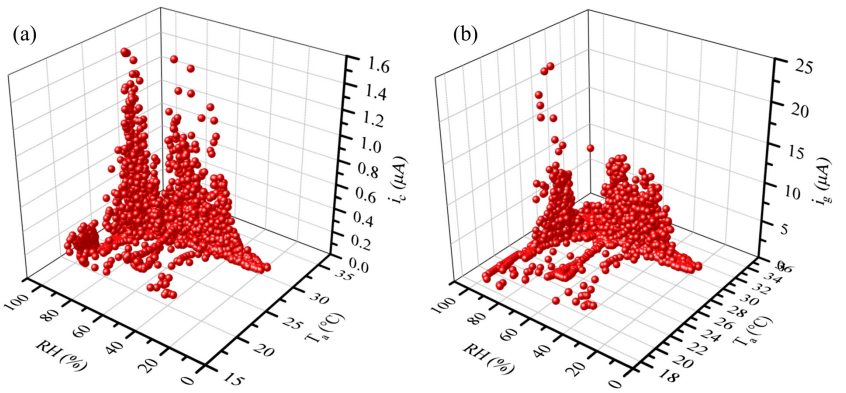

FIG. 8 Free corrosion (i_c) and galvanic corrosion (i_g) rate for NC SB coated MSPs as a function of time for the accelerated cyclic corrosion test (L2).

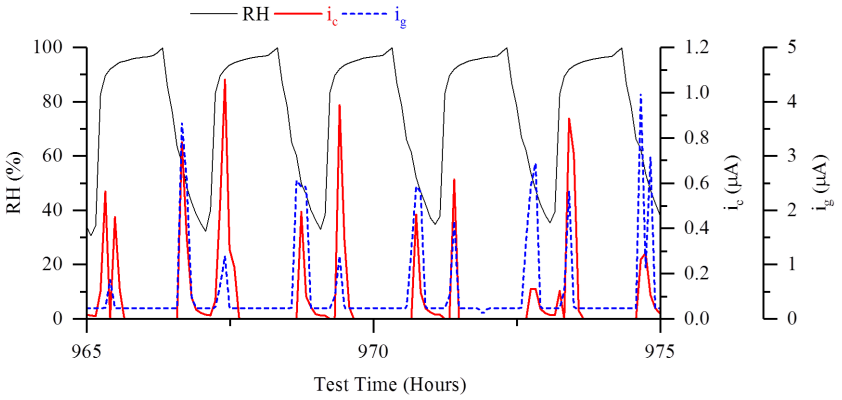

For each laboratory with three docking platforms, nine measurements of cumu lative free corrosion and galvanic corrosion were made (Fig. 9). The total corrosion was calculated for each time interval when conventional coated and scribed panels were pulled for coating condition and corrosion ratings. The conventional scribed panels were pulled at the prescribed intervals and rated for corrosion in the scribe, undercutting, and blistering. No coating creep back or blistering was observed, and only the corrosion in the scribe rating provided any performance discrimination.

FIG. 9 Cumulative (a) free corrosion and (b) galvanic corrosion for NC SB coated MSPs evaluated in cyclic accelerated corrosion tests performed at four laboratories. One laboratory (L4) conducted three replicated cyclic tests. Error bars are 95 % confidence intervals.

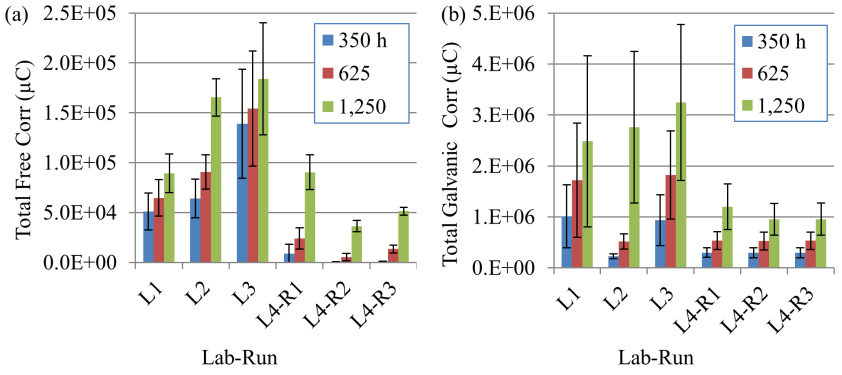

Corrosion in the scribe was determined by a visual rating method for percent length of scribe stained or corroded and a numerical score for severity of corrosion, with zero being bright and clean and five being severe corrosion product buildup. A sin gle panel score was determined by summing the product of the percentage and se verity ratings (Fig. 10).

Outdoor

Three coating systems are being tested at three exposure sites. Testing at Whidbey Island started later than the other locations, and corrosion results are limited. The free corrosion rate is typically maximum when the humidity is high (Fig. 11 and Fig. 12). The galvanic corrosion rate was very low for the exposure period and is at the low limits of detectability for the measurement system. Similarly, the sheltered docking platforms measure little or no corrosion at the Daytona Beach and Whid bey Island exposure sites. The cumulative free corrosion has been determined for the unsheltered docking platforms at the Ohio and Daytona Beach test sites (Fig. 13). One docking platform at the Ohio exposure site lost power from 1,000 to 2,500 h. The total corrosion data for the Ohio exposure site are reasonably well grouped, with differences in measured total corrosion of approximately 20 % of the maximum corrosion for each coating system after 150 days of exposure. The total corrosion measured at Daytona Beach for the chromate containing system (Cr SB) was approximately an order of magnitude higher than what was measured for the same length of time in Ohio. The nonchromate systems (*NC SB* and NC WB) had much more variation in performance relative to the chromate containing system (Cr SB) tested at Daytona Beach.

FIG. 10 Visual scribe corrosion ratings for conventional painted test panels exposed in cyclic accelerated tests performed at four laboratories. One laboratory (L4) conducted three replicated cyclic tests. Each bar represents an average of three replicate panel ratings.

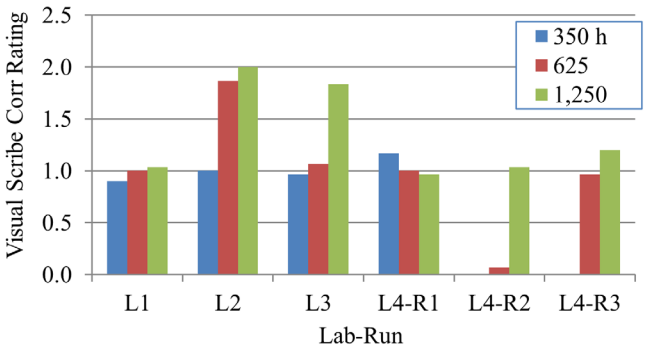

FIG. 11 Free corrosion rate (i_c) as a function of RH and temperature for an unsheltered MSP with an NC SB coating system tested at the Daytona Beach exposure site for 150 days.

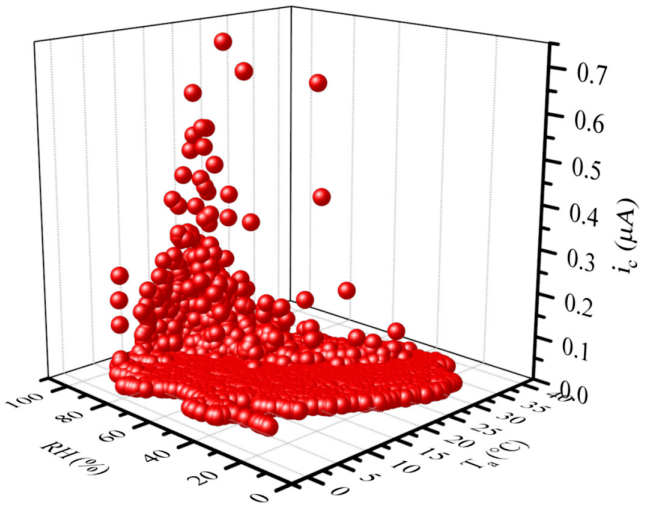

FIG. 12 Free corrosion (i_c) of an unsheltered MSP with an NC SB coating system tested at the Daytona Beach exposure site.

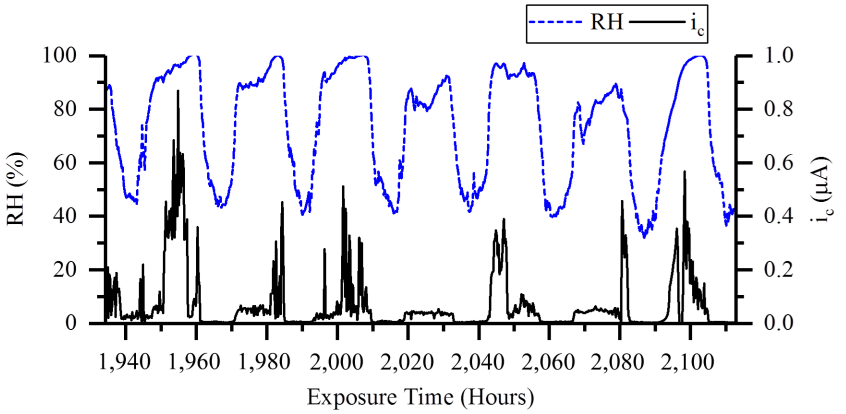

COATING BARRIER PROPERTIES

The coating barrier properties are determined by making high and low frequency measurements using gold IDE electrodes. The coating impedance varies with time and is dependent on the environmental conditions in cyclic corrosion tests and

FIG. 13 Cumulative free corrosion (i_c) for three coating systems tested at the (a) Ohio and (b) Daytona Beach exposure sites.

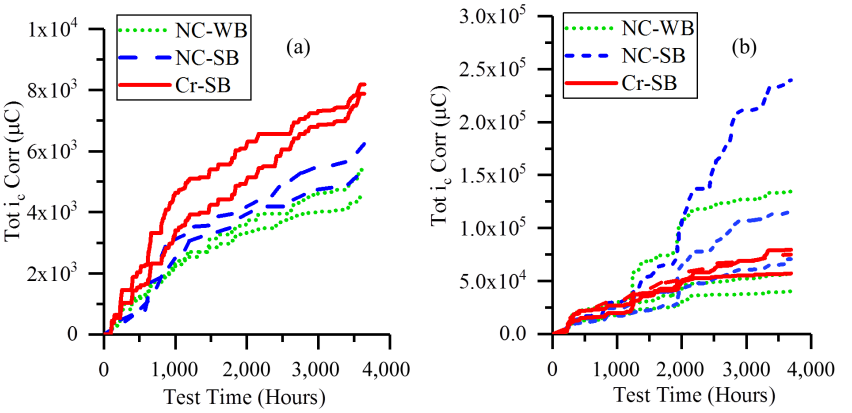

outdoor exposures (Fig. 14 and Fig. 15). Both the high and low frequency coating impedances had a similar response to environmental conditions in both the laboratory tests and outdoor exposures.

Discussion

The coating evaluation system has demonstrated utility for continuous measurements of coating impedance, free corrosion, galvanic corrosion, and environmental parameters.

FIG. 14 High frequency impedance modulus as a function of time for an NC SB coating system in a cyclic corrosion test (L3).

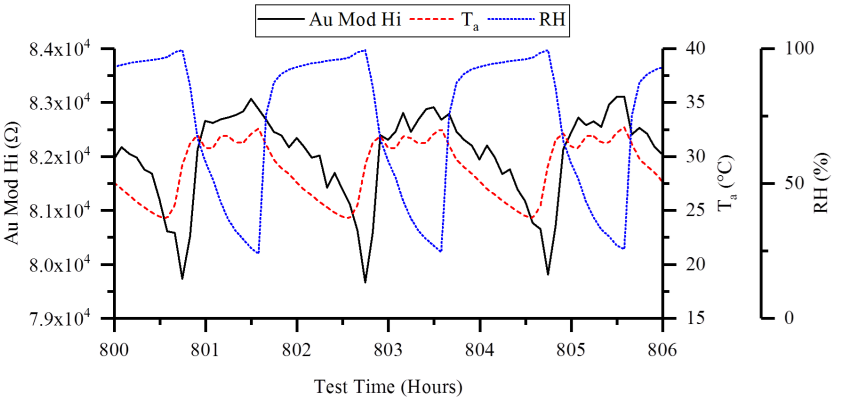

FIG. 15 (a) Low and (b) high frequency impedance modulus for 40 cycles of ASTM G85 A5 testing (L3) and approximately 4 days of outdoor exposure in Daytona Beach.

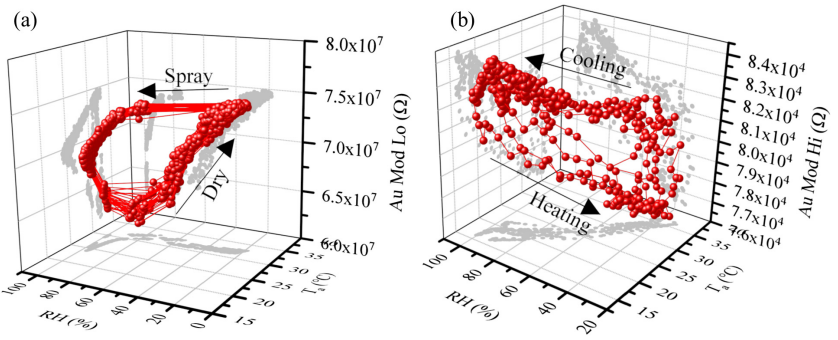

ENVIRONMENTAL PARAMETERS

Environmental conditions within the chamber were determined to have greater variability than the inherent measurement system variability for temperature and RH (Fig. 3). The average panel temperature and RH had measureable systematic dependence on position within the chamber. The range of differences in these average temperature and RH values was only 2°C and 5 %, respectively. More significant differences may exist in the distributions of the temperature and humidity, cyclic profiles, and extreme values of the environmental data achieved within a given chamber (Fig. 4). The environmental test profiles measured by triplicate docking platforms in four laboratories, shown in Fig. 4, are unique for each laboratory and docking platform. For the ASTM G85 A5 test performed three separate times at the same laboratory, the environmental test profile was different for each run. One critical parameter that is not currently measured with the coating evaluation system is salt deposition.

Relative to cyclic corrosion testing, outdoor environments have much slower fluctuations between nighttime, high RH and low temperature, and daytime, low RH and high temperature, conditions (Fig. 5a). In general, RH is inversely dependent on temperature in the outdoor environments, although this functional dependence may be altered by short term weather events or long term seasonal changes (Fig. 5b). The environmental data from the docking platforms sheltered within the SAS boxes did have smoother RH and temperature dependence as a function of time, or less short term (approximately minutes) environmental transients as compared to the unsheltered systems (Fig. 6). This likely is due to the thermal mass of the SAS box, shading from direct solar irradiance, and sheltering from precipitation. The temperature and RH within the SAS boxes did trend with ambient environment diurnal cycling.

CORROSION

Free corrosion and galvanic corrosion are dependent on the environmental conditions (Fig. 7). Corrosion rate peaks during wet and dry transitions in the accelerated chambers (Fig. 8). Cumulative corrosion is significantly different among the test laboratories, and the cumulative corrosion is in rank order agreement with the visual rating of conventional scribed panels (Fig. 9). Although the environmental conditions for each laboratory are very unique, the significance to corrosion of the environmental parameters is not yet known. Given the amount of galvanic and free corrosion occurring during the wet and dry transitions, future efforts to improve corrosion test chamber operation should consider the time dependence and RH and temperature combinations that define the environmental pathway between wet and dry states.

The total free corrosion data for replicate individual MSPs tested on multiple docking platforms with one coating system (NC SB) at four different laboratories have been used to assess the system variability. The average total free corrosion is statistically different for the different laboratories (Fig. 8). This is not a surprising result given the differences in the environmental conditions among the laboratories (Fig. 4). Within a given laboratory, the coefficient of variation (CoV, standard deviation divided by the mean) for all the MSPs tested in each laboratory was statistically equivalent across all the laboratories. The average variation between docking platforms (CoV = 27 % for 1,125 h data) at a laboratory is greater than the within docking platform variation (CoV = 18 % for 1,125 h data) (Fig. 16). The average coefficient of variation for all the MSPs tested in each laboratory decreased as a function of test time, although the variation increased with average total free corrosion (Fig. 9). The inherent variation in the measurement system is still unknown

FIG. 16 Average coefficient of variation for each laboratory at three test times. Average coefficient of variation for individual docking platforms after 1,125 h is also given.

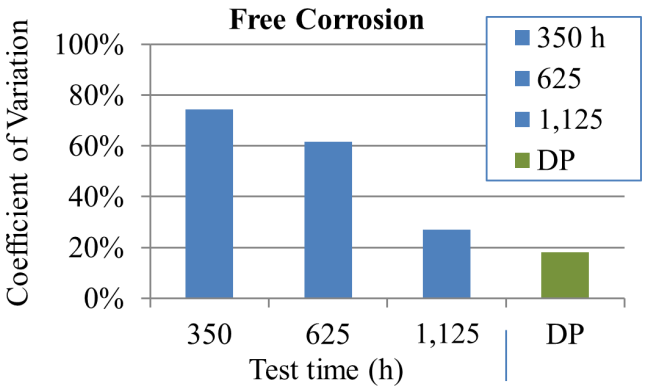

since the measurements are no more consistent than the environmental chambers used to test them.

High corrosion rate transients during wetting and drying in the outdoor test environments are not as obvious as with the accelerated tests (**Fig. 8** and **Fig. 12**). The reason for this is not clear, but some obvious differences between the cyclic accelerated tests and outdoor exposures exist. One obvious difference is that the cyclic test has much shorter transition times between the wet and dry states. Also, the ASTM G85 A5 cyclic test wets the surface with a salt solution, while corrosivity of the outdoor environment is controlled, in part, by wet and dry deposition of salts and the hygroscopic properties of these surface contaminants. Corrosive periods due to diurnal RH fluctuations would wet and dry the surface due to the hygroscop ic properties of the deposited contaminants [23]. Precipitation and condensation events in the outdoor environment are expected to wash the surface and reduce the amount of soluble salts that enhance corrosion. Slower transitions, milder environ mental conditions, and differences in hygroscopic properties and processes may all contribute to the differences in corrosion rate observed between the accelerated test and outdoor exposure. It is expected that improved understanding of these differ ences and the significance of these processes on coating performance and corrosion would be important in establishing more realistic accelerated tests that better simu late service environments.

As expected, based on proximity to the coastline, the Ohio test site was measured to be much less aggressive than the coastal Daytona Beach location. One docking platform at the Ohio exposure site lost power from 1,000 to 2,500 h, but other than this outage, the data were well grouped by coating system for this first 150 days of exposure. Higher amounts of cumulative corrosion occurred for the coatings exposed in Daytona Beach, with the nonchromate systems (NC SB and NC WB) having more variation in performance relative to the chromate containing system (Cr SB). The higher degree of variability in performance of the nonchromate coating systems at the Daytona Beach site may be due to the higher severity and their poorer perfor mance relative to the coating with chromate inhibitor.

BARRIER PROPERTIES

Barrier properties are measured at low and high frequencies to expand the coating impedance measurement range, with the low frequency impedance being much larger than the high frequency impedance. The low and high frequency coating impedance was dependent on the environmental conditions in cyclic corrosion and outdoor exposure tests (**Fig. 14** and **Fig. 15**).

Organic coatings can be modeled using equivalent circuits to fit electrochemical impedance spectroscopy data [16,19,24]. Coating impedance tests typically are per formed in immersion cells using three electrode measurements, and a basic circuit model is given in **Fig. 17a**. For the two electrode, gold IDE measurements using the MSP, both electrodes are covered by the coating, and the circuit model may be adjusted to account for this altered electrode geometry (**Fig. 17b**). The three electrode

FIG. 17 Equivalent circuit models for (a) an organic coating where one electrode is in the solution and the other is the metal substrate and (b) for a two electrode IDE sensor where both electrodes are covered by the organic coating, as is the case for the gold IDE of the MSP.

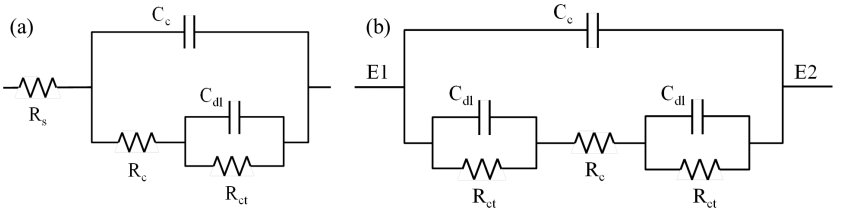

immersion measurement includes uncompensated solution resistance (R_s) that is typically very low relative to the ionic pore resistance of the coating (R_c). The gold IDE equivalent circuit includes the coating resistance (R_c) and capacitance (C_c), along with the interface electrochemical elements of double layer capacitance (C_{dl}), Warburg impedance (Z_w), and charge transfer resistance (R_{ct}) for each of the two gold electrodes. Based on these assumed equivalent circuits for coatings, it is expected that the high frequency measurements would be increasingly dependent on the coating resistance while the low frequency measurements would have increasing contributions from the charge transfer resistance.

The coating barrier properties are measured at two frequencies, low (10 Hz) and high (25 kHz), using the gold IDE. Both the low and high frequency impedances were dependent on the ionic resistance of the coating (**Fig. 17**). Ionic coating resistance and coating capacitance are dependent on the properties of the coating with respect to water uptake in the polymer matrix. Important properties for determining R_c and C_c are water equilibrium concentration of the polymer and water diffusion rates that are both dependent on temperature and RH [25,26]. The ionic coating resistance and capacitance are also dependent on the existence of pores and possibly the hygroscopic properties of the inhibitors.

The high frequency impedance likely is dominated initially by the low coating capacitance (C_c) and high coating resistance. With water uptake, the coating capacitance increases and the coating resistance decreases, resulting in a drop in impedance. At low frequencies, electrochemical processes have a larger contribution to the impedance and would be dependent on the double layer capacitance and charge transfer resistance. The low frequency impedance response is expected to be dominated by coating resistance and charge transfer resistance. Therefore, at high frequency, environmental conditions would have the largest impact on impedance response, while at low frequencies, environmental conditions and interfacial electrochemical response would both contribute to impedance. Both low and high frequency impedance are expected to respond to coating degradation and changes

in electrode area with respect to coating blistering and disbonding, but these depen dencies were not considered in the present investigation.

Assuming a strong dependence of high frequency impedance on environmental parameters, a multiparameter linear fit was performed for the high frequency im pedance. The high frequency impedance of an NC SB coating system with a shel tered exposure at Daytona Beach was a strong function ($R^2 = 0.95$) of temperature and RH (Fig. 18a). For the unsheltered docking platform, the variation in the high frequency impedance for the NC SB coating system was not as strongly correlated as the sheltered coating, although a significant fraction of the variation ($R^2 = 67$ %) is accounted for by the environmental parameters of temperature and RH (Fig. 18b).

In general, the high frequency impedance is inversely dependent on tempera ture and humidity, and this is consistent with the expectation of higher water con tent and diffusivity with increased humidity and temperature (Fig. 18). An inverse dependence of impedance on RH is also observed for the low frequency measure ments (Fig. 19a). An inverse dependence of low frequency impedance on tempera ture is not apparent in Fig. 19b, but it should be noted that, at the higher temperatures, RH is likely to be low. The dependence of impedance on water con tent and diffusion into and out of the coating would explain the hysteresis observed in the impedance response during the wetting and drying processes (Fig. 15). Fur thermore, this may explain the improved high frequency impedance prediction for the SAS box, where the changes in temperature and RH were more gradual com pared to the unsheltered exposed coating (Fig. 18).

A similar analysis was performed on the low frequency data for an NC SB coat ing system exposed (unsheltered) at Daytona Beach (Fig. 19). A multiparameter linear

FIG. 18 Predicted high frequency impedance versus measured impedance for an NC SB coating exposed at the Daytona Beach test site. The two plots are for (a) sheltered and (b) unsheltered conditions.

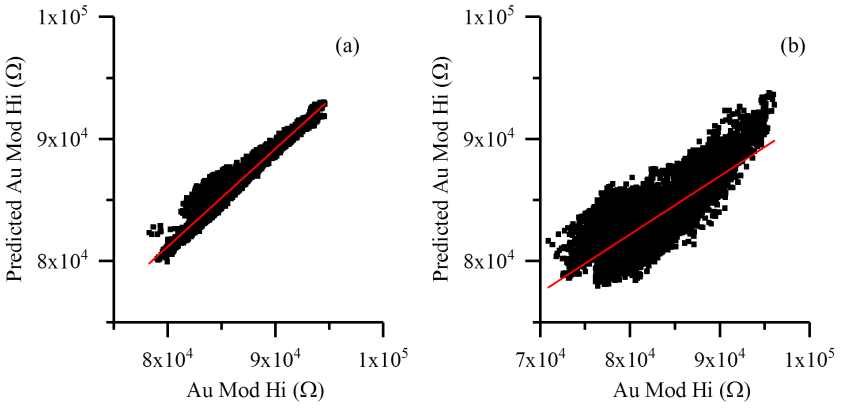

FIG. 19 Low frequency coating impedance modulus versus (a) RH and (b) air temperature for an NC SB coating unsheltered at the Daytona Beach test site.

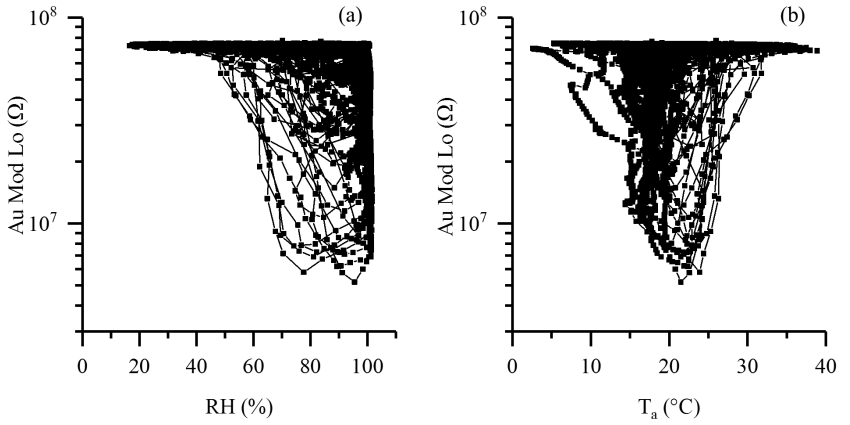

fit using air temperature and RH was investigated. The low frequency impedance data did not have an obvious linear dependence on either temperature or humidity. The low frequency data did behave a lot like bare metal low frequency corrosion data, where the impedance has a nonlinear dependence on RH due to salt hydration and is dominated by the charge transfer resistance. These data are qualitatively consistent with the equivalent circuit model, where high frequency impedance is dominated by environmental interactions with the coating, and low frequency behavior is dependent on interfacial electrochemical processes.

Conclusions

The coating evaluation system has been demonstrated for obtaining continuous environmental, corrosion, and barrier property data throughout accelerated corrosion tests and during outdoor exposures. Testing was performed using multiple coating evaluation systems within individual chambers, in multiple replicate tests, and at four different laboratories. Significant variability exists for environmental conditions within an individual chamber, for each replicate run of a given chamber, and between laboratories all running nominally the same cyclic accelerated corrosion test (ASTM G85 A5). These differences in conditions between laboratories resulted in significantly different amounts of corrosion. The free corrosion and galvanic corrosion rates were highest during transitions between wet and dry conditions in the cyclic accelerated test, but these peak corrosion transients were not as apparent in outdoor exposure tests. The coating barrier properties were inversely dependent on temperature and RH, and hysteresis was observed in the high and low frequency impedance in both the laboratory and outdoor tests. A strong

correlation between temperature and RH was obtained for high frequency coating impedance in sheltered conditions, but for unsheltered and accelerated testing, this correlation was reduced likely due to these hysteresis effects.

The system has been demonstrated to produce continuous time based measurements of environmental and coating performance parameters in laboratory chamber tests and outdoor exposures. The relationships between environmental conditions and corrosion rates have not been determined, and knowledge of salt deposition rates is needed to obtain a more complete picture of the conditions that determine corrosivity in chamber tests and outdoor exposures. The measurement system described here may be useful for determining these dependencies in future efforts. Improved knowledge of measurement system variability for corrosion and barrier properties would be beneficial, but this would require test condition consistency that is possibly beyond what can be achieved in laboratory chambers and that may only be possible in outdoor exposure tests. It is expected that the coating evaluation systems will have utility for coating formulation, product qualification, and materials selection.

ACKNOWLEDGMENTS

This material is based upon work supported by the U.S. Air Force under Contract No. FA8501 13 C 0017 and the Office of Naval Research under Contract No. N00014 15 C 5053. Any opinions, findings, and conclusions or recommendations expressed in this material are those of the authors and do not necessarily reflect the views of the U.S. Air Force and Office of Naval Research. The authors thank the program managers David Ellicks, with the Air Force Life Cycle Management Center, and William Nickerson, with the Office of Naval Research, for their support and guidance. Boeing, the University of Dayton Research Institute, and the Southwest Research Institute are acknowledged for accelerated and outdoor corrosion testing. In particular, Alexander Khramov of the University of Dayton Research Institute performed materials preparation and panel ratings; James Dante and Travis Kostan of the Southwest Research Institute provided data interpretation and statistical analysis; and Kristen Williams, Richard Wire, and Wes Quigley managed the corrosion testing at Boeing.

References

[1] Herzberg, E., "Determining Corrosion's Effect on the Cost and Availability of DOD Weapon Systems and Equipment," Report SAL4ITI, Logistics Management Institute, Tysons, VA, 2015.

[2] Benavides, S., "Corrosion Control in the Aerospace Industry," Woodhead, Cambridge, UK, 2009, p. 320.

[3] Montgomery, E., Curran, J., Calle, L., and Kolody, M., "Timescale Correlation between Marine Atmospheric Exposure and Accelerated Corrosion Testing," NACE-11353, presented at *CORROSION 2011*, Houston, TX, March 13–17, 2011, NACE International, Houston, TX, p. 27.

[4] LeBozec, N., Blandin, N., and Thierry, D., "Accelerated Corrosion Tests in the Automotive Industry: A Comparison of the Performance towards Cosmetic Corrosion," *Mater. Corros.*, Vol. 59, No. 11, 2008, pp. 889–894.

[5] Boelen, B., Schmitz, B., Defourny, J., and Blekkenhorst, F., "A Literature Survey on the Development of an Accelerated Laboratory Test Method for Atmospheric Corrosion of Precoated Steel Products," *Corros. Sci.*, Vol. 34, No. 11, 1993, pp. 1923–1931.

[6] "GMW14872 Cyclic Corrosion Laboratory Test," General Motors Co., Detroit, MI, 2013, p. 27.

[7] "Global Laboratory Accelerated Cyclic Corrosion Test," *Corporate Engineering Test Procedure*, Ford Motor Co., Dearborn, MI, 2009, p. 14.

[8] "Corrosion Test by Automatic Change of Phases of Salt Spray, Drying and Humidity (ECC1)," Renault, Boulogne-Billancourt, France, 2014, p. 18.

[9] Fowler, S., "Atmospheric Corrosion in the Laboratory and the Role of Mass Loss Coupons in Test Monitoring," NACE-9125, presented at *CORROSION 2017*, New Orleans, LA, March 26–30, 2017, NACE International, Houston, TX, 2017, p. 15.

[10] ASTM D1654-08(2016)e1, *Standard Test Method for Evaluation of Painted or Coated Specimens Subjected to Corrosive Environments*, ASTM International, West Conshohocken, PA, 2016, www.astm.org

[11] Feng, Z. and Frankel, G., "Galvanic Test Panels for Accelerated Corrosion Testing of Coated Al Alloys: Part 2—Measurement of Galvanic Interaction," *Corrosion*, Vol. 70, No. 1, 2014, pp. 95–106.

[12] Matzdorf, C., Nickerson, W. C., Rincon Troconis, B. C., Frankel, G. S., Li, L., and Buchheit, R. G., "Galvanic Test Panels for Accelerated Corrosion Testing of Coated Al Alloys: Part 1—Concept," *Corrosion*, Vol. 69, No. 12, 2013, pp. 1240–1246.

[13] Feng, Z., Frankel, G., and Matzdorf, C., "Quantification of Accelerated Corrosion Testing of Coated AA7075-T6," *J. Electrochem. Soc.*, Vol. 161, No. 1, 2014, pp. C42–C49.

[14] NACE-TM0416-2016, *Test Method for Monitoring Atmospheric Corrosion Rate by Electrochemical Measurements*, NACE International, Houston, TX, 2016, pp. 1–24.

[15] Ellicks, D., Friedersdorf, F., Merrill, M., and Kramer, P., "Continuous Monitoring of Atmospheric Corrosion and Coating Degradation," NACE-8834 presented at *CORROSION 2017*, New Orleans, LA, March 26–30, 2017, NACE International, Houston, TX, 2017, p. 13.

[16] Mansfeld, F., Kendig, M., and Tsai, S., "Evaluation of Corrosion Behavior of Coated Metals with AC Impedance Measurements," *Corrosion*, Vol. 38, No. 9, 1982, pp. 478–485.

[17] Mansfeld, F., "Use Of Electrochemical Impedance Spectroscopy for the Study of Corrosion Protection by Polymer Coatings," *J. Appl. Electrochem.*, Vol. 25, No. 3, 1995, pp. 187–202.

[18] Schindelholz, E. and Kelly, R., "Wetting Phenomena and Time of Wetness in Atmospheric Corrosion: A Review," *Corros. Rev.*, Vol. 30, Nos. 5–6, 2012, pp. 135–170.

[19] Amirudin, A. and Thiery, D., "Application of Electrochemical Impedance Spectroscopy to Study the Degradation of Polymer-Coated Metals," *Prog. Org. Coat.*, Vol. 26, No. 1, 1995, pp. 1–28.

[20] *Metals and Alloys in the Unified Numbering System, 13th ed.,* SAE International, Warrendale, PA, 2017, p. 687.

[21] Lawrence, M., "The Relationship between Relative Humidity and the Dewpoint Temperature in Moist Air: A Simple Conversion and Applications," *Bull. Am. Meteorol. Soc.*, Vol. 86, No. 2, 2005, pp. 225–233.

[22] ASTM G85-11, *Standard Practice for Modified Salt Spray (Fog) Testing*, ASTM International, West Conshohocken, PA, 2011, www.astm.org

[23] Cole, I. and Paterson, D., "Mathematical Models of Dependence of Surface Temperatures of Exposed Metal Plates on Environmental Parameters," *Corros. Eng. Sci. Technol.*, Vol. 41, No. 1, 2006, pp. 67–76.

[24] Murray, J., "Electrochemical Test Methods for Evaluating Organic Coatings on Metals: An Update. Part I. Introduction and Generalities Regarding Electrochemical Testing of Organic Coatings," *Prog. Org. Coat.*, Vol. 30, No. 4, 1997, pp. 225–233.

[25] Feickert, A. and Wagner, A., "Optimizing Coating Performance for Diffusion under Cyclic Moisture Exposure," *Phys. Rev. Mater.*, Vol. 1, No. 3, 2017, p. 10.

[26] Strand, K., Feickert, A., and Wagner, A., "Fourth-Order Analysis of a Diffusive Lattice Boltzmann Method for Barrier Coatings," *Phys. Rev. E*, Vol. 95, No. 6, 2017, http://dx.doi.org/10.1103/PhysRevE.95.063311

STP 1609, 2019 / available online at www.astm.org / doi: 10.1520/STP160920170224

William Nelson,[1,2] Justin Grostefon,[1] Thomas Camino,[1] and Robert Hastings[1]

Electrochemical Testing of Modular Taper Junctions: Effect of Assembly Force and Head Offset

Citation

Nelson, W., Grostefon, J., Camino, T., and Hastings, R., "Electrochemical Testing of Modular Taper Junctions: Effect of Assembly Force and Head Offset," *Advances in Electrochemical Techniques for Corrosion Monitoring and Laboratory Corrosion Measurements, ASTM STP1609*, S. Papavinasam, R. B. Rebak, L. Yang, and N. S. Berke, Eds., ASTM International, West Conshohocken, PA, 2019, pp. 114–136, http://dx.doi.org/10.1520/STP160920170224[3]

ABSTRACT

Examinations of retrieved orthopedic implants have demonstrated corrosion; however, the extent of corrosion damage can be quite variable. There are a number of factors that may influence this corrosion, including device design and materials, surgical technique, and patient factors such as lifestyle, activity, and comorbidities that affect the local physiological environment around the hip prosthesis. This study evaluated the effect of a number of those factors on the corrosion of the head-stem junction of a modular hip using an electrochemical method. Several groups of head-stem taper coupons were immersed in phosphate-buffered saline and held at a constant anodic potential in an electrochemical cell while being mechanically loaded. Femoral head size, diameter, offset, and assembly force were varied. Incrementally increasing cyclic loads were applied to the femoral head. After the short-term incremental test was completed, some specimens were subjected to a long-term 4-kN cyclic load ($R = 0.1$) that was applied for 10^6 cycles. Current was continually monitored, and

Manuscript received November 10, 2017; accepted for publication March 12, 2018.

[1]DePuy Synthes Joint Reconstruction, 700 Orthopaedic Dr., Warsaw, IN 46581 0988, USA

W. N. http://orcid.org/0000 0002 0942 266X

[2]Theoris Services, 8900 Keystone Crossing, Suite 150, Indianapolis, IN 46240, USA

[3]ASTM Symposium on *Advances in Electrochemical Techniques for Corrosion Monitoring and Laboratory Corrosion Measurements* on November 13 14, 2017 in Atlanta, GA, USA.

displacement sensors monitored the relative micromotion of the assembled components. Test specimens assembled with less than 4 kN of load experienced a statistically significant increase in corrosion current during both the short-term and long-term tests compared to specimens assembled with higher loads. The larger +12-mm head offset exhibited a statistically significant increase in corrosion current compared to the +8.5-mm offset in the long-term test when assembled with the 1-kN load. It is recommended that taper assembly force and head offset should be controlled in future corrosion tests of taper junctions. Although there are measurable differences in corrosion current reported in this laboratory experiment, the values for corrosion current have not been correlated with clinical performance or outcomes. This study has shown that assembly technique and head offset are factors that affect corrosion current measured in the laboratory.

Keywords

mechanically assisted crevice corrosion, modularity, fretting, micromotion, corrosion, electrochemistry, onset load

Introduction

Total hip arthroplasty (THA) is a common orthopedic procedure involving surgical removal of the articular surfaces of the femoral head (ball) and the acetabulum (socket) and replacement with prosthetic hip implants. Modern hip prostheses generally are comprised of a metallic femoral stem that affixes to the femoral bone, a modular femoral head that is made of either metal or ceramic that affixes to the femoral stem through a modular head stem taper junction, a metallic acetabular shell that affixes to the acetabular bone, and an acetabular bearing that affixes to the acetabular shell and is made of either ultra high molecular weight polyethylene or ceramic. Annual rates of THA in industrialized countries typically range between 50 and 100 surgeries per 100,000 people [1]. THA surgery is currently one of the most successful surgical procedures available; the National Joint Registry for the United Kingdom has reported 10 year revision rates for metal on polyethylene prostheses ranging between 3 % and 6 % in their population for all causes of revision [2].

Most modern hip implant systems use a tapered modular junction between the femoral stem and femoral head to enable the surgeon to intraoperatively adjust patient biomechanics (i.e., leg length and offset). This modular taper junction may, in some cases, be susceptible to fretting and corrosion. One possible effect of this corrosion is the release of metal ions and wear debris into the joint space, which may contribute to osteolysis [3], adverse local tissue reactions [4,5], and head stem dissociation [6,7].

Corrosion that may occur at the head stem junction is thought to occur by an interaction between two corrosion mechanisms, fretting corrosion and crevice corrosion [8]. Fretting corrosion describes the corrosion of metals at sliding surfaces

resulting from the periodic destruction and regrowth of protective oxide layers. The metals most commonly used in THA implants are alloys of titanium (Ti) or cobalt chromium (CoCr). Alloys composed of these metals rely on a passive oxide layer for corrosion protection, and corrosion may occur on both alloys if this passive lay er is disrupted by cyclic mechanical stress [9]. Therefore, fretting is both a wear pro cess and a corrosion process. Fretting corrosion at modular taper junctions resulting from micromotion between the stem and the head has been recognized since the late 1980s and has been well documented [8,10 14]. Crevice corrosion describes a corrosion mechanism in which the products of corrosion build up inside an area wherein the geometry restricts the rate of diffusion of ions and corrosion products away from the corroding area. As crevice corrosion progresses, processes such as crevice acidification, chloride migration, hydrogen generation, and combi nations thereof can exacerbate corrosion inside the crevice, making crevice corro sion an autocatalytic process [15]. The morphology of the corrosion observed on retrieved tapers in some studies indicates that crevice corrosion occurs in vivo under certain conditions [16 18]. Laboratory testing has shown that mild crevice acidification and chloride migration occur in modular taper crevices even in the absence of mechanical loading, but these changes did not result in measurable cor rosion current in the absence of fretting [19]. It has been hypothesized that crevice corrosion does not occur at a taper junction unless severe fretting corrosion has occurred, in which case the continued repassivation processes may reduce the pH inside the crevice to a point beyond which the oxide layer of the CoCr head is no longer stable [20,21].

Numerous implant retrieval studies have investigated which design factors cor relate to an increase in head stem corrosion in vivo [18,22 26]. However, due to the nature of retrieval studies, it is difficult to control certain implant design factors in these series, such as the implant manufacturer or the sizes of the heads and stems used. Effects related to patient or surgeon factors are also unknown in these studies. Therefore, more in vitro testing is necessary to understand the relative importance of these design factors with regards to corrosion risk.

The tribocorrosion of modular hip implants at the head stem junction has been tested electrochemically for many years. ASTM F1875 98, *Standard Practice for Fretting Corrosion Testing of Modular Implant Interfaces: Hip Femoral Head Bore and Cone Taper Interface*, provides a framework for fretting corrosion testing of hip head stem taper interfaces [27]. Experiments based on this standard have used an electrochemical cell specifically designed to enable a materials test frame or hip sim ulator to apply load to an implant or head stem construct while electrochemical measurements are being taken, but within this standard, both electrochemical and nonelectrochemical methods of quantifying corrosion are specified. The standard contains two electrochemical procedures, with Procedure A covering all potentio static testing and Procedure B specifying a nonpotentiostatic testing. Nonpotentio static testing has perhaps been more common, with a number of authors [8,12,19,28 30] having published studies using this procedure. In these

nonpotentiostatic experiments, the open circuit potential of the working electrode is measured against a reference electrode, but the working electrode is not polarized. Instead, the working electrode is coupled to a counter electrode made of the same material and having the same surface area as the hip stem. Between the working and counter electrode, a zero resistance ammeter (ZRA) typically is used to mea sure any mechanically induced current between the two electrodes. This test meth od allows the open circuit potential of the hip stem construct to be measured and the fretting current to be estimated while fretting occurs. Results utilizing this meth od have shown that the open circuit potential of a modular hip stem or simplified head stem coupon becomes more cathodic in response to fretting [20].

In a conventional three electrode electrochemical cell connected to a potentio stat, if the working electrode is sufficiently anodically polarized, the current density of cathodic reactions at the working electrode will become negligible compared to the oxidation current, and most of the reduction reactions will happen at the coun ter electrode, allowing the current to be measured by the potentiostat [15]. In an open circuit test, this relationship is not guaranteed; local cathodes may form on parts of the working electrode outside the taper, and the portion of the current that passes through the ZRA to the counter electrode may vary based on differences in surface area available for cathodic reactions at the two electrodes. Therefore, while the open circuit test best represents in vivo corrosion, there is a potential for inac curacies and inconsistencies in the current measurements, especially when different sizes or designs are to be compared.

More recently, some investigators [14,31 34] have used a potentiostatic method to measure fretting corrosion at modular hip taper junctions. In this test method, an implant or coupon is fixed in an electrochemical cell and mechanically loaded, but the electrochemical setup differs. The construct is anodically polarized to a spe cific potential in the passive region for Ti and CoCr alloys. This polarization is maintained for the duration of the test. Anodic polarization of the specimen removes the need for the counter electrode to accurately represent the remainder of the hip stem and simplifies the analysis of the test. This test method does eliminate the possibility of measuring the potential change of the working electrode in response to fretting. While it is less representative of in vivo conditions, it may allow the fretting current to be measured with greater consistency among different designs than nonpotentiostatic testing.

In this study, a potentiostatic electrochemical technique was used to determine the corrosion response of head stem taper junction specimens under cyclic load in saline solution. The short term and long term corrosion characteristics were inves tigated using a short term, potentiostatic, incremental load method similar to the one used by Mali and Gilbert [14], followed by an additional long term potentio static test. Heads were quasistatically press assembled to the mating stems in a materials test frame using varying loads, and femoral heads with different sizes and offsets were used. Displacement sensors were used during the test in an attempt to quantify the micromotion of the head relative to the stem.

Few electrochemical tests have investigated the effect of assembly force and head offset on modular hip taper corrosion. To the authors' knowledge, no other published electrochemical test has yet investigated the effect of head size, and none have potentiostatically investigated the effect of assembly force and head offset variations in both short and long term contexts.

Materials and Methods

SPECIMEN PREPARATION AND ASSEMBLY

Test specimens used in this study consisted of finished product femoral heads attached to taper stem coupons specifically manufactured for this experiment. Femoral heads of varying diameter and offset (ARTICUL/EZE, DePuy Synthes, Warsaw, IN) made of Co Cr alloy (ASTM F1537, *Standard Specification for Wrought Cobalt 28 Chromium 6 Molybdenum Alloys for Surgical Implants* [*UNS R31537, UNS R31538, and UNSR31539*]) were paired with representative femoral stem taper coupons made of Ti 6Al 4V ELI (ASTM F136, *Standard Specification for Wrought Titanium 6Aluminum 4Vanadium ELI* [*Extra Low Interstitial*] *Alloy for Surgical Implant Applications* [35], UNS R56401) and manufactured to the same taper specifications as finished product femoral stems. Before assembly, the taper stem coupon was rinsed with phosphate buffered saline, removed, and then quickly hand pressed into the femoral head, such that a small amount of saline wetted the interlocking taper surface. This assembly method was intended to trap a small amount of saline in the taper, ensuring that some amount of electrolyte penetrated the junction. The noncontact displacement sensors (NC DVRT 1.0, LORD Microstrain, Williston, VT, or WayCon T05 G KA O, Munich, Germany) were then mounted to the stem such that they were aligned with the superior and inferior sides of the assembled specimen. A flat annulus of anodized aluminum was used as the target for the displacement sensor, which was attached to a plastic piece affixed to the head using waterproof epoxy. The coupons were then press assembled in a servohydraulic test frame under force control. The assembly load was applied at a rate of 200 N/s to a maximum force as shown in Table 1.

TEST FIXTURING AND ELECTROCHEMICAL SETUP

Test specimens were secured in fixturing such that the longitudinal axis of the specimens were at a 55 degree angle from the horizontal plane and cyclically loaded in MTS 370 servohydraulic test frames (MTS, Eden Prairie, MN) while simultaneously being held at a constant potential in an electrochemical cell by a Bio Logic SP 200 potentiostat (Bio Logic USA, Knoxville, TN). Specimens were inserted through the tank, such that the upper portion of the specimen was immersed in phosphate buffered saline with a pH of 7.0 to 7.2 (Thermo Scientific, Waltham, MA). The tank was filled such that the fluid level was just under the area where the actuator contacted the head in the test. The aeration of the saline was not controlled, but the saline was in contact with the atmosphere. A carbon counter electrode and a silver/silver

TABLE 1 Specimen groups tested in this experiment. Group 1 specimens were tested with the short term incremental load experiment only, while Group 2 specimens were exposed to the short term incremental load experiment followed by a 10^6 cycle experiment.

Group	Head Assembly Force (kN)	Head Diameter (mm)	Head Offset (mm)	Sample Size	Experiment
1 1	1.1	28	+12	5	Short term
1 2	2.2	28	+12	5	Short term
1 3	4.4	28	+12	5	Short term
1 4	6.7	28	+12	5	Short term
1 5	8.9	28	+12	5	Short term
1 6	13.3	28	+12	5	Short term
1 7	17.8	28	+12	5	Short term
2 1	1.1	28	+12	5	Short term + Long term
2 2[a]	4.4	28	+12	5	Short term + Long term
2 3	1.1	36	+12	5	Short term + Long term
2 4	1.1	28	+8.5	5	Short term + Long term
2 5	1.1	40	+8.5	5	Short term + Long term

[a]Specimens were cleaned and reused from Group 1 3.

chloride (Ag/AgCl) reference electrode were used to form an electrochemical cell with the stem head construct serving as the working electrode. The test setup is depicted in Fig. 1, while the test specimens are depicted in Fig. 2.

The potential of the specimen was fixed at −50 mV versus Ag/AgCl, which was chosen because it was within the passive region of the alloys being tested. Applying this potential in phosphate buffered saline consistently results in a small anodic current (less than 1 uA) when no load is applied.

MECHANICAL LOAD PROFILE

The −50 mV versus Ag/AgCl potential was maintained throughout the experiment and for at least 1 h prior to starting the experiment to allow the baseline current to reach a steady state value. After this waiting period, the sinusoidal load profile shown in Fig. 3 was applied. The initial sinusoidal load of 100 N ($R = 0.1$) was applied for 540 cycles, after which the load was increased to 200 N ($R = 0.1$) for another 540 cycles, after a 10 s dwell period. The load continued to be increased in this fashion until a load of 1,000 N ($R = 0.1$) was reached, after which the load was incremented by 200 N until a final load of 4,000 N ($R = 0.1$) was reached. All loads were applied at a frequency of 3 Hz. This loading regimen was utilized as it enabled determination of the corrosion "onset load" or the load at which corrosion began to occur. In these experiments, the onset load was defined as the first load level at which the average current exceeded 1 μA. This threshold was chosen because it was greater than the baseline current for all the specimens, which was about 0.5 μA on average at the beginning of the test. After 540 cycles at 4,000 N ($R = 0.1$), some specimens (Table 1) were additionally loaded for 1 million cycles at 4,000 N

FIG. 1 Experiment setup. The specimen is the working electrode in an electrochemical cell. The cell is placed in a servohydraulic test frame, and force is applied to the top of the head. The bearing surface is connected to the actuator via a thrust bearing to allow the specimen to deflect.

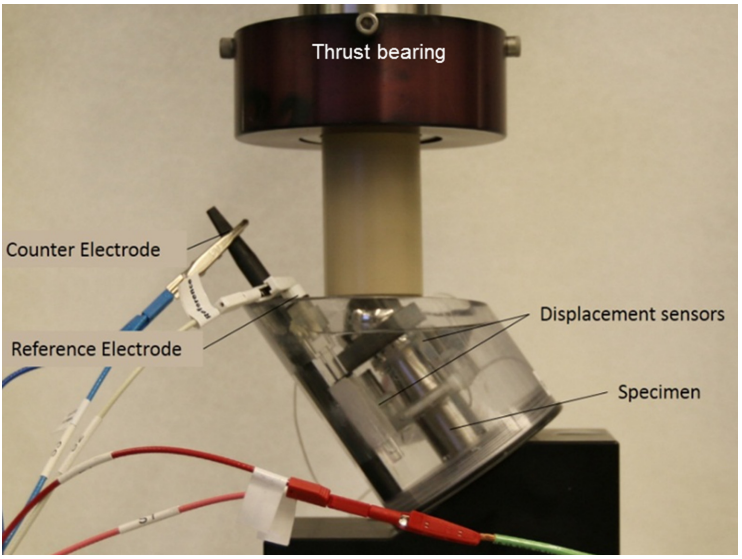

FIG. 2 The femoral heads used in this test. From left to right (all dimensions are in millimeters diameter + offset): 28 + 12, 36 + 12, 28 + 8.5, and 40 + 8.5.

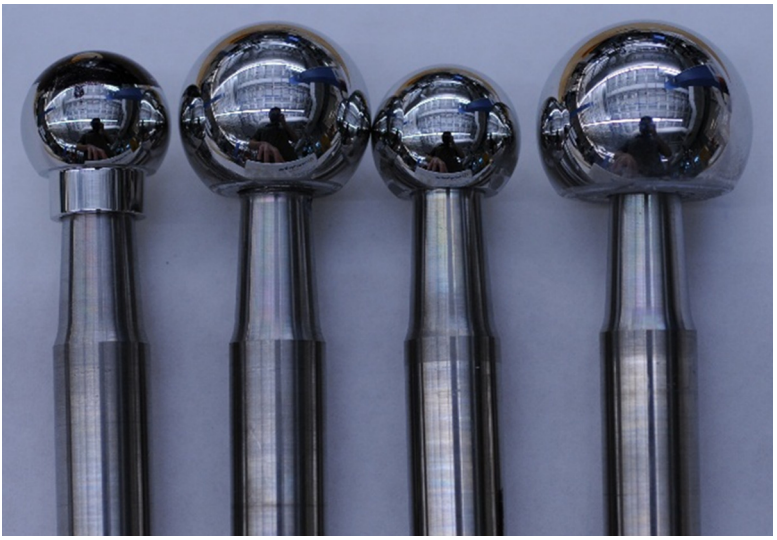

FIG. 3 The maximum load applied by the cyclic sinusoidal load profile. The frequency of the loading was 3 Hz and the minimum load was 10 % of the maximum load throughout the test. The Group 1 specimens were subjected to only the short term test, while Group 2 specimens were subjected to both the short term and the long term tests (Table 1).

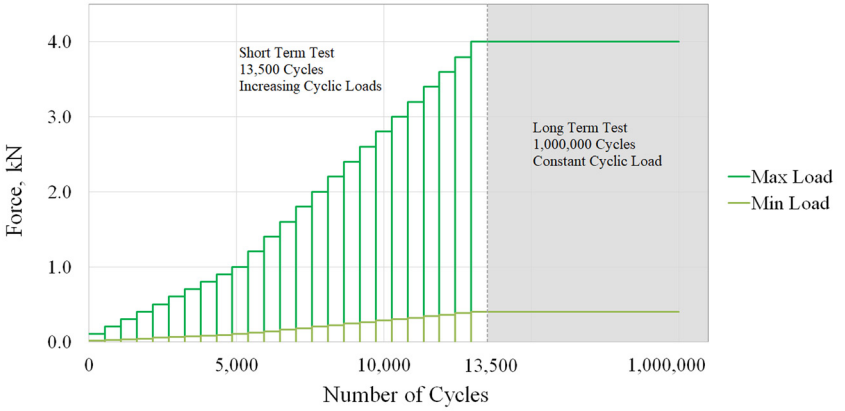

($R = 0.1$), which is a reasonable high estimate for the peak magnitude of the vertical component of the hip reaction force for activities such as walking and stair climbing [36]. During this portion of the test, current and relative micromotion of the head and taper coupon were monitored.

MOTION ANALYSIS

The motion of the head relative to the stem was monitored by two noncontact dis placement sensors secured on the superior and inferior side of the head. The two noncontact displacement sensors were fixed into custom polycarbonate mounts clamped around the stem coupon so that the displacement sensors were in superior and inferior positions on the stem, as shown in Fig. 1. These displacement sensors measured the distance from the sensor to an anodized aluminum target. Epoxy was used to bond the target to a custom plastic mount and the mount to the femoral head. A limitation with this test setup is that it is not possible to accurately isolate and measure the rigid motion of the head relative to the stem during loading due to the difficulty of separating the rigid and elastic components of the motion. Other authors have reported micromotion measurements in modular neck stem compo nents [13,37] but, in this test setup, there are challenges in making these measure ments with the stem immersed in saline and not interfering with the electrochemical measurements. To compensate, the displacement of the heads dur ing seating was measured accurately as there was no stem deflection to confound the measurement, and the displacements before and after seating could be

measured at zero load. The subsidence of the head after the short term incremental load test was also measured in a similar manner. The subsidence was then defined as the net motion of the head resulting from the applied cyclic load, which was measured at the end of the short term test when no load was applied to the head.

TEST GROUPS: ASSEMBLY FORCE, HEAD DIAMETER, AND OFFSET

In these tests, the assembly force of the femoral head, the head diameter, and the head offset were varied, and the effects on the current measured during cyclic load ing were observed. The assembly force of each group was varied in accordance with Table 1, and each group consisted of five specimens. During this time, current data were recorded by the potentiostat, and micromotion data were gathered by the dis placement sensors. These data were generated along with force and actuator dis placement from the test frame, collected by a data acquisition system (National Instruments, Austin, TX), and analyzed using a custom MATLAB program (Math Works, Natick, MA).

Both short term incremental load and long term experiments are summarized in Table 1. The heads and stems of one group were cleaned, reassembled, and retested, as noted.

Results

SHORT-TERM INCREMENTAL LOAD TEST: ASSEMBLY FORCE

Current versus time curves were obtained from the specimens, and Fig. 4 shows a typical curve for a specimen assembled with a low load in the short term test. These curves were most often characterized by three regions. At the beginning of the test, the average current was usually less than 1 μA, and there was no observable fretting current. As the cyclic load increased, an increase in current was observed. This cur rent had a cyclic waveform with the same frequency as the applied load, which is indicative of mechanically induced corrosion. Once fretting corrosion began to occur, the magnitude of the current often varied unpredictably in the short term test.

The average current versus time curves for three different groups assembled with varying force (Table 1) are shown in Fig. 5 and demonstrate some of the trends associated with the incremental test. First, the effect of assembly force on the amount of current in the incremental load test is identified by the visible difference in the load at which the current began to increase relative to the baseline current. Finally, as the overall amount of current increased, the variability of the current data between specimens also increased. This effect has been observed before in potentiostatic tests of taper corrosion [14].

The average current during the short term incremental experiment (Table 1, Group 1) was calculated for all specimens in the test (Fig. 6), and the overall average current was found to be less variable than peak currents or currents at a specific load. Additional mass loss that cannot be measured by the potentiostat has been previously reported to occur purely as a result of wear [38]; however, increased

FIG. 4 Typical current versus time data from the incremental load test. When corrosion occurs, the current waveform typically has the same frequency as the applied load. The cyclic load is briefly halted in between the step increases of the maximum applied load (Fig. 3). Repassivation likely occurs in these intervals, which would account for the sudden decreases in current observable in these periods.

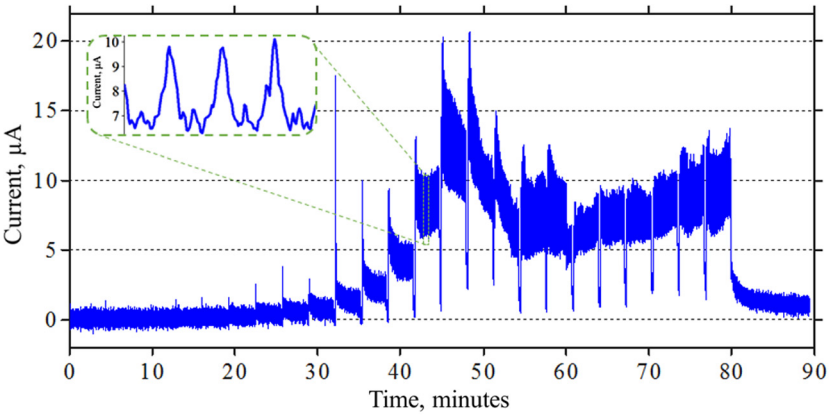

FIG. 5 The average current observed at each cyclic load level applied in the short term test at three of the assembly force groups tested (from Group 1, Table 1). Error bars are one standard deviation; N = 5 for each group.

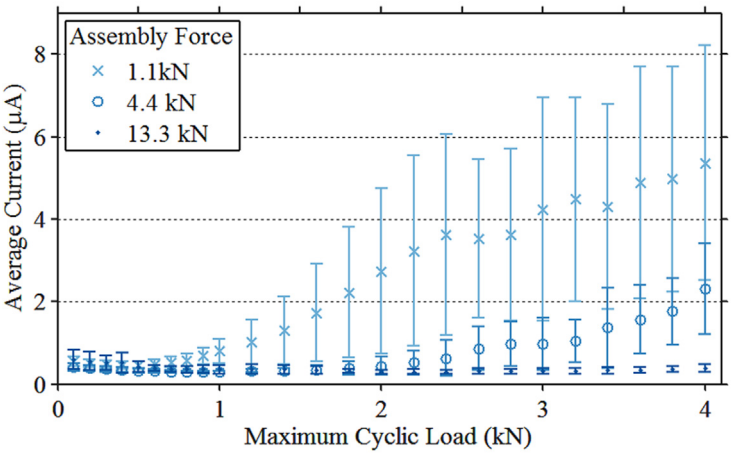

FIG. 6 Average current observed during the short term incremental fretting corrosion test for the Group 1 specimens in **Table 1**. Error bars represent 95 % confidence intervals calculated based on individual standard deviations. No significant differences were detected by the Games Howell multiple comparisons test.

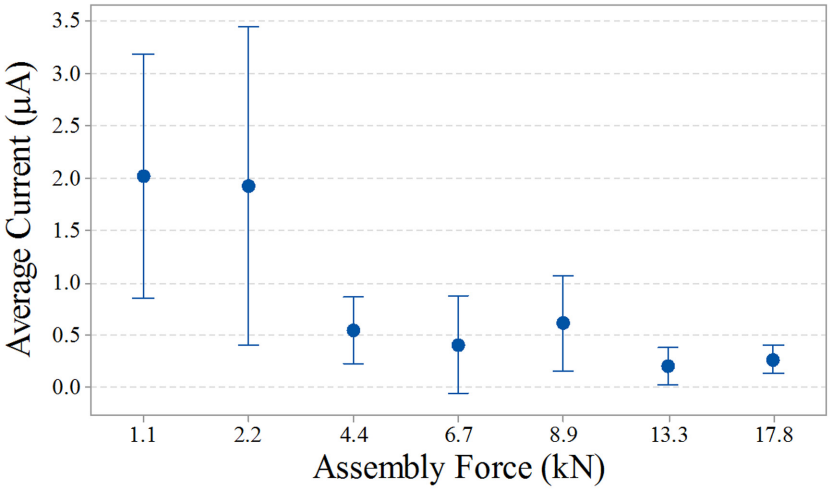

wear should result in a corresponding amount of increased measurable current. Therefore, the average current provides a reliable quantitative measure of the corro sion of the specimen.

Statistical analysis of the data presented in **Fig. 6** was complicated by the differ ence in variability between low assembly and high assembly groups. In this experi ment, groups with higher average currents had increased variability compared to groups with low currents. In the case of **Fig. 6**, Levene's method was used to deter mine that there were significant differences in the standard deviation among groups ($p = 0.026$). Because of this, the Games Howell post hoc test was used to determine significant differences among groups in these tests. In the case of the average cur rent data in **Fig. 6**, no significant differences were found using this method. Howev er, there is a steep drop in average current between the 2.2 and 4.4 kN assembly forces, which may be explained by the load profile used in the test. Because the maximum load applied in the test is 4 kN, the specimens assembled with loads of 4.4 kN or greater were not exposed to a force greater than the force used to push the head onto the taper during the test and therefore would be expected to experi ence less micromotion. This explanation is supported by the onset load (**Fig. 7**) and the motion data (**Fig. 8**) that were collected. In particular, the corrosion perfor mance falls into two groups based on whether the head was assembled with a great er force than was applied during the test. The average current of the ten specimens

FIG. 7 Onset load measured in the short term incremental fretting corrosion test for Groups 1 1, 1 2, and 1 3 in Table 1. The onset load is defined as the cyclic load during which the average current was greater than 1 microamp. No specimen from groups assembled with force greater than 4.4 kN had an onset load per this definition. Error bars represent 95 % confidence intervals calculated based on individual standard deviations. Groups that do not share a letter are statistically different as determined by the Games Howell multiple comparisons test.

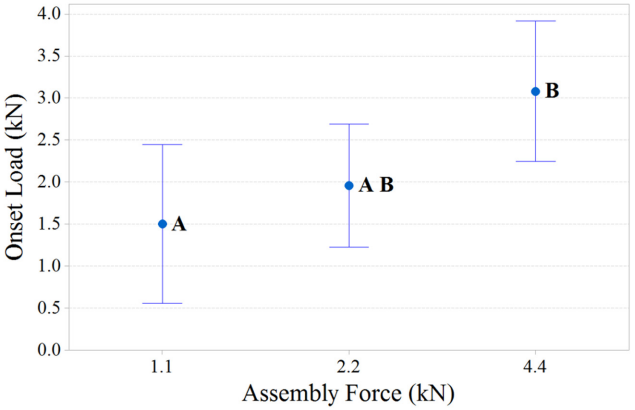

FIG. 8 Seating and subsidence observed in the short term incremental fretting corrosion test for the Group 1 specimens in Table 1. Seating is defined as the displacement of the head resulting from the application of the assembly load, while subsidence is defined as the displacement of the head occurring due to the cyclic loads applied in the short term corrosion test. Error bars are the combined standard deviation of the seating and subsidence. Positive subsidence (defined as the head moving further down the taper) is shown in red, while negative subsidence is shown in purple.

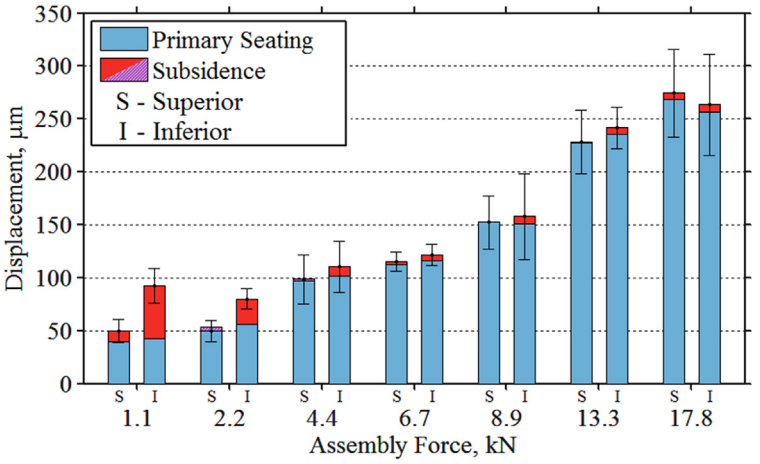

with an assembly force less than 4 kN was significantly ($p = 0.0004$) greater than the 25 specimens tested with greater assembly forces.

Fig. 7 shows a relationship between assembly force and onset load in the specimens from Group 1. There were significant differences in the onset load between specimens assembled with 1.1 and 4.4 kN loads, suggesting that specimens assembled with higher loads can withstand higher loads before fretting corrosion begins to occur. Specimens assembled with loads greater than 4.4 kN, with few exceptions, did not have an onset load as defined previously (the average corrosion at all loads in the incremental test was less than 1 μA).

SHORT-TERM INCREMENTAL LOAD TEST: OFFSET AND HEAD SIZE

In another experiment (Table 1, Group 2), five groups of specimens were tested with varying assembly forces, head sizes, and head offsets. These five groups of specimens were tested with the same short term incremental load test as before, but following that test, they were subjected to an additional long term experiment to determine how the corrosion of the specimens changed over time. The average current and onset load results from the incremental load portion of the test are shown in Fig. 9 and Fig. 10.

FIG. 9 Average current observed during the short term incremental fretting corrosion test for the Group 2 specimens in Table 1, which were subsequently tested in the long term test. Error bars represent 95 % confidence intervals calculated based on individual standard deviations. Significant differences detected by the Games Howell multiple comparisons test are as marked; means that do not share a letter are statistically different.

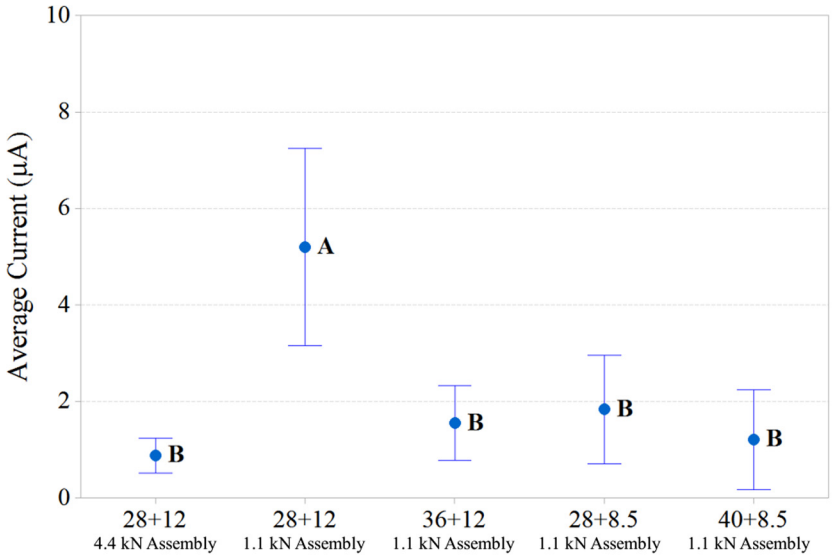

FIG. 10 Onset load measured in the short term test for the Group 2 specimens in Table 1. The onset load is defined as the cyclic load during which the average current was greater than 1 microamp. Error bars represent 95 % confidence intervals calculated based on individual standard deviations. Groups that do not share a letter are statistically different as determined by the Games Howell multiple comparisons test.

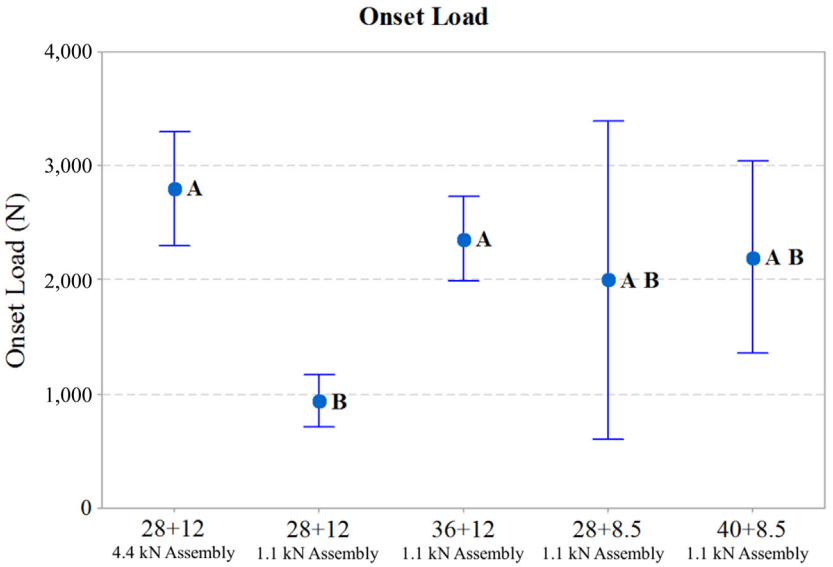

LONG-TERM CORROSION TEST: ASSEMBLY FORCE, OFFSET, AND HEAD SIZE

The current versus time relationship observed in the long term corrosion test was distinct from the short term test. In this test, the sinusoidal cyclic load was kept constant at 4 kN ($R = 0.1$), rather than being incrementally increased. The test continued until 10^6 cycles were complete. A typical graph of current versus time in this long term test is shown in Fig. 11.

In the long term fretting tests, the average current typically was elevated in the first 2 to 6 h of the test. This pattern is often observed at wear surfaces, in which interlocking asperities are worn down over time, leading to wear rates that decrease. Initial high rates of corrosion are termed "break in" wear. In many cases, the average current did stabilize, and a lower, steady state, cyclic current was maintained throughout the test. Specimens assembled with a high force and smaller offset heads (+8.5 mm) most often showed this behavior. However, in some cases, the average current steadily increased as the test continued. Specimens assembled with a low force and specimens with larger offsets (+12 mm) more often exhibited this behavior. Because these specimens generally had a high rate of corrosion in the short term as well, it is reasonable to infer that the corrosion rate may increase as a result

FIG. 11 A typical current versus time curve for two specimens with differing assembly forces in the long term corrosion tests. Each data point represents the average current over a 30 s time interval. The voltage was maintained for 2 h after the cyclic loading was ceased at the end of the test (after roughly 92 h of testing). In all cases, the baseline current prior to testing was below 1 μA, so a difference in the time it takes for the current to return to the pretest baseline can be determined from this graph.

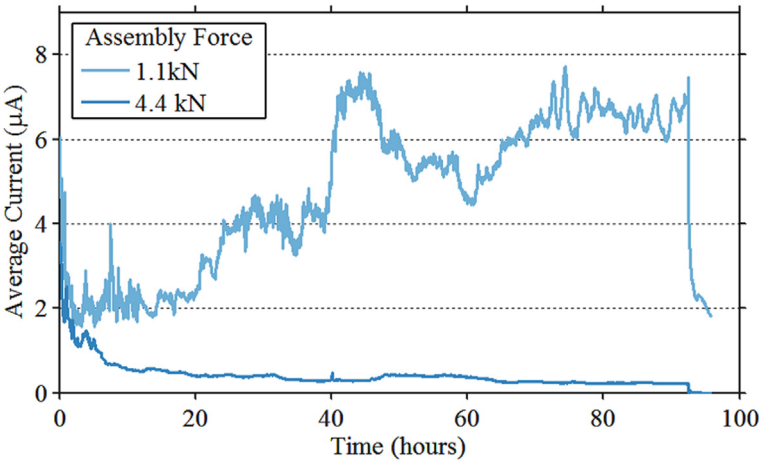

of cumulative damage to the taper surface, which may result in larger micromotions, which in turn cause greater damage. Crevice corrosion may also explain the increase in corrosion rates over time. Fig. 11 shows continuing corrosion of a specimen assembled with a low assembly force after cyclic loading has ceased, which is explained by ongoing crevice corrosion that diminishes over time as fresh solution diffuses into the crevice.

The average current measured in the long term test is presented in Fig. 12. Three design factors were investigated in this test: head size, head offset, and assembly force, and of these, low assembly forces and high head offsets both significantly increased the corrosion compared to the low offset and the high assembly force groups. Head size did not significantly affect the corrosion of the specimens in the long term test.

MOTION ANALYSIS

The seating motion of the head during the assembly procedure (primary seating) and the net displacement of the head resulting from the short term incremental load test (subsidence) are presented in Fig. 8 and Fig. 13. Seating displacement increased with increased assembly force; however, specimens assembled with less than 4 kN of force subsided more during the incremental load test. Most of the

FIG. 12 Average current observed during the long term fretting corrosion test. Error bars represent 95 % confidence intervals calculated based on individual standard deviations. Significant differences detected by the Games Howell multiple comparisons test are as marked; means that do not share a letter are statistically different.

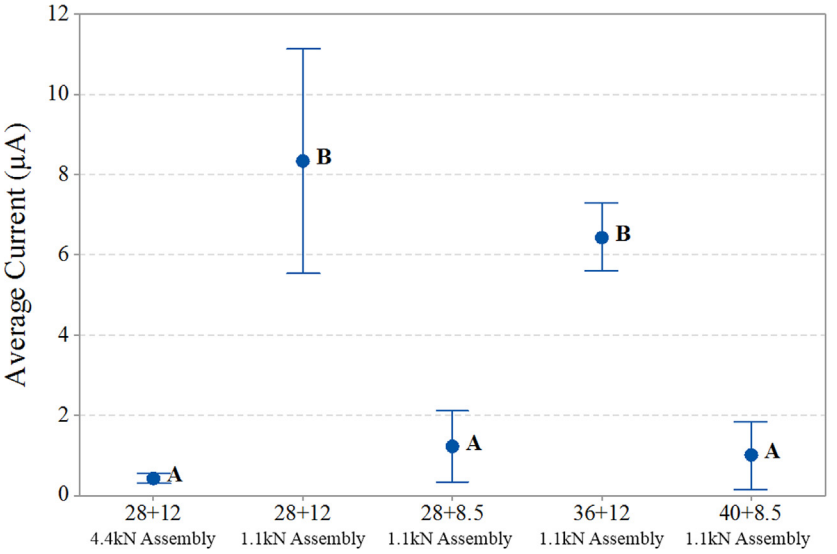

subsidence happened asymmetrically on the inferior side of the specimen as the inferior side experienced most of the visible corrosion during the long term test.

Discussion

In these experiments, low assembly force resulted in significant increases in mechanically induced fretting corrosion in the short term incremental load test as well as the long term test. Head offset also led to significantly increased corrosion in the long term test, although in the short term test, the results were mixed. In the short term test, the low assembly 28 + 12 (head diameter + head offset) group performed significantly worse from a corrosion perspective than the 36 + 12 group. This difference may be partly explained by the significantly higher onset load for the 36 + 12 group compared to the low assembly 28 + 12 group, but it is unknown why these specimens had a higher onset load. While the 36 + 12 specimens showed a greater initial resistance to corrosion, their corrosion performance in the long term test was not significantly different than the 28 + 12 group assembled with a similar load.

It is anticipated that hip taper junctions corroding in vivo would pass through a period of run in wear, as many wear surfaces do [12,39], and be affected by the buildup of wear debris and corrosion products. Therefore, it seems likely that the

FIG. 13 Seating and subsidence observed in the short term incremental fretting corrosion test in the specimens that went on to the long term test. Seating is defined as the displacement of the head resulting from the application of the assembly load, while subsidence is defined as the displacement of the head occurring due to the cyclic loads applied in the short term corrosion test. Error bars are the combined standard deviation of the seating and subsidence. Positive subsidence (defined as the head moving further down the taper) is shown in red, while negative subsidence is shown in purple.

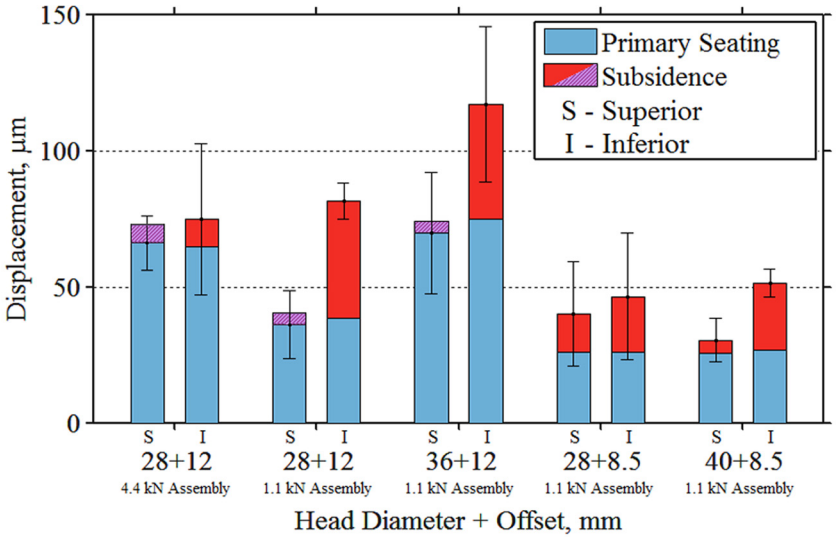

long term performance of the taper junction in this test would represent the performance of an actual implant more accurately than a short term test. Numerous corrosion effects have been shown to contribute to the buildup of wear/corrosion particles, such as third body wear and possible increases in crevice corrosion [9]. It is not clear to what degree any of these processes occurred in the long term test. If time and progressively increasing mechanical damage must occur before the most severe corrosion damage can occur, it can be inferred that short term testing may not be suitable to study this type of corrosion. Optical microscopy of taper junctions from the long term test showed moderate amounts of damage, with a larger amount of debris visible on the inferiodistal portion of the taper (**Fig. 14**). Similar asymmetric wear patterns have been described on retrieved prostheses, and finite element modeling of weakly assembled tapers has also predicted asymmetric wear [40,41].

Overall, the results of this work confirm the body of available literature regarding taper assembly force and its relationship to taper corrosion. It has often been suggested that increased assembly force should reduce corrosion rates by decreasing the amount of micromotion between the head and the stem. Although the

FIG. 14 Superior (left) and inferior (right) halves of a corroded trunnion of a low assembly, high offset specimen from the long term test.

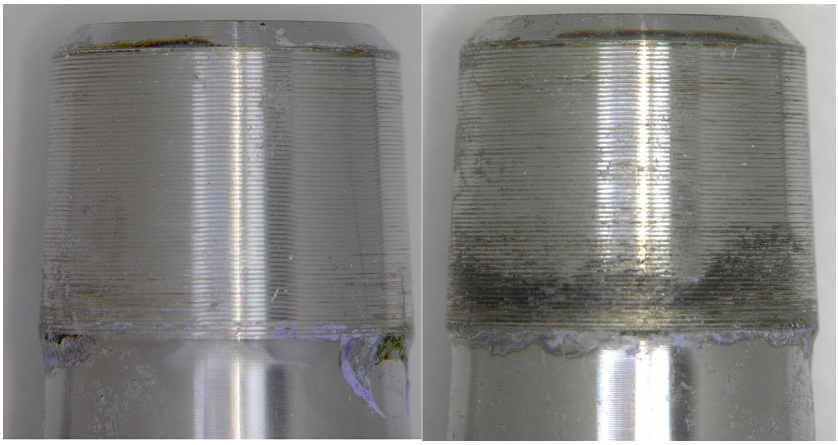

micromotion of the head relative to the stem could not be isolated and measured directly in this test, seating was measured both during assembly and after the test, and it was shown that the head seated further down the taper with higher assembly loads. When the assembly force was less than the maximum force applied during the test, the head subsided asymmetrically over the course of the test, and corrosion generally increased, possibly because of this asymmetric motion. Other authors have observed that an increased seating force reduces subsidence resulting from cyclic loading in modular necks [42]. In addition, finite element modeling has predicted that head assembly force can significantly influence long term wear rates [41], and electrochemical tests [30] have shown that minimal assembly loads can result in significantly increased short term fretting current. The average force a surgeon can deliver to a femoral head in a clinical setting has been measured to be roughly 4.4 kN [43], while the peak load applied to a femoral head during some strenuous activities can be much higher [36]. These data highlight the importance of assembling the femoral head to the femoral stem with sufficient force.

The results of this work also agree with previous literature on the effects of head offset, which has suggested that larger head offsets place greater moments on the taper junction. High offset heads have been associated with increased corrosion in some retrieval studies [44] but not others [22]. One electrochemical study showed no significant difference in currents between hip stems coupled with +6 mm and +0 mm offset heads [12], but considering the relatively low corrosion experienced by +8.5 mm offset heads in this test at a low assembly force, those results are not necessarily conflicting.

There is little agreement in the literature regarding the effect of head size on taper corrosion. Although some finite element analysis studies [45,46] have

predicted that larger heads create increased stress at the taper junction, retrieval studies have shown mixed results [25,47 49]. A recent review of retrieval studies reported that the effect of head size on fretting and corrosion was inconclusive [50]. No effect can be reliably attributed to head size based on these data, but this may be because the load in this test was applied uniaxially. It has been theorized that a torque applied to the specimen by friction when moving naturally against a bearing surface in vivo or in a hip simulator may lead to greater micromotion at the taper when a larger head is used due to frictional torque at the bearing interface being transmitted to the taper junction. This test may not accurately determine the effect of head size on corrosion because it does not produce motions characteristic of hip articulation.

This study has other limitations, including the fact that this test was by design less representative of in vivo conditions than many electrochemical tests that have been done in the past. In this study, a potentiostatic test method was used rather than having a representative counter electrode coupled to the working electrode through a ZRA and measuring the open circuit potential. In addition, phosphate buffered saline was used as an electrolyte rather than simulated body fluid, and the test was conducted at room temperature rather than body temperature. Lastly, machined Ti 6Al 4V coupons were used instead of actual hip stems; however, care was taken to utilize design specifications representative of actual hip stems. These experiment parameter choices were made to increase the simplicity and reproduc ibility of the test, but it is recognized that these tests may not accurately reproduce the corrosion that occurs in vivo. They do, however, serve as a methodology to be used to comparatively evaluate different parameters and designs.

Conclusions

- Increased assembly force reduced average currents due to corrosion in the short term incremental test as well as the long term test. Femoral heads assembled with greater assembly forces seated further down the taper and did not progressively subside as far down the taper as a result of cyclic loading. It is believed that increased assembly force also reduces the cyclic micromotions that cause fretting corrosion, but this was not measured in this test.
- Heads with larger offsets experienced significantly more corrosion during the long term test when assembled with a low assembly force (1.1 kN).
- Short term current was significantly less and onset load was significantly greater for 36 + 12 heads than 28 + 12 heads, but these differences did not persist in the long term test. It is possible that more complicated loading sce narios could potentially cause fretting damage that would increase with head size. This would have to be evaluated in future testing.
- The short term potentiostatic incremental cyclic fretting corrosion test can determine differences in corrosion performance between different modular taper combinations and assembly techniques. Short term testing is best com bined with a long term test so that the effect of the run in period of mechani cally induced corrosion damage can be understood.

References

[1] Merx, H., Schrader, P., Sturmer, T., Dreinhofer, K., Puhl, W., Gunther, K., and Brenner, H., "International Variation in Hip Replacement Rates," *EUROHIP: Health Technology Assessment of Hip Arthroplasty in Europe*, Springer Berlin, Heidelberg, Germany, 2009, pp. 5–19, http://dx.doi.org/ 10.1007/978-3-540-74137-4 2

[2] National Joint Registry, "12th Annual Report," NJR, Hemel Hempstead, UK, 2015.

[3] Urban, R. M., Jacobs, J. J., Gilbert, J. L., and Galante, J. O., "Migration of Corrosion Products from Modular Hip Prostheses. Particle Microanalysis and Histopathological Findings," *J. Bone Joint Surg. Am.*, Vol. 76, No. 9, 1994, pp. 1345–1359.

[4] Lawrence, H., Deehan, D., Holland, J., Kirby, J., and Tyson-Capper, A, "The Immunobiology of Cobalt: Demonstration of a Potential Aetiology for Inflammatory Pseudotumours after Metal-on-Metal Replacement of the Hip," *Bone Joint J.*, Vol. 96–B, No. 9, 2014, pp. 1172–1177, http://dx.doi.org/10.1302/0301-620X.96B9.33476

[5] Daniel, J., Holland, J, Quigley, L., Sprague, S., and Bhandari, M., "Pseudotumors Associated with Total Hip Arthroplasty," *J. Bone Joint Surg.*, Vol. 94, No. 1, 2012, pp. 86–93, http://dx.doi.org/10.2106/JBJS.J.01612

[6] Talmo, C. T., Sharp, K. G., Malinowska, M., Bono, J. V., Ward, D. M., and LaReau, J., "Spontaneous Modular Femoral Head Dissociation Complicating Total Hip Arthroplasty," *Orthopedics*, Vol. 37, No. 6, 2014, pp. e592–e595, http://dx.doi.org/10.3928/01477447-20140528-62

[7] Matsen Ko, L., Chen, A. F., Deirmengian, G. K., Hozack, W. J., and Sharkey, P. F., "Catastrophic Femoral Head-Stem Trunnion Dissociation Secondary to Corrosion," *J. Bone Jt. Surg.*, Vol. 98, No. 16, 2016, pp. 1400–1404, http://dx.doi.org/10.2106/JBJS.15.00914

[8] Gilbert, J. L. and Jacobs, J., "The Mechanical and Electrochemical Processes Associated with Taper Fretting Crevice Corrosion: A Review," *Modularity of Orthopedic Implants, ASTM STP1301*, D. Marlowe, J. Parr, and M. Mayor, Eds., ASTM International, West Conshohocken, PA, 1997, pp. 45–59, http://dx.doi.org/10.1520/STP12020S

[9] Gilbert, J. L., "Mechanically Assisted Corrosion of Metallic Biomaterials," *ASM Handbook, Volume 23: Materials for Medical Devices*, ASM International, Materials Park, OH, 2012, pp. 79–89.

[10] Brown, S. A., Hughes, P. J., and Merritt, K., "In Vitro Studies of Fretting Corrosion of Orthopaedic Materials," *J. Orthop. Res.*, Vol. 6, No. 4, 1988, pp. 572–579, http://dx.doi.org/10.1002/jor.1100060415

[11] Geringer, J., Forest, B., and Combrade, P., "Fretting-Corrosion of Materials Used as Orthopaedic Implants," *Wear*, Vol. 259, Nos. 7–12, 2005, pp. 7–12, http://dx.doi.org/10.1016/j.wear.2004.11.027

[12] Gilbert, J. L., Mehta, M., and Pinder, B., "Fretting Crevice Corrosion of Stainless Steel Stem-CoCr Femoral Head Connections: Comparisons of Materials, Initial Moisture, and Offset Length," *J. Biomed. Mater. Res. Part B Appl. Biomater.*, Vol. 88B, No. 1, 2009, pp. 162–173, http://dx.doi.org/10.1002/jbm.b.31164

[13] Jauch, S. Y., Huber, G., Sellenschloh, H., Haschke, H., Baxmann, M., Grupp, T. M., and Morlock, M. M., "Micromotions at the Taper Interface between Stem and Neck Adapter of a Bimodular Hip Prosthesis during Activities of Daily Living," *J. Orthop. Res.*, Vol. 31, No. 8, 2013, pp. 1165–1171, http://dx.doi.org/10.1002/jor.22354

[14] Mali, S. A. and Gilbert, J. L., "Correlating Fretting Corrosion and Micromotions in Modular Tapers: Test Method Development and Assessment," *Modularity and Tapers in Total Joint Replacement Devices, ASTM STP1591*, A. S. Greenwald, S. Kurtz, J. Lemons, and

W. Mihalko, Eds., ASTM International, West Conshohocken, PA, 2015, pp. 259–282, http://dx.doi.org/10.1520/STP159120140136

[15] McCafferty, E., *Introduction to Corrosion Science*, Springer, New York, NY, 2010.

[16] Cook, S. D., Barrack, R. L., and Clemow, A. J., "Corrosion and Wear at the Modular Interface of Uncemented Femoral Stems," *J. Bone Joint Surg. Br.*, Vol. 76, No. 1, 1994, pp. 68–72.

[17] Gilbert, J. L., Buckley, C. A., and Jacobs, J. J., "In Vivo Corrosion of Modular Hip Prosthesis Components in Mixed and Similar Metal Combinations," *J. Biomed. Mater. Res.*, Vol. 27, No. 12, 1993, pp. 1533–1544, http://dx.doi.org/10.1002/jbm.820271210

[18] Goldberg, J. R., Gilbert, J. L., Jacobs, J. J., Bauer, T. W., Paprosky, W., and Leurgans, S., "A Multicenter Retrieval Study of the Taper Interfaces of Modular Hip Prostheses," *Clin. Orthop. Relat. Res.*, Vol. 401, No. 401, 2001, pp. 149–161, http://dx.doi.org/10.1097/00003086-200208000-00018

[19] Goldberg, J., Buckley, C., Jacobs, J., and Gilbert, J. L., "Corrosion Testing of Modular Hip Implants," *Modularity of Orthopedic Implants, ASTM STP1301*, D. Marlowe, J. Parr, and M. Mayor, Eds., ASTM International, West Conshohocken, PA, 1997, pp. 157–176, http://dx.doi.org/10.1520/STP12030S

[20] Goldberg, J. R. and Gilbert, J. L., "In Vitro Corrosion Testing of Modular Hip Tapers," *J. Biomed. Mater. Res. B. Appl. Biomater.*, Vol. 64, No. 2, 2003, pp. 78–93, http://dx.doi.org/10.1002/jbm.b.10526

[21] Gilbert, J. L., Mali, S. A., and Sivan, S., "Corrosion of Modular Tapers in Total Joint Replacements: A Critical Assessment of Design, Materials, Surface Structure, Mechanics, Electrochemistry, and Biology," *Modularity and Tapers in Total Joint Replacement Devices, ASTM STP1591*, A. S. Greenwald, S. Kurtz, J. Lemons, and W. Mihalko, Eds., ASTM International, West Conshohocken, PA, 2015, pp. 192–223, http://dx.doi.org/10.1520/STP159120140135

[22] Arnholt, C., Underwood, R., MacDonald, D. W., Higgs, G. B., Chen, A. F., Klein, G., Hamlin, B., et al., "Microgrooved Surface Topography Does Not Influence Fretting Corrosion of Tapers in Total Hip Arthroplasty: Classification and Retrieval Analysis," *Modularity and Tapers in Total Joint Replacement Devices, ASTM STP1591*, A. S. Greenwald, S. Kurtz, J. Lemons, and W. Mihalko, Eds., ASTM International, West Conshohocken, PA, 2015, pp. 99–122, http://dx.doi.org/10.1520/STP159120140149

[23] Pourzal, R., Hall, D. J., Ha, N. Q., Urban, R. M., Levine, B. R., Jacobs, J. J., and Lundberg, H. J., "Does Surface Topography Play a Role in Taper Damage in Head-Neck Modular Junctions?," *Clin. Orthop. Relat. Res.*, Vol. 474, No. 10, 2016, pp. 2232–2242, http://dx.doi.org/10.1007/s11999-016-4933-x

[24] Higgs, G. B., Macdonald, D. W., Chen, A. F., Klein, G. R., Hamlin, B. R., Lee, G., Mont, M. A., et al., "Does Taper Size Have an Effect on Taper Damage in Retrieved Total Hip Devices?," *J. Arthroplasty*, Vol. 31, No. 9, 2016, pp. 277–281, http://dx.doi.org/10.1016/j.arth.2016.06.053

[25] Dyrkacz, R. M. R., Brandt, J. M., Ojo, O. A., Turgeon, T. R., and Wyss, U. P., "The Influence of Head Size on Corrosion and Fretting Behaviour at the Head-Neck Interface of Artificial Hip Joints," *J. Arthroplasty*, Vol. 28, No. 6, 2013, pp. 1036–1040, http://dx.doi.org/10.1016/j.arth.2012.10.017

[26] Tan, S. C., Teeter, M. G., Del Balso, C., Howard, J. L., and Lanting, B. A., "Effect of Taper Design on Trunnionosis in Metal on Polyethylene Total Hip Arthroplasty," *J. Arthroplasty*, Vol. 30, No. 7, 2015, pp. 1269–1272, http://dx.doi.org/10.1016/j.arth.2015.02.031

[27] ASTM F1875–97, *Standard Practice for Fretting Corrosion Testing of Modular Implant Interfaces: Hip Femoral Head-Bore and Cone Taper Interface*, ASTM International, West Conshohocken, PA, 2010, www.astm.org

[28] Brown, S., Abera, A., D'Onofrio, M., and Flemming, C., "Effects of Neck Extension, Coverage, and Frequency on the Fretting Corrosion of Modular THR Bore and Cone Interface," *Modularity of Orthopedic Implants, ASTM STP1301*, D. Marlowe, J. Parr, and M. Mayor, Eds., ASTM International, West Conshohocken, PA, 1997, pp. 189–198, http://dx.doi.org/10.1520/STP12032S

[29] Swaminathan, V., Scholl, L., Lee, R., Faizan, M., Thakore, M., TenHuisen, K., and Nevelos, J., "Simultaneous Hip Head-Stem Taper Junction Measurements of Electrochemical Corrosion and Micromotion: A Comparison of Taper Geometry and Stem Material," *Modularity and Tapers in Total Joint Replacement Devices, ASTM STP1591*, A. S. Greenwald, S. Kurtz, J. Lemons, and W. Mihalko, Eds., ASTM International, West Conshohocken, PA, 2015, pp. 321–335, http://dx.doi.org/10.1520/STP159120140150

[30] Mroczkowski, M. L., Hertzler, J. S., Humphrey, S. M., Johnson, T., and Blanchard, C. R., "Effect of Impact Assembly on the Fretting Corrosion of Modular Hip Tapers," *J. Orthop. Res.*, Vol. 24, No. 2, 2006, pp. 271–279, http://dx.doi.org/10.1002/jor.20048

[31] Neville, A., Hesketh, J., Beadling, A. R., Bryant, M. G., and Dowson, D., "Incorporating Corrosion Measurement in Hip Wear Simulators: An Added Complication or a Necessity?," *Proc. Inst. Mech. Eng. Part H: J. Eng. Med.*, Vol. 230, No. 5, 2016, pp. 406–420, http://dx.doi.org/10.1177/0954411916642484

[32] Panagiotidou, A., Meswania, J., Osman, K., Bolland, B., Latham, J., Skinner, J., Haddad, F. S., Hart, A., and Blunn, G., "The Effect of Frictional Torque and Bending Moment on Corrosion at the Taper Interface: An In Vitro Study," *Bone Joint J.*, Vol. 97–B, No. 4, 2015, pp. 463–472, http://dx.doi.org/10.1302/0301-620X.97B4.34800

[33] Panagiotidou, A., Meswania, J., Hua, J., Muirhead-Allwood, S., Hart, A., and Blunn, G., "Enhanced Wear and Corrosion in Modular Tapers in Total Hip Replacement Is Associated with the Contact Area and Surface Topography," *J. Orthop. Res.*, Vol. 31, No. 12, 2015, pp. 2032–2039, http://dx.doi.org/10.1002/jor.22461

[34] Swaminathan, V. and Gilbert, J. L., "Fretting Corrosion of CoCrMo and Ti6Al4V Interfaces," *Biomaterials*, Vol. 33, No. 22, 2012, pp. 5487–5503, http://dx.doi.org/10.1016/j.biomaterials.2012.04.015

[35] ASTM F136-13, *Standard Specification for Wrought Titanium-6Aluminum-4Vanadium ELI (Extra Low Interstitial) Alloy for Surgical Implant Applications*, ASTM International, West Conshohocken, PA, 2013, www.astm.org

[36] Bergmann, G., Graichen, F., Rohlmann, A., Bender, A., Heinlein, B., Duda, G. N., Heller, M. O., and Morlock, M. M., "Realistic Loads for Testing Hip Implants," *Biomed. Mater. Eng.*, Vol. 20, No. 2, 2010, pp. 65–75, http://dx.doi.org/10.3233/BME-2010-0616

[37] Jauch, S. Y., Huber, G., Hoenig, E., Baxmann, M., Grupp, T. M., and Morlock, M. M., "Influence of Material Coupling and Assembly Condition on the Magnitude of Micromotion at the Stem–Neck Interface of a Modular Hip Endoprosthesis," *J. Biomech.*, Vol. 44, No. 9, 2011, pp. 1747–1751, http://dx.doi.org/10.1016/j.jbiomech.2011.04.007

[38] Yan, Y., Neville, A., Dowson, D., and Williams, S., "Tribocorrosion in Implants—Assessing High Carbon and Low Carbon Co–Cr–Mo Alloys by In Situ Electrochemical Measurements," *Tribol. Int.*, Vol. 39, No. 12, 2006, pp. 1509–1517, http://dx.doi.org/10.1016/j.triboint.2006.01.016

[39] Menezes, P. L., Nosonovsky, M., Ingole, S. P., Kailas, S. V., and Lovell, M. R., *Tribology for Scientists and Engineers*, Springer, New York, NY, 2013.

[40] Bishop, N., Witt, F., Pourzal, R., Fischer, M., Rutschi, M., Michel, M., and Morlock, M. M., "Wear Patterns of Taper Connections in Retrieved Large Diameter Metal-on-Metal Bearings," *J. Orthop. Res.*, Vol. 31, No. 7, 2013, pp. 1116–1122, http://dx.doi.org/10.1002/jor.22326

[41] English, A., Ashkanfar, A., and Rothwell, G., "The Effect of Different Assembly Loads on Taper Junction Fretting Wear in Total Hip Replacements," *Tribol. Int.*, Vol. 95, 2016, pp. 199–210, http://dx.doi.org/10.1016/j.triboint.2015.11.025

[42] Haschke, H., Jauch-Matt, S. Y., Sellenschloh, K., Huber, G., and Morlock, M. M., "Assembly Force and Taper Angle Difference Influence the Relative Motion at the Stem–Neck Interface of Bi-Modular Hip Prostheses," *J Eng. Med.*, Vol. 230, No. 7, 2016, pp. 690–699, http://dx.doi.org/10.1177/0954411916648717

[43] Heiney, J. P., Battula, S., Vrabec, G. A., Parikh, A., Blice, R., Schoenfeld, A. J., and Njus, G. O., "Impact Magnitudes Applied by Surgeons and Their Importance When Applying the Femoral Head onto the Morse Taper for Total Hip Arthroplasty," *Arch. Orthop. Trauma Surg.*, Vol. 129, No. 6, 2009, pp. 793–796, http://dx.doi.org/10.1007/s00402-008-0660-4

[44] Del Balso, C., Teeter, M. G., Tan, S. C., Lanting, B. A., and Howard, J. L., "Taperosis: Does Head Length Affect Fretting and Corrosion in Total Hip Arthroplasty?," *Bone Jt. J.*, Vol. 97–B, No. 7, 2015, pp. 911–916, http://dx.doi.org/10.1302/0301-620X.97B7.35149

[45] Lavernia, C. J., Iacobelli, D. A., Villa, J. M., Jones, K., Gonzalez, J. L., and Jones, W. K., "Trunnion-Head Stresses in THA: Are Big Heads Trouble?," *J. Arthroplasty*, Vol. 30, No. 6, 2014, pp. 1085–1088, http://dx.doi.org/10.1016/j.arth.2015.01.021

[46] MacLeod, A. R., Sullivan, N. P. T., Whitehouse, M. R., and Gill, H. S., "Large-Diameter Total Hip Arthroplasty Modular Heads Require Greater Assembly Forces for Initial Stability," *Bone Jt. Res.*, Vol. 5, No. 8, 2016, pp. 338–346, http://dx.doi.org/10.1302/2046-3758.58.BJR-2016-0044.R1

[47] Triantafyllopoulos, G. K., Elpers, M. E., Burket, J. C., Esposito, C. I., Padgett, D. E., and Wright, T. M., "Otto Aufranc Award: Large Heads Do Not Increase Damage at the Head-Neck Taper of Metal-on-Polyethylene Total Hip Arthroplasties," *Clin. Orthop. Relat. Res.*, Vol. 474, No. 2, 2016, pp. 330–338, http://dx.doi.org/10.1007/s11999-015-4468-6

[48] Huot Carlson, J. C., Van Citters, D. W., Curier, J. H., Bryant, A. M., Mayor, M. B., and Collier, J. P., "Femoral Stem Fracture and In Vivo Corrosion of Retrieved Modular Femoral Hips," *J. Arthroplasty*, Vol. 27, No. 7, 2012, pp. 1389–1396, http://dx.doi.org/10.1016/j.arth.2011.11.007

[49] Matthies, A. K., Racasan, R., Bills, P., Blunt, L., Cro, S., Panagiotidou, A., Blunn, G., Skinner, J., and Hart, A. J., "Material Loss at the Taper Junction of Retrieved Large Head Metal-on-Metal Total Hip Replacements," *J. Orthop. Res.*, Vol. 31, No. 11, 2013, pp. 1677–1685, http://dx.doi.org/10.1002/jor.22431

[50] Mistry, J. B., Chughtai, M., Elmallah, R. K., Diedrich, A., Le, S., Thomas, M., and Mont, M. A., "Trunnionosis in Total Hip Arthroplasty: A Review," *J. Orthop. Traumatol.*, Vol. 17, No. 1, 2016, pp. 1–6, http://dx.doi.org/10.1007/s10195-016-0391-1

STP 1609, 2019 / available online at www.astm.org / doi: 10.1520/STP160920170223

Bobbi Jo E. Merten,[1] Michael T. Walsh,[1] and Jessica D. Torrey[1]

Validation of Coated Infrastructure Examination by Electrochemical Impedance Spectroscopy

Citation

Merten, B. J. E., Walsh, M. T., and Torrey, J. D., "Validation of Coated Infrastructure Examination by Electrochemical Impedance Spectroscopy," *Advances in Electrochemical Techniques for Corrosion Monitoring and Laboratory Corrosion Measurements*, *ASTM STP1609*, S. Papavinasam, R. B. Rebak, L. Yang, and N. S. Berke, Eds., ASTM International, West Conshohocken, PA, 2019, pp. 137–159, http://dx.doi.org/10.1520/STP160920170223[2]

ABSTRACT

Field electrochemical impedance spectroscopy (EIS) measurement allows researchers and facility owners to examine protective coatings on existing infrastructure. Few other nondestructive coating inspection methods provide quantitative information, and none are as comprehensive. EIS measures the total resistance to water and ion permeation for the in-service coating, which indicates the degree of corrosion protection. A desired application of these results is to maximize coating service life and improve maintenance planning at facilities with valuable coated infrastructure. EIS evaluation of naturally aged coatings also offers the opportunity to advance coating service life prediction studies. Despite advances in hardware portability and progress in method development, however, field EIS testing and application to coating maintenance decision-making remain limited. The absence of a standardized procedure for conducting a field EIS survey and analyzing its results is a barrier to further implementation. This paper evaluates the repeatability of EIS measurements through an experimental design performed on coated infrastructure. The assessed

Manuscript received November 9, 2017; accepted for publication February 16, 2018.

[1]Bureau of Reclamation, Materials and Corrosion Laboratory, Denver Federal Center, PO Box 25007, Denver, CO 80225, USA B. J. E. M. http://orcid.org/0000 0001 9592 7340, M. T. W. http://orcid.org/0000 0003 0716 3710, J. D. T. http://orcid.org/0000 0002 1096 9347

[2]ASTM Symposium on *Advances in Electrochemical Techniques for Corrosion Monitoring and Laboratory Corrosion Measurements* on November 13 14, 2017 in Atlanta, GA, USA.

structures varied from high-to-low protective impedance values, and the service environments were atmospheric and constant immersion. All coatings were approaching the end of their service life. The tests demonstrate outcomes for many of the variables encountered when executing the proposed field method, including coating type, thickness, age, and exposure conditions. The results show good repeatability for specimens, but variation occurs in the values obtained from one specimen to the next. The paper also considers EIS test method parameters, including applied frequency range and number of data points collected, as well as the practical challenges of performing field EIS testing. The discussion proposes the best practices realized through these studies, such as the use of a two-cell setup and the illustration of results via probability plots. Final thoughts highlight the future work necessary to advance standardization and implementation of field EIS testing.

Keywords

electrochemical impedance spectroscopy, field impedance spectroscopy, in situ impedance spectroscopy, coating assessment, infrastructure inspection, field electrochemical impedance spectroscopy testing

Introduction

Organic protective coatings are the primary, and often sole, means of corrosion protection for the mild steel components of civil infrastructure. A protective coating functions as a barrier between the steel structure and its service environment, preventing electrolyte from completing a corrosion cell between anodic and cathodic sites on the steel surface. Electrochemical impedance spectroscopy (EIS) is an effective tool for measuring the barrier performance of coatings on steel and has the benefit of detecting coating degradation long before visible damage occurs [1].

EIS evaluation of protective coatings requires a basic understanding of the underlying protection mechanisms that govern coatings. The Sixth International Conference on Advances in Corrosion Protection by Organic Coatings resulted in several recent reviews on the state of the art [2–5]. There is agreement that coatings give protection by a combination of bulk and interfacial properties. The chemical and physical properties of the bulk polymer material control or limit the migration of water and ions to the substrate. A well formulated coating employs hydrophobicity through its chemical properties and minimizes voids through its physical properties. Obtaining the desired degree of homogeneity is an ongoing challenge, and many coatings have localized regions, known as "D areas," that have a direct relationship with the external ion solution and exhibit low electrical resistivity [3]. The D areas comprise a small percentage of the coating and have a resistance between that of the adjacent coating and that which would be expected of a pore. Multicoat systems sufficiently mask D areas to provide a more effective barrier [6]. Recent field application trends toward one coat systems to achieve shorter return to service times may prove problematic in the long term as D areas quickly break down and lead to corrosion of the underlying steel.

The polymer coating interface provides a concentrated zone of corrosion protection at the substrate. A durable adhesive bond structure ensures this by preventing the accumulation of an aqueous phase at the interface. The aqueous phase is required for electrochemical corrosion reactions to occur and proceed. Funke [7] argued that wet adhesion is a direct measure of a material's corrosion protection, but Marsh [8] showed that this claim is not applicable to all coating types. The adhesive interface in most polymer materials likely consists of covalent bonds, such as metal oxide carbon [9], and weaker attractive forces, such as weak acid weak base associations [10].

Protective coatings endure many stresses during their service lives. Among them are contractive stresses associated with curing, solvent drying, or loss of soluble material, expansive stresses due to water ingress, and thermal or mechanical cycling stresses induced by the service environment [7]. Hydraulic steel structures control or transfer water and are thus often exposed to either continuous or intermittent immersion conditions. Also, coatings in atmospheric service environments may be exposed to ultraviolet radiation. Negele and Funke [7] showed that some stress might be relieved through natural relaxation processes. Repeated cycles of stress and relaxation result in cumulative physical aging for most polymeric materials.

EIS can be used to monitor polymer degradation by measuring changes to the coating's dielectric properties [11 13]. The present study evaluates the application of EIS measurements to in situ coated infrastructure to determine the corrosion protection properties of the aging system. Provided that a standard and reliable approach can be developed, the resulting EIS data could aid maintenance programs and decision making by estimating the coating's remaining service life. Enhanced accuracy of coating system service life predictions will improve attempts to maximize a coating's useful life and thereby minimize its life cycle costs.

Field Impedance Spectroscopy

In 1948, Bacon, Smith, and Rugg [14] provided the first direct current resistance evaluations of organic coatings on metal substrates in immersion, ranking the performance of more than 300 coating systems. The ensuing decades brought advancements in the technique and equipment, resulting in a valuable approach for monitoring the long term effectiveness of protective coatings on substrates [15 17]. Several potentiostats are now marketed as portable for field use.

For more than two decades, researchers provided examples of field EIS experiments [18 20]; the 2009 ASTM symposia on Advances in Electrochemical Techniques for Corrosion Monitoring and Measurement provided a thorough citation list of early efforts [21]. The present research continues the effort to advance EIS for field use by demonstrating field experiments on coated structures conducted with emphasis on evaluating repeatability in the EIS data. This is a critical step in advancing field EIS practices and ensuring that the data are used appropriately. The techniques here include method improvements and lessons learned previously that

have been reported as a result of preliminary efforts by this group [22]. Notably, the electrochemical method used herein evolved to a nonsubstrate cell setup to forego direct metallic substrate connection, as reported by other authors in their laboratory electrochemical experiments [23,24].

Theory

EIS is a frequency dependent application of Ohm's law that incorporates real and imaginary components to provide a complex electrical resistance [11]. Eq 1 provides the basic relationship of resistance, R, to voltage, V, and current, I. Eq 2 provides the expression for impedance, Z, at frequency, ω, which illustrates that impedance of a material is a function of the oscillation frequency of the alternating current signal.

$$R = \frac{V}{I} \tag{1}$$

$$Z(\omega) = \frac{V(\omega)}{I(\omega)} \tag{2}$$

Furthermore, Eq 3 shows the total impedance for a material as it relates to its real, Z_{real}, and imaginary, Z_{im}, impedance components with $j = \sqrt{-1}$. Additional information on EIS theory and its applications to protective coatings is available in the literature [11,13,25 30].

$$Z = Z_{real} + jZ_{im} \tag{3}$$

In practice, EIS testing measures the current required to satisfy an applied sinu soidal voltage pattern across a given material. The lag of the current response is the phase angle, θ, which is a characteristic of the material's electrical behavior, ranging from $\theta = 0^\circ$ for a resistor to $\theta = -90^\circ$ for a capacitor.

The spectroscopic aspect of EIS allows for the evaluation of many physical properties at various frequencies. As an example, coating characteristics such as water uptake [31 33] and adhesion [12,34] appear in the middle to high measure ment frequencies. As the measurement frequency decreases, all current flows through resistive elements in the circuit, and the total impedance of the circuit is measured. Comparing the impedance magnitude, $|Z|$, at low frequencies, approxi mately 0.1 to 0.01 Hz, is the most common approach for EIS data interpretation of barrier coatings. As a general rule, a $|Z|$ greater than 10^8 ohm signifies good barrier performance, whereas less than 10^6 ohm is poor [4,14]. Additionally, the $|Z|$ pro vides a good approximation for polarization resistance, which allows for the calcu lation of corrosion rate via the Stearn Geary equation [26].

Equivalent circuit modeling (ECM) offers an additional form of data analysis. ECM uses analogous circuit elements to represent particular aspects of the corrod ing system. The circuit elements and the resulting model must provide a reasonable theoretical explanation for physical processes that occur within the material. A basic resistor capacitor provides a fair approximation for intact coatings on substrates.

The initiation and propagation of corrosion at the coating interface results in a second time constant in the data, requiring an additional resistor capacitor element for the model.

An organic coating often emulates the behavior of an imperfect capacitor. The inclusion of a so called constant phase element (CPE) in ECM provides greater sensitivity for modeling the coating's capacitive behavior, resulting in an improved overall model fit. The CPE incorporates an exponent, α, with values from -1 to 1 that allows the CPE to represent any θ in the EIS data (i.e., a resistor, capacitor, and so on). Eq 4 shows the simple relationship between θ and α.

$$\theta = \frac{\pi}{2} \times \alpha \tag{4}$$

EXPERIMENT

Several coated mild steel structures provided the in situ samples used in this experiment. Structure A is a trash chute in atmospheric service at a small dam. The actual coating system type is unknown but likely is a shop applied material suitable for light to medium duty exposure. Structures B through D are hydroelectric penstock pipes. The exterior coatings are CA 50 (cold applied) coal tar paint, accessible within a below grade tunnel. The interior linings are American Water Works Association (AWWA) C203 hot applied coal tar enamel. Table 1 provides additional structure information and condition notes.

Sampling Procedure

The proposed method prescribes the selection of several samples, each with multiple specimens. Fig. 1 provides a schematic of a coated structure and the distribution of samples and corresponding specimens. The proper selection of test specimens is key to the application of successful and meaningful field EIS measurements. The specimen selection process is as follows:

- Identify accessible areas of coated structure and perform a cursory inspection.
- Select testing areas where coating is likely to be completely saturated (i.e., in standing water until the day of testing, assuming that it can be dewatered

TABLE 1 Coating type and exposure information for coated structures.

ID	Service[a]	Coating	Condition Notes
A	Atmospheric	Unknown	Aged 25 years in outdoor exposure
B	Atmospheric	CA 50	Aged 85 years in a cool, humid tunnel
C	Immersion	AWWA C203	Aged 85 years as interior lining; freshwater reservoir; dewatered time < 4 %
D	Immersion	AWWA C203	Aged 85 years as interior lining; freshwater reservoir; dewatered time < 3 %

[a]Coated structure service elevation ranges from 7,700 to 7,800 ft.

FIG. 1 Schematic of experimental samples and specimens for EIS coated infrastructure evaluation; a specimen is made up of any combination of two test cells.

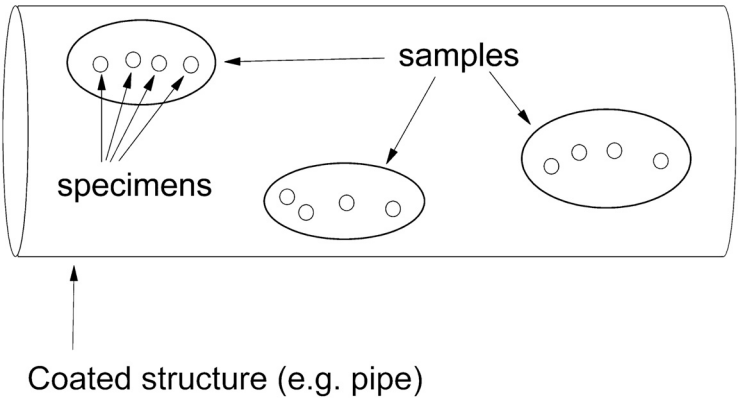

quickly for testing). Locations with a low likelihood of saturation have the dis advantage that they can require a long soaking period to equilibrate.

- Locate areas where the coating has a uniform appearance and represents the "best" condition observed. Areas of average to above average condition are acceptable.
- Select specimens that have no visible defects. Each sample should consist of at least four coating specimens. An area of 3 in. by 3 in. (7.6 cm by 7.6 cm) is appropriate to proceed with applying each temporary test cell.

The naming convention used in this experiment identifies each sample with an alphanumeric designation (e.g., B 1, B 2) and then appends an alphabetic suffix to identify the particular specimen (e.g., B 1a, B 1b). Repeatability tests of any particu lar specimen are identified by number (e.g., B 1a.1, B 1a.2).

Test Method

SPECIMEN PREPARATION

Each sample site was cleaned with a water soaked towel and then dried in prepara tion for the application of temporary test cells. Each specimen is made up of two test cells, and each test cell used a reservoir that was constructed from a 100 mL plastic beaker with its bottom removed. Underwater adhesive was applied to the top rim of the beaker, and the assembly was inverted and pressed firmly against the coated structure surface, thus forming the temporary test cell. The adhesive was allowed to cure in place for at least 2 h before the reservoirs were filled with approx imately 50 mL of dilute Harrison's solution (0.35 mass percent ammonium sulfate and 0.05 mass percent sodium chloride).

Before initiating a series of tests, each filled reservoir was given at least 30 min to saturate the coating and equilibrate as needed. It should be noted that while at mospheric coatings often require overnight saturation to achieve equilibrium, the freshly dewatered immersion coatings in this study needed less than 2 h given their normally saturated state.

EIS MEASUREMENT

Testing employed an Ivium CompactStat™ (Eindhoven, the Netherlands) mobile potentiostat and its dedicated software. Testing used the two cell measurement technique, which involved using one test cell for both a copper copper sulfate refer ence electrode and a platinum mesh counter electrode and a second test cell for a platinum mesh working electrode. The testing was absent of an electromagnetic shielding method or Faraday cage as would be standard for laboratory EIS testing to reduce noise.

Fig. 2 shows an example of a two cell test setup. Each two cell measurement en abled EIS evaluation of approximately 4 in.^{2} (25 cm^2) of the structure's coated sur face. Various combinations of two cell measurements, or specimens, comprised each sample.

The open circuit potential was observed at the beginning of each measurement. A negative and relatively stable potential during a 10 s observation indicated that the coating specimen was sufficiently saturated and at steady state (i.e., ready to ini tiate the EIS measurement).

FIG. 2 Field EIS test setup for measurement with no connection to the substrate shown as (a) schematic and (b) photograph.

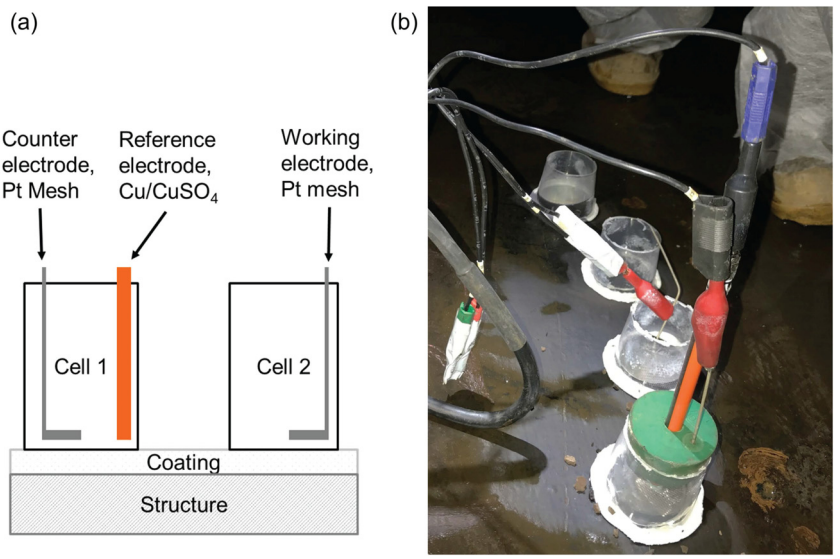

Table 2 provides experimental parameters for each structure, including the total number of data files produced for the particular sample and any experimental variations for the measurement. The initial test frequency was 10^5 Hz, and the final frequency was 0.1, 0.05, or 0.01 Hz. The tests recorded five points per decade using open circuit potential perturbations of 50 mV rms unless otherwise noted in Table 2.

PHYSICAL AND ENVIRONMENTAL DATA

The testing method matured over the course of the present work and ultimately included the collection of environmental data as a proxy for historic exposure and coating film thickness to improve coating condition characterization. Table 3 presents observed environmental conditions at the time of testing (air temperature, surface temperature, and relative humidity) and film thickness data. This information is representative of the typical service conditions, aiding the analysis of remaining coating service life and interpretation of the EIS test results. Environmental condition values for Structure A were estimated. Conditions for Structure C approximately matched conditions at Structure D.

Data Screening

Field EIS testing is subject to data anomalies, such as those arising from instrumental errors or uncontrolled electromagnetic noise sources. Data screening involves reviewing each data file upon test completion and subsequently evaluating outlier data points during desktop analysis. Screening the data enables removal of data sets

TABLE 2 EIS measurements for each coated structure and measurement variable notes.

ID	Samples	Specimens	Data Sets	Notes
A	1	3	13	Single test cell; saturated calomel reference; perturbation: 10 mV; final frequency: 0.1, 0.01 Hz
B	4	6	16	Final frequency: 0.05, 0.01 Hz
C	2	5	17	Final frequency: 0.1, 0.05, 0.01 Hz
D	6	25	46	Final frequency: 0.05, 0.01 Hz

TABLE 3 Environmental conditions and coating film thickness data for coated structures.

ID	Air Temperature (°F)	Surface Temperature (°F)	Relative Humidity (%)	Film Thickness, Avg (mils)	Film Thickness, Standard Deviation (mils)
A	Near 80	Near 80	Near 30	...	...
B	54	40	53	8.6	1.6
C	...	...	...	30.0	13.0
D	48	44	70	26.8	10.6

that indicate either significant operational errors or deviations from realistic physi cal coating properties or phenomena.

The experiments yielded a small subset of data with sufficient error to reject; the analysis nonetheless included data from all EIS tests that yielded a complete test scan. The present experiment did not apply the data screening process described in the previous paragraph. The incorporation of this errant data has the benefit of aid ing identification of anomalies and facilitating additional critical review of the data collection process (see Results and Discussion sections that follow).

Data Analysis

Data analysis involved both the evaluation of the $|Z|$ at low frequencies and the modeling of each coating system using equivalent circuits. The evaluation used raw impedance data (i.e., data not corrected for surface area). ZView® software (Scrib ner Associates, Southern Pines, North Carolina, USA) facilitated the ECM of the data sets.

Repeatability analysis involved the evaluation of data from multiple measure ments taken for each specimen. The characterizations were proceeded by calcula tion and evaluation of the sample mean, μ, standard deviation, s, and coefficient of variation, C_V. The sample size, n, was less than five observations for most repeat ability calculations, and this necessitated the use of Eq 5 for calculation of C_V. Data sets with a much larger n would enable the use of the simplified Eq 6.

$$C_V = \left(1 + \frac{1}{4n}\right) \times \frac{s}{\mu} \tag{5}$$

$$C_V = \frac{s}{\mu} \tag{6}$$

Test Results

SAMPLE VARIABILITY

The large volume of compiled EIS data allowed statistical evaluation of the raw data values. The first approach calculated the μ, s, and C_V of $|Z|$ values collected in the low frequency portion of the measurement. In particular, the $|Z|$ data at 0.05 Hz provided the input for this analysis. However, several EIS scans executed to a final frequency of 0.01 Hz did not include a measurement at 0.05 Hz; here, 0.04 Hz was the closest available data point and accordingly was selected. In addition, data col lection for Structures A and C ended at 0.1 Hz; data used the $|Z|$ value at that fre quency for the analysis. See Table 2 for a summary of the total number of samples, specimens, and data files evaluated.

Fig. 3 presents results for each sample except D 3. The D 3 measurements were unsuccessful because of test cell leaks that prevented complete scans. Results illus trate the variation of $|Z|$ at low frequencies for adjacent specimens. The μ of each

FIG. 3 Sample variability statistics for EIS |*Z*| data at 0.05 Hz.

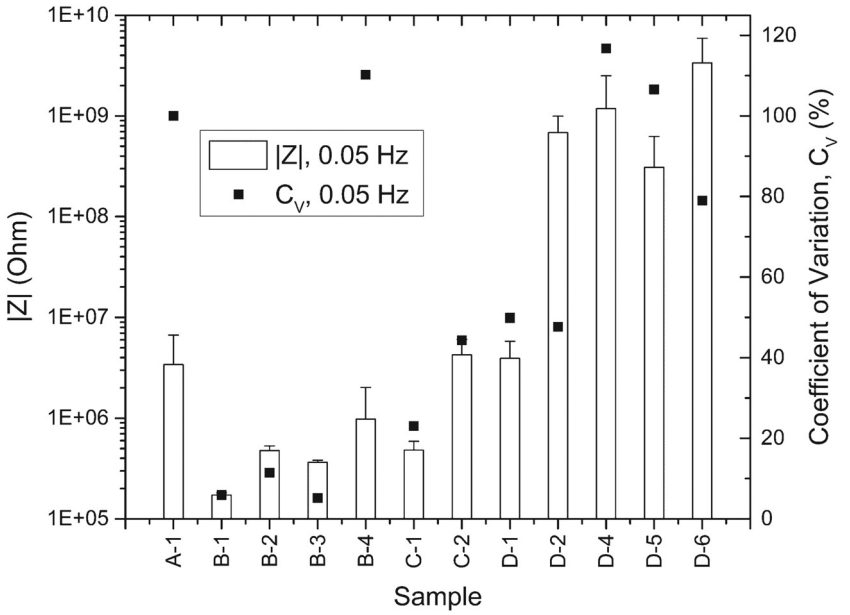

low frequency |*Z*| value appears as a column with an error bar showing *s* in the pos itive direction. The right ordinate axis indicates values of C_V, presented in scatter plot format. A lower C_V value indicates a high degree of uniformity for the adjacent coating properties.

Structures A and B provided examples of coatings on structures operating in atmospheric (as opposed to immersed) environments. The averaged low frequency |*Z*| values for Structure A are greater than 10^6 ohm, suggesting that the coating provides a low level of barrier protection. This is typical of a coating sys tem designed for atmospheric service, which may not have high barrier protection as a design feature. Structure A also has a high C_V, indicating poor uniformity among the measured specimens. However, the test also showed variation attribut able to both environmental and experimental variables, demonstrating a need to refine the testing technique. Corrections to the technique made after the collection of Structure A data, including implementation of the two cell setup and the removal of obvious sources of alternating curent noise interference from the experiment, such as in service power cords and cellular phones in transmitting mode, yielded results apparent in subsequent measurements. The ongoing process of method validation and refinement helped to determine the anticipated preci sion of measurement while also identifying appreciable errors that could be attrib uted to the technique itself.

Testing conducted at the sample locations for Structure B yielded the lowest $|Z|$ values, shown in Fig. 3. The measured values are near or less than 10^6 ohm. Considering that the coating system is a CA 50 coal tar paint of approximately 9 mils film thickness, the coating is providing poor barrier protection and nearing the end of its service life. The data indicate that the averaged low frequency $|Z|$ results for the specimens at samples B 1, B 2, and B 3 provided less barrier protection than the respective results for all other structures. The Structure B results also have the lowest C_V values, possibly indicative of greater coating or coating condition uniformity than that observed in the other samples.

Structure B 4 had only one specimen, which had a slightly higher average $|Z|$ and high variability. A review of the raw data and field notes indicated that significant test cell leakage occurred at B 4 during measurement, allowing completion of only two tests. The $|Z|$ values at 0.05 Hz measured 1.7×10^6 and 2.5×10^5 ohm for the two respective tests on the same specimen. Though the impedance data had minimal noise (i.e., undesirable fluctuation), the lack of repeatability and the leaking cup prevented the continuation of testing. It should be noted that data screening would have effectively removed sample B 4 from consideration if field EIS testing had been conducted for coating performance decision making purposes.

Noise level was likewise low at B 1, B 2, and B 3, and results provide sound information for further evaluation of this coating. B 1 through B 3 testing resulted in data collection for three distinct samples with a total of five distinct specimens.

Structures C and D, both in immersion service, have the widest range of test results. Both samples for Structure C measured an average $|Z|$ near 10^6 ohm, indicating poor barrier protection and the end of the coating service life (Fig. 3). A closer look at the data indicated that one specimen from C 2 should be discarded because the test cell leaked and was empty by the end of the measurement. The other specimens for C 2 were devoid of any adverse measurement issues. A recalculation of C 2 without the compromised specimen yielded a μ of 5.0×10^6 ohm and a C_V of 5 % (not shown in Fig. 3) . The testing for Structure C resulted in two samples and five specimens. One specimen would be discarded if the tests had been conducted for coating performance decision making.

The averages of the $|Z|$ values for four of the five Structure D samples ranged from 3.1×10^8 to 3.4×10^9 ohm, while the average value of the fifth sample (D 1) was 3.9×10^6 ohm. Despite the comparatively low average $|Z|$ at sample D 1, the raw data and testing notes do not provide any discernable reason to discard the results.

Fig. 4 presents each of the D 1 data sets in Nyquist and Bode plot formats. Results of D 1a and D 1b are similar. Results of both D 1c and D 1d indicate significantly lower impedance values, possibly suggesting that the coating provides a lower level of barrier protection for these particular specimens. It should be noted, however, that this variation could also be the result of fine hairline cracking or pinholes that provide electrolytic contact with the substrate despite being invisible to the naked eye.

FIG. 4 EIS data for all sample D 1 specimens shown as (a) Nyquist and (b) Bode plots.

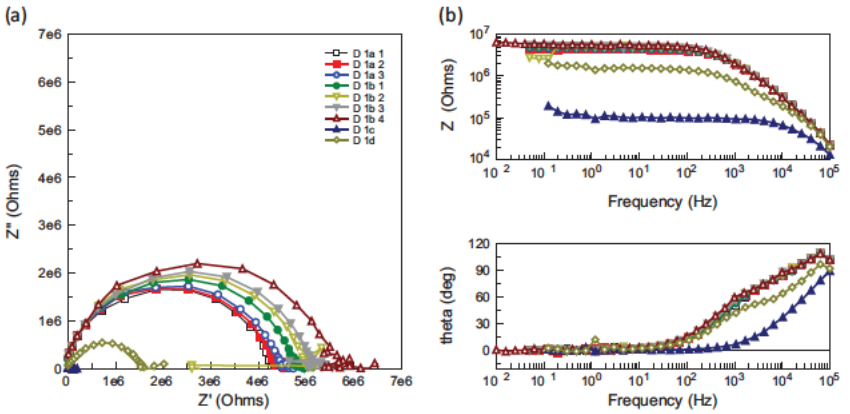

Tests in the remaining Structure D samples (i.e., D 2 through D 6) revealed relatively higher $|Z|$ values. Values of the observed magnitudes would indicate excellent barrier protection, but it is important to note that the data sets for these samples tended to have higher C_V values. Samples D 2, D 4, and D 5 each had six specimens, a greater quantity than any other samples reported in this work. Data variability increased the calculated values of C_V, but the greater quantity of specimens rendered the results more representative of the overall coating condition. Sample D 6 had only two specimens, both of which yielded $|Z|$ values higher than those observed in any other samples in this work.

Fig. 5 shows that several data sets, namely D 4b, D 4d, and D 4e, had an appreciable level of noise at low frequencies. The noise contributed to the high C_V value for sample D 4 but did not otherwise provide adequate justification for discarding any data. The observed collapse of the D 4a.4 curve at frequencies below 1 Hz cannot be attributed to any physical phenomena and likely represents an equipment artifact, possibly caused by a short circuit that developed midway through the experiment. Data for D 4a.4 would not be included in data analysis if the tests had been conducted for coating performance decision making.

Repeatability of Results

Fig. 6 illustrates the repeatability of individual test results using the same plotting conventions used in Fig. 3. Plotted data for each specimen shown represent the results of at least three tests, but not all specimens were subjected to repeated measurements. Specifically in Fig. 6, the data for specimens C 1a, D 1a, and D 2b represent three tests, A 1b represents nine tests, and D 6a represents six tests; the data for all other specimens represent four tests. Most tests proceeded from previous

FIG. 5 EIS data for all sample D 4 specimens shown as (a) Nyquist and (b) Bode plots.

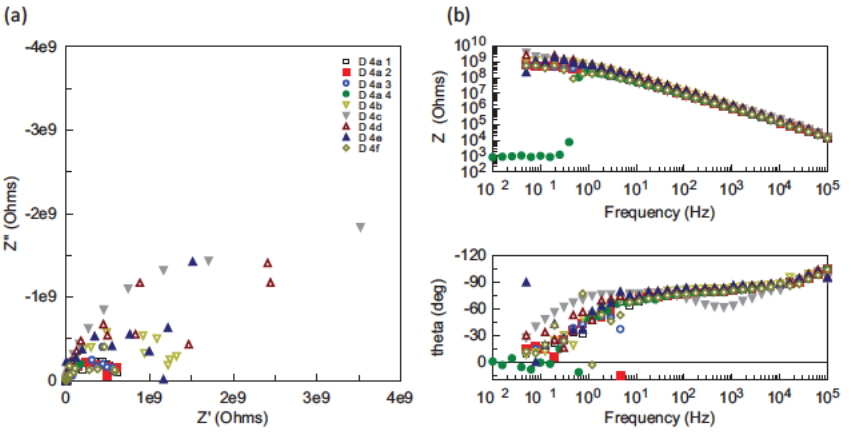

FIG. 6 Repeatability statistics for each specimen using EIS |Z| data at 0.05 Hz.

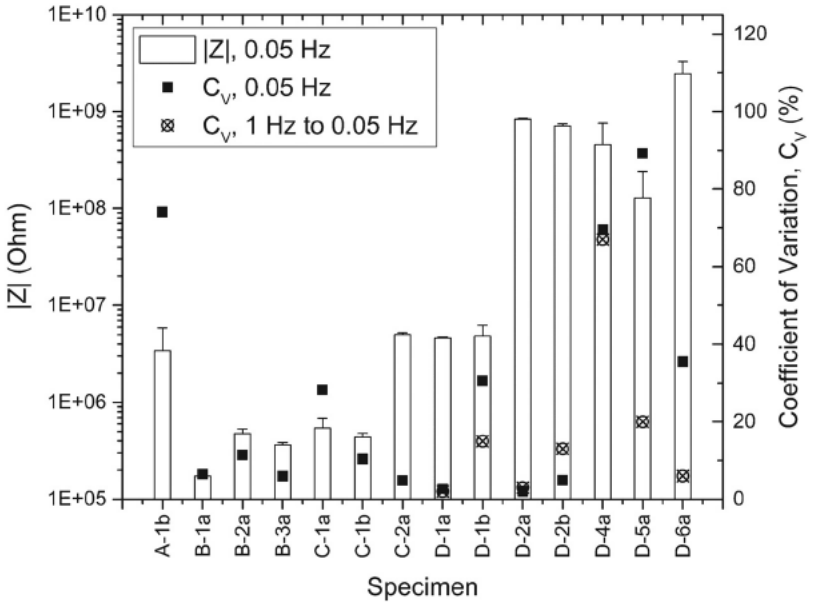

tests without any equipment adjustment or intermediate equipment use. Reported results do not distinguish the few cases in which testing of a different specimen required adjustment of equipment; variation was deemed insignificant.

The general trends of the values presented in Fig. 3 are similar to the trends that appear in the Fig. 6 specimen repeatability results. This is expected because the data in Fig. 6 constitute a significant portion of the Fig. 3 data. Fig. 6 does, however, show a distinct reduction in the C_V magnitudes between the two figures, indicating a high degree of measurement repeatability.

An additional C_V parameter for the average of the raw $|Z|$ values measured at frequencies from 1 to 0.05 Hz appears in Fig. 6 for the Structure D specimens. Averaging the low frequency $|Z|$ values reduces the effects of noise on any particular $|Z|$ value in this region. This resulted in a significant reduction of the C_V values for most specimens; six of the seven specimens showed C_V values of less than 20 % when smoothed $|Z|$ data were used. The outlier, D 4a, has a high C_V as a result of the errant D 4a.4 measurement, as discussed earlier and highlighted in Fig. 5. A recalculation of D 4a with the remaining data sets provides a μ of 9.1×10^8 ohm and a C_V of 4 %. The data averaging, or smoothing, approach reduces the consequences of reporting a single value, which would inherently incorporate some degree of measurement inaccuracy. Incorporating smoothing or a similar technique into a formalized field EIS method should be considered further.

EQUIVALENT CIRCUIT MODELING

Test data for Structure D underwent ECM. Structure D was selected because it represented the most matured application of the field EIS test method and yielded the largest data set. Fig. 7 shows the model employed to represent the aged coating system in the present work. The use of ECM for this particular coating system type with more than 80 years of service is not found in other published works and thereby affording an opportunity for discussion of a more suitable model. Furthermore, the two cell setup used here also necessitated the experimental validation of suitable models. Fig. 8 and Fig. 9 show the D 5a and D 6a specimen data, respectively, and include an ECM fit line for a representative data set. The D 6a has a pronounced second time constant and much higher $|Z|$ values at the low frequencies. The two Bode plots are similar at frequencies greater than 10^2 Hz.

FIG. 7 Equivalent circuit model for an aged coating system.

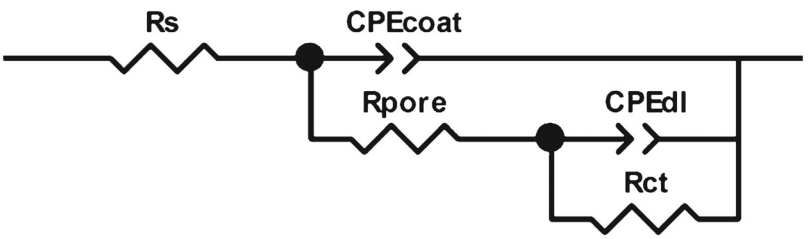

FIG. 8 EIS data for repeated measurements of specimen D 5a and the ECM fitted line for D 5a.3 shown as (a) Nyquist and (b) Bode plots.

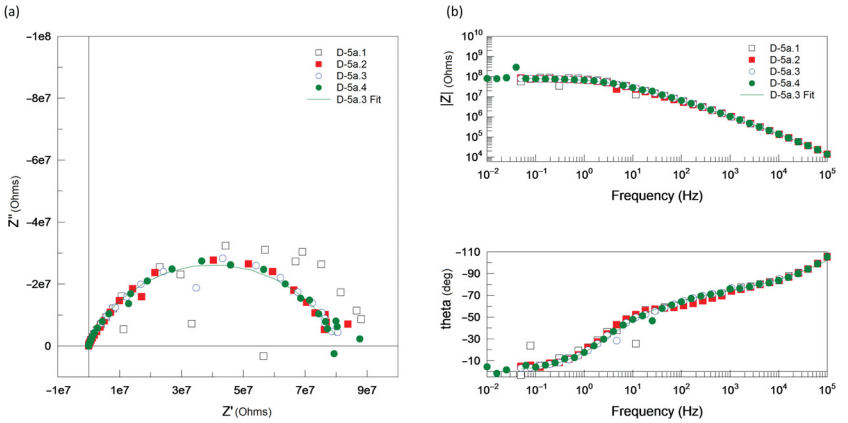

FIG. 9 EIS data for repeated measurements of specimen D 6a and the ECM fitted line for D 6a.4 shown as (a) Nyquist and (b) Bode plots.

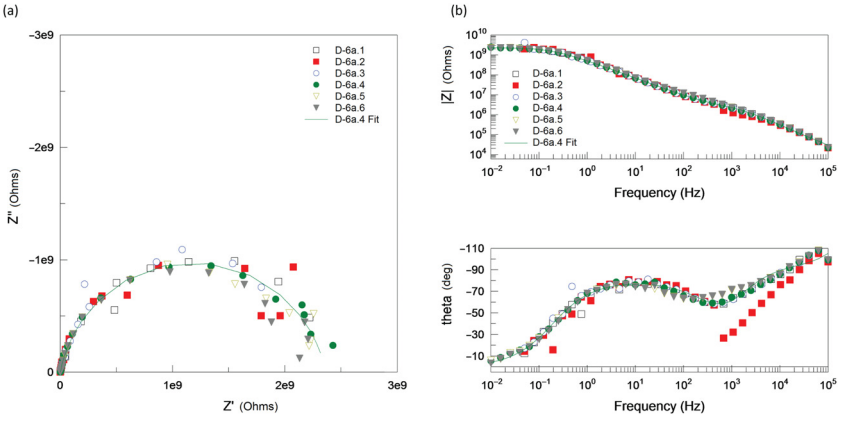

ECM data for D 5a.3 provided the best fit, as shown in Fig. 8. Fitting for this data set required the removal of one data point, at 3 Hz, to allow the model to calculate a proper fit. The other three data sets required the removal of several additional anom alous data points to yield a proper fit. Table 4 presents the model data. The solution resistance, R_s, values are approximated as negative values, as is typical given poor instrument resolution at these small resistances. The coating CPE, CPE_{coat}, values are

TABLE 4 Specimens D 5a and D 6a ECM outputs.

ID	R_s[a] (ohm)	CPE_{coat}[b] (F)	α_{coat}[c]	R_{pore}[d] (ohm)	CPE_{dl}[e] (F)	α_{dl}[f]	R_{ct}[g] (ohm)	Sum of Squares
D 5a.1	1,508	8.7E 12	1.19	4.9E+04	1.5E 09	0.71	9.7E+07	0.14
D 5a.2	1,317	4.7E 12	1.23	2.3E+04	1.7E 09	0.71	8.4E+07	0.26
D 5a.3	1,777	1.4E 11	1.16	8.2E+04	1.4E 09	0.71	8.3E+07	0.09
D 5a.4	2,378	3.3E 11	1.09	1.6E+05	1.5E 09	0.68	8.3E+07	0.37
D 5a, C_V	**28**	**86**	**5**	**79**	**8**	**2**	**8**	**61**
D 6a.1	22,471	6.2E 11	0.98	4.0E+06	2.8E 10	0.89	2.4E+09	0.25
D 6a.2	20,229	1.6E 10	0.90	5.9E+06	1.7E 10	0.93	2.3E+09	0.48
D 6a.3	21,911	6.3E 11	0.98	4.1E+06	2.9E 10	0.88	2.4E+09	0.22
D 6a.4	26,835	8.3E 11	0.95	5.1E+06	2.8E 10	0.87	2.3E+09	0.30
D 6a.5	31,562	1.2E 10	0.92	1.1E+07	2.4E 10	0.87	2.2E+09	0.36
D 6a.6	31,458	1.3E 10	0.92	1.2E+07	2.3E 10	0.87	2.2E+09	0.37
D 6a, C_V	**20**	**40**	**4**	**55**	**18**	**3**	**4**	**30**

Note: Boldface values are the coefficient of variation (C_V) for all respective specimen measurements (i.e., preceding table rows).
[a]Solution resistance.
[b]Coating CPE.
[c]Coating CPE exponent.
[d]Pore resistance.
[e]Double layer CPE.
[f]Double layer CPE exponent.
[g]Charge transfer resistance.

approximately 10^{-11} F, but α is slightly higher than 1, which should not theoretically be possible. The highest frequency measured values could be contributing to greater measurement error. The coating pore resistance, R_{pore}, and the charge transfer resis tance, R_{ct}, are approximately 10^5 and 10^8 ohm, respectively.

The removal of the two highest frequency data points effectively improved the fit of the D 6a specimen data and yielded a more reasonable α value, suggesting that the instrument was not accurately measuring these data points. Fitting the D 6a.2 data set required removal of anomalous data points between 10^3 and 10^4 Hz. The results (Table 4) again show the CPE_{coat} to be a near perfect capacitor with a value of 10^{-10} F, which is an order of magnitude greater than the capacitance measured in D 5a. The R_{pore} and R_{ct} are also one order of magnitude greater than the respective values observed for D 5a.

Table 4 also includes C_V values for each parameter of interest. The C_V values for CPE_{dl} and R_{ct} indicate that the observed values and ECM results are more repeatable than the CPE_{coat} and R_{pore} values. The reason for the disparity is unknown, though it could possibly be attributed to the modeling software's reduced ability to resolve and fit the higher frequency data. It should be noted that the ECM also includes a propagation of error from the measurement to the model outputs.

Discussion

Areas of coating with localized defects caused by debris or blistering, or those with other visible coating defects, are sufficiently classified by existing qualitative inspection standards as *damaged* and are outside the scope of the EIS evaluations conducted in the present work. This experiment evaluated *undamaged* areas (i.e., those experiencing general degradation not visible to the naked eye). The method presented here reveals the performance of the coating that appears to be in average to above average condition.

The objective of this work was to establish the feasibility of collecting sufficient and verifiable EIS data for application to the coating service life decision making process. The proposed method is expected to be capable of providing relevant and previously unavailable information to the decision makers who are responsible for determining coating maintenance needs and schedules for a given structure.

The approach taken with the method described and proposed herein is to assume that, with basic knowledge of the coating system, one can interpret the EIS data to project remaining service life for the undamaged areas. The outcomes provide the ability to identify practical coating maintenance options, which may include (1) performing spot or zone repairs to damaged areas and (2) applying full recoating.

The ensuing discussion focuses on key aspects vital to the standardization of field EIS methods. The first aspect is related to the test method and application of the test method on existing structures. The second aspect is the analysis and interpretation of the resulting data, providing a suggested data preparation procedure for communicating that information to decision makers.

Test Method

The EIS field test method used in this experiment involves a two cell measurement technique. The use of a two cell technique obviates both the need for a direct connection to metal, which may damage a functioning coating, and other challenges previously encountered with high contact resistance [22].

The sampling procedure dictates the use of at least four test cells per sample. A specimen consists of two test cells, and the number of specimens tested in the present work for each sample ranged from one to six. The results suggest that higher data quantities are preferable; thus, it would be reasonable to set guidelines such as "at least four samples per substantial area of the coated structure." An existing field coating evaluation method specifies evaluation of three samples for the initial 1,000 ft^2 of investigation and requires an additional sample for each following 1,000 ft^2 of coated structure [35].

The test method is not likely to find use on coated structures with limited or unsafe access. Structures that cannot be accessed for the amount of time needed for setup (fastening test cells and allowing adequate time for curing, saturating the

coating of interest with electrolyte, etc.) and testing will also present significant challenges. Setup time reduction occurred by using any one of a number of readily available marine epoxies and other adhesives capable of curing sufficiently within 1 or 2 h at ambient temperatures.

Selecting coating samples with high levels of existing saturation also reduces the wait time between water up and test commencement; completely dry coatings may need a full day to reach a proper saturation and equilibration. The length of time required is greatest for barrier coatings in good condition. The time required to achieve proper saturation may be the limiting factor that most greatly affects broader implementation of field EIS measurements.

Early deployments found the longest duration activity to be making the actual measurements [22]. Increasing the final test frequency value and decreasing the quantity of data points per decade reduces the specimen measurement time from more than 20 min to less than 5 min.

Data Analysis and Interpretation

The data analysis approaches used in this experiment closely follow common prac tice and manipulation of EIS data, specifically plotting the low frequency $|Z|$ data and conducting ECM. The implementation of several additional techniques described here increases the utility of processed data to decision makers and other stakeholders.

DATA SCREENING

Continuous monitoring of test cells and collected data during the test will prevent inclusion of anomalous data in test results. In particular, persons collecting field EIS data should ensure that initial open circuit potentials are realistic for the speci men of interest, adequate test cell electrolyte levels are maintained, excessive exter nal noise is not present, and changes in observed $|Z|$ values are steady and smooth.

DATA SMOOTHING

Data processing included evaluation of not only individual $|Z|$ values but also aver age values over limited ranges, in particular, those of the lowest frequencies observed. This process helped to reduce the effects of minor noise fluctuations as individual tests advanced from one frequency value to the next.

PROBABILITY PLOTS

Evaluating values at low frequencies is important because this is where EIS can detect reduced coating performance before defects, excessive wear, and so on are visible to the naked eye [1]. The use of a lognormal probability distribution plot in Fig. 10 demonstrates a possible approach for analyzing low frequency $|Z|$ data while also providing a practical tool that could aid coating maintenance or replacement decision making. Fig. 10 shows all tests' raw data measured at low frequencies using the data smoothing method described earlier for two particular Structures, B and D,

FIG. 10 Lognormal probability plot of averaged |Z| data from 1 Hz to 0.05 Hz for Structures B and D.

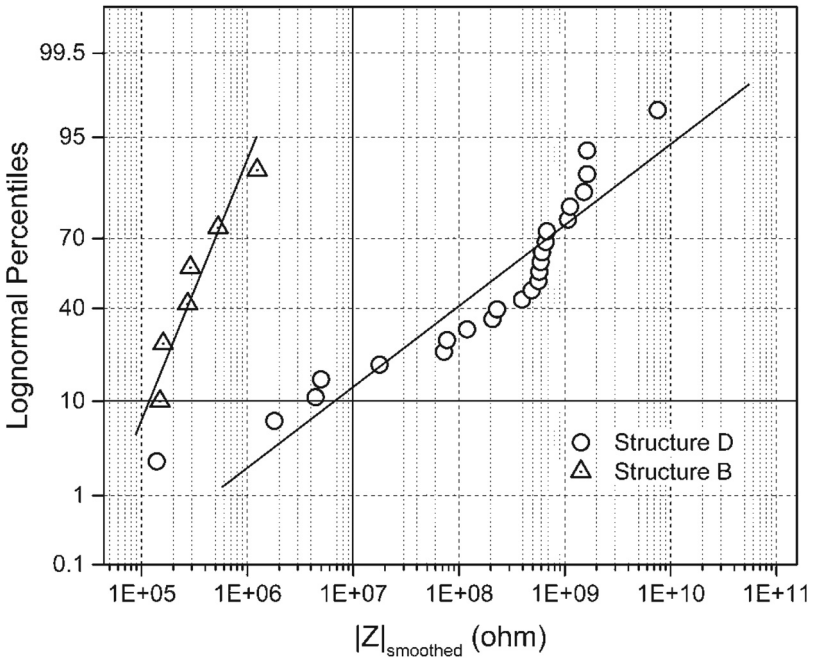

as well as a linear fit for each data set. The plot includes a designation of poor barrier protection as values below 1.0×10^7 ohm (vertical solid line) and a probability threshold of 10 % (horizontal solid line).

Producing probability plots facilitates identification of structures that have a high percentage of surface area with an underperforming coating (i.e., low barrier protection). For example, Structure B (Fig. 10) shows 100 % of the specimens tested exhibiting low barrier protection, while Structure D has only approximately 15 % of specimens exhibiting poor quality. The arbitrary threshold of 10 % probability allows an owner to use the method to set guidelines for decision making (e.g., "a full recoat will be implemented when 10 % of the coating measures impedance values below 1.0×10^7 ohm"). Structures B and D are both candidates for recoating based on this guideline.

The low measurement values reported in this research are important because they support the claim that EIS detects the reduction in coating properties before they are visible. Furthermore, they provide a basis for determining the percentage of undamaged coating that has fallen below an acceptable range of performance. The lognormal probability plot evaluation is adapted from a common technique used to make corrosivity determinations via soil resistivity measurements [36].

Future Work

Field EIS testing provides an opportunity to obtain quantitative, performance based data on apparently undamaged areas of coated structures. The present research effectively indicated each observed coating's current performance level to aid facility owners in determining when to perform coating maintenance or replacement activ ities. Future work will explore the use of field EIS testing on new coating systems as a tool for assessing conformance to performance based coating specifications. Facil ity owners could thus include field EIS testing as part of the contractor's field quali ty control testing, providing quantitative values that must be achieved. If performed early in the coating application schedule, the test could prevent application of nonconforming coatings to the entire structure. The implementation of field EIS testing for coating contracts could allow for timely course correction and prevent costly contract disputes after the fact.

The work presented here contributed to the body of knowledge associated with the repeatability of field EIS measurements. Additional work is needed to firmly establish the suitability and validity of field EIS testing and to evaluate other aspects not reviewed here (e.g., determination of guidelines for proper sample and speci men selection and performing round robin testing). Subsequent standardization of the technique could ensure that future implementation meets the quality sought by ASTM International.

An advanced maturation of field EIS testing would include emphasis on mod ifying the field equipment to improve portability and ease application of the mea surement. The portability of field potentiostats continues to improve and now includes handheld devices. The goal should be to maximize the portability with out significant change to measurement sensitivity or data quality. The test cell could also be improved, and use of a magnetic test cell apparatus, currently avail able, is possible for most steel structures. It may be desirable to combine the test cell, test solution, and potentiostat into a single magnetic unit that can be con nected to flat or partially curved surfaces at any orientation and left to perform the measurement.

Conclusion

The present research evaluated a field EIS testing method on coated infrastructure and included example structures in immersion service and atmospheric service. The field EIS tests applied a two cell measurement technique with no connection to substrate. Method validation is presented through a set of experiments that showed good repeatability of specimen measurements, particularly when compared to mea surement variability between adjacent specimens, or sample variability. The mea surement results for impedance magnitude at 0.05 Hz provided the input for the statistical analysis used in this validation. A subsequent data smoothing approach enhanced the measurement repeatability results by averaging all data between 0.05 and 1 Hz. The latter approach minimizes the effect of errors arising from

individual data points. Attempts to apply equivalent circuit modeling resulted in less repeatable outcomes for the individual circuit elements.

Data analysis also resulted in recommended approaches to aid in the presentation of EIS results. The emphasis is on the use of field EIS testing to quantify the coating condition of the areas of undamaged coating on structure (i.e., those without visible defects). The application of probability plots afforded an easily interpreted approach for presenting EIS data and conveying results to decision makers. The drawback of probability plots is that they require a significant data set, the size of which should be established, in addition to sample and specimen guidelines, by future research.

ACKNOWLEDGMENTS

The authors appreciate the funding support of the Bureau of Reclamation Science & Technology Program, Project ID 1884, and the Manuals & Standards Program. The authors are also grateful for the access and support provided by Reclamation facility managers, making the field EIS testing possible.

References

[1] Frankel, G. S., "Electrochemical Techniques in Corrosion: Status, Limitations, and Needs," *J. ASTM Int.*, Vol. 5, No. 2, 2008, http://dx.doi.org/10.1520/JAI101241

[2] Kendig, M. and Mills, D. J., "An Historical Perspective on the Corrosion Protection by Paints," *Prog. Org. Coat.*, Vol. 102, Part A, 2017, pp. 53–59, https://doi.org/10.1016/j.porgcoat.2016.04.044

[3] Lyon, S. B., Bingham, R., and Mills, D. J., "Advances in Corrosion Protection by Organic Coatings: What We Know and What We Would Like to Know," *Prog. Org. Coat.*, Vol. 102, Part A, 2017, pp. 2–7, https://doi.org/10.1016/j.porgcoat.2016.04.030

[4] Mills, D. J. and Jamali, S. S., "The Best Tests for Anti-Corrosive Paints. And Why: A Personal Viewpoint," *Prog. Org. Coat.*, Vol. 102, Part A, 2017, pp. 8–17, https://doi.org/10.1016/j.porgcoat.2016.04.045

[5] Sykes, J. M., Whyte, E. P., Yu, X., and Sharer Sahir, Z., "Does 'Coating Resistance' Control Corrosion?" *Prog. Org. Coat.*, Vol. 102, Part A, 2017, pp. 82–87, https://doi.org/10.1016/j.porgcoat.2016.04.015

[6] Mills, D. and Mayne, J., "Inhomogeneous Nature of Polymer Films and Its Effect on Resistance Inhibition," *Corrosion Control by Organic Coatings*, Leidheiser, H., Ed., NACE International, Houston, TX, 1981, pp. 12–17.

[7] Negele, O. and Funke, W., "Internal Stress and Wet Adhesion of Organic Coatings," *Prog. Org. Coat.*, Vol. 28, No. 4, 1996, pp. 285–289, http://dx.doi.org/10.1016/0300-9440(95)00606-0

[8] Marsh, J., Scantlebury, J. D., and Lyon, S. B., "The Effect of Surface/Primer Treatments on the Performance of Alkyd Coated Steel," *Corros. Sci.*, Vol. 43, No. 5, 2001, pp. 829–852, https://doi.org/10.1016/S0010-938X(00)00070-6

[9] Leidheiser, H., Jr. and Deck, P. D., "Chemistry of the Metal-Polymer Interfacial Region," *Science*, Vol. 241, No. 4870, 1988, pp. 1176–1181, http://dx.doi.org/10.1126/science.241.4870.1176

[10] Bolger, J. C., "Acid Base Interactions between Oxide Surfaces and Polar Organic Compounds," *Adhesion Aspects of Polymeric Coatings*, Mittal, K. L., Ed., Springer US, Boston, MA, 1983, pp. 3–18, http://dx.doi.org/10.1007/978-1-4613-3658-7_1

[11] Lvovich, V. F., *Impedance Spectroscopy: Applications to Electrochemical and Dielectric Phenomena*, Wiley, Hoboken, NJ, 2012.

[12] Scully, J. R., "Electrochemical Impedance of Organic-Coated Steel: Correlation of Impedance Parameters with Long-Term Coating Deterioration," *J. Electrochem. Soc.*, Vol. 136, No. 4, 1989, pp. 979–990, http://dx.doi.org/10.1149/1.2096897

[13] ASTM G106-89(2015), *Standard Practice for Verification of Algorithm and Equipment for Electrochemical Impedance Measurements*, ASTM International, West Conshohocken, PA, 2015, www.astm.org

[14] Bacon, R. C., Smith, J. J., and Rugg, F. M., "Electrolytic Resistance in Evaluating Protective Merit of Coatings on Metals," *Ind. Eng. Chem.*, Vol. 40, No. 1, 1948, pp. 161–167, http://dx.doi.org/10.1021/ie50457a041

[15] Kendig, M., Mansfeld, F., and Tsai, S., "Determination of the Long Term Corrosion Behavior of Coated Steel with A.C. Impedance Measurements," *Corros. Sci.*, Vol. 23, No. 4, 1983, pp. 317–329, https://doi.org/10.1016/0010-938X(83)90064-1

[16] Wolstenholme, J., "Electrochemical Methods of Assessing the Corrosion of Painted Metals—A Review," *Corros. Sci.*, Vol. 13, No. 7, 1973, pp. 521–530, https://doi.org/10.1016/S0010-938X(73)80002-2

[17] Beaunier, L., Epelboin, I., Lestrade, J. C., and Takenouti, H., "Etude Electrochimique, et par Microscopie Electronique a Balayage, du Fer Recouvert de Peinture (in French)," *Surface Technology*, Vol. 4, No. 3, 1976, pp. 237–254, https://doi.org/10.1016/0376-4583(76)90036-4

[18] Sonke, J. and Consultancy, S., "Qualification of Protective Coatings Using EIS," presented at *EUROCORR 2008,* Edinburgh, Scotland, September 7–11, 2008.

[19] Gray, L. G. S. and Appleman, B. R., "EIS: Electrochemical Impedance Spectroscopy," *JPCL*, Vol. 20, No. 2, 2003, pp. 66–74.

[20] Tsai, C. H. and Mansfeld, F., "Determination of Coating Deterioration with EIS: Part II. Development of a Method for Field Testing of Protective Coatings," *Corrosion*, Vol. 49, No. 9, 1993, pp. 726–737, http://dx.doi.org/10.5006/1.3316106

[21] Papavinasam, S., Attard, M., and Revie, R. W., "Electrochemical Impedance Spectroscopy Measurement during Cathodic Disbondment Experiment of Pipeline Coatings," *J. ASTM Intl.*, Vol. 6, No. 3, 2009, http://dx.doi.org/10.1520/JAI101246

[22] Merten, B. J., Skaja, A., Tordonato, D., and Little, D., "Re-Evaluating Electrochemical Impedance Spectroscopy (EIS) for the Field Inspector's Toolbox: A First Approach," presented at SSPC 2014, Orlando, FL, February 10–13, 2014, The Society for Protective Coatings, Pittsburgh, PA, pp. 1–17.

[23] Allahar, K., Su, Q., and Bierwagen, G., "Non-Substrate EIS Monitoring of Organic Coatings with Embedded Electrodes," *Prog. Org. Coat.*, Vol. 67, No. 2, 2010, pp. 180–187, http://dx.doi.org/10.1016/j.porgcoat.2009.10.001

[24] Mills, D., Picton, P., and Mularczyk, L., "Developments in the Electrochemical Noise Method (ENM) to Make It More Practical for Assessment of Anti-Corrosive Coatings," *Electrochim. Acta*, Vol. 124, 2014, pp. 199–205, https://doi.org/10.1016/j.electacta.2013.09.067

[25] Jones, D. A., *Principles and Prevention of Corrosion*, 2nd ed., Prentice Hall, Upper Saddle River, NJ, 1996, pp. 109–113.

[26] Kelly, R. G., Scully, J. R., Shoesmith, D., and Buchheit, R. G., *Electrochemical Techniques in Corrosion Science and Engineering*, CRC Press, Boca Raton, FL, 2002.

[27] Loveday, D., Peterson, P., and Rodgers, B., "Evaluation of Organic Coatings with Electrochemical Impedance Spectroscopy. Part 1: Fundamentals of Electrochemical Impedance Spectroscopy," *JCT Coatings Tech*., Vol. 1, No. 8, 2004, pp. 46–52.

[28] Loveday, D., Peterson, P., and Rodgers, B., "Evaluation of Organic Coatings with Electrochemical Impedance Spectroscopy. Part 2: Application of EIS to Coatings," *JCT Coatings Tech*., Vol. 1, No. 10, 2004, pp. 88–93.

[29] Loveday, D., Peterson, P., and Rodgers, B., "Evaluation of Organic Coatings with Electrochemical Impedance Spectroscopy. Part 3: Protocols for Testing Coatings with EIS," *JCT Coatings Tech*., Vol. 2, No. 13, 2005, pp. 22–27.

[30] Mansfeld, F. and Tsai, C. H., "Determination of Coating Deterioration with EIS: I. Basic Relationships," *Corrosion*, Vol. 47, No. 12, 1991, pp. 958–963, http://dx.doi.org/10.5006/1.3585209

[31] Brasher, D. M. and Kingsbury, A. H., "Electrical Measurements in the Study of Immersed Paint Coatings on Metal. I. Comparison between Capacitance and Gravimetric Methods of Estimating Water-Uptake," *J. Appl. Chem*., Vol. 4, No. 2, 1954, pp. 62–72, http://dx.doi.org/10.1002/jctb.5010040202

[32] Nguyen, A. S., Causse, N., Musiani, M., Orazem, M. E., Pébère, N., Tribollet, B., and Vivier, V., "Determination of Water Uptake in Organic Coatings Deposited on 2024 Aluminium Alloy: Comparison between Impedance Measurements and Gravimetry," *Prog. Org. Coat*., Vol. 112, 2017, pp. 93–100, https://doi.org/10.1016/j.porgcoat.2017.07.004

[33] Vosgien Lacombre, C., Bouvet, G., Trinh, D., Mallarino, S., and Touzain, S., "Water Uptake in Free Films and Coatings Using the Brasher and Kingsbury Equation: A Possible Explanation of the Different Values Obtained by Electrochemical Impedance Spectroscopy and Gravimetry," *Electrochim. Acta*, Vol. 231, 2017, pp. 162–170, https://doi.org/10.1016/j.electacta.2017.02.051

[34] Kendig, M. W., Jeanjaquet, S., and Lumsden, J., "Electrochemical Impedance of Coated Metal Undergoing Loss of Adhesion," *Electrochemical Impedance: Analysis and Interpretation, ASTM STP18082S*, Scully, J. R., Silverman, D. C., and Kendig, M. W., Eds., ASTM International, West Conshohocken, PA, 1993, pp. 407–427, http://dx.doi.org/10.1520/STP18082S

[35] SSPC SP 2, *Procedure for Determining Conformance to Dry Coatings Thickness*, The Society for Protective Coatings, Pittsburgh, PA, 2015.

[36] Bureau of Reclamation, *The 10 % Soil Resistivity Method,* MERL-05-19, U.S. Department of the Interior, Bureau of Reclamation, Denver, CO, 2005.

STP 1609, 2019 / available online at www.astm.org / doi: 10.1520/STP160920170220

Xueyuan Zhang[1] and Dominik Moosbauer[1]

Application of Harmonic and Total Harmonic Distortion Instrumentation in Corrosion

Citation

Zhang, X. and Moosbauer, D., "Application of Harmonic and Total Harmonic Distortion Instrumentation in Corrosion," *Advances in Electrochemical Techniques for Corrosion Monitoring and Laboratory Corrosion Measurements*, *ASTM STP1609*, S. Papavinasam, R. B. Rebak, L. Yang, and N. S. Berke, Eds., ASTM International, West Conshohocken, PA, 2019, pp. 160–179, http://dx.doi.org/10.1520/STP160920170220[2]

ABSTRACT

Linear polarization resistance and electrochemical impedance spectroscopy (EIS) are widely applied in corrosion for studying the electrode/solution interface, films, coatings, and corrosion rates. Most potentiostatic and galvanostatic EIS measurements are based on the use of a perturbation signal (i.e., frequency or amplitude modulation of a sine wave) applied to the specimen. The determination of corrosion rate via linear polarization resistance and EIS requires the constants of Tafel slopes in the cathodic and anodic reaction of a corrosion process, but these techniques cannot provide that. The present instrumentation research is related to the modulation of frequency and amplitude for development of harmonic analysis and total harmonic distortion. The main purpose of this preliminary study is to increase the signal-to-noise ratio and to obtain additional information about the corrosion system (e.g., corrosion rate, Tafel slope). Variable amplitude signals can increase the signal level for higher-quality EIS data. However, the voltage amplitude cannot follow a linear relationship when the impedance increases at lower frequencies. Even though a high-amplitude sine wave will bring distortion in the response signal when a signal with a high-amplitude sine wave is applied on the corrosion system, the corrosion rate and Tafel slope can be derived from higher harmonics

Manuscript received November 6, 2017; accepted for publication March 16, 2018.

[1]Gamry Instruments, 734 Louis Dr., Warminster, PA 18974, USA

[2]ASTM Symposium on *Advances in Electrochemical Techniques for Corrosion Monitoring and Laboratory Corrosion Measurements* on November 13 14, 2017 in Atlanta, GA, USA.

of the response signal. Frequency and amplitude modulation techniques and their application to corrosion are discussed and reviewed in the present research.

Keywords
corrosion rate, harmonic analysis, total harmonic distortion, steel, electrochemical impedance spectroscopy, diffusion

Introduction

The cost of corrosion in China was approximately 2,127.8 billion renminbi (approximately US$310 billion) in 2015 [1], and the global cost of corrosion is estimated to be US$2.5 trillion, roughly 3.4 % of the global gross domestic product, according to a study by NACE International. Corrosion monitoring, inspection, and lab testing are important issues in corrosion engineering. Determination of corrosion rates for materials in different environments is the main focus in corrosion testing via different techniques, for example, gravimetric methods, electrical resistance, linear polarization resistance (LPR), electrochemical impedance spectroscopy (EIS), electrochemical noise, electrochemical frequency modulation (EFM), harmonic analysis (HA), and nondestructive testing methods, including ultrasonic testing, radiographic testing, guided wave testing, and electromagnetic testing. With respect to the main role and nature of the electrochemical process in corrosion, electrochemical techniques have been developed specifically for corrosion measurement and research in the field and laboratory.

Traditional LPR/potentiodynamic (Pdy) polarization and EIS are powerful and practical electrochemical techniques in the study of corrosion rate, electrochemical corrosion reaction, and diffusion processes. They are widely applied in corrosion research and electrochemistry for understanding interfaces, films, coatings, and ion transport mechanisms. Normally, there are three constraints for a valid EIS measurement and analysis: stability, linearity, and causality relating to the electrochemical system and instruments. EIS results and the validity of data can be evaluated with Kramers Kronig (K K) transforms [2]. Based on the Butler Volmer equation to characterize the relationship between overpotential and current for an electrochemical reaction, a linear response of current exists only when the overpotential is small, typically $5/n$ mV root mean square (rms), where n is the number of electrons transferred in an electrochemical reaction [3]. In an actual EIS measurement, a sine wave perturbation with a fixed amplitude is applied to the system either as a potential for potentiostatic EIS or as a current for galvanostatic EIS. The corresponding cell current or voltage is measured and divided by the perturbation voltage or current at the sine wave frequency. In a further development, a perturbation containing power at multiple frequencies (i.e., a sum of sine waves) can be applied and measured. In a linear system, this is mathematically equivalent to applying each frequency independently and serially [4]. Gamry

Instruments' (Warminster, PA) OptiEIS™ algorithm software advances this approach by individually apportioning the power at each frequency of the perturbation in order to optimize the signal to noise ratio and experiment time. During monitoring of corrosion in the field, LPR and impedance techniques are common because of their fast and accurate measurements, while the constants of Tafel slopes can be found in the determination of corrosion rates based on the Stern Geary equation. It is necessary to develop other electrochemical instrumentation techniques for corrosion monitoring and research with direct knowledge of Tafel slopes.

Potentiostatic EIS is often advantageous because it allows much easier control of a perturbation voltage to obtain a linear response in these high impedance corrosion systems. On the other hand, in a fixed amplitude potentiostatic EIS experiment, the corresponding current drops with a higher impedance at the lower frequency, negating the previous K K assumptions. Wojcik and Orazem [5] and Agarwal [6] recognized this issue in traditional EIS instrumentation. They employed variable amplitude excitation currents in a galvanostatically modulated technique for a study of the corrosion process of copper. They demonstrated that the modulation in amplitude is a practical way to monitor the corrosion process via galvanostatic EIS measurement. Gamry Instruments has implemented this approach in its Hybrid EIS method.

Up to this point, we have been discussing experimental methods for relatively stable electrochemical processes that respond in a linear manner (i.e., those that behave according to the K K preconditions). However, much of the actual response in electrochemical systems is nonlinear and hence fertile ground for new measurement approaches. There is much to be learned by investigating the nonlinear behavior of electrochemical systems.

For example, the Butler Volmer equation (Eq 1):

$$i = i_o \cdot \left(e^{\left[\frac{\alpha_a zF}{RT}\Delta E\right]} - e^{\left[-\frac{\alpha_c zF}{RT}\Delta E\right]} \right) \tag{1}$$

gives rise to a linear region around $\Delta E = 0$, given by Eq 2:

$$i = i_o \frac{zF}{\alpha RT}\Delta E \tag{2}$$

but quickly becomes nonlinear as either half reaction becomes dominant, giving rise to the Tafel equation (Eq 3 and Eq 4):

$$\text{Anodic Limit: } i = i_o \cdot e^{\left[\frac{\alpha_a zF}{RT}\Delta E\right]} \tag{3}$$

$$\text{Cathodic Limit: } i = -i_o \cdot e^{\left[-\frac{\alpha_c zF}{RT}\Delta E\right]} \tag{4}$$

The Tafel region is accessible using a nonlinear form of EIS analysis known as EFM or, more properly, intermodulation distortion as described by Bosch and

Bogaerts [7]. In a previous work, two sine waves were simultaneously applied to a corrosion specimen at a larger than usual amplitude. The resulting response occur ring at frequencies $nf_1 + mf_2$, where n and m are signed integers, is caused by the mixing of the frequencies by the nonlinear Tafel response. Normal EIS does not cause this distortion. EFM, however, makes use of it to extract the Tafel coefficients and kinetic information. Darowicki developed a similar approach using harmonic distortion analysis where a single sine wave at frequency f creates harmonic content at nf. Darowicki [8] and Darowicki and Mjewska [9] have reviewed the state of har monic analysis. Devay and Meszaros previously employed the faradaic distortion method in a study of the rate of corrosion of metals [10].

Mass transport to the active charge transfer surface is another example of nonlinear electrochemical dynamics. Nonlinear response cannot be avoided when the diffusion process dominates the electrochemical reaction. The AC voltammetry technique is well developed to separate electrochemical reactions and diffusion pro cesses in a nonlinear electrochemistry system. Wilson, Schwartz, and Adler have applied harmonic signals and nonlinear EIS in solid oxide fuel cells for a better insight into the surface reaction and diffusion processes [11]. This study highlighted the rate variation in the second and third order harmonic responses. Harrington developed a theory for electrochemical impedance of surface reactions relating to harmonic and large amplitude perturbation signals [3]. Ramschak et al. [12] employed total harmonic distortion (THD) analysis as a diagnostic tool in polymer electrolyte membrane fuel cells and solid oxide fuel cells [13,14]. Bosch and Bogaerts studied the corrosion of steel in aqueous sodium sulfate (Na_2SO_4) with diffusion controlled processes via harmonic techniques [15]. The application of THD in the analysis of corrosion process has not been reported so far.

In the present paper, the instrumentation and basic analysis for nonlinear elec trochemical impedance as well as harmonic and total harmonic distortion are described and reviewed. We also present the preliminary application of these tech niques applied to a corrosion system for steel in a potassium hydroxide (KOH) and Na_2SO_4 electrolyte. More modifications in the instrumentation, testing, and improvements in THD technique will be reported in future publications.

Instrumentation

A basic setup for HA/THD measurement system is shown in **Fig. 1**. A Gamry Instru ments Interface™ 1000 potentiostat was used for the present measurements and study. The potentiostatic (controlled voltage) configuration is more suitable for cor rosion electrochemistry in most cases.

An analog signal is created as the sum of a DC voltage and an AC voltage at several harmonic frequencies (Eq 5):

$$I(t) = \sum_{k\ 0}^{N} I_k e^{jk\omega t} \tag{5}$$

FIG. 1 Diagram of harmonic and impedance instrumentation.

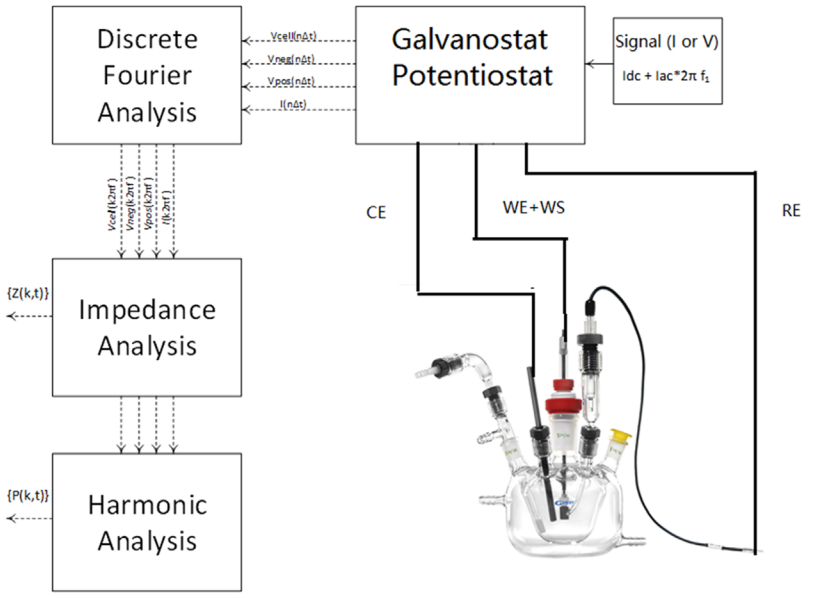

The DC signal is given by V_0. The fundamental frequency corresponds to the first harmonic, $k = 1$. For single frequency EIS and THD, the upper harmonics are not stimulated, and the signal is reduced to (Eq 6):

$$I(t) = I_{DC} + I_{AC}\sin(\omega t) \tag{6}$$

This signal is generated by the instrument and applied to the electrodes in the elec trochemical cell.

The time responses of the current and voltages are discretely sampled at time intervals, Δt, recorded as (Eq 7):

$$\begin{aligned} V_{cell}[n] &= V_{cs}[n] - V_{ws}[n] \\ V_{pos}[n] &= V_{cs}[n] - V_{ref}[n] \\ V_{neg}[n] &= V_{ws}[n] - V_{ref}[n] \\ I_{cell}[n] & \end{aligned} \tag{7}$$

where:

n = point number,
V_{ref} = reference voltage,
V_{cs} = counter sense voltage,
V_{ws} = working sense voltage,
V_{pos} and V_{neg} = working and counter electrodes,
V_{cell} = total cell voltage between the working and counter electrodes, and
I_{cell} = cell current through the working electrode.

These signals are then converted into the frequency domain using the discrete Fourier transform (Eq 8):

$$\tilde{X}[k] = \sum_{n\ 0}^{N-1} X[n] \cdot e^{-2\pi kn/N}, \quad X = V_{cell},\ V_{pos},\ V_{neg},\ I_{cell}. \tag{8}$$

From this point onward, the frequency domain signals are processed depending on the analysis required. For example, the traditional definition of impedance is given by Eq 9:

$$\tilde{Z}_{cell}[k] = \frac{\tilde{V}_{cell}[k]}{\tilde{I}_{cell}[k]}, \quad k = 1 \tag{9}$$

Likewise, the half cell impedance is defined as (Eq 10):

$$\tilde{Z}_{pos,neg}[k] = \frac{\tilde{V}_{pos,neg}[k]}{\tilde{I}_{cell}[k]}, \quad k = 1 \tag{10}$$

Other types of processing can be applied to the signal streams in **Fig. 1**. For example, higher order impedances have been defined in Eq 11:

$$\tilde{Z}[k] \approx \frac{\tilde{V}_{any}[k]}{\left|\tilde{I}_{cell}[1]\right|^k}, \quad k > 1 \tag{11}$$

The power of a signal at any harmonic of a fundamental signal can be calculated by Eq 12:

$$P_X[k] = |X[k]|^2, \quad X = V_{cell},\ V_{pos},\ V_{neg},\ I_{cell} \tag{12}$$

The present harmonic analysis implementation calculates the $P[k]$s and $\tilde{V}[k]$s through the tenth harmonic.

Total harmonic distortion, described by Ramschak et al. [12] and Mao and Krewer [13], is defined as the ratio of the signal power in the harmonics (up to ten) to the signal power in the fundamental frequency.

One can easily extend the mathematics to the potentiostatic case where the potential is applied and current is the result. In this case, THD is given by Eq 13:

$$THD_I = \sqrt{\frac{\sum_{k\ 2}^{L} P_I[k]}{P_I[1]}} \tag{13}$$

CASE I: ACTIVATION CONTROL

The relationship between potential (E) and current (j) for a charge transfer corro sion process can be represented by the following Butler Volmer equation in a cor rosion reaction (Eq 14) with activation control [16 20]:

$$j = j_{corr} e^{(\Delta E/\beta a)} - e^{(-\Delta E/\beta c)} \tag{14}$$

where $\beta_a = b_a/\ln 10$ and $\beta_c = b_c/\ln 10$.

When the perturbation signal is employed as a sinusoidal wave with an angular frequency of w and amplitude, U_0, over a time period t as given by Eq 15 and Eq 16:

$$\Delta E = U_0 \sin wt \tag{15}$$

$$j_F = j_{corr} e^{(U_0 \sin wt/\beta_a)} - e^{(-U_0 \sin wt/\beta_c)} \tag{16}$$

We can expand j_F as a Taylor series so that the amplitude of each harmonic wave can be obtained by Fourier series expansion (Eq 17):

$$j_F = j_0 + j_1 \sin wt - j_2 \cos 2wt - j_3 \sin 3wt + \cdots \tag{17}$$

where:

$$j_1 = 2j_{corr}\left[I_1\left(\frac{U_0}{\beta_a}\right) + I_1\left(\frac{U_0}{\beta_c}\right)\right],$$
$$j_2 = -2j_{corr}\left[I_2\left(\frac{U_0}{\beta_a}\right) + I_2\left(\frac{U_0}{\beta_c}\right)\right],$$
$$j_3 = -2j_{corr}\left[I_3\left(\frac{U_0}{\beta_a}\right) + I_3\left(\frac{U_0}{\beta_c}\right)\right], \text{ and}$$

I_n ($n = 1,2,3$ …) is from the first order modified Bessel functions. Normally Eq 18 could be given as follows:

$$I_1(\mathrm{x}) \approx \mathrm{x}/2$$
$$I_2(\mathrm{x}) \approx (1/2)(\mathrm{x}/2)^2 \tag{18}$$
$$I_3(\mathrm{x}) \approx (1/6)(\mathrm{x}/2)^3$$

where $I_n(z)$, based on Bessel functions, is given as the following (Eq 19):

$$I_n(z) = \left(\frac{z}{2}\right)\sum_{k\ 0}^{\infty}\left(\frac{z}{2}\right)^{2k}\left(\frac{1}{k!(n+k)!}\right) \quad n = 0,\ 1,\ 2\ldots \tag{19}$$

We can derive j_1, j_2, and j_3 as follows (Eq 20):

$$j_1 = j_{corr}\left(\frac{1}{\beta_a} + \frac{1}{\beta_c}\right)U_0$$
$$j_2 = -j_{corr}\left(\frac{1}{\beta_a^2} - \frac{1}{\beta_c^2}\right)\frac{U_0^2}{4} \tag{20}$$
$$j_3 = -j_{corr}\left(\frac{1}{\beta_a^3} - \frac{1}{\beta_c^3}\right)\frac{U_0^3}{24}$$

If we include the contribution of the third harmonic in j_{corr} (Eq 21),

$$j_1 = j_{corr}\left[\left(\frac{1}{\beta_a} + \frac{1}{\beta_c}\right)U_0 + \frac{1}{8}\left(\frac{1}{\beta_a^3} + \frac{1}{\beta_c^3}\right)U_0^3\right] \tag{21}$$

We can derive j_{corr} and the Tafel slope, $\beta_{a,c}$ as follows (Eq 22 and Eq 23):

$$j_{corr} = \frac{(j_1 + 3j_3)^2}{4\sqrt{3|2(j_1 + 3j_3)j_3 + i_2^2|^{1/2}}} \tag{22}$$

$$\frac{1}{b_{a,c}} = \frac{1}{4.6U_0}\left(\frac{j_1 + 3j_3}{j_{corr}} \pm 4\frac{j_2}{j_1 + 3j_3}\right) \tag{23}$$

CASE II: DIFFUSION CONTROL

When the perturbation frequency is high or the diffusion coefficient is large, the derivation of corrosion current and Tafel slope is similar to the aforementioned activation situation [15,21]. Further derivation of the corrosion current and Tafel slope with a lower diffusion coefficient implemented with least squares analysis will be reported in the future.

Experimental

ELECTRODE AND ELECTROCHEMICAL SETUP

A cylindrical specimen of C1018 mild steel 9.5 mm (0.37 in.) in length and 13 mm (0.5 in.) in diameter from the Metal Samples Company (Munford, AL) was used for the electrochemical measurement. A EuroCell™ electrochemical cell from Gamry Instruments was utilized, in which a graphite rod acted as the counter electrode, and saturated silver/silver chloride (Ag/AgCl) was the reference electrode. The cell was filled with 150 mL of electrolyte solution, and the working electrode was par tially immersed into the electrolyte. The electrolyte was 0.01 M KOH or 0.01 M KOH + 0.1 M Na_2SO_4. The surface area of the steel specimen immersed into the solution was about 4 cm^2. An Interface 1000E potentiostat (Gamry Instruments) was used for all the electrochemical measurements.

ELECTROCHEMICAL MEASUREMENT

Three EIS/THD experiments with amplitudes of 10, 20, and 50 mV, respectively, were carried out after the electrode was immersed into the solution for 30 min, fol lowed by EIS, EFM, LPR, and Pdy measurements. Following the sequence, OCP → EIS → OCP → EFM → OCP → LPR → OCP → LPR → OCP → Pdy → OCP → EFM → OCP → EIS. Open circuit potential (OCP) was frequently measured during the process.

The setup parameters for different electrochemical measurements were as follows:

OCP: 300 s before EIS, EFM, LPR, and Pdy experiments.

EIS: The amplitude for the perturbation signal was 10 mV rms. DC voltage was set to 0 V versus OCP. The scanning frequency ranged from 1 MHz to 0.004 Hz.

EFM: The base frequency was set to 0.1 and 0.01 Hz, respectively, in two EFM measurements; 2 times and 5 times base frequencies were synthesized as the

perturbation signals during EFM measurements. The amplitude was 10 mV rms, and DC voltage was set to 0 V versus end of charge.

LPR: The scanning voltage ranged from −20 to 20 mV versus OCP. The scanning rates were 1 and 0.167 mV/s, respectively. The measurements of OCP were carried out for 300 s for a steady state of steel in the solution before the LPR experiment in the experimental sequence.

Pdy: Two types of setup were employed in Pdy measurements. The scanning potentials of Pdy measurements in the sequence ranged from −0.08 to 0.03 V versus end of charge, and the scanning rate was 5 mV/s.

CYCLIC VOLTAMMETRY OF STEEL

Cyclic voltammetry (CV) scans of steel in KOH and KOH + Na_2SO_4 were measured for three cycles from OCP to −0.4 V versus OCP and then back to 0 or 0.5 V versus the Ag/AgCl reference electrode for a further understanding of film formation on steel and the influence of Na_2SO_4 on the properties of the film. The scanning rate was 5 mV/s.

EIS, HA, AND THD MEASUREMENTS

Potentiostatic EIS with varying amplitudes was employed in most measurements. The AC applied voltages were 10, 20, and 50 mV during potentiostatic measurements. The frequency varied from 10 kHz to 0.004 Hz in EIS measurements. Signal harmonics up to the tenth harmonic and THD were recorded and analyzed simultaneously. Voltage or current power of each harmonic signal was recorded for a further analysis.

Results and Discussions

TYPICAL CV CURVES FOR STEEL IN KOH + NA_2SO_4 SOLUTION

Fig. 2 shows a typical CV curve for steel in KOH and KOH + Na_2SO_4 scanning from OCV to −0.4 V versus OCV and then back to 0 and 0.5 V versus reference, respectively. As shown in Fig. 2a, an oxidation peak was found at about −500 mV, which possibly was caused by the transition between magnetite (Fe_3O_4)and maghemite (Fe_2O_3); and then the oxidation of the ferrous hydroxide, $Fe(OH)_2$, into lepidocrocite (γ FeOOH) occurred in the first cycle. The reduction peak of Fe_2O_3 to Fe_3O_4 appeared at −454 mV in the CV [22,23]. No further peaks were found even though the final potential reached 500 mV in the CV measurement. In Fig. 2b, with the addition of 0.1 M Na_2SO_4 into KOH, activation corrosion occurred at −576 mV without any film conversion or formation. No passivation effect was found because of the existence of sulfate.

TYPICAL EIS FOR STEEL IN KOH AND KOH + NA_2SO_4 SOLUTION

The typical EIS plots of steel in KOH purged with N_2, in the air without any purging gas, and the addition of Na_2SO_4 into KOH purged with N_2 are given in Fig. 3.

FIG. 2 CV curve for steel in (a) KOH and (b) KOH + Na_2SO_4.

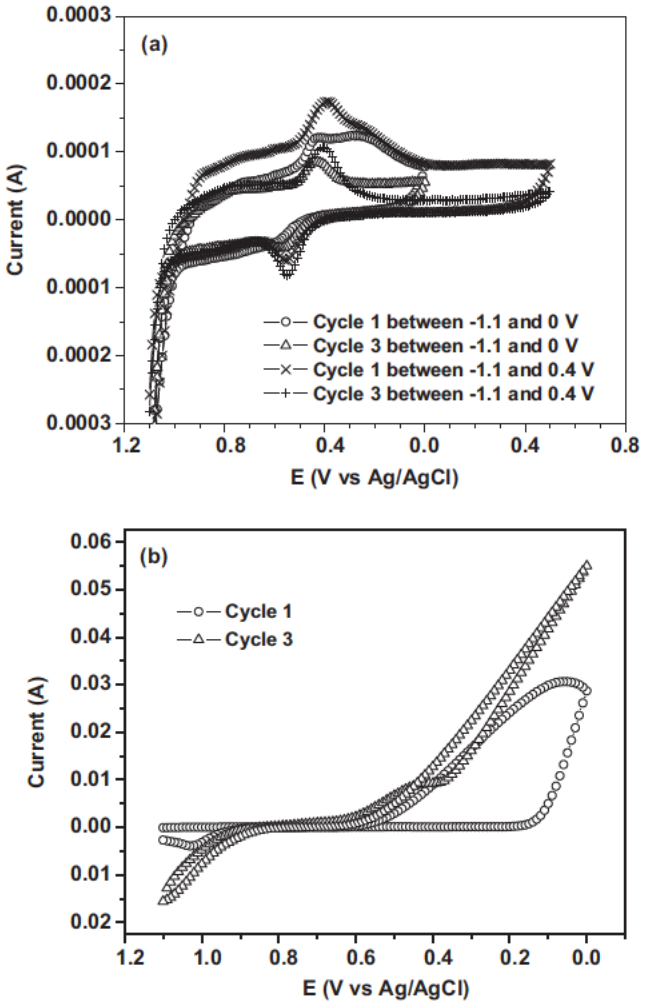

The Nyquist plots exhibited one time constant. The existence of O_2 in the solution increased the diameter of the circle in the Nyquist arc. The addition of Na_2SO_4 decreased the diameter of the Nyquist arc. The fitting of the Nyquist plots for steel in different solutions was modeled by a simple Randles equivalent circuit, except for a constant phase element (CPE) instead of a capacitor. The fitting results are listed in Table 1.

The polarization resistance (Rp) values for steel in 0.01 M KOH purged with N_2, in 0.01 M KOH with air, and in KOH + Na_2SO_4 + purged with N_2 are 1.98×10^5, 2.90×10^5, and 5.84×10^5 Ω, respectively. The existence of O_2

FIG. 3 Typical EIS for steel in KOH and KOH + Na_2SO_4 solution.

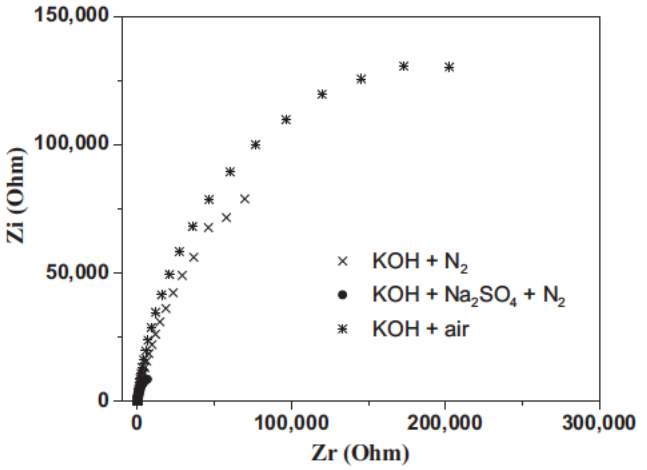

TABLE 1 Fitting parameters of solution resistance (Ru), polarization resistance (Rp), and constant phase element (CPE).

	KOH + N_2	KOH + Air	KOH + Na_2SO_4 + N_2
Rp (Ω)	1.98×10^5	2.90×10^5	5.84×10^5
Ru (Ω)	54.44	55	9.392
Y0	4.15×10^{-4}	2.13×10^{-4}	5.80×10^{-3}
α	0.845E 01	0.892	0.803

from the air in the solution induced a possible modification of the passivation film, or the formation of a more compact film with a different composition occurred. The addition of Na_2SO_4 to the KOH solution decreased the polarization resistance and deteriorated the film on steel, which was reported by Arzola, Palomar Pardavé, and Genesca [24]. There was a higher capacitance for the film formed on steel in the KOH + Na_2SO_4 solution, so possibly a porous film formed on steel.

TYPICAL HARMONIC CURRENT AND THD RESULTS

A typical current total harmonic distortion (ITHD) curve for steel in 0.01 M KOH with a perturbation of 50 mV is shown in Fig. 4a. Phase angle is from the phase shift between the perturbation voltage and the first order of harmonic current. ITHD at low frequency is constant because of the linear response of the solution resistance. The steady state of the ITHD below 100 mHz was caused by the stable surface at

FIG. 4 (a) A typical ITHD curve for steel in 0.01 M KOH. (b) Different orders of harmonic current for steel in 0.01 M KOH.

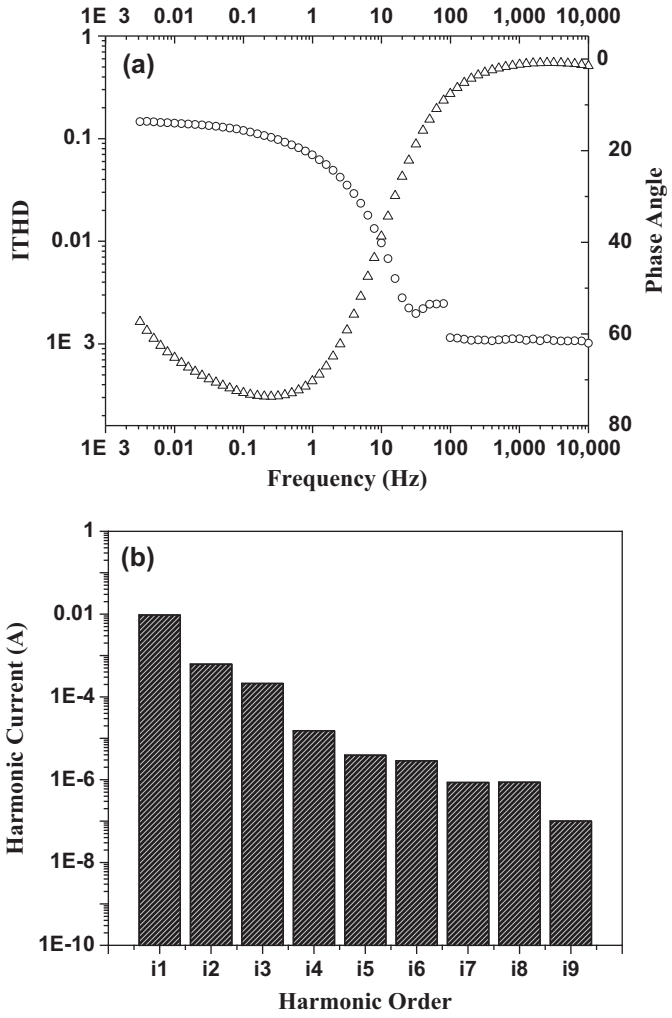

low frequencies. At each frequency, ten orders of harmonic signal can be finalized and acquired from the present instrumentation as shown in Fig. 4b. A frequency of 1 Hz was used as an example in Fig. 4b. The ninth order of the harmonic current was about 1×10^{-7} A. Harmonic current decreased with increasing order for the steel in the KOH solution.

The reason for the transition between two stable ITHDs in Fig. 4a is still under investigation.

THD AND EIS FOR STEEL IN KOH PURGED WITH N_2 AND IN AIR

The EIS Bode and THD plots with different amplitudes and frequencies for steel in a KOH solution purged with N_2 are given in Fig. 5a and b, respectively. No signifi cant change in modulus and phase angle in the EIS Bode plot could be observed

FIG. 5 (a) EIS Bode plot with different amplitudes for steel in KOH solution purged with N_2. (b) ITHD with different amplitudes for steel in KOH solution purged with N_2. (c) EIS Bode plot with different amplitude for steel in KOH solution in air. (d) ITHD plot with different amplitudes for steel in KOH solution in air.

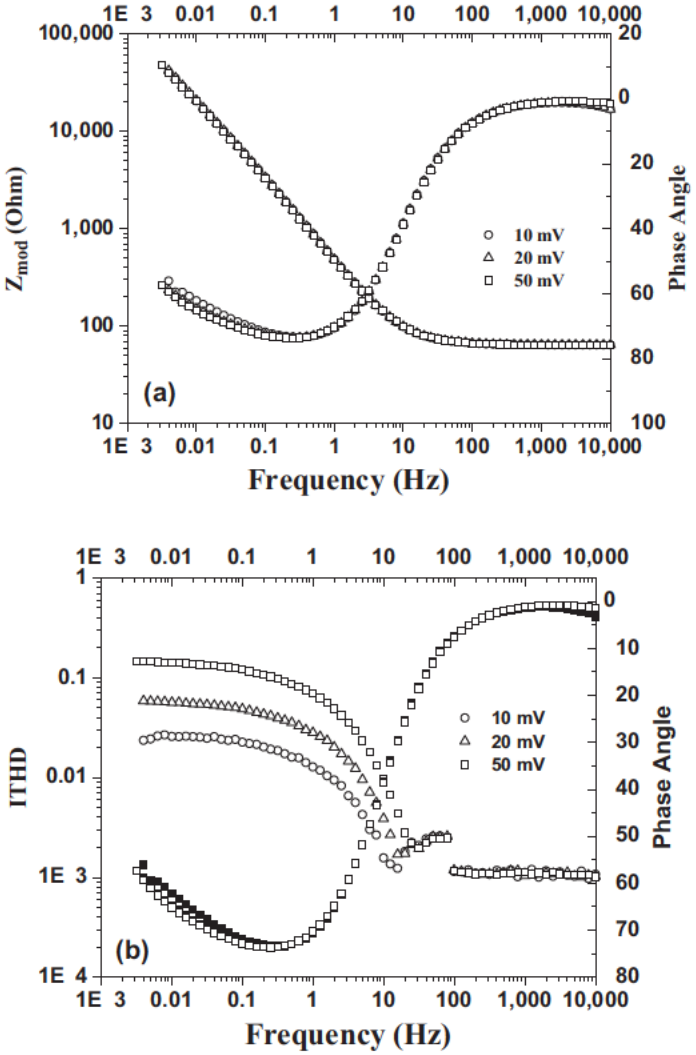

FIG. 5 (*Continued*).

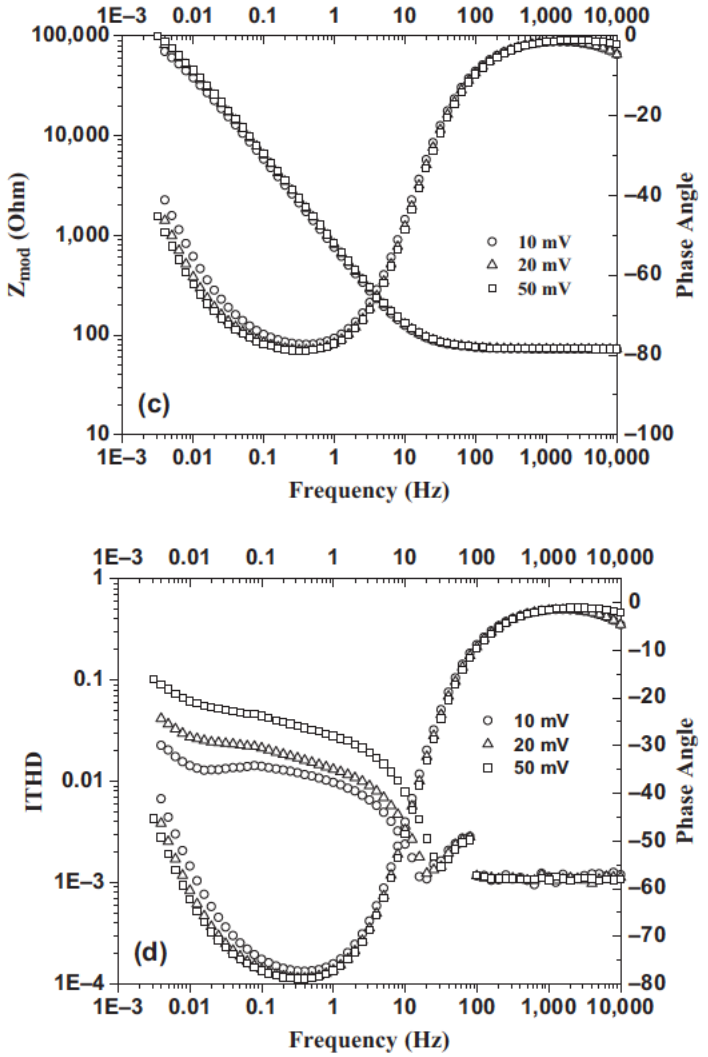

with various amplitudes of 10, 20, and 50 mV. In the THD curve, ITHD between 10 kHz and 100 Hz is constant with no distortion because of the linear response of solution resistance. The change in ITHD between 80 and 16 Hz can be distorted be cause of the AC line voltage at 50 Hz powering the potentiostat. ITHD increased starting from 16 Hz and then reached a steady value of 2.681 % at 10 mHz for the amplitude of 10 mV. The steady ITHD value increased with the amplitude in the perturbation signal.

Bode and ITHD plots for steel in a KOH solution exposed to the air are shown in Fig. 5c and d, respectively. The influence of amplitude on the modulus in the Bode plots is not significant. The behavior of ITHD at frequencies below 15 mHz is different from that purged with N_2. Another ramp line in the ITHD curve at lower frequencies was found, which may have been caused by the diffusion process of O_2 to the surface of the steel. The influence of amplitude on ITHD is similar to that for purging N_2, that is, the higher ITHD, the higher amplitude. Ramschak et al. [12] and Mao and Krewer [13] employed THD techniques to study the influence of O_2 on THD, demonstrating that it is a promising technique for monitoring the opera tion status of a fuel cell and the reduction mechanism of O_2 on platinum. In their reports, at frequencies below 10 Hz, the THD increased as frequency decreased. The change of ITHD with the concentration of O_2 in the solution can be utilized for the reduction mechanism of oxygen on steel.

THD AND EIS FOR STEEL IN KOH AND KOH + NA_2SO_4 SOLUTION

The influence of Na_2SO_4 on EIS Bode and ITHD plots for steel in KOH and KOH + Na_2SO_4 solution are shown in Fig. 6a and b, respectively. The addition of Na_2SO_4 decreased the solution resistance and modulus in impedance over the whole frequency range between 10 kHz and 0.004 Hz. ITHD increased with the addition of Na_2SO_4. The corrosion rate derived according to Eq 22 is plotted in Fig. 7. The corrosion rate decreased with frequency. The addition of Na_2SO_4 into the KOH solution increased the corrosion current. The choice of the chief fre quency in the determination of corrosion rate from harmonic techniques is dis cussed later.

THE INFLUENCE OF FREQUENCY IN HARMONIC/EFM AND SCAN RATE IN LPR ON THE CORROSION RATE

The Rp of steel measured with different techniques (LPR, EFM, EIS, and HA) in 0.01 M KOH purged with N_2 is shown in Fig. 8. The value of Rp fitted with EIS exhibits the largest, which is comparable with that via LPR measurements at a lower scan rate of 0.167 mV/s. The transformation between Rp, corrosion current, and Tafel slopes based on the Stern Geary equation is employed in EFM and HA. The difference in the value of Rp is significant because of the different scan rates in LPR and frequency in EFM.

Various amplitudes were used in HA/THD measurements for steel in KOH solution purged with N_2, as shown in Fig. 5a. The influence of amplitude on corrosion current in HA measurements was further analyzed at 0.1 Hz and is listed in Table 2.

The corrosion current increased with amplitude in HA measurements. The scan rate influenced the polarization resistance results via the LPR technique with respect to the contribution of the non faradaic process by the double layer and diffusion during corrosion. The scan rate was set to 0.6 V/h (i.e., 0.1667 mV/s) as per ASTM G59, *Standard Test Method for Conducting Potentiodynamic*

FIG. 6 (a) The influence of Na_2SO_4 on EIS plots for steel in KOH and KOH + Na_2SO_4 solution. (b) The influence of Na_2SO_4 on ITHD plots for steel in KOH and KOH + Na_2SO_4 solution.

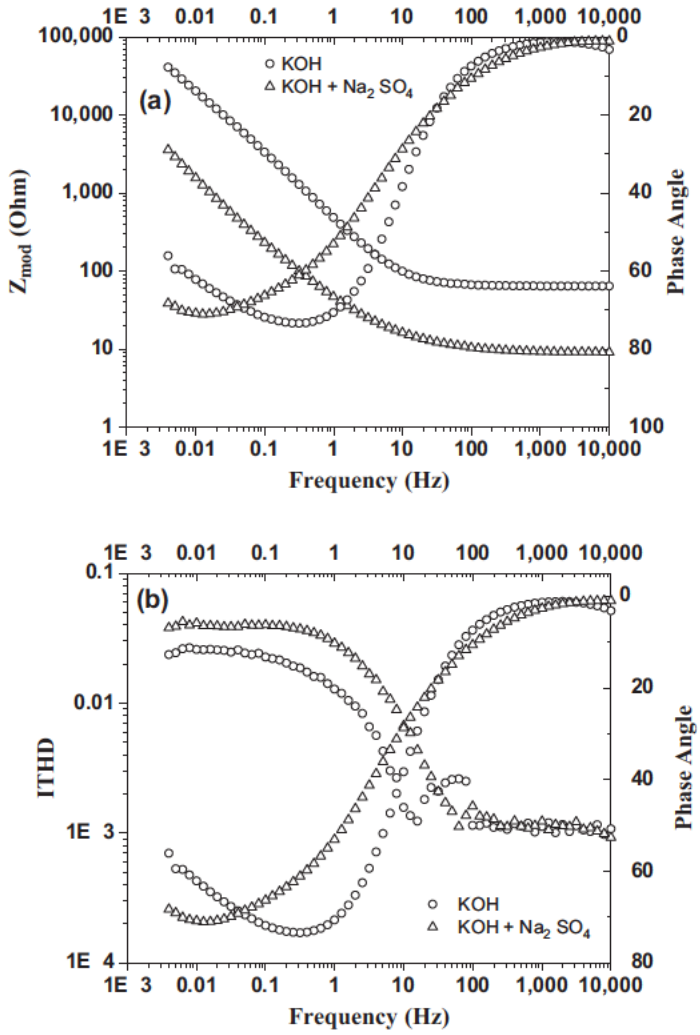

Polarization Resistance Measurements [25]. In the harmonic measurement for a determination of corrosion rate, the frequency employed in the harmonic tech nique can be equivalent to the scan rate in LPR. The selection of scan rate in LPR or frequency in harmonic measurements has been reported and discussed in sev eral studies [26 29]. The actual applied potential reaches 98 % of the stable value at infinite time only when the time is more than $4Rp \times C$, where C is the

FIG. 7 The corrosion rate for steel in 0.01 M KOH and 0.01 M KOH + 0.1 M Na_2SO_4.

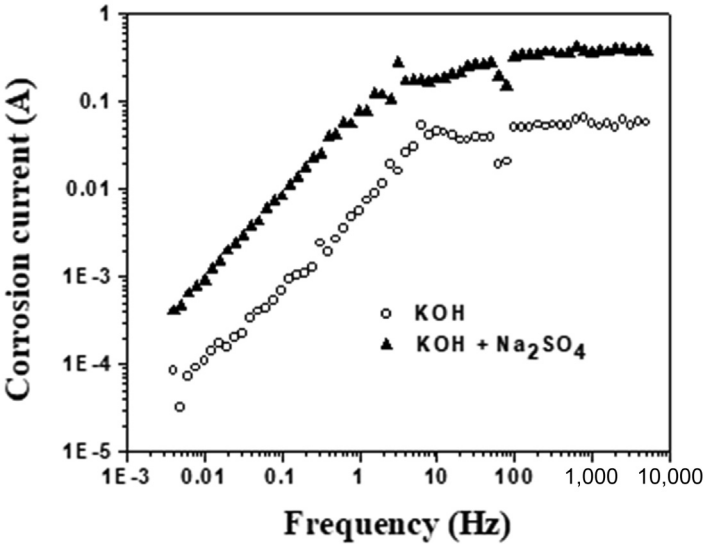

FIG. 8 Polarization resistance (Rp) measured with various techniques (LPR, EFM, EIS, and HA) for steel in 0.01 M KOH purged with N_2.

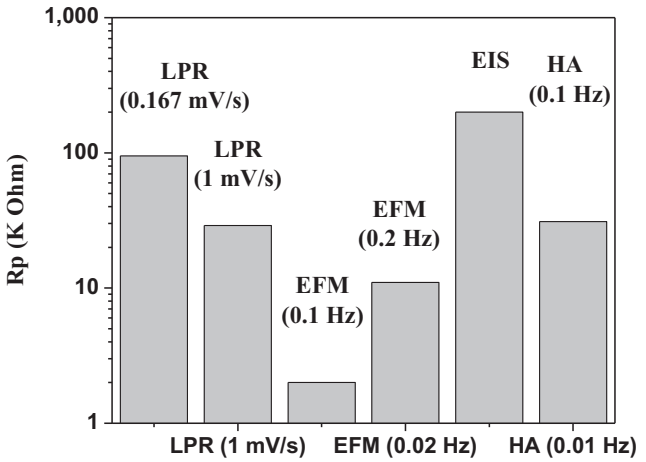

capacitance of the double layer. As for the corrosion system without a diffusion controlled process, the maximum frequency to acquire accurate $Rs + Rp$ is about $1/[2\pi \times C \times (Rs + Rp)]$.

TABLE 2 Corrosion current via HA/THD at 0.1 Hz with various amplitudes.

Amplitude (mV)	10	20	50
Corrosion current (A)	0.00069	0.00073	0.00081

Concerning the steel in the 0.01 M KOH solution, the optional frequency was determined to be 0.002 Hz according to Rp, Rs, and CPE values shown in Table 1. The frequencies used in the EFM and HA measurements (0.1, 0.02, and 0.01 Hz) were higher than 0.002 Hz, so the lower Rp values were acquired from EFM and HA measurements.

Summary

An HA/THD instrumentation technique was implemented in both potentiostatic and galvanostatic modes. HA/THD can provide corrosion rates, polarization resistances, and Tafel slopes comparable to established LPR, EFM, and EIS techniques. In this paper, we report the first use of THD to characterize the corrosion process. The ramp line was first reported in THD curves for the diffusion of oxygen in a corrosion pro cess. Harmonic and THD methods are influenced by the amplitude of the perturba tion signal and diffusion process in an electrochemical reaction. The influence of oxygen and sulfate ions on the corrosion process was discussed using THD results.

ACKNOWLEDGMENTS

We acknowledge discussions with Dr. Qing Mao at Dalian University of Technology concerning harmonic and THD techniques during the preparation of a draft of this report. Software engineers A. Kojevnikov and M. Yaffe at Gamry Instruments contrib uted to the software scripts for HA/THD instrumentation. Dr. Stephen M. Cohen at Gamry assisted with editing the text of this manuscript.

References

[1] Hou, B., Li, X., Ma, X., Du, C., Zhang, D., Zheng, D., Xu, W., Lu, D., and Ma, F., "The Cost of Corrosion in China," *npj Mater. Degrad.*, Vol. 1, No. 4, 2017, pp. 1–10, http://dx.doi.org/10.1038/s41529-017-0005-2

[2] Orazem, M. E. and Tribollet, B., *Electrochemical Impedance Spectroscopy*, Wiley, Hoboken, NJ, 2008.

[3] Harrington, D. A., "Theory of Electrochemical Impedance of Surface Reactions: Second-Harmonic and Large-Amplitude Response," *Can. J. Chem.*, Vol. 75, No. 11, 1997, pp. 1508–1517, http://dx.doi.org/10.1139/v97-181

[4] Creason, S. C. and Smith, D. E., "Fourier Transform Faradaic Admittance Measurements: I. Demonstration of the Applicability of Random and Pseudo-Random Noise as Applied Potential Signals," *J. Electroanal. Chem. Interfacial Electrochem.*, Vol. 36, No. 1, 1972, pp. A1–A7, http://dx.doi.org/10.1016/S0022-0728(72)80466-2

[5] Wojcik, P. T. and Orazem, M. E., "Variable-Amplitude Galvanostatically Modulated Impedance Spectroscopy as a Tool for Assessing Reactivity at the Corrosion Potential without Distorting Temporal Evolution of the System," *Corrosion*, Vol. 54, No. 4, 1998, pp. 289–298, http://dx.doi.org/10.5006/1.3284855

[6] Agarwal, W. P., Orazem, M. E., and Darowicki, K., "A Method for Maintaining a Constant Potential Variation during Galvanostatic Regulation of Electrochemical Impedance Measurements," *Electrochim. Acta*, Vol. 41, No. 7–8, 1996, pp. 977–983, http://dx.doi.org/10.1016/0013-4686(95)00428-9

[7] Bosch, R. W. and Bogaerts, W. F., "Instantaneous Corrosion Rate Measurement with Small-Amplitude Potential Intermodulation Techniques," *Corrosion*, Vol. 52, No. 3, 1996, pp. 204–212, http://dx.doi.org/10.5006/1.3292115

[8] Darowicki, K., "Fundamental-Harmonic Impedance of First-Order Electrode Reactions," *Electrochim. Acta*, Vol. 39, No. 18, 1994, pp. 2757–2762, http://dx.doi.org/10.1016/0013-4686(94)00302-5

[9] Darowicki, K. and Majewska, J., "Harmonic Analysis of Electrochemical and Corrosion Systems—A Review," *Corros. Rev.*, Vol. 17, Nos. 5–6, 1994, pp. 383–399, http://dx.doi.org/10.1515/CORRREV.1999.17.5-6.383

[10] Devay, J. and Meszaros, L., "Study of the Rate of Corrosion of Metals by a Faradaic Distortion Method, I.," *Acta Chim. Hung.*, Vol. 100, Nos. 1–4, 1979, pp. 183–202.

[11] Wilson, R., Schwartz, D. T., and Adler, S. B., "Nonlinear Electrochemical Impedance Spectroscopy for Solid Oxide Fuel Cell Cathode Materials," *Electrochim. Acta*, Vol. 51, Nos. 8–9, 2006, pp. 1389–1402, http://dx.doi.org/10.1016/j.electacta.2005.02.109

[12] Ramschak, W., Peinecke, V., Prenninger, P., Schaffer, T., and Hacker, V., "Detection of Fuel Cell Critical Status by Stack Voltage Analysis," *J. Power Sources*, Vol. 157, No. 2, 2006, pp. 837–840, http://dx.doi.org/10.1016/j.jpowsour.2006.01.009

[13] Mao, Q. and Krewer, U., "Total Harmonic Distortion Analysis of Oxygen Reduction Reaction in Proton Exchange Membrane Fuel Cells," *Electrochim. Acta*, Vol. 103, No. 30, 2013, pp. 188–198, http://dx.doi.org/10.1016/j.electacta.2013.03.194

[14] Zhang, X., Moosbauera, D., Kojevnikova, A., and Yaffea, M., "Total Harmonic Distortion for PEM Fuel Cell," *ECS Trans.*, Vol. 75, No. 38, 2017, pp. 17–28, http://dx.doi.org/10.1149/07538.0017ecst

[15] Bosch, R. W. and Bogaerts, W. F., "Harmonic Analysis of Corroding Systems Considering Diffusion Phenomena," *J. Electrochem. Soc.*, Vol. 143, No. 12, 1996, pp. 4033–4039, http://dx.doi.org/10.1149/1.1837332

[16] Pirnát, A., Mészáros, L., and Lengyel, B., "A Comparison of Electrochemical and Analytical Chemical Methods for the Determination of the Corrosion Rate with Very Efficient Inhibitors," *Corros. Sci.*, Vol. 37, No. 6, 1995, pp. 963–973, http://dx.doi.org/10.1016/0010-938X(95)00007-7

[17] Angst, U. M. and Elsener, B., "Measuring Corrosion Rates: A Novel AC Method Based on Processing and Analyzing Signals Recorded in the Time Domain," *Corros. Sci.*, Vol. 89, No. 12, 2014, pp. 307–317, http://dx.doi.org/10.1016/j.corsci.2014.09.013

[18] Durnie, W., Marco, R. D., Jefferson, A., and Kinsella, B., "Harmonic Analysis of Carbon Dioxide Corrosion," *Corros. Sci.*, Vol. 44, No. 6, 2002, pp. 1213–1221, http://dx.doi.org/10.1016/S0010-938X(01)00136-6

[19] Gill, J. S., Callow, L. M., and Scantlebury, J. D., "Corrosion Measurements Derived from Small Perturbation Non-Linearity—Part 1: Harmonic Analysis," *Corrosion*, Vol. 39, No. 2, 1983, pp. 61–66, http://dx.doi.org/10.5006/1.3580816

[20] Jafar, M. J., Dawson, J. L., and John, D. G., "Electrochemical Impedance and Harmonic Analysis Measurements on Steel in Concrete," *Electrochemical Impedance Analysis and Interpretation, ASTM STP1188*, J. R. Scully, D. C. Silverman, and M. W. Kendig, Eds., ASTM

International, West Conshohocken, PA, 1993, pp. 384–403, http://dx.doi.org/10.1520/STP18081S

[21] Darowicki, K., "Fundamental-Harmonic Impedance of First-Order Electrode Reactions," *Electrochim. Acta*, Vol. 39, No. 18, 1994, pp. 2757–2762, http://dx.doi.org/10.1016/0013-4686(94)00302-5

[22] Xu, W., Daub, K., Zhang, X., Noel, J. J., Shoesmith, D. W., and Wren, J. C., "Oxide Formation and Conversion on Carbon Steel in Mildly Basic Solutions," *Electrochim. Acta*, Vol. 54, No. 24, 2009, pp. 5727–5738, http://dx.doi.org/10.1016/j.electacta.2009.05.02

[23] Zhang, X., Shoesmith, D. W., and Wren, J. C., "Kinetics of H_2O_2 Reaction with Oxide Films on Carbon Steel," *Corros. Sci.*, Vol. 49, No. 12, 2007, pp. 4553–4567, http://dx.doi.org/10.1016/j.corsci.2007.04.012

[24] Arzola, S., Palomar-Pardavé, M. E., and Genesca, J., "Effect of Resistivity on the Corrosion Mechanism of Mild Steel in Sodium Sulfate Solutions," *J. Appl. Electrochem.*, Vol. 33, No. 12, 2003, p. 1233, http://dx.doi.org/10.1023/B:JACH.0000003855.95788.12

[25] ASTM G59–97 (2014), *Standard Test Method for Conducting Potentiodynamic Polarization Resistance Measurements*, ASTM International, West Conshohocken, PA, 2014, www.astm.org

[26] Pirnát, A., Mészáros, L., and Lengyel, B., "A Comparison of Electrochemical and Analytical Chemical Methods for the Determination of the Corrosion Rate with Very Efficient Inhibitors," *Corros. Sci.*, Vol. 37, No. 6, 1995, pp. 963–973, http://dx.doi.org/10.1016/0010-938X(95)00007-7

[27] Scully, J. R., "Polarization Resistance Method for Determination of Instantaneous Corrosion Rates," *Corrosion*, Vol. 56, No. 2, 2000, pp. 199–218, http://dx.doi.org/10.5006/1.3280536

[28] Mansfeld, F., "Tafel Slopes and Corrosion Rates from Polarization Resistance Measurements," *Corrosion*, Vol. 29, No. 10, 1973, pp. 397–402, http://dx.doi.org/10.5006/0010-9312-29.10.397

[29] Macdonald, D. D., "An Impedance Interpretation of Small Amplitude Cyclic Voltammetry: I. Theoretical Analysis for a Resistive-Capacitive System," *J. Electrochem. Soc.*, Vol. 125, No. 9, 1978, pp. 1443–1449, http://dx.doi.org/10.1149/1.2131693

STP 1609, 2019 / available online at www.astm.org / doi: 10.1520/STP160920170233

Lietai Yang[1] and Xiaodong Sun[1]

Experimental Studies on the Effect of Electrode Spacing in Coupled Multielectrode Array Sensors on Corrosion Rate Measurements

Citation

Yang, L. and Sun, X., "Experimental Studies on the Effect of Electrode Spacing in Coupled Multielectrode Array Sensors on Corrosion Rate Measurements," *Advances in Electrochemical Techniques for Corrosion Monitoring and Laboratory Corrosion Measurements, ASTM STP1609*, S. Papavinasam, R. B. Rebak, L. Yang, and N. S. Berke, Eds., ASTM International, West Conshohocken, PA, 2019, pp. 180–194, http://dx.doi.org/10.1520/STP160920170233[2]

ABSTRACT

The electrodes in a coupled multielectrode array sensor (CMAS) are usually flush-mounted in an insulator, and the spacing between adjacent electrodes is an important parameter. The common belief is that the smaller the spacing is, the better the multielectrode array simulates the behavior of a real one-piece metal. Experiments were conducted to study the effect of spacing in CMAS on the measurements of corrosion rates. The data suggest that the spacing has no significant effect on the measured nonuniform corrosion rate for carbon steel in simulated seawater when the spacing varies from 1 to 8 mm. Preliminary studies also suggest that the CMAS with 16 closely packed electrodes and small spacing (0.05–0.25 mm) may measure a lower than usual nonuniform corrosion rate because of the efficient chemical interaction among all of the electrodes packed within a small area. The efficient chemical interaction may have caused all the electrodes in the small area to be under active corrosion such that there were no effective cathodic electrodes left to support localized corrosion. This was

Manuscript received November 15, 2017; accepted for publication June 18, 2018.

[1]Corr Instruments, 23 Affonso Dr., Carson City, NV 89706, USA L. Y. http://orcid.ord/0000 0002 9704 8953

[2]ASTM Symposium on *Advances in Electrochemical Techniques for Corrosion Monitoring and Laboratory Corrosion Measurements* on November 13 14, 2017 in Atlanta, GA, USA.

evidenced by the measurement of the open-circuit potentials of individual electrodes soon after decoupling of the electrodes. The data showed that there is a small variation in the open-circuit potentials for the probe with closely packed electrodes (small standard deviation). In contrast, the standard deviations for the probes that have a spacing of 1 or 8 mm were larger. As a sensor, the loss of effective cathode may not represent the situation for industrial equipment where the cathodic sites in faraway locations may always be available when there is localized corrosion.

Keywords

multielectrode array, corrosion sensors, corrosion monitoring, coupled multielectrode, CMAS, CMA, coupled array, array electrode

Introduction

Coupled multielectrode arrays have been used to study the electrochemical behavior and localized corrosion of metals since the 1990s [1 3]. They are highly effective tools for studying the spatiotemporal behavior of metals in laboratories [4 12]. The coupled multielectrode arrays are also widely used as coupled multielectrode array sensors (CMASs) for monitoring nonuniform corrosion rates, especially localized corrosion rates, in laboratories and plants [13 26].

When a metal undergoes nonuniform corrosion, particularly localized corro sion such as pitting corrosion or crevice corrosion in a corrosive environment, elec trons are released from the anodic sites where the metal corrodes and they travel within the metal to the cathodic sites where the metal corrodes less or does not cor rode (upper section of **Fig. 1**) [2]. Such a phenomenon occurs because of local varia tions in the microstructure of the metal surface or in the environment chemistry (or both). If the metal is separated into multiple small pieces (or mini electrodes), some of the mini electrodes have properties that are close to the anodic sites and others have properties that are close to the cathodic sites of the corroding metal. When these mini electrodes are coupled by connecting each of them to a common joint through a multichannel zero voltage ammeter (ZVA) [27], the electrodes that exhibit anodic properties simulate the anodic areas, and the electrodes that exhibit the cathodic properties simulate the cathodic areas of the corroding metal (lower section of **Fig. 1**). The electrons released from the anodic electrodes are forced to flow through the coupling joint to the cathodic electrodes. Thus, the ZVA measures the anodic currents (I^{a}_{ex}) to the more corroding electrodes and cathodic currents (I^{c}_{ex}) from the less corroding or noncorroding electrodes. The quantitative localized or nonuniform corrosion rates on the individual electrodes can be determined from the anodic currents [2,13].

As discussed by Cong et al., the ability for a coupled multielectrode array to ef fectively simulate the electrochemical behavior of a one piece metal depends on two types of couplings. One is coupling through chemical interaction and the other is coupling through electrical potential field [7]. The effective coupling through

FIG. 1 Principle of CMAS probe: The upper section shows the electron flows from the corroding area to the less corroding areas inside a metal when localized corrosion takes place; the lower section shows the electron flows after the anodic and cathodic areas are separated into individual small electrodes and coupled through an external circuit that measures the anodic current (I^a_{ex}) and cathodic current (I^c_{ex}) through each of the individual electrodes [2].

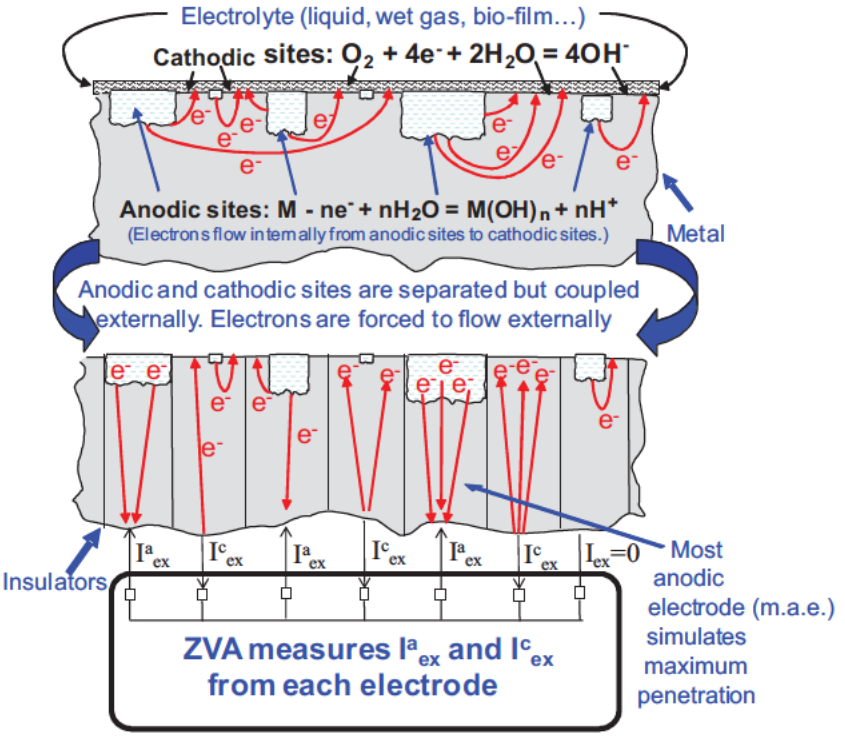

potential fields requires that both the voltage drop caused by the solution resistance [7] and the voltage imposed by the ZVA [27] must be negligibly low. The effective coupling through the chemical interaction requires that the spacing between the neighboring electrodes must be as small as reasonably achievable [7]. As the solu tion resistance also depends on the spacing of the electrodes, the effective coupling of electrical potential fields also requires that the electrode spacing be reasonably small. Theoretical calculations were performed by Cong et al. for the distributions of the electrical potential affected by the current flow and chemical interactions by diffusion surrounding a single 0.15 mm diameter electrode flush mounted on a flat surface. This paper describes the experimental results on the effect of the electrode spacing of CMAS probes with carbon steel electrodes on the measurement of the corrosion rate.

Experimental

Three CMAS probes with 16 functional electrodes made of Type 1018 carbon steel (UNS G10180) were tested in simulated seawater (0.5 M sodium chloride [NaCl] solution saturated with air). The electrodes were made of 1.0 mm diameter wires. The electrodes of the first CMAS probe (Probe A) were closely packed together in a random pattern as shown in Fig. 2a, with the spacing between the adjacent electro des being 0.05 to 0.25 mm. The electrodes of the second CMAS probe (Probe B) were packed in a regular four by four pattern as shown in Fig. 2b, with the spacing between the adjacent electrodes being 1.0 mm. The electrodes of both Probe A and Probe B were flush mounted in an epoxy. The electrodes of the third CMAS probe (Probe C) were spaced out in a regular four by four pattern as shown in Fig. 2c, with the spacing between the adjacent electrodes being 8 mm. The side surfaces of all of the electrodes of Probe C were coated with an epoxy, and the wire cross sectional areas at the tips were exposed to act as the active surfaces of the electrodes. The electrode arrangement of Probe C simulates the CMAS probes with finger like electrodes that are for application in systems containing a hydrogen sulfide (H_2S) environment. The finger like electrodes effectively prevent the formation of contig uous electron conducting corrosion products such as iron sulfide in the presence of H_2S between adjacent electrodes [28]. The electron conducting corrosion products between adjacent electrodes had been blamed for causing short circuiting of the

FIG. 2 Electro dearrangements on the CMAS probes (spacing was 0.05 0.25 mm for Probe A, 1.0 mm for Probe B, and 8.0 mm for Probe C).

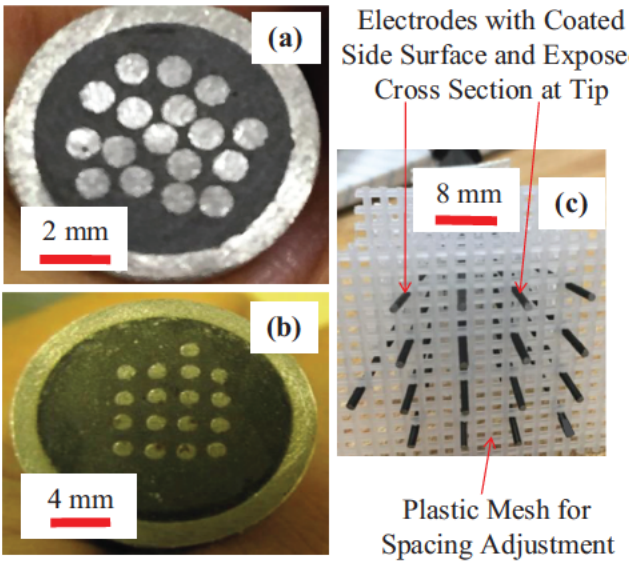

electrodes for electrochemical sensors [29].The cross sections of all the electrodes in the aforementioned probes were polished with 240 grit silicon carbide paper before the experiment, and the exposed surface area of each electrode was 0.785 mm^2.

A silver/silver chloride reference electrode filled with a saturated potassium chloride solution was used to measure the coupling potentials of the probes and the open circuit potentials of the individual electrodes on each probe after the electro des were decoupled from the coupling joint of each probe.

During the experiment, the CMAS probe was vertically immersed in the test solution contained in a beaker without agitation. The temperature was between 22°C and 25°C. Several nanoCorr® Model B 40 analyzers (Corr Instruments, San Antonio, TX) were used as the CMAS instruments, which measure the coupling currents from each of the individual electrodes of the CMAS probes and the cou pling potential of the CMAS probes against the reference electrode. These instru ments also have the ability to decouple a selected electrode so that its open circuit potential can be measured against the reference electrode or against the coupling joint to which all the other 15 electrodes are connected. Each of the Model B 40 analyzers was used for up to two CMAS probes with 16 electrodes or for up to 4 CMAS probes with 10 electrodes.

A conductivity meter was used to measure the conductivity of the solution and the conductance (or impedance) between a decoupled electrode and the coupling joint of the other electrodes. The measurement voltage supplied by the conductivity meter had an amplitude between 100 and 250 mV (depending on the conductivity of the solution) and a frequency of about 250 Hz. As shown in **Fig. 1**, the current flow on each electrode is between the electrode and the coupling joint of all the other electrodes. The solution resistance between the electrode and the coupling joint of the other electrodes is more directly related to the distribution of electrical potential.

Results and Discussions

NONUNIFORM CORROSION RATES FROM PROBES WITH DIFFERENT SPACING

Fig. 3 shows typical maximum nonuniform corrosion rates from the probes with different spacing (0.05 8 mm). The maximum nonuniform corrosion rate is derived from the current on the electrode that exhibits the most anodic behavior (most anodic electrode). The rates from Probe A (0.05 0.25 mm spacing) and Probe B (1 mm spacing) are very close to each other until the 130th hour. Between the 90th and 130th hour, the corrosion rates were about the same for all three probes. Then after the 130th hour, the nonuniform corrosion rates from Probe B (1 mm spacing) and C (8 mm spacing) were close to each other, but the corrosion rate from Probe A (0.05 0.25 mm spacing) began to deviate from those of Probes B and C and reached 0.5 mm/year at the 170th hour. The nonuniform corrosion rate from Probe A remained lower at about 0.5 mm/year, but the corrosion rates from

FIG. 3 Maximum nonuniform corrosion rate of carbon steel in simulated seawater from the CMAS probes with different spacing.

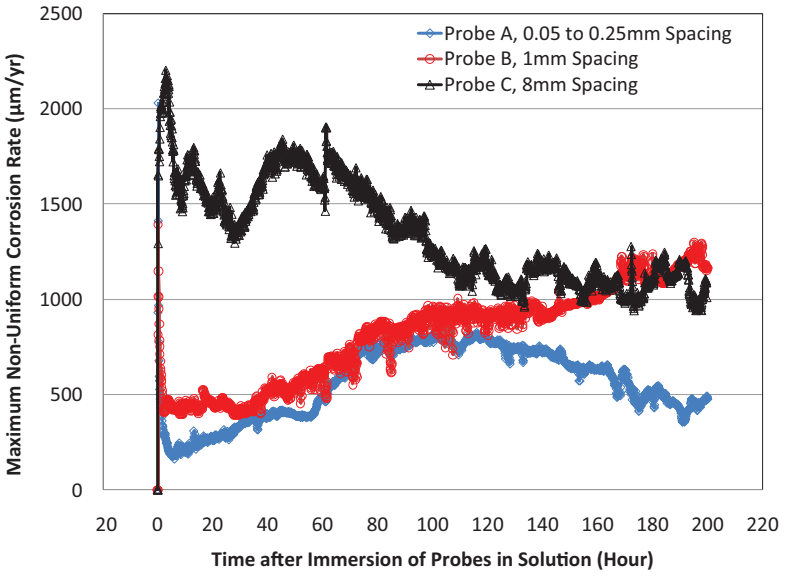

Probe B (1 mm spacing) and Probe C (8 mm spacing) were between 1.0 and 2.0 mm until the end of the experiment.

Considering the stochastic nature of nonuniform corrosion, especially localized corrosion, which may vary by a factor of five or more for the same metal immersed in similar solutions [30], the observed variation of the nonuniform corrosion rate from 0.5 mm/year for Probe A to 2 mm/year for Probes B and C is not large, and it may be due to the random effect. The measurements were repeated for Probes A and B side by side after repolishing. In all cases, the nonuniform corrosion rate from Probe A was lower than that from Probe B by at least 50 %. According to the data reported by Southwell and Alexander for the long term (1 year) exposure tests in Panama River seawater, the maximum pitting rate found on a large carbon steel coupon (two sides of a 230 cm by 230 cm plate) was 1.6 mm/year [31]. The corro sion rates, as shown in Fig. 3, for the three probes agree with the data reported for the 1 year tests, considering the large variations for localized corrosion. The non uniform corrosion rate from the probe that has 0.05 to 0.25 mm spacing was only marginally lower than that of the other probes.

Fig. 4 shows the maximum nonuniform corrosion rates from the probes with different spacing (0.05 8 mm) shortly before and after the immersion of the probes in the solution. The corrosion rates of all three probes were at the lower detection limit of the instruments (less than 0.2 µm/year) initially and increased immediately

FIG. 4 Maximum nonuniform corrosion rate of carbon steel in simulated seawater from the CMAS probes with different spacing immediately after the immersion.

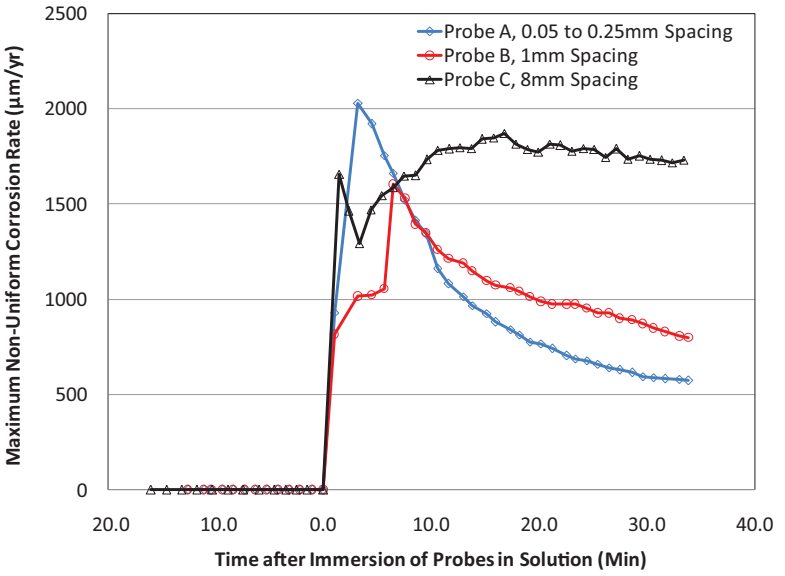

after the immersion in the solution. All rates were 1,500 µm/year or higher within the first 10 min. Interestingly, the corrosion rates from the two probes with flush mounted electrodes (Probe A and Probe B) exhibited a clear trend of rapid decrease with time. This decreasing trend is especially true for Probe A, which has smaller electrode spacing. Such a decreasing trend is not observed with Probe C, which has the individually exposed electrodes and large spacing (8 mm) between the adjacent electrodes. Repeated measurements for Probes A and B after repolishing also showed a similar trend.

OPEN-CIRCUIT POTENTIALS OF INDIVIDUAL ELECTRODES

At the end of the testing, the coupling potential (the potential at the coupling joint) of each probe was measured. Then, all the electrodes of each probe were decoupled from their coupling joints at the same time, and the open circuit potentials of the individual electrodes of the probes were measured shortly after the decoupling (within 10 to 20 min) and 20 h after the decoupling. Table 1 shows the coupling potentials of the probes (E_{coup}), the open circuit potentials of the individual electrodes (E) after decoupling, and standard deviations of the potentials. Surprisingly, the standard deviation of the individual potentials of Probe A (with spacing between 0.05 and 0.025 mm) is very low shortly after the decoupling. Fig. 5 shows the comparison of the standard deviations from the three probes. Shortly after the

TABLE 1 Open circuit potentials of individual electrodes after decoupling and coupling potentials of probes.

	Probe A				Probe B				Probe C			
	10 Min[a]		20 H[a]		10 Min[a]		20 H[a]		10 Min[a]		20 H[a]	
Electrode	*E* (mV)	Δ*E* (mV)	*E* (mV)	Δ*E* (mV)	*E* (mV)	Δ*E* (mV)	*E* (mV)	Δ*E* (mV)	*E* (mV)	Δ*E* (mV)	*E* (mV)	Δ*E* (mV)
1	637	4	642	2	618	10	563	78	609	4	608	3
2	639	2	636	8	625	3	681	40	609	4	606	5
3	641	0	648	4	626	2	677	36	640	35	645	34
4	646	5	663	19	628	0	621	20	612	7	615	4
5	640	1	646	2	[b]	[b]	[b]	[b]	483	122	497	153
6	645	4	643	1	[b]	[b]	[b]	[b]	520	85	506	105
7	642	1	649	5	669	41	702	61	611	6	610	1
8	643	2	648	4	644	16	647	6	608	3	607	4
9	644	3	648	4	602	26	675	34	624	19	625	14
10	636	5	626	18	622	6	594	47	612	7	613	2
11	641	0	642	2	632	4	634	7	611	6	612	1
12	640	1	628	16	633	5	635	6	628	23	630	19
13	648	7	661	17	629	1	630	11	[b]	[b]	[b]	[b]
14	636	5	603	41	605	23	666	25	605	0	601	10
15	641	0	647	3	613	15	645	4	642	37	646	35
16	638	3	622	22	629	1	622	19	[b]	[b]	[b]	[b]
E_{coup}	641		644		628		641		605		611	
SD	3.5		15.0		16.5		36.9		44.4		44.6	
Maximum |Δ*E*|	7.0		19.0			41.0		61.0		37.0		35.0

Note: *E* open circuit potential; E_{coup} coupling potential; SD standard deviation of *E*; Δ*E* *E* E_{coup}.
[a]Time after the electrodes on CMAS probes were decoupled.
[b]Electrodes not used because of broken wires.

FIG. 5 Comparison of the standard deviations and maximum $|\Delta E|$ from the three probes immediately after the decoupling and 20 h after the decoupling.

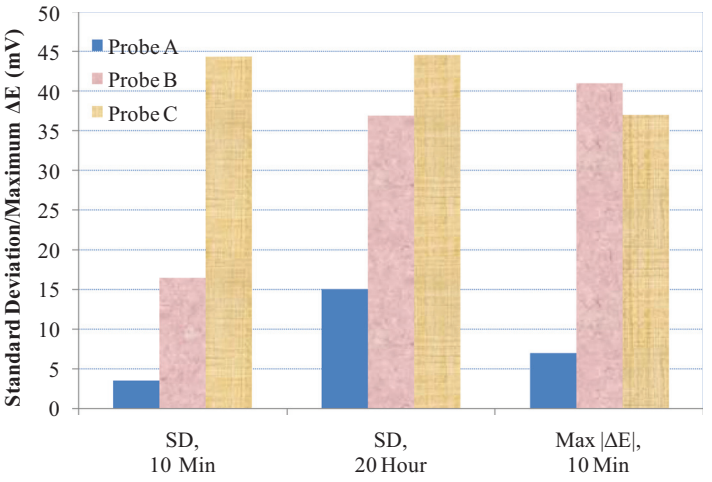

decoupling, the standard deviations of the potentials for the three probes were 3.5, 16.5, and 44.4 mV, respectively. The low standard deviation value for Probe A sug gests that both the local chemistry on the surface of each electrode and the metal lurgical properties of each electrode of Probe A were very close to each other before and shortly after the decoupling.

Because all electrodes of the three probes were from the same steel wire, but the standard deviations of the individual electrodes from the other two probes are large, the low standard deviation from Probe A must be due to the local chemistry effect. Therefore, the local chemistry at the individual electrodes of Probe A was affected by the process called coupling through chemical interaction.

As the driving force of the measured maximum nonuniform corrosion rate from each CMAS probe is how much lower the open circuit potential of the most anodic electrode is from the coupling potential (the maximum value of $|\Delta E|$ where $\Delta E = E - E_{coup}$) [7,32]. The values of $|\Delta E|$ are also presented in **Table 1**, and the maximum values of $|\Delta E|$ for each probe are also presented in **Fig. 5**.

It can be seen from **Fig. 5** that the standard deviation of Probe A increased from the initial value of 3.5 to 15 mV after the electrodes were decoupled for 20 h. After the decoupling, all the individual electrodes were corroding at their own open circuit potentials, and there was no net ionic flow between the anodic electrodes and the cathodic electrodes, which means that there was no accelerated chemical mixing by the electrical potential field (movement of the charged species in the elec trical field). In addition, the anodic electrodes, especially the most anodic electrodes, were not forced by the other electrodes to corrode at an accelerated rate because

their potentials were not raised by the other cathodic electrodes when there was no coupling.

The lower standard deviation and smaller maximum $|\Delta E|$ immediately after decoupling and higher standard deviation and larger maximum $|\Delta E|$ 20 h after decoupling for Probe A, which has spacing of 0.05 to 0.25 mm, may also explain why the maximum nonuniform corrosion rate of Probe A was high immediately after the probe were immersed in the solution (2,000 μm/year) but deceased rapidly to less than 700 μm/year in a few hours (Fig. 4). The lower standard deviation immediately after decoupling and the higher standard deviation 20 h after decou pling indicate the coupling effect on the standard deviation (i.e., coupling caused the standard deviation to decrease). Immediately after the immersion of the probe, there was no significant coupling effect, and the anodic electrodes were forced to corrode at a relatively high rate by the cathodic electrodes because of the larger standard deviation of the potentials (or larger maximum $|\Delta E|$ caused by the more effective cathodes), which is the driving force for nonuniform corrosion. The high corrosion rates produced relatively large amount of charged aggressive species such as hydrogen ions. These aggressive species were transported to the cathodic electro des by diffusion and by electrical force applied by the potential field, causing the cathodic electrodes to be less cathodic and to provide less driving force for nonuni form corrosion. Even though the nonuniform corrosion rate as measured by the CMAS probe decreased, it does not necessarily mean that total corrosion rate, which is the sum of the nonuniform portion and the uniform portion, has decreased because the CMAS probe does not measure the uniform portion of the corrosion. This is because the electrons associated with the uniform corrosion flow only internally within the same electrodes, and they cannot be measured by the ZVA in the external circuit.

For the spatiotemporal studies of localized corrosion, the common belief is that smaller spacing is better for the multielectrode array to simulate the behavior on the surface of a one piece metal. This is because the small spacing would provide more efficient coupling through the potential field (less potential drop) and more efficient coupling through chemical interaction, which is the combination effect of both diffusion and the electrical potential field.

As a sensor, however, the efficient coupling through the chemical interaction may not necessarily mean that the CMAS probes with closely packed electrodes and smaller spacing are more accurate than the CMAS probes with far spaced elec trodes. This is because the better chemical interaction among the multiple electro des that are all packed within a small area (less than 4 mm in Probe A) causes all the electrodes in the small area to behave the same (all of them were active as evi denced by the lower potentials for all the electrodes of Probe A as shown in Table 1), and there is no cathode to maintain the corrosion potential. This may not be the case for the metal surface in plant equipment because, unlike the CMAS probe, the surface of the equipment is large and it is always possible to have areas on the plant equipment that act as the cathodes and maintain the potential of the corroding site

to a high value if localized corrosion takes place, even though such cathodic sites may be far away from the corroding sites.

The low standard deviation values immediately after decoupling, as shown in Table 1 and Fig. 5, and the initial increase and then decrease of the maximum non uniform corrosion rates, as shown in Fig. 4, also indicate that there was some cou pling through chemical interaction for Probe B, which has a spacing of 1 mm, but no apparent chemical coupling for Probe C, which has a spacing of 8 mm. When the electrodes are far spaced, there is less chemical interaction by diffusion because of the increase in the diffusion path and by the electrical potential field because the electrical field (derivative of potential with respect to distance) is low, and there is more chance for the neutrality to be satisfied by the other nonaggressively charged species that are present in the space between the electrodes. That is, the transference number of the aggressive species may be lower when the electrodes are far spaced.

For long term corrosion monitoring, the results in Fig. 3 suggests that the spacing for Probe A (0.05 0.25 mm) is probably too small because the maximum nonuniform corrosion rate from Probe A continued to decrease, and the spacing of Probe B (1 mm) and Probe C (8 mm) was probably acceptable because their long term rates were about the same, and there was no continued decreasing trend observed with these two probes. In addition, their maximum $|\Delta E|$ (about 37 mV) was significantly higher than that of Probe A (7 mV). It should be noted that the standard deviation for Probe B was still relatively low (16.5 mV; Fig. 5) immediately after the decoupling, but the ultimate driving force for the maximum nonuniform corrosion rate from the CMAS probe is the maximum $|\Delta E|$. The maximum $|\Delta E|$ is related to the standard deviation in potentials, but it does not always mean that if the standard deviation is high, the maximum $|\Delta E|$ is also high. This is because the standard deviation also accounts for the variations of the cathodic electrode poten tials, which are important to raise the coupling potentials but do not directly deter mine the corrosion rate of the most anodic electrode whose corrosion rate is used to represent the maximum nonuniform corrosion rate in Fig. 3.

Repeated measurements after repolishing show that the standard deviation of the open circuit potentials was from 11.2 to 17 mV for Probe A and 35 to 61 mV for Probe B. The ratios between the probes were all above 2.5, which confirms that the standard deviation of the open circuit potentials were all lower from Probe A than from Probe B after the side by side exposure to the same solution.

IMPEDANCE BETWEEN INDIVIDUAL ELECTRODES AND THE COUPLING JOINT

The conductivity of the solution was measured before and after the testing. Both values were approximately 44 mS/cm, which is within the range of conductivity reported for seawater. Because the coupling current on each electrode in a CMAS probe is either from or to the rest of the electrodes that are coupled together, the resistance or impedance between each individual electrode and the coupling joint of the rest of the electrodes determines how the electrical potential field is affected by the coupling currents. Table 2 shows the impedance values measured with the

TABLE 2 Impedance measured between the individual electrodes and the coupling joint before the testing (immediately after the immersion) and after the testing.

	Impedance Immediately after Immersion (ohm)			Impedance after Testing (ohm)		
Electrode	Probe A	Probe B	Probe C	Probe A	Probe B	Probe C
1	118.6	126.2	155.9	169.7	170.5	152.5
2	120.0	126.1	[b]	178.6	135.4	138.0
3	116.3	122.1	[b]	186.1	131.1	146.8
4	100.1	121.5	145.5	174.9	189.3	176.2
5	113.4	[a]	[b]	188.0	[a]	[c]
6	112.9	[a]	147.3	170.6	[a]	[c]
7	102.8	118.4	[b]	170.6	234.1	148.7
8	107.6	121.7	[b]	179.6	214.2	168.9
9	110.0	122.9	[b]	178.9	135.4	143.2
10	118.4	119.7	[b]	126.1	231.7	138.5
11	100.7	117.9	[b]	204.6	182.5	121.5
12	111.6	118.3	[b]	148.9	233.0	146.2
13	106.0	125.1	[b]	169.9	185.1	[a]
14	113.1	120.8	[b]	127.0	135.7	[c]
15	100.1	122.1	[b]	199.8	141.2	111.7
16	117.6	120.5	[b]	159.5	196.0	[a]
Average	110.6	121.7	149.6	170.8	179.6	144.7
Maximum	120.0	126.2	155.9	204.6	234.1	176.2

[a]Electrodes not used because of broken wires.
[b]Electrodes not measured (only corner and middle electrodes were measured at very start of test).
[c]Electrodes whose coating was affected by cathodic disbonding because they were cathodes and their electrode surface areas were affected.

conductivity meter for each probe at the start of the test and at the end of the test. Compared with the potentials as shown in Table 1, most of the electrodes that had lower impedance after the long term immersion were cathodic electrodes. This indicates that the increase in impedance mainly was due to the layer of corrosion products formed on the electrodes.

The average values of the impedance were 110.6 ohm for Probe A, 121.7 ohm for Probe B, and 149.6 ohm for Probe C. Comparing with the five to eight fold increase in spacing (0.05 0.25 mm for Probe A, 1 mm for Probe B, and 8 mm for Probe C), the percentage increase in impedance from Probe A to Probe C is only a fraction of the base value. Therefore, a large portion of the measured impedance was probably due to the impedance at the electrode interface; the solution resistance is probably much less than the measured values as shown in Table 2.

Nonetheless, the highest impedance was only 234.1 ohm (for Probe C). The highest corrosion rate shown in Fig. 2 was 2.25 mm/year (Probe C shortly after the immersion), which corresponds to a total current of 1.52 μA for the carbon steel electrode with a surface area of 0.785 mm^2. Thus, the highest voltage drop caused

by the highest impedance is 0.352 mV. Simulation analyses on the effect of the voltage imposed by ammeters on coupling current measurements were performed using the Butler Volmer equation [32]. The analyses concluded that the effect of 0.5 mV voltage was less than 5 % for the worst case if the $|\Delta E|$ was 20 mV or higher. The simulated cases included a large range of the Tafel slopes from the liter ature ($\beta_a = 30$ 120 mV/Dec; $\beta_c = 50$ mV/Dec to infinity). As the effect of voltage drop caused by solution resistance is similar to the effect of the voltage imposed by the ZVAs [32], the value of 0.352 mV is not significant in causing an impact on the electrical potential field for a CMAS probe. So, the spacing of 8 mm is acceptable for carbon steel probes in simulated seawater as far as the coupling through electri cal potential is concerned.

Conclusion

Experiments were conducted to study the effect of spacing in CMASs on the meas urements of nonuniform corrosion rates for carbon steel in simulated seawater. No significant differences were observed between the long term nonuniform corrosion rates from the probe that had 1 mm spacing and the probe that had 8 mm spacing. The nonuniform corrosion rate from the probe that had 0.05 to 0.25 mm spacing was marginally lower than that of the other probes. The measurements of the im pedance between the selected electrode and the coupling joint of the remaining electrodes showed that the voltage drop caused by the impedance did not strongly depend on the spacing in the range of 0.05 to 8 mm.

The preliminary data from open circuit potential measurements suggest that the CMAS probe with 16 closely packed electrodes and small spacing (0.05 0.25 mm) may have measured a slightly lower than usual nonuniform corrosion rate. This is based on the observation that the standard deviation of the open circuit potentials from the probe with 0.05 to 0.25 mm spacing was smaller than those from the probes that had a spacing of 1 mm and 8 mm by a factor of 2.5 or more.

The small variations in the open circuit potentials may be an indication that the chemical interaction among all of the electrodes packed within a small area is highly efficient. The efficient chemical interaction caused all the electrodes in the small area to be under active corrosion, and there were no effective cathodic electro des left to support the nonuniform corrosion or localized corrosion. As a sensor, the loss of effective cathodes may not represent the true situation for industrial equipment because the cathodic sites may always be available when there is local ized corrosion because the surface of the equipment is large and the cathodic sites can be in faraway locations.

References

[1] Fei, Z., Kelly, R. G., and Hudson, J. L., "Spatiotemporal Patterns on Electrode Arrays," *J. Phys. Chem.*, Vol. 100, No. 49, 1996, pp. 18986–18991.

[2] Yang, L, "Multielectrode Systems," *Techniques for Corrosion Monitoring*, L. Yang, Ed., Woodhead, Cambridge, UK, 2008, pp. 187–235.
[3] Tan, Y. J., "Monitoring Localized Corrosion Processes and Estimating Localized Corrosion Rates Using a Wire-Beam Electrode," *Corrosion*, Vol. 54, No. 5, 1998, pp. 403–413.
[4] Lunt, T. T., Brusamarello, V., Scully, J. R., and Hudson, J. L., "Interactions among Localized Corrosion Sites Investigated with Electrodes Array," *Electrochem. Solid-State Lett.*, Vol. 3, No. 6, 2000, pp. 271–274.
[5] Budiansky, N. D., Hudson, J. L., and Scully, J. R., "Origins of Persistent Interaction among Localized Corrosion Sites on Stainless Steel," *J. Electrochem. Soc.*, Vol. 151, No. 4, 2004, pp. B233–B243.
[6] Bocher, F., Presuel-Moreno, F., Budiansky, N. D., and Scully, J. R., "Coupled Multi-Electrode Investigation of Crevice Corrosion of 316 Stainless Steel," *Electrochem. Solid-State Lett.*, Vol. 10, No. 3, 2007, pp. C16–C20.
[7] Cong, H., Bocher, F., Budiansky, N. D., Hurley, M. F., and Scully, J. R., "Use of Coupled Multi-Electrode Arrays to Advance the Understanding of Selected Corrosion Phenomena," *J. ASTM Int.*, Vol. 4, No. 10, 2007, http://dx.doi.org/10.1520/JAI101248
[8] Budiansky, N. D., Bocher, F., Cong, H., Hurley, M. F., and Scully, J. R., "Use of Coupled Multi-Electrode Arrays to Advance the Understanding of Selected Corrosion Phenomena," *Corrosion*, Vol. 63, No. 6, 2007, pp. 537–554.
[9] Bocher, F. and Scully, J. R., "Stifling of Crevice Corrosion and Repassivation: Cathode Area versus Controlled Potential Decreases Assessed with a Coupled Multi-Electrode Array," *Corrosion*, Vol. 71, No. 9, 2015, pp. 1049–1063.
[10] Tan, Y., "Sensing Electrode Inhomogeneity and Electrochemical Heterogeneity Using an Electrochemically Integrated Multielectrode Array," *J. Electrochem. Soc.*, Vol. 156, No. 6, 2009, pp. C195–C208.
[11] Mahdavi, F., Forsyth, M., and Tan, M. Y. J., "Understanding the Effects of Applied Cathodic Protection Potential and Environmental Conditions on the Rate of Cathodic Disbondment of Coatings by Means of Local Electrochemical Measurements on a Multi-Electrode Array," *Prog. Org. Coat.*, Vol. 103, 2017, pp. 83–92.
[12] Hinds, G. and Turnbull, A., "Novel Multi-Electrode Test Method for Evaluating Inhibition of Underdeposit Corrosion. Part 1: Sweet Conditions," *Corrosion*, Vol. 66, No. 4, 2010, https://dx.doi.org/10.5006/1.3381572
[13] Yang, L., Sridhar, N., Pensado, O., and Dunn, D., "An In-Situ Galvanically Coupled Multi-Electrode Array Sensor for Localized Corrosion," *Corrosion*, Vol. 58, 2002, https://dx.doi.org/10.5006/1.3280789
[14] Ashida, Y. and Sumiyoshi, I., "A Multielectrode Array Sensor for Coating and Pretreatment Evaluation on Carbon Steels," Paper No. 9011, presented at *CORROSION/2017*, New Orleans, LA, March 26–30, 2017, NACE International, Houston, TX, 2017, pp. 1–9.
[15] Yang, L. and Sridhar, N., "Coupled Multielectrode Online Corrosion Sensor," *Mater. Performance*, Vol. 42, No. 9, 2003, pp. 48–52.
[16] Yang, L., Sridhar, N., Brossia, C. S., and Dunn, D. S., "Evaluation of the Coupled Multielectrode Array Sensor as a Real Time Corrosion Monitor," *Corros. Sci.*, Vol. 47, No. 7, 2005, pp. 1794–1809.
[17] Anderko, A., Sridhar, N., Yang, L., Grise, S. L., Saldanha, B. J., and Dorsey, M. H., "Validation of a Localised Corrosion Model Using Real-Time Corrosion Monitoring in a Chemical Plant," *Corros. Eng. Sci. Technol.*, Vol. 40, No. 1, 2005, pp. 33–42.
[18] Yang, B., Gershun, A. V., Marinho, F. J., and Woyciesjes, P. M., "Effect of Fluoride on Corrosion of Cooling System Metals in Ethylene Glycol-Based Antifreeze/Coolants," *J. ASTM Int.*, Vol. 3, No. 1, 2006, https://dx.doi.org/10.1520/JAI100505

[19] Yang, B., Marinho, F. J., and Gershun, A. V., "New Electrochemical Methods for the Evaluation of Localized Corrosion in Engine Coolants," *J. ASTM Int*., Vol. 4, No. 1, 2007, https://dx.doi.org/10.1520/JAI100502

[20] Pickthall, T., Morris, V., and Gonzalez, H., "Corrosion Monitoring of a Crude Oil Pipeline A Comparison of Multiple Methods," Paper No. 07340, presented at *CORROSION/2007*, Nashville, TN, March 11–15, 2007, NACE International, Houston, TX, 2007, p. 1–17.

[21] Colbert, R. and Reich, R., "Corrosion Monitoring of a Water Based Rolling Facility with Coupled Multielectrode Array Sensors and the Correlations with Other Process Variables: Conductivity, pH, Temperature, Dissolved Oxygen and Corrosion Potential," presented at *CORROSION/2008*, Paper No. 08295, New Orleans, LA, March 16–20, 2008, NACE International, Houston, TX, 2008, pp. 1–15.

[22] Chiang, K. T. and Yang, L., "Development of Crevice-Free Electrodes for Multielectrode Array Sensors for Applications at High Temperatures," *Corrosion*, Vol. 64, No. 10, 2008, pp. 805–812.

[23] Yang, L. and Chiang, K. T., "A Review of Coupled Multielectrode Array Sensors for Corrosion Monitoring and a Study on the Behaviors of the Anodic and Cathodic Electrodes," *J. ASTM Int*., Vol. 6, No. 3, 2009, https://dx.doi.org/10.1520/JAI101253

[24] Chiang, K. T. and Yang, L., "High-Temperature Electrochemical Sensor for Online Corrosion Monitoring," *Corrosion*, Vol. 66, No. 9, 2010, pp. 095002-1–095002-8.

[25] Yang, L., Chiang, K. T., Shukla, P. K., and Shiratori, N., "Internal Current Effects on Localized Corrosion Rate Measurements Using Coupled Multielectrode Array Sensors," *Corrosion*, Vol. 66, No. 9, 2010, https://dx.doi.org/10.5006/1.3490307

[26] Yang, L., Chiang, K. T., Yu, H., Pabalan, R. T., Dasgupta, B., and Ibarra, L., "Threshold Chloride Levels for Localized Carbon Steel Corrosion in Simulated Concrete Pore Solutions Using Coupled Multielectrode Array Sensors," *Corrosion*, Vol. 70, No. 8, 2014, pp. 850–857.

[27] Yang, L. and Yang, A. A., "On Zero-Resistance Ammeter and Zero-Voltage Ammeter," *J. Electrochem. Soc*., Vol. 164, No.13, 2017, pp. C819–C821.

[28] Yang, L., Sun, X., and Barnes, R., "Coupled Multielectrode Array Sensors with Solid Electrolyte-Coated Finger-Like Electrodes for Applications in Oil-Water Mixtures and Natural Gas Systems Containing Hydrogen Sulfide, presented at *CORROSION/2014*, Paper No. 4406, San Antonio, TX, March 9–13, 2014, NACE International, Houston, TX, 2014.

[29] Papavinasam, S., "Electrochemical Techniques for Corrosion Monitoring," *Corrosion Monitoring Techniques*, L. Yang, Ed., Woodhead, Sussex, UK, 2008, p. 80.

[30] Dorsey, M. H., Licina, G. J., Saldanha, B. J., and Ebersole, R. C., "Monitoring for Corrosion and Microbiological Activity in a Cooling Water System," presented at *CORROSION/2002*, Paper No. 02009, Denver, CO., April 7–11, 2002, NACE International, Houston, TX, 2002, p. 14.

[31] Southwell, S. R. and Alexander, A. L., "Corrosion of Metals in Tropical Waters, Structural Ferrous Metals," *Mater. Prot*., Vol. 9, No. 1, 1970, pp. 14–23.

[32] Yang, L., "Effect of Voltage between Electrodes of a Coupled Multielectrode Array Sensor on Corrosion Rate Measurement," presented at *CORROSION/2016*, Paper No. 7911, Vancouver, BC, March 6–10, 2016, NACE International, Houston, TX, 2016, pp. 1–14.

STP 1609, 2019 / available online at www.astm.org / doi: 10.1520/STP160920170205

H. Burak Gunay,[1] Mustafa Salehi,[2] Sankara Papavinasam,[3]
Nihal U. Obeyesekere,[4] and O. Burkan Isgor[5]

Investigation of Corrosion Inhibitor Persistency Using Electrochemical Quartz Crystal Nanobalance

Citation

Gunay, H. B., Salehi, M., Papavinasam, S., Obeyesekere, N. U., and Isgor, O. B., "Investigation of Corrosion Inhibitor Persistency Using Electrochemical Quartz Crystal Nanobalance," *Advances in Electrochemical Techniques for Corrosion Monitoring and Laboratory Corrosion Measurements*, *ASTM STP1609*, S. Papavinasam, R. B. Rebak, L. Yang, and N. S. Berke, Eds., ASTM International, West Conshohocken, PA, 2019, pp. 195–210, http://dx.doi.org/10.1520/STP160920170205[6]

ABSTRACT

This paper presents an electrochemical quartz crystal nanobalance (EQCN) and scanning electron microscopy study conducted to better understand the inhibitor film formation and destruction processes in pipelines. The kinetics of the inhibitor film formation and destruction processes were investigated through the laboratory-scale EQCN experiments. The results of this study demonstrate that the EQCN is a promising alternative to the macroscale methods that have been commonly used to study inhibitor persistency. Scanning electron microscopy results show that corrosion of specimens protected with an inhibitor film was due to pitting corrosion mostly concentrated around the flow cell inlet. Specimens on which a protective inhibitor film did not develop exhibited uniform

Manuscript received October 21, 2017; accepted for publication April 27, 2018.

[1]Dept. of Civil and Environmental Engineering, Carleton University, 1125 Colonel By Dr., Ottawa, ON K1S 5B6, Canada https://orcid.org/0000 0003 3214 700X

[2]Giatec Scientific Inc., 245 Menten Place, Suite 300, Ottawa, ON K2H 9E8, Canada

[3]CorrMagnet Consulting Inc., 6 Castlemore St., Ottawa, ON K2G 6K8, Canada

[4]Clariant Oil and Mining Services, 2730 Technology Forest Blvd., The Woodlands, TX 77381, USA

[5]Dept. of Civil and Construction Engineering, Oregon State University, 101 Kearney Hall, Corvallis, OR 97331, USA https://orcid.org/0000 0002 0554 3501

[6]ASTM Symposium on *Advances in Electrochemical Techniques for Corrosion Monitoring and Laboratory Corrosion Measurements* on November 13 14, 2017 in Atlanta, GA, USA.

corrosion. Energy-dispersive X-ray spectroscopy results show that chlorine accumulation only occurs inside the pits.

Keywords
EQCN, SEM, corrosion inhibition, kinetics of steel passivation and depassivation

Introduction

Corrosion inhibition chemicals are widely employed in the hydrocarbon industry to protect metals used in drilling, refining, production, and transport from the cor rosive effects of small amounts of aggressive phase (brine) in the large amounts of nonaggressive phase (oil).

Batch corrosion inhibition has been used in crude oil pipelines since the 1960s. The technique involves a slug of inhibitor traveling downstream with the product in a pipeline inspection gauge. Batch corrosion inhibitor use is based on a set of industry rules of thumb: (1) A protective film of 0.0254 to 0.0762 mm is assumed to form upon contact with the inhibitor [1]. The amount of inhibitor, called the inhibitor slug, is determined based upon this assumption. (2) The inhibitor needs to be diluted to increase the contact time to a minimum of 10 to 15 s [2]. (3) Acceptable dilution ratios for inhibitors are in the range of one to one and one to five [2]. Each of these variables impacts the inhibitor performance in a nebulous way. **Fig. 1** provides an overview of these variables. The effect of contact time needs to be investigated by changing the inhibitor slug, dilution rate, and the flow rate independently.

Adsorption of inhibitors occurs as a result of electrostatic forces between the ion ic charges or dipoles in the inhibitor molecules and the electric charges on the metal [3]. Consequently, an inhibitor film forms on the metal surface. These inhibitor films, despite the assumption of being 0.0254 to 0.0762 mm in thickness by the industry, range from 28 nm to 2.5 μm in thickness as suggested in the literature [1,4]. Further more, the kinetics of the inhibitor film formation process is not well understood, and research on batch corrosion inhibitor films is quite limited due to the challenges asso ciated with the use of conventional techniques such as linear polarization resistance, electrochemical impedance spectroscopy, and electrochemical noise [5,6].

FIG. 1 Factors that influence the inhibitor performance.

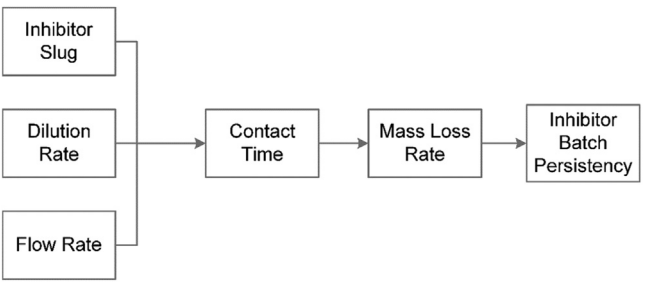

The process of selecting the corrosion inhibitors starts with a laboratory evaluation and is followed by testing/use in the field [7]. Efficiency of an inhibitor is measured by the reduction in the corrosion rate upon the addition of the inhibitor to the system [3]. Common laboratory methodologies to classify the inhibition efficiency are the wheel test, bubble test, static test, rotating disc electrode, rotating cylinder electrode, jet impingement, and rotating cage. Among these methods, the wheel test, bubble test, jet impingement, and rotating cage test rely on the weight loss measurements of macroscale coupons. The test procedures involve measuring the mass difference on coupons exposed to the simulated exposure conditions in a finite amount of time. The air formed oxides before the experiments and the corrosion products after the experiments are removed by mechanical abrasion and chemical cleaning, typically in a supersonic acid bath. The major shortcomings of measuring mass loss on macroscale coupons (e.g., 40 gr) in this fashion is that it relies on (1) the complete removal of the corrosion products from the metal surface and (2) the measurement of small mass changes (e.g., ±0.1 mg) on an analytical balance. ASTM G1 03, *Standard Practice for Preparing, Cleaning, and Evaluating Corrosion Test Specimens* [8], suggests that inadequate corrosion product removal or overcleaning can significantly affect the precision. This may lead to the misinterpretation of the corrosion rate.

On the other hand, the electrochemical quartz crystal nanobalance (EQCN) can be used to precisely study the kinetics of adsorption and dissolution of the batch inhibitor film through the associated mass gain/loss rate processes. The EQCN technique exploits the piezoelectric properties of quartz crystal (QC) integrated to an oscillator circuit. The changes in the resonance frequency of a QC exhibit an inverse linear relationship with the changes in the thin metal mass deposited on the crystal [9]. Thin metal films (approximately 100 nm thick) are deposited on the crystals using a process called sputtering. In this physical process, accelerated ions bombard solid targets in a potential gradient environment [10] to deposit thin films of metals in a precise thickness and uniformity (±1 Å). Despite the potential of EQCN to improve batch inhibitor treatment processes, only a few researchers have employed it to study inhibitor adsorption/dissolution [11 13]. Hepel and Cateforis [13] studied the copper corrosion inhibition. Cattanach et al. [11,12] studied corrosion in gas pipelines on precorrosion inhibitor employed samples.

A laboratory scale experimental procedure to estimate an inhibitor's efficiency through the mass loss rate can be developed by using a thin film deposited QC. In such a test, the oscillation inevitably stops as the mass loss causes the metal plate to uniformly (as general corrosion) or partially (as pitting corrosion) disappear, cutting the crystal off from the circuitry. Given that 1 mm/year corrosion is equivalent to a 114 nm/h mass loss rate, at typical pipeline corrosion rates with/without inhibitor presence (0.3 0.05 mm/year), the QC with a 100 nm thin metal film is expected to stop oscillating between 2 and 20 h. Using this approach the operant dependent error due to improper corrosion product removal observed in conventional approaches (e.g., using ASTM G1 03) can be eliminated.

With the long term vision to guide the development of an EQCN based inhibitor persistency test procedure, this paper presents a preliminary parametric study. The inhibitor amount, the inhibitor dilution rate, and the flow rate were the studied parameters. The kinetics of inhibitor film adsorption and dissolution, and subsequent metal mass loss, were studied with the EQCN and open circuit potential (OCP) measurements. Imaging and spectral analysis of the specimens were also necessary to better understand the inhibitor film failure mechanisms and their relationship with the batch contact time and to support the electrochemical discussions. Scanning electron microscopy (SEM) and electron dispersive X ray spectroscopy (EDS) techniques were utilized for imaging the surface topography to identify the corrosion type (i.e., pitting or uniform) and to reveal the elemental distribution of critical species such as chlorine or oxygen over the surface of failed specimens.

Experimental

EXPERIMENTAL SETUP

The experimental setup is schematically presented in **Fig. 2**. An AT cut 10 MHz QC is oscillated using an oscillator circuit. The oscillator is designed to withstand the viscous inhibitor batch. The QC has two thin metal films (approximately 100 nm) sputtered on both sides of it. One of these (gold, Au) is in contact with the air and is assumed to be inert in air. The other one (iron, Fe) is in contact with the flowing brine, which was 3.5 % aerated sodium chloride (NaCl) solution (pH = 6.8). The experimental solution is prepared by dissolving analytical grade NaCl inside deionized water. A syringe infusion pump with less than 0.2 % reproducibility is used to sustain the flow between the inlet and outlet reservoirs. The OCP is measured with respect to a silver silver chloride (Ag AgCl) reference electrode. The frequency of the working oscillator is subtracted from a precision reference oscillator of 10 MHz to accurately measure frequency changes due to mass variations on the QC. A commercial EQCN flow cell (**Fig. 3a**) is used. The flow cell is kept inside a Faraday cage at all times. **Fig. 3b** shows one of the QCs used in this study.

A widely used commercial oil soluble corrosion inhibitor is used in this study. Batch inhibitor use is simulated by pumping a slug of inhibitor over the iron for a certain period prior to the experiment. The inhibitor batch is prepared by diluting with analytical grade methanol to ratios between 1:4 and 1:20. The frequency measurements are converted to mass changes using the following equation [9]:

$$\Delta f = -\frac{2f_o^2}{A\sqrt{\rho_q \mu_q}}\Delta m \tag{1}$$

where:

f_o = frequency of the unloaded QC, Hz,
A = area of the piezoelectrically active surface, m^2,

FIG. 2 Experimental setup.

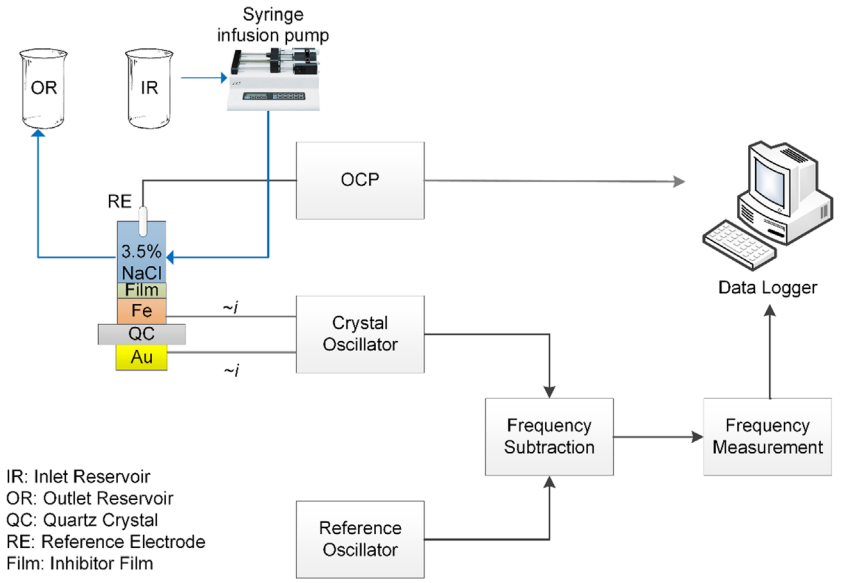

FIG. 3 EQCN (a) flow cell and (b) quartz crystal.

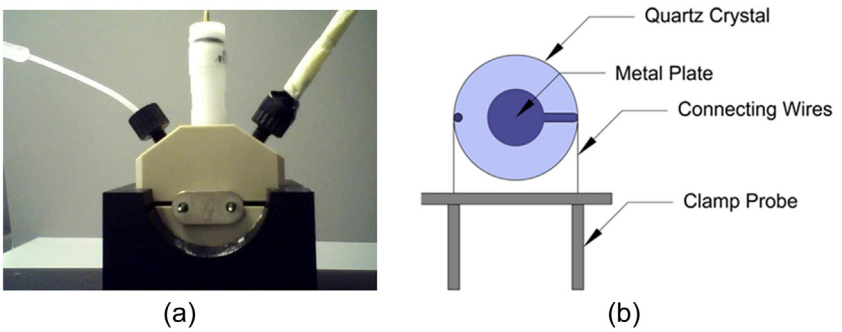

ρ_q = density of the quartz, kg/m^3, and

μ_q = shear modulus of the AT cut QC, N/m^2.

For small mass changes of 10 MHz QC, Eq 1 is reduced to an inverse linear relationship as follows (Eq 2):

$$\Delta f = -0.867 \Delta m \tag{2}$$

The SEM and EDS analyses are carried out using a TESCAN VEGA II XMU VPSEM (Brno, Czech Republic) and Oxford Instruments Inca Energy 250X EDS

(Abingdon, UK), respectively. A copper conducting tape is attached to the specimens to sustain a current flow of 1 pA to 2 μA. A small portion of this copper tape is included in the SEM images as a visual reference, meaning that if a location on the image is darker than the copper tape, it indicates that its atomic mass is smaller than the copper. The elements that have a smaller atomic mass than copper include Fe, oxygen (O), and chlorine (Cl) elements commonly observed on a corroding iron surface. In regions where elements with an atomic mass larger than Cu are found (distinguishable with a lighter color than the Cu tape), we can interpret that the Fe on the QC is thoroughly consumed and SEM imagery points out the Au substrate only. Moreover, EDS analysis provides auxiliary information about the elemental composition such as silicon (Si) from the quartz substrate, carbon from the organic contamination, or Au from the noble side of the crystal. We removed these elements when we presented the EDS results.

EXPERIMENTAL PROGRAM

Batch inhibitor application is simulated by pumping the batch inhibitor through 1.3 mm diameter silicon tubing. The EQCN flow cell is located between the inlet reservoir and the outlet reservoir (Fig. 3a). As the inhibitor batch is slowly pumped from the inlet reservoir, it comes into contact with the iron electrode mounted on the QC. The contact time of the inhibitor batch is varied by changing the inhibitor amount, dilution rate, and the flow rate during the batch inhibitor application. Table 1 shows the experimental program.

All independent variables (i.e., inhibitor slug, dilution rate, and flow rate during the batch inhibitor application) are varied individually by keeping the other two constant. This way the effect of changing the contact time by changing any of these independent variables individually can be studied. The inhibitor slug is varied from

TABLE 1 Experimental program.

Analysis	Contact Time (s)	Inhibitor Slug (μL)	Dilution Rate (%)	Flow Rate (μL/min)
Inhibitor slug	9	9	15	400
	15	15	15	400
	23	23	15	400
	45	45	15	400
Dilution rate	9	15	25	400
	15	15	15	400
	23	15	10	400
	45	15	5	400
Flow rate	9	15	15	667
	15	15	15	400
	23	15	15	266
	45	15	15	133

9 to 45 μL. The dilution rate is varied from 5 % to 25 %. The flow rate during the batch inhibitor application is varied from 133 to 667 μL/min.

Once an inhibitor batch application is complete, a brine solution starts to be pumped. The iron electrode remains exposed to the brine solution until the QC fails to oscillate. The flow rate in the tubing is selected through a nondimensional analy sis to scale down a generic crude oil pipe 0.75 m in diameter and 1 m/s flow rate. The non Newtonian viscosity at room temperature and the density of the waxy crude oil are assumed as 400 mPa/s and 800 kg/m^3, respectively. Thus, the flow rate of the brine in the 1.3 mm diameter silicon tubing is selected as 400 μL/min.

In order to verify the experimental reliability, a few duplicate experiments were conducted. Fig. 4 shows two sets of repeat experiments: (a) 9 s of batch exposure at 25 % dilution and 400 μL/min flow rate and (b) 15 s of batch exposure at 15 % dilu tion and 400 μL/min flow rate. Mass change and the OCP data for the repeats at 9 s of batch exposure at 25 % dilution and 400 μL/min flow rate show high repeatabili ty, as shown in Fig. 4a. Mass reduction in both specimens continues at an increasing rate, reaching approximately −5,000 ng just before the QCs stop oscillating. The OCP is approximately −0.33 V/Ag AgCl. The QCs stop oscillating after approxi mately 300 min of exposure to the flowing brine. Mass change and the OCP data for the repeats of 15 s of batch exposure at 15 % dilution and 400 μL/min flow rate show similar mass change and OCP responses, as shown in Fig. 4b. The results indi cate that a 550 ng thick inhibitor film forms on the specimens. The OCPs of both specimens converge to approximately −0.1 V/Ag AgCl after 720 min of exposure to the flowing brine. The QCs stop oscillating after approximately 900 min and approximately 1,000 min after the inhibitor application.

Failed QCs are then taken to a desiccator to eliminate further oxidation of the specimens and kept until the microscopic and spectral analyses are carried out.

FIG. 4 Verification of the experimental reliability by repeating (a) 9 s of batching at 25 % dilution and 400 μL/min flow rate and (b) 15 s of batching at 15 % dilution and 400 μL/min flow rate.

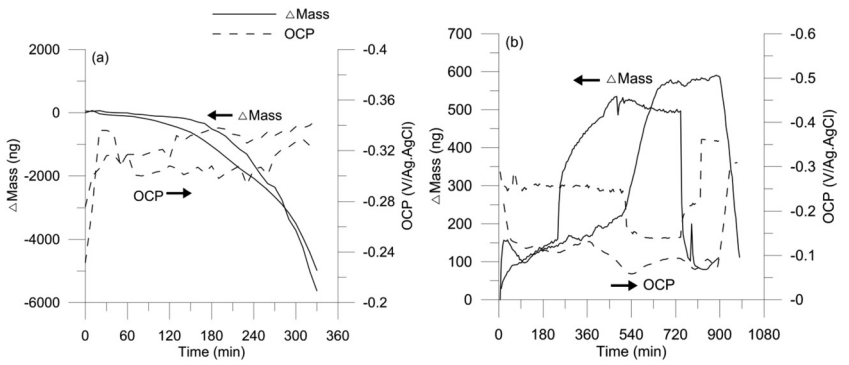

Images of the specimens are taken at ×40 to reveal the overall topography and up to ×5,000 to reveal the pit distribution and geometry. Spectral analysis is carried out inside the visible pits, protected surfaces, and thoroughly corroded surfaces to show the differences among the relative distribution of Fe, O, and Cl at locations with different levels of activity.

Results

INHIBITOR SLUG ANALYSIS

Fig. 5 shows the change in mass and OCP of the iron upon a 9 s, 15 s, 23 s, and 45 s exposure to a 15 % diluted inhibitor solution (e.g., the inhibitor slug is varied from 9 μg to 45 μg). Results reveal that extending the contact time increases the in hibitor film adsorption amount. The inhibitor films formed on the 0.2 cm^2 iron electrodes are 200 (Fig. 5a), 500 (Fig. 5b), 450 (Fig. 5c), and 800 ng (Fig. 5d) for 9, 15, 23, and 45 s of batch inhibitor exposure, respectively; 15 (Fig. 5b), 23 (Fig. 5c), and

FIG. 5 The change in mass and the OCP of the iron after (a) 9 s, (b) 15 s, (c) 23 s, and (d) 45 s of batching with 15 % diluted inhibitor inside flowing brine at a 400 μL/min rate by varying the inhibitor slug 9 to 45 μL.

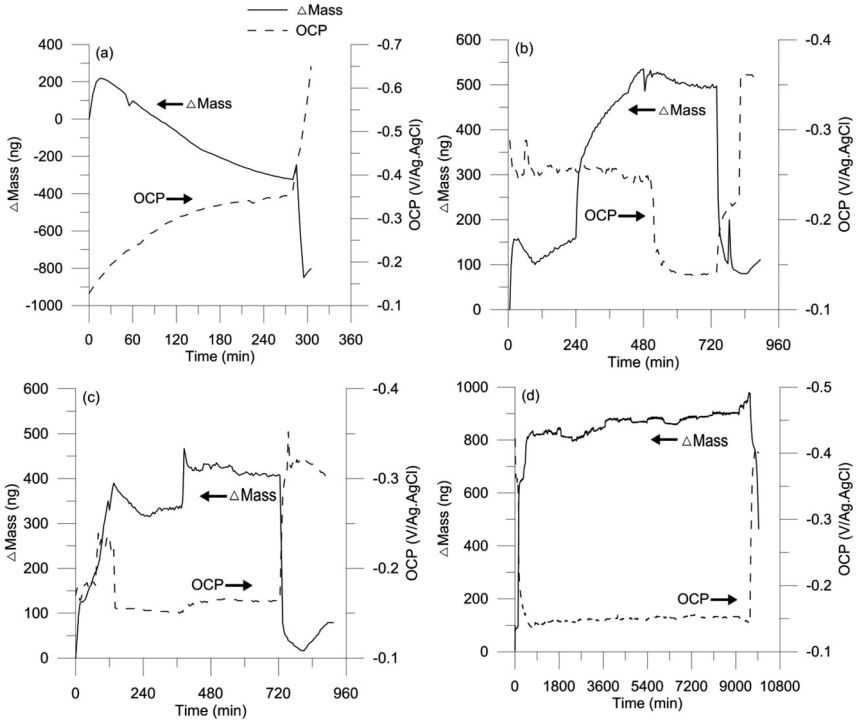

45 s (Fig. 5d) of inhibitor batch exposure results in an increase in the OCP during the film formation process. This can be interpreted as a reduction in the surface activity during the inhibitor film formation. However, the OCP of the specimens exposed to the inhibitor batch for only 9 s (Fig. 5a) does not increase. This can be explained as the inhibitor film that forms upon 9 s of batch inhibitor contact on the iron surface is not protective. The inhibitor film formation is followed by a passive state in OCP (less than −0.2 V/Ag AgCl) and a relatively stable mass change in specimens exposed to the batch inhibitor for 15 (Fig. 5b), 23 (Fig. 5c), and 45 s (Fig. 5d). This passive state is ended with a reduction in the OCP (greater than −0.3 V/Ag AgCl) and in the iron mass after 720 min for 15 and 23 s of batch inhibitor exposure and after 10,000 min for 45 s of batch inhibitor exposure. This can be explained as the initiation of pitting after the loss of the inhibitor film. Without the inhibitor film, iron experiences active corrosion in the 3.5 % NaCl solution with a pH of 6.8. At this pH, iron does not produce a passive film, and the oxide film that forms due to this corrosion is not protective. Shortly after the loss of passive state, the QC stops oscillating. In brief, the results indicate that a relatively better inhibition efficiency can be achieved by increasing the inhibitor to iron contact time through an increase in the inhibitor slug.

DILUTION RATE ANALYSIS

Fig. 6 shows the changes in the mass and the OCP of the iron electrodes upon 9, 15, 23, and 45 s of exposure to a diluted inhibitor batch with a 15 μg inhibitor. In order to increase the contact time without changing the inhibitor slug, the batch dilution ratio is increased from 1:4 to 1:20. Results show that changing the contact time by increasing the dilution rate affects the inhibitor film adsorption kinetics. The inhibitor films formed on approximately 0.2 cm^2 iron electrodes are 100 (Fig. 6a), 500 (Fig. 6b), 450 (Fig. 6c), and 600 ng (Fig. 6d) for 9, 15, 23, and 45 s of batch exposure, respectively. OCP results can be interpreted as an indication of the corrosion induced surface activity; 15 (Fig. 6b), 23 (Fig. 6c), and 45 s (Fig. 6d) of batch inhibitor exposure on the iron electrodes yield an increase in the OCP during the film formation process. This can be interpreted as a reduction of the surface activity during the inhibitor film formation. However, the OCP of the specimens exposed to the batch inhibitor for only 9 s (Fig. 6a) does not increase. This can be explained as the inhibitor film formed after 9 s of batching is not protective. The inhibitor film formation is followed by a passive state in the OCP (less than −0.2 V/Ag AgCl) and a relatively stable mass change in the specimens exposed to the batch inhibitor for 15 (Fig. 6b), 23 (Fig. 6c), and 45 s (Fig. 6d). This passive state is ended with a reduction in the OCP (greater than −0.3 V/Ag AgCl) and a decreasing trend in the electrode mass after 720 min for 15 s, after 2,400 min for 23 s, and after 3,000 min for 45 s of batch inhibitor exposure. This can be explained as the initiation of pitting after the loss of the inhibitor film. Shortly after the loss of a passive state, the QC stops oscillating. Simply put, a relatively better inhibition efficiency can be achieved by increasing the inhibitor to iron contact time through an increase in the inhibitor batch dilution rate.

FIG. 6 The change in mass and the OCP of the iron after (a) 9 s, (b) 15 s, (c) 23 s, and (d) 45 s of batching with a 15 μL inhibitor slug inside flowing brine at a 400 μL/min rate by varying dilution rate from 25 % to 5 %.

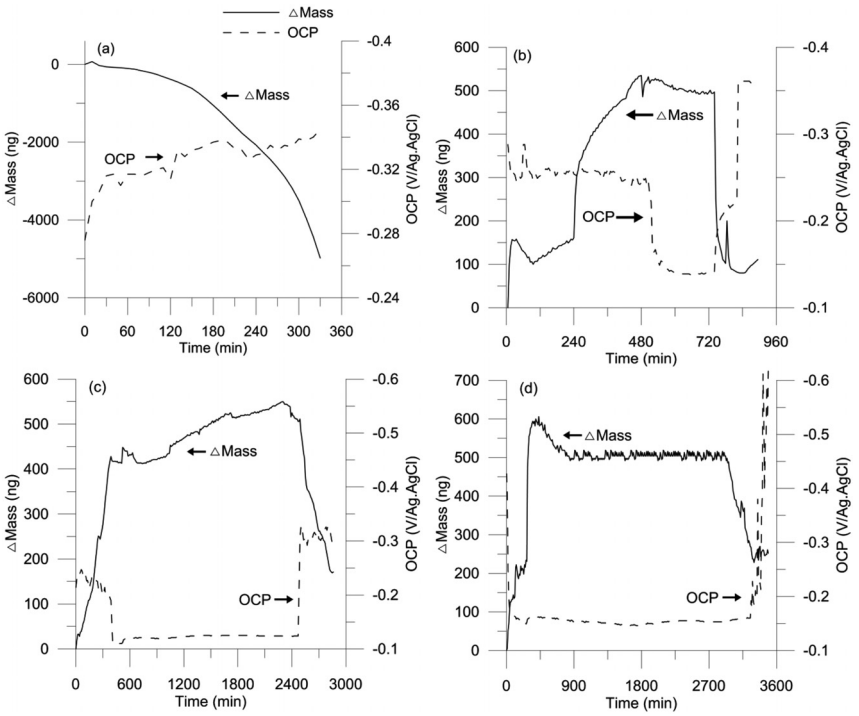

FLOW RATE ANALYSIS

Fig. 7 shows the changes in the mass and the OCP of the iron electrode upon 9, 15, 23, and 45 s of exposure to 15 μg of inhibitor batch at 15 % dilution rate. In order to change the inhibitor to iron contact time, the flow rate during the inhibitor batch application is varied from 166 to 667 μL/min. However, it should be noted that the flow rate after the batch application remained 400 μL/min to keep the experimental conditions consistent. Results show that changing the contact time by decreasing the flow rate affects the inhibitor film adsorption kinetics. The films developed on the 0.2 cm^2 iron electrodes resulted in a mass change of 100 (Fig. 7a), 500 (Fig. 7b), 450 (Fig. 7c), and 550 ng (Fig. 7d) after 9, 15, 23, and 45 s of batch inhibitor exposure, respectively. The OCP of the electrodes after 15 (Fig. 7b), 23 (Fig. 7c), and 45 s (Fig. 7d) of batch inhibitor application attained values more than −0.2 V/Ag AgCl. This can be interpreted as lower surface activity, which can be related to a protective inhibitor film. However, the OCP of the specimens after 9 s (Fig. 7a) of batch inhibitor application was less than −0.3 V/Ag AgCl. This can be

FIG. 7 The change in mass and OCP of the iron after (a) 9 s, (b) 15 s, (c) 23 s, and (d) 45 s of batching with a 15 μL inhibitor slug inside flowing brine at a 15 % dilution rate by varying the flow rate from 133 to 667 μL/min.

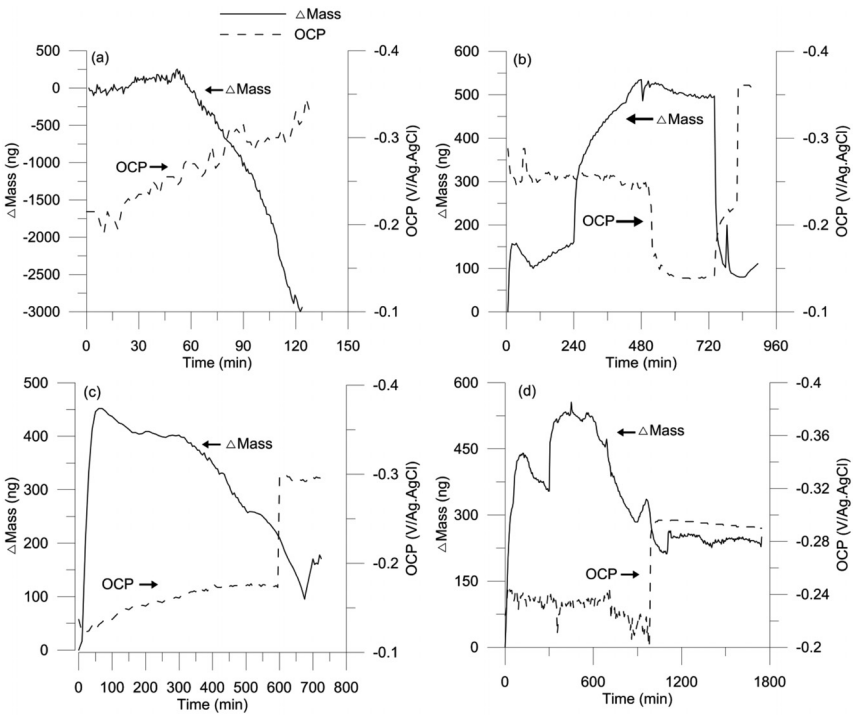

explained as the inhibitor film that formed after 9 s of batching may not be protec tive. This passive state is ended with a potential drop and a reduction in the elec trode mass. Shortly after the loss of the passive state, the QC stops oscillating. In brief, our preliminary observations point out that the flow rate during an inhibitor batch application is an important parameter influencing the effectiveness of the application.

MICROSCOPIC AND SPECTRAL ANALYSIS

SEM images shown in Fig. 8b indicate that the specimens that were exposed to the inhibitor batch for 15, 23, and 45 s exhibit pitting corrosion concentrated at the flow cell inlet. In these failed QC specimens (i.e., specimens no longer oscillate due to the loss of iron electrode continuity), the metal loss is partial. The EDS results at a pit location (as shown in Fig. 9b) reveal the relative mass ratio of Fe, O, and Cl as 0.51, 0.44, and 0.05, respectively. However, EDS results for the same specimen at a protected region (Fig. 9c) show the relative mass ratio of Fe, O, and Cl as 0.92, 0.08, and 0, respectively.

FIG. 8 SEM images showing the overall surface topography (×40) of samples failed after (a) 9 s, (b) 15 s, (c) 23 s, and (d) 45 s of batching.

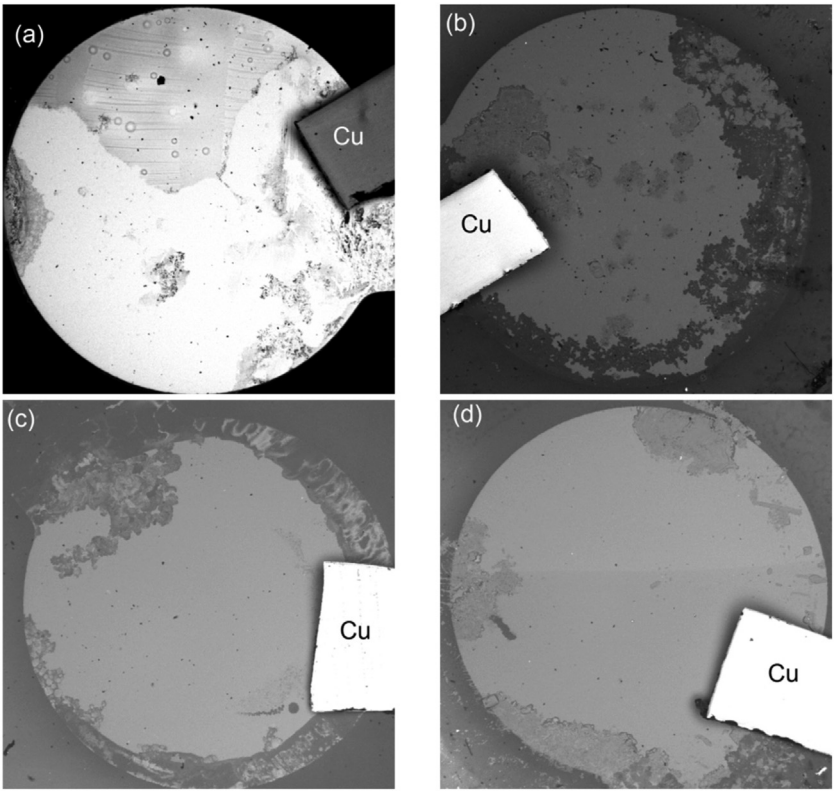

FIG. 9 Images where the EDS analysis is carried out showing the relative mass ratios of Fe O Cl at (a) a uniform corrosion region of sample shown in **Fig. 8a**, (b) a pit location of the sample shown in **Fig. 8b**, and (c) a protected region of the sample shown in **Fig. 8b**.

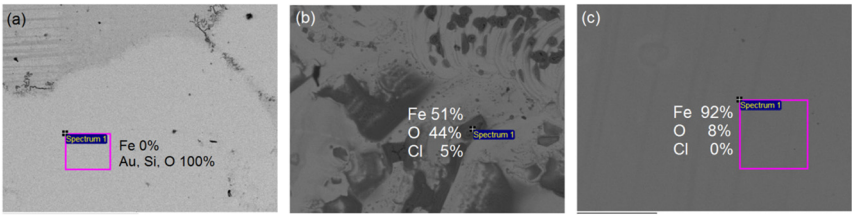

However, specimens exposed to the inhibitor batch for 9 s exhibit uniform corrosion (Fig. 8a), which confirms the inadequacy of the inhibitor films for protecting the metal substrate. The electrode surface is brighter overall than the copper reference (i.e., Au substrate dominates the image), indicating the Fe is essentially consumed on the entire surface before the QC stops oscillating. EDS results at a uniformly corroded region (Fig. 9a) confirm these observations by showing Au and Si from the substrate without any Fe.

Discussion

EQCN studies using a typical batch corrosion inhibitor that is commonly used in pipelines show that an inhibitor film of 1 to 4 μg/cm^2 can form on an iron electrode. The inhibitor film formation process is likely related to the batch inhibitor contact duration. A protective inhibitor film forms after a batch inhibitor application for 15, 23, and 45 s. The adsorbed inhibitor film, if protective, tends to have a mass of at least 2 μg/cm^2. Assuming an inhibitor density of 1 g/cm^3, the inhibitor film thickness can be estimated as 20 nm. This is in line with the microscopic/spectral observations in McMahon [4], which found that a 28 nm thick monolayer inhibitor film forms on iron.

The inhibitor film remains protective for a certain period inside a flowing brine. Then, the OCP drops. This is followed by mass loss, which can be inferred as the loss of the inhibitor film and the metal substrate. Shortly after the inhibitor film loses its protectivity, the iron on the surface of the QC is corroded, cutting off the electrical circuit and causing the QC to stop oscillating. Therefore, a correlation between the inhibition efficiency and the duration the QC continues oscillating can be suggested. Fig. 10 shows the pitting rate (C_r) in terms of mm/years. This is estimated by dividing 100 nm thick iron film by the duration the QC remained oscillating. This estimation holds because all specimens stop oscillating shortly after the inhibitor loses its protectivity. The preliminary results indicate that the pitting rate appears to exhibit an exponential relationship with the contact time (Eq 3):

$$\ln(C_r) = A \ln(t) + B \tag{3}$$

where:

C_r = pitting rate, mm/year,

t (s) = batch inhibitor contact time, s, and

A and B = multiplier coefficients.

The coefficients of the determination (R^2) values for these fits were between 0.79 and 0.88. Note that this relationship is developed with only a limited number of observations. Although the results are promising, the readers should be cautious in extrapolating them to other contexts. We plan to collect more EQCN data and seek to develop a more reliable relationship between the batch inhibitor exposure time and pitting rate.

Changing the contact time by changing the inhibitor slug, dilution rate, and flow rate results in different inhibition efficiencies. For example, increasing the

FIG. 10 Estimated pitting rate (C_r) as a function of contact time varied by changing the inhibitor slug, dilution rate, and the flow rate.

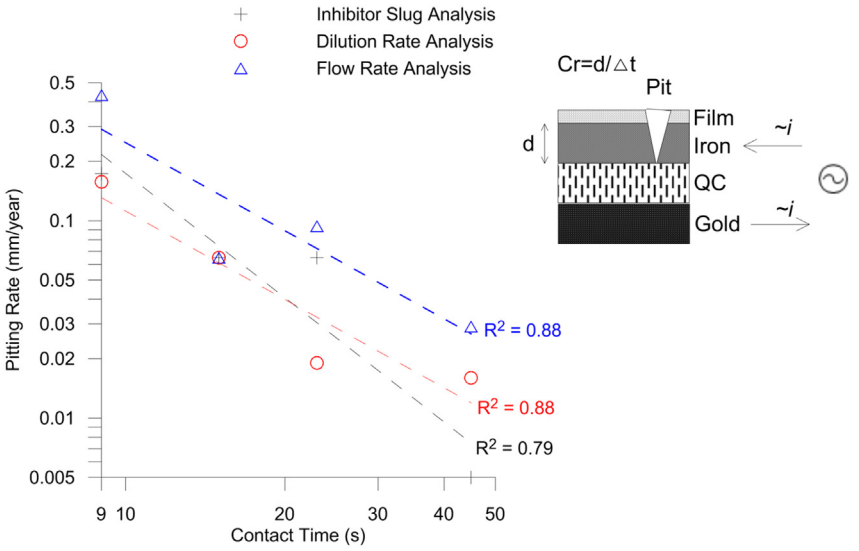

contact time to 45 s by decreasing the inhibitor flow rate yields a pitting rate greater than 0.029 mm/year. Increasing the contact time to 45 s by increasing the dilution rate results in a pitting rate greater than 0.016 mm/year. Increasing the contact time to 45 s by increasing the inhibitor slug results in a pitting rate greater than 0.005 mm/year. Similarly, 23 s of contact time acquired by an increased dilution rate results in pitting rates five times less than the same inhibitor to iron contact time acquired by the decreased flow rate (i.e., greater than 0.019 and greater than 0.094). Therefore, inhibition efficiency is a complex process related not only to the contact time but also to the way the contact time is changed.

SEM results show that the majority of the pits are located at the inlet of the flow cell. Therefore, flow assisted corrosion may be the prevailing mode of failure in a pipeline protected with an inhibitor batch. However, when batching time is not enough to develop a protective film, iron exhibits severe uniform corrosion. EDS results show that chloride likely accumulates only at active pits, while on the inhibi tor protected surfaces, chloride is not observed.

It is worth noting that the linear relationship between the frequency change and the mass change proposed by the Sauerbrey equation best applies to cases in which the deposited mass is rigid and evenly distributed onto the surface. However, it is unclear whether or not the adsorbed inhibitor film layer joins the oscillations of the QC substrate. To minimize the viscoelastic effects, the inhibitors of this study were diluted at low dilution rates (e.g., 5 % 25 %). Arguably, higher dilution rates

would have exacerbated these viscoelastic effects. A potential solution to handle the increased viscosity due to an increase in the inhibitor fraction in the batch can be using the Kanazawa and Gordon [14] relationship. However, the main objective of this paper was to put forward a testing procedure for inhibitor persistence assessment using the EQCN technique. The readers should be cautious in extending these preliminary results to other contexts. Future research is needed to verify the physical significance of the frequency change observations through repeated experiments and with alternative relationships to the Sauerbrey equation. Moreover, in this study, the potential explanatory variables for the inhibitor persistence (i.e., dilution rate, inhibitor slug, flow rate) were investigated in a univariate fashion. Potential multicollinearities among these variables were neglected. Future work should develop a multivariate experimental approach to examine these multivariate effects.

Conclusions

The EQCN experiments conducted on iron deposited QCs indicated the formation of an inhibitor film of 1 to 4 $\mu g/cm^2$. It was observed that the inhibition efficiency of these films depends on the iron to inhibitor contact duration. A protective inhibitor film was observed to form after a batch inhibitor exposure of 15, 23, and 45 s. The adsorbed inhibitor film, if protective, had a mass of at least 2 $\mu g/cm^2$.

It is observed that the QCs stop oscillating when the deposited iron plates experience excessive pitting. Therefore, the pitting rate could be estimated by correlating the time QCs keep oscillating in contact with the flowing brine and the thickness of the iron plates. It was found that changing the contact time by changing the inhibitor slug, dilution rate, and flow rate results in different inhibition efficiencies. Therefore, inhibition efficiency of a batch inhibitor application is a complex process related not only to the contact time but also to the way the contact time is changed. The results of this study provided experimental support for the potential use of EQCN as a technique to replace existing macroscale laboratory methodologies.

SEM results show that corrosion of the specimens protected with an inhibitor film is via pitting corrosion and that the pits were mostly concentrated near the flow cell inlet, indicating flow assisted corrosion. Specimens on which a protective inhibitor film did not develop exhibited uniform corrosion. EDS results showed that chlorine accumulation only occurs inside the pits.

References

[1] Menendez, C., Bojes, J. M., and Lerbscher, J., "Obtaining Batch Corrosion Inhibitor Film Thickness Measurements Using an Optical Profiler," *Corrosion*, Vol. 67, No. 3, 2011, https://dx.doi.org/10.5006/1.3560117

[2] Bojes, J. M., Girgis, M., Goerz, K. G., and Rippon, I. J., "A Laboratory Evaluation of the Variables That Affect the Application of Batch Corrosion Inhibitors-Phase I," presented at *CORROSION 2002*, Denver, CO, April 7–11, 2002.

[3] Papavinasam, S., "Corrosion Inhibitors," *Uhlig's Corrosion Handbook*, 3rd ed., R. W. Revie, Ed., Wiley, Hoboken, NJ, 2011, pp. 1021–1032.
[4] McMahon, A., "The Mechanism of Action of an Oleic Imidazoline Based Corrosion Inhibitor for Oilfield Use," *Colloid. Surface*, Vol. 59, 1991, pp. 187–208.
[5] Tan, Y.-J., Bailey, S., and Kinsella, B., "An Investigation of the Formation and Destruction of Corrosion Inhibitor Films Using Electrochemical Impedance Spectroscopy (EIS)," *Corros. Sci.*, Vol. 38, No. 9, 1996, pp. 1545–1561.
[6] Papavinasam, S., Revie, R., Attard, M., Demoz, A., and Michaelian, K., "Comparison of Techniques for Monitoring Corrosion Inhibitors in Oil and Gas Pipelines," *Corrosion*, Vol. 59, No. 12, 2003, pp. 1096–1111.
[7] Papavinasam, S., Revie, R., Attard, M., Demoz, A., and Michaelian, K., "Comparison of Laboratory Methodologies to Evaluate Corrosion Inhibitors for Oil and Gas Pipelines," *Corrosion*, Vol. 59, No. 10, 2003, pp. 897–912.
[8] ASTM G1-03(2017)e1, *Standard Practice for Preparing, Cleaning, and Evaluating Corrosion Test Specimens*, ASTM International, West Conshohocken, PA, 2017, www.astm.org
[9] Sauerbrey, G. Z., "Use of Quartz Vibration for Weighing Thin Films on a Microbalance," *J. Physik*, Vol. 155, 1959, pp. 206–212.
[10] Martin, P., "Ion-Based Methods for Optical Thin Film Deposition," *J. Mater. Sci.*, Vol. 21, No. 1, 1986, pp. 1–25.
[11] Cattanach, K., Ramachandran, S., Jovancicevic, V., and Sherik, A., "A New Methodology for Monitoring Corrosion under Sales Gas Conditions Using the Quartz Crystal Microbalance," presented at *CORROSION 2011*, Houston, TX, March 13–17, 2011.
[12] Cattanach, K., Jovancicevic, V., Ramachandran, S., and Sherik, A., "Development of New Corrosion Inhibitor to Prevent Black Powder Formation Using Quartz Crystal Microbalance Technique," presented at *CORROSION 2011*, Houston, TX, March 13–17, 2011.
[13] Hepel, M. and Cateforis, E., "Studies of Copper Corrosion Inhibition Using Electrochemical Quartz Crystal Nanobalance and Quartz Crystal Immittance Techniques," *Electrochim. Acta*, Vol. 46, Nos. 24–25, 2001, pp. 3801–3815.
[14] Kanazawa, K. K. and Gordon, J. G., "Frequency of a Quartz Microbalance in Contact with Liquid," *Anal. Chem.*, Vol. 57, No. 8, 1985, pp. 1770–1771.

STP 1609, 2019 / available online at www.astm.org / doi: 10.1520/STP160920170196

Sheldon W. Dean, Jr.[1]

Electrode Potential as a Key Indicator of Corrosion Performance

Citation

Dean, Jr., S. W., "Electrode Potential as a Key Indicator of Corrosion Performance," *Advances in Electrochemical Techniques for Corrosion Monitoring and Laboratory Corrosion Measurements*, *ASTM STP1609*, S. Papavinasam, R. B. Rebak, L. Yang, and N. S. Berke, Eds., ASTM International, West Conshohocken, PA, 2019, pp. 211–230, http://dx.doi.org/10.1520/STP160920170196[2]

ABSTRACT

The electrode potential of a metal surface in a corrosive environment (e.g., natural water) is a key indicator of the material's tendency to corrode. This fact has become more important as technologies for measuring the electrode potential have evolved. Electrode potential measurements are essential for assessing the performance of cathodic protection systems. These measurements have also been important in determining whether reinforcing bar in concrete is corroding. In addition, electrode potential measurements are important in the polarization resistance technique of monitoring corrosion rates. They have also been used to evaluate the tendency of alloys to develop pitting and crevice corrosion in chloride-containing environments. ASTM G215, *Standard Guide for Electrode Potential Measurement*, covers the measurement of electrode potentials, including the care and maintenance of reference electrodes used for measuring electrode potentials. This new standard is discussed along with more details on the errors and problems that can arise with these measurements.

Keywords

electrode potential, corrosion potential, polarization resistance, calomel electrode, reference electrode, polarization, liquid junction potential

Manuscript received October 11, 2017; accepted for publication November 30, 2017.

[1]Dean Corrosion Technology, Inc., 306 Marshall Lndg., Glen Mills, PA 19346, USA http://orcid.org/0000 0003 0611 7384

[2]ASTM Symposium on *Advances in Electrochemical Techniques for Corrosion Monitoring and Laboratory Corrosion Measurements* on November 13 14, 2017 in Atlanta, GA, USA.

Introduction

The term "electrode potential" has been accepted to cover the reversible energy required to transport a unit of positive electrical charge across the electrode interface with its environment [1]. This term includes surfaces that are polarized by current flowing through the interface as well as surfaces that do not have any current flowing from external sources. In the case where no external sources of current are present, the potential is usually designated as the "corrosion potential." The term "electrochemical potential" has also been used occasionally for these values, but this term has long been used to designate the partial derivative of the total electrochemical Gibbs free energy of a system with respect to the concentration of a specific ion in the solution. In order to avoid confusion, the term "electrochemical potential" should not be used to refer to electrode potential [1].

The concept of electrode potential was developed in the nineteenth century by physical chemists, including Nernst, Haber, and Arrhenius [2]. When the mechanism of most corrosion processes was recognized to be electrochemical in nature, the importance of electrode potential became apparent [3]. The use of electrode potential measurements in corrosion monitoring and testing became more prevalent when instruments became available that allowed accurate potential measurements to be made using extremely small currents. This then enabled the use of reference electrodes without the risk of encountering errors caused by polarizing the reference electrode.

Thereafter, the development of the potentiostat occurred, and that has allowed electrochemical corrosion testing to be based on electrode potential as an independent variable. Although electrode potentials do not include any loss that occurs from current flowing in the environment, such losses can occur with most measurement systems, which results in an error in the result. In most cases, this error can be minimized using design features, but an error is still present.

The purpose of this paper is to review the applications where electrode potential measurements are used, including corrosion testing, corrosion monitoring, and cathodic protection. These different applications have different requirements for accuracy and precision, so it is important to understand the requirements of the application to be able to assess the importance of the errors that can occur.

Thereafter, the various reference electrodes that are used for these measurements are discussed, and information is provided on the maintenance and storage of reference electrodes so that they can be used with confidence.

Applications Using Electrode Potential Measurement

CORROSION RATE ESTIMATION BY POLARIZATION RESISTANCE

Electrode potential measurements are used in corrosion rate estimation by at least two techniques. The polarization resistance approach uses the Stern Geary analysis

of charge transfer kinetics [4]. In corrosion monitoring situations, the corrosion potential is established, and then the test electrode is polarized either ±10 mV. The current is measured when it becomes stabilized (i.e., when the current drift is less than about 1 % in a 10 min period) [5]. In the two electrode system, it is assumed that each electrode has a 10 mV polarization so that the total potential drop across the two electrodes is 20 mV. The resistance loss in the solution is ignored.

In the three electrode system, one of the electrodes is used as the working elec trode, so the system polarizes this electrode either ±10 mV, and the current is mea sured. The second electrode is the auxiliary electrode that supplies the current, and the third electrode is used as the reference electrode. In both the two and three electrode systems, the electrodes are often identical in size, shape, and alloy, but in some cases a platinum mesh counter electrode is used. The current supplied to achieve the 10 mV polarization is approximately proportional to the corrosion rate so the system can be used as a continuous monitor of the rate. However, in systems where the resistivity of the solution is significant, the error that results causes the rate to be underestimated, and the magnitude of this error is proportional to the solution resistivity [6].

CORROSION RATE ESTIMATION BY POTENTIAL SCAN

The potential scan technique for corrosion rate estimation also assumes that the corrosion reactions are limited by charge transfer kinetics. These kinetics show an exponential relationship between the current density and electrode potential. At electrode potentials near the corrosion potential, both anodic and cathodic reac tions are occurring at rates that are similar, so only the difference between these two currents is flowing in the external circuit. However, if the polarization is increased in either direction, a linear relationship should be found when the loga rithm of the current density is plotted against the electrode potential. The corrosion rate can then be estimated by extrapolating this line back to the corrosion potential (**Fig. 1**) [7]. As a practical matter, the linear relationship usually develops when the polarization exceeds 50 mV from the corrosion potential. The procedure for calcu lating corrosion rates from current density measurements is covered in ASTM G102, *Standard Practice for Calculation of Corrosion Rates and Related Information from Electrochemical Measurements* [6].

DETERMINING PASSIVITY

Metals that develop a thin, nonporous layer of corrosion product on their surface usually exhibit a rate of corrosion that is limited by the solubility of this layer. This condition is known as passivity, and it is observed with many metals and alloys. One consequence of this process is that, as the layer develops, the corrosion poten tial of the metal increases significantly. Therefore, the corrosion potential of a metal can be used to reveal if the metal is in a passive condition. This phenomenon has been used in the case of carbon steel rebar in concrete [8]. The aqueous solution that results when concrete is wet contains a significant concentration of calcium

FIG. 1 Schematic plot of a corrosion process in which both anodic and cathodic reactions are charge transfer controlled and showing Tafel behavior, from ASTM G3 [7].

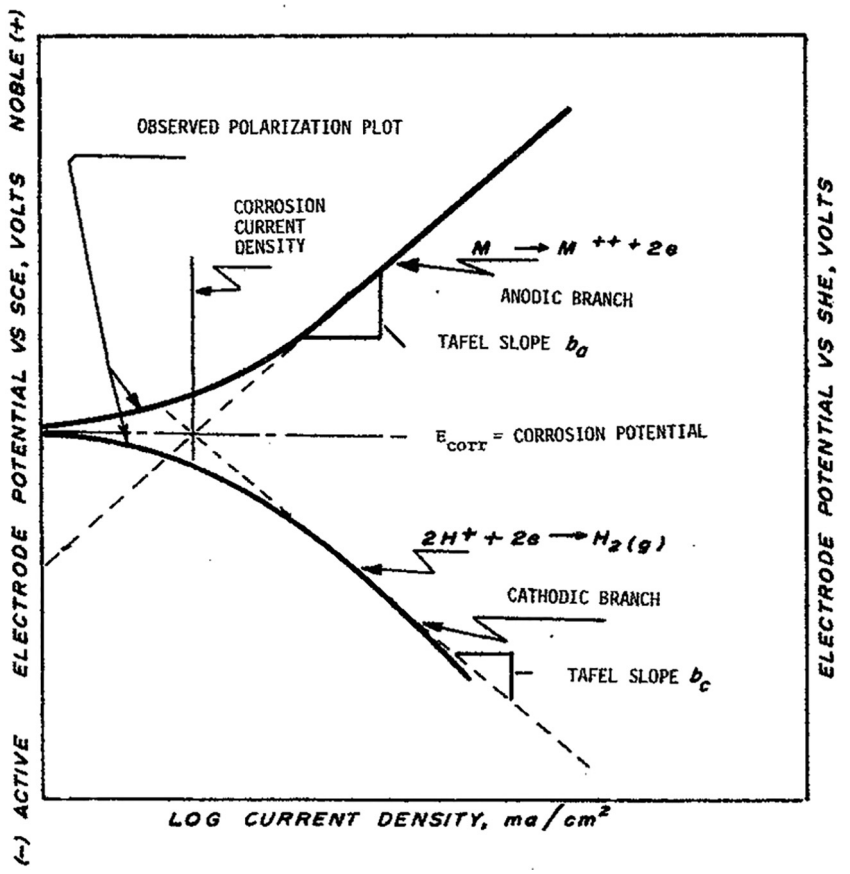

hydroxide that causes the pH of the solution to be around 12 or above. As a result, the steel rebar in the concrete is passive, and its corrosion potential reflects this condition. However, if the concrete has become carbonated from long exposure to the carbon dioxide in the atmosphere, or if chlorides from road salt application or marine exposure have permeated into the concrete, the passive condition may be compromised, and accelerated corrosion of the steel can occur. The corrosion potential of the rebar will reflect this condition by showing a significant decrease. This fact has been used as an evaluation technique to signal when serious damage is likely in concrete structures such as bridges and parking garages.

A similar situation occurs with stainless steels in concentrated sulfuric acid. Usually sulfuric acid at concentrations above 92 % contains sufficient oxidizing

agents to maintain stainless steel alloys, such as Type 304L (UNS S30403), in a pas sive condition at ambient temperature. However, if the acid contains reducing agents such as certain organic impurities, or if the acid is warmed above the temperature where the passive layer dissolves, accelerated corrosion will occur. The corrosion potential of the steel will reflect this situation by showing a negative shift when the accelerated corrosion occurs. As a result, corrosion potential monitoring has been an effective way to monitor stainless steels in concentrated sulfuric acid systems.

TESTING FOR PITTING AND CREVICE CORROSION

In the case of alloys that owe their corrosion resistance to their ability to retain their passive film in oxidizing conditions, the phenomena of pitting and crevice corro sion are important failure mechanisms that can occur in certain environments. In these environments, the passive film protecting the metal will tend to break down locally when the electrode potential exceeds a specific value. If the electrode poten tial is decreased, the accelerated corrosion will cease when the potential reaches the repassivation potential. It is generally believed that alloys with higher repassivation potentials are more resistant to pitting and crevice corrosion than alloys with lower values. Crevice corrosion occurs in areas where the surface is partially shielded from the environment, and it usually initiates at lower electrode potentials than pitting. Pitting corrosion initiates at inclusions and other singularities in the passive film.

In either case, the localized attack will continue unless the electrode potential falls below the repassivation potential. The question of how to measure the repassi vation potential has been addressed in several ASTM test methods, including ASTM G61, *Standard Test Method for Conducting Cyclic Potentiodynamic Polariza tion Measurements for Localized Corrosion Susceptibility of Iron , Nickel , or Cobalt Based Alloys* [9], ASTM G100, *Standard Test Method for Conducting Cyclic Galvanostaircase Polarization* [10], and ASTM G192, *Standard Test Method for Determining the Crevice Repassivation Potential of Corrosion Resistant Alloys Using a Potentiodynamic Galvanostatic Potentiostatic Technique* [11]. ASTM G150, *Standard Test Method for Electrochemical Critical Pitting Temperature Testing of Stainless Steels and Related Alloys* [12], was created to determine the critical pitting temperature for iron base alloys with chromium and molybdenum additions such as UNS S31603 and UNS S31254. In this case, the specimen electrode is held at +0.700 mV versus saturated calomel electrode (SCE) as the temperature is increased. When pitting occurs, the current required to maintain this potential increases abruptly.

TESTING FOR INTERGRANULAR CORROSION

Stainless steels have long been known to be susceptible to intergranular corrosion if the carbon content of the alloy is allowed to react with the chromium in the alloy during a high temperature exposure. The reaction occurs most rapidly at grain boundaries where the area adjacent to the grain boundary becomes depleted of chromium, with the result that these areas tend to suffer accelerated attack in

corrosive environments. Chemical tests have been used detect this condition, which is known as sensitization [13]. However, the electrochemical reactivation (EPR) test, ASTM G108, *Standard Test Method for Electrochemical Reactivation (EPR) for Detecting Sensitization of AISI Type 304 and 304L Stainless Steels* [14], was devel oped by the nuclear industry as a quantitative measurement of the degree of sensiti zation. This test relies on the fact that sensitized Type 304 and Type 304L (UNS S30400 and S30403) will exhibit a significant anodic current increase when their electrode potential is scanned from a positive passive value in the negative direction as the potential approaches the primary passivation potential. The method mea sures the electric charge that passes during reverse scan from +200 mV versus SCE to 50 mV above the corrosion potential with a scan rate of −1.67 mV/s. The specimen is examined after the scan to determine the grain boundary area, and the measured charge value is divided by the grain boundary area exposed to the envi ronment. In this case, the environment is 0.50 M sulfuric acid, H_2SO_4 + 0.01 M potassium thiocyanate.

TESTING ALUMINUM ALLOYS FOR HEAT TREATMENT CONDITION

The mechanical properties of precipitation hardening aluminum alloys are largely determined by the degree to which certain elements, such as copper and zinc, pre cipitate from solid solution. This precipitation process is carried out by heat treat ments. However, the corrosion potential of these alloys in certain environments is also determined by the solid solution content of these elements in the alloys. As a result, the heat treatment of the alloy can be determined by measuring the corrosion potential in the test solution. This approach provides a rapid and nondestructive method for establishing the condition of the alloy. ASTM G69, *Standard Test Method for Measurement of Corrosion Potentials of Aluminum Alloys* [15], uses the corrosion potential of aluminum alloys measured against an SCE in a 1.0 M sodium chloride solution containing 3 g/L hydrogen peroxide at 25°C. The measured potential value can then be compared to the required values for the alloy and heat treatment condi tion. Although this test method was developed as an acceptance test for high strength aluminum alloys, it can also be used in failure analyses.

CONTROL AND EVALUATION OF CATHODIC PROTECTION SYSTEMS

Cathodic protection systems are widely used to provide protection for steel struc tures and pipelines in soil and aqueous environments. In these cases, the steel usual ly is coated, and the cathodic protection provides protection for holidays in the coating [16]. Buried pipelines are major users of cathodic protection systems. Because the rate of penetration from corrosion occurs as rapidly at a holiday in the coating as it would if no coating were present, the cathodic protection system is essential in maintaining these pipelines as leak free. Flat bottom storage tanks and buried fuel tanks are similar in that the coating system usually is not sufficient to ensure a leak free condition for long term performance [17]. Steel structures in aqueous environments are also coated to protect them from corrosion damage, and

cathodic protection is used to protect holidays in the coating systems in these applications.

Electrode potential measurement is an important monitoring method for cathodic protection systems. In this case, the measurement approach must deal with the potential field that the current flow in the environment creates. The reason for this is that the reference electrode usually cannot be placed close to the point where the polarization of the electrode is occurring. In most cases, the current interruption method is used to obtain the electrode potential of the surface in question.

In soils, the copper/saturated copper sulfate electrode (CSE) reference electrode is most commonly used. This electrode is not used in marine applications because chloride contamination causes a significant error. Silver/silver chloride electrodes and pure zinc electrodes are often used in these cases [18].

One approach in using this technology is to establish that the item under protection is at a potential more negative than −0.850 mV versus CSE. At this level, the rate of corrosion is negligible. Another approach is to determine how much polarization has occurred because of the cathodic protection current. If the electrode potential shows a negative shift greater than 100 mV, the protection level generally is accepted as sufficient [16].

HYDROGEN OVERVOLTAGE AND PERMEATION MEASUREMENT

In aqueous systems, the reduction of hydrogen ions is a common cathodic reaction. This reaction is shown in Eq 1.

$$2H_3O^+ + 2e^- \rightarrow H_2(g) + 2H_2O \tag{1}$$

This equilibrium potential, E (volts), for this reaction at 25°C and 101.3 kPa hydrogen partial pressure, is given by Eq 2.

$$E = -0.0597(\text{pH}) \tag{2}$$

An electrode in an aqueous solution at a potential of U (volts) on the standard hydrogen scale will have a hydrogen overvoltage, HOV, given by Eq 3 [18].

$$HOV = E - U \tag{3}$$

The hydrogen overvoltage is an important parameter in understanding some corrosion related issues that occur. In particular, hydrogen embrittlement cracking of high strength steels and other alloys occurs because hydrogen enters the metal and diffuses to grain boundaries in the metal. When the metal is under tensile stress, the hydrogen atoms in the grain boundaries can cause decohesion and result in crack formation. The hydrogen overvoltage provides the driving force for entry of the hydrogen atoms into the metal. The composition of the solution is also important because some compounds, such as hydrogen sulfide, promote hydrogen entry into the metal. In this case, the electrode potential is a direct contributor to the entry of hydrogen into the metal.

ASTM G148, *Standard Practice for Evaluation of Hydrogen Uptake, Permeation, and Transport in Metals by an Electrochemical Technique* [19], was developed to measure the hydrogen uptake, permeation, and transport through metals. This practice uses a two compartment test cell with the metal specimen providing a barrier between the compartments. The test solution is placed in one compartment, and the other compartment contains a solution that allows the hydrogen that emerges from the specimen to be oxidized electrochemically. The rate of oxidation is measured as the current required for the electrochemical process.

This technique was developed by Devanathan and Stachurski [20] and has been helpful in understanding the transport of hydrogen through steels and similar alloys. Hydrogen overvoltage is an important parameter in this practice.

Measurement of Electrode Potentials

STANDARD REFERENCE ELECTRODES

The process of making an electrode potential measurement is simple and easy with modern instruments. The diagram shown in **Fig. 2**, from ASTM G3, *Standard*

FIG. 2 Schematic diagram of an apparatus to measure the electrode potential of a specimen using a Luggin Haber capillary probe, from ASTM G3 [7].

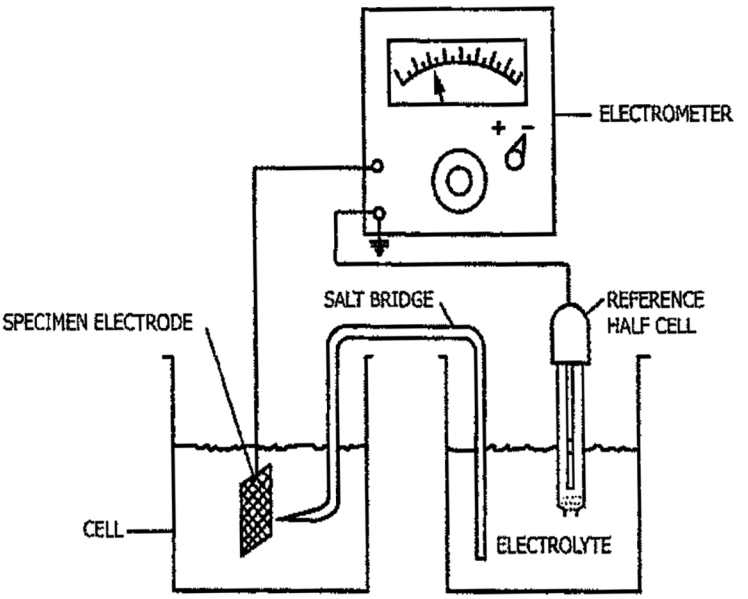

NOTE 1—The electrode potential of specimen is negative as shown.

Practice for Conventions Applicable to Electrochemical Measurements in Corrosion Testing [7], is applicable to most laboratory measurements. There are several issues that are important in making these measurements. The reference electrode is an essential element in the measurement process. In most cases, the SCE reference electrode has been the preferred reference electrode for laboratory applications because this electrode has been available, accurate, and compatible with most ambient temperature glassware setups. Commercial electrometers have sufficient input resistance so that polarization of the electrode is not an issue.

Ives and Janz published a key monograph on reference electrodes in 1961 that covers most of the theory and application of reference electrodes [21]. The concept of a reference electrode is based on the principle that the potential of an electrochemical reaction is directly proportional to the Gibbs free energy of the reaction. The free energy is determined at equilibrium conditions so the reaction is stationary. In the case of an electrochemical reaction involving a metal, the condition of equilibrium requires that the rate of oxidation (the anodic reaction) exactly equals the rate of reduction (the cathodic reaction), that is, the electrodeposition of the metal.

This condition is usually represented by an equation of the type shown in Eq 4:

$$Me = Me^{n+} + ne^{-} \tag{4}$$

where:

Me = a metal with a valence of n.

The equilibrium electrode potential of this reaction is given by Eq 5:

$$E = E^0 + 0.0592n(T + 273.2)(298.2)^{-1} \log[Me^{n+}] \tag{5}$$

where:

E = electrode potential of the half cell, V,

E^0 = standard potential of the reaction with all reactants and products at unit activity,

$[Me^{n+}]$ = activity of the Me ion,

n = number of electrons transferred (i.e., the valance of the metal), and

T = electrode temperature, °C.

Conventional practice considers the hydrogen reduction reaction at its standard state as the reference point for electrode potential values (Eq 6).

$$2H_3O^{+} + 2e^{-} = H_2(g) + 2H_2O \tag{6}$$

The standard state condition is 25°C, hydrogen partial pressure of 101.3 KPa (1.0 atm), and hydrogen ion at unit activity (pH = 0.0).

Although the hydrogen electrode can be constructed and utilized, it seldom is employed in corrosion studies because of the difficulties in setting up and maintaining this electrode.

SCE

The calomel electrode is based on the oxidation of mercury and the reduction of mercurous ions (Eqs 7 and 8):

$$2Hg + Hg_2^{++} + 2e \tag{7}$$

$$Hg_2^{++} + 2Cl^- = Hg_2Cl_2 \tag{8}$$

Calomel is the trivial name for mercurous chloride. In this case, the mercurous ion concentration is not unity but rather is determined by the solubility of mercurous ions in a chloride solution. Mercurous ions are slightly soluble in chloride environments with their concentration determined by the solubility product relationship. In the case of the calomel electrode, the chloride concentration is based on the solubility of potassium chloride (KCl). The SCE should always have KCl crystals and mercurous chloride (Hg_2Cl_2) crystals present. This electrode has been used as a reference electrode for pH meters for many years, and it has proven to be accurate and reliable in most situations.

Unfortunately, mercury has been banned by some governments in their locations because of the toxicity of some mercury compounds. As a result, it may not be possible to use these electrodes in these locations. Although this situation is still being resolved, it may be necessary to develop alternatives to the SCE.

SILVER/SILVER CHLORIDE ELECTRODE

The silver/silver chloride electrode is a possible replacement for the SCE (Eqs 9 and 10).

$$Ag = Ag^+ + e^- \tag{9}$$

$$Ag^+ + Cl^- = AgCl \tag{10}$$

This electrode is similar to the SCE in that the silver ion concentration is determined by the chloride ion concentration because silver chloride is only slightly soluble in aqueous solutions. Traditionally, the silver/silver chloride electrodes have been used with KCl concentrations of 0.1 and 1.0 M and seawater. More recently, silver/silver chloride electrodes have been supplied with saturated KCl solutions similar to the SCE. The lower chloride concentrations have the advantage of having more silver ions in solution, and that makes them less prone to polarization errors during the measurement process. However, with modern electrometers, this concern is usually not an issue. As a result the saturated KCl silver/silver chloride electrode may be the logical replacement for the SCE if that becomes necessary.

COPPER/CSE

The copper/CSE was developed for situations where a more robust reference electrode was needed (Eqs 11 and 12).

$$Cu = Cu^{++} \tag{11}$$

$$Cu^{++} + SO_4^- = CuSO_4 \tag{12}$$

These electrodes have been widely used in cathodic protection applications. The solution used for these electrodes is a saturated copper sulfate solution containing a

small amount of sulfuric acid to maintain the copper metal surface in an active state. Based on the information in Pourbaix's *Atlas of Electrochemical Equilibria in Aqueous Solutions* [22], the pH of a solution should not exceed 2.9 in order to maintain a copper surface free of an oxide film. This pH would require the addition of about 0.19 g/L sulfuric acid to attain this value. Although the addition of sulfuric acid will suppress the solubility of copper sulfate, this effect is negligible with regard to the resulting half cell potential.

The CSE is widely used for soil and similar potential measurements. It has also been used for electrode potential measurements of rebar in concrete and steel in freshwater environments. It is not applicable for seawater because of the possible contamination of the fill solution with chloride. Because of the high copper ion con tent of the fill solution, these electrodes are more resistant to polarization from the measurement process. However, in field applications, the temperature will vary so temperature corrections are necessary.

ZINC ELECTRODES

Pure zinc electrodes are used occasionally for seawater and other aqueous environ ments as reference electrodes. In these cases, the corrosion potential of the zinc is the basis for the measurement. Although these electrodes are more variable than the pre viously described electrodes, they are sufficient for some applications. Because the zinc is immersed directly in the system, there is no liquid junction potential to create an unknown error. In addition, the effective resistivity of the electrode is low, so they are not likely to show polarization effects. However, they will drift with time and tend to be less accurate than the previously described electrodes.

NONSTANDARD REFERENCE ELECTRODES

In applications where the actual value of the electrode potential is not necessary for the test, a variety of other reference electrodes can be used. The main requirement for these electrodes is that they remain stable during the procedure (i.e., their value does not drift). Probably the most widely used system employs reference electrodes that are identical to the test electrode. This approach is used in polarization resis tance measurements where the goal is to polarize the test electrode 10 mV and mea sure the current required to achieve this polarization. When these measurements are made periodically, the reference electrode is usually connected to the test elec trode during the time that measurements are not being made. This procedure helps to keep both electrodes in a similar condition.

A similar approach is used for electrochemical noise measurements [23]. The coupled multielectrode array system also uses this approach for measuring nonuni form corrosion [24].

Errors in Electrode Potential Measurements

There are a number of different types of errors that can arise in electrode potential measurements. These errors can result from potential drops in the environment

when the reference electrode is not placed close to the test electrode, and current is flowing in the environment where the electrodes are placed. Another source of error occurs when reference electrodes have a specific environment in which to produce the desired half cell potential. The junction between the reference electrode's environment and the test electrode's environment can cause errors from the potential difference that develops at that junction and the possible high electrical resistance created by the junction. Also, when the reference electrode has a specific environment, contamination or dilution of this environment will create an error in the potential measurement.

LIQUID JUNCTION POTENTIAL

In cases where the reference electrode has a specific environment that is necessary for the reference electrode half cell potential to achieve its desired level, the junction point where the reference electrode environment and the test electrode's environment connect can develop a charge imbalance that creates the liquid junction potential. This charge imbalance occurs because the diffusivity of positive and negative ions can differ. As a result, positive ions may accumulate on one side of the junction while negative ions accumulate on the other side. This will cause a potential difference across the junction. Usually, this potential difference can be minimized by choosing a compound that has positive and negative ions that have similar diffusivities. KCl is such a compound, and that it why it has been used in the SCE and silver/silver chloride reference electrodes. The liquid junction potentials for half cells with KCl are +3 mV for a saturated solution, +2 mV for a 1.0 M solution, and +1 mV for a 0.1 M solution [7]. This error is a constant for the reference electrode that is chosen so that in most corrosion tests it is not an issue. This error is smaller than the random errors that can occur in these procedures. It is mainly a concern when the potential measurements are being used to determine Gibbs free energy values.

TEMPERATURE EFFECTS

In cases where the test temperature is not at 25°C, it may be necessary to make a correction for the actual test temperature. This situation can develop when the measured potential is being used to determine if a protection level is adequate, and the reference electrode is a standard reference electrode such as the SCE or CSE. In some cases, the test environment is at a different temperature than the reference electrode. This situation is likely when a salt bridge is being used to connect the test environment to the reference electrode. For example, ASTM G5, *Standard Reference Test Method for Making Potentiodynamic Anodic Polarization Measurements*, requires that the test be carried out at 30°C [25]. In this case, the SCE reference electrode is connected to the test cell by a salt bridge, so the reference electrode is probably close to the laboratory temperature, which in most cases is probably between 22 and 24°C. The temperature correction in this case is relatively small, approximately 1 mV, but in other cases a significant error may occur, so a correction might be necessary.

There are two temperature corrections that have been established for reference electrodes [26]. The thermal coefficient is obtained when the potential of the elec trode at temperature, *T*, is measured against the same electrode at 25°C, and the difference is divided by (*T* 25). The isothermal temperature coefficient is obtained by measuring the potential of the reference electrode at 25°C against a standard hydrogen electrode (SHE) also at 25°C and then repeating the measurements with both electrodes at *T*. The isothermal coefficient is calculated as the difference between these two potentials divided by (*T* 25). The isothermal coefficient may be calculated from the thermal coefficient by subtracting 0.87 mV/°C from the thermal coefficient. In most cases, the thermal temperature coefficient is used for making temperature corrections for reference electrodes. However, in cases where electrode potentials are being compared to thermodynamic values where the standard state condition is referred to the SHE potential, the isothermal coefficient is required. For example, this situation occurs when potential/pH (Pourbaix) diagrams at different temperatures are being created.

Another error that can occur in cases where the reference electrode and test electrode are at different temperatures is related to the thermal effects on diffusion. In most cases, this error is smaller than the temperature effect on the electrode itself; but in cases where large temperature differences are encountered, it should be evaluated.

ERRORS IN MEASURING POLARIZED ELECTRODES

In cases where the electrode in question is polarized by current flowing in the envi ronment, an error in the measured potential will occur because of the potential cre ated by the current flowing through a resistive medium between the test electrode and the reference electrode. The current flow creates a potential field around the test electrode so that the placement of the reference electrode within this field deter mines the potential that is measured. In the case of laboratory measurements, this error can be minimized by the use of a Luggin Haber capillary probe that is placed close to the test electrode. The Luggin Haber probe provides a column of electrolyte that excludes current except that which is necessary to make the measurement. The probe will also shield the test electrode from the current, and that will create anoth er error if the shielding covers a significant portion of the specimen area. As a prac tical matter, the optimum placement of the probe to minimize both errors is obtained when the distance between the probe tip and the test electrode is equal to the outer diameter of the probe. In this case, there is a benefit from using a fine capillary because it allows the probe tip to be placed very close to the test electrode. However, this benefit is negated if the probe has a thick wall capillary. Some experi mental designs have used this approach to minimize damage to the probe tip, but this does not achieve the desired reduction in error.

Another approach for minimizing the error from reference electrode placement in cases where close placement is not possible is to make the potential measurement after interrupting the current flowing in the environment. The potential field

resulting from the current flow will disappear instantly when the current is interrupted, but the polarization effect on the electrode decays much more slowly. As a result, it is possible to obtain reasonably good electrode potential readings on polarized electrodes by interrupting the current flow. Some investigators make several potential measurements after the current is interrupted at known times and extrapolate the resulting decay curve back to the instant of interruption. This approach is helpful when it is not possible to make the potential readings rapidly enough to avoid significant decay issues. However, in most cases, this approach is not necessary to obtain the desired potential value with sufficient accuracy. Current interruption measurements are used extensively for evaluation cathodic protection systems in soils.

In the case of laboratory measurements, an experimental approach for dealing with resistivity errors is to superimpose a high frequency signal on the polarization current. In this case, the high frequency signal essentially short circuits the electrode, but it does respond to the resistance in the electrolyte [27]. Computer systems used in some potentiostats will carry out the calculations and provide corrected potential values for electrochemical tests requiring specimen polarization.

In cases where the geometry of the setup is simple and can be modeled, some investigators have used finite element analysis on electrolytes with known resistivities to create the potential field resulting from the current flow. In this case, the placement of the reference electrode must be known. When the current is flowing, the error can be compensated using the calculated error correction. This approach is reasonable when the errors are small and the accuracy of the potential required is not crucial.

RANDOM ERRORS

In any measuring activity, random errors occur for a variety of reasons. Usually, these errors are distributed normally and occur for reasons that are not understood, but they occur consistently. The use of interlaboratory testing procedures is intended to identify the magnitude of these errors. The variations that occur when a procedure is carried out by one operator using the same apparatus on identical specimens sequentially is known as the repeatability error, and it is characterized by its standard deviation, s_r. When a procedure is carried out by several laboratories using their measurement systems according to the test method on identical specimens, the variations that occur are known as the reproducibility error, and it is characterized by its standard deviation, s_R.

In the case of electrode potential measurements, several ASTM standard test methods have had interlaboratory test programs run, and the repeatability and reproducibility standard deviations have been determined. Table 1 shows a listing of the values that have been obtained for test methods developed by ASTM Committee G01. Generally, these methods have used the SCE reference electrode, and the reproducibility standard deviations have ranged from 7 to 11 mV [11,15]. The silver/silver chloride electrode with a saturated KCl fill solution showed a 25 mV

TABLE 1 Experimental errors in electrode potential measurements.

Electrode	s_rmV	s_RmV	Ref.	Note
Hg/Hg_2Cl_2/Sat. KCl (SCE)	3.0	7.0	ASTM G69 [15]	
Hg/Hg_2Cl_2/Sat KCl (SCE)	5.6	9.6	ASTM G69 [15]	[a]
Hg/Hg_2Cl_2/Sat. KCl (SCE)	10.2	10.6	ASTM G192 [11]	[b]
Cu/$CuSO_4$/Sat. $CuSO_4$ (CSE)	16	19	ASTM C876 [8]	[c]
Ag/AgCl/Sat. KCl	15	25	ASTM C876 [8]	[c]

[a]Measurement of chemically etched 5052 H32.
[b]Measured at 92°C with 10 mV steps.
[c]Measurement of bare steel rebar encased in concrete.

reproducibility standard deviation when used on concrete for rebar potentials [8]. The CSE in this application showed 19 mV for its reproducibility standard deviation [8]. In this case, the source of the error was probably related to the variability of the concrete for both the silver/silver chloride and CSEs. One test method, ASTM G192 [11], was run at 90°C with decreasing steps of 10 mV, and those factors may have been responsible for the higher reproducibility standard deviation found in this method.

Reference Electrode Maintenance

Electrometric pH measurements have been used for more than 75 years. The SCE has been an integral component in this measurement system, and as a result, these electrodes have been widely available and reliable. They have been the standard reference electrodes for electrochemical corrosion testing during this time. In laboratories where many test procedures are carried out, the reference electrodes may become damaged or contaminated. ASTM G215, *Standard Guide for Electrode Potential Measurement*, outlines several procedures for maintaining and storing these electrodes [18].

STORAGE

The use of an elastomeric cap covering the tip of the SCE is a simple and effective approach for protecting the leak path of the electrode. This cap can minimize evaporation of the KCl solution and thereby prevent crystals from plugging the tip. It also provides some protection from mechanical damage. However, it is not a long term solution for storage of these electrodes. Another approach is keep the tip immersed in purified water between uses. In such cases, it is important to keep the water level below the level of the KCl solution in the electrode. This will allow the solution to leak out of the electrode during its inactive period. This situation is not desirable for long term storage, but it prevents back diffusion of water into the electrode and minimizes the possibility of contamination through the tip. Another approach is to keep the tip immersed in a saturated KCl solution during its periods

of inactivity. This approach is effective, but in some cases the development of KCl crystals above the liquid level during extended periods of storage has been unsightly and problematic. This phenomenon occurs because of the Marangoni effect, which occurs when the liquid surrounding the KCl crystals has a higher surface tension than the bulk liquid and evaporation of water from the solution increases the con centration of KCl, which in turn increases the surface tension of the solution.

CONTAMINATION

The fill solution used in reference electrodes is essential for maintaining the stan dard half cell potential of the electrode. Anything that affects the metal ion concen tration in the fill solution will affect the half cell potential. For example, the presence of hydrogen sulfide, even at miniscule concentrations, will suppress the solubility of mercurous, cupric, or silver ions. As a result, laboratories that use or handle hydrogen sulfide must be very careful to prevent this compound from enter ing their reference electrodes. Many organic compounds will also affect the solubili ty of these ions. In the case of the SCE and silver/silver chloride electrodes, other halogen ions such as bromide and iodide will affect the solubility of the metal ions and so affect the electrode potential. The CSE electrode is also affected by halide ions and should not be used when contamination with these ions is possible.

In situations where the test environment contains compounds that can damage the reference electrode, it is good practice to clean the exterior of the electrode after every usage before it is stored. In many cases, a simple rinse with purified water and wipe with a clean absorbent paper wipe is sufficient. In cases where the environ ment is viscous or adherent, it may be necessary to use more aggressive procedures to remove the contamination before storage. The use of detergent solutions fol lowed by rinsing with purified water may be adequate. Mechanically wiping the exterior surface is also effective for some situations. In any case, the electrode should be examined carefully before being stored.

Electrodes that have a fill solution such as saturated KCl should be inspected before use. KCl crystals should be visible in the electrode if the solution is in good condition. It may be desirable to add solution and KCl crystals from time to time if the fill level becomes too low.

In situations where several reference electrodes are being used in a laboratory, it is necessary to check them occasionally to verify that they are in good condition. This can be carried out by measuring each one against a master electrode. If the potential difference between the test electrode and the master electrode is less than about 3 mV, the test electrode is probably in good condition. Some laboratories use a different type of master electrode so the measured potential is not close to zero. This avoids the possible mistake of forgetting to turn on the electrometer, seeing a zero value, and concluding that the test electrode is in good condition when no measurement has been made.

In cases where several electrodes are stored in a common container, there is a possibility that contamination has occurred to the solution and that it is affecting

all of the electrodes in the container. As a result, the master electrode should never be stored in the same container as the other reference electrodes.

When an electrode shows an unacceptable potential against the master electrode, an action must be taken. One approach is to discard the electrode. However, some laboratories attempt to rehabilitate the offending electrode. This can be accomplished by removing the fill solution and cleaning the reference electrode glass tube. Then a fresh fill solution can be added. It is important to realize that, when this procedure is carried out, it may take some time for the metal ion concentration to reach the desired level in the reference electrode. As a result, it is necessary to check the rehabilitated electrode against the master before it is used in a test procedure. This check should be carried out for at least 10 to 20 min to be sure that the electrode potentials are not drifting. The rehabilitated electrode should be within 2 mV of its desired value before being used. In cases where the reference metal is contaminated with insoluble compounds such as silver sulfide, this rehabilitation will not be adequate, so a postrehabilitation check is essential to verify that the problem has been solved.

Discussion

The concept of using the electrode potential of a metal surface in an electrolyte has evolved during the last century. The early work was used to develop thermodynamic properties of metallic elements, and it was a valuable technique for establishing the Gibbs free energy for many electrochemical oxidation/reduction reactions. Latimer carried out a monumental study to characterize these elements' oxidation potentials [28]. Later, Pourbaix expanded this work with the development of the potential/pH diagram [22]. Latimer's work considered the reactions as oxidation reactions, and his table of standard oxidation potentials was widely published. This table showed the potentials for the oxidation reactions with all of the reactants and products in their standard states (i.e., 25°C and unit activity). The application of Latimer's work for understanding corrosion issues was difficult, although Pourbaix's *Atlas* continues to be an important resource.

The development of cathodic protection systems for pipelines was a key step in the evolution of electrode potential applications. In this case, it was obvious that coatings would not be adequate to protect pipelines from corrosion failures because there was no practical means to provide a coating that would remain completely free of holidays for the anticipated life of the pipeline. The problem with cathodic protection systems was determining when the protection was sufficient to prevent corrosion without applying excessive protection, which is expensive and can damage coating systems. Measuring the electrode potential of the protected surface was found to be a reasonable approach for this determination. An extensive technology system has grown up around this understanding [29].

The use of electrode potential measurement in corrosion testing also has evolved with the development of instruments that can measure electrical potential

using tiny current flows. The first electrometers relied on measuring the attractive force that develops between the plates of a parallel plate capacitor. These devices were very susceptible to spurious static electric charge accumulations, so they were housed in chambers covered with a grounded metallic mesh to create a Faraday cage. These devices were accurate but very clumsy to use.

Thereafter, with the development of vacuum tubes and amplifiers based on these tubes, it became possible to measure potentials with a typical voltmeter design but with a very high input impedance (e.g., 11×10^6 Ω). This concept also allowed the development of potentiostat designs for controlling current based on potential measurement. The development of solid state transistors allowed the use of smaller units with much better portability. The incorporation of computer control into the potentiostat also made these units able to carry out a wide variety of functions more easily and with better precision than was previously possible.

The electronic potentiostat made possible the automatic polarization scans that revealed the active/passive behavior of stainless steels in acid environments, as illustrated by the ASTM G5 reference test method [25]. The development of the concept of polarization resistance and its relationship to corrosion rate also came out of this understanding. Further work was carried out to demonstrate the characteristics of pitting, crevice corrosion, and hydrogen embrittlement cracking. In all of these studies, the measurement and control of electrode potential are essential.

One key concept in the development of these technologies is the fact that a reference electrode composed of a pure metal in a specific controlled environment can be connected to the test environment using a simple slow leak liquid junction, and it will produce a meaningful potential value. Although most scientists and engineers today accept this concept without question, it is still a remarkable development.

Conclusions

1. Electrode potential is a key parameter for understanding the corrosion mechanism that applies to many metals and alloys.
2. Corrosion potential is a type of electrode potential that occurs when the metal surface being measured is not undergoing any external polarization (i.e., it is not receiving or supplying current to an external electrode).
3. Electrode potential measurements require the use of a reference electrode. Two types of reference electrodes are commonly used: standard reference electrodes and nonstandard reference electrodes. Standard reference electrodes include the SHE, SCE, and the CSE.
4. Nonstandard reference electrodes usually are identical to the test electrode material, but in some cases pure zinc is used because its corrosion potential is relatively stable and well known in the test environment. Nonstandard reference electrodes mainly are used in cases where only the change in potential is needed.
5. The silver/silver chloride electrode with a KCl saturated fill solution is a likely replacement for the SCE reference electrode because of the ban on mercury containing compounds in some locations. This situation will require that new

precision statements be developed for the test methods that currently require the SCE standard reference electrode. Interlaboratory testing will be necessary if this is carried out. The KCl concentration for the silver/silver chloride elec trode will also have to be specified.

6. A variety of errors can occur in electrode potential measurements. These errors can result from contamination of the reference electrode environment, from placement of the electrode tip in the test environment when current is flowing, or from problems occurring at the tip where the reference electrode solution makes contact with the test environment. Several techniques have been developed for successfully dealing with these errors.
7. The random experimental errors that occur with electrode potential measure ments have been discussed, and the standard deviations of these errors in sev eral test methods are shown to be in the range of 3 to 25 mV, depending on the reference electrode and the system under investigation.

References

[1] ASTM NACE/ASTM G193-12d, *Standard Terminology and Acronyms Relating to Corrosion*, ASTM International, West Conshohocken, PA, 2012, www.astm.org

[2] Moore, W. J., *Physical Chemistry,* 2nd ed., Prentice-Hall, Englewood Cliffs, NJ, 1955, pp. 435–497.

[3] Evans, U. R., "An Outline of Corrosion Mechanisms, Including the Electrochemical Theory," *The Corrosion Handbook,* H. H. Uhlig, Ed., Wiley, New York, 1948, pp. 3–10.

[4] Stern, M. and Geary, A. I., "Electrochemical Polarization, I. A Theoretical Analysis of the Shape of Polarization Curves," *J. Electrochemical Soc.*, Vol. 104, No. 1, 1957, p. 56.

[5] ASTM G96-90, *Standard Guide for Online Monitoring of Corrosion in Plant Equipment (Electrical and Electrochemical Methods)*, ASTM International, West Conshohocken, PA, 2018, www.astm.org

[6] ASTM G102-89, *Standard Practice for Calculation of Corrosion Rates and Related Information from Electrochemical Measurements*, ASTM International, West Conshohocken, PA, 2015, www.astm.org

[7] ASTM G3-14, *Standard Practice for Conventions Applicable to Electrochemical Measurements in Corrosion Testing*, ASTM International, West Conshohocken, PA, 2014, www.astm.org

[8] ASTM C876-15, *Standard Test Method for Corrosion Potentials of Uncoated Reinforcing Steel in Concrete*, ASTM International, West Conshohocken, PA, 2015, www.astm.org

[9] ASTM G61-86, *Standard Test Method for Conducting Cyclic Potentiodynamic Polarization Measurements for Localized Corrosion Susceptibility of Iron-, Nickel-, or Cobalt-Based Alloys*, ASTM International, West Conshohocken, PA, 2018, www.astm.org

[10] ASTM G100-89, *Standard Test Method for Conducting Cyclic Galvanostaircase Polarization*, ASTM International, West Conshohocken, PA, 2015, www.astm.org

[11] ASTM G192-08, *Standard Test Method for Determining the Crevice Repassivation Potential of Corrosion Resistant Alloys Using a Potentiodynamic-Galvanostatic-Potentiostatic Technique*, ASTM International, West Conshohocken, PA, 2014, www.astm.org

[12] ASTM G150-18, *Standard Test Method for Electrochemical Critical Pitting Temperature Testing of Stainless Steels and Related Alloys*, ASTM International, West Conshohocken, PA, 2018, www.astm.org

[13] ASTM A262-15, *Standard Practices for Detecting Susceptibility to Intergranular Attack in Austenitic Stainless Steels, Annual Book of ASTM Standards,* Vol. 01.03, ASTM International, West Conshohocken, PA, 2015, www.astm.org

[14] ASTM G108-94, *Standard Test Method for Electrochemical Reactivation (EPR) for Detecting Sensitization of AISI Type 304 and 304L Stainless Steels*, ASTM International, West Conshohocken, PA, 2015, www.astm.org

[15] ASTM G69-12, *Standard Test Method for Measurement of Corrosion Potentials of Aluminum Alloys*, ASTM International, West Conshohocken, PA, 2012, www.astm.org

[16] NACE TM0497-2012, *Measurement Techniques Related to Criteria for Cathodic Protection on Underground or Submerged Metallic Piping Systems*, NACE International (NACE), Houston, TX, 2012.

[17] NACE TM0101-2012, *Measurement Techniques Related to Criteria for Cathodic Protection of Underground Storage Tank Systems*, NACE International (NACE), Houston, TX, 2012.

[18] ASTM G215-17, *Standard Guide for Electrode Potential Measurement*, ASTM International, West Conshohocken, PA, 2017, www.astm.org

[19] ASTM G148-97, *Standard Practice for Evaluation of Hydrogen Uptake, Permeation, and Transport in Metals by an Electrochemical Technique*, ASTM International, West Conshohocken, PA, 2018, www.astm.org

[20] Devanathan, M. A. V. and Stachurski, Z., "The Adsorption and Diffusion of Electrolytic Hydrogen in Palladium," *P. Roy. Soc. A—Math. Phy.,* Vol. 270, No. 1340, 1962, pp. 90–102.

[21] Ives, D. J. G. and Janz, G. J., *Reference Electrodes, Theory and Practice,* Academic, New York, 1961, pp. 1–70.

[22] de Zoubov, N., Van Leugenhaghe, C., and Pourbaix, M., "Copper," *Atlas of Electrochemical Equilibria in Aqueous Solutions,* M. Pourbaix, Ed., NACE International, Houston, TX, 1974, pp. 384–392.

[23] ASTM G199-09, *Standard Guide for Electrochemical Noise Measurement*, ASTM International, West Conshohocken, PA, 2014, www.astm.org

[24] ASTM G217-16, *Standard Guide for Corrosion Monitoring in Laboratories and Plants with Coupled Multielectrode Array Sensor Method*, ASTM International, West Conshohocken, PA, 2016, www.astm.org

[25] ASTM G5-14e1, *Standard Reference Test Method for Making Potentiodynamic Anodic Polarization Measurements*, ASTM International, West Conshohocken, PA, 2014, www.astm.org

[26] de Bethune, A. J. and Swendeman Loud, N. A., *Standard Aqueous Electrode Potentials and Temperature Coefficients,* Clifford A. Hampel, Skokie, IL, 1964, pp. 1–19.

[27] ASTM G106-89, *Standard Practice for Verification of Algorithm and Equipment for Electrochemical Impedance Measurements*, ASTM International, West Conshohocken, PA, 2015, www.astm.org

[28] Latimer, W. M., *The Oxidation States of Elements and Their Potentials in Aqueous Solutions,* 2nd ed., Prentice Hall, New York, 1952.

[29] Peabody, A. W., *Peabody's Control of Pipeline Corrosion,* 2nd ed., R. L. Bianchetti, Ed., NACE International, Houston, TX, 2001.

STP 1609, 2019 / available online at www.astm.org / doi: 10.1520/STP160920170145

Raul B. Rebak,[1] Timothy B. Jurewicz,[1] and Young-Jin Kim[2]

Electrochemical Behavior of Accident Tolerant Fuel Cladding Materials under Simulated Light Water Reactor Conditions

Citation

Rebak, R. B., Jurewicz, T. B., and Kim, Y.-J., "Electrochemical Behavior of Accident Tolerant Fuel Cladding Materials under Simulated Light Water Reactor Conditions," *Advances in Electrochemical Techniques for Corrosion Monitoring and Laboratory Corrosion Measurements*, *ASTM STP1609*, S. Papavinasam, R. B. Rebak, L. Yang, and N. S. Berke, Eds., ASTM International, West Conshohocken, PA, 2019, pp. 231–243, http://dx.doi.org/10.1520/STP160920170145[3]

ABSTRACT

After the Fukushima reactor accidents following Japan's March 2011 tsunami, the U.S. Department of Energy engaged with nuclear fuel vendors to develop improved fuels for the current fleet of light water power reactors. General Electric and Oak Ridge National Laboratory have proposed using iron-chrome-aluminum (FeCrAl) ferritic alloys as cladding material for the existing uranium dioxide fuel (UO_2). This is a simple approach that leaves unchanged the present coolable geometry in the reactor. FeCrAl alloys have outstanding resistance, in accident conditions, to attack by superheated steam compared to the current zirconium alloys. Since ferritic FeCrAl alloys have not been used before in nuclear power reactors, extensive characterization has been performed to determine their behavior in light water reactor conditions (e.g., normal operation and accident). The present work deals with the electrochemical behavior of the newer alloys in high-temperature water (near 300°C) containing either excess hydrogen gas or excess oxygen. Results show that chromium-containing ferritic

Manuscript received August 14, 2017; accepted for publication December 4, 2017.

[1]GE Global Research, 1 Research Circle, Schenectady, NY 12309, USA R. B. R. http://orcid.org/0000 0002 8070 4475

[2]FNC Technology, 44 Tapsil ro, Yongin si, Gyeounggi do, 17084, Republic of Korea

[3]ASTM Symposium on *Advances in Electrochemical Techniques for Corrosion Monitoring and Laboratory Corrosion Measurements* on November 13 14, 2017 in Atlanta, GA, USA.

FeCrAl have similar electrochemical high-temperature behavior like other common existing reactor alloys containing chromium for passivation (such as X-750, Alloy 600, and Type 304SS). The use of FeCrAl alloy cladding would also eliminate existing common degradation mechanisms such as shadow corrosion in boiling water reactors.

Keywords

accident tolerant fuels, cladding, FeCrAl, electrochemical behavior, high-temperature water, hydrogen, boiling water reactor, shadow corrosion

Introduction

After the accident and plant blackout caused by a tsunami at the Fukushima Daiichi nuclear power plant in northeast Japan, the international scientific community was determined to find a fuel system that would be more resistant to these types of acci dents. The plant blackout prevented the recirculation of cooling water to remove radioactivity heat [1]. Therefore, the zirconium (Zr) of the fuel cladding, both in the reactor and in the spent fuel in the cooling pools, reacted with water and steam to produce large amounts of ignitable hydrogen gas and even more heat because of the exothermic oxidation: $Zr + 2H_2O === ZrO_2 + 2H_2 + Heat$.

In 2012, the U.S. Department of Energy (DOE) called for proposals from U.S. commercial nuclear fuel producers for an accident tolerant fuel (ATF). Currently, many in the industry prefer to call this effort advanced technology fuel [2]. There are several ATF concepts being developed by the industry in cost sharing efforts with the DOE. General Electric and its partners including Oak Ridge National Laboratory (ORNL), Sandvik Materials Technology, and Exelon and Southern Nuclear power utility companies are developing an iron chrome aluminum (FeCrAl) cladding for the existing fuel uranium dioxide fuel pellets [3]. The main characteristic of this FeCrAl alloy is its outstanding resistance to oxidation in high temperature water and steam, which was the Achilles heel of the Zr alloy in the Fukushima reactors. However, even though austenitic stainless steel was used for fuel rod cladding in the first pressurized water reactors, FeCrAl alloys have never been used in light water reactors. Their corrosion and electrochemical behavior in approximately 300°C water thus needs to be characterized. Currently, two FeCrAl alloys are being evaluated, APMT (powder metallurgy) and C26M (a traditionally melted alloy developed by ORNL) (**Table 1**).

The objective of this study was to perform high temperature electrochemical testing to determine if the behavior of the newer ferritic FeCrAl materials compared to the well known behavior of traditional reactor materials. **Table 1** lists some of the alloys that were studied. The corrosion potential of the materials depends on the water chemistry conditions and the oxide surface nature, such as oxide thickness, composition, conductivity, microstructure, and so on. Also, a change in the electro catalytic nature of the surface associated with the chemical compositions of the oxide layers can play a significant role in the free corrosion potential behavior of

TABLE 1 Nominal compositions in mass percent of the studied materials.

Element	Zircaloy-2 HCP	304SS Austenitic	Alloy 33 Austenitic	X-750 Austenitic	C26M Ferritic	APMT Ferritic
Zr	~ 98					
Fe	0.07 0.2	~ 70	32	7	~ 80	~ 70
Ni	0.03 0.08	8	31	~ 72		
Cr	0.05 0.15	19	~ 33	15	12	22
Al				0.7	6	5
Mo			1.6		2	3
Si		0.75 max	0.5 max	0.5 max	0.2	0.7 max
Mn		2 max	2 max	1 max		0.4 max
C		0.08 max	0.015 max	0.08 max	0.01 max	0.08 max
Other	1.5 Sn		0.6 Cu, 0.4 N	2.5 Ti, 1 Nb	0.05 Y	Y, Hf

Note: HCP hexagonal close packed; Ni nickel; Mo molybdenum; Si silicon; Mn manganese; C carbon; Sn tin; Cu copper; N nitrogen; Ti titanium; Nb niobium; Y yttrium; Hf hafnium.

the materials. The relative values of the corrosion potentials could be an indication of the likelihood of galvanic corrosion when or if the materials are coupled in the reactor environment.

Experimental Technique

The electrochemical measurements in pure water at 288°C and 10 MPa pressure were conducted in a 1 gal (3.78 L) stainless steel autoclave by controlling the water chemistry conditions at a water flow rate of 100 cm^3/min (**Fig. 1**). The specimens for the electrochemical testing were cut in the form of strips 0.5 cm wide by 2.5 cm long and then polished using a wet 600 grit emery paper. This geometry was required to fit the specimens through the autoclave top penetrations (**Fig. 2**). All the test specimens were rinsed ultrasonically with high purity water. The specimens for electrochemical measurements were spot welded to a polytetrafluorethylene insulated stainless steel wire that was mounted in a special fitting around the platinum (Pt) counter electrode (**Fig. 2**). Water in the loop was purified to 18 Mohm cm through a demineralizer, an organic removal column, and a submicron filter before passing into a 1 gal (3.78 L) glass conditioning column. The water was equilibrated with appropriate mixtures of argon (Ar), oxygen gas (O_2), or hydrogen gas (H_2) to establish the desired water chemistry. Oxygen and hydrogen monitors were used for measuring the dissolved oxygen and hydrogen in the inlet and outlet streams, respectively. The studied aqueous environments were simulated reactor environments with the addition of only hydrogen or oxygen to high purity water and without the addition of lithium or boron. The pH of high temperature water (near 300°C) is approximately 5.6. A Pt electrode was used to monitor the effective redox potential of the water.

FIG. 1 Recirculating autoclave system. The autoclave is at center left.

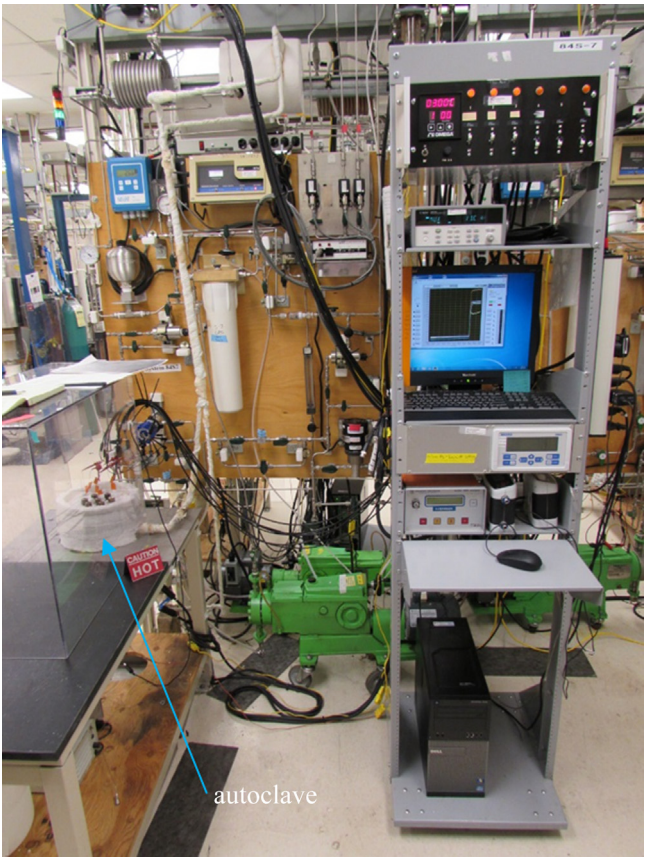

The materials used to manufacture the specimens for the electrochemical measurements (Table 1) were not cladding tubes or spacers but rods. The type of oxides formed on the specimens, which control the values of corrosion potential in the hydrogen or oxygen rich environments, depend mainly on the chemical composition of the alloys (Table 1) and have little or no correlation with other properties of the alloys, such as grain size and mechanical strength.

Experimental Results

CORROSION POTENTIAL

Fig. 3 shows the corrosion potential behavior of five engineering alloys for 3 weeks (Table 1) and Pt in high temperature water at 288°C. The potential measurements were performed using a zirconia high temperature pH sensor with a copper/copper

FIG. 2 Six specimens mounted in the autoclave head. The Pt counter electrode is at the center.

oxide internal junction as a reference electrode and an Agilent Model 34970A elec trometer (Agilent Technologies, Santa Clara, CA). The measurements were taken every 10 min. The measured potential values were converted to the standard hydro gen electrode (SHE) scale. For the first approximately 480 h of immersion, the water contained dissolved hydrogen gas (300 ppb H_2), and for the last period, the water contained dissolved oxygen gas (1,000 ppb O_2). In the very first few hours of the measurements, the potential showed typical transient behavior and then it quickly stabilized for all the materials involved. Under hydrogen conditions, the corrosion potential for the six materials was low and between −600 and −800 mV (SHE). The maximum separation among the corrosion potential for all the materi als was generally in a band of less than 50 mV. At approximately 480 h of immer sion, the gas was changed from hydrogen to oxygen, and a sudden increase in the

FIG. 3 Corrosion potential versus immersion time in pure water at 288°C. In the first period, the water contained 0.3 ppm hydrogen and, in the last period, 1 ppm oxygen.

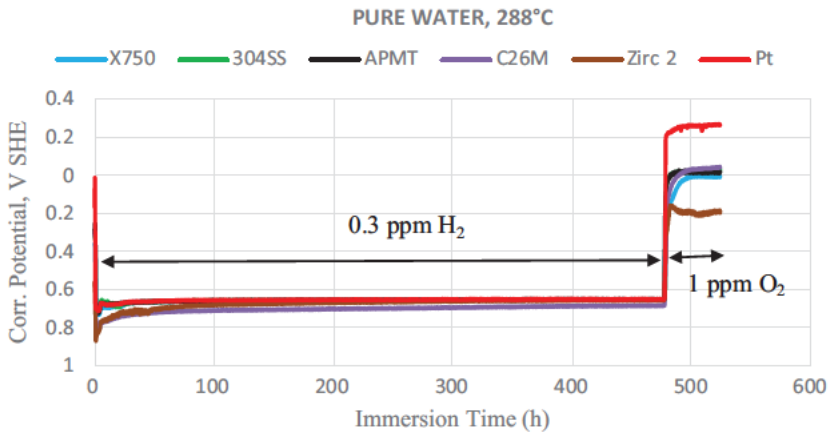

corrosion potential for all the materials was observed (Fig. 4). While in the hydrogen atmosphere the potential of all the materials was approximately the same, in the oxygen atmosphere there was a clear separation of the corrosion potential values. The highest (most noble) potential was for Pt and the lowest (less noble) was

FIG. 4 Detail of the corrosion potential versus immersion time in pure water at 288°C. In the first period, the water contained 0.3 ppm hydrogen and, in the last, 1 ppm oxygen.

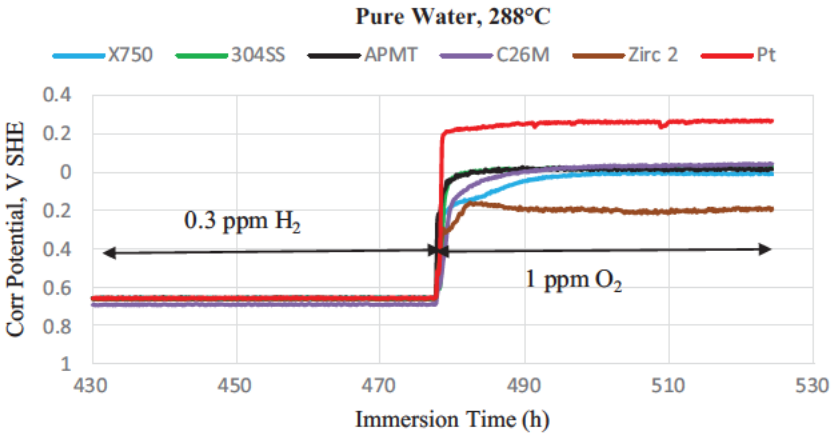

for Zircaloy 2. The potentials of all the other materials including nickel based X 750, austenitic stainless steel Type 304, and the two newer ferritic FeCrAl materials (APMT and C26M) were similar to each other and near 0 V SHE. This is not surprising because these alloys contain Cr for passivation. Based on the corrosion potential data, it is evident that the redox kinetics on FeCrAl are like the well known behavior of traditional nuclear reactor materials, such as Type 304SS and X 750, in high temperature water. Fig. 5 and Fig. 6 show replotted corrosion potentials for other materials under (a) hydrogen atmosphere and (b) oxygen atmosphere [4]. Again, in the oxidizing environment, there was a separation of the corrosion potentials (Pt highest and Zircaloy 2 lowest) and the other materials, including nanoferritic 14Cr alloy (NFA), Alloy 33, nickel alloy X 750, and Type 304SS were all in a narrow band of less than 100 mV. In the hydrogen atmosphere, the corrosion potential of all the materials was grouped in a narrow band of less than 50 mV on the order of −0.6 V (SHE).

SHADOW CORROSION

An enhanced growth of Zr oxides may occur in boiling water reactor nuclear power plants on areas of Zr alloys that are "facing" other metals such as nickel based alloys

FIG. 5 Corrosion potential versus immersion time in pure water containing 1,000 ppb dissolved oxygen. S30400 and N07750 are the unified numbering system numbers of Type 304SS and the nickel based alloy X 750, respectively.

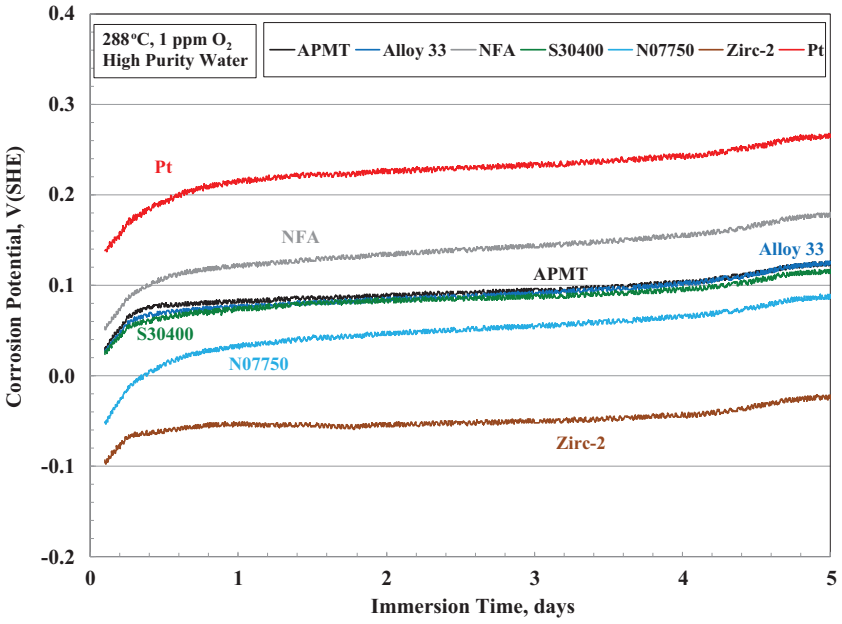

FIG. 6 Corrosion potential versus immersion time in pure water containing 150 ppb dissolved hydrogen. S30400 and N07750 are the unified numbering system numbers of Type 304SS and the nickel based alloy X 750, respectively.

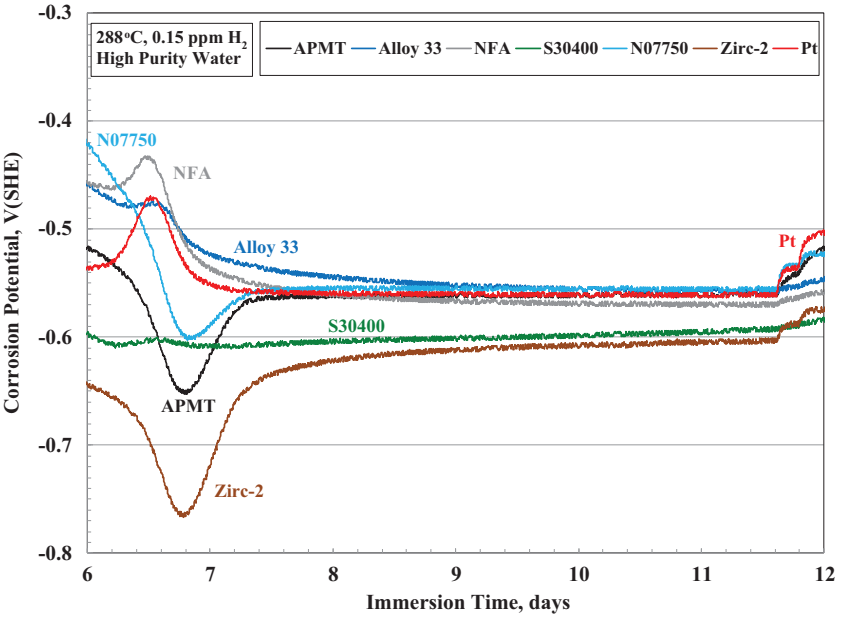

and stainless steels. This anomalous growth in the oxide of the Zr alloy is called "shadow" corrosion because the higher corrosion rate shape on the zirconium alloy component resembles the imprint of the other stainless steel or nickel alloy metallic component [5,6]. Two hypotheses have been used to explain this phenomenon: (1) galvanic corrosion and (2) local radiolysis; however, there is evidence that these two hypotheses may not explain all the occurrences of shadow corrosion. Lysell, Nystrand, and Ullberg argue that the most likely cause of shadow corrosion is the theory of galvanic corrosion [6]. Shadow corrosion in reactors has been explained by a separation in the corrosion potential of the materials under irradiation. Under irradiation, the corrosion potential of nickel alloys such as X 750 and Zircaloy 2 go in separate directions, the Zircaloy becomes more cathodic, and the nickel alloy becomes more anodic [7]. In current reactors, the fuel cladding is Zircaloy, and other components such as the separation grits and handles generally are stainless steels or nickel based alloys. In the ATF concept proposed by General Electric and ORNL, the tubes for the fuel will be ferritic FeCrAl alloys (such as APMT and C26M), and the other components are expected to remain stainless steels and nickel based alloys. Therefore, it would be important to determine how the effect or irradiation might affect the behavior of FeCrAl alloys as compared to the current Zircaloy materials.

In laboratory autoclaves, plant irradiation behavior has been simulated using ultraviolet (UV) illumination [4,7]. The energy of UV irradiation used here was too low to produce radiolytic species of the water, which do exist in an actual reactor environment. The present UV treatment was meant to study only the response of the oxide films on the surface of the alloys. Fig. 7 shows the corrosion potential behavior of three alloys in high purity water with 1 ppm oxygen at 288°C. In the absence of illumination, the corrosion potential of APMT and X 750 are very close at near 0.1 V (SHE), while the corrosion potential of Zircaloy 2 was approximately 100 mV lower. During the period of UV illumination, the corrosion potential of both X 750 and APMT became more anodic (noble), that is, they both moved in the same direction. However, the corrosion potential of Zircaloy 2 became more cathodic (less noble). This separation in the corrosion potential in the presence of irradiation may explain the occurrence of shadow corrosion on zirconium in boil ing water reactor nuclear power plants [7]. The changes in the corrosion potential in the presence of UV light is due to the photoexcitation of n type zirconium dioxide formed on Zircaloy 2 and p type nickel oxide on X 750. If a FeCrAl tube is used for the ATF cladding, shadow corrosion may not occur because under

FIG. 7 UV illumination effect on the corrosion potential of Zircaloy 2 and APMT versus X 750 in 288°C water containing 1 ppm dissolved O_2. Under UV irradiation, there is a separation in the potentials of Zircaloy and X 750, but there is no separation between APMT and X 750.

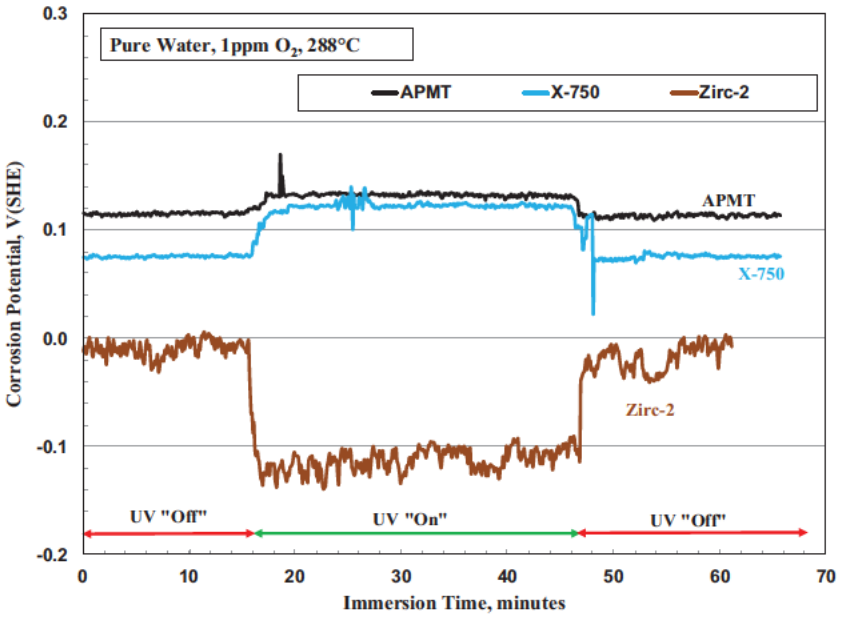

irradiation the corrosion potential of FeCrAl and nickel alloys such as X 750 would be practically the same.

GALVANIC CORROSION

Galvanic corrosion occurs when two different metals enter into contact (or are connected by an electrical conductor) and are exposed to a conductive electrolyte. A difference in electrical potential exists between different metals and serves as the driving force in passing current through metals. This current flow results in increased corrosion of one of the metals in the couple [7].

The galvanic current behavior of Zircaloy 2 and APMT separately coupled to X 750 were measured in 288°C water containing 1 ppm dissolved O_2. The coupled electrodes for galvanic corrosion measurement had a gap of approximately 1 mm between an anode electrode (Zircaloy 2 or APMT) and the cathode electrode (X 750) [4]. The test specimens were irradiated through a sapphire window from a penetration in the bottom of the autoclave. A thin diamond disk made by chemical vapor deposition was placed on the top of sapphire window to protect it from dissolution in high temperature water and did not affect the UV intensity [4,7]. An anodic galvanic current was measured when Zircaloy 2 was galvanically coupled with X 750 in the hot water environment (Fig. 8). This anodic galvanic current

FIG. 8 Galvanic current of Zirc 2 and APMT coupled to X 750 in 288°C water plus 1 ppm O_2 with and without UV illumination. Under UV irradiation, there is an increase of the anodic current for Zircaloy 2 but no change in the cathodic current for APMT.

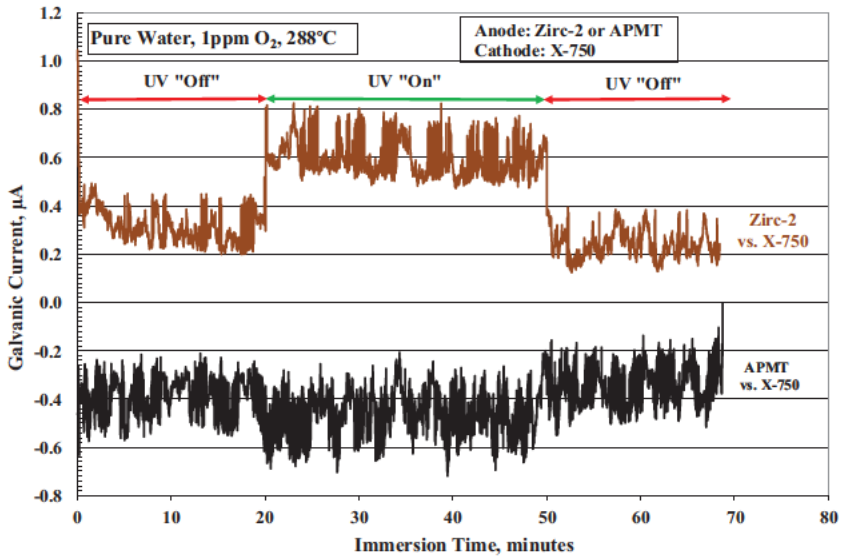

mainly is attributed to a larger and positive difference in the corrosion potential between Zircaloy 2 and X 750 in water with oxygen (**Figs. 3 5**). The anodic gal vanic current for the dissolution of Zircaloy 2 was increased when illumination was on, showing the increased oxidation of Zircaloy in the presence of irradiation [7]. On the contrary, the galvanic current between APMT and X 750 was cathodic; that is, the X 750 was slowly preferentially corroding in presence of APMT, how ever with a smaller absolute current than when X 750 was coupled to Zircaloy. This is the result of the closer values of corrosion potentials between APMT and X 750 as shown in **Fig. 5**. The galvanic current between X 750 and APMT was not affected by the UV illumination (**Fig. 8**). These galvanic corrosion results suggest that the FeCrAl alloy APMT as an ATF cladding material would be less suscepti ble to enhanced shadow or galvanic corrosion when it is electrically connected to a X 750 spacer grid or any other nickel alloy or stainless steel component in the reactor.

Final Remarks

Currently and worldwide, most of the cladding for uranium dioxide fuel in light water power reactors is made with Zr based alloys. Under severe accident condi tions such as the events of March 2011 at the Fukushima site, the Zr alloys may react rapidly with water and steam, forming hydrogen gas that may lead to explosions. It has been proposed in several countries that one of the options for resolving this issue is to replace Zr alloys with FeCrAl ferritic alloys such as APMT or C26M. Because FeCrAl alloys were never used in light water reactors, it is important to characterize their electrochemical behavior in comparison with well tested present reactor alloys, which have been used successfully for more than 60 years. Current results show that the corrosion potential of the newer FeCrAl alloys is the same as those of the common existing materials such as Type 304SS or nickel based X 750. That is, by introducing the FeCrAl materials into the reactor, there will be no change in the redox potential system in the reactor. It was reported that the type of oxide films that form on FeCrAl alloys in light water reactor environments are very similar to the oxide films that form on austenitic stainless steels or nickel based alloys containing Cr for passivation [8].

Some of the adverse attributes of FeCrAl compared to Zr alloys for cladding include higher neutron absorption and possibly a higher release of tritium into the coolant. These two traits may be minimized by reducing the cladding wall thickness to half of the current value (for neutron compensation) and by the formation of oxides on the surface (for tritium release abatement).

Summary and Conclusions

1. The electrochemical behavior of ferritic FeCrAl alloys APMT and C26M in high temperature water was investigated.

2. In hydrogenated 288°C water, the corrosion potential of FeCrAl is the same as for the other tested materials such as nickel based X 750, austenitic stainless steel Type 304, Zircaloy 2, and Pt.
3. Under excess oxygen 288°C water, the corrosion potential of FeCrAl is the same as the corrosion potential of Cr containing alloys such as Type 304SS and X 750.
4. By using FeCrAl alloys as ATF fuel cladding, the likelihood of shadow corro sion and galvanic corrosion between the cladding and austenitic X 750 or 304SS in the reactor will be eliminated because they behave electrochemically in the same manner in high temperature water.

ACKNOWLEDGMENTS

This material is based upon work supported by the DOE (National Nuclear Security Administration) under Award No. DE NE0008221. This report was prepared as an account of work sponsored by an agency of the U.S. government. Neither the U.S. government nor any agency thereof, nor any of their employees, makes any warranty, express or implied, or assumes any legal liability or responsibility for the accuracy, completeness, or usefulness of any information, apparatus, product, or process dis closed, or represents that its use would not infringe on privately owned rights. Refer ence herein to any specific commercial product, process, or service by trade name, trademark, manufacturer, or otherwise does not necessarily constitute or imply its endorsement, recommendation, or favoring by the U.S. government or any agency thereof. The views and opinions of the authors expressed herein do not necessarily state or reflect those of the U.S. government or any agency thereof.

References

[1] Rebak, R. B., "Iron-Chrome-Aluminum Alloy Cladding for Increasing Safety in Nuclear Power Plants," *EPJ Nuclear Sci. Technol.*, Vol. 3, No. 34, 2017, http://dx.doi.org/10.1051/epjn/2017029

[2] Nuclear Energy Institute (NEI), "Advanced Technology Fuels—Potential Nuclear Industry Game Changer," http://web.archive.org/web/20181110144456/https://www.nei.org/advocacy/make-regulations-smarter/accident-tolerant-fuel (accessed Nov. 10, 2018).

[3] Stachowski, R. E., Rebak, R. B., Gassmann, W. P., and Williams, J., "Progress of GE Development of Accident Tolerant Fuel FeCrAl Cladding," *Proceedings of TopFuel 2016*, September 11–16, 2016, American Nuclear Society, Boise, ID, pp. 179–187.

[4] Kim, Y. J., Wagenbaugh, F., Jurewicz, T. B., Blair, R. J., and Rebak, R. B., "Environmental Behavior of Light Water Reactor Accident Tolerant Candidate Cladding Materials under Design Conditions," Paper C2015-5817, *Proceedings of Corrosion 2015 Conference* (NACE International), Dallas, TX, March 15–19, 2015, pp. 1–15.

[5] Lemaignan, C., "Corrosion or Zirconium Alloy Components in Light Water Reactors," *ASM Metals Handbook, Vol. 13C Corrosion: Environments and Industries*, ASM International, Metals Park, OH, 2006, p. 415.

[6] Lysell, G., Nystrand, A.-C., and Ullberg, M., "Shadow Corrosion Mechanism of Zircaloy," *Zirconium in the Nuclear Industry: Fourteenth International Symposium, ASTM STP1467*,

P. Rudling, and B. Kammenzind, Eds., ASTM International, West Conshohocken, PA, 2005, pp. 445–461, http://dx.doi.org/10.1520/STP37520S

[7] Kim, Y.-J., Rebak, R. B., Lin, Y.-P., Lutz, D., Crawford, D., Kucuk, A., and Cheng, B., "Photoelectrochemical Investigation of Radiation-Enhanced Shadow Corrosion Phenomenon," *J. ASTM Int.*, Vol. 7, No. 7, 2010, pp. 1–18, http://dx.doi.org/10.1520/JAI102952

[8] Rebak, R. B., Larsen, M., and Kim, Y.-J., "Characterization of Oxides Formed on Iron-Chromium-Aluminum Alloy in Simulated Light Water Reactor Environments," *Corros. Rev.*, Vol. 35, No. 3, http://dx.doi.org/10.1515/corrrev-2017-0011

STP 1609, 2019 / available online at www.astm.org / doi: 10.1520/STP160920170229

Liang He,[1] Gaoxiang Wu,[1] and Preet M. Singh[1]

Study on the Repassivation Behavior of Steels Using Electrochemical Test Methods

Citation

He, L., Wu, G., and Singh, P. M., "Study on the Repassivation Behavior of Steels Using Electrochemical Test Methods," *Advances in Electrochemical Techniques for Corrosion Monitoring and Laboratory Corrosion Measurements*, *ASTM STP1609*, S. Papavinasam, R. B. Rebak, L. Yang, and N. S. Berke, Eds., ASTM International, West Conshohocken, PA, 2019, pp. 244–261, http://dx.doi.org/10.1520/STP160920170229[2]

ABSTRACT

Passive film stability is very important for the reliable use of many alloys in a given environment. Passive film should also be able to repair or regrow upon damage to provide a reliable protection to alloys. Breakdown and repassivation behavior of passive film plays an important role in localized corrosion of engineering alloys. This paper aims to give a general review of the electrochemical methods used to study the repassivation behavior of alloys and to present two different film removal methods used for repassivation study—namely the scratch test and the electrochemical film-reduction methods. The film reduction method was conducted using carbon steel A569 in borate buffer solution (pH = 8.4) to study the effects of retained plastic strain on the repassivation kinetics of carbon steels. Plastic strain was found to improve the initial repassivation kinetics of carbon steel. The scratch tests were performed on a duplex stainless steel UNS S32003 in both chloride (Cl^-) and thiosulfate plus chloride ($S_2O_3^{2-} + Cl^-$) solutions. Addition of $S_2O_3^{2-}$ slows down the repassivation of UNS S32003. Repassivation kinetics of the separated single ferrite phase of UNS S32003 were slower than those of the bulk material.

Manuscript received November 11, 2017; accepted for publication February 13, 2018.

[1]Georgia Institute of Technology, 500 10th St. NW, Atlanta, GA 30318, USA L. H. http://orcid.org/0000 0002 9533 7137, G. W. http://orcid.org/0000 0002 5092 651X, P. M. S. http://orcid.org/0000 0002 2360 3061

[2]ASTM Symposium on *Advances in Electrochemical Techniques for Corrosion Monitoring and Laboratory Corrosion Measurements* on November 13 14, 2017 in Atlanta, GA, USA.

Keywords
repassivation kinetics of steels, scratch test method, electrochemical film reduction method, duplex stainless steels, carbon steels

Introduction

Passive film formed on the surface of metals/alloys provides protection from the aggressive/corrosive environment. However, film breakdown often occurs through chemical or mechanical damage, during the initiation of pits in solutions containing aggressive anions, or during stress corrosion cracking and corrosion fatigue. The repair of the passive film, namely repassivation behavior, is very important to the study of these forms of corrosion.

FILM REMOVAL TECHNIQUES

To study the repassivation of film in a given environment, film is intentionally removed and allowed to regrow while the kinetics of film reformation is determined by recording and analyzing the current activities during this process. Different methods to remove the initial passive film have been developed during the past few decades, such as the manual scratch test [1 8], fracturing thin film electrode [9 11], straining wire [12,13], fast fracture technique [14,15], and electrochemical reduction method [16 19].

In straining wire methods, metal wires several millimeters in diameter are potentiostatically polarized and slowly strained, while the current is recorded at the same time [12,13]. However, for the oxide films with high ductility, the phenomena observed through this method may cause film thinning instead of film fracture [20]. The fast fracture technique involves the fast weight drop on the specimen, leading to the exposure of bare metal surface to the solution [14,15].

Among these methods, the scratch test method is the most commonly used. In a scratch test, while the specimen is typically polarized at a fixed potential value using a potentiostat, the passive film is removed through a mechanical scratch using a diamond scriber, and the current transient is recorded at the same time. If the repassivation rate is fast, for example in stainless steels and aluminum alloys, the already scratched area may repassivate during the depassivation of the remaining area, reducing the peak current. Thus, the time spent to make the scratch needs to be minimized in this method. Burstein and Marshall [1] and Marshall and Burstein [2,3] used a stylus to scratch the surface of a rotating disc electrode with a 100 Hz rotating frequency with contact time of about 1 ms. A surface that has a rectangular shape with a small thickness of hundreds of micrometers has been utilized for the scratch test to minimize the contact time [4,5]. Special attention needs to be paid to determine the area of the scratch, which can easily be measured and characterized after the test. Another issue is the potential drop caused by solution resistance (IR drop) between the specimen and

the reference electrode, which is largest at the peak current [21,22]. Because the current changes during depassivation and repassivation, the IR drop also changes correspondingly, leaving the potential drop across the film not constant. Attention has also been paid to the capacitive current between the passive film and the scratched bare metal surface [23,24]. It was observed that both ohmic drop and capacitive current led to the decrease in the peak current, which could be mitigated by using a small scratched area and a solution with high conductivity. Other improvements can be achieved through reduction in the passive area or by covering the surface with insulating layers [10,11,24]. The scratch test method has also been used to study the pitting corrosion resistance of stainless steels in thiosulfate containing environments [25].

In an effort to resolve the slow depassivation and large ohmic drop issues, Frankel et al. developed the breaking thin film electrode method [9]. Metal film was deposited onto the glass or silicon wafers; the thickness of the film was typically no more than 1 μm, and the metal film was covered by an insulating layer to reduce the influence from the surrounding passive area [9 11]. This method allows for a very small exposed bare metal area in the order of 10^{-5} cm^2, reducing the ohmic drop. The time for depassivation is several microseconds, a much faster depassivation rate compared to the scratch tests. High current density after the fracture of film was observed to be as high as hundreds of ampere per centimeter square (A/cm^2). Although the resistance is reduced in this method, the large IR drop issue is not resolved [10].

Another method to remove the passive film is the electrochemical film reduction method, where the passive film is removed through potentiostatic cathodic polarization for a long period of time [16 19]. The repassivation of the specimen is realized by fast polarization of the specimen at a potential within the passive region while the current transient is recorded simultaneously. This method does not involve mechanical removal of the passive film, but it can also cause some problems. One of the main issues is the uncertainty in the complete removal of the passive film. Angeliu, Andresen, and Pollick used both electrochemical reduction and the fast straining by drop weight method to study the repassivation of alloy 600, and they observed lower current density during the initial stage of repassivation when using electrochemical reduction method, indicating a noncomplete reduction of the passive film [17]. In addition, researchers developed an electrochemical method to study the repassivation potential to predict the long term resistance to localized corrosion of stainless steels and other alloys [26 28]. In this method, a high potential is applied to the specimen to induce localized corrosion such as pitting and crevice corrosion. After some time for the growth of localized corrosion, the potential is reduced until repassivation occurs, and this potential is defined as the repassivation potential. It should be noted that the repassivation potential also depends on the scan rate during the reduction of potential, and different models can be applied according to the scan rate used [27].

REPASSIVATION KINETICS THEORIES

During repassivation, the current transient decays from the peak current, when the bare metal surface is exposed to the environment, to the stable passive current when the passive film is reformed at the surface. Several models have been proposed to simulate the film growth and repassivation. The high field conduction model considers the passive film as an oxygen lattice with the metal ions filling the interstitial sites, and the potential drop across the film draws the metal ions from the bulk metal [29,30]. Because the passive film is typically very thin (several nanometers for stainless steels), the electric field within the film is high, and as the film grows, this electric field drops, leading to a decrease in the current flow. The high field conduction model has been applied to study the effect of pH of environmental and alloying elements on the repassivation kinetics of austenitic and ferritic stainless steels [1–4].

According to the high field conduction model [29,30], the electrolytic current density within the passive film because of the metal ion flow is expressed by Eq 1:

$$i = \alpha \cdot \exp\left(B\frac{V}{x}\right) \tag{1}$$

where α and B are constant and (V/x) is the electric field, with V the potential drop across the film and x the thickness of the passive film. If the current only contributes to the passive film growth and no metal dissolution is considered, the charge density and the thickness of the passive film can be related through Eq 2:

$$q(t) = \frac{\rho zF \cdot x(t)}{M} \tag{2}$$

where ρ is the density of passive film, z is the charge of metal ions, F is the Faraday's constant, and M is the molecular weight of the film; $i(t)$ can then be expressed as (Eq 3):

$$i(t) = \alpha \cdot \exp\left(\frac{B \cdot \rho VzF}{q(t) \cdot M}\right) \tag{3}$$

with $\frac{\rho zF}{M}$ being a constant, which can be represented by c; the relationship then becomes (Eq 4):

$$\log i(t) = A + \frac{cBV}{q(t)} \tag{4}$$

Kwon, Cho, and Yeom have shown that when comparing similar alloy/environment systems containing aggressive anions such as chloride, the higher the value of cBV, the higher the susceptibility of stainless steels to pitting corrosion and stress corrosion cracking [31].

However, the high field conduction model assumes that all the current after film breakdown contributes to the film growth and does not contribute to the dissolution of bare metal during the initial stages of repassivation. Alternatively, Beck

argued that metal dissolution current is dominant at the early passivation stage; therefore the metal dissolution current $I_{diss} \gg I_{film}$, the film formation current, making I_{film} negligible at early times [32]. Along with this argument, Fleischmann and Thirsk developed an expression (Eq 5) to model the metal dissolution current as

$$I_{tot} = I_{diss} = (i_0 \cdot a)(1 - \theta) \cdot \exp\{\beta_a \cdot \eta\} \tag{5}$$

where i_o is the exchange current density for the bare metal surface, a is the scratch area, β_a is the anodic Tafel slope, η is the polarization potential, and θ is the coverage of film formation and was derived from the Avrami relationship (dimensionless) [33].

Ratzer Sheibe and Buhl took a slightly different approach by incorporating the I_{film} current into the mathmetical model to account for nonuniform repassivation progresses at various scratching surfaces [34]. Ratzer Sheibe and Buhl employed two terms to simulate the repassivation current. This model treated repassivation as a film thickening process. The first term represents the dissolution current, and it can be used to model monolayer growth at the early repassivation stage (Eq 6):

$$I_{mono} = cv\, Q_{ox}\, (1 - \theta) \tag{6}$$

where v is the scratch speed, Q_{ox} is the charge density to form a monolayer of oxide, and c is a constant.

The second term reflects the thickening of the film by the addition of another monolayer (Eq 7):

$$I_{film} = \theta\, A t^{-b} \tag{7}$$

where θ is a "covering coefficient" and A and b are empirical constants.

Similar to Beck's and Ratzer Sheibe's models, Lillard's model was developed by Lillard, Vasquez, and Bahr [7], and it splits the repassivation current I_{total} into the dissolution current I_{diss} and the film passive current I_{film}, as is given by Eq 8:

$$I_{total} = I_{diss} + I_{film} = (1 - \theta) \cdot I_{bare} + \theta \cdot A \cdot t^{-b} \tag{8}$$

where I_{bare} is the very initial dissolution current from the bare metal, roughly taken as the first current recorded, and θ is the fraction of area covered by the passive film and is expressed by Eq 9:

$$\theta = 1 - \exp(-k \cdot t^{-n}) \tag{9}$$

where A, b, and n are constants that need to be computed accordingly [7].

In this paper, a scratch test method was used to study the repassivation of a duplex stainless steel UNS S32003 in Cl^- and $S_2O_3^{2-}$ containing solutions. Kwon's model, derived from the high field conduction model, is used to study the repassivation kinetics. In comparison, the film reduction method was conducted on carbon steel A569 in borate buffer solution (pH = 8.4) to study the effects of

retained plastic strain on the repassivation of carbon steel, and Lillard's model was found to apply to this system. These two different techniques are used in two different alloy/environment systems to demonstrate their applicability in different systems.

Experimental Procedures

All electrochemical tests were conducted using the potentiostatic chronoamperome try test method to monitor the repassivation current because this technique is more sensitive to short time data acquisition. The test cell was composed of a three electrode system with a saturated calomel electrode (SCE) as the reference electrode and platinum as the counter electrode. Before each test, the samples were polished to 2,000 grit and cleaned with ethanol and acetone.

In the study of repassivation behavior of duplex stainless steels in Cl^- and ($S_2O_3^{2-}$ + Cl^-) solutions, the mechanical scratch method was used because of the presence of $S_2O_3^{2-}$, which could be reduced at lower potentials during electrochem ical reduction. The duplex stainless steel (DSS) used for this study was UNS S32003, and the chemical composition of this alloy is shown in Table 1. The test solution was made from reagent grade sodium chloride and sodium thiosulfate in deionized water with concentrations of 1 M Cl^- and (1 M Cl^- + 0.1 M $S_2O_3^{2-}$). During the chronoamperometry test, the specimen was polarized at 0 V_{SCE}, which was within the passive region for UNS S32003 in the tested environment, and a mechanical scratch was made with a diamond scriber after the current had stabi lized at the passive current level after 60 s of immersion. The current was recorded for another 60 s after the scratch. To compare the repassivation behavior of the ferrite phase with that of the bulk DSS, preferential dissolution of the austenite phase was conducted in 2 M sulfuric acid + 0.5 M hydrochloric acid (HCl) fol lowing the method developed by Tsai and Chen [35]. Potentiodynamic polariza tion was first performed within the active region of UNS S32003, and potentials at which the two peaks corresponding to the maximum preferential dissolution of the ferrite phase and the austenite phase were recorded. Potentiostatic polariza tion was then conducted at the two potentials for 10 h to get the single phase microstructure. The resulting sample surface was characterized by scanning elec tron microscopy/energy dispersive X ray spectroscopy to identify the remaining phase. The space within the single ferrite phase, which was previously occupied by the austenite phase, was then filled with lacquer to obtain a smooth surface.

TABLE 1 Chemical composition of the materials used in this study (in weight percent).

	Cr	Ni	Mo	Mh	Cu	C	P	S	N	Si	Fe
DSS 2003	21.7	4.0	1.64	1.72	0.17	0.015	0.025	<0.001	0.17	0.32	Bal.
A569				<0.6	=0.2	<0.15	<0.035	<0.04			Bal.

In this way, any austenite phase that was remaining but had lower height than that of the ferrite phase could be covered. The electrochemical response then only came from the ferrite phase. This single ferrite phase specimen was then used in the study of repassivation kinetics. Because the surface area is important in determining both the current density and the charge density, especially for the single phase specimen, the scratched area was characterized after each test. The thickness of the specimen of bulk UNS S32003 is 850 μm. For single ferrite phase specimens, the thickness varies from 200 to 420 μm because only one phase is exposed and the length of the scratched ferrite phase also depends on the local microstructure. Tests under each condition were repeated at least four times to verify the reproducibility of data.

In another study, the effect of strain on the corrosion and repassivation behavior of carbon steel in borate buffer solution was examined. Carbon steel specimens were cold rolled at room temperature; %CR indicates the percentage of thickness reduction and %CR used in this study were 0 % (no cold rolling), 5 %, 10 %, 25 %, and 50 %. In this case, mechanical scratch could not be used as that would have generated surface strain from scratching action with a scriber. Therefore, electrochemical reduction of the passive film method was used. Carbon steel A569 was used in this study, and its chemical composition is shown in Table 1. The specimen was reduced at -1 V_{SCE} for different times and immediately anodically polarized at a potential ($+0.15$ mV_{SCE}) in the passivation range. Precautions were taken to address whether the cathodic reduction induced hydrogen diffused into the materials, which could also interfere with the oxidation current signal in the following step when the sample was anodically polarized.

Results

REPASSIVATION OF DUPLEX STAINLESS STEELS IN Cl AND (Cl $+ S_2O_3^{2}$) SOLUTION

Fig. 1 shows the microstructure of UNS S32003 and the two phases are elongated along the rolling direction, and scratches were made perpendicular to the rolling direction. Potentiodynamic polarization of UNS S32003 in (2 M H_2SO_4 + 0.5 M HCl) is shown in Fig. 2, and there are two peaks present within the active region. Energy dispersive X ray spectroscopy analysis after the separation of the two phases confirmed that the potential for the maximum active corrosion rate of the ferrite phase was -352 mV_{SCE}, while the potential for the maximum active corrosion of the austenite phase was -299 mV_{SCE}. Chemical composition of the single phase left at the surface after potentiostatic polarization is shown in Table 2. The ferrite phase is enriched in chromium (Cr) and molybdenum (Mo), while the austenite phase has higher nickel, manganese, and nitrogen (N) content. The space in the remaining phase that was previously occupied by the other phase was then filled with lacquer to obtain a smooth surface, as shown in Fig. 3. The ferrite phase is interconnected, while the austenite phase forms single islands.

FIG. 1 Microstructure of UNS S32003 specimen: α = ferrite phase; γ = austenite phase.

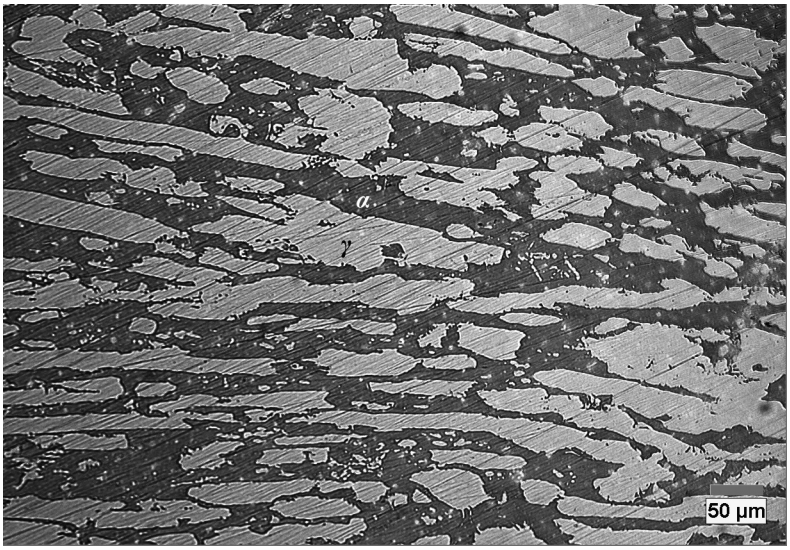

FIG. 2 Potentiodynamic polarization of UNS S32003 in (2 M H_2SO_4 + 0.5 M HCl) acid solution.

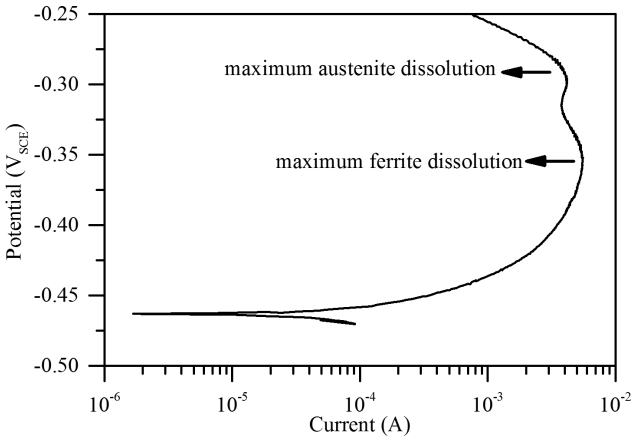

Fig. 4 shows the current density decay after the mechanical scratch where the time 0s represents the moment from which the current started to decay and the passive film started to form. Fig. 4a shows the linear linear plot of current density versus time curves for the three tested systems. For the bulk material UNS S32003

TABLE 2 Chemical composition of ferrite phase and austenite phase analyzed by energy dispersive X ray spectroscopy. Eight different sites were analyzed for each phase. Numbers represent the average value.

	Cr	Ni	Mo	Mn	N	Fe
Ferrite	22.9	3.0	1.5	1.6	0.08	65.8
Austenite	20.5	4.6	0.9	1.9	0.2	67.6

FIG. 3 Single phase microstructure after etching and mounting in epoxy: (a) ferrite phase; (b) austenite phase.

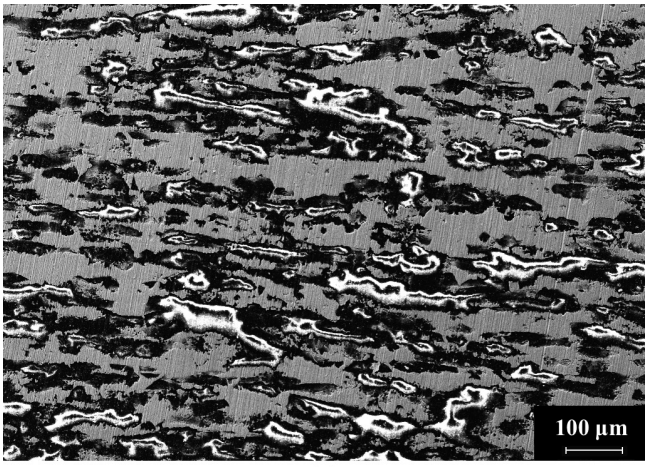

(a)

(b)

FIG. 4 Current density decay during repassivation after scratch in: (a) linear scale; (b) log log scale.

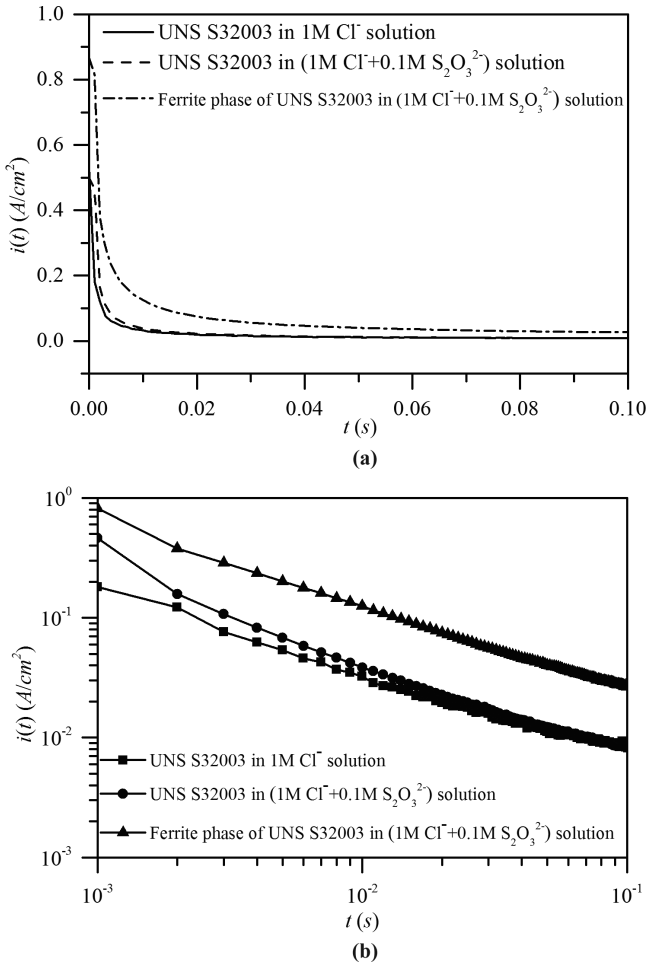

with both phases exposed, the current density decreased to the passive current density within 0.1 s after the scratch was made, while the time period for the single ferrite phase in UNS S32003 was more than 0.2 s. The addition of $S_2O_3^{2-}$ slowed down the repassivation process of the specimen, which can be better observed in the log log plot of current density versus time shown in Fig. 4b.

In this work, a MATLAB code (MathWorks, Inc., Natick, MA) was generated to check if log $i(t)$ versus $q(t)^{-1}$ followed the relationship described by Eq 4 proposed by Cho et al. [6]. Charge density was calculated through integration of the current density versus time, and the last data point before the scratch where the specimen was passive was used as time zero. Fig. 5a shows the $i(t)$ versus $q(t)^{-1}$

FIG. 5 (a) Log $i(t)$ versus $q(t)^{-1}$ in different test conditions. (b) One example showing curve fitting and value of R^2.

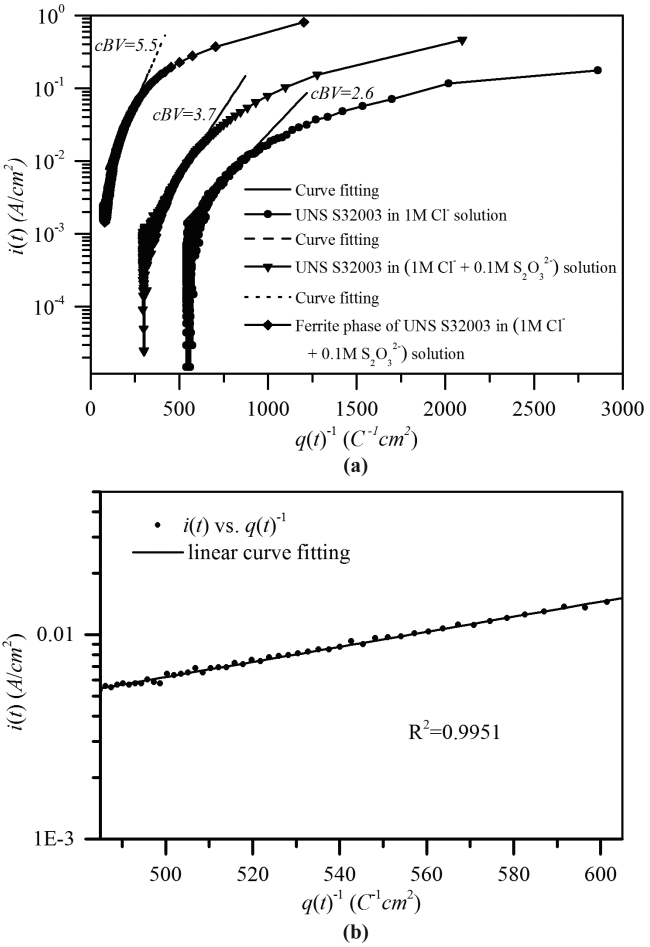

relationship, in which $q(t)^{-1}$ was calculated from data sets shown in **Fig. 4a**. The $i(t)$ versus $q(t)^{-1}$ curves exhibited a linear region; this region was analyzed through a linear curve fit, and the R^2 value was above 99.5 %. **Fig. 5b** shows one example of the curve fitting and the R^2 value. Numbers shown next to the linear region are *cBV* values calculated according to Eq 4 [6]; *cBV* values increased with the addition of $S_2O_3^{2-}$ to Cl^- containing solution, and the *cBV* value for the ferrite phase was much higher than that for the bulk DSS specimen.

From the log $i(t)$ versus $q(t)^{-1}$ curves analysis, the *cBV* value increased with the addition of $S_2O_3^{2-}$ to the Cl^- containing solution, indicating that the susceptibility of duplex stainless steels to pitting and stress corrosion cracking would increase.

The presence of $S_2O_3^{2-}$ has been shown to largely decrease the repassivation potential of duplex stainless steels in Cl^- containing environment and pits preferentially develop into the ferrite phase [36 38]. Pitting corrosion of stainless steels in $S_2O_3^{2-}$ containing environments depends on the $S_2O_3^{2-}/Cl^-$ ratio, and there is a critical $S_2O_3^{2-}/Cl^-$ range within which the pitting corrosion would happen [25]. The applied potential is also important, and at high potentials, $S_2O_3^{2-}$ could not be reduced to sulfur and promoted pitting corrosion. Future work will be done on the effects of $S_2O_3^{2-}/Cl^-$ as well as applied potential on the repassivation kinetics of DSS. The pitting corrosion susceptibility of the two phases in DSS can also be different according to the heat treatment procedures [39 41]. Chemical composition and the pitting corrosion resistance of the two phases can be altered through annealing treatment, providing evidence that the higher susceptibility to pitting corrosion of one phase in DSS is mainly because of the chemical composition difference. Although the ferrite phase is enriched in Cr and Mo, austenite has a higher N content, which probably contributes to the higher corrosion resistance of the austenite phase.

EFFECT OF STRAIN ON THE REPASSIVATION OF CARBON STEELS

To study the effects of strain on the repassivation of carbon steels, carbon steel A569 with different retained plastic deformation are used in borate buffer solution. To avoid additional stress/strain caused by mechanical scratch, the electrochemical reduction method was used to remove the film.

During potentiostatic repassivation, the current densities at the applied potential of +0.15 V applied potential decayed with time very rapidly for the cold rolled specimens, as shown in Fig. 6. The passive film was almost completely formed

FIG. 6 Repassivation current density at +0.15 V_{SCE} for 0 %CR, 5 %CR, 10 %CR, 25 %CR, and 50 %CR specimens in borate buffer solution.

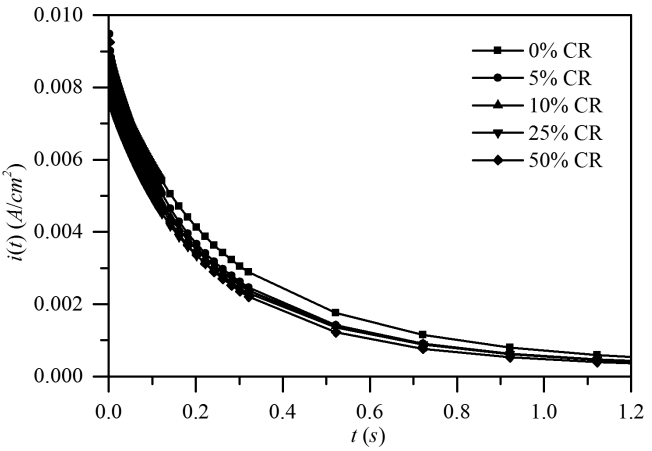

within the initial 1.2 s, indicated by the converging current density at the end of each curve. Faster repassivation kinetics, represented by the faster decay in current density, were noticed for the specimens with higher degrees of cold rolling. Each of these repassivation tests was repeated at least five times, and the results were consis tent. The log current density versus log time plot is presented in **Fig. 7**. A distinct discontinuity of slope is manifested in **Fig. 7**, likely indicating two different repassi vation kinetic mechanisms. Region I possesses a shallower slope for all five curves, meaning repassivation was slower in the beginning. This is likely due to the fact that the initial stage of strain influenced repassivation of A569 in borate buffer was metal dissolution dominated. On the contrary, Region II reflects a much faster repassivation process than Region I, signified by a steeper slope. This is probably because this stage was controlled by the film formation mechanism. Compared to the high field conduction model, which typically is characterized by a single slope region, the two slope trend of the curves presented in **Fig. 7** again evidence the importance of the repassivation model developed by Beck [32], Ratzer Sheibe and Buhl [24], and Lillard, Vasquez, and Bahr [7].

Lillard's model was used to analyze the repassivation current for each sample, and above 99.5 % fitting was obtained for each curve [7]. A MATLAB code was written to fit the repassivation current data; hence, the fraction of completion or the fraction of area covered by passive film, θ, versus time plot could be derived accord ing to Eqs 9 and 10. Fraction of repassivation completion θ was extracted from the mathematical simulation; θ is plotted with respect to time in **Fig. 8**. The resultant graph again indicates that the repassivation kinetics are accelerated due to the pres ence of strain, as shown in **Fig. 8**. This is likely due to the accelerated active

FIG. 7 Log repassivation current density versus log time for 0 %CR, 5 %CR, 10 %CR, 25 %CR, and 50 %CR specimens.

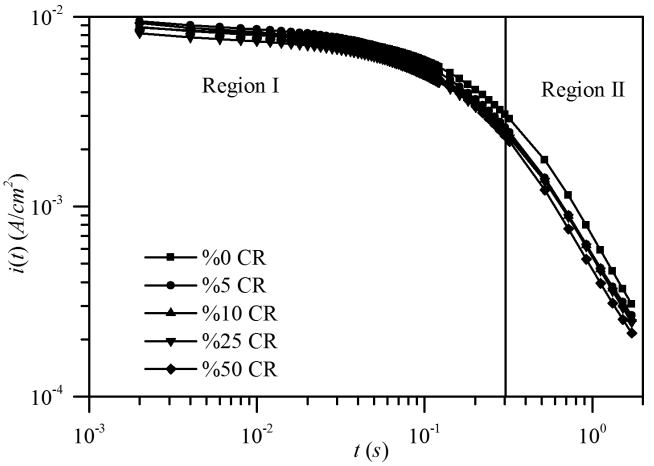

FIG. 8 Fraction of completion of film formation θ as a function of time for 0 %CR, 5 %CR, 10 %CR, 25 %CR, and 50 %CR specimens.

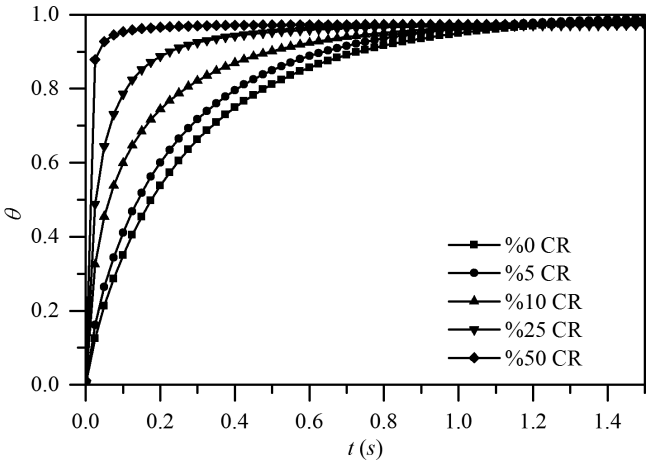

dissolution rate of the bare metal surface because of the additional strain energy in the material. Several authors have demonstrated that strain can increase the metal's active dissolution rate [42 45]. These results indicate that the effect of strain is dominant before the large part of the surface area is repassivated in the early stages of passive film formation.

Discussions

Comparing the two film removal methods used to study the repassivation kinetics, namely the mechanical scratch test method and the electrochemical film reduc tion method, the differences and applicability are shown in Table 3. In both test methods, data acquisition is realized through the potentiostatic chronoamperom etry technique, which is sensitive to short time data collection. For example, the sample period is 1 ms in this study. Because of less stability in the manual scratch, the depassivated area needs to be examined after each test, while in electrochemi cal reduction of the film, the depassivated area is simply the area that is exposed to the test solution. In the systems where external stress/strain due to mechanical scratch need to be avoided, the electrochemical film reduction method can be used. On the other hand, if the potential for film removal could induce a chemical reaction of some species in the test solution, in those cases the mechanical scratch test method is a better suited method for repassivation study. In addition, atten tion should be paid to the time period needed for the reduction of passive film because the time of reduction should be long enough to completely reduce the passive film.

TABLE 3 Comparison between the two depassivation test methods for the study on repassivation kinetics.

	Scratch Test Method	Electrochemical Film Reduction
Data acquisition	Potentiostatic chronoamperometry	Potentiostatic chronoamperometry
Area of film removal	Area that has been scratched by the stylus (needs characterization after tests)	Area exposed to the test solution (relatively constant)
Disadvantage	1. Introduce external stress/strain to the surface of specimen. 2. The microstructure in the area scratched by the stylus may not represent the microstructure of the whole surface of the specimen.	1. Potential for film removal may induce reduction reaction of chemical species in the solution. 2. Solution near the surface may be different from the bulk solution. 3. It is not definite that passive film on materials such as stainless steels can be fully electrochemically reduced or if it is just a film thinning process.

Conclusions

1. Presence of thiosulfate slows down the repassivation kinetics of DSS compared with the repassivation kinetics in an aqueous solution with only chloride. Repassivation kinetics of the ferrite phase is lower than that of the bulk DSSs that contain both ferrite and austenite in environments containing both chlo ride and thiosulfate.
2. Plastic strain improves the initial repassivation kinetics of carbon steel. This can be ascribed to the increased active dissolution rate at the initial stage.
3. Both the mechanical scratch test method and electrochemical film reduction method are versatile and can complement each other where one method does not apply to a certain alloy/environment system, making the technique a pow erful tool for the study of repassivation kinetics.

ACKNOWLEDGMENTS

Liang He and Gaoxiang Wu would like to thank the Renewable Bioproducts Institute at Georgia Tech for the Paper Science and Engineering graduate student fellowship. The authors would also like to acknowledge the member companies of the Renewable Bioproducts Institute for partial financial support for this project.

References

[1] Burstein, G. T. and Marshall, P. I., "The Coupled Kinetics of Film Growth and Dissolution of Stainless Steel Repassivating in Acid Solutions," *Corros. Sci.*, Vol. 24, No. 5, 1984, pp. 449–462, https://dx.doi.org/10.1016/0010-938X(84)90070-2

[2] Marshall, P. I. and Burstein, G. T., "The Effect of pH on the Repassivation of 304L Stainless Steel," *Corros. Sci.*, Vol. 23, No. 11, 1983, pp. 1219–1228, https://dx.doi.org/10.1016/0010-938X(83)90049-5

[3] Marshall, P. I. and Burstein, G. T., "Effects of Alloyed Molybdenum on the Kinetics of Repassivation on Austenitic Stainless Steels," *Corros. Sci.*, Vol. 24, No. 5, 1984, pp. 463–478, https://dx.doi.org/10.1016/0010-938X(84)90071-4

[4] Newman, R. C., "The Dissolution and Passivation Kinetics of Stainless Alloys Containing Molybdenum-I. Coulometric Studies of Fe-Cr and Fe-Cr-Mo Alloys," *Corros. Sci.*, Vol. 25, No. 5, 1985, pp. 331–339, https://dx.doi.org/10.1016/0010-938X(85)90111-8

[5] Bastek, P. D., Newman, R. C., and Kelly, R. G., "Measurement of Passive Film Effects on Scratched Electrode Behavior," *J. Electrochem. Soc.*, Vol. 140, No. 7, 1993, pp. 1884–1889, https://dx.doi.org/10.1149/1.2220733

[6] Cho, E. A., Kim, C. K., Kim, J. S., and Kwon, H. S., "Quantitative Analysis of Repassivaion Kinetics of Ferritic Stainless Steels Based on the High Field Ion Conduction Model," *Electrochim. Acta*, Vol. 45, No. 12, 2000, pp. 1933–1942, https://dx.doi.org/10.1016/S0013-4686(99)00415-6

[7] Lillard, R. S., Vasquez, G. Jr., and Bahr, D. F., "The Kinetics of Anodic Dissolution and Repassivation on Stainless Steels 304L in Solutions Containing Nitrate," *J. Electrochem. Soc.*, Vol. 158, No. 6, 2011, pp. 194–201, https://dx.doi.org/10.1149/1.3574367

[8] Newman, R. C., Sieradzki, K., and Isaacs, H. S., "Stress-Corrosion Cracking of Sensitized Type 304 Stainless Steel in Thiosulfate Solutions," *Metall. Trans. A*, Vol. 13, No. 11, 1982, pp. 2015–2026, https://dx.doi.org/10.1007/BF02645947

[9] Frankel, G. S., Rush, B. M., Jahnes, C. V., Farrell, C. E., Davenport, A. J., and Isaacs, H. S., "Repassivation Transients Measured with Thin Film Breaking Electrodes," *J. Electrochem. Soc.*, Vol. 138, No. 2, 1991, pp. 643–644, https://dx.doi.org/10.1149/1.2085652

[10] Frankel, G. S., Jahnes, C. V., Brusic, V., and Davenport, A. J., "Repassivation Transients Measured with the Breaking-Electrode Technique on Aluminum Thin-Film Samples," *J. Electrochem. Soc.*, Vol. 142, No. 7, 1995, pp. 2290–2295, https://dx.doi.org/10.1149/1.2044289

[11] Kolman, D. G. and Scully, J. R., "Limitations of Potentiostatic Repassivation Techniques and Their Relationship to the Applicability of the High Field Approximation to the Repassivation of Titanium," *J. Electrochem. Soc.*, Vol. 142, No. 7, 1995, pp. 2179–2188, https://dx.doi.org/10.1149/1.2044272

[12] Hoar, T. P. and Ford, F. P., "Electrode Reaction Rates on Straining Aluminum-Magnesium Wires in Chloride and Sulfate Solutions," *J. Electrochem. Soc.*, Vol. 120, No. 8, 1973, pp. 1013–1019, https://dx.doi.org/10.1149/1.2403619

[13] Engseth, P. and Scully, J. C., "Repassivation Studies on an Austenitic Stainless Steel in Chloride Solutions," *Corros. Sci.*, Vol. 15, Nos. 6–12, 1975, pp. 505–519, https://dx.doi.org/10.1016/0010-938X(75)90016-5

[14] Beck, T. R., "Stress Corrosion Cracking of Titanium Alloys. II. An Electrochemical Mechanism," *J. Electrochem. Soc.*, Vol. 115, No. 9, 1968, pp. 890–896, https://dx.doi.org/10.1149/1.2411463

[15] Beck, T. R., "Reactions and Kinetics of Newly Generated Titanium Surfaces and Relevance to Stress Corrosion Cracking," *Corrosion*, Vol. 30, No. 11, 1974, pp. 408–414, https://dx.doi.org/10.5006/0010-9312-30.11.408

[16] Angeliu, T. M. and Andresen, P. L., "Effect of Zinc Additions on Oxide Rupture Strain and Repassivation Kinetics of Iron-Based Alloys in 288°C Water," *Corrosion*, Vol. 52, No. 1, 1996, pp. 28–35, https://dx.doi.org/10.5006/1.3292092

[17] Angeliu, T. M., Andresen, P. L., and Pollick, M. L., "Repassivation and Crack Propagation of Alloy 600 in 288°C Water," *Corrosion*, Vol. 53, No. 2, 1997, pp. 114–119, https://dx.doi.org/10.5006/1.3280439

[18] Oh, K. N., Toor, I. H., Ahn, S. H., and Kwon, H. S., "Influence of Cu on the Passivation Behavior of Fe-20Cr-xCu (x 0, 2, 4 wt%) Alloys in Sulfuric Acid Solution," *Corrosion*, Vol. 69, No. 6, 2013, pp. 560–567, https://dx.doi.org/10.5006/0673

[19] Wu, G. and Singh, P. M., "Effect of Strain on Repassivation and Corrosion Behavior of Carbon Steel A569," presented at *Corrosion 2017*, New Orleans, LA, March 26–30, 2017, NACE International, Houston, TX, Paper No. C2017–9083.

[20] Keddam, M., Oltra, R., Colson, J. C., and Desestret, A., "Depassivation of Iron by Straining and by Abrasion: An A.C. Impedance Study," *Corros. Sci.*, Vol. 23, No. 4, 1983, pp. 441–451, https://dx.doi.org/10.1016/0010-938X(83)90072-0

[21] Newman, R. C., "Measurement and Interpretation of Electrochemical Kinetics on Bare Metal Surfaces," *Corrosion Chemistry within Pits, Crevices and Cracks*, A. Turnbull, Ed., HMSO, Butterworth, London, 1987, p. 317.

[22] Pearson, H. J., Burstein, G. T., and Newman, R. C., "Resistance to Flow of Current to Scratched Electrodes," *J. Electrochem. Soc.*, Vol. 128, No. 11, 1981, pp. 2297–2303, https://dx.doi.org/10.1149/1.2127238

[23] Wei, R. P., Gao, M., and Xu, P. Y., "Peak Bare-Surface Current Densities Overestimated in Straining and Scratching Electrode Experiments," *J. Electrochem. Soc.*, Vol. 136, No. 6, 1989, pp. 1835–1836, https://dx.doi.org/10.1149/1.2097038

[24] Bastek, P. D., Newman, R. C., and Kelly, R. G., "Measurement of Passive Film Effects on Scratched Electrode Behavior," *J. Electrochem. Soc.*, Vol. 140, No. 7, 1993, pp. 1884–1889, https://dx.doi.org/10.1149/1.2220733

[25] Newman, R. C., Wong, W. P., Ezuber, H., and Garner, A., "Pitting of Stainless Steels by Thiosulfate Ions," *Corrosion*, Vol. 45, No. 4, 1989, pp. 282–287, https://dx.doi.org/10.5006/1.3577855

[26] Tsujikawa, S. and Kojima, Y., "Repassivation Method to Predict Long Term Integrity of Low Alloy Titanium for Nuclear Waste Package," *MRS Proceedings*, Vol. 212, 1990, p. 261, https://dx.doi.org/10.1557/PROC-212-261

[27] Sridhar, N. and Cragnolino, G. A., "Applicability of Repassivation Potential for Long-Term Prediction of Localized Corrosion of Alloy 825 and Type 316L Stainless Steel," *Corrosion*, Vol. 49, No. 11, 1993, pp. 885–894, https://dx.doi.org/10.5006/1.3316014

[28] Dunn, D. S., Cragnolino, G. A., and Sridhar, N., "An Electrochemical Approach to Predicting Long-Term Localized Corrosion of Corrosion-Resistant High-Level Waste Container Materials," *Corrosion*, Vol. 56, No. 1, 2000, pp. 90–104, https://dx.doi.org/10.5006/1.3280526

[29] Cabrera, N. and Mott, N. F., "Theory of the Oxidation of Metals," *Rep. Prog. Phys*, Vol. 12, 1949, pp. 163–184.

[30] Verwey, E. J. W., "Electrolytic Conduction of a Solid Insulator at High Fields," *Physica*, Vol. 2, Nos. 1–12, 1935, pp. 1059–1063, https://dx.doi.org/10.1016/S0031-8914(35)90193-8

[31] Kwon, H. S., Cho, E. A., and Yeom, K. A., "Prediction of Stress Corrosion Cracking Susceptibility of Stainless Steels Based on Repassivation Kinetics," *Corrosion*, Vol. 56, No. 1, 2000, pp. 32–40, https://dx.doi.org/10.5006/1.3280519

[32] Beck, T. R., "Electrochemistry of Freshly Generated Titanium Surfaces—II. Rapid Fracture Experiments," *Electrochim. Acta*, Vol. 18, No. 11, 1973, pp. 815–827, https://dx.doi.org/10.1016/0013-4686(73)85033-9

[33] Fleischmann, M. and Thirsk, H. R., *Advances in Electrochemistry and Electrochemical Engineering*, Wiley, New York, 1963, p. 123.

[34] Ratzer-Scheibe, V. H. J. and Buhl, H., "Zum Repassivierungsverhalten Metallischer Werkstqffc, am Beispiel einer Titanlegierung," *Werkst. Korros.*, Vol. 30, 1979, pp. 846–853.

[35] Tsai, W. T. and Chen, J. R., 2007, "Galvanic Corrosion between the Constituent Phases in Duplex Stainless Steel," *Corros. Sci.*, Vol. 49, No. 9, 1979, pp. 3659–3668, https://dx.doi.org/10.1016/j.corsci.2007.03.035

[36] He, L., Wang, Y., and Singh, P. M., "Pitting Behavior of Lean Duplex Stainless Steels in Thiosulfate-Containing Paper Machine Environment," presented at *Corrosion* 2017, New Orleans, LA, March 26–30, 2017, NACE International, Houston, TX, Paper No. C2017–9163.

[37] Wang, Y. and Singh, P. M., "Corrosion Behavior of Austenitic and Duplex Stainless Steels in Thiosulfate- and Chloride-Containing Environments," *Corrosion*, Vol. 71, No. 8, 2015, pp. 937–944, https://dx.doi.org/10.5006/1694

[38] Wang, Y., Wu, G., He, L., and Singh, P. M., "Effect of Thiosulfate on Metastable Pitting of 304L and S32101 in Chloride- and Thiosulfate-Containing Environment," *Corrosion*, Vol. 72, No. 5, 2016, pp. 628–635, https://dx.doi.org/10.5006/1955

[39] Zhang, L., Zhang, W., Jiang, Y., Deng, B., Sun, D., and Li, J., "Influence of Annealing Treatment on the Corrosion Resistance of Lean Duplex Stainless Steel 2101," *Electrochim. Acta*, Vol. 54, No. 23, 2009, pp. 5387–5392, https://dx.doi.org/10.1016/j.electacta.2009.04.023

[40] He, L. and Singh, P. M., "Effects of Annealing Temperature on Pitting Corrosion of LDX 2003 and LDX 2404 Duplex Stainless Steels," presented at *Corrosion* 2017, New Orleans, LA, March 26–30, 2017, NACE International, Houston, TX, Paper No. C2017–9156.

[41] Naghizadeh, M. and Moayed, M. H., "Investigation of the Effect of Solution Annealing Temperature on Critical Pitting Temperature of 2205 Duplex Stainless Steel by Measuring Pit Solution Chemistry," *Corros. Sci.*, Vol. 94, 2015, pp. 179–189, https://dx.doi.org/10.1016/j.corsci.2015.01.051

[42] Johnston, H. A., "Effect of Strain on Corrosion Rates of Copper in Sulfuric Acid Solutions," master's thesis, University of British Columbia, Vancouver, Canada, 1955.

[43] Yang, Y. and Chang, F., "Stress Enhanced Corrosion at the Tip of Near-Neutral PH Stress Corrosion Cracks on Pipelines," *Corrosion*, Vol. 72, No. 8, 2016, pp. 1035–1043, https://dx.doi.org/10.5006/2045

[44] Yaguchi, S. and Yonezawa,T., "Intergranular Stress Corrosion Cracking Growth Perpendicular to Fatigue Pre-Cracks in T–L Oriented Compact Tension Specimens in Simulated Pressurized Water Reactor Primary Water," *Corros. Sci.*, Vol. 86, 2014, pp. 326–336, https://dx.doi.org/10.1016/j.corsci.2014.06.003

[45] Ralston, K. D. and Birbilis, N., "Effect of Grain Size on Corrosion: A Review," *Corrosion*, Vol. 66, No. 7, 2010, pp. 075005–075005–13, https://dx.doi.org/10.5006/1.3462912

STP 1609, 2019 / available online at www.astm.org / doi: 10.1520/STP160920170207

Mike Horton[1]

Corrosion Rates of Ductile Iron Pipe in Drilling Fluids: A Comparison of ASTM Electrochemical Standards G59, G102, and G106 to ASTM Weight Loss Standard G162

Citation

Horton, M., "Corrosion Rates of Ductile Iron Pipe in Drilling Fluids: A Comparison of ASTM Electrochemical Standards G59, G102, and G106 to ASTM Weight Loss Standard G162," *Advances in Electrochemical Techniques for Corrosion Monitoring and Laboratory Corrosion Measurements*, *ASTM STP1609*, S. Papavinasam, R. B. Rebak, L. Yang, and N. S. Berke, Eds., ASTM International, West Conshohocken, PA, 2019, pp. 262–279, http://dx.doi.org/10.1520/STP160920170207[2]

ABSTRACT

One of the most commonly used piping materials for transport of water and wastewater in the United States is ductile iron pipe (DIP). Although this piping normally is installed using open trench cuts, a trenchless installation method that is finding increased popularity for DIP is horizontal directional drilling (HDD). Many HDD installations utilize specialized drilling fluids, commonly called "drilling muds," which may be composed of bentonite clay, various organic and inorganic additives, polymers, lubricants, wetting agents, or polymers mixed with water (or any combination thereof). To evaluate the corrosion characteristics of these fluids in contact with DIP, a 1-year corrosion study involving more than 200 ductile iron pipe specimens was conducted comparing five commercially available directional drilling fluids. Corrosion tests were conducted using electrochemical test methods described in ASTM G59, *Standard Test Method for Conducting Potentiodynamic*

Manuscript received October 25, 2017; accepted for publication January 30, 2018.

[1]U. S. Pipe and Foundry Company, Technology and Product Development Dept., 2023 St. Louis Ave., Bessemer, AL 35020, USA http://orcid.org/0000 0003 0570 4149

[2]ASTM Symposium on *Advances in Electrochemical Techniques for Corrosion Monitoring and Laboratory Corrosion Measurements* on November 13 14, 2017 in Atlanta, GA, USA.

Polarization Resistance Measurements, ASTM G102, *Standard Practice for Calculation of Corrosion Rates and Related Information from Electrochemical Measurements*, and ASTM G106, *Standard Practice for Verification of Algorithm and Equipment for Electrochemical Impedance Measurements*, and these results were compared to 1-year weight loss test results obtained using ASTM G162, *Standard Practice for Conducting and Evaluating Laboratory Corrosions Tests in Soils*. This paper discusses which electrochemical test method and method of analysis gave results closest to those obtained with ASTM G162 weight loss evaluation.

Keywords

ductile iron pipe, drilling fluids, corrosion, electrochemical testing, polarization resistance, linear polarization, electrochemical impedance spectroscopy, trenchless technology, horizontal directional drilling, HDD

Introduction

Aging water and wastewater infrastructure problems have been widely publicized. The 2017 American Society of Civil Engineers (ASCE) Infrastructure Report Card rated the water industry infrastructure a "D" and stated: "According to the American Water Works Association, an estimated $1 trillion is necessary to maintain and expand services to meet demands over the next 25 years" [1]. At an ASCE conference titled *Beneath Our Feet Challenges and Solutions*, Allouche and Ariaratnam reported: "Faced with an urgent need to rehabilitate or replace their aging utility systems on one hand, and dwindling budgets, tight environmental restrictions and an increased emphasis on user costs on the other hand, owners of utility networks are seeking alternate methods for repairing, replacing, and expanding their underground assets" [2].

One alternate method of pipeline installation to meet these demands the popularity of which is growing rapidly in the water and wastewater industry is trenchless technology (TT). Compared to traditional "open cut" trench installations of pipelines, TT methods offer installation advantages in many areas such as highly congested/populated areas; under utilities, rivers, busy roads, and driveways; areas where there are environmental restrictions; burials greater than 15 ft; and areas where trenching operations would cause major inconveniences to the public such as at hospitals, airports, office buildings, and so on or loss of business to merchants (or any combination thereof) [3].

One such TT method is horizontal directional drilling (HDD), and a growing piping material being utilized in HDD installations is ductile iron pipe (DIP). Drilling fluids are used during the HDD process to support and lubricate the pipe, to reduce required pulling forces, to clean and cool the cutting bit, to stabilize the bore hole formation, and to remove cuttings from the bore hole [4]. The type and formulation of drilling fluids utilized are based on soil characteristics and typically consist of water based mixtures of bentonite clay or polymers, or both. A literature search on the corrosivity of drilling fluids with respect to DIP, however, failed to reveal

any reported research in this area. This absence of information is one of the factors that prompted this study.

To evaluate the corrosion characteristics of drill fluids in contact with DIP, a 1 year corrosion study involving more than 200 DIP samples was conducted comparing five commercially available directional drilling fluids. Electrochemical corrosion tests were conducted using procedures and analysis discussed in the following ASTM electrochemical test standards: ASTM G59, *Standard Test Method for Conducting Potentiodynamic Polarization Resistance Measurements* [5], ASTM G102, *Standard Practice for Calculation of Corrosion Rates and Related Information from Electrochemical Measurements* [6], and ASTM G106, *Standard Practice for Verification of Algorithm and Equipment for Electrochemical Impedance Measurements* [7]. Corrosion rate results from electrochemical test methods were then compared to 1 year weight loss test results obtained using method ASTM G162, *Standard Practice for Conducting and Evaluating Laboratory Corrosions Tests in Soils* [8].

Ductile Iron Pipe

Since replacing gray cast iron pipe in the mid 1970s, millions of feet of DIP have been successfully installed and utilized in many types of environments [9]. Reported advantages of DIP in HDD installations include but are not limited to quick and easy joint assembly, standard pressure capabilities up to 350 psi (2.4 MPa) or greater upon special request, better distribution of thrust or pulling force, and joint deflection with simultaneous joint restraint. DIP can be located from the surface with commonly used locators [10]. In addition to the strength and toughness of DIP, the authors also report that it is utilized in some areas for its impermeability where distribution lines are installed in areas subject to groundwater contamination by organic compounds.

The two methods of installing restrained joint DIP with HDD equipment are either a cartridge method or an assembled line method [11]. The preferred method where there is a limited right of way or easements is the cartridge method, where the joints are connected in the pit one at a time and then pulled through the bore hole. With the second method of installation, the joints are preassembled and the pipes are strung out along the right of way prior to pulling through the bore hole.

Corrosion Study

The purpose of this study was twofold to evaluate and compare the corrosivity of various commercially available drilling fluids used in HDD installations of DIP and to compare corrosion rate results obtained utilizing various ASTM electrochemical techniques with those obtained using ASTM G162 [8], which is based on coupon weight loss. This 1 year study was conducted as part of a master's thesis titled "Evaluation of the Corrosivity of Drilling Fluids Utilized in Horizontal Direction Drilling (HDD) Installations of Ductile Iron Pipe" [12]. A detailed discussion of the

entire study can be found in this thesis, and a discussion primarily comparing the corrosivity of commercially available drilling fluids and the benefits of asphalt coating may be found in Horton [3].

The purpose of this ASTM technical paper is to specifically compare and discuss corrosion rate results obtained using ASTM electrochemical procedures and analysis methods described in ASTM G59, ASTM G102, and ASTM G106 [5–7], with corrosion rates determined based on weight loss determined using ASTM G162 [8].

DIP TEST SPECIMENS

Two hundred and twenty two 4 in. by 4 in. test specimens were cut from a production 8 in. diameter DIP that was verified as meeting all requirements of American Water Works Association (AWWA) Standard C151 [13]. One half of the coupons (111 specimens) were uncoated and sandblasted, and the other one half (111 specimens) were coated utilizing standard production asphaltic cutback "shopcoat." Cut edges and internal surfaces of the specimens were coated with a 100 % solids two part epoxy. The specimens utilized for the study are shown in **Fig. 1** and **Fig. 2**.

DRILL FLUID/ELECTROLYTE DESCRIPTION

Based on discussions with HDD contractors, drilling fluid manufacturers, and DIP manufacturers, five commercially available and commonly used HDD drilling fluids were selected for study. To verify the results of the methods and procedures, a control salt solution of 3.5 % (by weight) laboratory grade sodium chloride and distilled water was included. Previous corrosion studies in saltwater have shown the

FIG. 1 Photograph showing 222 DIP specimens used in the study.

FIG. 2 Photograph showing representative standard shopcoated DIP O.D. surface (left) and uncoated, sandblasted DIP O.D. surface (right).

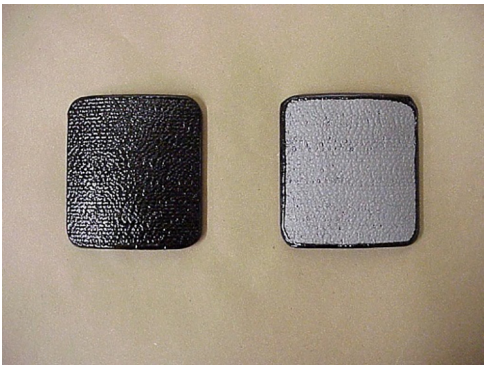

corrosion rate of unprotected DIP in this environment typically to be between 3 and 6 mils per year (e.g., 0.003 in. [0.075 mm] to 0.006 in. [0.15 mm] per year) [14]. The test environments and their corresponding symbols assigned during the study are as follows:

W = Standard 3.5 % saltwater (control)
P = A commercially available Wyoming bentonite blended with special extenders
BB = A commercially available Wyoming sodium bentonite
BZ = A commercially available Wyoming sodium bentonite plus corrosion inhibitors
CV = A commercially available polymer emulsion hydrolyzed polyacrylamide/polyacrylate copolymer mixed into virgin bentonite
CZ = A commercially available sodium bentonite clay with special polymer additive

All drilling fluids were mixed in strict accordance with the manufacturer's instructions, yielding concentrations based on the manufacturer's technical data sheets.

Soil test methods to determine if a soil in contact with DIP should be considered corrosive or not are described in detail in AWWA C105, Appendix A [15]. Two of the tests having the most impact on corrosion (resistivity and pH) were conducted for the six different environments. Laboratory resistivity tests were conducted in accordance with the soil box test method as described in ASTM G57, *Standard Test Method for Field Measurement of Soil Resistivity Using the Wenner Four Electrode Method* [16], and laboratory pH tests were conducted in accordance with ASTM G51, *Standard Test Method for Measuring pH of Soil for Use in Corrosion Testing* [17]. The resistivity of the drilling fluids varied from 380 to 1,120 Ω cm, and the pH varied from 9.0 to 10.6. The resistivity of the sodium

FIG. 3 (a) Resistivities and (b) pHs of test environments.

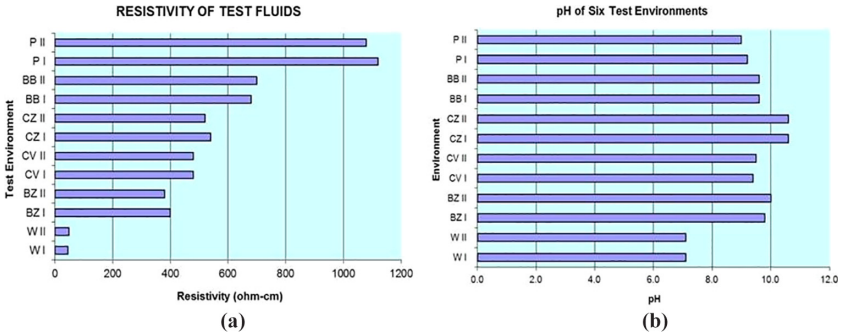

chloride (NaCl) control solution was between 40 and 50 Ω cm, and the pH was 7.1. Resistivities and pHs of the test environments are shown in Fig. 3a and b, respectively.

DESCRIPTION OF WEIGHT LOSS TESTING

Weight loss testing was conducted on 180 DIP specimens in six environments in accordance with ASTM G162 [8]. Ninety specimens were sandblasted, and 90 specimens were coated with a standard asphaltic coating. Triplicate specimens in each environment were evaluated at intervals of 1, 3, 6, 9, and 12 months. After exposure, all specimens were cleaned in accordance with procedures described in ASTM G1 03, *Standard Practice for Preparing, Cleaning, and Evaluating Corrosion Test Specimens*, using C.3.2 procedure [18]. Three sandblasted coupons and three asphalt coated coupons were also evaluated at zero exposure time to determine weight loss attributable to the ASTM G 1 cleaning process. All weight loss measure ments were determined to the nearest 0.001 g and were corrected to account for baseline loss from the cleaning loss.

Minimum environment volume requirement based on specimen size required 8.3 gal (31.9 L) of mixed drilling fluid or test solution utilized for every three 4 in. (100 mm) by 4 in. (100 mm) coupons. More than 5,000 lb (2,270 kg) of drilling flu ids and control solution were mixed for the study. A total of 60 containers with each containing three DIP specimens were utilized for the weight loss evaluation phase of the study.

DESCRIPTION OF ELECTROCHEMICAL TESTING

Electrochemical Test Equipment

Potentiodynamic polarization measurements, linear polarization resistance mea surements, and electrochemical impedance spectroscopy (EIS) measurements were conducted utilizing an EG&G Princeton Applied Research (Oak Ridge, TN) Model 263A potentiostat/galvanostat with two phase Model 5210 lock in amplifier.

Electrochemical Test Cell

A typical test cell used in electrochemical testing is described in ASTM G5, *Standard Reference Test Method for Making Potentiodynamic Anodic Polarization Measurements* [19], and is shown in **Fig. 4a** and **b**.

Initial testing of drilling fluids in this test cell revealed problems with the size and surface of the DIP working electrode. The DIP working electrode was approximately 1 cm^2 in size and was machined on all exposed surfaces to fit the electrode holder. Results revealed the corrosion test results on the smooth, machined surface specimens were significantly different than results on as cast DIP surfaces, which have a peen pattern roughness, annealing oxide, and asphaltic shopcoat. To resolve this problem and test the representative DIP outside diameter (O.D.) pipe surfaces, which would be exposed to the drilling fluids, 24 specially designed electrochemical cells that fit the curvature of an 8 in. DIP external surface were constructed. These specially designed and constructed cells increased the test area to approximately 100 cm^2. This specially designed corrosion test cell is shown in **Fig. 5a** and **b**.

Electrochemical Test Methods

Corrosion is an electrochemical process and, as such, can be studied using various electrical testing techniques. Faraday's law can be used to calculate the corrosion rate using formulas given in ASTM G59 [5] and ASTM G102 [6]. A detailed discussion of electrochemical theory and associated calculations used to obtain corrosion rates can be found in numerous publications, ASTM standard test methods, and ASTM standard practices and are beyond the scope of this paper. However, a brief discussion of the test methods and calculations specific to DIP used during this study follows.

Polarization Resistance

As discussed in ASTM G59 [5], standard polarization resistance can be related to the rate of general corrosion for metals that are at or near their corrosion potential and

FIG. 4 Components of test cell (a) and actual test cell filled with salt water (b).

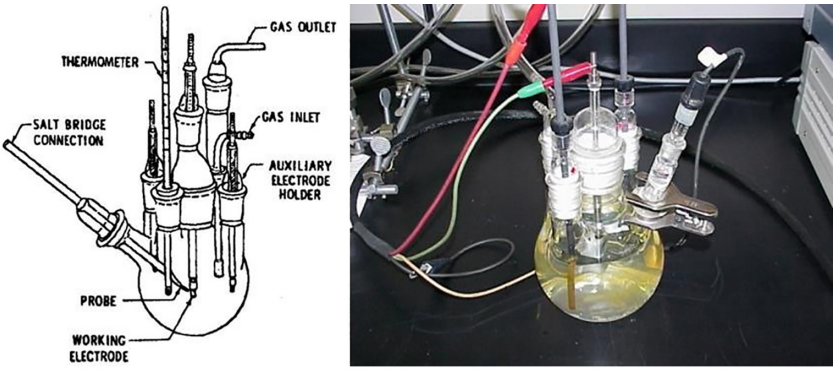

(a) (b)

FIG. 5 Components of test cell (a) and test cell filled with drilling fluid (b).

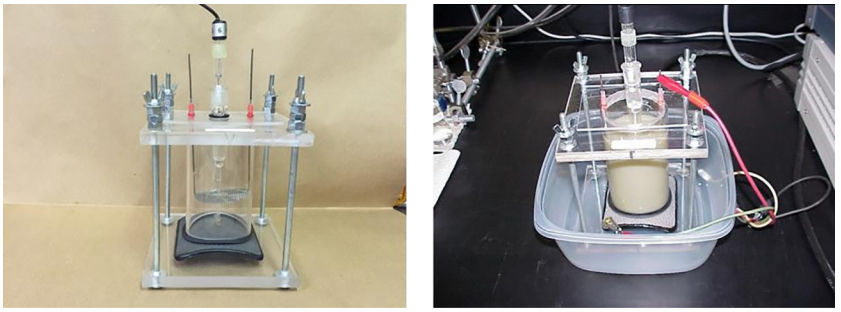

(a) (b)

commonly referred to as E_{corr}. This DC test method utilizes a small potential scan, $\Delta E(t)$, applied to a metal sample. The resultant currents, i, are recorded and the polarization resistance, R_p, of the corroding electrode is determined. R_p is defined as the slope of the potential versus the current density at $i = 0$ in accordance with Eq 1:

$$R_p = (\partial \Delta E / \partial i)_{i\ \ 0,\ dE/dt \to 0} \tag{1}$$

The corrosion current density, i_{corr}, is related to the polarization resistance by the Stern Geary coefficient, β, by Eq 2:

$$i_{corr} = 10^6 \beta / R_P \tag{2}$$

The dimension of R_p is Ω cm^2, i_{corr} is $m\mu A/cm^2$, and β is in volts. The Stern Geary coefficient is related to the anodic, β_a, and cathodic, β_c, Tafel slopes per Eq 3.

$$\beta = \beta_a \beta_c / 2.303(\beta_a + \beta_c) \tag{3}$$

The units of the Tafel slopes are volts and the corrosion rate, *CR*, can be determined from Eq 4 based on equivalent weight, *EW*, of the metal (expressed in grams), and ρ, the density of the metal, in g/cm^3. The density of ductile iron is 7.86 g/cm^3.

$$CR = 3.27 \times 10^{-3}(i_{corr} EW / \rho) \tag{4}$$

DIP O.D. Pipe Surfaces

As discussed in ASTM G102 [6], the equivalent weight, *EW*, can be described as the mass of metal in grams that will be oxidized by the passage of one Faraday (96,489 ± 2°C [amp s]) of electric charge. For pure elements, the equivalent weight is given by Eq 5:

$$EW = W / n \tag{5}$$

where:

W = atomic weight of the element, and

n = number of electrons required to oxidize an atom of the element in the cor rosion process (e.g., the valence of the element).

The equivalent weight of iron is 27.56 g/equivalent.

Once the polarization resistance is determined, the corrosion rate can be esti mated using the Tafel slopes and the Stern Geary relationship, utilizing Eq 6:

$$i_{corr} = \beta_a\beta_c/[2.303\ R_P(\beta_a + \beta_c)] \tag{6}$$

where:

i_{corr} = corrosion current density, amps/cm^2,
R_p = polarization resistance, Ω cm^2,
β_a = anodic Tafel slope, V/decade or mV/decade of current density, and
β_c = cathodic Tafel slope, V/decade or mV/decade of current density.

Corrosion current can be converted to a corrosion rate, in mils/year (MPY), utilizing Eq 7:

$$\text{MPY} = i_{corr}(\Lambda)(1/\rho)(EW) \tag{7}$$

where:

i_{corr} = corrosion current density in amps/cm^2,
Λ = combination of several conversion terms and is 1 2866 × 10^5 *MPY* g/A cm,
ρ = iron density of 7.86 g/cm^3,
EW = equivalent weight of iron, 27.56 g/equivalent, which is considered dimen sionless in this calculation, or Eq 8:

$$MPY(\text{for ductile iron}) = 0.45 i_{corr} \tag{8}$$

with the units of i_{corr} in μA/cm^2.

Tafel Analysis

A Tafel plot, also known as an E log I curve, is a scan that applies a known current density to obtain a voltage shift from E_{corr}, the freely corroding potential. The measurements are computer controlled and performed at an optimum scan rate represented in millivolts per second over a range of anodic and cathodic poten tials. The corrosion current, i_{corr}, is obtained from a Tafel plot by extrapolating the linear portions of the cathodic and anodic legs of the curve with their intersec tion corresponding to the total corrosion current [20]. Tafel plots can be used to estimate anodic and cathodic Tafel slopes, estimate corrosion rates, and determine what type of geochemical process controls corrosion rates.

Electrochemical Data Analysis

Softcorr III DC Corrosion Software and Powersine™ EIS software manufactured by Princeton Applied Research were used for computer analysis of data [21]. Two different methods of analysis were utilized in this study for both the polarization resistance test and the EIS test. In the first method, anodic and cathodic software default Tafel constants of 0.100 were used, and corrosion rates were determined using the equations given in ASTM G102. In the second method, the actual Tafel constants obtained from the Tafel scan were utilized in the equations to determine

corrosion rate. As a result, a total of five different methods of electrochemical analysis for determining corrosion rate were utilized for the study and are listed here:

- Method 1 Polarization resistance using assigned Tafel constants of 0.100
- Method 2 EIS using assigned Tafel constants of 0.100
- Method 3 Polarization resistance using Tafel constants from Tafel scan
- Method 4 EIS using Tafel constants from Tafel scan
- Method 5 Tafel scan using Tafel constants generated by the test

Discussion of Results

Results from a 1 year weight loss study were compared to various types of electrochemical tests and methods of analysis. Average weight loss results over the 12 month exposure period were compared to five different electrochemical test methods, with 1 week, 1 month, 2 months, 3 months, 4 months, and 6 months as the exposure periods, to determine if meaningful results could be determined by an electrochemical test method(s) in a shorter time period than the 6 month or 1 year test required for weight loss comparisons. The average weight loss of sandblasted coupons over the 1 year test period is shown in Fig. 6, and the average weight loss of coated coupons over the 1 year test period is shown in Fig. 7.

Visual examination of weight loss samples after 1 year revealed the asphaltic shopcoat on samples in all fluids except BZ and CV was approximately 66 % gone.

FIG. 6 Average mils per year (MPY) corrosion rate of sandblasted coupons over 12 month exposure (based on weight loss).

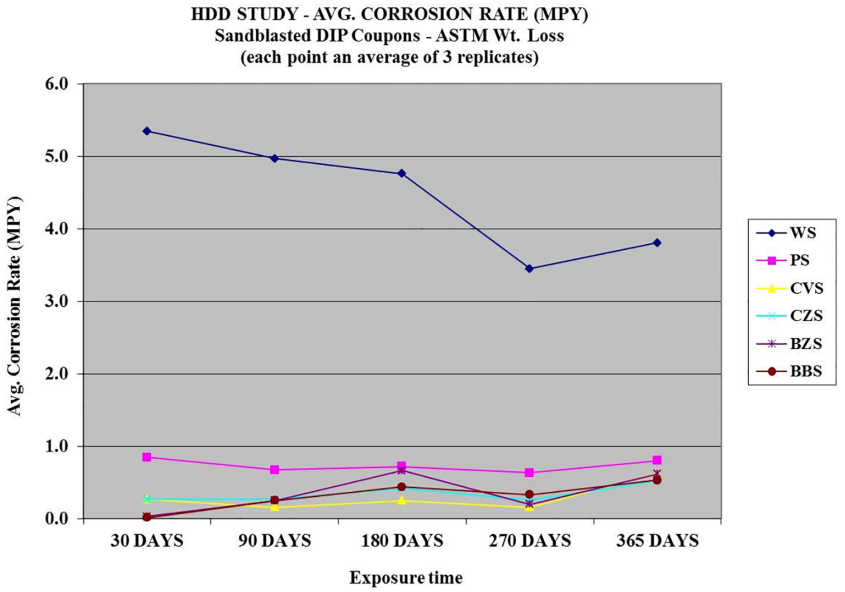

FIG. 7 Average MPY corrosion rate of coated coupons over 12 month exposure (based on weight loss).

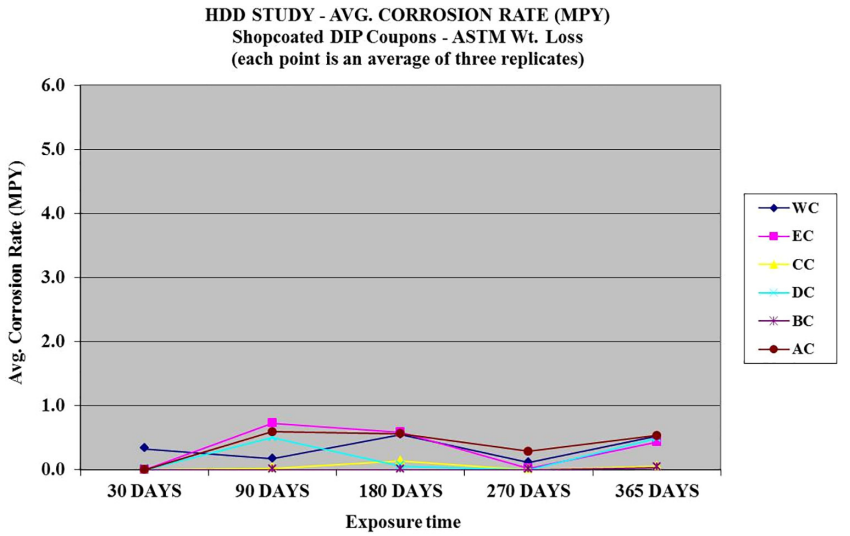

Preliminary electrochemical testing of the coated coupons revealed these corrosion rate data were very inconsistent. A normality test indicated the coated coupon's weight loss corrosion rate data for four of the six environments were not normally distributed. Therefore, the following analysis of the electrochemical test results is restricted to the blasted coupons only.

Average MPY results for blasted coupons in 3.5 % NaCl control solution obtained utilizing five different electrochemical analysis techniques are shown in Fig. 8. Average corrosion rates from weight loss results for 1, 3, and 6 months are included for comparison. In the NaCl control solution, EC Method 1 produced the results closest to the weight loss results at 6 months.

Average MPY results for blasted coupons in P drill fluid obtained utilizing five different electrochemical analysis techniques are shown in Fig. 9. Average corrosion rates from weight loss results for 1, 3, and 6 months are included for comparison. In the P drill fluid, EC Method 2 produced the results closest to the weight loss results during the 6 month test period, and EC Method 3 had the poorest correla tion with the weight loss results.

Average MPY results for blasted coupons in BB drill fluid obtained utilizing five different electrochemical analysis techniques are shown in Fig. 10. Average cor rosion rates from weight loss results for 1, 3, and 6 months are included for com parison. In the BB drill fluid, EC Method 2 produced the results closest to the weight loss results during the 6 month test period, and EC Method 3 had the poor est correlation with the weight loss results.

FIG. 8 Average MPY corrosion rate of blasted DIP coupons in 3.5 % NaCl solution over 6 month exposure (weight loss results vs. results from five EC analysis methods).

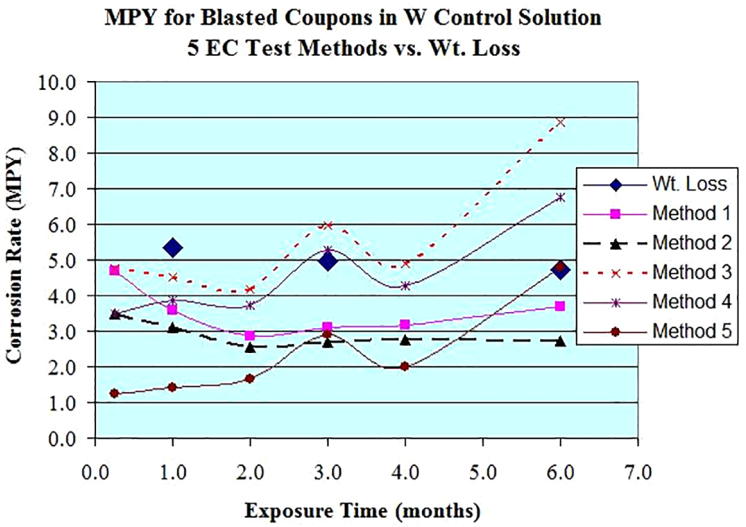

FIG. 9 Average MPY corrosion rate of blasted DIP coupons in P drill fluid over 6 month exposure (weight loss results versus results from five electrochemical analysis methods).

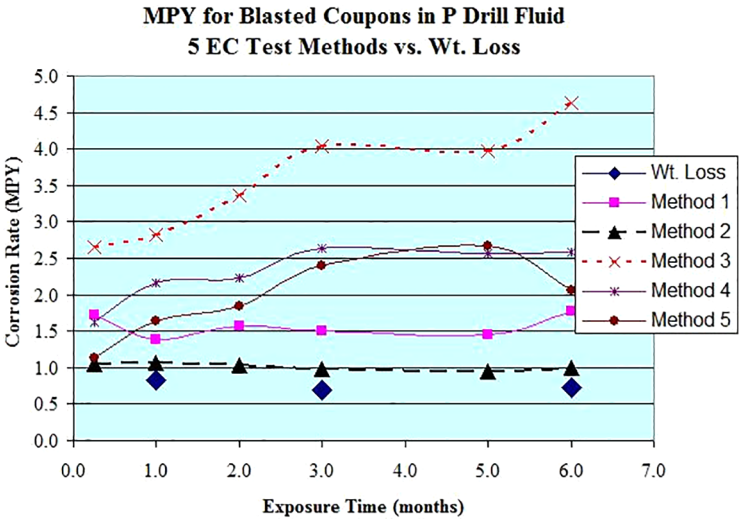

FIG. 10 Average MPY corrosion rate of blasted DIP coupons in BB drill fluid over 6 month exposure (weight loss results vs. results from five EC analysis methods).

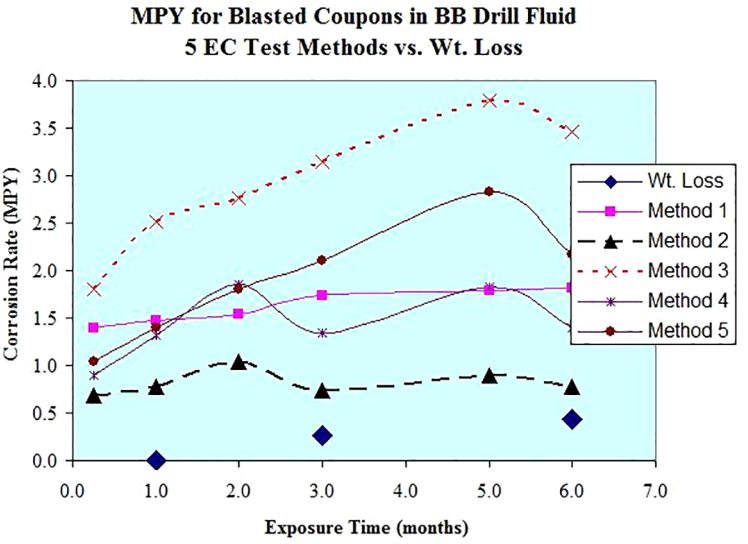

Average MPY results for blasted coupons in BZ drill fluid obtained utilizing five different electrochemical analysis techniques are shown in Fig. 11. Average corrosion rates from weight loss results for 1, 3, and 6 months are included for comparison. In the BZ drill fluid, EC Methods 2 and 4 produced the results closest to the weight loss results during the 6 month test period, and EC Methods 1 and 3 had the poorest correlation with the weight loss results.

Average MPY results for blasted coupons in CV drill fluid obtained utilizing five different electrochemical analysis techniques are shown in Fig. 12. Average corrosion rates from weight loss results for 1, 3, and 6 months are included for comparison. In the CV drill fluid, EC Method 2 produced the results closest to the weight loss results during the 6 month test period, and EC Method 3 had the poorest correlation with the weight loss results.

Average MPY results for blasted coupons in CZ drill fluid obtained utilizing five different electrochemical analysis techniques are shown in Fig. 13. Average corrosion rates from weight loss results for 1, 3, and 6 months are included for comparison. In the CZ drill fluid, EC Methods 2 and 4 produced the results closest to the weight loss results during the 6 month test period, and EC Method 3 had the poorest correlation with the weight loss results.

One reason for conducting laboratory electrochemical corrosion tests is to obtain corrosion rate results quickly rather than waiting a year or more for actual

FIG. 11 Average MPY corrosion rate of blasted DIP coupons in BZ drill fluid over 6 month exposure (weight loss results vs. results from five EC analysis methods).

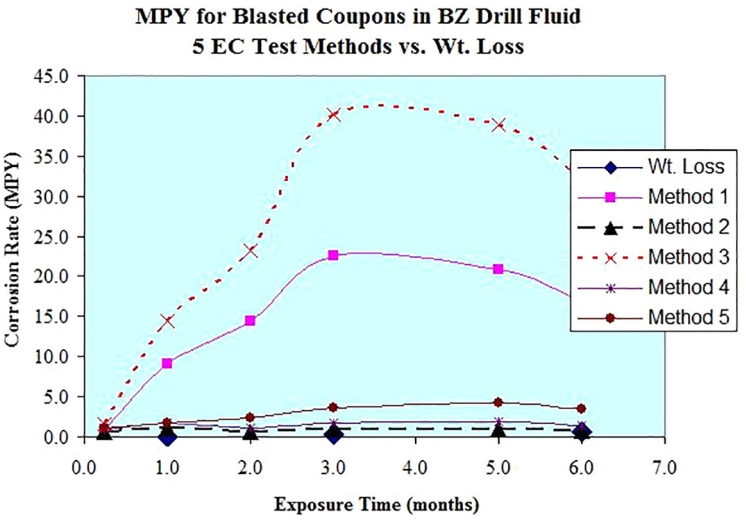

FIG. 12 Average MPY corrosion rate of blasted DIP coupons in CV drill fluid over 6 month exposure (weight loss results vs. results from five EC analysis methods).

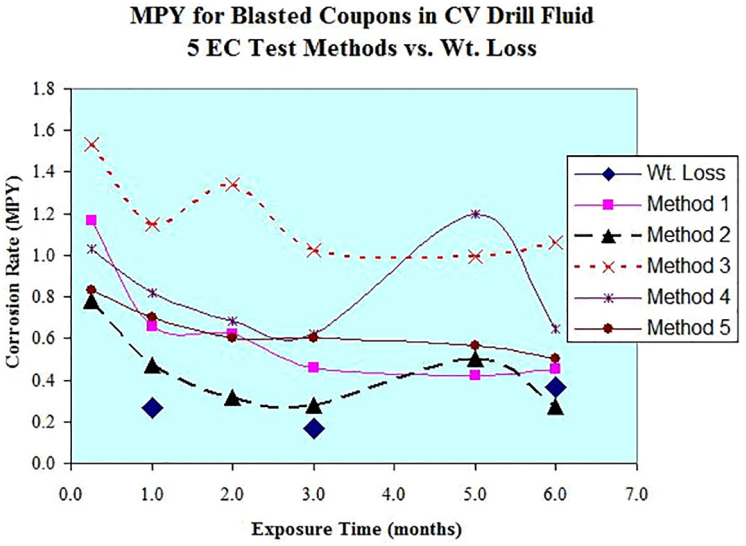

FIG. 13 Average MPY corrosion rate of blasted DIP coupons in CZ drill fluid over 6 month exposure (weight loss results vs. results from five EC analysis methods).

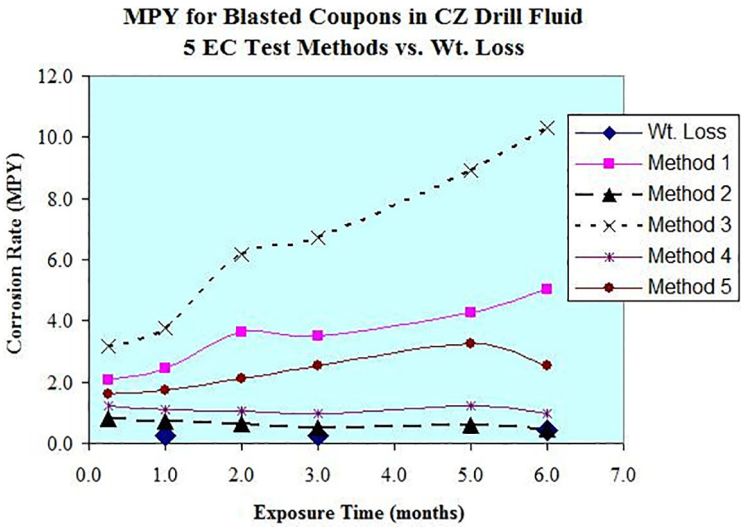

weight loss results. As part of this study, five different electrochemical test methods were performed after a 1 week exposure to six different fluids, and these results were compared to the average weight loss in each fluid after 1 year of exposure. These results are shown in Table 1.

When comparing DIP corrosion rate results from electrochemical test methods conducted at 1 week to average corrosion rates based on weight loss at 12 months,

TABLE 1 Comparison of MPY corrosion results from electrochemical test methods conducted at 1 week to corrosion results based on average weight losses at 12 months of exposure.

Environment	12 Mo. Avg. Wt. Loss (MPY)	EC Method 1 @ 1 week (MPY)	EC Method 2 @ 1 week (MPY)	EC Method 3 @ 1 week (MPY)	EC Method 4 @ 1 week (MPY)	EC Method 5 @ 1 week (MPY)
W 3.5 % NaCl (control)	3.8	4.7	3.5	4.8	3.5	1.2
P drill fluid	0.8	1.7	1.1	2.7	1.6	1.1
BB drill fluid	0.5	1.4	0.7	1.8	0.9	1.0
BZ drill fluid	0.6	0.9	0.7	1.5	1.0	1.1
CV drill fluid	0.6	1.2	0.8	1.5	1.0	0.8
CZ drill fluid	0.5	2.1	0.8	3.2	1.2	1.6

Note: All MPY results are an average of results from three replicate coupons.

EC Method 2 (i.e., EIS analysis using assigned Tafel constants of 0.100) produced the closest correlation for sandblasted DIP coupons in all six environments. The next best correlation was for EC Method 4 (EIS using Tafel constants from the Tafel scan). Correlation coefficients in order of best to worst for the comparison were as follows:

- Method 2 (EIS using assigned Tafel constants of 0.100): 0.9973
- Method 4 (EIS using Tafel constants from Tafel scan): 0.9815
- Method 1 (polarization resistance using assigned Tafel constants of 0.100): 0.9502
- Method 3 (polarization resistance using Tafel constants from Tafel scan): 0.8463
- Method 5 (Tafel scan using Tafel constants generated by the test): 0.0995

These results are specific to DIP in the described environments and may or may not be applicable to other materials and environments.

Summary

- HDD methods are being utilized more and more frequently for pipeline instal lations in the United States. DIP is a piping material that is increasing in popularity for HDD installations due to its successful service record, imperme ability, inherent strength, and toughness.
- Drilling fluids are used during the HDD process to support and lubricate the pipe, to reduce required pulling forces, to clean and cool the cutting bit, to sta bilize the bore hole formation, and to remove cuttings from the bore hole. Weight loss testing conducted in accordance with ASTM G162 revealed none of the five most common commercially available drilling fluids evaluated in this study would be considered corrosive to bare or shopcoated DIP. Average weight loss corrosion rates in all mixtures were less than 1 mil (0.001 in.) per year (0.025 mm/year) over the 1 year test period.
- One year weight loss testing in a control solution of 3.5 % NaCl revealed an average corrosion rate of 3.8 MPY (0.095 mm/year). These results are in agreement with published literature, which reports a corrosion rate between 3 and 6 MPY for DIP in a 3.5 % NaCl nonflowing environment. The standard shopcoat on DIP did provide some extra corrosion protection lowering the weight loss corrosion rate in a 3.5 % standard saltwater solution from an average of 3.8 MPY (0.095 mm/year) to an average of 0.5 MPY (0.013 mm/year).
- Electrochemical testing of the coated DIP coupons revealed these corrosion rate data were very inconsistent. A normality test indicated the coated cou pon's weight loss corrosion rate data for four of the six environments were not normally distributed. Therefore, analysis of the electrochemical test results and comparison to weight loss results were restricted to the blasted coupons.
- The following five methods were used to analyze electrochemical test results on blasted DIP coupons over a 6 month time period:
  - Method 1 Polarization resistance using assigned Tafel constants of 0.100
  - Method 2 EIS using assigned Tafel constants of 0.100

  - Method 3 Polarization resistance using Tafel constants from Tafel scan
  - Method 4 EIS using Tafel constants from Tafel scan
  - Method 5 Tafel scan using Tafel constants generated by the test
- Correlation of weight loss results with electrochemical test method results var ied by environment and exposure time. In all of the five most common drill fluids evaluated, EC Method 2 (i.e., EIS analysis using assigned Tafel constants of 0.100) on blasted DIP coupons consistently gave the closest correlation to weight loss results. EC Method 2 also gave the best correlation to 12 month weight loss results in the different environment of 3.5 % NaCl control solution.
- One reason for conducting laboratory electrochemical corrosion tests is to ob tain corrosion rate results quickly rather than waiting a year or more for actual weight loss results. When comparing DIP corrosion rate results from electro chemical test methods conducted at 1 week to average weight loss corrosion rates over 12 months, EC Method 2 (i.e., EIS analysis using assigned Tafel con stants of 0.100) produced the closest correlation for DIP coupons in all six envi ronments. EC Method 2 also gave the best correlation to weight loss results in ranking the drilling fluids from most corrosive to least corrosive. The next best correlation was for EC Method 4 (EIS using Tafel constants from the Tafel scan). These results are specific to DIP in the described environments and may or may not be applicable to other materials and environments.
- This study indicates correlation of an electrochemical test method to actual weight loss results is dependent upon the characteristics of the DIP material being tested (i.e., as cast annealing oxide surface, machined surface, sand blasted surface, coated, and so on), the type of electrolyte being evaluated, the time of exposure, and the method of electrochemical analysis. Laboratory elec trochemical corrosion testing will give a quick indication of corrosion rates of a specific material in a specific environment and will yield an informative comparison of corrosion rates of a material in various environments, but results should be verified under actual field or use conditions.

ACKNOWLEDGMENTS

In addition to the U.S. Pipe and Foundry Company, acknowledgement and appreciation are given to Dr. Robert Peters of the University of Alabama at Birmingham Civil Engi neering Department, the Ductile Iron Pipe Research Association, American Cast Iron Pipe Company, and Bariod Industrial Products for their assistance in this investigation.

References

[1] American Society of Civil Engineers, "2017 Infrastructure Report Card (A Comprehensive Assessment of America's Infrastructure)," ASCE, Reston, VA, 2017.

[2] Allouche, E. N. and Ariaratnam, S. T., "State-of-the-Art-Review of No-Dig Technologies for New Installations," *Proceedings of Pipelines 2002, Beneath Our Feet: Challenges and Solutions*, Cleveland, OH, August 4–7, 2002, G. E. Kurz, Ed., ASCE, Reston, VA, 2002, pp. 1–12.

[3] Horton, A. M., "Evaluation of the Corrosivity of HDD Drilling Fluids Utilized for Ductile Iron Pipe Installations," *Proceedings of Pipelines 2007, Advances and Experiences with Trenchless Pipeline Projects*, Boston, MA, July 8–11, 2007, M. Najafi and L. Osborn, Eds., ASCE, Reston, VA, 2007, pp. 1–15.

[4] Knight, M., Duyvestyn, G., and Gelinas, M., "Excavation of Surface Installed Pipelines," *J. Infrastruct. Syst.*, Vol. 7, No. 3, 2001, pp. 123–129.

[5] ASTM G59-97 (2014), *Standard Test Method for Conducting Potentiodynamic Polarization Resistance Measurements*, ASTM International, West Conshohocken, PA, 2014, www.astm.org

[6] ASTM G102-89 (2015), *Standard Practice for Calculation of Corrosion Rates and Related Information from Electrochemical Measurements*, ASTM International, West Conshohocken, PA, 2015, www.astm.org

[7] ASTM G106-89 (2015), *Standard Practice for Verification of Algorithm and Equipment for Electrochemical Impedance Measurements*, ASTM International, West Conshohocken, PA, 2015, www.astm.org

[8] ASTM G162-99 (2010), *Standard Practice for Conducting and Evaluating Laboratory Corrosions Tests in Soils*, ASTM International, West Conshohocken, PA, 2010, www.astm.org

[9] Bonds, R. W., Barnard, L. M., Horton, A. M., and Oliver, G. L., "Corrosion and Corrosion Control of Iron Pipe," *J. Am. Water Works Ass.*, Vol. 97, No. 6, 2005, pp. 88–98.

[10] Carpenter, R. and Conner, R., "The Versatility of Ductile Iron Pipe in Trenchless Construction," *Proceedings of Pipelines 2003: New Pipeline Technologies, Security, and Safety*, Baltimore, MD, July 13–16, 2003, M. Najafi, Ed., ASCE, Reston, VA, 2003, pp. 1312–1322.

[11] Griffin, J., "Ductile Iron Proves Effective with HDD, Pipe Bursting," *Underground Construction*, Vol. 58, No. 6, 2003, pp. 12–15.

[12] Horton, A. M., "Evaluation of the Corrosivity of Drilling Fluids Utilized in Horizontal Directional Drilling (HDD) Installations of Ductile Iron Pipe," M.S. thesis, University of Alabama, Birmingham, AL, 2005.

[13] AWWA C151-09 Standard, "Ductile-Iron Pipe, Centrifugally Cast," American Water Works Association, Denver, CO, 2009.

[14] Walton, C. F., Ed., *Gray and Ductile Iron Castings Handbook*, Gray and Ductile Iron Founders' Society, Inc., Cleveland, OH, 1971, p. 320.

[15] AWWA C105-10 Standard, "Polyethylene Encasement for Ductile-Iron Pipe Systems," American Water Works Association, Denver, CO, 1999.

[16] ASTM G57-06(2012), *Standard Test Method for Field Measurement of Soil Resistivity Using the Wenner Four-Electrode Method*, ASTM International, West Conshohocken, PA, 2012, www.astm.org

[17] ASTM G51-95 (2012), *Standard Test Method for Measuring pH of Soil for Use in Corrosion Testing*, ASTM International, West Conshohocken, PA, 2012, www.astm.org

[18] ASTM G1-03 (2017)e1, *Standard Practice for Preparing, Cleaning, and Evaluating Corrosion Test Specimens*, ASTM International, West Conshohocken, PA, 2017, www.astm.org

[19] ASTM G5-14e1, *Standard Reference Test Method for Making Potentiodynamic Anodic Polarization Measurements*, ASTM International, West Conshohocken, PA, 2014, www.astm.org

[20] Princeton Applied Research, "PAR Application Notes: PAR CORR 1, CORR-4, AC-1, and AC-5," PAR, Oak Ridge, TN, 2005.

[21] EG&G Instruments, Inc., PowerSine™ Software, EG&G Instruments, Inc., Oak Ridge, TN, 1998.

STP 1609, 2019 / available online at www.astm.org / doi: 10.1520/STP160920170245

Van Anh Nguyen,[1] Anatolie G. Carcea,[1]
Mahmoudreza Ghaznavi,[1] and Roger C. Newman[1]

Status of Pitting Corrosion Prediction in Mixed Solutions Containing Reduced Sulfur Species

Citation

Nguyen, V. A., Carcea, A. G., Ghaznavi, M., and Newman, R. C., "Status of Pitting Corrosion Prediction in Mixed Solutions Containing Reduced Sulfur Species," *Advances in Electrochemical Techniques for Corrosion Monitoring and Laboratory Corrosion Measurements*, *ASTM STP1609*, S. Papavinasam, R. B. Rebak, L. Yang, and N. S. Berke, Eds., ASTM International, West Conshohocken, PA, 2019, pp. 280–293, http://dx.doi.org/10.1520/STP160920170245[2]

ABSTRACT

Pitting of stainless steels and nickel-base alloys in solutions containing reduced sulfur species has features that are distinct from ordinary chloride-induced pitting. In particular, very severe pitting of molybdenum-free alloys occurs in neutral sodium sulfate solution containing thiosulfate ions for a certain range of sulfate to thiosulfate concentration ratio and a certain range of potential. Such pitting is hard to initiate without mechanical damage of the metal surface in situ; thus, the potentiostatic scratch test is particularly appropriate in this case. For chloride-thiosulfate mixtures, mechanical damage is not mandatory, and the quantification of pitting susceptibility is more complex because pitting can also occur in solutions containing only chloride anions. The signature of catalyzed (thiosulfate-induced) pitting is a large drop in pitting potential compared with the pure chloride case. The chloride-thiosulfate case is also notable in that the favorable ratio of chloride to thiosulfate concentration is very large for nickel-base alloys but much smaller for stainless steels. Reaction-transport modeling

Manuscript received December 9, 2017; accepted for publication June 20, 2018.
[1]Dept. of Chemical Eng., University of Toronto, Toronto, ON, M5S 3E5, Canada V. A. N. http://orcid.org/0000 0001 8299 611X, A. G. C. http://orcid.org/0000 0001 7267 8265, M. G. http://orcid.org/0000 0001 6106 0814, R. C. N. http://orcid.org/0000 0002 2422 619X
[2]ASTM Symposium on *Advances in Electrochemical Techniques for Corrosion Monitoring and Laboratory Corrosion Measurements* on November 13 14, 2017 in Atlanta, GA, USA.

has been used to elucidate two particular features of pitting in these systems—the B value in Galvele's pitting potential equation and the enrichment of anions in pits as a function of their charge. It is found that the B value for chloride solutions is around 100 mV, in agreement with experiments, if one assumes that chromium cations exist mainly in the form of chloro-complexes. When thiosulfate is present, it is much more strongly enriched in pits than chloride. For sulfate-based solutions, the B value is around 50 mV, in line with the double charge of sulfate (and thiosulfate). Sulfide, not being an anion in the acidic conditions of a pit, shows different behavior in that deeper pits are less stable than shallow pits because the limiting flux of sulfide to the bottom of the pit decreases.

Keywords
stainless steel, nickel alloy, corrosion, pitting, thiosulfate

Introduction

Reduced sulfur anions (meaning more reduced than sulfate) are potent catalysts of both acid dissolution and pitting corrosion in nickel (Ni), iron (Fe), and their alloys. With pure Ni dissolving in aqueous sulfuric acid, the catalysis by adsorbed sulfur is perfect, meaning that a single monolayer can dissolve macroscopic amounts of Ni [1]. For stainless steels or Ni base alloys, and especially alloys containing molybdenum (Mo), the catalysis is only partial, and a continued supply of reduced sulfur is required [2,3]. The adsorbed sulfur attracts electron density from neighboring Ni or Fe atoms, thus becoming what can be termed $S_{ads}^{\delta-}$ [4].

Pitting of Type 304 stainless steel (304SS) in chloride solutions containing a range of reduced sulfur anions was first studied systematically by Newman, Isaacs, and Alman [5]. Thiosulfate was very aggressive over a range of concentrations, but the catalyzed pitting vanished at high thiosulfate concentration. This was attributed to consumption of acid within the pit by disproportionation or electroreduction of thiosulfate (or both). Sulfide showed a different behavior, with no upper concentration threshold being apparent, and this was attributed to its nonanionic nature in the pit and thus being unable to enrich in the pit by electromigration.

Later on, it was found that chloride was unnecessary, with severe catalyzed pitting of 304SS being demonstrated in sulfate thiosulfate mixtures [6,7]. This was relevant to corrosion issues in paper machines [8] and also to microbially influenced corrosion [9]. This type of pitting was found to persist at very low ionic strengths, provided the sulfate to thiosulfate concentration ratio was kept in the aggressive range of roughly 10 to 25. Potentiostatic scratch testing was mandatory to obtain conservative results in such solutions; without in situ damage of the metal surface, pit initiation was extremely sluggish. Possibly this indicates that chloride does indeed have a special role in "breaking down" the passive film, as argued by Marcus in the *Faraday Discussions* on corrosion chemistry [10].

Recently, the focus was switched to Ni base alloys and high alloy stainless steels used for steam generator tubing in water cooled nuclear power plants [10]. Three

alloys (600, 800, and 690) were shown to demonstrate sulfate thiosulfate pitting over a range of potentials and sulfate thiosulfate concentration ratios. Some of those results are reproduced in this paper. However, a disconnect was identified between the early results for stainless steel and the new results for Ni rich alloys when using chloride thiosulfate mixtures. For stainless steel, the most aggressive sulfate thiosulfate and chloride thiosulfate ratios were thought to be similar, in the range of 10 to 50 [5,11]. But for the Ni rich alloys, the most aggressive chloride thiosulfate mixtures had chloride thiosulfate ratios of more than a thousand, compared with 40 for sulfate thiosulfate. The data of Roberge [12] go only part of the way in resolving this issue. We will return to this point later, after presenting some experimental results.

In order to make better sense of the data on reduced sulfur effects, we recently instituted a program of one dimensional reaction transport modeling. One focus is the B value in Galvele's pitting potential equation (Eq 1) that should apply to any metal or alloy [13]:

$$E_{pit} = A - B\log[Cl^-] \tag{1}$$

and its adaption to sulfate thiosulfate or chloride thiosulfate pitting. Another is the co enrichment behavior of differently charged anions in a pit, as in the chloride thiosulfate case. There are persuasive arguments, stemming from Galvele, to suggest that B is an increment in ohmic potential drop (IR drop) in the pit or pit nucleus due to the electrolyte resistance in the pit and the ionic current flowing per decade of external chloride concentration [13,14]. The B value is of fundamental interest but also of practical importance. It enables the extrapolation of pitting data to dilute conditions or long exposure times (or both) based on science rather than empirical observation. In the specific case of sulfate thiosulfate pitting, as discussed in this paper, the low B value facilitates pitting at very low ionic strength and needs to be understood.

Finally, we will make a few comments on the behavior of sulfide in pits [15] and on the special phenomena that result from its inability to enrich by electromigration.

Experimental Procedures

The 600, 800, and 690 alloys were obtained in the form of 1.5 mm sheets from Metal Samples Inc. (Munford, AL). Their compositions with respect to the main alloying elements are shown in **Table 1**. They were solution annealed at 1,050°C for 1 h in 97.5 % argon/2.5 % H_2 gas mixture and water quenched.

TABLE 1 Compositions of the alloys studied, in wt.%.

Compositions	Alloy 600	Alloy 690	Alloy 800
Ni	Balance	Balance	31.2
Fe	9.53	10.1	Balance
Cr	16.1	29.6	20
C	0.06	0.03	0.07

After mounting in epoxy resin, samples were used as working electrodes in a three electrode cell containing the sulfate thiosulfate or chloride thiosulfate solu tion. Tracepur® sodium sulfate, assay greater than 99 %; sodium thiosulfate, assay 99.5 % 100.5 %; sodium chloride, assay less than 99 % were from EMD Chemicals Inc., an affiliate of Merck KGaA (Darmstadt, Germany). The resistivity of the deionized water was 18.2 MΩ cm. A platinum counter electrode and a mercury mercurous sulfate reference electrode (MSE) filled with saturated potassium sulfate (0.65 V vs. standard hydrogen electrode at 25°C) were also immersed for the sulfate thiosulfate experiments; for chloride thiosulfate, the reference electrode was silver silver chloride filled with saturated potassium chloride (0.197 V vs. standard hydrogen electrode at 25°C). All experiments reported here used an open beaker as the electrochemical cell, with freshly poured solution the oxidation rate of thiosul fate is slow enough to allow such a procedure, even in highly diluted solutions, and confirmed by detailed ion chromatography measurements [10].

All the scratching was done in situ, with the potential applied and the sample immersed. A diamond engraving pencil was used for scratching the scratches were approximately 0.1 mm wide and 9.5 mm long. All the results shown here relate to a solution temperature of 60°C.

The procedure for a sulfate thiosulfate pitting test was as follows, exploiting the fact that sulfate thiosulfate pitting ceases at a sufficiently positive potential, where thiosulfate can no longer be electroreduced in the pit [8]. First, the sample was pas sivated at 0 V (MSE) in 0.1 M sodium sulfate (Na_2SO_4) for half an hour. Then it was transferred to the test cell and polarized at −0.91 V (MSE), below any possible pitting onset potential. The current was allowed to stabilize for 30 s. Then a scratch was made at this potential and the current transient (the scratch current) recorded for 180 s. Then, when no pitting occurred, the potential was stepped upward by 100 or 25 mV, depending on the resolution required, and the process was repeated. If pitting occurred, as indicated by an increase in the current after initial repassivation (the scratch pitting current), the pits on the scratch were repassivated anodically by applying 0 V (MSE) for 10 s, then the potential was stepped back to the next scratch ing potential. All of this is possible because sulfate thiosulfate pitting is reluctant to initiate on undisturbed surfaces, although it does do so eventually.

In order to define carefully the ranges of potential and anionic concentration ratio for pitting, various interpolations and repeat scratches were made, and some sequences started at high potential and worked down to low potential. The final charts shown in this paper were the result of at least five repeat tests.

For chloride thiosulfate pitting, anodic potentials could not be applied to repas sivate the pits because ordinary chloride pitting would have occurred, but an anodic passivation in pure sulfate solution was still used, as before, to minimize the base currents and delay spontaneous pitting away from the scratches.

Pitted scratches were examined by scanning electron microscope and energy dispersive X ray analysis, usually after allowing a longer time for pit development than was used in the main electrochemical procedure.

Experimental Results and Discussions

SULFATE–THIOSULFATE SOLUTIONS

Fig. 1 shows typical results of scratching tests for cases where pitting did, and did not, occur on Alloy 600. The increase in current due to pitting is obvious in this example but was more subtle for the other alloys, especially Alloy 690.

Fig. 2 shows the scratch pitting current for Alloy 600 after 180 s as a function of potential. The initial increase with increasing potential is due mainly to greater pit growth rate, while the decrease after the peak is due mainly to a decreased number of pit nuclei on each scratch. The other two alloys showed much lower pitting currents at the most aggressive potential (−0.51 V), as follows: Alloy 600, 1,100 μA; Alloy 800, 120 μA; and Alloy 690, 9 μA. These differences were partly due to different pit nucleation densities and partly to different pit growth rates, as revealed by scanning electron microscope examination of the scratches [10].

For a baseline concentration of 0.1 M Na_2SO_4, the dependence of pitting on thiosulfate concentration was examined for all three alloys. To a remarkable precision, the most severe anionic ratio was 40 for all three alloys. This can only be due to a mutual electromigration of sulfate and thiosulfate into the pits, preserving their concentration ratio in the bulk solution.

Moreover, the most severe anionic concentration ratio remained close to 40 as the ionic strength was varied over several orders of magnitude, as indicated by Fig. 3

FIG. 1 Typical raw data for the scratch experiments: annealed Alloy 600 in 0.1 M Na_2SO_4 + 0.005 M $Na_2S_2O_3$ at 60°C [10].

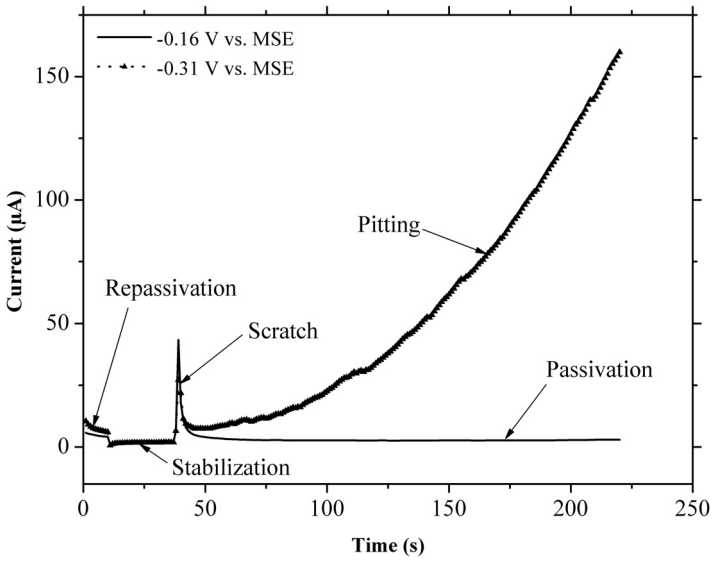

FIG. 2 Dependence of scratch pitting current after 180 s on potential for tests done in 0.1 M Na_2SO_4 + 0.0025 M $Na_2S_2O_3$ on Alloy 600 at 60°C [10].

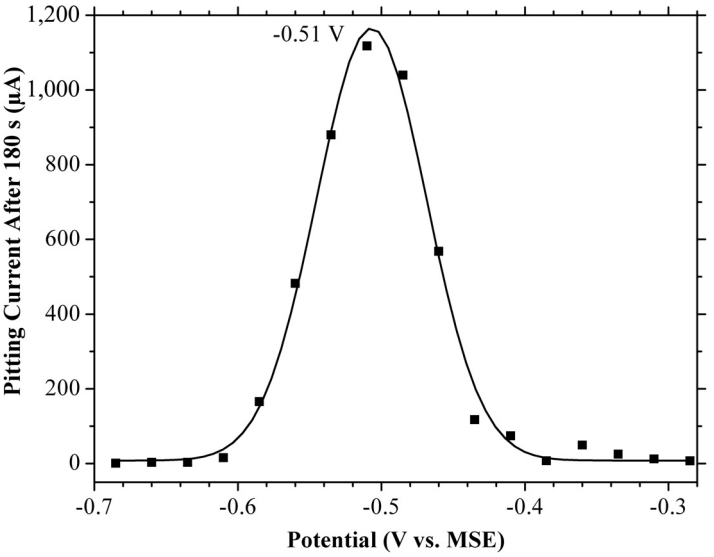

FIG. 3 The dependence of pitting rate on potential for annealed Alloy 600 in 1 × 10^{-3} M Na_2SO_4 with different concentrations of $Na_2S_2O_3$ at 60°C, showing that the most severe anionic concentration ratio remains at 40 [10].

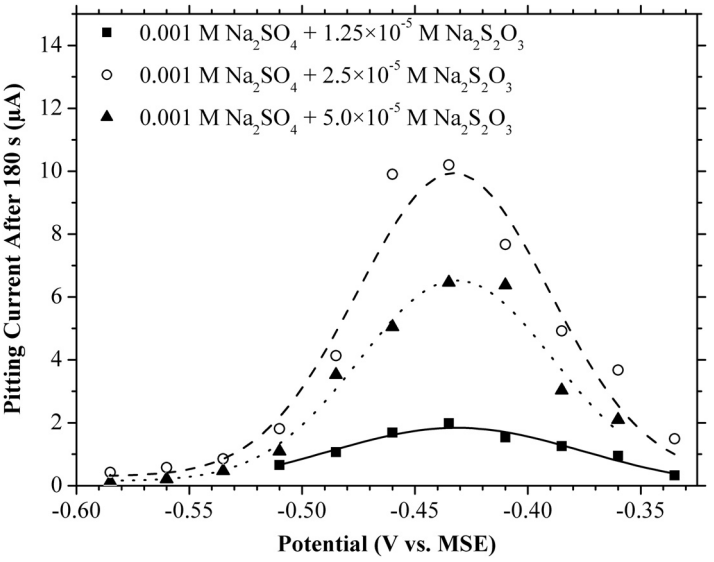

for 1 mM sulfate. Stable pitting was obtained in tests with thiosulfate concentrations as low as 1 μM, using the same anionic concentration ratio of 40 [10].

CHLORIDE–THIOSULFATE SOLUTIONS

Initial scratch testing on Alloy 600, with no thiosulfate present, demonstrated some degree of pitting resistance up to at least −100 mV (Ag/AgCl) in 0.3 M NaCl at 60°C, and when it did show persistent pitting at potentials around 0 V, the currents were low (sub μA) and unstable. Given this result, there was no difficulty distinguishing ordinary chloride pitting from thiosulfate catalyzed pitting, which invariably gave scratch currents of at least 0.5 μA, up to 150 μA in the most severe cases (after 180 s), with a smooth current increase as shown in **Fig. 4**. There is often a subtle peak or shoulder in the rate of thiosulfate catalyzed chloride pitting with potential (not well shown in **Fig. 4**), but this was not nearly as easy to discern as in the case of sulfate thiosulfate pitting, where pitting ceased altogether at high potentials. In chloride thiosulfate solutions, thiosulfate catalyzed pitting starts at a certain potential, and depending on the solution composition and alloy, may start to decrease in rate at higher potentials until normal uncatalyzed chloride pitting starts, and the current increases again.

It was immediately apparent that the amount of thiosulfate required for catalyzed pitting of Alloy 600 was much less in (strong) chloride than in (strong) sulfate

FIG. 4 Pitting corrosion of annealed Alloy 600 in 0.1 M NaCl with different concentrations of $Na_2S_2O_3$ at 60°C showing that pitting is rapid for chloride thiosulfate concentration ratios in the range from 1,000 to 4,000. Little or no catalyzed pitting occurred at ratios of 400 or 10,000 [10].

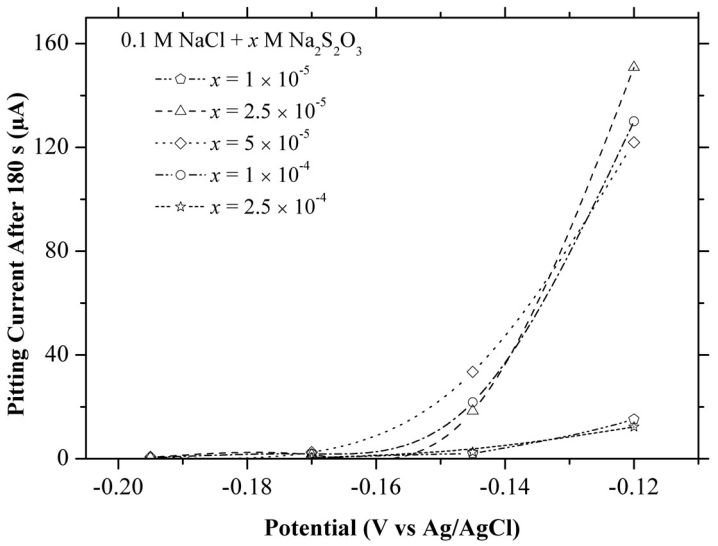

solution. Pitting was very active for chloride thiosulfate ratios of 1,000 to 4,000. An obvious reason for this is that the double charge of the thiosulfate causes it to enrich relative to chloride but not relative to sulfate, as discussed later on in the modeling section. But more work is required to harmonize this result with the behavior of Type 304SS, where the original work of Newman, Isaacs and Alman [5] suggested an optimal chloride to thiosulfate ratio of no more than 25, while Franz [11] also used a ratio of 25 in her work on growth of single pits in 304SS. One possible explanation is that adsorbed sulfur (S) is more catalytic (activating) for dissolution of Ni than Fe due perhaps to the latter's greater affinity for oxygen or to a difference in the degree of charge transfer on to the adsorbed S atoms; there are several interrelated possibilities. In that case, a lower flux of thiosulfate will be required to maintain activation of a Ni base than an Fe base alloy, other things being equal, but then why does this not apply to the sulfate thiosulfate system? Another possibility is that Alloy 600 has different behavior simply because it is kinetically more noble in acids than Type 304SS. Given that electroreduction of thiosulfate is required to stabilize dissolution in the pit, the rate of this reduction will be lower, at the onset of pitting, in Alloy 600 than in 304SS, owing to the displacement of the catalyzed pitting to higher potentials. To put it another way, the potential in the pits formed on stainless steel in chloride thiosulfate is lower, so thiosulfate is reduced at a higher rate than is required to form the catalyzing monolayer; thus, most of the thiosulfate is "wasted."

Another difference from the sulfate based system was that pitting was much more difficult to stabilize in diluted chloride thiosulfate solutions because the "optimal" thiosulfate concentration became absurdly low. So there are two answers to the question, which is more severe in Alloy 600, sulfate thiosulfate or chloride thiosulfate pitting? From the perspective of relatively concentrated systems, chloride is more severe because less thiosulfate is required for pitting. But sulfate thiosulfate pitting persists in solutions with much lower overall ionic strength, so it is a more plausible practical issue in dilute systems.

CHLORIDE–SULFIDE SYSTEM

As already mentioned, there is no apparent maximum concentration or concentration ratio of sulfide to chloride at which pitting vanishes [5]. This is due to the nonanionic nature of sulfide in acidic solutions, so that it cannot be enriched in a pit by electromigration. A further consequence of this is that pits in chloride sulfide solutions become less stable with increasing depth because the limiting flux of the activating sulfide to the pit bottom decreases [15]. This poses yet another challenge for the application of standardized test methods.

GALVELE'S B VALUE—EXPERIMENTS

The B value was estimated for sulfate thiosulfate as shown in **Fig. 5**. Although there were only a few experiments, the value is clearly neither 60 mV, as predicted by Galvele for chloride, nor 30 mV, as would be expected from Galvele's model with a

FIG. 5 Experimental determination of the B value for sulfate thiosulfate mixtures at 60°C. The data points are the lowest potentials measured versus the MSE reference electrode where pitting was detected in the scratch test.

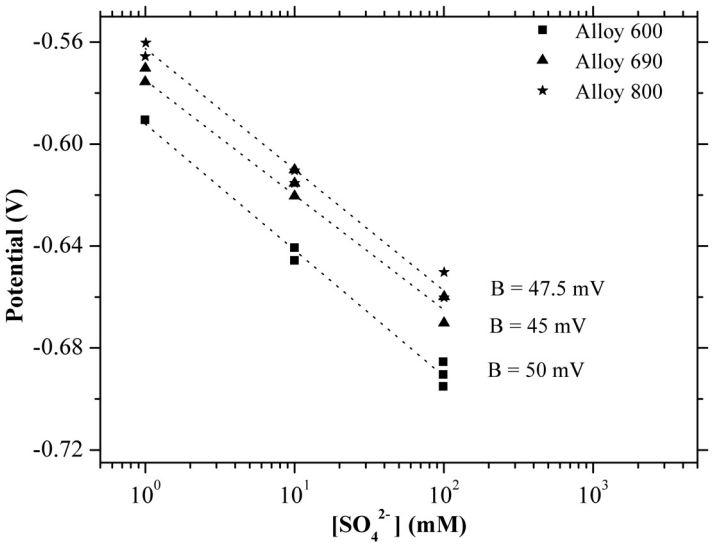

doubly charged anion, nor 100 mV, as found experimentally for chloride (these numbers are given for clarity as the present experiments were done at 60°C, they need to be multiplied by 333/298, which is 1.117). The experimental B value is about 50 mV. An economical hypothesis to explain this value is that it is half of 100 mV (i.e., whatever the reason is for the 100 mV value), and it applies to the sulfate thiosulfate pitting, but with a factor of two to account for the double charge of the sulfate ion.

REACTION-TRANSPORT MODELING

The modeling was done primarily to address the old problem of the different B values for Fe and stainless steel but also enabled us to contribute to the nuclear steam genera tor corrosion issue by accounting for the occurrence of thiosulfate catalyzed pitting at extremely low ionic strengths. The low B values found in sulfate thiosulfate solutions are a key aspect of this. Thus, this modeling exercise focuses solely on the B value, which is dependent on IR drop as mentioned previously and contains no explicit kinet ics. Full details are given elsewhere [16]. The assumptions are as follows:

- Fixed dissolved Ni concentration at the bottom of the one dimensional pit
- Ideal solution theory applies (but calculations have also been done with concentration dependent diffusivities)
- Usual application of the Nernst Planck equation, electroneutrality, Nernst Einstein relation

- Presence or absence of chromium (Cr) cationic chloro complexes or sulfate complexes with particular (high) stability constants
- Equal diffusivities for all ionic species (this can easily be relaxed of course)

Making these assumptions, the steady state potential and species distributions, and the cation flux at the pit bottom, are calculated. The latter is not very relevant to this paper. The potential difference (IR drop) between the bottom and the top of the pit is plotted against the log of the external solution concentration. It should be noted that some initial and boundary conditions allow analytical solutions and pro vide a check on the numerical modeling.

Finally, the sulfate thiosulfate and chloride thiosulfate systems are contrasted by displaying the very different thiosulfate concentrations that arise at the bottom of the pit. This is an initial step toward understanding the different concentration dependencies described in the preceding sections.

B Value for Pure Chloride or Pure Sulfate Systems

This was a fully expected result B values of 60 and 30 mV, respectively. This is an analytical result for low bulk solution concentrations, but as Fig. 6 shows, there is some curvature at high chloride revealed by the numerical computation. Most of the data show some such departure from a constant B value at the higher ionic strengths, and this is already just visible in Fig. 6.

FIG. 6 IR drop within a pit when Ni dissolves at limiting current density and no complexes form in either NaCl or Na_2SO_4; C_{bulk} (bulk concentration of NaCl or Na_2SO_4) is varied up to 1,500 mM; fitted B values are 59 and 30 mV in NaCl and Na_2SO_4, respectively.

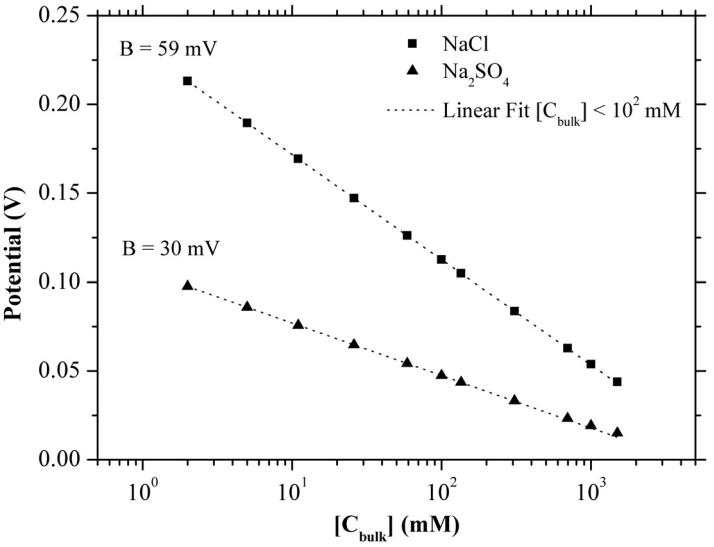

B Value for Pure Chloride or Pure Sulfate Systems with One or Other Very Stable Cationic Complex of Cr

Fig. 7 shows an illuminating result as we increase the number of chloride ions in the complex from 0 to 1 to 2, assuming high stability for the complexes (as indicated by OLI Analyzer Studio 9.3 database) [16], B increases from 60 to 108 mV. This is a very promising basis for a model of the high B value seen in stainless steels or Ni base alloys.

Fig. 8 shows the equivalent result for sulfate, with a maximum B value of 43 mV. This agrees closely with the experimental result shown in Fig. 5, allowing for the temperature correction already mentioned.

Relative Enrichment of Thiosulfate at the Pit Bottom for Chloride-Thiosulfate

For sulfate thiosulfate with no complexation, the anionic concentration ratio in the bulk solution is preserved at the bottom of the pit. For chloride thiosulfate, the results are as shown in Table 2 for a fixed chloride bulk concentration of 0.1 M. This table contains B values, but we have no experimental data on those. The important parts, for present purposes, are the last two columns showing chloride and thiosulfate concentrations at the bottom of the pit. We can see that anionic concentration ratios of 10,000, 1,000, 100, and 10 in the bulk solution translate into ratios of 102, 11.7, 2.00, and 0.50, respectively, at the bottom of the pit. Thus, having two anions

FIG. 7 IR drop in Ni 17 wt.% Cr when Cr cations form $CrCl^{2+}$ or $CrCl_2^{+}$ in NaCl solutions at stability constant values for the respective complexes of $K = 1\ mM^{-1}$ and $1\ mM^{-2}$.

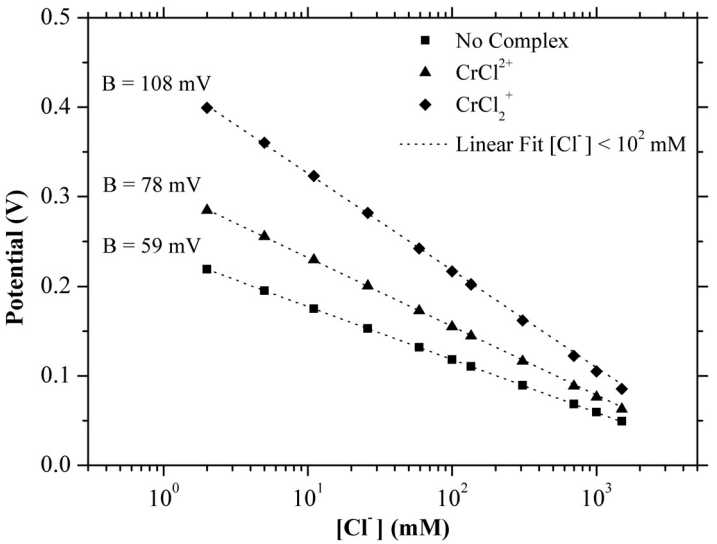

FIG. 8 IR drop in Ni 17 wt.% Cr when Cr cations form $CrSO_4^+$ in Na_2SO_4 solutions at two stability constant values: $K = 10^{-3}$ mM^{-1} and 5 mM^{-1}.

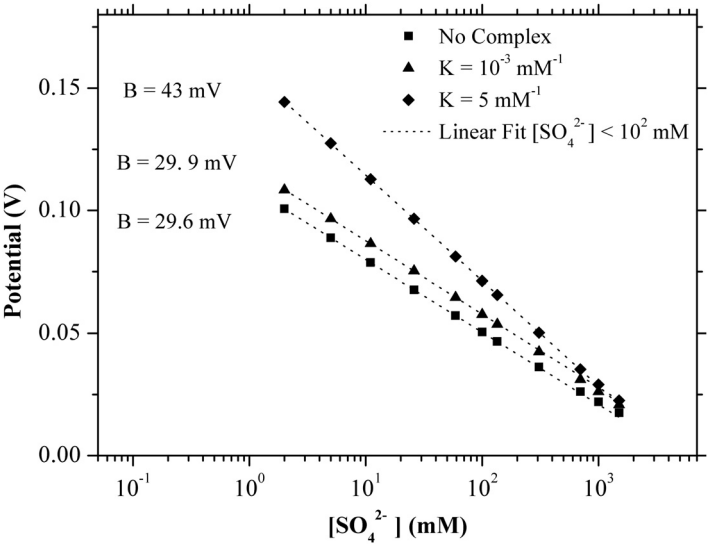

TABLE 2 Enrichment of thiosulfate relative to chloride for the chloride thiosulfate pit model at different bulk ratio of chloride to thiosulfate.

$[Cl^-]_{bulk}$, mM	$[Cl^-]/[S_2O_3^{2-}]$[a]	B value, mV	$[Cl^-]_{bottom}$, mM	$[S_2O_3^{2-}]_{bottom}$, mM
100	10,000	52.5	9,788	96
100	1,000	41.8	8,538	729
100	100	34.0	5,014	2,514
100	10	31.0	2,010	4,039

[a]Ratio at bulk concentrations.

of different charge has a profound effect on the pit chemistry as already noted by Galvele in one figure in his 1976 paper [13].

Conclusions

1. Pitting of stainless alloys in sulfate thiosulfate solutions is a unique form of localized corrosion that obeys strict rules reflecting the mutual enrichment of anions inside the pit. It is very resistant to the use of standard test techniques.
2. Pitting of stainless alloys in chloride thiosulfate solutions is more complex than previously thought. Calculations show that thiosulfate should enrich vastly more than chloride in a pit, and results on Ni rich alloys reflect that; but for

stainless steels, the results look more similar to those obtained in sulfate thiosulfate mixtures.

3. The most likely explanation for the different behavior of Fe rich and Ni rich stainless alloys is the generally more positive potential required to pit the Ni rich alloys, which reduces the rate of thiosulfate reduction occurring inside a pit.
4. Reaction transport modeling has illuminated the variation of Galvele's B value with solution composition in these systems.
5. Chloride sulfide systems are different because sulfide is not an anion in acidic solution and cannot enrich in a pit. Pits become less stable (higher repassiva tion potential) with increasing depth. Again, such phenomena are not easily accessible using standard test techniques.

ACKNOWLEDGMENTS

This research was supported by the Natural Sciences and Engineering Research Council (Canada) and by the University Network of Excellence in Nuclear Engineering. The contributions of William Zhang to earlier work in this area are gratefully acknowledged.

References

[1] Oudar, J. and Marcus, P., "Role of Adsorbed Sulfur in the Dissolution and Passivation of Nickel and Nickel-Sulfur Alloys," *Appl. Surf. Sci.*, Vol. 3, No. 1, 1979, pp. 48–67.

[2] Elbiache, A. and Marcus, P., "The Role of Molybdenum in the Dissolution and the Passivation of Stainless Steels with Adsorbed Sulphur," *Corros. Sci.*, Vol. 33, No. 2, 1992, pp. 261–269.

[3] Newman, R. C., "The Dissolution and Passivation Kinetics of Stainless Alloys Containing Molybdenum–II. Dissolution Kinetics in Artificial Pits," *Corros. Sci.*, Vol. 25, No. 5, 1985, pp. 341–350.

[4] Yang, H. and Whitten, J. L., "Adsorption of SH and OH and Coadsorption of S, O and H on Ni(111)," *Surf. Sci.*, Vol. 370, Nos. 2–3, 1997, pp. 136–154.

[5] Newman, R. C., Isaacs, H. S., and Alman, B., "Effects of Sulfur Compounds on the Pitting Behavior of Type 304 Stainless Steel in Near-Neutral Chloride Solutions," *Corrosion*, Vol. 38, No. 5, 1982, pp. 261–265.

[6] Newman, R. C., "Pitting of Stainless Alloys in Sulfate Solutions Containing Thiosulfate Ions," *Corrosion*, Vol. 41, No. 8, 1985, pp. 450–453.

[7] Newman, R. C., Wong, W. P., and Ezuber, H., "Pitting of Stainless Steels by Thiosulfate Ions," *Corrosion*, Vol. 45, No. 4, 1989, pp. 282–287.

[8] Garner, A., "Thiosulfate Corrosion in Paper-Machine White Water," *Corrosion*, Vol. 41, 1985, No. 10, pp. 587–591.

[9] Newman, R. C., Wong, W. P., and Garner, A., "A Mechanism of Microbial Pitting in Stainless Steel," *Corrosion*, Vol. 42, No. 8, 1986, pp. 489–491.

[10] Zhang, W., Carcea, A. G., and Newman, R. C., "Pitting of Steam-Generator Tubing Alloys in Solutions Containing Thiosulfate and Sulfate or Chloride," *Faraday Discussions,* Vol. 180, 2015, pp. 233–249.

[11] Newman, R. C. and Franz, E. M., "Growth and Repassivation of Single Corrosion Pits in Stainless Steel," *Corrosion*, Vol. 40, No. 7, 1984, pp. 325–330.

[12] Roberge, R., "Effect of the Nickel Content in the Pitting of Stainless Steels in Low Chloride and Thiosulfate Solutions," *Corrosion*, Vol. 44, No. 5, 1988, pp. 274–280.

[13] Galvele, J. R., "Transport Processes and the Mechanism of Pitting of Metals," *J. Electrochem. Soc.*, Vol. 123, No. 4, 1976, pp. 464–474.

[14] Laycock, N. J. and Newman, R. C., "Localised Dissolution Kinetics, Salt Films and Pitting Potentials," *Corros. Sci.*, Vol. 39, Nos. 10–11, 1997, pp. 1771–1790.

[15] Mat, S. and Newman, R. C., "Local Chemistry Aspects of Hydrogen Sulfide-Assisted Stress-Corrosion Cracking of Stainless Steels," Paper #228, *Proceedings of Corrosion 94*, Baltimore, MD, February 28–March 4, 1994, NACE, Houston, TX.

[16] Nguyen, V. A., Carcea, A. G., Ghaznavi, M., and Newman, R. C., "The Effect of Cation Complexation on the 'B' Value in Galvele's Pit Model—Results of Reaction-Transport Modeling" (manuscript in preparation).

STP 1609, 2019 / available online at www.astm.org / doi: 10.1520/STP160920170230

Piyush Khullar[1] and Robert G. Kelly[1]

Electrochemical Measurements in Thin Electrolyte Layers Using Sintered Silver/Silver Chloride Electrodes

Citation

Khullar, P. and Kelly, R. G., "Electrochemical Measurements in Thin Electrolyte Layers Using Sintered Silver/Silver Chloride Electrodes," *Advances in Electrochemical Techniques for Corrosion Monitoring and Laboratory Corrosion Measurements*, *ASTM STP1609*, S. Papavinasam, R. B. Rebak, L. Yang, and N. S. Berke, Eds., ASTM International, West Conshohocken, PA, 2019, pp. 294–322, http://dx.doi.org/10.1520/STP160920170230[2]

ABSTRACT

There remains a need to be able to make electrochemical measurements in thin films in a way that allows accurate assessment of the electrochemical kinetics. Methods used to date suffer from uneven current distribution and can cause modifications of the thin electrolyte, both of which can affect the kinetics measured. The present work investigates the use of commercially available sintered silver/silver chloride (SSSC) electrodes as combined reference electrodes/counter electrodes to allow electrochemical measurements in thin electrolyte films. A range of working electrode type, electrolyte geometry, and electrolyte compositions were studied. Where possible, direct comparisons were made between results using the SSSC and a standard three-electrode arrangement. In all cases, the SSSC results well reproduced those obtained with the conventional arrangement. In addition, a range of electrochemical measurements in thin films, including during ASTM B117, *Standard Practice for Operating Salt Spray (Fog) Apparatus*, salt spray testing, were conducted and demonstrated the utility of this arrangement. Limitations of the use of SSSC electrodes are also discussed,

Manuscript received November 12, 2017; accepted for publication March 5, 2018.

[1]Center for Electrochemical Science and Engineering, Dept. of Materials Science and Engineering, University of Virginia, 395 McCormick Rd., Charlottesville, VA 22904, USA P. K. https://orcid.org/0000 0002 2441 4422, R. G. K. https://orcid.org/0000 0002 7354 0978

[2]ASTM Symposium on *Advances in Electrochemical Techniques for Corrosion Monitoring and Laboratory Corrosion Measurements* on November 13 14, 2017 in Atlanta, GA, USA.

including the fact that currents above 1 mA led to polarization of the SSSC electrode of approximately 20 mV. Although this paper focused on one particular cell configuration, the concept of combined reference electrodes/counter electrodes can be extended to different configurations requiring measurements of corrosion behavior either through continuous electrochemical impedance spectroscopy/linear polarization resistance monitoring or polarization scans.

Keywords
thin electrolyte films, electrochemical methods, atmospheric corrosion

Introduction

Atmospheric corrosion is an electrochemical process that is often controlled by the characteristics of the thin electrolyte film inherent in this type of exposure. Deposit ed atmospheric aerosols absorb moisture from the air and form a thin solution film on the surface. The relative humidity (RH) in the atmosphere plays an important role in this phenomenon. As the RH increases above the deliquescence threshold [1], a thin electrolyte film is formed on the surface whose concentration depends on the thermodynamic equilibrium with the RH.

Although most of structures are exposed to atmospheric conditions, the majori ty of the corrosion studies have been conducted in full immersion conditions. Under these conditions, many aspects of the corrosion behavior for a material can be obtained by the anodic and cathodic polarization scans or by using electrochemi cal impedance spectroscopy (EIS) techniques (or both). Monitoring corrosion potential combined with linear polarization resistance (LPR) measurements is another useful way to obtain polarization behavior. While conventional full immer sion experimental techniques offer the ease of measurement, they cannot be used to study atmospheric corrosion due to the experimental challenges of placing a refer ence electrode (RE) and a counter electrode (CE) reliably into a thin film. All the aforementioned electrochemical techniques, although straightforward to use in full immersion, are nontrivial in thin electrolyte films, where the physical setup suffers from ohmic potential drop (IR) constraints.

Traditional bulk electrochemical measurement methods also assume that the solution concentration is constant. Although this assumption may hold true in full immersion conditions, in atmospheric conditions, the solution concentration depends on the RH. Depending on the electrolyte composition, the diurnal cycles can change the equilibrium solution concentration of the salts by up to an order of magnitude. This change in turn affects the electrolyte thickness and oxygen avail ability, which is a major factor in determining the cathodic current available.

Although the presence of a thin electrolyte layer or droplets on the substrate make the electrochemical measurement process difficult, various approaches have been used to determine electrochemical kinetics in thin films. Kelvin probes [2 4] have been used to obtain the surface Volta potentials, which are then converted to corrosion potentials using calibration curves. This technique allows noncontact

measurement of potentials through dielectric media such as air or electrolyte films. The conversion from measured Volta potential to corrosion potential relies on the assumption that both are linearly related and not affected by the change in humidi ty and thus changes in solution composition. Impedance based sensors have also been developed to characterize atmospheric corrosion [5 7]. Lyon and coworkers developed a three electrode cell by embedding electrodes in epoxy and creating a well to place the reference electrode in contact with the electrolyte [8 11]. Other techniques involving a platinum (Pt) wire [12] or a conventional saturated calomel electrode (SCE) [13,14] as an RE with a CE in a nearby well or larger volume of solution have been reported in literature.

In all of these measurement approaches, as the electrolyte layer thinned, the current distribution across it became distorted due to the location of the CE. In some cases, it is reasonable to expect that the RE lost ionic contact with the working electrode (WE) as well. Thus, accurate thin film measurements remain a challenge, and new techniques are needed to develop a better electrochemical understanding of the atmospheric corrosion processes.

A few measurement tools and techniques have been developed recently to overcome the aforementioned drawbacks. For example, Kramer, Friedersdorf, and Merrill [15] developed a thin film atmospheric cell that utilizes a carbon cloth as CE and a silver/silver chloride (Ag/AgCl) electrode as RE. The authors used a hydrophilic membrane to establish a thin electrolyte film. By controlling the volume of electrolyte and RH during the experiment, the authors were able to control the electrolyte film thickness. The authors demonstrated a two orders of magnitude increase in the diffusion limited oxygen reduction kinetics (vs. full immersion) on stainless steel Type 316 (SS316) when a 40 μm sodium chloride (NaCl) solution film was established on the metal. Hangarter and Policastro [16] used microelectro des (with Ag/AgCl as RE and a Pt wire as CE) in a Pasteur pipette tip to measure cathodic kinetics in a droplet cell. The authors were able to show increased oxygen reduction kinetics on different metallic substrates under droplet cells (vs. full immersion).

While the recently developed methods and techniques highlight the importance of measuring thin film kinetics, they suffer from complex design and nonuniform current distributions due to placement of the CE. This paper reports the use of a commercially available sintered Ag/AgCl electrode as a combined RE and CE for polarization measurements in thin films. The use of the combined electrode in a thin film cell ensures uniform current distribution with limited ohmic drop. In addition, the products of the reduction/oxidation reaction on the Ag/AgCl do not significantly alter the thin film electrolyte as is the case with a nearby Pt CE.

Experimental Procedures

Sintered Ag/AgCl electrodes are commercially available through a variety of manu facturers. For this project, the sintered Ag/AgCl disc electrodes were obtained from

Warner Instruments (Hamden, CT). The electrodes are available in different sizes and configurations. Fig. 1 shows the different sizes of disc electrodes used for this study, namely 4 , 8 , and 12 mm diameter disc electrodes.

Different materials were chosen as the WE for demonstrating the electrochemical capabilities of the sintered Ag/AgCl as a combined RE and CE: (1) 99.9 % Pt wire, (2) carbon steel (C1010), and (3) aluminum alloy 5083 (AA5083). A conventional flat cell was used to obtain polarization curves on the WE under full immersion with an SCE and Pt mesh counter electrode. The same cell was used for obtaining polarization curves with a sintered Ag/AgCl acting as a combined RE and CE in full immersion. Rotating disc electrodes (5 mm diameter Pt) were used to obtain polarization curves under forced convection conditions to achieve an accurate diffusion layer for comparison purposes. Once proven in bulk solution, the concept was then further extended to thin film experiments.

Fig. 2 shows a schematic of the experimental arrangement used to obtain thin film electrolyte polarization scans with a sintered Ag/AgCl as a combined RE and CE. The WE samples were embedded in epoxy and polished to a 1,200 grit finish. Before exposure, samples were plasma cleaned to improve the wettability of the surface. For thin film electrochemical measurements, the electrolyte layer was established with the help of a custom three dimensional (3D) printed disk of known thickness or polyester tape of known thickness. The 3D printed setup was then placed in a small chamber (Fig. 3) with inlet ports to introduce air or any other

FIG. 1 Sintered Ag/AgCl disc electrodes available from Warner Instruments (Hamden, CT).

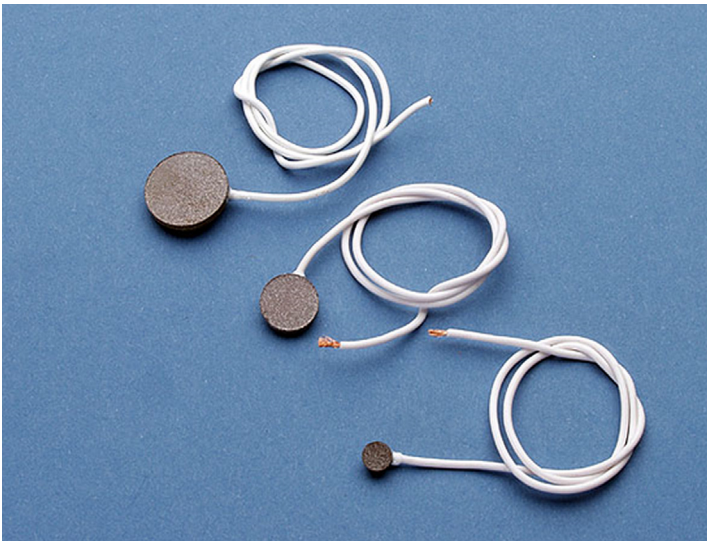

FIG. 2 (a) Orthogonal and (b) cross sectional view of the 3D printed setup with the WE embedded in epoxy.

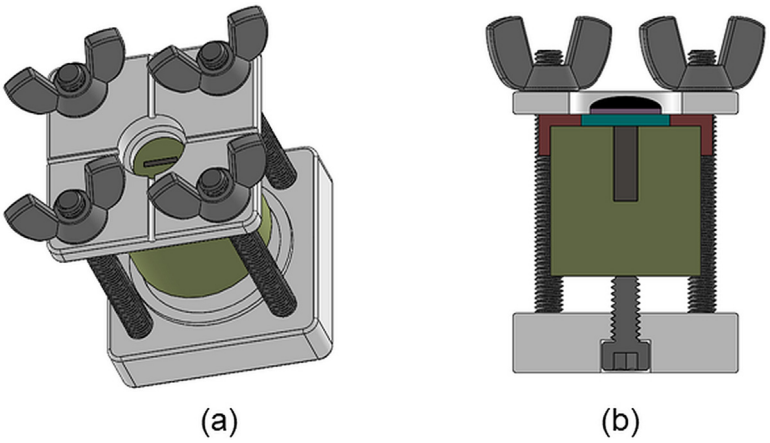

FIG. 3 Thin film electrochemical cell with a sintered Ag/AgCl as combined RE and CE.

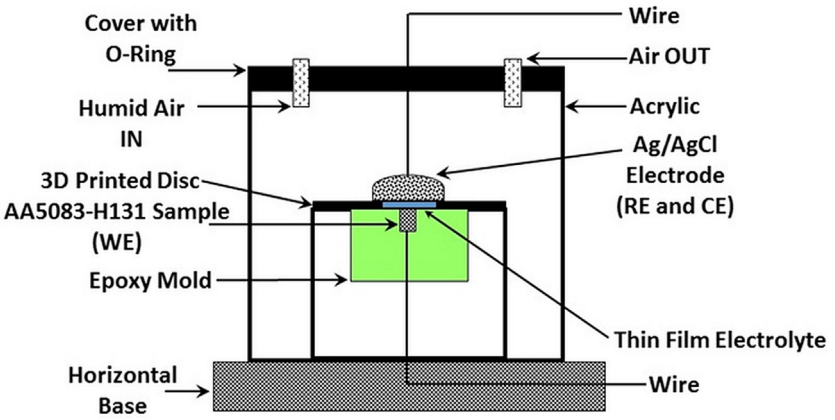

gaseous species. Humid air was pumped into the chamber to achieve equilibrium humidity corresponding to the NaCl concentration used. The Ag/AgCl disc elec trode was kept on top of the WE for uniform current distribution. An SP 150 or SP 200 potentiostat (Bio Logic Science Instruments, Seyssinet Pariset, France) was used to perform polarization measurements. Open circuit potential (OCP) was allowed to stabilize for 1 h before performing any polarization. A scan rate of 1 mV/s was used to perform anodic or cathodic polarization (or both). For

demonstrations in this study, a 12 mm diameter Ag/AgCl disc was chosen as the electrode, and all experiments were performed at room temperature (22°C).

Results

FULL IMMERSION MEASUREMENTS

Fig. 4 shows a plot of the potential of the sintered Ag/AgCl electrode as a function of chloride composition over a wide range of concentration (0.001 M to 3 M sodium chloride). The potential of sintered Ag/AgCl was allowed to stabilize and was recorded versus SCE in full immersion. As expected, the electrode follows Nernstian behavior, albeit with a slope of 51 mV/decade. Fig. 5 shows the anodic and cathodic polarization curves of the sintered Ag/AgCl electrode in 0.6 M NaCl. The OCP of approximately 10 mV versus SCE is as expected for a 0.6 M chloride concentration. A high apparent exchange current density of 1.5 mA/cm^2 is observed. There is minimal (less than 20 mV) polarization of the electrode until an anodic (and cathodic) current density of 2.5 mA/cm^2 is applied. Further cathodic polarization leads to the peak in current density at −200 mV (SCE) followed by a diffusion limited current density regime.

Fig. 6 shows the cathodic polarization curves for a Pt WE in quiescent full immersion conditions using (a) a conventional SCE with a Pt mesh as the CE and (b) a sintered Ag/AgCl as a combined RE and CE. An electrolyte of 1 M NaCl

FIG. 4 Potential of the sintered Ag/AgCl versus SCE as a function of chloride concentration.

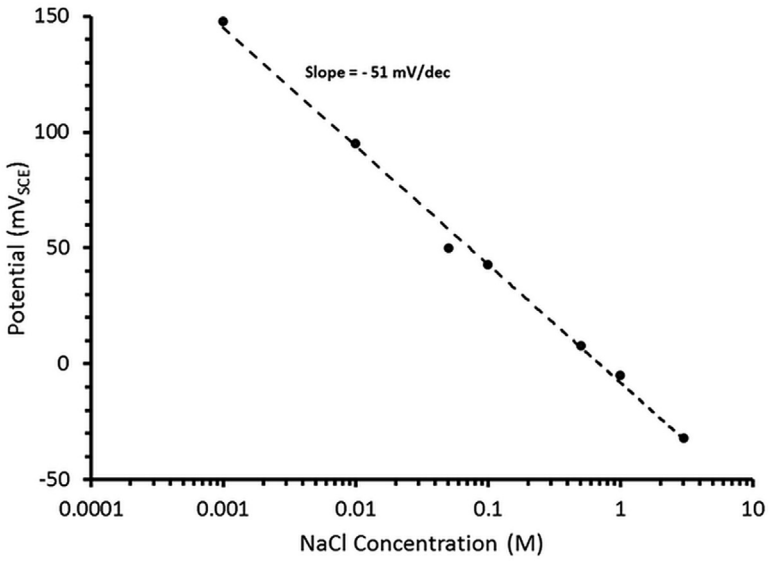

FIG. 5 Polarization curve of the sintered Ag/AgCl electrode (12 mm diameter disc) in 0.6 M NaCl.

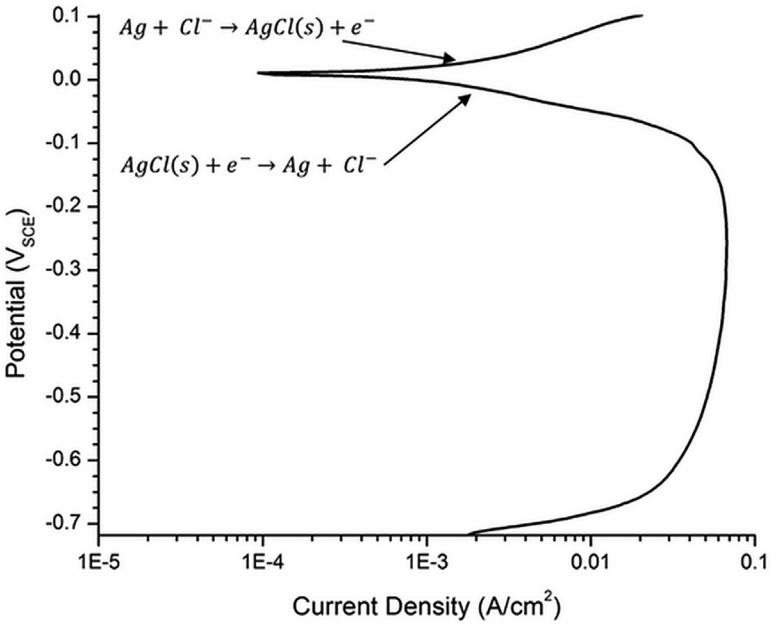

FIG. 6 Cathodic polarization curves for 1 mm diameter Pt WE in quiescent full immersion solution of 1 M NaCl.

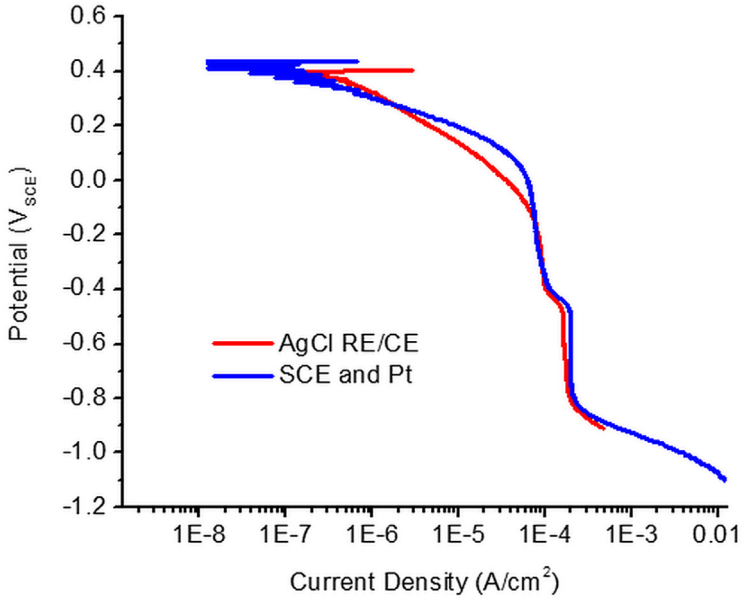

(pH 3) was used, and the potential of the sintered Ag/AgCl was converted to the SCE reference scale using Fig. 4. The diffusion limited oxygen reduction and proton reduction regimes followed by water reduction can be clearly seen in the aforementioned scans. Minor differences between the two scans are expected and attributed to differences in diffusion layer thickness in quiescent conditions.

Fig. 7 shows the anodic and cathodic polarization curves for C1010 steel using (a) a conventional SCE with Pt mesh in full immersion and (b) a sintered Ag/AgCl as combined RE and CE in full immersion. An electrolyte of 0.6 M NaCl (pH 6) was used, and the potential of the sintered Ag/AgCl electrode was converted to the SCE reference scale using Fig. 4. As observed for the Pt WE, the anodic and cathodic scans obtained using the sintered Ag/AgCl as a combined RE and CE are similar to ones obtained using SCE as RE and Pt as CE. The proton reduction currents are not appreciable at pH 6 and hence not observed in Fig. 7. Also, as expected, the diffusion limited oxygen reduction kinetics are slower on C1010 versus a Pt WE.

A Pine Research (Durham, NC) modular speed rotator with a rotating disc electrode (RDE) (5 mm diameter Pt WE) was used to overcome the experiment to experiment differences in the diffusion layer established in quiescent conditions. Fig. 8 shows the cathodic and anodic polarization curves obtained using the Pt RDE

FIG. 7 Cathodic and anodic polarization curves for C1010 steel sample (1 cm^2) in quiescent full immersion solution of 0.6 M NaCl.

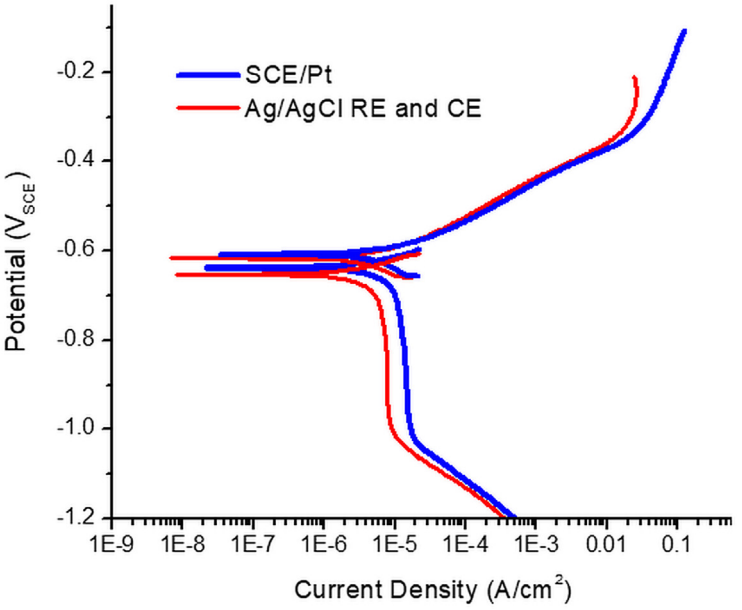

FIG. 8 Cathodic and anodic polarization curves for 5 mm diameter Pt RDE in 1 M NaCl solution at a rotating speed of 100 rpm.

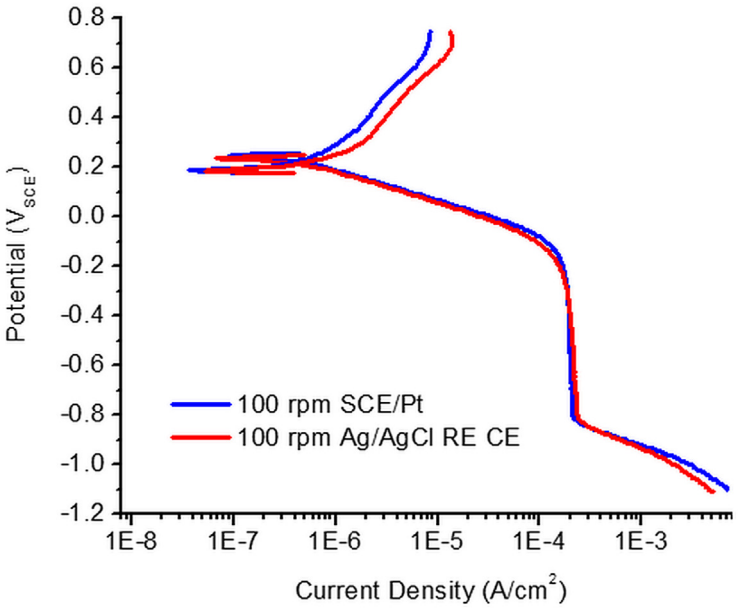

at 100 rpm; 1 M NaCl (pH 5.6) was used as electrolyte. Compared to Fig. 6, the anodic and cathodic curves with the sintered Ag/AgCl combined RE and CE are indistinguishable from those generated with the conventional SCE and Pt CE. Using the Levich equation,[3] the diffusion layer at a speed of 100 rpm is calculated to be approximately 60 μm.

THIN FILM MEASUREMENTS

The thin measurements shown in this section were conducted using sintered Ag/AgCl as a combined RE and CE. Fig. 9 shows the OCP measurement on a 1 mm diameter Pt WE using a sintered Ag/AgCl electrode. At time $t = 0$, a 100 μm film was established on the WE by depositing an electrolyte of known volume using a micropipette. The OCP kept rising before stabilizing at approximately 280 mV. After 45 min, LPR of the surface was measured using a fast scan rate of 5 mV/s.

[3]Levich current $I_L = (0.620)nFAD^{\frac{2}{3}}\omega^{\frac{1}{2}}\upsilon^{-\frac{1}{6}}C$, where, I_L is the Levich current (Amp), n is the number of moles of electrons transferred, F is the Faraday constant, A is the area of the electrode (cm^2), D is the diffusion coefficient (cm^2/s), ω is the angular rotation speed (rad/s), υ is the kinematic viscosity (cm^2/s), and C is the analyte concentration (mol/cm^3). Diffusion layer δ can be obtained by equating Levich current to the steady state diffusion limited current, which yields $\delta = 1.61\omega^{-1/2}\upsilon^{1/6}D^{1/3}$.

FIG. 9 Open circuit potential of a 1 mm diameter Pt WE exposed to 1 M NaCl 100 μm thin solution film.

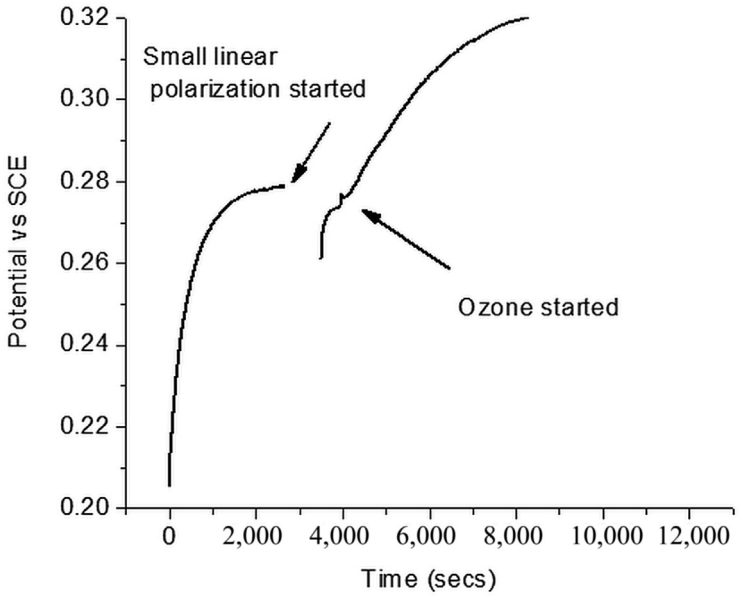

At the end of the LPR measurement, 8 ppm ozone was introduced in the chamber. The OCP of the Pt WE increased after introducing ozone in the chamber because of faster ozone reduction kinetics.

Fig. 10 shows the measurement of OCP and LPR when a 1 mm electrolyte film was established on an AA5083 alloy. The OCP was continuously monitored and LPR scans were conducted every hour. The OCP at the beginning of the scan was approximately −760 mV. With time, the corrosion potential went down. The polarization resistance went up during the same time, indicating a decrease in cathodic kinetics. Once all the oxidizer was consumed (after approximately 4 h), the potential started increasing. At the end of 12 h, the oxidizer was replenished and the OCP started out at a higher value as it did at the start of the exposure. This quick experiment shows the ability of sintered Ag/AgCl to not only detect changes in surface potential (role of RE) but also to provide information regarding the polarization resistance (role of CE) to get information regarding the kinetics and the changes in anode/cathode.

Fig. 11 shows the cathodic scans on 1 mm diameter Pt WE in a 100 μm thin film solution of 0.6 M NaCl. The cathodic polarization scans clearly show the oxygen reduction kinetics followed by the water reduction region. Different trials to perform the scan show that the diffusion limited behavior of the alloy is reproducible.

FIG. 10 Potential and linear polarization resistance measurements on 0.36 cm^2 AA5083 alloy WE exposed to 1 mm thin film of 2 M NaCl+ 0.022 M $AlCl_3$+0.05 M $K_2S_2O_8$.

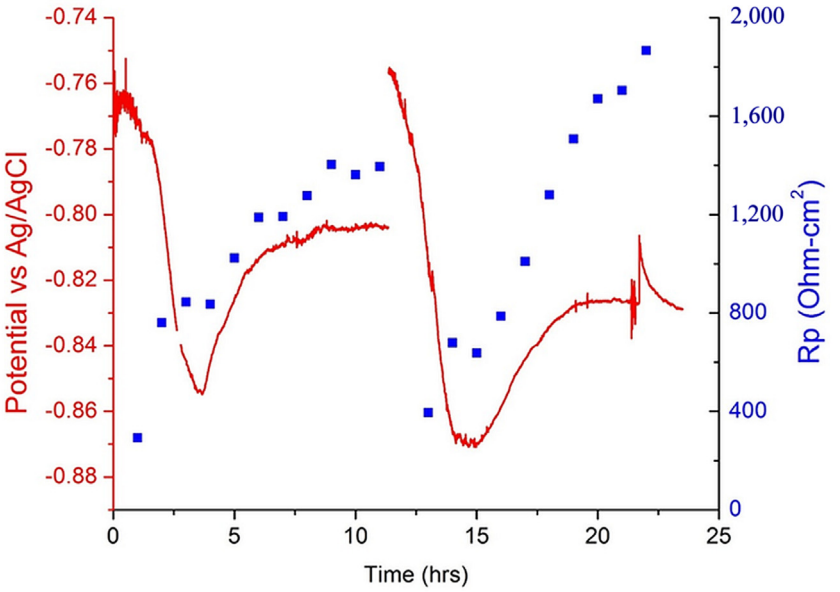

FIG. 11 Cathodic polarization scans on 1 mm diameter Pt WE exposed to 100 μm thin film of 0.6 M NaCl.

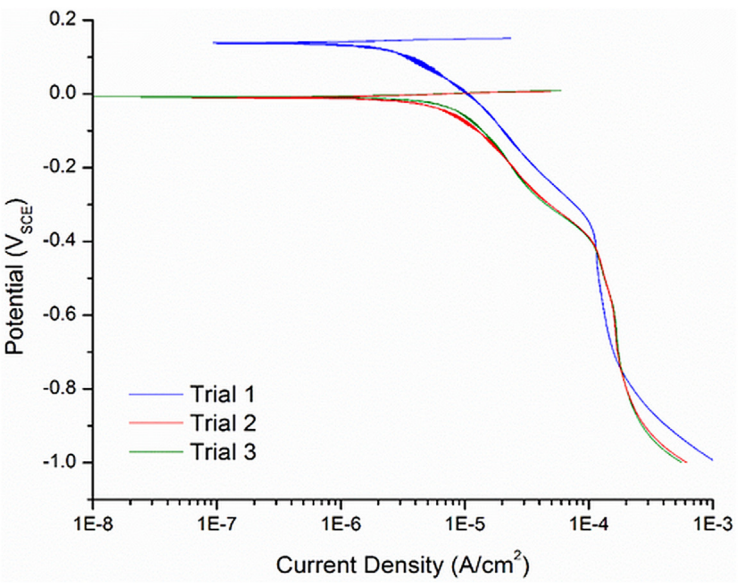

FIG. 12 Cathodic and anodic polarization scans on 1 cm^2 C1010 alloy WE exposed to 250 μm thin film of 0.6 M NaCl overlaid on the full immersion scans as shown in Fig. 7.

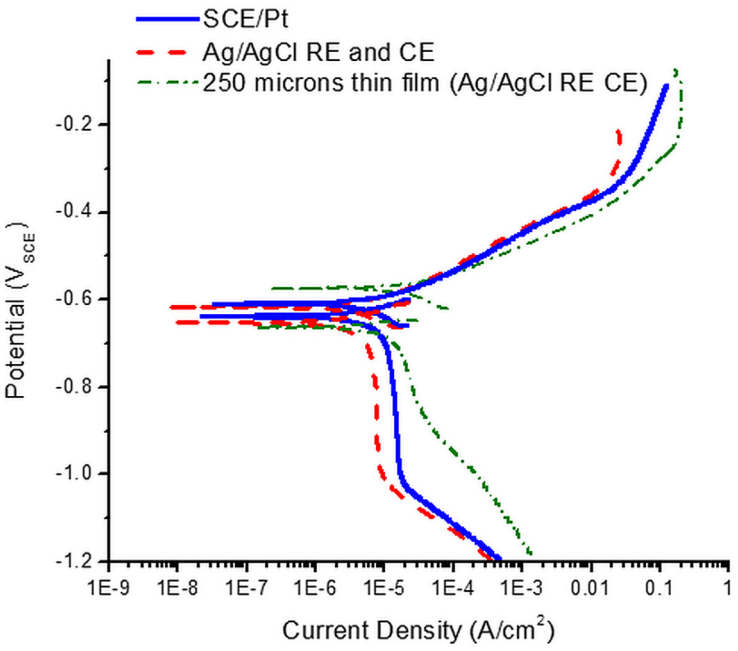

Fig. 12 shows the cathodic scans on C1010 WE in a 0.6 M NaCl electrolyte film approximately 250 μm thick. The thin film scans have been overlaid on the full immersion scans from Fig. 7 for comparison. The corrosion potential for the case with thin film electrolyte is higher, which is as expected due to faster oxygen reduction kinetics. Fig. 13 shows the cathodic scans obtained on an AA5083 degree of sensitization 50 sample with different film thicknesses. As expected, the cathodic kinetics measurement on AA5083 is slower when compared to Pt WE.

As mentioned earlier, EIS is a powerful technique to probe the electrochemical behavior of the substrate undergoing corrosion. The EIS measurements (10^{-1} to 10^5 Hz) shown in Fig. 14 were conducted potentiostatically on an AA5083 alloy using a potential wave of amplitude 10 mV. The Nyquist plot in bulk solution shown here using a conventional SCE/Pt setup is indistinguishable from the one obtained using sintered Ag/AgCl as RE/CE. Fig. 15 shows the Nyquist plots obtained on AA5083 in 100 μm of 1 M NaCl solution. The plots obtained at different time intervals can be used to monitor changes in corrosion behavior.

FIG. 13 Cathodic polarization measurements on 0.36 cm^2 AA5083 alloy WE exposed to 0.6 M NaCl electrolyte of different film thickness.

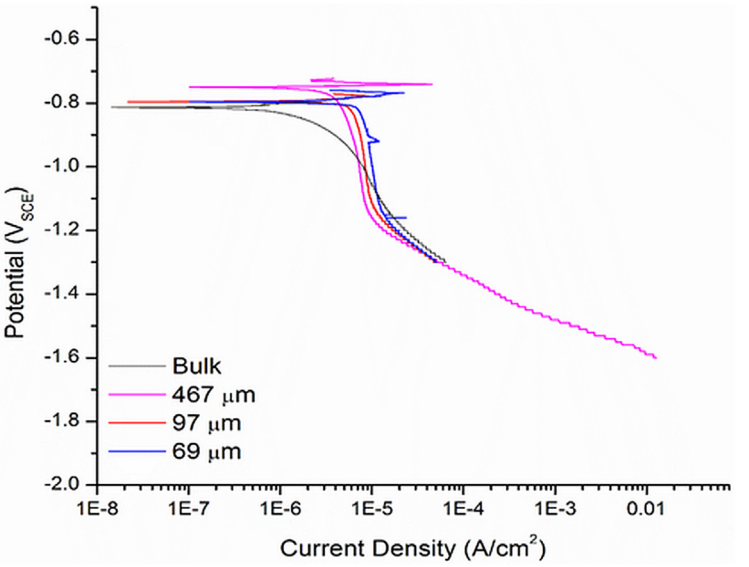

FIG. 14 EIS measurements on an AA5083 alloy exposed to 1 M NaCl solution in full immersion.

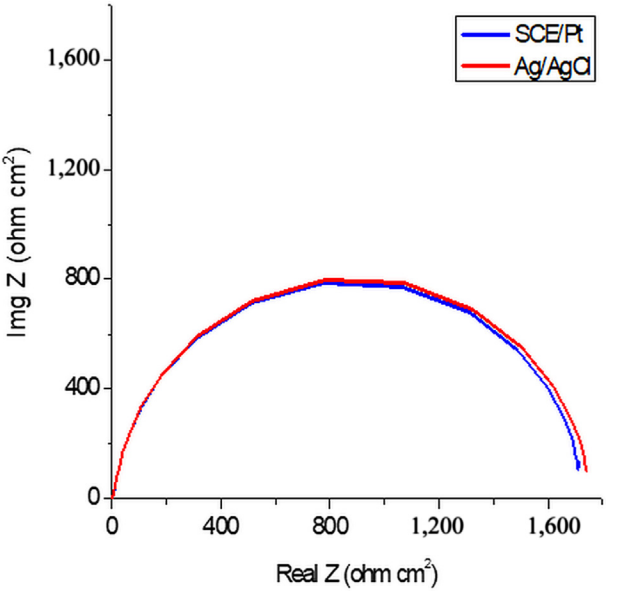

FIG. 15 EIS measurements on an AA5083 alloy exposed to 100 μm of 1 M NaCl solution. Each semicircle represents a measurement with an interval of 1 h.

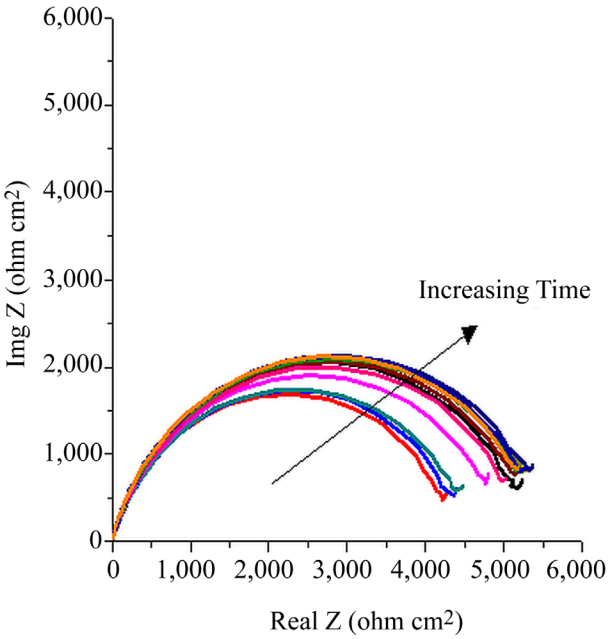

Discussion

The role of an RE in an electrochemical cell is to provide a stable potential for measurement and control of the WE potential. In conventional three electrode electrochemical experiments, the RE is exposed to extremely small currents in the range of 10 pA; hence, polarization of the RE is negligible. On the other hand, the role of a CE is to support the reactions occurring at the WE by acting as a source/sink for the electrons consumed/produced at the WE. So, when the WE is undergoing anodic polarization, the CE becomes the sink for the electrons released at WE. When the WE needs to be cathodically polarized, the electrons required for the reduction reactions are supplied by the anodic reactions at the CE. Hence, the current at the WE will always be equal (and of the opposite sign) to the CE. This equivalence in current is also the historical reason for the recommendation of having a high CE:WE area. If the surface of the CE is small compared to the WE, it might lead to a high current density on the CE and high potential difference between the two electrodes, which can create problems depending on the allowable potential limit of the potentiostat.

Platinum or another inert material is a good choice for the CE in bulk solutions. However, for thin film solutions, the products of the reaction at the CE can

alter the pH of the electrolyte and thus interfere with the reactions of interest at the WE. For example, a Pt CE in aqueous chloride solution produces O_2 and H^+ (and possibly OCl^-) during cathodic polarization of the WE and H_2 and OH^- during anodic polarization of the WE.

Ag/AgCl is a well known reference electrode characterized by its stability. When no current flows between the electrode and solution, the potential observed is the half cell potential, or the Nernst potential, as given by the Nernst equation (Eq 1). Although, the theoretical Nernst slope is −59 mV/decade (at 25°C), the sintered Ag/AgCl electrodes used for this study had a stable slope of −51 mV/decade as shown in **Fig. 4** at a lab temperature of 22°C. **Fig. 4** was used to convert the potentials measured by sintered Ag/AgCl to an SCE scale.

$$E = E^o - \frac{2.303RT}{F}\log[Cl^-] = E^o - 0.0591\log[Cl^-] \quad (1)$$

However, if current passes through the electrode, the potential observed is altered. The difference between the potential at zero current and measured potential when current is passing is known as overpotential. Ag/AgCl electrodes exhibit characteristics that are comparable to an essentially nonpolarizable electrode. Ag/AgCl electrodes can be fabricated by starting with an Ag base (wire or coupon) and electrochemically growing the AgCl on its surface. Although the electrode produced this way can be used for most applications, it is not a sturdy construction because the AgCl film deposited is removed after repeated use. Sintered Ag/AgCl electrodes offer a more stable design. The sintered matrix consists of finely divided Ag and AgCl powder pressed together in desired shapes. In addition, sintering creates a high surface area that increases the effective kinetics of the Ag/AgCl electrodes that already have a high exchange current density and a low Tafel slope. This effect inherently limits the polarization of the electrode as seen in **Fig. 5**. For sufficiently small currents, an Ag/AgCl electrode can serve simultaneously as RE and CE as its potential would not be altered. Thus, it can supply significant currents with minimal polarization the ability required for a combined RE/CE. The limits on using any electrode as a combined RE/CE can be defined by the current density at which the polarization of the electrode exceeds a user specified maximum deviation from the OCP and the charge capacity (to establish when the electrode needs to be discarded).

As mentioned before, anodic polarization of the WE requires the CE to be polarized cathodically. This polarization will result in the reduction of AgCl to metallic silver and the release of chloride according to Eq 2:

$$AgCl + e^- \leftrightarrow Ag + Cl^- \quad (2)$$

As shown in the polarization curve of the sintered Ag/AgCl electrode in **Fig. 5**, eventually all of the electrochemically accessible AgCl in the electrode is consumed, and the current decreases after reaching a maximum at approximately −200 mV (vs. SCE). During anodic polarization of the Ag/AgCl electrode (i.e., as would occur

during cathodic polarization of the WE), Eq 2 leads to oxidation of Ag to form more AgCl on the electrode (in an electrolyte containing chloride ions). The anodic current density reaches a maximum at approximately 100 mV (SCE) at a current density of 30 mA/cm^2. The large quantity of AgCl present in a sintered Ag/AgCl electrode (compared to one in which a bare Ag wire is chloridized to obtain AgCl) is the main reason it can be used as a combined CE and RE.

Integration of the current revealed that the charge capacity of the 12 mm diameter electrode shown in Fig. 4 was approximately 100°C. Depending on the size of the electrode (and hence the amount of AgCl present), the charge for other sintered Ag/AgCl electrodes was found to be between 50 and 800°C for electrodes between 4 and 24 mm in diameter.

Although the Ag/AgCl electrode can supply substantial current, it can be clearly seen that the electrode undergoes polarization at higher current densities. Fig. 16 shows the deviation of the potential versus OCP of an Ag/AgCl electrode in 0.6 M NaCl during anodic and cathodic polarization of the electrode. Essentially, this graph plots the potential (vs. OCP) and current density in the electrochemical re gion close to OCP. When no current is drawn from the electrode, the potential recorded is the OCP (or a deviation of 0 V from OCP). As the electrode is polarized (in either direction), the potential starts to drift in the positive direction (anodic polarization) and the negative direction (cathodic polarization). As the polarization in the cathodic and anodic direction is almost identical, as shown in Fig. 5, the deviation

FIG. 16 The deviation from the OCP of the sintered Ag/AgCl electrode during polarization in 0.6 M NaCl solution.

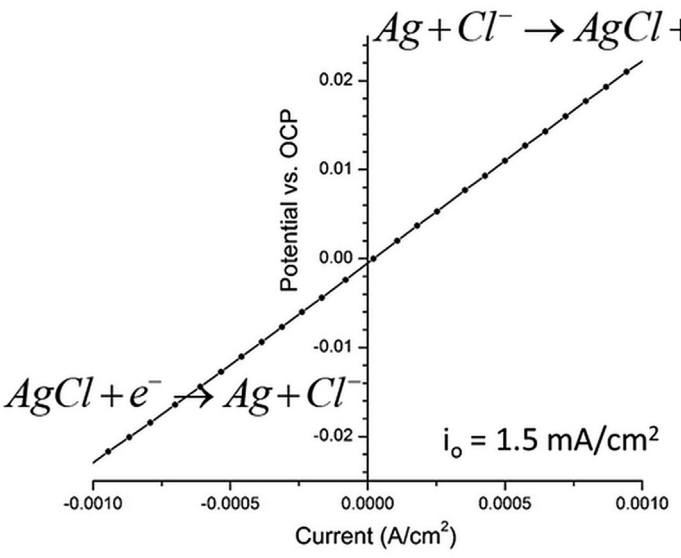

from OCP also looks identical in either direction. For example, when about 1 mA/cm^2 current is drawn from the electrode, the deviation is less than 20 mV in either direc tion. For many corrosion applications, anodic current densities of 1 mA/cm^2 (and even lower cathodic current densities) are more than sufficient to characterize the behavior of a metal. For linear polarization measurements and EIS characterization, the current drawn is always small, but it should be noted that this 1 mA/cm^2 current density can be easily increased by choosing an appropriate CE:WE ratio.

This deviation from the OCP was measured during a polarization experiment where the sintered Ag/AgCl electrode was used as RE and CE and is shown in Fig. 17. The y axis shows the deviation of OCP (vs. SCE) in volts and the x axis shows the time in seconds. The experiment was done in 1 M NaCl bulk solution on a 5 mm Pt WE. The OCP of the WE was measured for 1 h and the WE polarized cathodically to -1.2 V_{SCE} (after the OCP hold). The combined RE/CE sintered Ag/AgCl was not being polarized during OCP measurement (of the WE); hence, there is no deviation from -10 mV (versus SCE) potential during the OCP hold. At the end of the OCP hold, the WE starts to get polarized, which in turn leads to polarization of the RE/CE. The deviation of the sintered Ag/AgCl from the OCP is not noticeable initially but, eventually, at higher current densities, the potential deviates as much as 1 5mV from the OCP (-0.025 V_{SCE}). As soon as the experi ment ends and the RE/CE is no longer being polarized, it returns back to its OCP of approximately -0.010 V_{SCE}. A similar behavior was obtained when the WE was

FIG. 17 The deviation from the OCP of the sintered Ag/AgCl electrode (used as combined RE and CE) during anodic polarization of a 5 mm diameter Pt RDE.

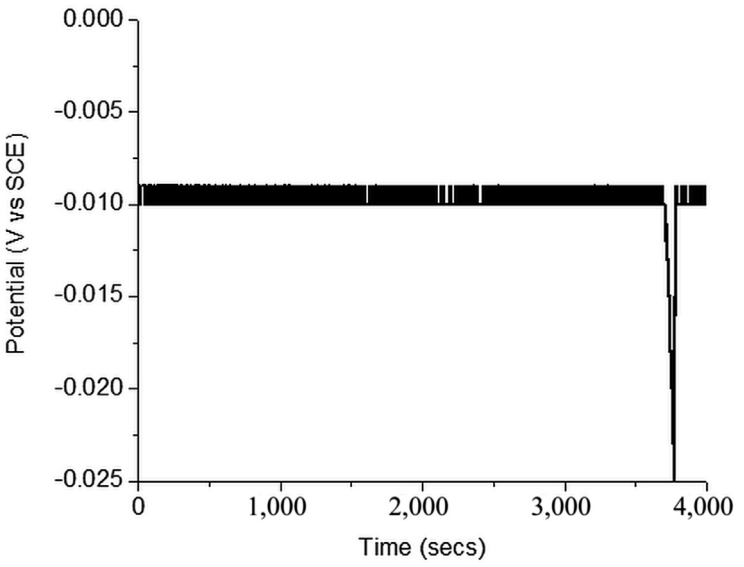

FIG. 18 The deviation from the OCP of the sintered Ag/AgCl electrode (used as combined RE and CE) during cathodic polarization of a 5 mm diameter Pt RDE.

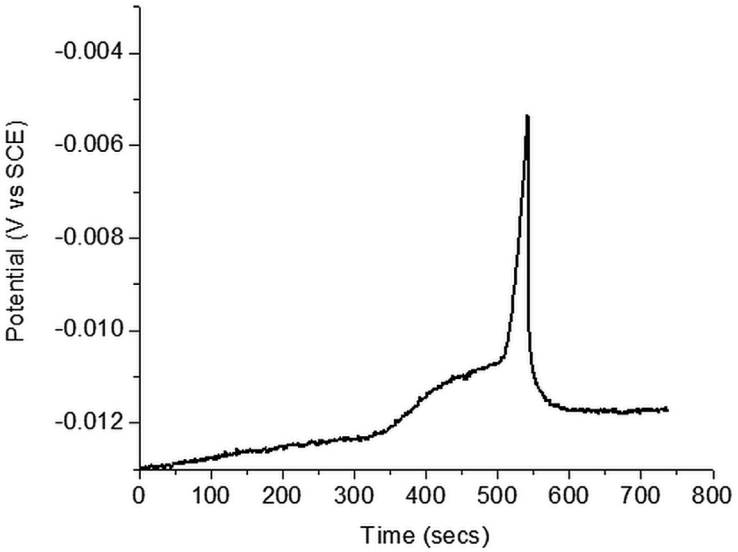

anodically polarized as shown in Fig. 18, with the maximum deviation from OCP occurring when the maximum current was drawn by the WE.

Fig. 19 shows the deviation of the RE/CE and the polarization of WE (C1010) on the same graph. The left y axis shows the deviation from the OCP of the RE/CE, while the right y axis shows the current density at WE. The bottom x axis shows the time for both curves, and the top x axis shows the corresponding WE potential. At the beginning of the scan, the RE/CE did not deviate from its OCP. As more current was drawn from the RE/CE (due to the increasing polarization of WE), the sintered Ag/AgCl began to deviate from its OCP (vs. SCE). When WE current density reached 1 mA/cm^2, the RE/CE had deviated by approximately 30 mV from its OCP. The deviation of the RE/CE from its OCP can be used to adjust the WE potential measured (to compensate for the RE/CE deviation).

Comparing the cathodic kinetics obtained on 1 mm Pt WE using a sintered Ag/AgCl as RE and CE showed that the electrode yielded a curve that was indistinguishable from the one obtained using a conventional SCE RE and Pt CE. The ORR diffusion limited current density was found to be approximately 10^{-4} A/cm^2. COMSOL Multiphysics modeling (Liu, C., personal communication, 2016) showed that for a WE that is 1 mm in diameter, the edge diffusion of oxygen accounts for approximately half of the total current observed. When the WE size is increased to about 1 cm^2 (C1010), the cathodic scans as obtained in Fig. 7 show a reasonable ORR diffusion limited current density of 2×10^{-5} A/cm^2. As expected, the ORR is

FIG. 19 The deviation from the OCP of the sintered Ag/AgCl electrode (used as combined RE and CE) during cathodic polarization of a C1010 WE in 0.6 M NaCl solution.

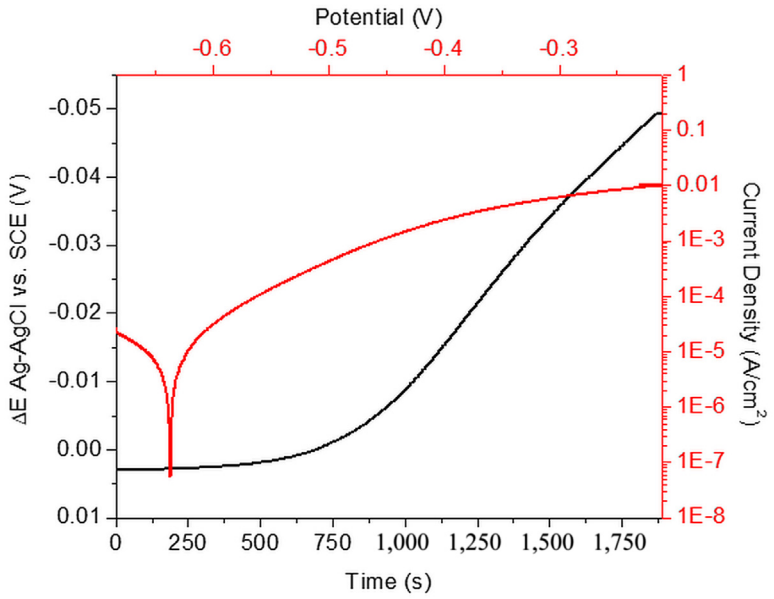

faster on Pt WE when compared to ORR on C1010. Cathodic and anodic scans obtained in Fig. 8 again showcase the ability of the sintered Ag/AgCl to produce curves that are indistinguishable from the ones obtained using conventional methods.

Fig. 12 overlays an anodic and cathodic scan on C1010 obtained under a thin film of 250 μm. In the region of the OCP, the thin film polarization scan differs from the full immersion curve as expected. This deviation can be attributed to the more rapid oxygen reduction kinetics on the C1010 as seen by Nishikata, Ichihara, and Tsuru [17]. At higher potentials and current densities, ohmic losses in solution lead to deviation from Tafel behavior. The primary limitation is the value of the maximum current needed and how this current translates to a current density on the Ag/AgCl, which controls the amount of polarization away from its OCP. For example, for the cathodic scan shown in Fig. 12, only 0.2°C of charge was consumed with the total available charge being approximately 100°C for a new 12 mm diameter disc electrode.

Fig. 11 shows three different trials of cathodic scans on Pt WE using the sintered Ag/AgCl in a 100 μm thin film of solution. These curves show that the diffusion limited behavior is reproducible, and faster ORR kinetics are observed in thin films. Compared to Pt WE, the cathodic scans for AA5083 alloy (Fig. 13) show reduced

kinetics. Even though the kinetics increase with the decrease in film thickness, the overall kinetics are slower when compared to Pt WE. The slower kinetics (espe cially) at lower film thickness can be attributed to the oxide formation on the sur face (Liu, C., personal communication, 2016).

In cases where the RE/CE deviation during polarization is not acceptable, elec trochemical techniques like LPR and EIS measurements can be used to obtain the corrosion behavior of the metal. A reference electrode by itself can only provide the corrosion potential but not information regarding the corrosion kinetics. For exam ple, increasing corrosion potential can be ascribed to either an increase in cathodic kinetics or a decrease in anodic kinetics. Fig. 10 shows the measurement of potential and LPR (inversely proportional to corrosion current). At the beginning of the exposure, the oxidizer concentration was maximum and it decreased with time due to consumption in the cathodic reactions. Fig. 20 shows the cathodic kinetics for different concentrations of potassium persulfate in a 500 μm thin electrolyte on AA5083 WE. As expected, the kinetics decrease with a decrease in concentration of the oxidizer. This decrease in cathodic kinetics can be related to an increase in polarization resistance. Thus, the decrease in potential during the first 4 h (Fig. 10) can be attributed to a decrease in cathodic kinetics only because it was paired with polarization resistance measurements during the exposure. However, the potential rises again at the end of 4 h and stabilizes to a value slightly lower than the initial

FIG. 20 Cathodic polarization scans obtained on AA5083 exposed to 0.5 mm thin film of 2 M NaCl + 0.022 M $AlCl_3$ concentrations of $K_2S_2O_8$.

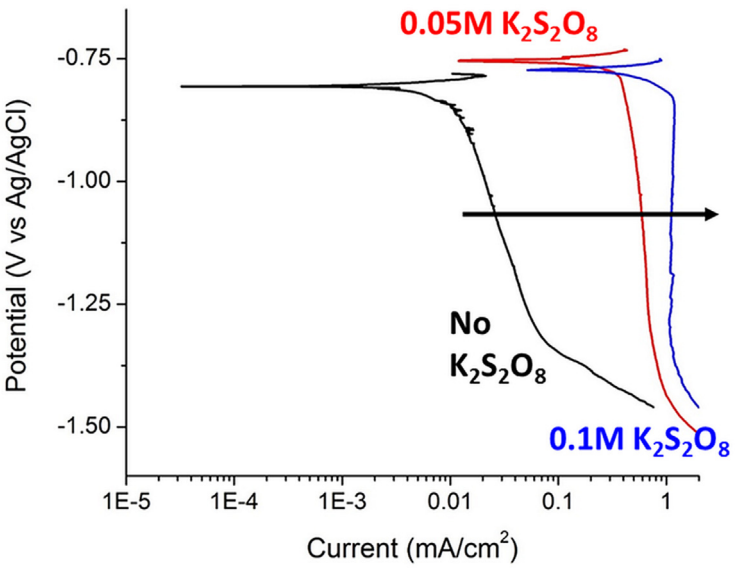

potential at the end of 12 h. Without the available R_p data, this increase could be (incorrectly) interpreted as an increase in cathodic kinetics. However, the R_p kept increasing during this time period, which indicates a decrease in corrosion kinetics. The decrease in kinetics and increase in corrosion potential can be attributed to a decrease in anodic kinetics or surface repassivation. Thus, the mixed potential theory can be used to interpret the potential and R_p data measured by the sintered Ag/AgCl in thin electrolyte films during atmospheric corrosion to ascertain and study the dominating corrosion processes.

Nondestructive techniques like EIS can be used to get even more information about the WE such as polarization resistance, solution resistance, and double layer capacitance. **Fig. 14** shows the EIS spectra obtained in full immersion conditions on an AA5083 alloy. Once again, the sintered Ag/AgCl produced an EIS spectra identical to the one obtained with conventional electrodes. **Fig. 15** shows the ability of the sintered Ag/AgCl to perform EIS in a thin film 100 μm in thickness. The thin film EIS measurements can be used for continuous corrosion monitoring in a standardized accelerated corrosion test like ASTM B117, *Standard Practice for Operating Salt Spray (Fog) Apparatus* [18]. In this standard test, the samples are exposed to 5 % NaCl solution for a specific period before the corrosion damage can be assessed. The sintered Ag/AgCl can be used to measure the OCP and obtain EIS spectra of the WE (assuming constant chloride concentration). **Fig. 21** and **Fig. 22** show the OCP measurement on an AA2060 T3 alloy and the EIS measurement after 1 h of exposure in ASTM B117. These measurements can be used to better

FIG. 21 OCP measurement of an AA2060 alloy during ASTM B117 test exposure.

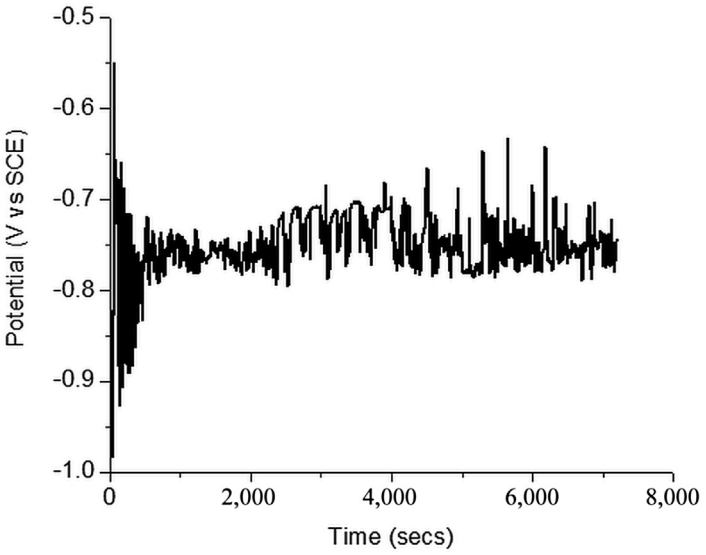

FIG. 22 EIS measurement (Nyquist plot) obtained for AA2060 at the end of 1 h of exposure in an ASTM B117 test.

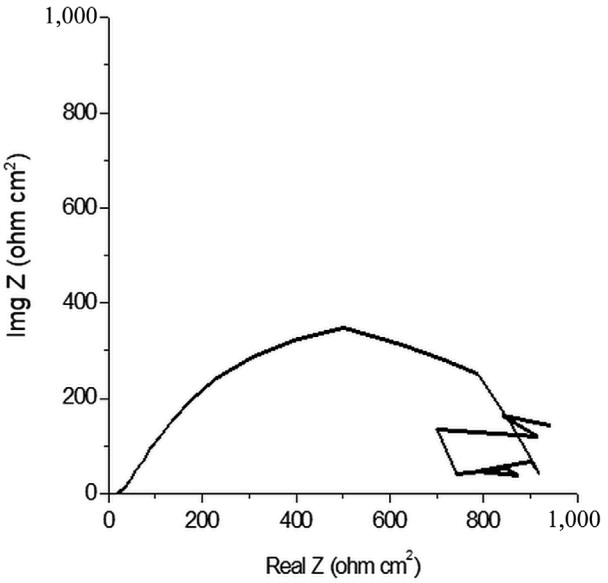

understand the electrochemical underpinnings of thin film corrosion and to develop improved accelerated lab tests.

However, there are several other experiments where the sample needs to be polarized electrochemically to accelerate atmospheric conditions. Fig. 23 shows the potential as a function of time when AA5083 was held galvanostatically at 1 mA/cm^2 under a 1 mm thin electrolyte film of 0.6 M NaCl. By keeping the WE area small, the amount of charge consumed (from a 12 mm diameter sintered Ag/AgCl electrode) in this experiment was approximately 20°C. For higher charge requirements, either for longer duration of exposure or larger WE, the sintered Ag/AgCl can be discarded and replaced by a new electrode during the exposure.

Two other characteristics of the sintered Ag/AgCl electrode that are important in thin film electrochemical studies of corrosion are its minimal effect on the solu tion composition and the uniform current distribution it affords in the apparatus schematically shown in Fig. 1. As shown in Eq 2, each coulomb of AgCl reduced releases one coulomb of chloride into solution. In the case of the scan for the 0.250 mm thick solution layer on C1010 (Fig. 12), the concentration of chloride in the lay er increased by 5 mM, a change of less than 1 %.

The uniform current distribution afforded by the arrangement of Fig. 3 is a major advantage of using the sintered Ag/AgCl as a combined RE/CE. Current dis tribution is one of the most significant challenges in thin film electrochemical

FIG. 23 Potential measurement during anodic galvanostatic polarization on AA5083 exposed to 1 mm thin film of 1 M NaCl.

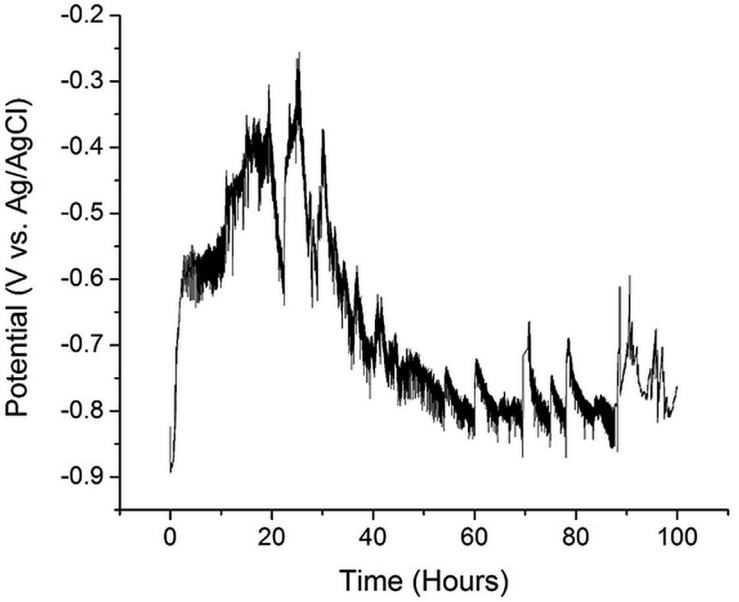

measurements. In previous measurement approaches, the placement of the CE with respect to the WE led to nonuniform current distributions. Standard methods gen erally use a Pt wire/mesh as the CE coiled around the WE. That arrangement leads to a focusing of the current at the edges of the electrode. This inhomogeneity com plicates interpretation of the current because the area over which it is spread can vary substantially with electrolyte layer thickness. One manifestation of that was the observation by Zhou et al. [13] of increased corrosion products at the edges of their samples during cathodic polarization. The arrangement of **Fig. 3**, in which the CE is directly above the WE, ensures uniform current distribution. As the RE is the same as CE, the potential measured also has a far more limited ohmic drop than in previ ous experimental arrangements. In fact, ohmic drop decreases as the electrolyte film becomes thinner as opposed to the standard approaches discussed earlier where the ohmic drop becomes more important with thinner films.

Considering that the WE is closed off by the RE/CE in the setup shown in **Fig. 3**, access to atmospheric gases can be an issue especially during cathodic polari zation of the WE. **Fig. 24** shows the cathodic polarization scans on a 1 mm Pt WE exposed to a 100 μm thin electrolyte solution of 1 M NaCl. The cathodic scans were run from OCP to −1.1 V (vs. SCE). As oxygen is consumed during the cathodic reaction (oxygen reduction), it would take a finite amount of time before the oxygen concentration levels are replenished in the thin film. These scans show

FIG. 24 Series of cathodic scans performed on 1 mm diameter Pt WE in 100 μm 1 M NaCl solution. Different time intervals represent the amount of time before a new cathodic scan was performed.

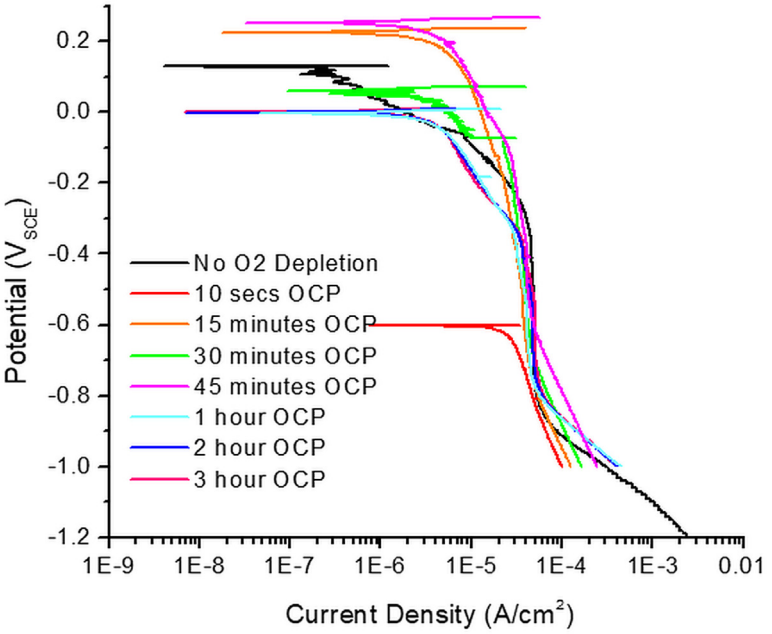

the amount of time it would take for the oxygen replenishment. The first cathodic scan was run after a 1 h OCP hold, and this scan is labeled as "no O_2 depletion." Subsequent scans were performed at different intervals from the first scan. For example, the next cathodic scan was performed 10 s after the first cathodic scan finished. In effect, oxygen replenishment was allowed to occur for only 10 s before the next cathodic scan. As it can be seen, the cathodic scan performed after 10 s had a lower diffusion limited current density (and lower corrosion potential), indicating that the oxygen had not returned to its pretest saturation level. However, the diffusion limited regime of the cathodic scan performed after 15 min was indistinguishable from the "no O2 depletion" scan, indicating that the oxygen levels are replenished between a 10 s and 15 min interval window. With a conservative estimate, allowing 15 min between successive cathodic scans is advised.

A similar experiment was also performed in full immersion conditions, and the results are shown in Fig. 25. Assuming a diffusion layer of 800 μm (in full immersion) and oxygen diffusion coefficient as 2×10^{-5} cm^2/s, it would take approximately 300 s for oxygen to diffuse through this layer. From Fig. 25, it can be seen that the OCP does recover within 5 min after the initial cathodic scan. The

FIG. 25 Series of cathodic scans performed on 1 mm diameter Pt WE in 1 M NaCl bulk solution. Different time intervals represent the amount of time before a new cathodic scan was performed.

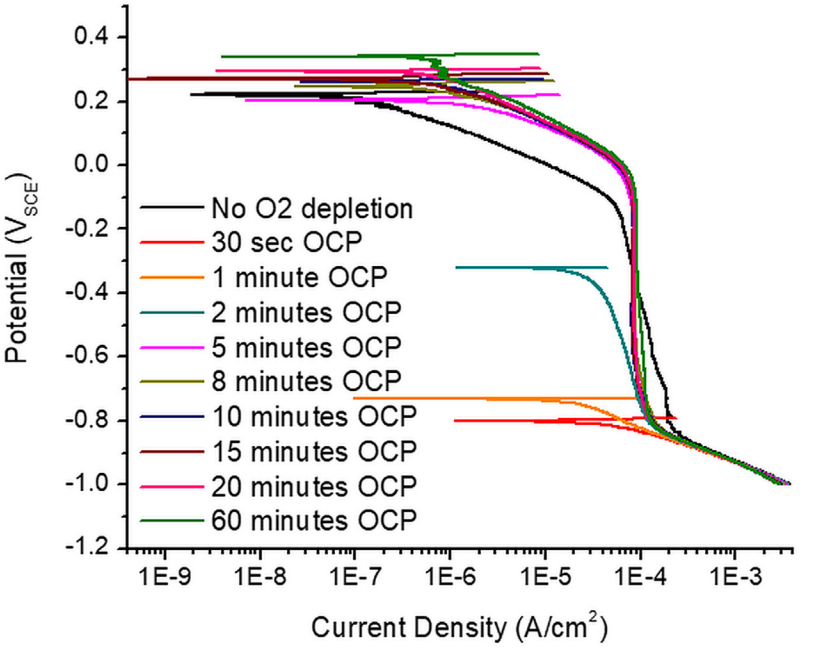

subsequent cathodic scans (i.e., after 8, 10, 15, 20, and 60 min) are indistinguish able, indicating completion of oxygen replenishment.

As mentioned before, the sintered Ag/AgCl electrode can be bought in different shapes such as a disc, pellet, or wire. Depending on the application and acceptable deviation from the OCP, the sintered electrodes can be used in different setups for making thin film electrochemical measurements. For example, based on the work shown in this paper, Rafla, Davenport, and Scully [19] embedded a 12 mm sintered Ag/AgCl disc in epoxy with an AA7050 multielectrode array (**Fig. 26**). The authors then polished the epoxy to reveal the sintered electrode and AA7050 array. Using an Ag/AgCl electrode as both RE and CE, the authors were able to probe the cathodic kinetics under a thin electrolyte film of 70 μm as shown in **Fig. 27**. The full immersion and rotating disc cathodic scans have also been shown using the same setup for comparison purposes.

Steiner, Burns, and Kelly [20] have used the sintered Ag/AgCl electrode to mea sure the potential of an AA5456 alloy during stress corrosion cracking experiments (**Fig. 28**) in misting, wicking, and full immersion conditions. They also employed the Ag/AgCl electrode as a combined RE/CE to perform cracking experiments

FIG. 26 Sintered Ag/AgCl used as combined RE/CE in a multielectrode array setup [19].

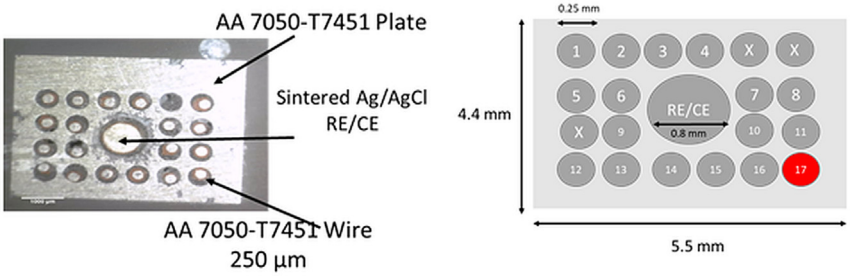

FIG. 27 Cathodic polarization scans performed on AA7050 in 0.6 M NaCl using sintered Ag/AgCl as RE/CE [19].

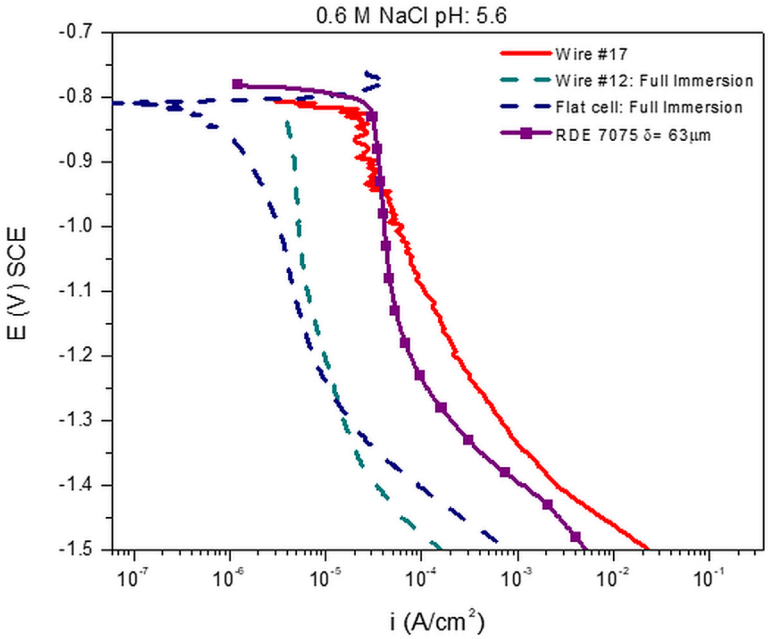

under potentiostatic conditions. As expected, the authors found that the location of electrode placement played an important role in misting or thin film conditions due to the IR constraints. Fig. 29 shows the effect of thin film polarization on the cracking behavior of AA5456. By placing the electrode closer to the crack, the authors were also able to show that the potentiostatic polarization in misting conditions can lead to behavior similar to that observed in full immersion.

FIG. 28 Schematic of an AA5456 specimen with an Ag/AgCl electrode used as RE/CE [20].

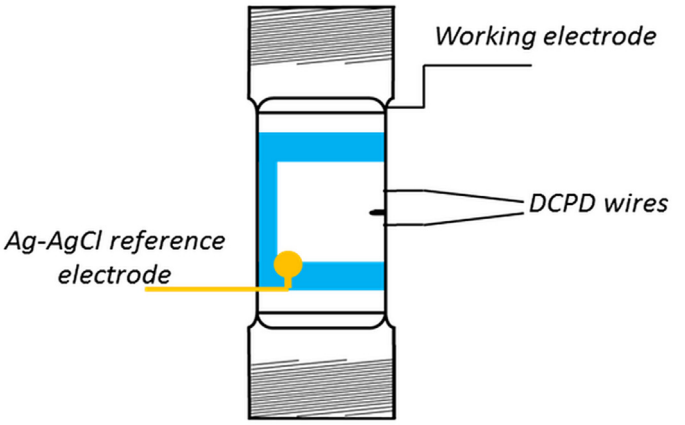

FIG. 29 Crack growth rate measurements performed in misting, wicking, and full immersion conditions. The potentiostatic conditions during misting and wicking were obtained using sintered Ag/AgCl as a combined RE/CE [20].

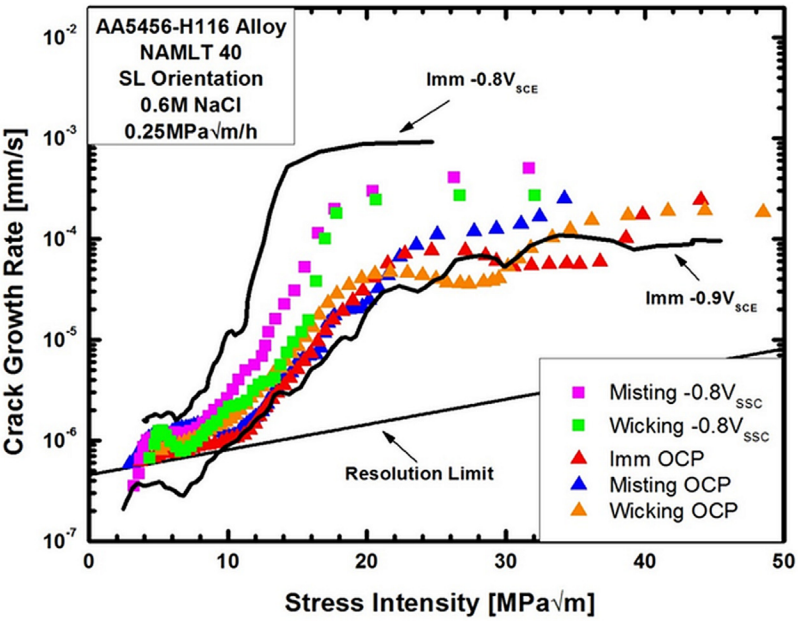

Limitations on the approach described here are important to understand. The increased polarization observed for currents greater than 5 mA (for the 12 mm diameter electrode) can pose a limit to its use for applications requiring higher currents. That said, the deviation of potential from the OCP of the Ag/AgCl RE and CE could be taken into account if the polarization characteristics were known. The area of WE can also be reduced to avoid this issue. If the chloride released from the electrode influences the surface under study (e.g., at very low chloride concentrations), then a different type of electrode would be needed. Finally, it is important to understand and characterize the conditions at which electrode depletion (charge/current) occurs. Some of the sintered Ag/AgCl electrodes used for this study showed aberrant electrochemical behavior that led to deposition of Ag on the WE. Although observed only sporadically, the problem can be resolved by placing a Nafion membrane [21] between the electrolyte and the Ag/AgCl electrode to prevent Ag ions from getting in solution while maintaining ionic conduction between the WE and combined RE/CE.

Summary

Sintered Ag/AgCl electrodes have been shown to be useful as a combined RE/CE to allow electrochemical measurements in thin electrolyte films. These inexpensive, commercially available electrodes can be used to perform polarization of WE without changing the pH of the electrolyte and do so with minimal ohmic drop. They have been shown to function well as part of two electrode electrochemical cells up to currents of 1 mA with polarization of approximately 20 mV. Although this paper focused on one particular cell configuration, the concept of combined RE/CE can be extended to different setups requiring measurements of corrosion behavior either through continuous EIS/LPR monitoring or polarization scans.

References

[1] Schindelholz, E. and Kelly, R. G., "Wetting Phenomena and Time of Wetness in Atmospheric Corrosion: A Review," *Corros. Rev.*, Vol. 30, Nos. 5–6, 2012, https://dx.doi.org/10.1515/corrrev-2012-0015

[2] Stratmann, M. and Streckel, H., "On the Atmospheric Corrosion of Metals Which Are Covered with Thin Electrolyte Layers—II. Experimental Results," *Corros. Sci.*, Vol. 30, Nos. 6–7, 1990, pp. 697–714.

[3] Stratmann, M., Streckel, H., Kim, K. T., and Crockett, S., "On the Atmospheric Corrosion of Metals Which Are Covered with Thin Electrolyte Layers—III. The Measurement of Polarisation Curves on Metal Surfaces Which Are Covered by Thin Electrolyte Layers," *Corros. Sci.*, Vol. 30, Nos. 6–7, 1990, pp. 715–734.

[4] Yee, S., Oriani, R. A., and Stratmann, M., "Application of a Kelvin Microprobe to the Corrosion of Metals in Humid Atmospheres," *J. Electrochem. Soc.*, Vol. 138, No. 1, 1991, pp. 55–61.

[5] Shitanda, I., Okumura, A., Itagaki, M., Watanabe, K., and Asano, Y., "Screen-Printed Atmospheric Corrosion Monitoring Sensor Based on Electrochemical Impedance Spectroscopy," *Sens. Actuators B Chem.*, Vol. 139, No. 2, 2009, pp. 292–297.

[6] Thee, C., Hao, L., Dong, J., Mu, X., Wei, X., Li, X., and Ke, W., "Atmospheric Corrosion Monitoring of a Weathering Steel under an Electrolyte Film in Cyclic Wet–Dry Condition," *Corros. Sci.*, Vol. 78, 2014, pp. 130–137.

[7] Li, C., Ma, Y., Li, Y., and Wang, F., "EIS Monitoring Study of Atmospheric Corrosion under Variable Relative Humidity," *Corros. Sci.*, Vol. 52, No. 11, 2010, pp. 3677–3686.

[8] Cox, A. and Lyon, S. B., "An Electrochemical Study of the Atmospheric Corrosion of Mild Steel—I. Experimental Method," *Corros. Sci.*, Vol. 36, No. 7, 1994, pp. 1167–1176.

[9] Cox, A. and Lyon, S. B. "An Electrochemical Study of the Atmospheric Corrosion of Iron—II. Cathodic and Anodic Processes on Uncorroded and Pre-Corroded Iron," *Corros. Sci.*, Vol. 36, No. 7, 1994, pp. 1177–1192.

[10] Zhang, S. H. and Lyon, S. B., "Anodic Processes on Iron Covered by Thin, Dilute Electrolyte Layers (I)—Anodic Polarisation," *Corros. Sci.*, Vol. 36, No. 8, 1994, pp. 1289–1307.

[11] Zhang, S. H. and Lyon, S. B., "Anodic Processes on Iron Covered by Thin, Dilute Electrolyte Layers (II)—A.C. Impedance Measurements," *Corros. Sci.*, Vol. 36, No. 8, 1994, pp. 1309–1321.

[12] Song, S. and Chen, Z., "Initial Corrosion of Pure Zinc under NaCl Electrolyte Droplet Using a Zn-Pt-Pt Three-Electrode System," *Int. J. Electrochem. Sci.,* Vol. 8, No. 5, 2013, pp. 6851–6863.

[13] Zhou, H. R., Li, X. G., Ma, J., Dong, C. F., and Huang, Y. Z., "Dependence of the Corrosion Behavior of Aluminum Alloy 7075 on the Thin Electrolyte Layers," *Mater. Sci. Eng. B*, Vol. 162, No. 1, 2009, pp. 1–8.

[14] Cheng, Y. L., Zhang, Z., Cao, F. H., Li, J. F., Zhang, J. Q., Wang, J. M., and Cao, C. N., "A Study of the Corrosion of Aluminum Alloy 2024-T3 under Thin Electrolyte Layers," *Corros. Sci.*, Vol. 46, No. 7, 2004, pp. 1649–1667.

[15] Kramer, P., Friedersdorf, F., and Merrill, M., "Corrosion Measurements under Atmospheric Conditions," presented at the *DoD Allied Nations Technical Corrosion Conference*, Aug. 7–10, 2017, Birmingham, AL.

[16] Hangarter, C. M. and Policastro, S. A., "Electrochemical Characterization of Galvanic Couples under Saline Droplets in a Simulated Atmospheric Environment," *Corrosion*, Vol. 73, No. 3, 2017, pp. 268–280.

[17] Nishikata, A., Ichihara, Y., and Tsuru, T., "Electrochemical Impedance Spectroscopy of Metals Covered with a Thin Electrolyte Layer," *Electrochim. Acta*, Vol. 41, Nos. 7–8, 1996, pp. 1057–1062.

[18] ASTM B117-16, *Standard Practice for Operating Salt Spray (Fog) Apparatus*, ASTM International West Conshohocken, PA, 2016, www.astm.org

[19] Rafla, V. N., Davenport, A. J., and Scully, J. R., "Localized Corrosion Damage Morphology and Corrosion Electrochemistry for Al-Zn-Mg-Cu and Stainless Steel 316 Fastener Galvanic Couples in Simulated Marine Environments," *Meet. Abstr.*, MA2017-02, 2017, https://dx.doi.org/10.18130/V35D8ND84

[20] Steiner, P., Burns, J., and Kelly, R., "Intergranular Stress Corrosion Cracking of 5XXX Series Al-Alloys under Atmospheric Exposure Conditions," presented at the *DoD Allied Nations Technical Corrosion Conference*, Aug. 7–10, 2017, Birmingham, AL.

[21] "Nafion™ Membranes—Delivering on the Promise of Clean Energy," https://web.archive.org/web/20180305195230/http://www.fuelcellsetc.com/store/Nafion (accessed Nov. 11, 2017).

STP 1609, 2019 / available online at www.astm.org / doi: 10.1520/STP160920170234

Dhinakaran Sampath[1] and Raghu V. Prakash[2]

Fatigue Crack Growth Behavior of a Mn-Ni-Cr Steel in 3.5 % NaCl Medium and Its Modeling

Citation

Sampath, D. and Prakash, R. V., "Fatigue Crack Growth Behavior of a Mn-Ni-Cr Steel in 3.5 % NaCl Medium and Its Modeling," *Advances in Electrochemical Techniques for Corrosion Monitoring and Laboratory Corrosion Measurements*, *ASTM STP1609*, S. Papavinasam, R. B. Rebak, L. Yang, and N. S. Berke, Eds., ASTM International, West Conshohocken, PA, 2019, pp. 323–344, http://dx.doi.org/10.1520/STP160920170234[3]

ABSTRACT

Understanding the fatigue crack growth behavior of marine steel at low frequencies in a corrosive environment under cathodic protection is essential for the design and prognosis of offshore structures. Experimental results demonstrate that the corrosion fatigue crack growth rate increases with a decrease in frequency, and this behavior can be mitigated by reducing the corrosion rates with the application of a cathodic potential. Knowledge of an optimum cathodic protection potential for corrosion fatigue crack growth without entering the domain of hydrogen-assisted cracking potentials is vital. To that end, the corrosion processes within the enclave of a stationary crack and a pulsating fatigue crack under different crack mouth potentials are elucidated through modeling of mass transport of electrolytic species and electrode reactions. Effect of crack tip strain enhanced electrochemical reaction rates on electrochemical parameters such as pH, potential, and corrosion current density at the crack tip is evaluated. The corrosion current density at the crack tip is reduced significantly when the applied crack mouth potential is changed from −550 to −1,050 mV SCE for both stationary and pulsating cracks. In the case of

Manuscript received November 20, 2017; accepted for publication April 7, 2018.

[1]School of Materials, University of Manchester, Manchester M13 9PL, United Kingdom
http://orcid.org/0000 0003 3324 5971
[2]Dept. of Mechanical Engineering, Indian Institute of Technology Madras, Chennai 600 036, India
http://orcid.org/0000 0002 8888 022X

[3]ASTM Symposium on *Advances in Electrochemical Techniques for Corrosion Monitoring and Laboratory Corrosion Measurements* on November 13 14, 2017 in Atlanta, GA, USA.

strain-enhanced corrosion processes, the corrosion current density is increased significantly when compared with the equivalent model without considering the straining effects. However, the corrosion current density is the same for the applied crack mouth potential below −900 mV SCE. The crack solution becomes alkaline as the crack tip pH increases with a decrease in cathodic potential. This result agrees with the experimental observation of the minimum corrosion fatigue crack growth rate of a steel in sodium chloride solution at around −900 and −950 mV SCE.

Keywords

corrosion fatigue, low frequency, fatigue crack growth rate, cathodic potential, steel, sodium chloride (NaCl) medium, modeling, electrochemistry

Introduction

Corrosion fatigue is defined as the phenomenon of material degradation due to the conjoint action of cyclic load and aggressive environment, and it poses a serious concern for the performance of marine, offshore, and power plant structures. The crack growth kinetics of structural materials under corrosion fatigue is enhanced by several orders of magnitude when compared with their crack growth kinetics in inert environments or air at low cyclic frequencies (less than 0.1 Hz) in the low stress intensity factor range (ΔK) regime [1 6]. Corrosion fatigue crack growth rate is influenced by material properties, fatigue parameters, environmental parameters, and their interactions. The combination of electrochemical crack tip driving forces and mechanical crack tip driving forces results in the synergistic effect of environment and cyclic load on fatigue crack growth kinetics [7 9]. Most often, mechanisms such as active path dissolution [9,10], film rupture process [11 14], adsorption induced dislocation emission [15 17], hydrogen induced localized plasticity [18,19], and hydrogen enhanced decohesion [20 22] are proposed to explain the crack growth response in different material environment systems. The traditional principles of fatigue for life prediction using Paris' Law are not valid for life prediction of a component susceptible to corrosion fatigue crack growth as the crack growth kinetics is enhanced in the lower ΔK regime. This is because the net result of crack growth rate is greater than the sum of crack growth rate due to mechanical loading and crack growth rate due to prolonged exposure to the operating environment. This necessitates the need for data generation for corrosion fatigue crack growth rates at various operating frequencies of an offshore structure. Experience has shown that many of these structures undergo very slow rates of cyclic loading, typically one cycle of loading in a day. The generation of corrosion fatigue crack growth data over a range of low frequencies, for example, 0.1 to 0.001 Hz, is time consuming using the traditional single frequency, fatigue crack growth experiments. High throughput experimental methodologies such as the frequency scanning method [23] and the frequency shedding method [24] are proposed to obtain corrosion fatigue crack growth data at low frequencies in the low ΔK regime.

Apart from this, one of the significant interests among offshore industries is the minimization of the effect of environment on fatigue life of offshore structures. Cathodic protection is one of the mitigating techniques to reduce the corrosion contribution to corrosion fatigue crack growth rate. The effect of cathodic potential on crack growth rate shows that the corrosion fatigue crack growth rate of a steel is reduced to the minimum at a potential of around −900 and −950 mV SCE [25,26]. However, a further decrease in cathodic potential accelerates the crack growth rate due to hydrogen assisted cracking [27 29]. It is essential to study the electrochemi cal reactions that take place in the material environment interface and within the crack enclave to determine the appropriate mechanism operating at the crack tip. A considerable amount of work has progressed in this direction beginning with Brown, Fujii, and Dahlberg [30] and others [31 34] on experimental measurement of chemistry and electrochemistry at the crack tip and electrode potential. The po larization of an electrode is nothing but the departure of electrode potential from its free corrosion potential [35]. The extent of polarization of a crack tip depends on the pH value of the solution, applied potential, and cyclic mechanical loading parameters such as cyclic stress intensity factor and cyclic frequency among others [36,37]. Several researchers attempted experimental measurements to characterize the local environment, and a detailed analysis has been carried out by Turnbull [31]. The pH potential data of a crevice in carbon steel and stainless steel in a sodium chloride (NaCl) solution [38] present the increase in pH within a crevice with an increase in cathodic polarization. This implies that the crevice/crack solution becomes less acidic with an increase in cathodic potential and so the contribution of corrosion is reduced. However, it is difficult to measure the solution composition accurately and the corro sion current and electrode potential within the crack experimentally owing to the dimensions of the crack feature itself. There is also a possibility that the experimental artifact itself would alter the solution composition within the crack, and this hinders accurate measurements. Therefore, mathematical models have been developed by Turnbull and Ferriss [37], Sharland and Tasker [39], Engelhardt and Macdonald [40], and Vankeerberghen [41] to describe the electrochemistry existing at the crack tip during stress corrosion and corrosion fatigue cracking. Therefore, the mathemati cal modeling of electrochemical processes in a corrosion fatigue crack gives a frame work to draw an understanding of various aspects of this issue and also improves predictive capability. This understanding also underpins the informed interpretation of the crack growth responses obtained experimentally.

Modeling corrosion fatigue crack growth is a complex problem involving the aspects of cyclic deformation at the crack tip and the apparent interaction with elec trochemical processes. The continuously varying strain rate and the aggressive chemi cal composition of the occluded solution at the crack tip are to be accounted for in the model. The highly stressed crack tip surface will preferentially become anodic, and its surface area is tiny compared to the surface area of the cathodic crack [7,8,42,43]. This situation will affect the corrosion activity significantly at the crack tip. The average increase in current density of iron dissolution on freshly created slip

steps is several orders of magnitude greater than the current density of iron dissolution in an unstrained surface [44]. Similarly, the current density for hydrogen generation on freshly created slip step surfaces is also greater by several orders of magnitude when compared with the equivalent current density in an unstrained surface [9,45,46]. Thus, an electrochemical approach is vital to understanding corrosion fatigue phenomenon by combining the effects of fatigue parameters such as cyclic frequency and stress intensity factor on electrochemical parameters such as corrosion current, electrode potential, and concentration of species in the occluded crack solution. This paper presents the modeling of corrosion fatigue cracks through a time dependent Nernst Planck equation to understand the effect of applied cathodic potential on corrosion current at the crack tip. This modeling work on mass transport of species in the crack solution is divided into three parts: First is the determination of electrochemical parameters at the crack tip (species concentration, pH, potential, and corrosion current) for a stationary crack, involving diffusion, and ion migration alone, for a range of applied crack mouth potentials. Next is the determination of electrochemical parameters at the crack tip for a pulsating corrosion fatigue crack, subjected to diffusion, ion migration, and advection, for a range of applied crack mouth potentials. The transport of species in the solution by advection occurs due to the fluid flow within the pulsating crack. Finally, the effects of strain enhanced iron dissolution and hydrogen reduction reaction rates on electrochemical parameters in a stationary crack and a pulsating crack are discussed.

Model Description

The synergistic action of mechanical stress and corrosion on crack growth rate is modeled based on linear superposition or competitive superposition of these processes [47]. The synergism arises from the contribution of local environment and crack tip stresses, resulting in increased crack growth as described in Eq 1 based on linear superposition.

$$V = V_{mechanical} + V_{corrosion} \tag{1}$$

where:

V = total crack growth rate,

$V_{mechanical}$ = crack growth rate due to mechanical load, and

$V_{corrosion}$ = crack growth rate due to the local environment.

The baseline fatigue crack growth rate in lab air, which constitutes the mechanical component of crack growth rate, can be obtained using Paris' Law. The contribution of corrosion to crack growth rate can be determined from the metal corrosion/dissolution rate at the crack tip (i_{av}). The metal dissolution rate ($V_{corrosion}$) can be obtained using Eq 2 based on Faraday's law:

$$V_{corrosion} = \frac{M_{Fe} i_{av}}{\rho_{Fe} Z_{Fe} F} \tag{2}$$

where:

M_{Fe} (molecular weight of iron) = 56 g/mol,

i_{av} = average corrosion current at the crack tip,

Z_{Fe} (charge number of iron) = 2,
ρ_{Fe} (density of iron) = 7.86 g/cm^2, and
F (Faraday's constant) = 96,500 C/mol.

CRACK GEOMETRY

The schematic of a crack as a simple parallel slot with a width of w_m and a length of L is illustrated in Fig. 1. The origin of the coordinate ($x = 0$) is fixed at the crack tip. The change in concentration in the thickness direction is assumed to be negligible to begin with, which is reasonably accurate for the modeling of stress corrosion cracks [48,49]. Moreover, the solution flow along the thickness direction is also neglected as it does not significantly influence the concentration distribution and electrochemical parameters [36]. Thus, the corrosion fatigue crack can be approxi mated as a one dimensional crack with a dissolving crack tip at one end and a crack mouth at the other end and an inactive crack walls. In this analysis, it is assumed that the electrolytic solution moves back and forth only along the direction of crack length due to cyclic motion of crack walls.

The assumptions made in this model are described as follows:

1. The crack tip alone is reactive and the crack walls are inert. The influence of polarization due to passive walls is not included in this model.
2. The crack tip is stationary. This means that the crack length remains the same throughout the analysis. Crack growth is not considered.
3. The effect of crack closure due to mechanical fatigue cycling is not included.

CRACK CHEMISTRY

Several studies mention that the simulation of localized corrosion behavior in a crevice or a crack requires at least six electrolytic species [39,40,48]. To replicate the conditions close to solution within a crack on a steel specimen in NaCl solution of pH 8 units, the following six chemical species were considered: (1) ferrous ions from anodic dissolution (Fe^{2+}); (2) ferrous hydroxyl ion from hydrolysis of ferrous ions ($FeOH^+$); (3) sodium (Na^+); (4) chloride (Cl^-) ions from the electrolyte (NaCl solution); (5) hydrogen (H^+); and (6) hydroxyl (OH^-) ions from dissociation of water molecules. The inclusion of oxygen in the species space is deemed to be

FIG. 1 Geometry considered for the analysis of corrosion fatigue cracks.

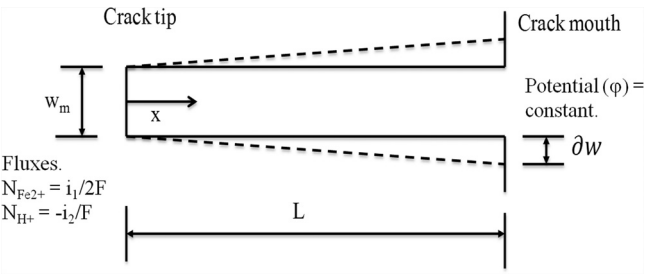

important in the case of corrosion fatigue as one would expect the replenishment of occluded crack solution with oxygen from bulk solution as a result of sinusoidal movement of crack walls. However, the concentration of oxygen is found to be negligible within the crack solution at a low cyclic frequency (less than 1 Hz) [40]. Moreover, the rate of transport of oxygen molecules is slow as it moves only by diffusion, and it is unaffected by potential gradients within the crack. The dissolved oxygen present in the electrolyte depletes in the initial corrosion process, and then the hydrogen reduction reaction becomes a prominent cathodic reaction to sustain the dissolution of iron (a major element in steel). For this reason, an oxygen species is not included in this model.

CHEMICAL AND ELECTROCHEMICAL REACTIONS

Homogeneous chemical reactions occur in the electrolytic solution among the existing species, which leads to the production of new species and other existing species in the solution. These reactions are reported to alter the solution concentration significantly [36,39,50]. In this model, hydrolysis of ferrous ions and dissociation of water molecules are considered, whose chemical reactions (Eq 3 and Eq 4) are given as follows:

$$Fe^{2+} + H_2O \rightarrow H^+ + FeOH^+ \tag{3}$$

$$H_2O \rightarrow H^+ + OH^- \tag{4}$$

The forward and backward reaction rates of these reactions are obtained from Mousson, Vuillemin, and Oltra [56] and the references cited therein, and they are given in **Table 1**. Even though this analysis pertains to a steel in NaCl solution, it is assumed that dissolution of iron alone takes place inside the crack as per the following dissolution reaction of iron into ferrous ion (Eq 5):

$$Fe \rightarrow Fe^{2+} + 2e^- \tag{5}$$

The reduction reaction of hydrogen ion at the crack mouth is considered in this model as per Eq 6.

$$H^+ + e^- \rightarrow {}^1/_2H_2 \tag{6}$$

The expressions for current density of iron oxidation (Eq 7) and hydrogen ion reduction (Eq 8) are given as Tafel's equations [51], and the same are as follows:

$$i_1 = p\ i_{01} \exp\left[\frac{F(V_m - \emptyset)}{RT}\right] \tag{7}$$

$$i_2 = q\ k_H + C_H + \exp\left[\frac{-0.5F(V_m - \emptyset)}{RT}\right] \tag{8}$$

where:

i_1 and i_2 = current densities for iron oxidation (dissolution) and hydrogen ion (evolution) reduction reactions, respectively.

The values of i_{01}, k_{H^+}, and C_{H^+} are given in **Table 1**. For a condition without the consideration for crack tip strain enhanced electrochemical rates, the anodic dissolution and hydrogen reduction reaction rates are same as Eq 7 and Eq 8 with $p = 1$

TABLE 1 Parameters used in corrosion fatigue model.

Notation	Description	Values/Units
C_i	Concentration of species *i* inside the crevice	mol/m^3
$C_{i,0}$	Concentration of species *i* at the crevice mouth	mol/m^3
D_i	Diffusion coefficient of species *i* except H^+ and OH ions	10^{-9} m^2/s
D_{H^+}	Diffusion coefficient of H^+ ion	9.3×10^{-9} m^2/s
D_{OH}	Diffusion coefficient of OH ion	5.3×10^{-9} m^2/s
F	Faraday's constant	96,483 C/mol
i_{01}	Exchange current density of ferrous ion	27×10^{10} A/m^2
k_{ref}	Kinetic constant (for Eq 3)	1/s
k_{feb}	Kinetic constant (for Eq 3)	10^{95} L/mol/s
k_{wf}	Kinetic constant (for Eq 4)	1 L/mol/s
k_{wb}	Kinetic constant (for Eq 4)	10^{14} L/mol^2/s
k_{H^+}	Constant for hydrogen ion	2×10^{-4} A L/mol/m^2
L	Crack length	10×10^{-3} m
N_i	Flux of species, *i*	mol/s/m^2
pH_{bulk}	pH of bulk solution	8
R	Gas constant	8.314 J/mol/K
T	Temperature	298 K
w	Crack width	m
φ	Electrostatic potential	V
V_m	External potential of the metal	V

and $q = 1$. For the effects of crack tip strain, the anodic dissolution and hydrogen reduction reactions rates are enhanced by equating p and q to 10^2 [7,46].

The crack walls become passive due to the acidic nature of the solution, but there is no mechanical disruption of corrosion products, unlike at the crack tip.

GOVERNING EQUATIONS AND BOUNDARY CONDITIONS

Mass transport in an electrolytic solution involves the movement of ionic species, mass balance, current flow, electroneutrality, and fluid flow. The movement of all the species in the solution follows any one or combination of three modes of transport: migration of a charged species in an electric field, diffusion due to concentration gradient, and advection due to the average fluid velocity. According to dilute solution theory, mass transport of each ionic species *i* is given by the Nernst Planck equation involving all three modes of transport in terms of the flux density of each species N_i [52–54] as in Eq 9.

$$N_i = -D_i \nabla C_i - z_i u_{m,i} F C_i \nabla \emptyset + u \nabla C_i \tag{9}$$

where:

N_i = flux density of species *i*, mol/(m^2/s),

D_i = diffusion coefficient of species *i*, m^2/s,

∇C_i = concentration gradient of species *i*, mol/m^4,

z_i = valency of the metal,
$u_{m,i}$ = mobility coefficient of species i, s mol/kg,
F = Faraday's constant,
C_i = concentration of species i, mol/m^3,
$\nabla\emptyset$ = potential gradient, V, and
u = velocity of the fluid, m/s.

The first term on the right side of Eq 9 defines the diffusion of species due to the concentration gradient, the second term considers migration due to the potential gradient, and the third term is for the motion of species due to advection. It can be noted that the ion migration term is peculiar and important for electrochemical systems in addition to diffusion and advection terms due to the presence of ionic species. The transport properties involved in Nernst Planck equations that are required a priori are D_i (diffusion coefficient) and $u_{m,i}$ (mobility coefficient). The fluid velocity within the system is required to be considered for the estimation of flux density in the case of corrosion fatigue cracks, which depends significantly on the type of external force that is acting on the fluid.

The mass balance equation (law of conversation of mass) of each species i [53,55] can be given in the following form (Eq 10):

$$\frac{\partial C_i}{\partial t} = -\nabla(N_i) + R_i \tag{10}$$

The rate of accumulation of species within the system depends on the inward and outward movement of species ($-\nabla N_i$) plus the rate of production of species due to the chemical reaction among the existing ionic species R_i in mol/(m^3/s). The occluded crack solution is considered to be electrically neutral [48,52,54], which can be expressed in the form given in Eq 11.

$$\sum{}_i z_i C_i = 0 \tag{11}$$

In this model, the analysis is confined to only the crack geometry with the crack tip ($x = 0$) and the crack mouth ($x = L$). The boundary conditions at the crack tip and crack mouth are related to the flux density of a species due to the current flow and the definition of concentration of bulk solution and electrode potential, respectively.

The transport of species (flux) generates current in the electrolytic solution, and it is proportional to the current density. The relationship between flux of a species and current density [54] has the form given in Eq 12.

$$N_i = \frac{i}{Fz_i} \tag{12}$$

The fluxes of ferrous and hydrogen ions considered [56] in this analysis at the crack tip ($x = 0$) are as follows (Eq 13):

$$N_{Fe^{2+}} = \frac{i_1}{2F} \text{ and } N_{H^+} = \frac{-i_2}{F} \tag{13}$$

The boundary condition at the crack mouth defines the concentration of ionic species equal to that of those species in bulk solution [56]. Moreover, the electrode potential at the crack mouth is equal to the potential applied to the metal surface. Eq 14 defines the boundary condition at the crack mouth. At the crack mouth ($x = L$),

$$C_{Fe^{2+}} = 0; C_{FeOH^+} = 0; C_{Na^+} = C_{bulk}^{Na^+}; C_{Ci} = C_{bulk}^{Cl}; C_{H^+} = C_{bulk}^{H^+}; C_{OH} = C_{bulk}^{OH} \quad \text{and electrode potential} = V_m \tag{14}$$

The assumption of electroneutrality gives the relation: $2C_{Fe^{2+}} + C_{FeOH^+} + C_{Na^+} + C_{H^+} = C_{Cl} + C_{OH}$ and this completes the set of equations for obtaining a numerical solution.

The movement of crack walls during cyclic loading results in advection of corrosive fluid within the crack. Advection of a fluid can be defined as the motion of fluid in the horizontal direction against the action of gravity under the influence of an external stimulating agency. The fluid velocity averaged across the width of the crack can be estimated from the law of conservation of fluid flow for an incompressible fluid [53], which is given by Eq 15:

$$V(x,t) = -\frac{1}{w}\int_x^L \frac{\partial w}{\partial x} dx \tag{15}$$

One could infer that the velocity of the fluid within the crack can be estimated if the motion of the pulsating crack is known; it is inferred that the fluid velocity varies as a function of crack length. The motion of the crack walls is given by the varying width of the crack during cyclic loading. The crack is assumed as a parallel sided slot of length L and width w_m. The motion of the crack walls for a sinusoidal waveform can be characterized by the following function (Eq 16):

$$w(t) = w_m + \left(\frac{x}{L}\right)\partial w \sin(2\pi f t) \tag{16}$$

where:

w_m = mean width,
∂w = amplitude,
f = cyclic frequency, and
x = any point on the crack length measured from the crack tip.

The fraction (x/L) in Eq 16 defines the variation in the crack width along the crack length during cyclic loading.

Therefore, the average fluid velocity within the crack can be written in the following form (Eq 17):

$$V(x,t) = \frac{-\frac{x^2}{L} 2\pi f \ \partial w \cos(2\pi f t)}{w_m + \left(\frac{x}{L}\right)\partial w \sin(2\pi f t)} \tag{17}$$

where:

x = any point on the crack measured from the crack tip,
$L = 10$ mm, and
$w_m = 10^{-4}$ m.

The width of crack tip (w_m) is assumed as 0.1 mm, and the movement (∂w) of each point on the crack walls during cyclic load is assumed as half of the crack opening displacement calculated for the stress intensity factor range of 18 MPa $\sqrt{}$m. This fluid velocity within the crack depends strongly on the applied frequency. A generalized form of fluid velocity within the crack enclave of a one dimensional crack proposed by Engelhardt [53] also returned the same velocity as obtained in this analysis.

Mass Transport in a Stationary Crack

The general analytical solution to mass transport of ionic species within a crack or a crevice using the Nernst Planck equation is scarce due to its rigidity and dependence on the initial conditions. In the case of a large system where the number of species in the electrolyte is more than two, it is challenging to solve analytically. Moreover, analytical solutions are usually restricted to the systems where diffusion and migration of species is predominant for determining steady state responses. The numerical solution is preferred in a system where time dependent responses are to be determined involving fluid motion due to the cyclical movements of the crack walls.

For validating the model described in the previous section, it is proposed to simulate the steady state concentration profiles of ionic species for a crack 2 mm in length, similar to the work of Mousson, Vuillemin, and Oltra [56] on the simulation of crevice corrosion of steel in NaCl solution. The governing equations and boundary conditions are solved for a steady state condition without considering the effect of fluid motion due to advection. The diffusion coefficients of each species, equilibrium constants of homogeneous chemical reactions, and kinetic data of electrochemical reactions are obtained from the open literature based on the analysis of crevice corrosion of steel in NaCl solution [56]. In this work, the model was developed in COMSOL® Multiphysics (COMSOL Multiphysics Pvt. Ltd., Bengaluru, India) and Mathematica® (Wolfram Alpha LLC, Bengaluru, India). The governing equations, along with prescribed boundary conditions, were numerically solved to estimate the steady state concentration profile of species within the crack. The number of finite elements that constitutes this one dimensional model is 2,500 with a maximum element size of 2 μm.

Fig. 2 presents the concentration profiles of different species along the crack length obtained from the present model, and they are observed to have a similar trend when compared with the results reported by Mousson, Vuillemin, and Oltra [56]. This result confirms that the described model presents the reasonable repeatability of species concentration.

Similarly, the steady state behavior of a 10 mm crack was modeled for different crack mouth potentials between −550 mV SCE (close to open circuit potential) and −1,050 mV SCE (a cathodic potential). A series of species concentration profiles for different crack mouth potentials is presented in Fig. 3. The ferrous ion

FIG. 2 Steady state concentration profiles of species across the crack length of 2 mm for a steel in an NaCl solution system reproduced using a COMSOL® model. These responses are in close agreement with Mousson, Vuillemin, and Oltra [56].

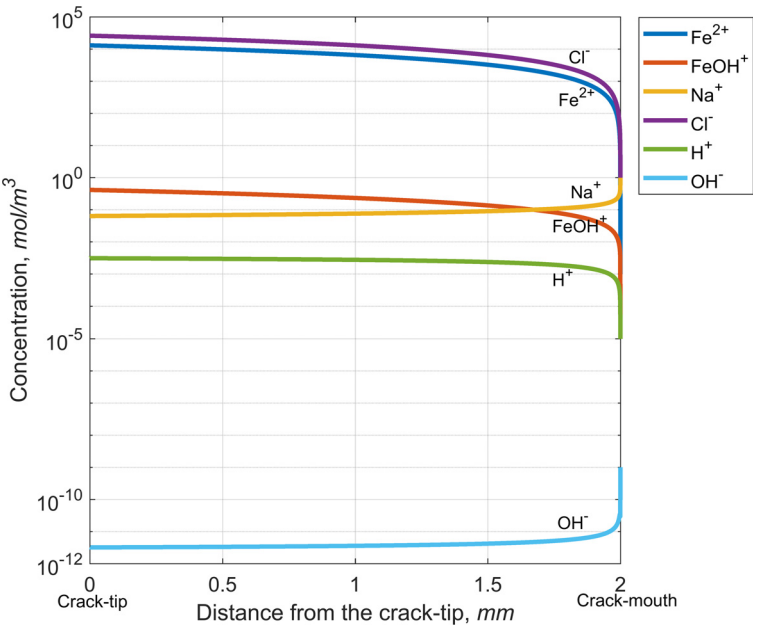

concentration at the crack tip is reduced by several orders as the crack mouth potential is reduced from −550 to −1,050 mV, implying the reduction in corrosion rate of iron at the crack tip. Consequently, the hydrolysis reaction of ferrous ions to ferrous hydroxyl ions is also reduced. Another species of interest is the hydrogen ions (H^+), based on which the solution chemistry within the crack enclave is deter mined in terms of solution pH. The pH at the crack tip is gradually increased with the application of more negative cathodic potentials due to the reduction in H^+ ion concentration at the crack tip.

The effect of crack tip straining enhanced electrochemical reaction rates on crack solution chemistry is simulated by increasing the anodic dissolution and hydrogen evolution reaction rates by two orders of magnitude [7,12,42]. The enhanced anodic dissolution and hydrogen evolution rates at the crack tip have modified the crack solution chemistry significantly when compared with the crack solution chemistry response of a model without straining effects for the equivalent crack mouth potentials, as shown in **Fig. 4**. It has to be noted in **Fig. 5** that more negative crack mouth potential is required for a strained state to reduce the enhanced crack tip current density of dissolution than the potential required for noninclusion of straining effects.

FIG. 3 Species concentration within the crack enclave of a crack of 10 mm for various crack mouth potentials (vs. SCE), (a) 550 mV, (b) 650 mV, (c) 750 mV, (d) 850 mV, (e) 950 mV, and (f) 1,050 mV, when the crack tip strain effects are not considered.

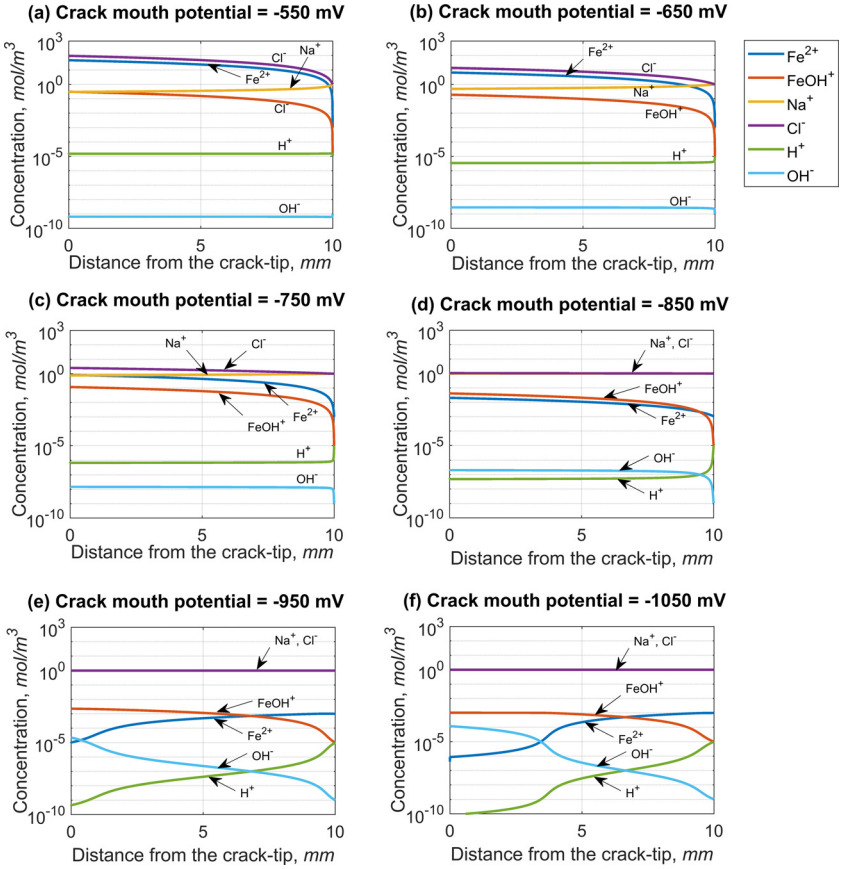

Mass Transport in a Pulsating Corrosion Fatigue Crack

The extension of the stationary crack model is valid with the inclusion of a time dependent flux term and an advection term in the governing equation. The solution pH, electrode potential, and current density at the crack tip of a 10 mm long crack in NaCl solution subjected to a stress intensity factor range (ΔK) of 18 MPa $\sqrt{m}$, stress ratio (R) of 0.1, and frequencies of 0.001, 0.01, and 0.1 Hz are presented in Fig. 6. The evolution of electrochemical parameters at the crack tip over time is

FIG. 4 Species concentration within the crack enclave of a crack of 10 mm for various crack mouth potentials (vs. SCE), (a) 550 mV, (b) 650 mV, (c) 750 mV, (d) 850 mV, (e) 950 mV, and (f) 1,050 mV, under crack tip straining enhanced electrochemical reaction rates.

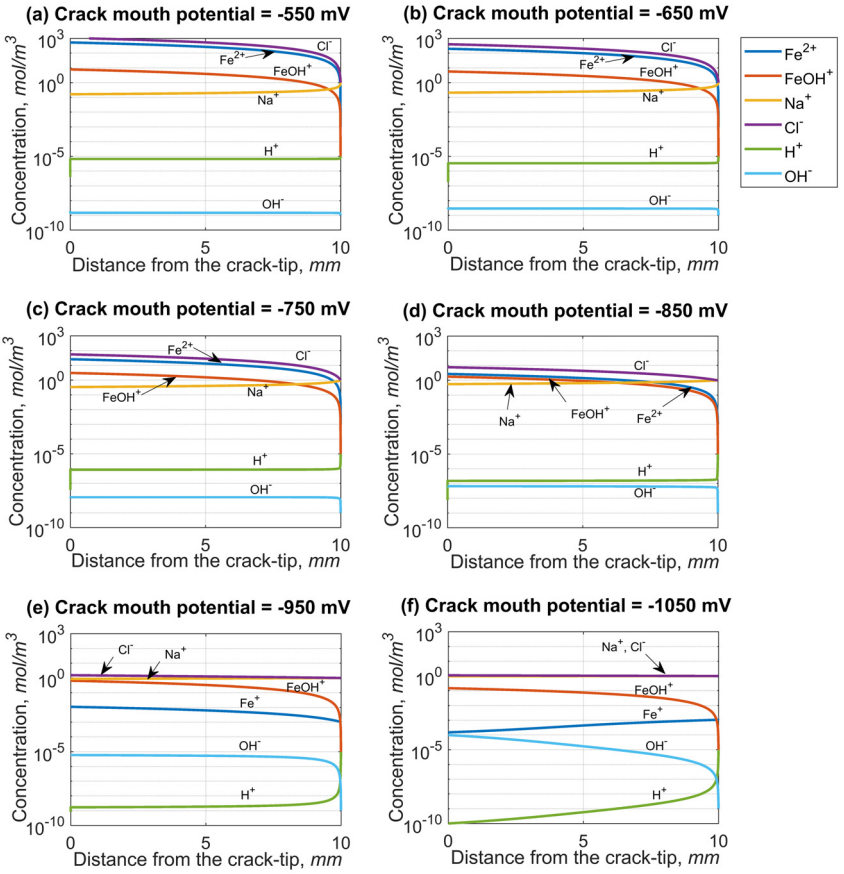

obtained for models with and without considering the straining effects, and these parameters are averaged over at least 1,000 fatigue cycles.

The anodic dissolution and hydrogen evolution rates are enhanced by two orders of magnitude ($p = q = 10^2$) to account for and understand the effect of applied stress intensity on electrochemical parameters.

The crack tip pH increases with the decrease in applied crack mouth potential for a bulk pH of 8 units. This trend of increasing alkalinity of the crack tip solution at more negative potentials is also observed by Turnbull and Ferriss [36] and by Peterson and Lennox [38]. A small reduction in crack tip pH (0.25 units) is observed when the frequency is changed from 0.1 to 0.001 Hz at crack mouth

FIG. 5 A plot of (a) pH, (b) electrode potential, and (c) current density at the crack tip as a function of applied crack mouth potentials (vs. SCE) with and without considering the straining effects at the crack tip.

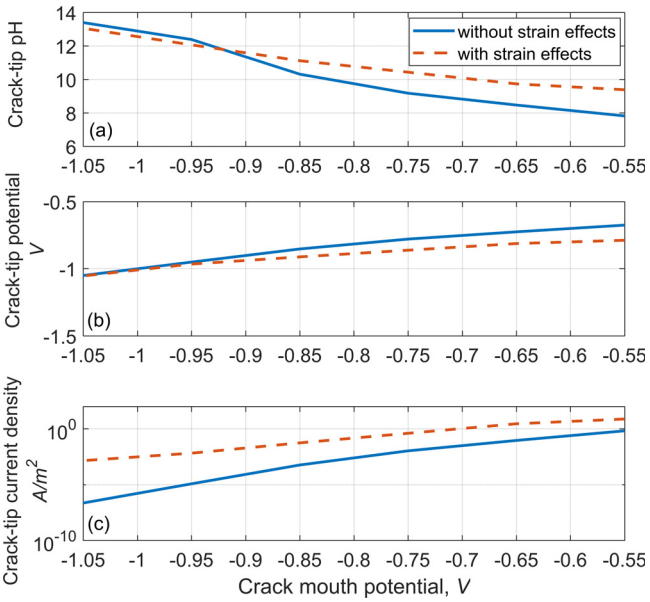

potentials up to −850 mV. For further reductions in crack mouth potential below −950 mV, the crack tip pH for 0.001 and 0.01 Hz reversed the other way around and increased to around 14 units. Also, the potential drop across the crack is almost zero when the applied crack mouth potential is less than −900 mV. In this region, the crack tip current density falls by three orders of magnitude.

For the strain enhanced anodic dissolution and hydrogen evolution, the pH increases by at least 1 unit for crack mouth potentials between −550 and −950 mV as in Page, McMinn, and Hudak [57]. The potential drop across the crack is increased significantly (decrease in crack tip potential) for all crack mouth potentials above −900 mV due to the strain enhanced electrochemical reaction rates for both 0.001 and 0.01 Hz when compared with the potential drop for the model without considering the strain effects. For further reduction in mouth potential below −900 mV, the potential drop becomes the same in both conditions. The current density is also higher for the strained state, but it reduces substantially when the mouth potential falls below −900 mV for both 0.001 and 0.01 Hz. This observation implies that the corrosion contribution to crack growth at a cathodic protection potential of −900 and −950 mV SCE is suppressed at low frequencies as observed in the experimental results [26,58]. The corrosion fatigue crack growth kinetics (provided in terms of crack growth enhancement ratio) of a marine steel

FIG. 6 A plot of (a) pH, (b) electrode potential, and (c) current density at the crack tip as a function of applied crack mouth potential (vs. SCE) for a crack subjected to cyclic load from the models, with and without considering the straining effects on electrochemical reaction rates. Cyclic load parameters: ΔK of 18 MPa $\sqrt{m}$, *R* of 0.1, and frequencies between 10^{-3} and 10^{-1} Hz. Labels that start with "s" are used to link the curves to the respective legends for clarity purposes.

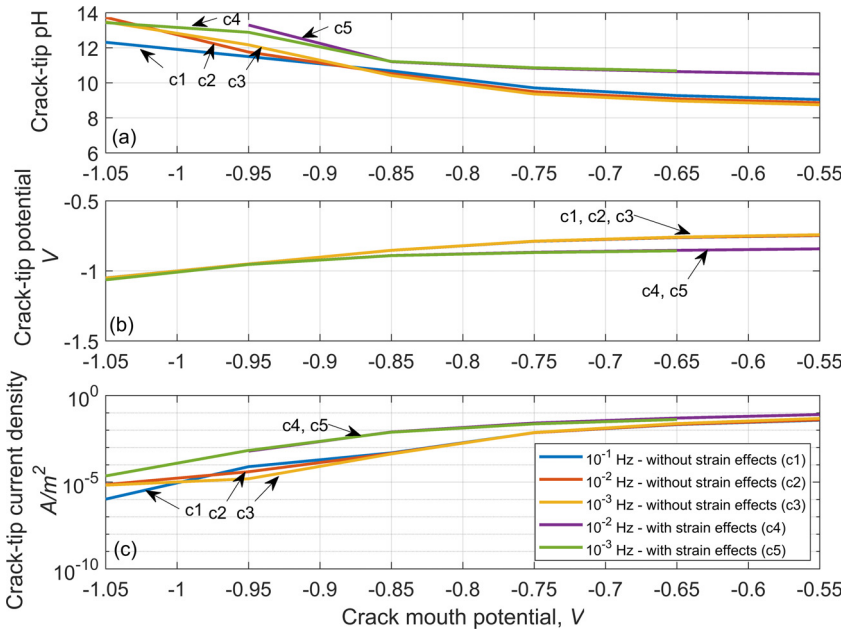

(manganese nickel chromium [Mn Ni Cr] steel) in 3.5 % NaCl solution increased by an order of magnitude over a range of frequencies between 5 and 0.01 Hz when evaluated using a frequency shedding method (**Fig. 7**) [24,59]. Crack growth enhancement ratio is a normalized crack growth rate in the corrosive environment with respect to crack growth rate in air at the same applied stress intensity factor range. The crack growth kinetics in the frequency domain are divided into three regions (log linear, plateau, and steep crack growth regions). One can observe that corrosion fatigue crack growth enhancement ratio decreases substantially with the application of −900 mV SCE over the range of low frequencies [59]. Thus, a cathodic potential of −900 mV SCE appeared to reduce the crack growth rate sig nificantly, as close as to the crack growth rate in air up to 0.1 Hz.

Further investigation on the effect of cathodic potential on corrosion fatigue crack growth rate of this steel via cathodic potential scanning tests at low frequen cies of 0.01 and 0.1 Hz illustrated that the crack growth rate attained its minimum

FIG. 7 Corrosion fatigue crack growth enhancement ratio (normalized with respect to crack growth rate corresponding to the applied stress intensity factor range) for Mn Ni Cr steel in 3.5 % NaCl solution as a function of cyclic frequencies for different applied stress intensity factor range (in MPa $\sqrt{m}$) [60].

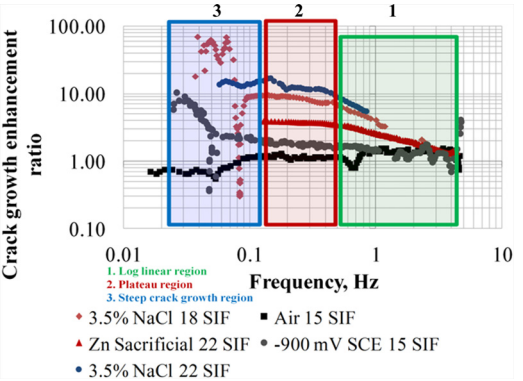

FIG. 8 Corrosion fatigue crack growth rate as a function of applied potential for frequencies 0.1 Hz and 0.01 Hz at a constant ΔK of 15 MPa $\sqrt{m}$ [59].

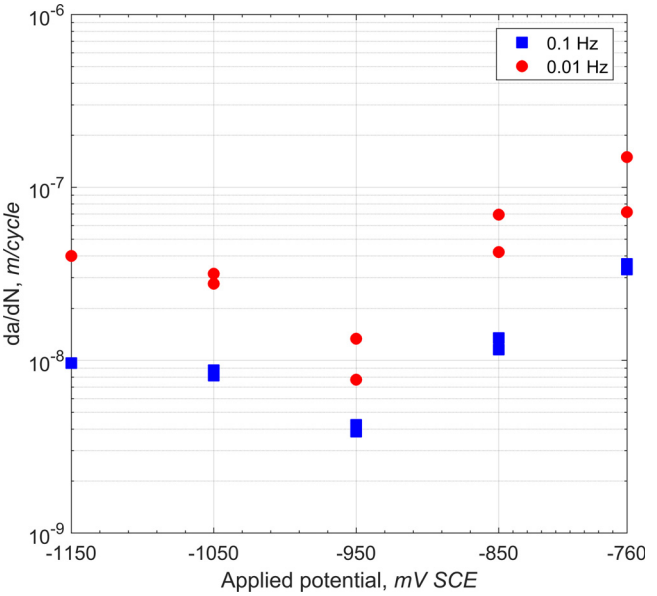

at −950 mV SCE [59] (Fig. 8). However, the corrosion fatigue crack growth rate increased from its minimum value when the cathodic potential was decreased fur ther. This acceleration in crack growth rate was observed to be mainly due to the enhanced hydrogen production and adsorption at the crack tip at a cathodic poten tial below −950 mV SCE [29,45,60]. The enhanced electrochemical reaction rates at the crack tip are able to capture the trends in the corrosion fatigue crack growth experiments.

Fig. 9 presents the results of pH variation for a pulsating crack over 10 cycles of mechanical loading for frequencies of 0.01 and 0.001 Hz. It is observed that the effect of pulsation of pH is significant below a potential of −950 mV for both the test frequencies. Further, the pH at 10^{-3} Hz is slightly lower than that of the pH at 10^{-2} Hz, indicating isolation of crack solution from bulk solution at low frequencies.

The variation in corrosion rate (current density at the crack tip) with respect to frequency for all crack mouth potentials is very moderate as per this model. When the current density is converted from "time" domain to "cycle" domain, the corro sion contribution to crack growth during corrosion fatigue is enhanced significantly for low frequencies. This contribution is further increased when the crack tip strain enhanced electrochemical reaction rates are considered. The enhancement of elec trochemical reaction rates used in this model is a first order approximation. The effect of varying crack tip strain and strain rate on electrochemical reaction rates [12,45] is of paramount interest to fully understand the corrosion fatigue crack growth mechanisms and to delineate corrosion and mechanical components of crack tip driving forces. The next steps in this research will be to understand the strain and strain rate effects on electrochemical reaction rates.

FIG. 9 Variation of pH for a pulsating crack at a mechanical loading frequency of (a) 0.001 Hz and (b) 0.01 Hz.

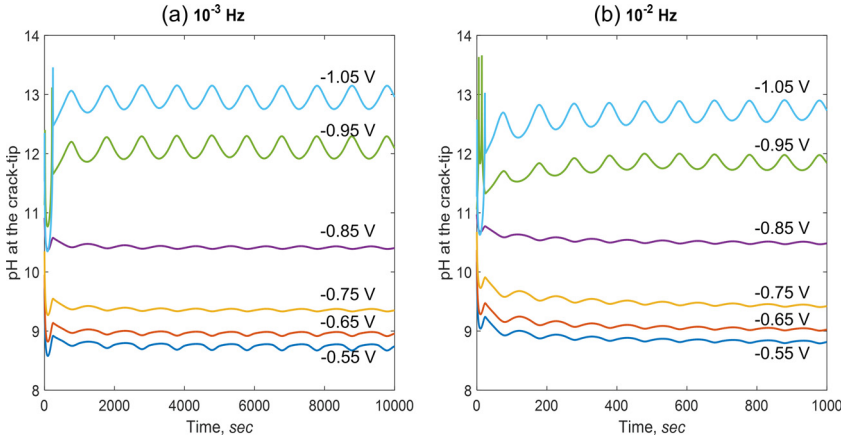

Summary and Conclusions

Mass transport of electrolytic species in a stationary crack and a pulsating corro sion fatigue crack present in a Mn Ni Cr steel under 3.5 % NaCl solution is mod eled using the Nernst Planck equation to understand the effect of applied crack mouth potential on electrochemical parameters such as solution chemistry, poten tial, and corrosion current density at the crack tip. In the case of corrosion fatigue crack, the advection term is added to the governing equation to account for load frequency induced fluid flow velocity within the crack enclave. An enhancement factor is introduced to consider the effect of crack tip straining enhanced electro chemical reaction rates on electrochemical parameters. The following conclusions are made:

1. The concentration profiles of electrolytic species in a stationary crack model are validated with the results reported in the literature for the same electro chemical conditions and crack length.
2. The concentration of ferrous ion at the crack tip (associated with corrosion current density) is reduced significantly when the crack mouth potential is decreased from −550 to −1,050 mV SCE. This behavior is accompanied by an increase in crack tip pH and a decrease in the crack tip potential drop.
3. The concentration of ferrous ion at the crack tip is increased significantly when the crack tip strain enhanced electrochemical reaction rates are consid ered for all crack mouth potentials. However, the corrosion current density tends to decrease with a decrease in crack mouth potential. Enhanced anodic dissolution leads to further increase in the crack tip pH and decrease in the potential drop.
4. An increase in corrosion contribution to corrosion fatigue crack growth in the cycle domain with a decrease in cyclic frequency is observed. Further, crack tip corrosion current density decreases with the decrease in the poten tial drop, and the corrosion contribution becomes very low for crack mouth potential below −900 mV SCE. The crack tip corrosion current density is higher for crack tip strain enhanced electrochemical reaction rates than the current density for the model without crack tip straining effects. However, the crack tip corrosion density for both cases becomes the same when the crack mouth potential is reduced below −900 mV. This conclusion supports the experimental observation of the minimum corrosion fatigue crack growth rate of a marine steel in NaCl solution at around a cathodic potential of −900 and −950 mV SCE.

References

[1] Wei, R. P. and Simmons, G. W., "Recent Progress in Understanding Environment Assisted Fatigue Crack Growth," *Int. J. Fract.*, Vol. 17, No. 2, 1981, pp. 235–247.

[2] Pao, P. S., Wei, W., and Wei, R. P., "Effect of Frequency on Fatigue Crack Growth Response of AISI 4340 Steel in Water Vapor," *Environment Sensitive Fracture of Engi-neering Materials: Proceedings of a Symposium Held at the Fall Meeting of the*

Metallurgical Society of AIME, Chicago, IL, October 24–26, 1977, A. Foroulis, Ed., TMS-AIME, Englewood, CO, 1979, pp. 565–580.

[3] Knop, M., Heath, J., Sterjovski, Z., and Lynch, S. P., "Effects of Cycle Frequency on Corrosion-Fatigue Crack Growth in Cathodically Protected High-Strength Steels," *Procedia Eng.*, Vol. 2, No. 1, 2010, pp. 1243–1252.

[4] Madduri, C. and Prakash, R. V, "Corrosion Fatigue Crack Growth Studies in Ni-Cr-Mn Steel," *Int. J. Mech. Mater. Eng.*, Vol. 4, No. 12, 2010, pp. 1402–1407.

[5] Seifert, H. P. and Ritter, S., "Corrosion Fatigue Crack Growth Behaviour of Low-Alloy Reactor Pressure Vessel Steels under Boiling Water Reactor Conditions," *Corros. Sci.*, Vol. 50, No. 7, 2008, pp. 1884–1899.

[6] Dawson, D. B. and Pelloux, R. M. M., "Corrosion Fatigue Crack Growth of Titanium Alloys in Aqueous Environments," *Metall. Trans.*, Vol. 5, No. 3, 1974, pp. 723–731.

[7] Despic, A. R., Raicheff, R. G., and Bockris, J. O., "Mechanism of the Acceleration of the Electrodic Dissolution of Metals during Yielding under Stress," *J. Chem. Phys.*, Vol. 49, No. 2, 1968, pp. 926–938.

[8] Hoar, T. P. and West, J. M., "Mechano-Chemical Anodic Dissolution of Austenitic Stainless Steel in Hot Chloride Solution," *Proc. R. Soc. A Math. Phys. Eng. Sci.*, Vol. 268, No. 1334, 1962, pp. 304–315, http://dx.doi.org/10.1098/rspa.1962.0142

[9] Hall, M. M., "Environmental Crack Driving Force," *Metall. Mater. Trans. A Phys. Metall. Mater. Sci.*, Vol. 44, No. 3, 2013, pp. 1200–1208, http://dx.doi.org/10.1007/s11661-012-1439-3

[10] Hall, M. M., "Crack Tip Strain Rate Equation with Applications to Crack Tip Embrittlement and Active Path Dissolution Models of Stress Corrosion Cracking," *Environment-Induced Cracking of Materials*, S. A. Shipilov, R. H. Jones, J.-M. Olive, and R. B. Beak, Eds., Elsevier Science, Amsterdam, 2008, pp. 59–68.

[11] Logan, H. L., "Film-Rupture Mechanism of Stress Corrosion," *J. Res. Natl. Bur. Stand.*, Vol. 48, No. 2, 1952, pp. 99–105.

[12] Hall, M. M., "Film Rupture Model for Aqueous Stress Corrosion Cracking under Constant and Variable Stress Intensity Factor," *Corros. Sci.*, Vol. 51, No. 2, 2009, pp. 225–233, http://dx.doi.org/10.1016/j.corsci.2008.08.052

[13] Congleton, J., Shih, H. C., Shoji, T., and Parkins, R. N., "The Stress Corrosion Cracking of Type 316 Stainless Steel in Oxygenated and Chlorinated High Temperature Water," *Corros. Sci.*, Vol. 25, Nos. 8-9, 1985, pp. 769–788, http://dx.doi.org/10.1016/0010-938X(85)90010-1

[14] Shoji, T., Takahashi, H., Suzuki, M., and Kondo, T., "New Parameter for Characterizing Corrosion Fatigue Crack Growth," *J. Eng. Mater. Technol. Trans. ASME*, Vol. 103, No. 4, 1981, pp. 298–304.

[15] Lynch, S. P., "Environmentally-Assisted Cracking: Overview of Evidence for an Adsorption-Induced Localized-Slip," *Process. Acta Met.*, Vol. 36, No. 10, 1988, pp. 2639–2661.

[16] Lynch, S. P., "Mechanisms and Kinetics of Environmentally Assisted Cracking: Current Status, Issues, and Suggestions for Further Work," *Metall. Mater. Trans. A Phys. Metall. Mater. Sci.*, Vol. 44, No. 3, 2013, pp. 1209–1229, http://dx.doi.org/10.1007/s11661-012-1359-2

[17] Lynch, S., "Hydrogen Embrittlement Phenomena and Mechanisms," *Corros. Rev.*, Vol. 30, Nos. 3–4, 2012, pp. 105–123, http://dx.doi.org/10.1515/corrrev-2012-0502

[18] Ladna, B. and Birnbaum, H. K., "A Study of Hydrogen Transport during Plastic Deformation," *Acta Metall.*, Vol. 35, No. 7, 1987, pp. 1775–1778.

[19] Birnbaum, H. K. and Sofronis, P., "Hydrogen-Enhanced Localized Plasticity–A Mechanism for Hydrogen-Related Fracture," *Mater. Sci. Eng. A*, Vol. 176, Nos. 1–2, 1994, pp. 191–202, http://dx.doi.org/10.1016/0921-5093(94)90975-X

[20] Gerberich, W. W. and Chen, Y. T., "Hydrogen-Controlled Cracking—An Approach to Threshold Stress Intensity," *Metall. Trans. A*, Vol. 6, 1975, pp. 271–278, http://dx.doi.org/10.1007/BF02667281

[21] Gerberich, W. W., Oriani, R. A., Lii, M., Chen, X., and Foecke, T., "The Necessity of Both Plasticity and Brittleness in the Fracture Thresholds of Iron," *Philos. Mag. A*, Vol. 63, No. 2, 1991, pp. 363–376, http://dx.doi.org/10.1080/01418619108204854

[22] Pfeil, L. B., "The Effect of Occluded Hydrogen on the Tensile Strength of Iron," *Proc. R. Soc. A Math. Phys. Eng. Sci.*, Vol. 112, No. 760, 1926, pp. 185–195, http://dx.doi.org/10.1098/rspa.1983.0054

[23] Buitrago, J., Weir, M. S., Kan, W. C., Hudak, S. J., Jr., and McMaster, F., "Effect of Loading Frequency on Fatigue Performance of Risers in Sour Environment," *Proceedings of ASME 2004, 23rd International Conference on Offshore Mechanics and Arctic Engineering*, OMAE 2004-51641, Vancouver, BC, June 20–25, 2004, American Society of Mechanical Engineers, New York, 2004, pp. 1059–1068.

[24] Prakash, R. V. and Sampath, D., "Estimation of Corrosion Fatigue-Crack Growth through Frequency Shedding Method," *J. ASTM Int.*, Vol. 9, No. 5, 2012, pp. 1–13, http://dx.doi.org/10.1520/JAI103988

[25] Murakami, R. and Ferguson, W. G., "The Effects of Cathodic Potential and Calcareous Deposits on Corrosion Fatigue Crack Growth Rate in Seawater for Two Offshore Structural Steels," *Fatigue Fract. Eng. Mater. Struct.*, Vol. 9, No. 6, 1987, pp. 477–488.

[26] Dhinakaran, S. and Prakash, R. V., "Effect of Low Cyclic Frequency on Fatigue Crack Growth Behavior of a Mn-Ni-Cr Steel in Air and 3.5% NaCl Solution," *Mater. Sci. Eng. A*, Vol. 609, 2014, pp. 204–208, http://dx.doi.org/10.1016/j.msea.2014.05.001

[27] Vigilante, G. N., Underwood, J. H., Crayon, D., Tauscher, S., Sage, T., and Troiano, E., "Hydrogen Induced Cracking Tests of High Strength Steels and Nickel-Iron Base Alloys Using the Bolt-Loaded Specimen," *Fatigue and Fracture Mechanics: 28th Volume, ASTM STP1321*, J. H. Underwood, B. D. Macdonald, and M. R. Mitchell, Eds., ASTM International, West Conshohocken, PA, 1997, pp. 602–616, http://dx.doi.org/10.1520/STP12332S

[28] Murtaza, G. and Akid, R., "Corrosion Fatigue Short Crack Growth Behaviour in a High Strength Steel," *Int. J. Fatigue*, Vol. 18, No. 8, 1996, pp. 557–566.

[29] Gangloff, R. P., "Hydrogen Assisted Cracking of High Strength Alloys," *Comprehensive Structural Integrity*, I. Milne, R. O. Ritchie, and B. Karihaloo, Eds., Elsevier Science, New York, NY, 2003, pp. 31–101.

[30] Brown, B. F., Fujii, C. T., and Dahlberg, E. P., "Methods for Studying the Solution Chemistry within Stress Corrosion Cracks," *J. Electrochem. Soc.*, Vol. 116, No. 2, 1969, p. 218, http://dx.doi.org/10.1149/1.2411799

[31] Turnbull, A., "The Solution Composition and Electrode Potential in Pits, Crevices and Cracks," *Corros. Sci.*, Vol. 23, No. 8, 1983, pp. 833–870.

[32] Turnbull, A., Saenz de Santa Maria, M., and Thomas, N. D., "Steady-State Electrochemical Kinetics of Structural Steel in Simulated Fatigue Crack-Tip Environments," *Corros. Sci.*, Vol. 28, No. 10, 1988, pp. 1029–1038, http://dx.doi.org/10.1016/0010-938X(88)90019-4

[33] Andresen, P. L. and Ford, F. P., "Fundamental Modeling of Environmental Cracking for Improved Design and Lifetime Evaluation in BWRs," *Int. J. Press. Vessel. Pip.*, Vol. 59, Nos. 1-3, 1994, pp. 61–70, http://dx.doi.org/10.1016/0308-0161(94)90142-2

[34] Cooper, K. R. and Kelly, R. G., "Crack Tip Chemistry and Electrochemistry of Environmental Cracks in AA 7050," *Corros. Sci.*, Vol. 49, No. 6, 2007, pp. 2636–2662.

[35] Revie, R. W. and Uhlig, H. H., *Corrosion and Corrosion Control*, 4th Ed., Wiley, Hoboken, NJ, 2007.

[36] Turnbull, A. and Ferriss, D. H., "Mathematical Modelling of the Electrochemistry in Corrosion Fatigue Cracks in Steel Corroding in Marine Environments," *Corros. Sci.*, Vol. 27, No. 12, 1987, pp. 1323–1350, http://dx.doi.org/10.1016/0010-938X(87)90129-6

[37] Turnbull, A. and Ferriss, D. H., "Mathematical Modelling of the Electrochemistry in Corrosion Fatigue Cracks in Structural Steel Cathodically Protected in Sea Water," *Corros. Sci.*, Vol. 26, No. 8, 1986, pp. 601–628, http://dx.doi.org/10.1016/0010-938X(86)90027-2

[38] Peterson, M. H. and Lennox, T. J., Jr., "A Study of Cathodic Polarization and pH Changes in Metal Crevices," *Corrosion*, Vol. 29, No. 10, 1973, pp. 406–412.

[39] Sharland, S. M. and Tasker, P. W., "A Mathematical Model of Crevice and Pitting Corrosion—I. The Physical Model," *Corros. Sci.*, Vol. 28, No. 6, 1988, pp. 603–620.

[40] Engelhardt, G. R. and Macdonald, D. D., "Modeling of Corrosion Fatigue Chemistry in Sensitized Stainless Steel in Boiling Water Reactor Environments," NACE-00227, *Proceedings of CORROSION 2000*, Orlando, FL, March 26–31, 2000, NACE International, Houston, TX, 2000, pp. 1–12.

[41] Vankeerberghen, M., "1D Steady-State Finite-Element Modelling of a Bi-Carrier One-Layer Oxide Film," *Corros. Sci.*, Vol. 48, No. 11, 2006, pp. 3609–3628.

[42] Sarkar, S. and Aquino, W., "Changes in Electrodic Reaction Rates Due to Elastic Stress and Stress-Induced Surface Patterns," *Electrochim. Acta*, Vol. 111, 2013, pp. 814–822, http://dx.doi.org/10.1016/j.electacta.2013.08.085

[43] Hishida, M., Begley, J. A., McCright, R. D., and Staehle, R. W., "Anodic Dissolution and Crack Growth Rate in Constant Strain Rate Tests at Controlled Potentials," *Stress Corrosion Cracking—Slow Strain Rate Technology, ASTM STP665*, G. M. Ugiansky, and J. H. Payer, Eds., ASTM International, West Conshohocken, PA, 1979, pp. 47–60, http://dx.doi.org/10.1520/STP38108S

[44] Howard, D. and Pyle, T., "The Dissolution of Atoms from Steps on a Metal Surface," *Philos. Mag.*, Vol. 14, 1966, pp. 1179–1189, http://dx.doi.org/10.1080/14786436608224283

[45] Hall, M. M., "Effect of Inelastic Strain on Hydrogen-Assisted Fracture of Metals," *Gaseous Hydrogen Embrittlement of Materials in Energy Technologies: Mechanisms, Modelling and Future Developments*, R. P. Gangloff, and B. P. Somerday, Eds., Woodhead, Cambridge, UK, 2012, pp. 378–429, http://dx.doi.org/10.1533/9780857095374.2.378

[46] Hall, M. M., "Effect of Variable Stress Intensity Factor on Hydrogen Environment Assisted Cracking," *Metall. Mater. Trans. A Phys. Metall. Mater. Sci.*, Vol. 42, No. 2, 2011, pp. 304–318, http://dx.doi.org/10.1007/s11661-010-0226-2

[47] McEvily, A. J. and Wei, R. P., "Fracture Mechanics and Corrosion Fatigue," *Proceedings of International Conference on Corrosion Fatigue: Chemistry, Mechanics and Microstructure*, Storrs, CT, June 14–18, 1971, NACE International, Houston, TX, 1972, pp. 25–30.

[48] Engelhardt, G. R. and Macdonald, D. D., "Development of Fast Algorithms for Estimating Stress Corrosion Crack Growth Rate," *Corros. Sci.*, Vol. 41, No. 12, 1999, pp. 2267–2302.

[49] Stroe, M., Oltra, R., and Vuillemin, B., "Modeling of Crevice Corrosion of Fe–Cr Alloys in Chloride Media," *ECS Trans.*, Vol. 11, No. 12, 2008, pp. 1–9.

[50] Walton, J. C., "Mathematical Modeling of Mass Transport and Chemical Reaction in Crevice and Pitting Corrosion," *Corros. Sci.*, Vol. 30, Nos. 8–9, 1990, pp. 915–928.

[51] Turnbull, A. and Thomas, J. G. N., "A Model of Crack Electrochemistry for Steels in the Active State Based on Mass Transport by Diffusion and Ion Migration," *J. Electrochem. Soc.*, Vol. 129, No. 7, 1982, pp. 1412–1422.

[52] Newman, J. and Karen, T. A., *Electrochemical Systems*, 3rd Ed., Wiley, Hoboken, NJ, 2004.

[53] Engelhardt, G. R. and Macdonald, D. D., "Modelling the Crack Propagation Rate for Corrosion Fatigue at High Frequency of Applied Stress," *Corros. Sci.*, Vol. 52, No. 4, 2010, pp. 1115–1122, http://dx.doi.org/10.1016/j.corsci.2009.11.031

[54] Kyosti, K., Lasse, M., and José, M., *Ionic Transport Processes in Electrochemistry and Membrane Science*, 1st Ed., Oxford University, Oxford, UK, 2008.

[55] Newman, J. S. and Tobias, C. W., "Theoretical Analysis of Current Distribution in Porous Electrodes," *J. Electrochem. Soc.*, Vol. 109, No. 12, 1962, pp. 1183–1191, http://dx.doi.org/10.1149/1.2425269

[56] Mousson, J., Vuillemin, B., and Oltra, R., "Modeling of the Propagation of Crevice Corrosion," *Proceedings of EUROCORR 2004: Long-Term Prediction and Modeling of Corrosion*, Nice, France, September 12–16, 2004, International Nuclear Information System (INIS) Repository, France, 2004, Ref. No. 36105073, pp. 1–9.

[57] Page, R. A., McMinn, A., and Hudak, S., Jr., "Characterization of Crack Tip Electrochemistry Using a Simulated Crack," *Corrosion*, Vol. 44, No. 9, 1988, pp. 623–631.

[58] Scott, P. M., Thorpe, T. W., and Carney, R. F. A., "Corrosion Fatigue Crack Initiation from Blunt Notches in Structural Steel Exposed to Seawater," *Proceedings of Seventh International Conference on Fracture*, Houston, TX, March 20–24, 1989, Elsevier, New York, 1989, pp. 1595–1602.

[59] Prakash, R. V. and Sampath, D., "Understanding Fatigue Crack Growth Behavior at Low Frequencies for a Mn–Ni–Cr Steel in 3.5 % NaCl Solution under Controlled Cathodic Potential," *Mater. Perform. Charact.*, Vol. 4, No. 2, 2015, pp. 157–167, http://dx.doi.org/10.1520/MPC20140018

[60] Scully, J. R., Dogan, H. R., Li, D. R., and Gangloff, R. P., "Controlling Hydrogen Embrittlement in Ultra-High Strength Steels," *Proceedings of CORROSION 2004*, New Orleans, LA, March 28–April 1, 2004, NACE International, Houston, TX, 2004, Paper No. 04563.

STP 1609, 2019 / available online at www.astm.org / doi: 10.1520/STP160920170191

Sankara Papavinasam[1]

Use of Electrochemical Techniques in Measuring Corrosion in the Laboratory and Monitoring Corrosion in the Field

Citation

Papavinasam, S., "Use of Electrochemical Techniques in Measuring Corrosion in the Laboratory and Monitoring Corrosion in the Field," *Advances in Electrochemical Techniques for Corrosion Monitoring and Laboratory Corrosion Measurements*, *ASTM STP1609*, S. Papavinasam, R. B. Rebak, L. Yang, and N. S. Berke, Eds., ASTM International, West Conshohocken, PA, 2019, pp. 345–362, http://dx.doi.org/10.1520/STP160920170191[2]

ABSTRACT

Most corrosion mechanisms are electrochemical in nature. Therefore, electrochemical techniques are widely used to understand corrosion in many corrosion education institutes and research organizations. Electrochemical techniques are also used in plant monitoring of corrosion mainly because of their ability to produce instantaneous corrosion rates. This paper presents the status of application of electrochemical techniques for measuring corrosion in the laboratory and for monitoring corrosion in the field. The information presented in the paper was collected based on a survey of corrosion professionals from education institutes, from research organizations, and from those working in the field. The salient features of the survey include: a large percentage of professionals are not following any standard procedures in conducting corrosion tests using electrochemical techniques; a fairly large percentage of field personnel are not aware of procedures used to calculate general corrosion rates (this practice prevails because many field-deployable devices have inbuilt general corrosion rate calculators); almost 50 % of these professionals do not

Manuscript received October 9, 2017; accepted for publication February 6, 2018.

[1]CorrMagnet Consulting Inc., 6, Castlemore St., Ottawa, ON K2G 6K8, Canada

[2]ASTM Symposium on *Advances in Electrochemical Techniques for Corrosion Monitoring and Laboratory Corrosion Measurements* on November 13 14, 2017 in Atlanta, GA, USA.

evaluate localized corrosion (because localized corrosion may lead to catastrophic failures in the field, 80 % of field operators evaluate the susceptibility of materials to localized corrosion); the involvement of education professionals in field corrosion rate monitoring is very limited (given the safety and security procedures to be followed in the field, the lesser involvement of academic community in the field is understandable; however, the establishment of paths for exposing students in the field will be useful in the long run); and the knowledge transfer cycle is broken at the field operator to educationists step (consequently, field use of electrochemical techniques is not taught during education). The findings of the survey should be considered within the limitations of it. A major limitation of the survey is that it summarized responses of only 55 professionals.

Keywords

electrochemical techniques, standards, education, potentiostat, corrosion monitoring, corrosion measurement, field monitoring

Introduction

Electrochemical techniques are used in the laboratory in a simulated environment to measure corrosion rates. The laboratory testing includes an apparatus (such as glass cell or autoclave) to simulate corrosion conditions and a technique to measure the corrosion rate simulated in the laboratory apparatus. The setup that consists of the apparatus to simulate the corrosion rate and the use of electrochemical techniques to measure corrosion rate is commonly known as an electrochemical test. Because of the availability of tools (e.g., potentiostats) to measure corrosion rates, electrochemical techniques are widely used to measure corrosion rates in the laboratory. The electro chemical techniques are also used in the field to monitor corrosion rates.

ASTM International G01.11 Subcommittee on Electrochemical Measurements in Corrosion Testing was started in 1965 to address three issues that had been inhibiting the development of electrochemical tests:

- Lack of reproducibility of electrochemical tests and lack of understanding of the variations in results
- Absence of standardized procedures for carrying out these tests
- Use of several conventions to present electrochemical data that made inter preting the test results difficult

To address these issues, G01.11 has been organizing symposia on the develop ments on electrochemical measurements and monitoring, publishing special techni cal publications (STPs), and developing standards on promising techniques.

The three most recently published STPs by ASTM G01.11 are:

- *Electrochemical Impedance: Analysis and Interpretation, ASTM STP1188* [1]
- *Electrochemical Noise Measurement for Corrosion Applications, ASTM STP1277* [2]
- *Advances in Electrochemical Techniques for Corrosion Monitoring and Mea surement, ASTM STP1506* [3]

At present G01.11 has the following 19 standards under its jurisdiction:

1. ASTM G3, *Standard Practice for Conventions Applicable to Electrochemical Measurements in Corrosion Testing* [4]
2. ASTM G5, *Standard Reference Test Method for Making Potentiodynamic An odic Polarization Measurements* [5]
3. ASTM G59, *Standard Test Method for Conducting Potentiodynamic Polariza tion Resistance Measurements* [6]
4. ASTM G61, *Standard Test Method for Conducting Cyclic Potentiodynamic Polarization Measurements for Localized Corrosion Susceptibility of Iron , Nickel , or Cobalt Based Alloys* [7]
5. ASTM G69, *Standard Test Method for Measurement of Corrosion Potentials of Aluminum Alloys* [8]
6. ASTM G71, *Standard Guide for Conducting and Evaluating Galvanic Corro sion Tests in Electrolytes* [9]
7. ASTM G82, *Standard Guide for Development and Use of a Galvanic Series for Predicting Galvanic Corrosion Performance* [10]
8. ASTM G96, *Standard Guide for Online Monitoring of Corrosion in Plant Equipment* (*Electrical and Electrochemical Methods*) [11]
9. ASTM G100, *Standard Test Method for Conducting Cyclic Galvanostaircase Polarization* [12]
10. ASTM G102, *Standard Practice for Calculation of Corrosion Rates and Relat ed Information from Electrochemical Measurements* [13]
11. ASTM G106, *Standard Practice for Verification of Algorithm and Equipment for Electrochemical Impedance Measurements* [14]
12. ASTM G108, *Standard Test Method for Electrochemical Reactivation* (*EPR*) *for Detecting Sensitization of AISI Type 304 and 304L Stainless Steels* [15]
13. ASTM G148, *Standard Practice for Evaluation of Hydrogen Uptake, Perme ation, and Transport in Metals by an Electrochemical Technique* [16]
14. ASTM G150, *Standard Test Method for Electrochemical Critical Pitting Tem perature Testing of Stainless Steels and Related Alloys* [17]
15. ASTM G189, *Standard Guide for Laboratory Simulation of Corrosion under Insulation* [18]
16. ASTM G192, *Standard Test Method for Determining the Crevice Repassivation Potential of Corrosion Resistant Alloys Using a Potentiodynamic Galvanostatic Potentiostatic Technique* [19]
17. ASTM G199, *Standard Guide for Electrochemical Noise Measurement* [20]
18. ASTM G215, *Standard Guide for Electrode Potential Measurements* [21]
19. ASTM G217, *Standard Guide for Corrosion Monitoring in Laboratories and Plants with Coupled Multielectrode Array Sensor Method* [22]

Other associations including NACE International and ISO also develop stand ards on electrochemical techniques for corrosion measurements and monitoring. These standards provide specific procedures or sets of requirements for a particular electrochemical technique that attains a consensus of knowledgeable people [23]. Compliance with standards is voluntary unless mandated by law. Electrochemical standards are useful for:

- Students, new researchers, and technicians learning electrochemical techniques
- Professors teaching and overseeing laboratories using electrochemical techniques
- Engineers, designers, managers, and government regulatory bodies reviewing and supervising integrity of infrastructures and industry operations, such as pipelines, power plants (thermo and nuclear), chemical processing, automo bile, buildings, bridges, transmission lines (overhead and underground), and water (drinking water and wastewater).

Use of standards in the aforementioned activities:

- Avoids duplication of efforts
- Harmonizes teaching and learning around the globe
- Improves efficiency of learning
- Improves reliability and safety of equipment, systems, and operations
- Minimizes unplanned shutdowns
- Reduces cost of learning and operation

Currently, fewer students are majoring in engineering or science, half the young professionals switch their job about every 3.5 years, and the number of experienced engineers is dramatically decreasing (e.g., the number of people working in the oil and gas industry fell from 700,000 in 1980 to 300,000 in 1998) [24]. All these factors make knowledge transfer from experienced engineer to novice engineer difficult. Further, no system is in place to transfer practical knowledge from the industry to the academicians and students. In an ideal situation, education, research and devel opment, standards, and field application should all be interlinked (**Fig. 1**), but cur rently, the circle is incomplete or nonexistent.

It is critical at this stage to develop a knowledge management process. Knowl edge management consists of four steps [24]:

- Capture knowledge
- Determine the most critical knowledge to retain and share
- Retain knowledge
- Share knowledge

The standards development process inherently performs these four steps. Therefore, using standards to educate, conduct research, and carry out field activi ties is beneficial and essential.

The objective of this paper is to evaluate the current status of using the stand ards on electrochemical techniques for corrosion measurement and monitoring in education, research, and in real field applications.

Survey

A survey consisting of ten questions was distributed to more than 275 professionals around the world using a commercial online tool [25]; 55 professionals responded to the survey. These professionals were broadly classified into three groups:

- Education (professors and lecturers who teach at universities and colleges)
- Research (professionals carrying out research in government and private laboratories)

FIG. 1 Ideal knowledge management circle.

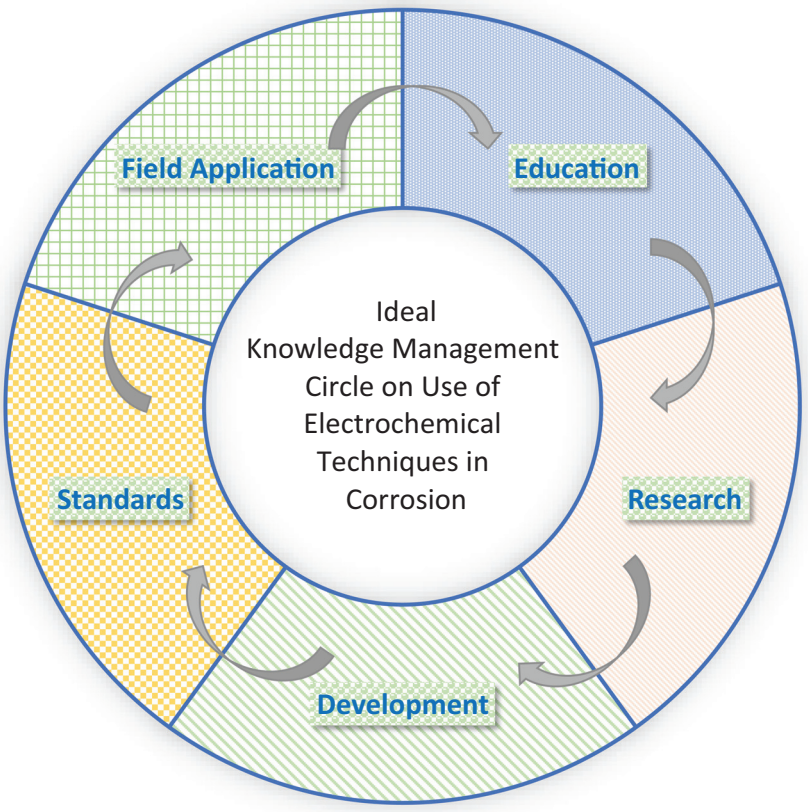

- Field application (professionals controlling corrosion in the actual field; most of the professionals who participated in the survey were from the oil and gas industry)

The ten questions were slightly modified for each group (Table 1), but they es sentially sought the same information from all three groups. The ten questions broadly covered four aspects:

- General use of electrochemical techniques
- Use of electrochemical techniques in the laboratory for general corrosion rate measurements and monitoring
- Use of electrochemical techniques in the laboratory for localized corrosion rate measurements and monitoring
- Use of electrochemical techniques in the field for monitoring corrosion rate

Fig. 2 presents details of the number of survey forms (distributed and responses received), and Fig. 3 details the various countries these responders were from.

TABLE 1 Questions distributed to different groups of professionals.

	Education	Research	Field Application
1	Do you teach corrosion?	Are you conducting research on corrosion and corrosion control?	Are you involved in corrosion and corrosion control (e.g., corrosion inhibitor, coating) monitoring or measurement?
2	Do you teach electrochemical techniques in your course?	Do you use electrochemical techniques in your corrosion research?	Do you use electrochemical techniques in corrosion monitoring?
3	Does your course include laboratory experiments involving electrochemical techniques?	Does your research include laboratory experiments involving electrochemical techniques?	Does your work include laboratory experiments involving electrochemical techniques?
4	Do you use any basic standards in your course?	Do you use any basic standards in your research?	Do you use any basic standards in your work?
5	How do students convert electrochemical parameters measured into general corrosion rate?	How do you convert electrochemical parameters measured into general corrosion rate?	How do you convert electrochemical parameters measured into general corrosion rate?
6	Do your laboratory tests include measurement of localized corrosion using electrochemical techniques?		
7	Does your course follow any of the standards on localized corrosion measurements using electrochemical techniques?	Does your research follow any of the standards on localized corrosion measurements using electrochemical techniques?	Does your work follow any of the standards on localized corrosion measurements using electrochemical techniques?
8	Are the students taught field measurements of corrosion using electrochemical techniques following any standards?	Does your research involve field measurements of corrosion using electrochemical techniques following any standards?	Does your work involve field measurements of corrosion using electrochemical techniques following any standards?
9	Do you teach the limitations of electrochemical techniques in the field?	Do you evaluate the limitations of electrochemical techniques in the field?	Do you evaluate the limitations of electrochemical techniques in the field?
10	Please provide any suggestions on areas for improvement		

Use of Electrochemical Techniques in Corrosion and Corrosion Control

The majority of the responders are involved in corrosion and corrosion control (**Fig. 4**), and almost all are using electrochemical techniques (**Fig. 5**). Information presented in **Fig. 4** and **Fig. 5** provides the confidence that the survey data were obtained from relevant and knowledgeable persons.

FIG. 2 Response to the survey on electrochemical techniques for corrosion measurements and monitoring.

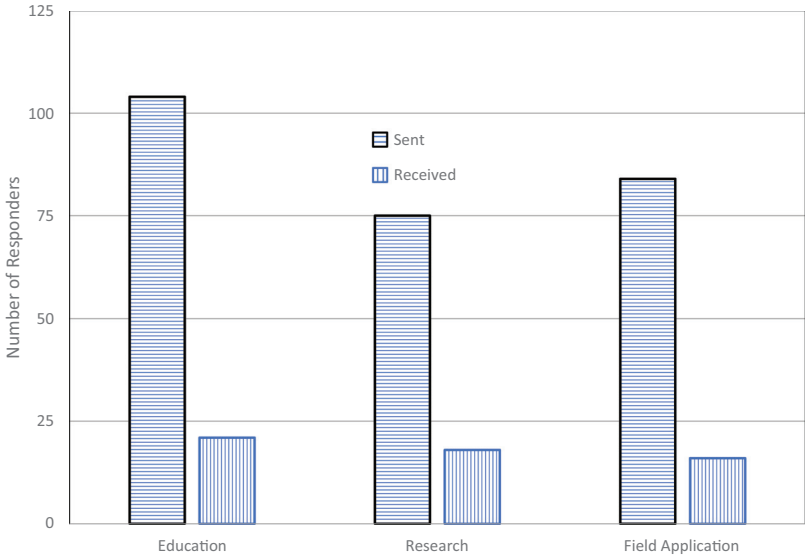

FIG. 3 Countries of responders.

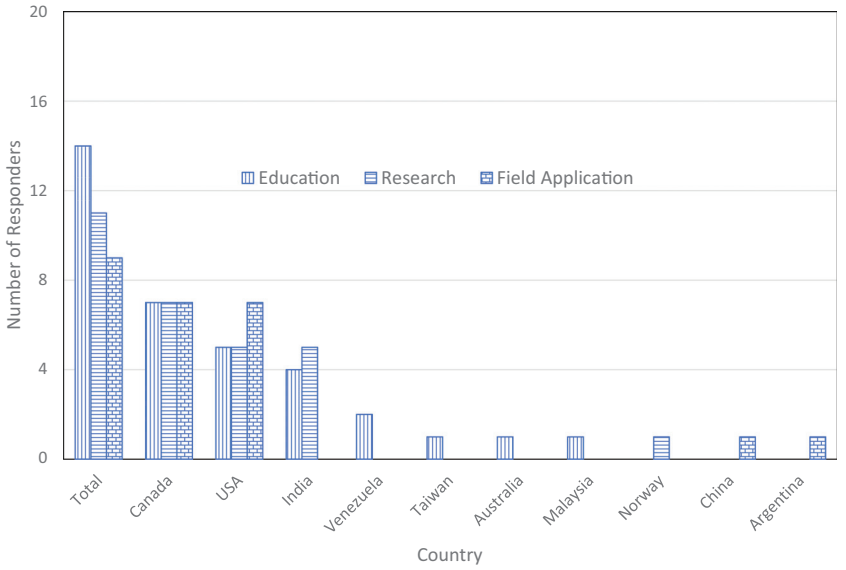

FIG. 4 Involvement in corrosion and corrosion control.

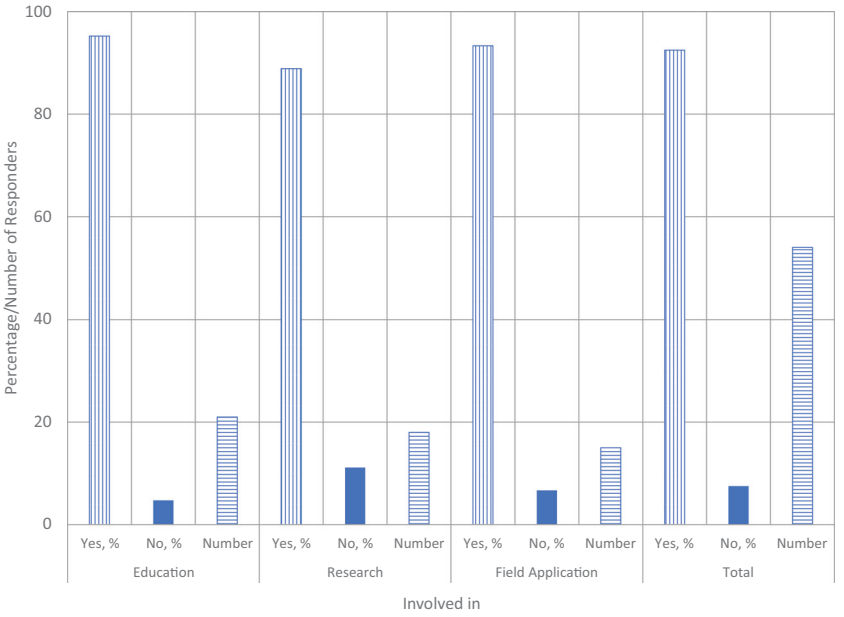

FIG. 5 Usage of electrochemical techniques in corrosion and corrosion control.

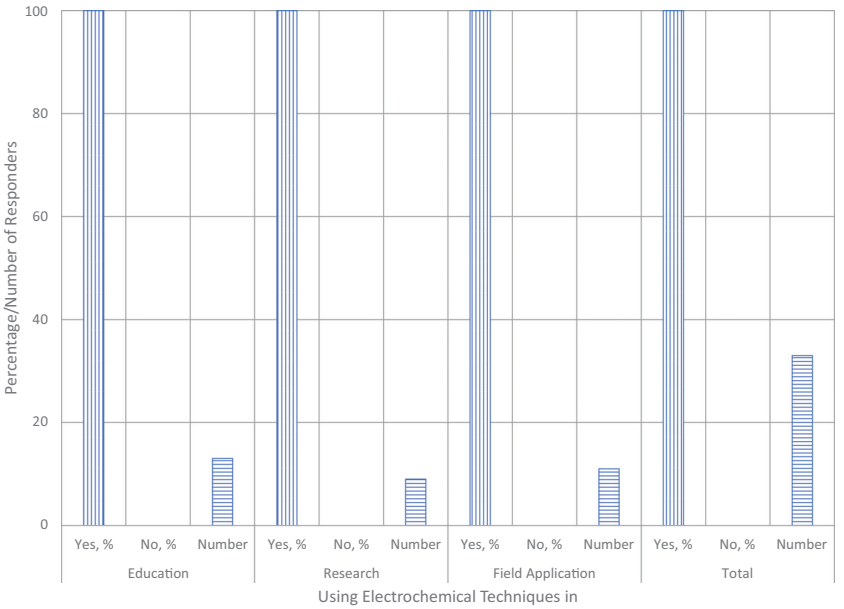

Electrochemical Techniques for Measuring General Corrosion Rate in the Laboratory

Laboratory evaluation is the first step in understanding corrosion. Therefore, con ducting laboratory tests using electrochemical techniques is vital for both education and research. Laboratory tests also play a vital role in predicting field behavior as well as in reducing the number of options for field testing and deployment.

With regard to the question on inclusion of laboratory tests, the survey pro duced surprising results (Fig. 6). Fifty percent of the corrosion courses are con ducted without laboratory tests involving electrochemical techniques. On the other hand, almost all responders working in the actual field see the value of laboratory tests and are using them.

Several standards have been published on various electrochemical techniques for the measurement of general corrosion rates in the laboratory. Fig. 7 presents the response as to the use of standards on electrochemical techniques. Salient features of the response are listed as follows:

- ASTM G5 the flagship standard of G01.11 is by far the most widely used standard among educationists, researchers, and field operators. This standard test method is commonly used to test and qualify the functionality of potentio stats as well as the to test the capability of technicians to conduct electrochem ical tests.

FIG. 6 Use of electrochemical techniques in the laboratory.

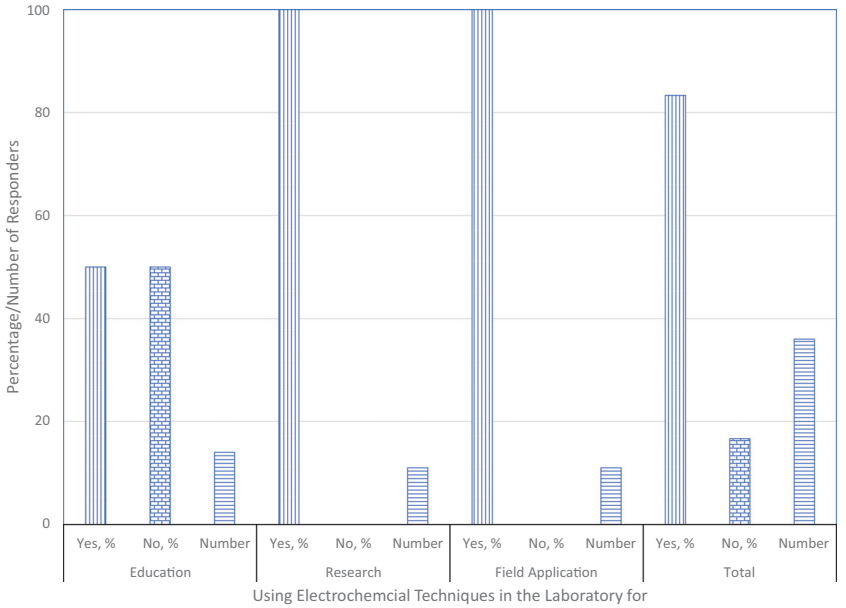

FIG. 7 Use of basic standards on electrochemical techniques in corrosion measurement.

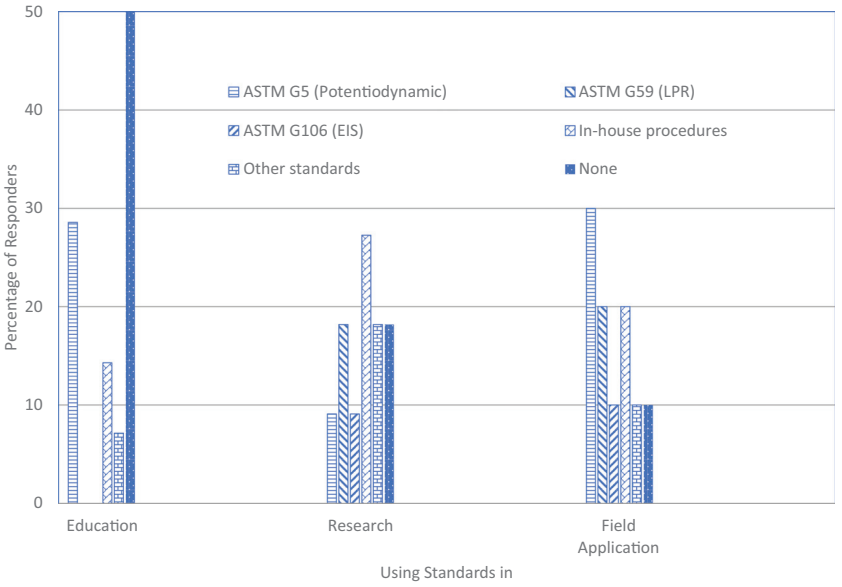

- Use of in house developed procedures to carry out corrosion tests using elec trochemical techniques is also common. The practice of using in house devel oped procedures is more common among research communities than other groups. This is not surprising because researchers tend to develop new proce dures. Further, it would be nice to know if the in house developed procedures are adopted from any of the standards and if they are similar to procedures presented in the standards. However, that exercise was not within the scope of this survey/paper.
- A surprisingly large percentage of professionals are not following any standard procedures in conducting corrosion tests using electrochemical techniques. The percentage of professionals not following any standards decreases in the order: education (50 %) research (18 %) field operators (10 %).
- Repeat measurements of corrosion rates using the linear polarization resis tance method following ASTM G59 is most common among field operators, whereas education institutes are not using it at all.
- About 10 % of researchers and field operators are using ASTM G106 (on the electrochemical impedance spectroscopy [EIS] technique), whereas education institutes do not use this standard at all. It should be noted that ASTM G106 provides practical guidelines for verifying the algorithm and equipment used in impedance measurements. Using this standard in education will augment students understanding the complexity of EIS.

- The survey options included ASTM G199 (electrochemical noise), ISO 17093 (electrochemical noise), and ISO 16773 (EIS). However, no responders indicated that they use these standards.

Electrochemical techniques measure electrochemical parameters, and general corrosion rates are calculated from those measured parameters. This calculation includes corrosion current measurements, use of Tafel slopes, and determination of equivalent weight of material tested. **Fig. 8** presents the methods corrosion professionals use to convert electrochemical parameters to general corrosion rates. Salient features of the response are listed here:

- ASTM G102 provides detailed procedures to calculate general corrosion rates from the electrochemical parameters measured. The survey indicates that it is the commonly used standard.
- Corrosion professionals extensively use in house or individual procedures. In fact, a higher percentage of corrosion professionals use in house or individual procedures rather than using ASTM G102. Further, it would be nice to know if the in house developed procedures are adopted from any of the standards and if they are similar to procedures presented in the standards. However, that exercise was not within the scope of this survey/paper.
- It is disturbing to note that a fairly large percentage of field personnel are not aware of procedures used to calculate general corrosion rates. This practice prevails because many field deployable devices have built in general corrosion rate calculators.

FIG. 8 Procedures to calculate general corrosion rates from electrochemical parameters.

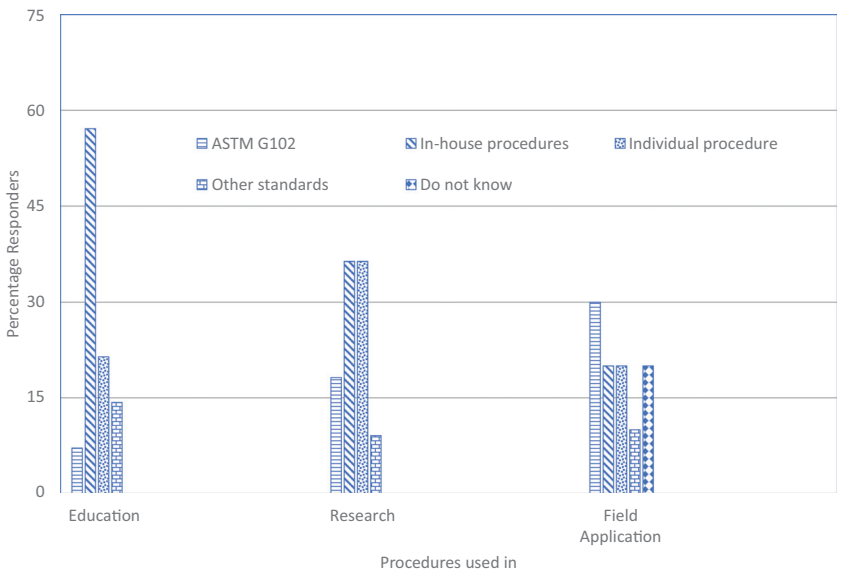

Electrochemical Techniques for Measuring Localized Corrosion Rate in the Laboratory

Almost all corrosion incidences in engineering structures occur due to localized corrosion rather than general corrosion. Therefore, evaluating the susceptibility of materials to localized corrosion is paramount. Localized corrosion occurs in different forms including but not limited to pitting corrosion, crevice corrosion, erosion corrosion, galvanic corrosion, hydrogen damage, sensitization, and corrosion under insulation. Fig. 9 presents the professionals' responses on evaluation of localized corrosion of materials in the laboratory. Salient features of the responses are listed here:

- The percentage evaluation of localized corrosion by education institutes and research professionals is lower. Almost 50 % of these professionals do not evaluate localized corrosion.
- Because localized corrosion may lead to catastrophic failures in the field, 80 % of field operators evaluate the susceptibility of materials to localized corrosion.

Several standards are available to evaluate the susceptibility of materials to localized corrosion. Fig. 10 presents the usage of standards on localized corrosion utilizing electrochemical techniques. The salient features are as follows:

FIG. 9 Measurement of localized corrosion susceptibility in the laboratory using electrochemical techniques.

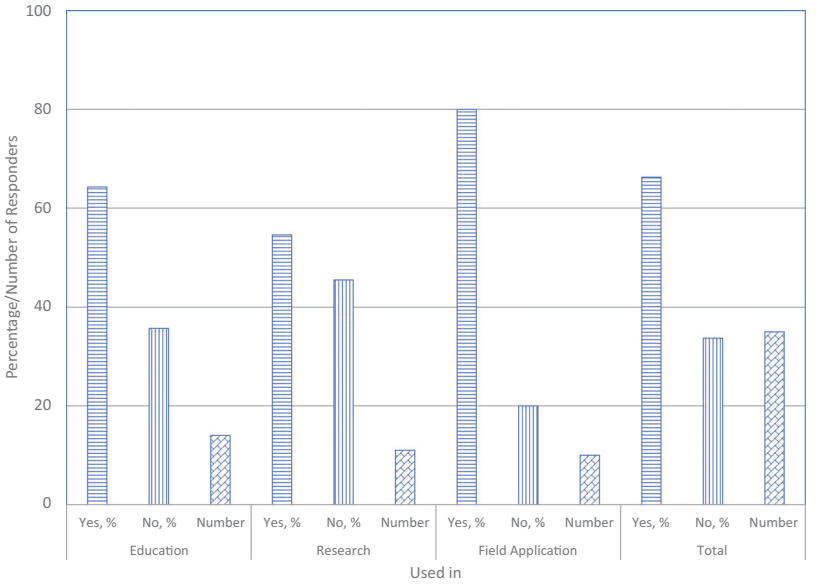

FIG. 10 Standards to evaluate localized corrosion using electrochemical techniques.

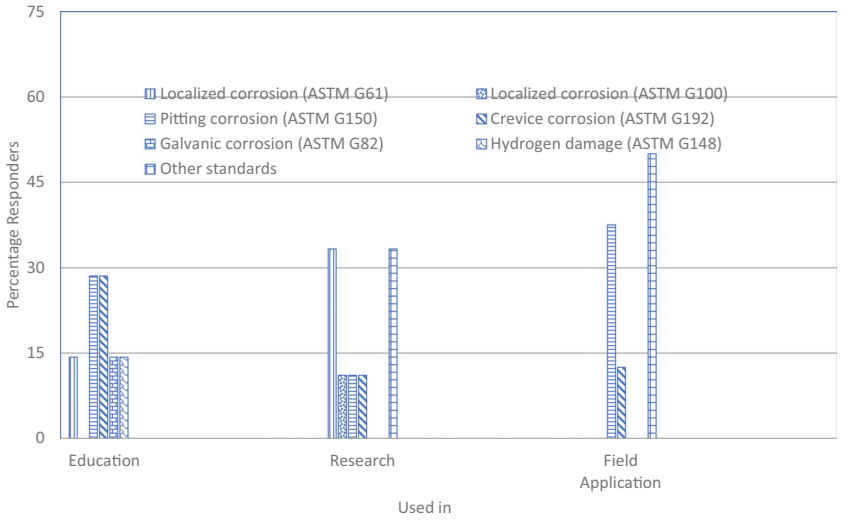

- No one standard is preferred by any group, though a slightly higher percentage of professionals use ASTM G150 (pitting corrosion). This is normal because, depending on the material and environment, different forms of localized corrosion may take place. Therefore, a variety of standards are used.
- This survey question also included ASTM G71 (galvanic corrosion), ASTM G108 (sensitization), and ASTM G189 (corrosion under insulation). But no responders indicated that they are using these standards.

Electrochemical Techniques for Monitoring Corrosion Rate in the Field

On time and online monitoring of corrosion rates is vital in the field. Because electrochemical techniques can provide instantaneous corrosion rates, they are used for online monitoring purposes. Fig. 11 presents the practices for online monitoring of corrosion using electrochemical techniques in the operating field. The salient features are as follows:

- Standards on electrochemical techniques are used in a limited way in the field.
- Many professionals use in house procedures to monitor corrosion rates. This may be justifiable because the field operating conditions may be diverse. Therefore, adaptation of standard procedures to specific conditions is required. Further, it would be nice to know if the in house developed procedures are adopted from any of the standards and if they are similar to procedures presented in the standards. However, that exercise was not within the scope of this survey/paper.

FIG. 11 Use of standards on electrochemical techniques in the field.

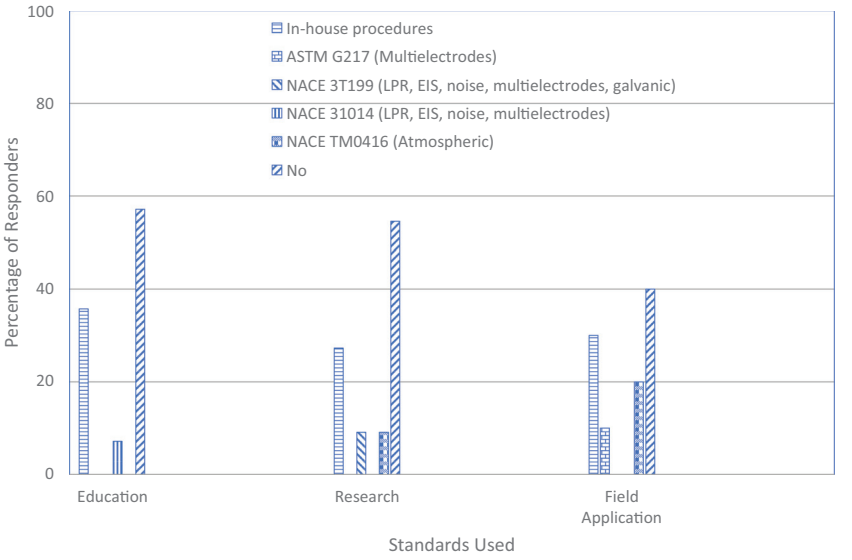

- It is startling to note that a large percentage of professionals do not have any standards/procedures for monitoring corrosion rates in the field using electro chemical techniques.
- The involvement of education professionals in field corrosion rate monitoring is very limited. Given the safety and security procedures to be followed in the field, the lesser involvement of the academic community in the field is under standable. However, the establishment of paths for exposing students in the field will be useful in the long run.

Every technique has limitations and boundaries. It is important to understand the limitations and boundaries of various electrochemical techniques and use them within the boundary of operation. Fig. 12 presents the understanding of corrosion professionals on the limitations of electrochemical techniques for corrosion moni toring. The salient features are as follows:

- Most corrosion professionals do understand the limitations of electrochemical techniques for corrosion monitoring based on their own experience and knowledge.
- Some standards describe in detail the limitations of electrochemical techni ques; however, corrosion professionals use the standards only in a very limited way.
- Many corrosion professionals (up to 40 % of the responders) involved in field operations use electrochemical techniques without understanding the limita tions/boundaries of those techniques.

FIG. 12 Understanding the limitations of electrochemical techniques.

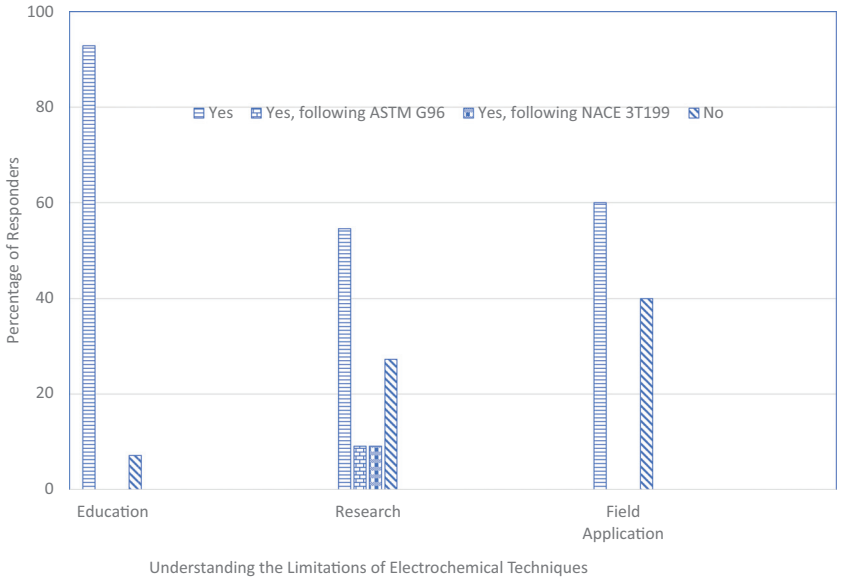

Discussion

Standards are developed based on input and volunteer participation of many knowledgeable people in a common field. Standards are mutually agreed upon min imum values or conditions that suppliers, users, producers, third party laboratories, academicians, and scientists are comfortable with, based on the current state of knowledge on that subject. Standards are periodically updated every 4, 5, or 10 years based on current and new knowledge.

Standards are normally used in implementing a product or process, in a com pany's product or service specifications, in government regulations, and in promoting a technology or knowledge. Adoption and use of standards help the industry as a whole to at least meet a minimum value, parameter, or practice. Associations such as ASTM International, NACE International, and ISO have developed several standards on electrochemical techniques for corrosion measurements and monitoring.

Using standards in corrosion education, research, and field practice helps to disseminate and retain knowledge. Most corrosion occurs by electrochemical mech anisms; therefore, fundamental and thorough knowledge of electrochemical techni ques in corrosion measurement and monitoring will help the community to control corrosion effectively and economically across the globe. Toward that end, the use of standards in corrosion education, research, and field practice should be encouraged, mandated, and practiced as second nature.

The survey results presented in the paper indicate that developed standards are only used in a limited way in corrosion education, research, and field application. Increased use of standards will facilitate retention of knowledge, seamless knowl edge transfer, and effective knowledge management.

Summary

- Most corrosion occurs by electrochemical mechanisms. Therefore, electro chemical techniques are widely used to measure and monitor corrosion. Sever al standards for using various electrochemical techniques have been published by ASTM International, NACE International, ISO, and other organizations.
- This paper presents results from a survey on the use of standards on electro chemical techniques in corrosion education, research, and field applications.
- The survey was distributed to more than 275 professionals and 55 responses were obtained.
- Among basic standards on electrochemical techniques for corrosion measure ments, use of ASTM G5 is common among corrosion educationists, research ers, and field users. However, a large percentage of them follow no standards.
- Use of ASTM G102 to convert the measured electrochemical parameter into a general corrosion rate is common among field professionals; but corrosion educationists and researchers follow their own procedures. Fifty percent of field professionals are unaware of procedures used in the conversion.
- Almost 50 % of the professionals are neither aware of standards on electro chemical techniques for localized corrosion measurements nor evaluate local ized corrosion potential of materials.
- The knowledge transfer cycle is broken at the field operator to educationists step. Consequently, field use of electrochemical techniques is not taught dur ing education.
- The findings of this survey should be considered within its limitations. A ma jor limitation of this survey is that it summarized responses of only 55 profes sionals and that most of these responders are from the oil and gas industry.

References

[1] Scully, J. R., Silverman, D. C., and Kendig, M. W., Eds., *Electrochemical Impedance: Analysis and Interpretation, ASTM STP1188*, ASTM International, West Conshohocken, PA, 1993, http://dx.doi.org/10.1520/STP1188-EB

[2] Kearns, J. R., Scully, J. R., Roberge, P. R., Reichert, D. L., and Dawson, J. L., Eds., *Electrochemical Noise Measurement for Corrosion Applications, ASTM STP1277*, ASTM International, West Conshohocken, PA, 1996, http://dx.doi.org/10.1520/STP1277-EB

[3] Papavinasam, S., Berke, N., and Brossia, S., Eds., *Advances in Electrochemical Techniques for Corrosion Monitoring and Measurement, ASTM STP1506*, ASTM International, West Conshohocken, PA, 2009, http://dx.doi.org/10.1520/STP1506-EB

[4] ASTM G3-14, *Standard Practice for Conventions Applicable to Electrochemical Measurements in Corrosion Testing*, ASTM International, West Conshohocken, PA, 2014, www.astm.org

[5] ASTM G5-14e1, *Standard Reference Test Method for Making Potentiodynamic Anodic Polarization Measurements*, ASTM International, West Conshohocken, PA, 2014, www.astm.org
[6] ASTM G59-97(2014), *Standard Test Method for Conducting Potentiodynamic Polarization Resistance Measurements*, ASTM International, West Conshohocken, PA, 2014, www.astm.org
[7] ASTM G61-86(2018), *Standard Test Method for Conducting Cyclic Potentiodynamic Polarization Measurements for Localized Corrosion Susceptibility of Iron-, Nickel-, or Cobalt-Based Alloys*, ASTM International, West Conshohocken, PA, 2018, www.astm.org
[8] ASTM G69-12, *Standard Test Method for Measurement of Corrosion Potentials of Aluminum Alloys*, ASTM International, West Conshohocken, PA, 2012, www.astm.org
[9] ASTM G71-81(2014), *Standard Guide for Conducting and Evaluating Galvanic Corrosion Tests in Electrolytes*, ASTM International, West Conshohocken, PA, 2014, www.astm.org
[10] ASTM G82-98(2014), *Standard Guide for Development and Use of a Galvanic Series for Predicting Galvanic Corrosion Performance*, ASTM International, West Conshohocken, PA, 2014, www.astm.org
[11] ASTM G96-90(2018), *Standard Guide for Online Monitoring of Corrosion in Plant Equipment (Electrical and Electrochemical Methods)*, ASTM International, West Conshohocken, PA, 2018, www.astm.org
[12] ASTM G100-89(2015), *Standard Test Method for Conducting Cyclic Galvanostaircase Polarization*, ASTM International, West Conshohocken, PA, 2015, www.astm.org
[13] ASTM G102-89(2015)e1, *Standard Practice for Calculation of Corrosion Rates and Related Information from Electrochemical Measurements*, ASTM International, West Conshohocken, PA, 2015, www.astm.org
[14] ASTM G106-89(2015), *Standard Practice for Verification of Algorithm and Equipment for Electrochemical Impedance Measurements*, ASTM International, West Conshohocken, PA, 2015, www.astm.org
[15] ASTM G108-94(2015), *Standard Test Method for Electrochemical Reactivation (EPR) for Detecting Sensitization of AISI Type 304 and 304L Stainless Steels*, ASTM International, West Conshohocken, PA, 2015, www.astm.org
[16] ASTM G148-97(2018), *Standard Practice for Evaluation of Hydrogen Uptake, Permeation, and Transport in Metals by an Electrochemical Technique*, ASTM International, West Conshohocken, PA, 2018, www.astm.org
[17] ASTM G150-18, *Standard Test Method for Electrochemical Critical Pitting Temperature Testing of Stainless Steels and Related Alloys*, ASTM International, West Conshohocken, PA, 2018, www.astm.org
[18] ASTM G189-07(2013), *Standard Guide for Laboratory Simulation of Corrosion under Insulation*, ASTM International, West Conshohocken, PA, 2013, www.astm.org
[19] ASTM G192-08(2014), *Standard Test Method for Determining the Crevice Repassivation Potential of Corrosion-Resistant Alloys Using a Potentiodynamic-Galvanostatic-Potentiostatic Technique*, ASTM International, West Conshohocken, PA, 2014, www.astm.org
[20] ASTM G199-09(2014), *Standard Guide for Electrochemical Noise Measurement*, ASTM International, West Conshohocken, PA, 2014, www.astm.org
[21] ASTM G215-17, *Standard Guide for Electrode Potential Measurements*, ASTM International, West Conshohocken, PA, 2017, www.astm.org
[22] ASTM G217-16, *Standard Guide for Corrosion Monitoring in Laboratories and Plants with Coupled Multielectrode Array Sensor Method*, ASTM International, West Conshohocken, PA, 2016, www.astm.org
[23] Dean, S. W., Jr., "Corrosion Standards, Who Needs Them?" *Plenary Lecture Presented at CORROSION 2010 Conference and Expo*, San Antonio, TX, March 14–18, 2010, NACE International, Houston, TX, 2010.

[24] Hack, H., "Knowledge Transfer from Experienced to Novice Engineers," *Plenary Lecture Presented at CORROSION 2012 Conference & Expo*, March 11–15, 2012, Salt Lake City, UT, NACE International, Houston, TX, 2012.

[25] Survey Monkey, https://www.surveymonkey.com/ (accessed December 6, 2018).

STP 1609, 2019 / available online at www.astm.org / doi: 10.1520/STP160920170175

Sankara Papavinasam[1]

Use of Standards on Electrochemical Techniques in Establishing Quality Education (QE), Quality Assurance (QA), and Quality Control (QC) Processes in Corrosion Control

Citation

Papavinasam, S., "Use of Standards on Electrochemical Techniques in Establishing Quality Education (QE), Quality Assurance (QA), and Quality Control (QC) Processes in Corrosion Control," *Advances in Electrochemical Techniques for Corrosion Monitoring and Laboratory Corrosion Measurements*, *ASTM STP1609*, S. Papavinasam, R. B. Rebak, L. Yang, and N. S. Berke, Eds., ASTM International, West Conshohocken, PA, 2019, pp. 363–377, http://dx.doi.org/10.1520/STP160920170175[2]

ABSTRACT

Most corrosion mechanisms are electrochemical in nature. Therefore, electrochemical techniques are widely used to investigate corrosion and to develop strategies to control it. Many electrochemical techniques are available to measure corrosion in the laboratory and to monitor corrosion in the field, including linear polarization resistance, electrochemical impedance spectroscopy, electrochemical noise, multielectrode technique, scanning reference electrode technique, and electrochemical quartz crystal microbalance. Several standardization organizations, including ASTM International, International Organization for Standardization, and NACE International have published standards on these techniques. For instance, ASTM International has published 19 standards on electrochemical techniques. These standards are further referenced and used in another 50 standards. These

Manuscript received September 25, 2017; accepted for publication April 2, 2018.

[1]CorrMagnet Consulting Inc., 6 Castlemore St., Ottawa, ON K2G 6K8, Canada

[2]ASTM Symposium on *Advances in Electrochemical Techniques for Corrosion Monitoring and Laboratory Corrosion Measurements* on November 13 14, 2017 in Atlanta, GA, USA.

standards are valuable to educate students in academic institutions, to evaluate corrosion behavior of materials and environments to establish their quality, and to ensure that the equipment, instruments, and infrastructure are safe and reliable for continued operation. This paper discusses the advances made in recent years in using electrochemical techniques in quality education, quality assurance, and quality control and proposes additional steps that could be taken to further improve the quality education, quality assurance, and quality control processes.

Keywords
corrosion education, electrochemical techniques, LPR, electrochemical noise, EIS, standards, corrosion management, corrosion workforce, potentiodynamic, quality education

Introduction

"In God we trust; all others bring data" (motto of the Apollo astronauts)

Reliable data on corrosion is necessary for making appropriate decisions such as evaluation, selection, and deployment of materials and corrosion control strategies. Most corrosion occurs by electrochemical principles. Therefore, electrochemical techniques to measure and monitor corrosion are widely used.

Over the past century, several advancements have been made that enable reliable corrosion monitoring and measurement using electrochemical techniques. Table 1 presents salient discoveries and advancements that have been made as well as standards that have been published. From Table 1, it is obvious that standards organizations have readily and diligently developed standards on promising techniques.

This paper discusses and emphasizes the importance of using standards on electrochemical techniques in quality education (QE), quality assurance (QA), and quality control (QC) processes.

Characteristics of Standards

Standards are minimum requirements with which suppliers, users, producers, third party laboratories, academicians, and scientists are comfortable. International associations, such as ASTM International, the International Organization for Stan dardization (ISO), and NACE International, develop standards on electrochemical techniques for corrosion measurements and monitoring.

Standards are developed based on the input and voluntary participation of many people in a common field. Standards are valuable for developing a product or process, writing specifications, implementing government regulations, promoting technology or knowledge, and for educating next generation professionals. Adop tion of standards helps the community and industry as a whole to at least meet a minimum value, parameter, or practice.

TABLE 1 Significant advancements in determining corrosion rates using electrochemical techniques.[a]

Year	Significant Advancement
1905	Tafel Equation Relationship between "potential" and "current" (corrosion rate)
1919	Butler Volmer Equation Relationship between "potential" and "current"
1929	Evans Diagram Relationship between "potential" and "current" (corrosion rate)
1938	Wagner and Traud (mixed potential theory) Development of the concept of local anodes and local cathodes
1942	Hickling Introduction of the term "potentiostat"
1950	Pourbaix Development of the potential and pH diagram
1957	Stern and Geary Equation Relationship between polarization resistance and general corrosion rate[a]
1959	Sauerbrey Equation Relationship between piezoelectric crystal oscillation and mass deposited on it (origin of electrochemical quartz crystal microbalance)
1960	Epelboin Development of electrochemical impedance spectroscopy (EIS)
1962	Devanathan and Stachurski Electrochemical measurement of hydrogen permeation
1968	Iverson Observation of potential fluctuations (first observation of electrochemical noise)
1968	ASTM G3, *Standard Practice Conventions Applicable to Electrochemical Measurements in Corrosion Testing* (2014)[b]
1969	ASTM G5, *Standard Reference Test Method for Making Potentiodynamic Anodic Polarization Measurements* (2014)[b]
1978	ASTM G59, *Standard Test Method for Conducting Potentiodynamic Polarization Resistance Measurements* (2014)[a,b]
1981	ASTM G69, *Standard Test Method for Measurement of Corrosion Potentials of Aluminum Alloys* (2012)[b]
1981	ASTM G71, *Standard Guide for Conducting and Evaluating Galvanic Corrosion Tests in Electrolytes* (2014)[b]
1983	ASTM G82, *Standard Guide for Development and Use of a Galvanic Series for Predicting Galvanic Corrosion Performance* (2014)[b]
1986	ASTM G61, *Standard Test Method for Conducting Cyclic Potentiodynamic Polarization Measurements for Localized Corrosion Susceptibility of Iron , Nickel , and Cobalt Based Alloys* (2018)[b]
1989	ASTM G100, *Standard Test Method for Conducting Cyclic Galvanostaircase Polarization* (2015)[b]
1989	ASTM G102, *Standard Practice for Calculation of Corrosion Rates and Related Information from Electrochemical Measurements* (2015)[a,b]
1989	ASTM G106, *Standard Practice for Verification of Algorithm and Equipment for Electrochemical Impedance Measurements* (2015)[b]
1990	ASTM G96, *Standard Guide Online Monitoring of Corrosion in Plant Equipment (Electrical and Electrochemical Methods)* (2018)[a,b]
1992	ASTM G108, *Standard Test Method for Electrochemical Reactivation (EPR) for Detecting Sensitization of AISI Type 304 and 304L Stainless Steels* (2015)[b]
1997	ASTM G148, *Standard Practice for Evaluation of Hydrogen Uptake, Permeation, and Transport in Metals by an Electrochemical Technique* (2018)[b]
1997	ASTM G150, *Standard Test Method for Electrochemical Critical Pitting Temperature Testing of Stainless Steels and Related Alloys* (2018)[b]

TABLE 1 *(Continued).*

Year	Significant Advancement
1999	NACE Technical Report 3T199, *Techniques for Monitoring Corrosion and Related Parameters in Field Applications* (2012)[b]
2007	ISO Standard 16773 1, *Electrochemical Impedance Spectroscopy (EIS) on Coated and Uncoated Metallic Specimens Part 1: Terms and Definitions* (2016)[b]
2008	ASTM G192, *Standard Test Method for Determining the Crevice Repassivation Potential of Corrosion Resistant Alloys Using a Potentiodynamic Galvanostatic Potentiostatic Technique* (2014)[b]
2009	ASTM G199, *Standard Guide for Electrochemical Noise Measurement* (2014)[b]
2014	ISO 17081, *Standard Method of Measurement of Hydrogen Permeation and Determination of Hydrogen Uptake and Transport in Metals by an Electrochemical Technique*
2014	NACE Technical Committee Report 31014, *Field Monitoring of Corrosion Rates in Oil and Gas Production Environments Using Electrochemical Techniques* (2014)[a,b]
2015	ISO 17093, *Corrosion of Metals and Alloys Guidelines for Corrosion Test by Electrochemical Noise Measurements* (2015)[b]
2015	ASTM G215, *Standard Guide for Electrode Potential Measurement* (2017)[a,b]
2016	ASTM G217, *Standard Guide for Corrosion Monitoring in Laboratories and Plants with Coupled Multielectrode Array Sensor Method* (2016)[b]
2016	NACE TM0416, *Standard for Monitoring Atmospheric Corrosion Rate* (2016)[b]

[a]These developments enabled measurement of corrosion rates in the laboratories and instantaneous monitoring of corrosion in the field using electrochemical techniques.
[b]Year of first publication of the standards in "year" column, with most recent version indicated in parentheses. Standards developing organizations (such as ASTM International) typically revise and update the standards every 5 years. Check with standards making organizations for the most recent version of these standards.

Standards on electrochemical techniques may be broadly classified into three categories:

- Standard Guide or State of the Art Report (Bronze level[a])
- Standard Practice (Silver level[a])
- Standard Test Method (Gold level[a])

Standard Guide or State of the Art Report (Bronze Level[a])

Standards in this category present general aspects of the methodology/technique; provide general guidelines on using the methodology/technique; describe general procedures for conducting the test using the methodology/technique; and identify general limitations of the methodology/technique. Some electrochemical techniques that fall into the "Standard Guide" category include:

[a]As defined by the author for simplification; standards do not identify such levels.

- ASTM G71, *Standard Guide for Conducting and Evaluating Galvanic Corro sion Tests in Electrolytes*
- ASTM G82, *Standard Guide for Development and Use of a Galvanic Series for Predicting Galvanic Corrosion Performance*
- ASTM G96, *Standard Guide for Online Monitoring of Corrosion in Plant Equipment* (*Electrical and Electrochemical Methods*)
- ASTM G189, *Standard Guide for Laboratory Simulation of Corrosion under Insulation*
- ASTM G199, *Standard Guide for Electrochemical Noise Measurement*
- ASTM G215, *Standard Guide for Electrode Potential Measurements*
- ASTM G217, *Standard Guide for Corrosion Monitoring in Laboratories and Plants with Coupled Multielectrode Array Sensor Method*
- NACE Technical Report 31014, *Field Monitoring of Corrosion Rates in Oil and Gas Production Environments Using Electrochemical Techniques*
- NACE Technical Publication 3T199, *Techniques for Monitoring Corrosion and Related Parameters in Field Applications*

Standard Practice (Silver Level[a])

Standards in this category present specific aspects of the methodology/technique; provide step by step procedures to measure or monitor corrosion using the meth odology/technique; identify specific limitations of the methodology/technique; and do not provide any anticipated results. It is the responsibility of the user of the stan dard to determine if all aspects of the standard are properly and adequately fol lowed. Some electrochemical techniques that fall into the "Standard Practice" category include:

- ASTM G3, *Standard Practice for Conventions Applicable to Electrochemical Measurements in Corrosion Testing*
- ASTM G102, *Standard Practice for Calculation of Corrosion Rates and Related Information from Electrochemical Measurements*
- ASTM G106, *Standard Practice for Verification of Algorithm and Equipment for Electrochemical Impedance Measurements*
- ASTM G148, *Standard Practice for Evaluation of Hydrogen Uptake, Perme ation, and Transport in Metals by an Electrochemical Technique*
- NACE SP0207, *Performing Close Interval Potential Measurements on Buried or Submerged Metallic Pipelines*
- ISO 16773, *Electrochemical Impedance Spectroscopy on Coated and Uncoated Metallic Specimens*

Standard Test Method (Gold Level[a])

Standards in this category provide clear direction in using the methodology/tech nique; provide step by step procedures to measure or monitor corrosion using the methodology/technique; describe conditions of using the standard; and publish the anticipated test result. The anticipated test result, published by the Standard Test Methods, is developed based on round robin tests involving several laboratories.

The round robin test results are analyzed by various parameters to define boundaries of the standards. Some typical terms used to define the round robin tests results in the standards are (Dean, S. W., Jr., personal communication via email, June 13, 2017):

***C_{ave}*:** The average corrosion rate (or an appropriate parameter related to corrosion, for example, repassivation potential) is the most likely result if the measurements are carried out for a sufficient number of times and the errors are normally distributed.

***SD*:** The standard deviation presents the difference between the average and the measurement result (occurring on either side of the average) where about 68 % of the results will fall (again if the errors are normally distributed).

Repeatability, *s_r*: The repeatability standard deviation is the standard deviation that is observed if the measurement procedure is repeated by the same operator using the same apparatus sequentially on the same or identical samples.

***r*:** The repeatability is the difference between the average and the measured value where 95 % of the measurements will end up when the measurement is repeated by the same operator using the same apparatus on the same or identical samples.

Reproducibility, *S_R*: The reproducibility standard deviation is the standard deviation that occurs when the same procedure is carried out by *different operators* using a different apparatus (usually in different organizations or laboratories) on the same or identical samples.

***R*:** The reproducibility is the limit of the range for the difference between the measured value and the average for 95 % of the measurements, when the procedure is carried out by different operators using a different apparatus (as previously noted) on identical samples.

***CV_r*:** The coefficient of variation is the standard deviation (s_r) divided by the average value and is usually expressed as a percentage.

***CV_R*:** The coefficient of variation is the standard deviation (S_R) divided by the average value and is usually expressed as a percentage.

The user must reproduce the anticipated test result to demonstrate that they met the requirements of the Standard Test Method. Following are some methods used to demonstrate that the user has met the standards requirement.

***C_{ave}*:** The average result is the goal in carrying out the test to demonstrate that the test was carried out in accordance with the standard method.

Some variations in corrosion measurement and monitoring are inevitable if the same operator performs repeat corrosion measurements and monitoring using the same or similar equipment. The repeatability statement is used whether the operator can carry out the procedure and obtain an acceptable result. The repeatability data are used as a test for an operator or technician to determine if he/she could carry out the method in an acceptable fashion. If the operator cannot meet the repeatability requirement, then one cannot allow his/her result to be used. For this purpose, s_r and r values are used to provide limits as to what is acceptable for a single operator.

S_r and r: If the operator is very accurate, the result is within the s_r range; if the operator is acceptable, the result is within the r range. Anything beyond that is not acceptable most of the time.

Values quoted in the reproducibility statement (S_R and R) could be to verify multiple operators (e.g., the producer of a technology, the user of a technology, and others) carrying out the measurements or monitoring. The producer and user normally would agree upon a range for any value that would be acceptable. In this case, the result of not meeting the acceptable range is rejection by the user of the technique/methodology developed by the producer.

CV_r and CV_R: The CV values are used in measurements/monitoring where the variation that occurs is proportional to the average value. Many methodologies for corrosion rate measurement yield a value that depends upon the material tested or on other variables that are part of the test method. In order to have a measure of the rate variability that is not dependent on the average result, the CV value is a reasonable approach.

However, it should be noted that Test Methods produced by some standards making organizations do not conduct round robin tests and do not publish the anticipated results. In such cases, the ability of the user to meet the requirements of the standard cannot be easily verified. Such standards should be considered as "silver standards," even though they are published as "Test Methods."

Some electrochemical techniques that fall into the "Standard Test Method" category include:

- ASTM G5, *Standard Reference Test Method for Making Potentiodynamic Anodic Polarization Measurements*
- ASTM G59, *Standard Test Method for Conducting Potentiodynamic Polarization Resistance Measurements*
- ASTM G61, *Standard Test Method for Conducting Cyclic Potentiodynamic Polarization Measurements for Localized Corrosion Susceptibility of Iron, Nickel, or Cobalt Based Alloys*
- ASTM G69, *Standard Test Method for Measurement of Corrosion Potentials of Aluminum Alloys*
- ASTM G100, *Standard Test Method for Conducting Cyclic Galvanostaircase Polarization*

- ASTM G108, *Standard Test Method for Electrochemical Reactivation (EPR) for Detecting Sensitization of AISI Type 304 and 304L Stainless Steels*
- ASTM G150, *Standard Test Method for Electrochemical Critical Pitting Tem perature Testing of Stainless Steels and Related Alloys*
- ASTM G192, *Standard Test Method for Determining the Crevice Repassivation Potential of Corrosion Resistant Alloys Using a Potentiodynamic Galvanostatic Potentiostatic Technique*
- NACE TM0416, *Test Method for Monitoring Atmospheric Corrosion Rate by Electrochemical Measurements*
- ISO 17093, *Corrosion of Metals and Alloys Guidelines for Corrosion Test by Electrochemical Noise Measurements*

Electrochemical Techniques in Quality Education

Corrosion education is the primary source for producing the next generation work force. In recent years, three independent analyses have been carried out on the gen eral status of corrosion education. The salient findings from these studies are briefly summarized in the following paragraphs [1 6].

In 2009, the status of corrosion education in the United States was assessed by the National Research Council [1]. This study divided the workforce of graduating and practicing engineers into the following categories:

- Technologists who perform repeated critical tasks
- Undergraduate engineering students in materials science and engineering (MSE) who, upon graduation, should be knowledgeable in materials selection
- Undergraduate students in other engineering disciplines
- MSE graduate students who, upon graduation, should be very knowledgeable in materials selection

The study further developed a pyramid of the corrosion workforce (**Fig. 1**):

- Technologists who perform repeated crucial functions
- MSE students who, upon graduation, are knowledgeable in materials
- Other engineering professionals who are knowledgeable in materials, their selection, and corrosion
- Corrosion engineers who are knowledgeable about the current status of corro sion and its control and who are considered as specialists
- Corrosion scientists who advance new knowledge on corrosion and develop innovative new solutions for controlling corrosion

In 2014, NACE International conducted a study entitled *International Measures of Prevention, Application, and Economics of Corrosion Technologies* (*IMPACT*) [3]. This study developed a corrosion management system (CMS) pyramid (**Fig. 2**) and found out the following about the current education and training course:

- The contents are heavily focused on the lower levels of the CMS pyramid (i.e., procedures and working practices).
- They are not geared for the upper levels of the CMS pyramid (i.e., policy, strat egy, and objectives).

FIG. 1 Corrosion Workforce Pyramid (adapted from [1]).

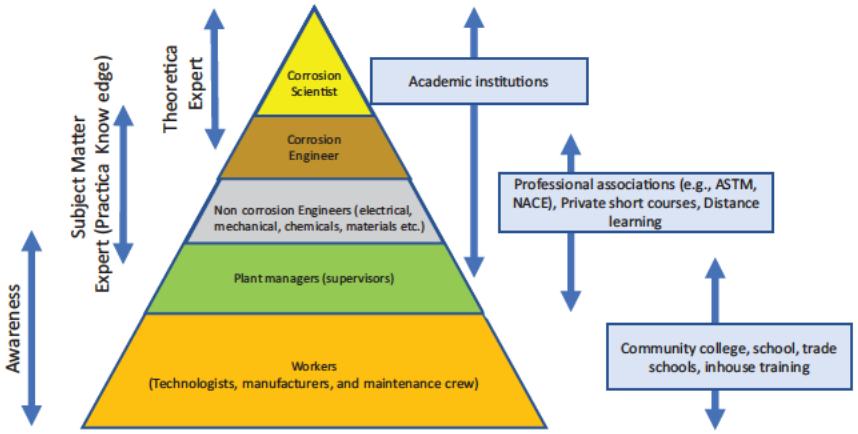

FIG. 2 Corrosion Management System (CMS) Pyramid [3] IMPACT Study. © NACE International 2016. All rights reserved by NACE. Reprinted with permission. NACE standards are revised periodically. Users are cautioned.

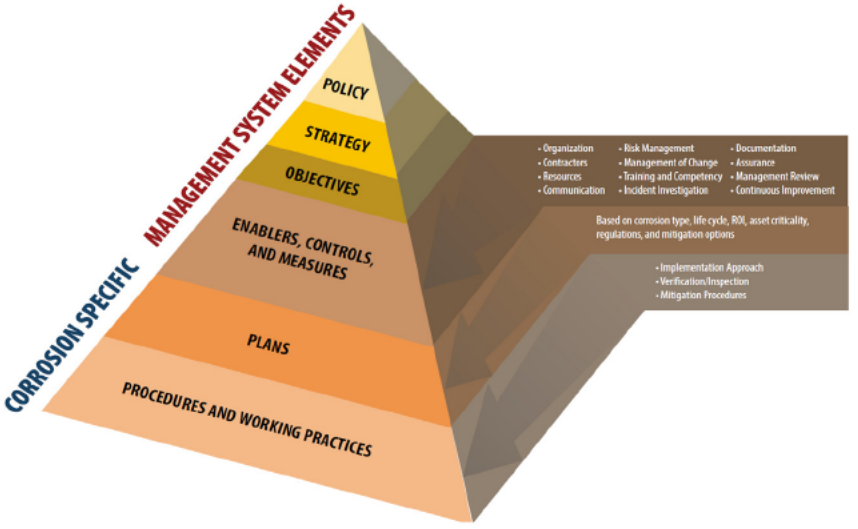

This study further observed that education and training programs:

- Will play an important role in the integration of corrosion management into an organization's management system.

- Must prepare corrosion professionals to communicate better with those out side of the profession.
- Must emphasize business strategy or public policy (or both) when advocating positions to those outside of the corrosion profession.

Another study by the World Corrosion Organization [5] observed that:

- Education in corrosion and corrosion control needs to be tuned to the differ ent levels in basic schools and universities.
- Responsible bodies should be established or identified in each country to install local corrosion control management systems.
- A network of independent experts worldwide who disseminate experiences (good and bad) and best practices should be established.
- It is important to support higher education to enable specialists in electro chemistry, corrosion, and materials science to increase knowledge of corrosion mechanisms and materials protection from the macro down to the nanoscale.

All these studies illustrate that there are three distinct stages of corrosion knowledge/interest (**Fig. 3a**) and, in reality, there exists a gap between each level (**Fig. 3b**) [5 7]. The reasons are too many to describe in this paper but are well dis cussed in the studies themselves. In addition, none of the studies have emphasized the importance of standards in education and skills development. One solution to fill the gap is to integrate the existing corrosion standards into the education system at the corrosion science level, in general, and with regard to electrochemical techni ques in particular [5].

One possible sequence for educating students and professionals both on theory and in the practical use of standards might be as follows:

Step 1: Before carrying out electrochemical testing, it is important to understand vari ous conventions and terminologies used in electrochemical techniques. ASTM G3[b] provides information on various conventions applicable to electrochemi cal measurements.

Step 2: The corrosion potential provides information on the tendency of a metal or alloy to undergo corrosion in a particular environment. Knowledge of corrosion po tential and the procedure for properly measuring it will help in understanding corrosion tendencies in laboratory and field environments. ASTM G215[b] and ASTM G69[c] provide detailed procedures for measuring corrosion potential.

Step 3: Once the student is familiar and comfortable with measuring corrosion poten tial, the next step is to study corrosion rates, linear polarization resistance (LPR), electrochemical noise, EIS, and potentiodynamic polarization techni ques. The following standards may be used for this reason:

- ASTM G59 (LPR)[b]
- ASTM G5 (Potentiodynamic)[b]

[b]At basic minimum level.
[c]At intermediate level.
[d]At advance level.
[e]For field experience/knowledge.

FIG. 3 Situations of corrosion education.

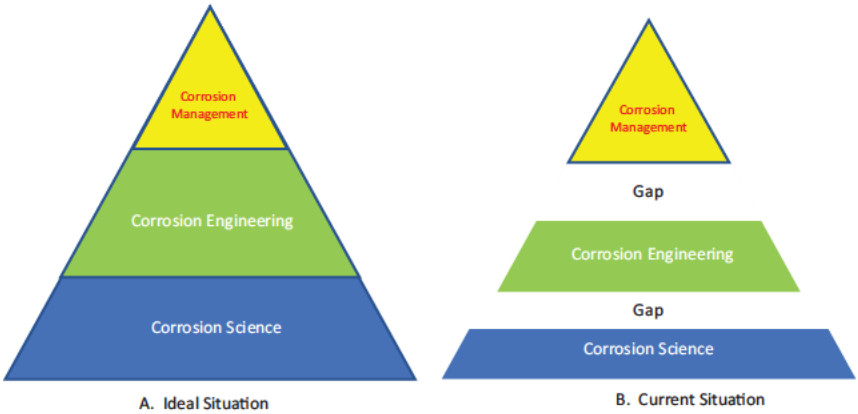

- ASTM G106[c] and ISO 16773[c] (EIS)
- ASTM G199[c] and ISO 17093[c]

Step 4: The measured electrochemical parameter (in Step 3) should be converted into the corrosion rate. ASTM G102[b] provides guidelines on calculating the corrosion rate from electrochemical parameters.

Step 5: The corrosion rate measured in Step 3 is the general corrosion rate. However, in real life, several forms of localized corrosion take place. Susceptibility of metals and alloys to some commonly occurring localized corrosion may be evaluated by electrochemical techniques, including localized corrosion (ASTM G61[d], ASTM G100[d]), pitting corrosion (ASTM G150[d]), crevice corrosion (ASTM G192[d]), galvanic corrosion (ASTM G71[d] and ASTM G82[d]), hydrogen damage (ASTM G148[d]), sensitization (ASTM G108[d]), and corrosion under insulation (ASTM G189[d]). Once the students/professionals are familiar with measuring general corrosion rates using electrochemical techniques, they should be trained to measure localized corrosion using electrochemical techniques.

Step 6: Obviously, measuring and monitoring field corrosion rates using electrochemical techniques are of practical value. In addition, students/professionals may be trained in monitoring the corrosion rate. The following standards may be used for this purpose:

- NACE SP0207[e] (electrode potential)
- ASTM G96[e] (LPR)
- ASTM G217[e] (multielectrodes)
- NACE 31014[e] (LPR, EIS, noise, and multielectrodes)
- NACE 3T199[e] (LPR, EIS, noise, multielectrodes, and galvanic couples)
- NACE TM0416[e] (atmospheric corrosion)

Step 7: It is equally important to educate students/professionals about the limitations of electrochemical techniques for corrosion monitoring. The following standards may be used for this purpose:

- ASTM G96[e] (LPR)
- NACE 3T199[e] (LPR, EIS, noise, multielectrodes, and galvanic couples)

Using the aforementioned sequence, educational institutions will prepare students to be appropriately trained for the practical world or for taking on advanced research or teaching (or any combination thereof). It is important that standards are introduced to students/young professionals at the early stages of their education. This approach will help:

- To train students/young professionals about the fundamentals of electrochemical techniques for corrosion monitoring in a uniform manner
- To emphasize the importance of producing data and acquiring knowledge in a standardized way
- To develop a workforce that has a thorough and solid foundation in the fundamentals of corrosion monitoring

Electrochemical Techniques in Quality Assurance

QA is a proactive quality process or activity to ensure the quality of products produced or in how a process is carried out. The objective of QA is to prevent defects in the product produced or to prevent deviation in the production process. To establish QA, it is essential to implement a good quality management system and to periodically assess/monitor that management system. Corrosion during a process/manufacture/activity will result in deviations in the process and will affect the quality of the product produced. Therefore, corrosion monitoring is an essential fundamental step in the QA process. Corrosion monitoring in the field is performed for two reasons:

- To obtain information on current conditions
- To determine a maintenance and repair schedule

Reliable techniques are used for monitoring, inspection, and early detection of defect conditions [8 12]. NACE 3T 199 provides an overview of more than 40 techniques (including electrochemical techniques). To understand the field experience with these techniques, a 20 question survey was conducted. Detailed results of the survey are available elsewhere [13], but the salient features are presented here:

- Among the electrochemical techniques, LPR is a widely used monitoring technique in the oil and gas industry (**Fig. 4**).
- The 20 questions could be broadly classified into four categories: What do you use? What do you prefer to use? Which technique do you find most unreliable? What do you want the monitoring techniques to be? Most of the responders answered the first set of questions only. The responders either skipped the remaining questions or provided descriptive answers in the first question itself. Analysis of the survey indicated that the users of electrochemical techniques have no or little knowledge regarding the science of the

FIG. 4 Usage of electrochemical techniques in corrosion monitoring in the oil and gas industry [13].

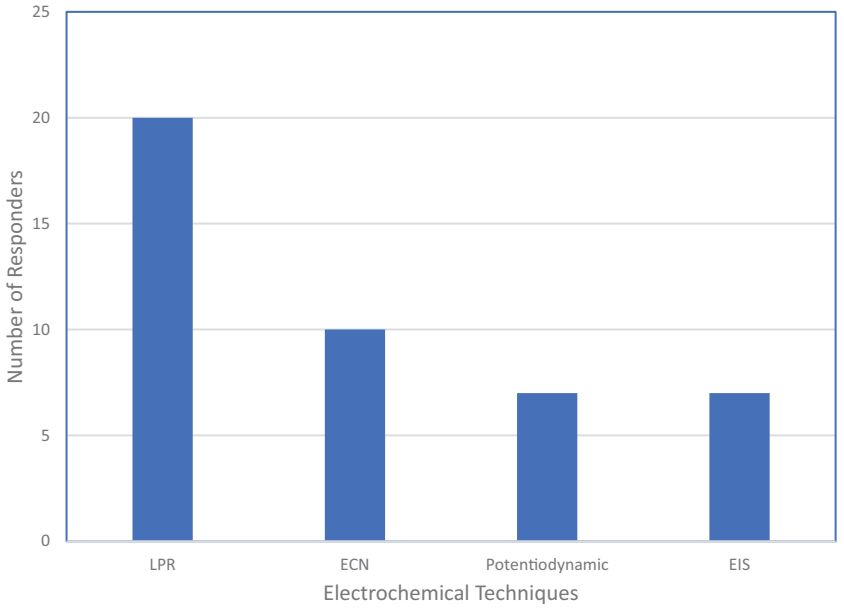

electrochemical techniques they use, and they heavily depend on the "technology provider (commercial vendors of the electrochemical technique)" to be knowledgeable about these techniques. The technology providers, on the other hand, have little or no knowledge of the process/environment to which the electrochemical probes are exposed. As a consequence, no correlation is established between electrochemical measurements and process deviation, if any.

- Data from these monitoring techniques are transmitted from the field to the decision makers in the office. Advancements in computer and information technologies have enabled transmission of the data that is rapid, reliable, and delivered in a user friendly fashion. However, users are unaware that most of the advancements have happened in transmitting the data to the user, after the probe/technique has collected the data, and that the process of the sensor/probe monitoring of corrosion essentially remains unchanged.

One of the main reasons for the problems in establishing a QA process using electrochemical techniques is a lack of fundamental electrochemical knowledge among the field operators. Training them using electrochemical techniques stand ards will overcome this problem and will help:

- To effectively use electrochemical corrosion rate monitoring in the QA process
- To avoid misuse of these techniques

Steps 6 and 7 (discussed earlier) provide essential elements of such training. Individual companies/industries may develop courses/procedures for establishing the QA process.

Electrochemical Techniques in Quality Control

QC is a set of activities to ensure the quality of a product or process [14]. The objective of the QC process is to identify and correct defects in a product or process. QC is a reactive process (i.e., it is carried out after a product is produced or a process is completed). It is the final step before a product or process is released to the end user.

It is essential that corrosion professionals and corrosion control products (i.e., instruments, equipment) are evaluated before they enter the workforce and the market. QC is critical to ensure that knowledgeable professionals and appropriate products enter the workforce and the market. Electrochemical standards may be conveniently and effectively used to establish QC relating to both professionals and products.

Professional associations such as ASTM International may develop certification programs to establish QC standards for the workforce and for corrosion control products.

Summary

- Most corrosion is electrochemical in nature. Therefore, corrosion professionals should have a fundamental and thorough knowledge of electrochemical principles and techniques. Such knowledge can only be obtained by using standards developed by various organizations.
- Standards are mutually agreed upon minimum values or conditions with which suppliers, users, producers, third party laboratories, academicians, and scientists are comfortable based on the current state of knowledge on a particular subject. International associations, including ASTM International, NACE International, and the ISO, develop standards regarding electrochemical techniques for corrosion control.
- Standards should be used for QE of corrosion professionals, for QA of corrosion control processes, and for QC of both corrosion professionals and corrosion control products.
- This paper presents a systematic approach toward establishing QE, QA, and QC using more than 25 international standards.

References

[1] National Research Council, *Assessment of Corrosion Education*, National Academies Press, Washington, DC, 2009, https://dx.doi.org/10.17226/12560

[2] Koch, G. H., Brongers, M. P. H., Thompson, N. G., Virmani, Y. P., and Payer, J. H., *Corrosion Costs and Preventive Strategies in the United States*, Publication # FHWA-RD-01-156, U.S. Department of Transportation, Federal Highway Administration, Washington, DC, 2003.

[3] Koch, G., Varney, J., Thompson, N., Moghissi, O., Gould, M., and Payer, J., *International Measures of Prevention, Application, and Economics of Corrosion Technologies* (*IMPACT*) *Study*, NACE International, Houston, TX, 2016.

[4] Schmitt, G., "Global Needs for Knowledge Dissemination, Research, and Development in Materials Deterioration and Corrosion Control," World Corrosion Organization, New York, 2009.

[5] Silverman, D. C., "A Perspective on Generating and Handling Corrosion Inhibitor Related Data," *Corrosion*, Vol. 60, No. 1, 2004, pp. 3–4.

[6] Dimond, J. R. and Ansuini, F. J., "Effect of Measurement and Instrumentation Errors on Potential Readings," Paper No. 1294, presented at *CORROSION 2001*, Houston, TX, March 11–16, 2001, NACE International, Houston, TX, 2001.

[7] Ansuini, F. J. and Dimond, J. R., "Factors Affecting the Accuracy of Reference Electrodes," *Mater. Performance*, Vol. 33, No. 11, 1994, pp. 14–17.

[8] Dean, S. W., Jr., "Electrochemical Corrosion Testing," *Laboratory Corrosion Testing*, Materials Technology Institute, St. Louis, MO, 2014, pp. 96–128.

[9] Hedges, B., Papavinasam, S., Sprague, K., and Knox, T., "Monitoring and Inspection Techniques for Corrosion in the Oil and Gas Production," Paper No. 5503, presented at *CORROSION 2015*, Dallas, TX, March 15–19, 2015, NACE International, Houston, TX, 2015.

[10] Papavinasam, S., Doiron, A., Attard, M., Demoz, A., and Rahimi, P., "Non-Intrusive Techniques to Monitor Internal Corrosion of Oil and Gas Pipelines," Paper No. 2012-1261, presented at *CORROSION 2012*, Salt Lake City, UT, March 11–15, 2012, NACE International, Houston, TX, 2012.

[11] Demoz, A., Papavinasam, S., Michaelian, K., and Revie, R.W., "Measurement of Corrosion Potentials of the Internal Surface of Operating High-Pressure Oil and Gas Pipelines," *J. ASTM Int.*, Vol. 5, No. 6, 2008, https://dx.doi.org/10.1520/JAI101244

[12] Papavinasam, S., Attard, M., Revie, R. W., Demoz, A., and Michaelian, K., "Comparison of Techniques for Monitoring Corrosion Inhibitors in Oil and Gas Pipelines," *Corrosion*, Vol. 59, No. 12, 2003, pp. 1096–1111.

[13] Papavinasam, S., Doiron, A., and Revie, R. W., "Industry Survey on Techniques to Monitor Internal Corrosion," *Mater. Performance*, Vol. 51, No. 2, 2012, pp. 2–6.

[14] Mitra, A., *Fundamentals of Quality Control and Improvement*, Wiley, Hoboken, NJ, 2008.

ASTM INTERNATIONAL
Helping our world work better

ISBN: 978-0-8031-7663-8
Stock #: STP1609

www.astm.org